INSIGHTS IN PLANT CELL BIOLOGY: 2021

EDITED BY: Simon Gilroy

PUBLISHED IN: Frontiers in Plant Science

frontiers Research Topics

ISSN 1664-8714
ISBN 978-2-83250-273-0
DOI 10.3389/978-2-83250-273-0

About Frontiers

Frontiers is more than just an open-access publisher of scholarly articles: it is a pioneering approach to the world of academia, radically improving the way scholarly research is managed. The grand vision of Frontiers is a world where all people have an equal opportunity to seek, share and generate knowledge. Frontiers provides immediate and permanent online open access to all its publications, but this alone is not enough to realize our grand goals.

Frontiers Journal Series

The Frontiers Journal Series is a multi-tier and interdisciplinary set of open-access, online journals, promising a paradigm shift from the current review, selection and dissemination processes in academic publishing. All Frontiers journals are driven by researchers for researchers; therefore, they constitute a service to the scholarly community. At the same time, the Frontiers Journal Series operates on a revolutionary invention, the tiered publishing system, initially addressing specific communities of scholars, and gradually climbing up to broader public understanding, thus serving the interests of the lay society, too.

Dedication to Quality

Each Frontiers article is a landmark of the highest quality, thanks to genuinely collaborative interactions between authors and review editors, who include some of the world's best academicians. Research must be certified by peers before entering a stream of knowledge that may eventually reach the public - and shape society; therefore, Frontiers only applies the most rigorous and unbiased reviews.
Frontiers revolutionizes research publishing by freely delivering the most outstanding research, evaluated with no bias from both the academic and social point of view. By applying the most advanced information technologies, Frontiers is catapulting scholarly publishing into a new generation.

What are Frontiers Research Topics?

Frontiers Research Topics are very popular trademarks of the Frontiers Journals Series: they are collections of at least ten articles, all centered on a particular subject. With their unique mix of varied contributions from Original Research to Review Articles, Frontiers Research Topics unify the most influential researchers, the latest key findings and historical advances in a hot research area! Find out more on how to host your own Frontiers Research Topic or contribute to one as an author by contacting the Frontiers Editorial Office: frontiersin.org/about/contact

INSIGHTS IN PLANT CELL BIOLOGY: 2021

Topic Editor:
Simon Gilroy, University of Wisconsin-Madison, United States

Citation: Gilroy, S., ed. (2022). Insights in Plant Cell Biology: 2021. Lausanne: Frontiers Media SA. doi: 10.3389/978-2-83250-273-0

Table of Contents

frontiers in Plant Science

ORIGINAL RESEARCH
published: 06 October 2021
doi: 10.3389/fpls.2021.737139

Cell Wall Composition and Structure Define the Developmental Fate of Embryogenic Microspores in *Brassica napus*

Carolina Camacho-Fernández[1†], Jose M. Seguí-Simarro[1], Ricardo Mir[1], Kim Boutilier[2] and Patricia Corral-Martínez[1,2†]*

[1] Cell Biology Group, COMAV Institute, Universitat Politècnica de València, Valencia, Spain, [2] Bioscience, Wageningen University and Research, Wageningen, Netherlands

OPEN ACCESS

Edited by:
Francisco Javier Medina, Margarita Salas Center for Biological Research, Spanish National Research Council, Spain

Reviewed by:
Alison M. R. Ferrie, National Research Council Canada (NRC-CNRC), Canada
John Laurie, Lethbridge Research Center, Agriculture and Agri-Food Canada, Canada

***Correspondence:**
Jose M. Seguí-Simarro
seguisim@btc.upv.es

†Present address:
Carolina Camacho-Fernández, HZPC Research B.V., Metslawier, Netherlands
Patricia Corral-Martínez, Nunhems Netherlands B.V., Nunhem, Netherlands

Specialty section:
This article was submitted to Plant Cell Biology, a section of the journal Frontiers in Plant Science

Received: 06 July 2021
Accepted: 17 September 2021
Published: 06 October 2021

Citation:
Camacho-Fernández C, Seguí-Simarro JM, Mir R, Boutilier K and Corral-Martínez P (2021) Cell Wall Composition and Structure Define the Developmental Fate of Embryogenic Microspores in Brassica napus. Front. Plant Sci. 12:737139. doi: 10.3389/fpls.2021.737139

Microspore cultures generate a heterogeneous population of embryogenic structures that can be grouped into highly embryogenic structures [exine-enclosed (EE) and loose bicellular structures (LBS)] and barely embryogenic structures [compact callus (CC) and loose callus (LC) structures]. Little is known about the factors behind these different responses. In this study we performed a comparative analysis of the composition and architecture of the cell walls of each structure by confocal and quantitative electron microscopy. Each structure presented specific cell wall characteristics that defined their developmental fate. EE and LBS structures, which are responsible for most of the viable embryos, showed a specific profile with thin walls rich in arabinogalactan proteins (AGPs), highly and low methyl-esterified pectin and callose, and a callose-rich subintinal layer not necessarily thick, but with a remarkably high callose concentration. The different profiles of EE and LBS walls support the development as suspensorless and suspensor-bearing embryos, respectively. Conversely, less viable embryogenic structures (LC) presented the thickest walls and the lowest values for almost all of the studied cell wall components. These cell wall properties would be the less favorable for cell proliferation and embryo progression. High levels of highly methyl-esterified pectin are necessary for wall flexibility and growth of highly embryogenic structures. AGPs seem to play a role in cell wall stiffness, possibly due to their putative role as calcium capacitors, explaining the positive relationship between embryogenic potential and calcium levels.

Keywords: androgenesis, arabinogalactan proteins, callose, cell wall, cellulose, microspore embryogenesis, subintinal layer, cell totipotency

INTRODUCTION

During the development of the male gametophyte (microsporogenesis and microgametogenesis), cells go through several stages before becoming mature, functional pollen grains. After meiosis, four young microspores are released from the tetrad. Microspores grow and mature and eventually divide asymmetrically to give rise to pollen grains, within which the male gametes will be produced. This natural pathway can be altered when microspores/pollen are cultured *in vitro*. Microspore

embryogenesis is an *in vitro* process whereby microspores are induced to become microspore-derived embryos. There are several ways to induce microspore embryogenesis, all of which rely on the application of a stress treatment (Seguí-Simarro et al., 2021). *Brassica napus* is considered a model species to study this process, since most of the knowledge gained in the last decades comes from the use of this species to investigate molecular, cellular, physiological, and developmental aspects of microspore embryogenesis (Jouannic et al., 2001; Corral-Martínez et al., 2013; Soriano et al., 2013; Rivas-Sendra et al., 2017, 2019; Corral-Martinez et al., 2020). In *B. napus* and many other species, microspore embryogenesis is triggered by the application of a heat stress treatment to isolated microspores. This treatment is associated with a series of cellular changes at different levels, involving the cytoskeleton, nucleus, cytoplasm, organelles, and cell wall (Simmonds and Keller, 1999; Seguí-Simarro and Nuez, 2008; Seguí-Simarro et al., 2011; Corral-Martínez et al., 2013; Parra-Vega et al., 2015a; Rivas-Sendra et al., 2019).

The cell wall is not only the protective layer of a plant cell, but also its connection with the environment and neighbor cells, as well as the mechanical force that compensates cell turgor and keeps cells firmly attached. Plant cell walls are formed from different polysaccharides, including pectin, hemicellulose, and cellulose. In different cell types, cell walls may have different proportions of these polysaccharides that define their cell properties and reflect their specific roles. Different polysaccharides can establish different physical and chemical interactions with each other, thereby conferring different properties to the wall. Thus, a combined analysis of the different cell wall components is needed to obtain a good overview of the types and functions of different cell walls.

Pectin is a polymer of galacturonic acid, represented by three major types: homogalacturonan (HG), and rhamnogalacturonan-I (RH-I) and -II (RH-II). They are synthesized in the Golgi system and then packed into vesicles and transported along the actin cytoskeleton to the cell wall, where they form the middle lamella separating adjacent cell walls. Pectin levels and modifications in the middle lamella are crucial for the regulation of cellular adhesion (Bou Daher and Braybrook, 2015). The stiffness of cell walls is also regulated by the pectin composition and level of esterification and by the presence of calcium and cell wall-remodeling enzymes like pectin methylesterases or polygalacturonases (Palin and Geitmann, 2012; Bou Daher and Braybrook, 2015). Cellulose is a linear polymer that is initially required for cell plate stabilization, and then for maintenance of cell wall shape and rigidity (Chen et al., 2018). Arabinogalactan proteins (AGPs) are a large family of heavily glycosylated hydroxyproline-rich cell surface proteins that are present in all higher plants and involved in many different aspects of plant growth and development, including differentiation, cell division, reproduction and, specifically during embryogenesis, cell survival, and embryo patterning (Cheung and Wu, 1999; Gaspar et al., 2001; Seifert and Roberts, 2007; Pereira et al., 2015). Several studies have revealed their involvement in plant reproduction, but their precise role is still unknown. In 2013, a new model about the role of periplasmic AGPs proposed them as calcium capacitors that control the release of calcium to the cytoplasm for cell signaling. Callose is a polymer that is involved in different plant processes, including sexual reproduction, where it is present at different stages. During microsporogenesis, callose is first present in the cell walls of the tetrad, young microspore, generative cell, beneath the intine at the aperture regions of mature pollen grains and at the pollen tube tip and plugs formed during pollen tube growth (Gorska-Brylass, 1967; Dong et al., 2005; Chebli et al., 2012). However, the most general role of callose relates to cell wall formation, where it is essential for cell plate establishment (Seguí-Simarro et al., 2008). All these cell wall components are sequentially added during cell wall biogenesis. The first component transported to the nascent cell plate is HG-pectin. Next, callose is locally synthesized for cell plate expansion. Then, callose is removed in parallel with the onset of cellulose biosynthesis and transport of hemicellulose. Cellulose combines with hemicellulose to create a cellulose–hemicellulose network, while pectin reorganizes into the middle lamella (Albersheim et al., 2011).

During microspore embryogenesis, the cell wall must adapt from covering a single cell, the microspore, to cover a larger, multicellular structure. It seems reasonable to predict that such adaptation requires profound changes in cell wall structure and composition. During the earliest stages of microspore embryogenesis, the sequence of steps described above and the mechanisms of synthesis and/or deposition of cell wall components are altered, resulting in the transient formation of abnormal, irregular, and fragmented cell walls separating the first divided cells, which has profound consequences in further embryo development (Parra-Vega et al., 2015b). These changes are paralleled by altered levels of xyloglucans, pectin, and AGPs (Corral-Martínez et al., 2019), and by the formation of a unique, callose-rich cell wall beneath the intine of the microspore, the subintinal layer (Parra-Vega et al., 2015b). The subintinal layer was proposed to act as a transient physical barrier that protects embryogenic microspores from osmotic changes in the surrounding *in vitro* environment (Rivas-Sendra et al., 2019). Although the specific role of AGPs in microspore embryogenesis is not known, they differentially accumulate in the newly formed cell walls (inner walls and subintinal layer) of induced microspores (Corral-Martínez et al., 2019) and are important for embryo viability and development (Borderies et al., 2004; Corral-Martínez and Seguí-Simarro, 2014).

It is widely accepted that microspore cultures are heterogeneous systems where different cell populations coexist (Seguí-Simarro and Nuez, 2008). Some microspores are not induced and become developmentally arrested or die. Others follow a gametophytic-like development, becoming pollen-like structures that express many of the features of mature pollen grains (Satpute et al., 2005) that develop *in planta*. A third group of microspores develop as embryos. However, not all these embryogenic structures are similar. During zygotic embryogenesis, embryos comprise an embryo proper and a transient basal structure called the suspensor (Dresselhaus and Jürgens, 2021). Previous studies in *B. napus* showed the presence of exine-enclosed (EE), suspensorless structures, and suspensor-bearing structures, both described as embryogenic based on the expression of embryo-reporter genes (Soriano et al., 2013, 2014),

and two types of embryogenic callus-like structures, loose and compact (Telmer et al., 1995; Li et al., 2014; Soriano et al., 2014). Recently, a time-lapse imaging study defined the developmental fate of these structures (Corral-Martinez et al., 2020) and distinguished two main groups of microspore-derived structures according to their ability to form differentiated embryos. EE structures and suspensor-bearing embryos (SUS) are considered highly embryogenic because a high proportion of them develop into differentiated embryos, while only a low percentage become callus-like structures or die. Compact callus (CC) and loose callus (LC) structures are considered barely embryogenic because they have a very low viability and ability to form differentiated embryos.

Due to this remarkable heterogeneity and the well-known role of cell wall in shaping *in vitro* morphogenesis, a new approach for understanding cell wall dynamics in each type of microspore-derived structure is required to determine the relationship between their cell wall characteristics and their competence for the successful completion of embryo development. In this work, we performed a detailed study of the cell wall structure and composition in the different structures found in *B. napus* microspore cultures, focusing on pectin (both highly and low methyl-esterified), callose, and AGPs, using confocal and transmission electron microscopy (TEM) and immunogold labeling. Our results uncover a relationship between cell wall composition and structure and the developmental fate of each type of microspore-derived structure, providing new insights on the role of these cell wall components during microspore embryogenesis. This study also provides a broader framework for understanding cell fate and morphogenic processes during *in vitro* embryogenesis.

MATERIALS AND METHODS

Plant Material

DH4079 plants were used as donor plants for microspore culture. DH4079 is a doubled haploid line derived from *B. napus* L. cv. Topas, and highly responsive to induction of microspore embryogenesis. Plants were grown continuously at 18°C in growth chambers in 20 cm pots at 60% relative humidity under a 16/8 h photoperiod until just before flowering, and then transferred to 10°C/5°C (day/night) with the same photoperiod.

Microspore Culture

Flower buds containing a majority of late, vacuolated microspores and early bicellular pollen grains were collected from donor plants. The isolation, induction, and culture was performed according to Corral-Martínez et al. (2021). Flower buds were surface sterilized with 4 g/L sodium hypochlorite and then washed three times with sterile water. Microspores were isolated from anthers by crushing buds with a sterile syringe piston in isolation medium (13% w/v sucrose in dH_2O, pH 5.8) and filtering the suspension through a 30 μm nylon mesh (Millipore). This was followed by three rounds of centrifugation (100 × *g*, 4 min each) and resuspension of the microspores in isolation medium. After the last centrifugation, microspores were resuspended in culture medium (NLN-13 medium), made with NLN basal medium (Duchefa, Netherlands), 13% (w/v) sucrose, and 0.5 g/L $Ca(NO_3)_2{\cdot}4H_2O$, pH 5.8. Microspore density was adjusted with a hemocytometer (Camacho-Fernández et al., 2018) to 40,000 microspores/ml with culture medium. Microspores were plated in 6 cm tissue culture dishes (3 ml suspension per plate) and incubated in darkness for 1 day at 32°C. Afterward, plates were kept at 25°C in darkness for progression of embryogenesis.

Staining and Observation by Confocal Laser Scanning Microscopy

Brassica napus microspore cultures were collected at days 0, 2, 5, and 8 after culture initiation and fixed overnight at 4°C with 4% paraformaldehyde in PBS (pH 7.4). Afterward, samples were washed three times with PBS and then stored at 4°C in 0.1% paraformaldehyde in PBS until use. Staining of callose and cellulose in microspores was performed according to Parra-Vega et al. (2015b) and Rivas-Sendra et al. (2019). For callose detection, samples were incubated first with 10 μg/ml propidium iodide (PI; Fluka) for 10 min, and then with 0.1% aniline blue (AB; Fluka) for 20 min. PBS was used for preparation of all staining solutions and for the three washes after each staining. Samples were mounted in 17% Mowiol 4-88 (Sigma-Aldrich) and 33% glycerol (v/v) in PBS. For cellulose detection, samples were stained with 0.01% Direct Red (Sigma) in 0.1 M PBS for 30 min, washed three times with PBS, mounted in a 1:1 mix of Mowiol and 2.5 μg/ml 4′,6-diamidine-2′-phenylindole dihydrochloride (DAPI; Sigma-Aldrich) prepared as described in Custers (2003), and then incubated for at least 15 min. Fluorochromes were excited with 405 nm (for DAPI and aniline blue) and 561 nm (for PI and Direct Red) laser lines, and emission was recorded between 450–490 and 580–650 nm, respectively. All the samples were incubated in darkness and observed with a ZEISS 780 Axio Observer confocal laser scanning microscope. Images were processed with Zeiss Efficient Navigation (ZEN) and FIJI software (Schindelin et al., 2012).

To observe cell wall thickness, the fixed samples were stained with Direct Red as described above and with SCRI Renaissance Cell 2200 (SR2200). Staining of SCRI Renaissance 2200 was performed according to Musielak et al. (2015), incubating samples 30 min before observation. SR2200 was excited with a 405 nm laser line and emission was recorded between 415 and 476 nm. At least 100 embryogenic structures were examined with a Leica SP5 confocal laser scanning microscope. Images were processed with Leica Application Suite Advanced Fluorescence (LAS AF) and FIJI software (Schindelin et al., 2012).

Processing of Samples for Transmission Electron Microscopy

Five-day-old cultured microspores were collected for TEM. Processing was performed as described in Seguí-Simarro and Nuez (2007) with some modifications. Samples were fixed in Karnovsky fixative (Karnovsky, 1965), post-fixed with 2% OsO_4 in 0.05 M cacodylate buffer and washed three times with 0.025 M cacodylate. Microspores were immobilized and concentrated as

follows: cacodylate buffer was removed and 1–2 drops of warm (liquid) 15% gelatin in cacodylate buffer were added. Microspores were then resuspended in the liquid gelatin, centrifuged (1 min at 125 × *g*) and allowed to cool on ice for gelatin solidification. Once solid, 20 μl of 1% paraformaldehyde in cacodylate buffer was added, and the samples stored overnight at 4°C. Finally, gelatin-embedded samples were cut in small pieces and kept in cacodylate buffer until use. Samples were dehydrated in a progressive methanol series and embedded and polymerized in Embed 812 resin (Electron Microscopy Sciences). Ultrathin (80 nm) sections were obtained from at least three different blocks of each sample with a Leica UC6 ultramicrotome for TEM observation. Sections were mounted on carbon and formvar-coated, 200-mesh nickel grids (Electron Microscopy Sciences), stained with uranyl acetate in 70% methanol (6 min) and lead citrate (30 s). Images were taken with a Jeol JEM 1010 TEM. For morphometric studies of the cell wall, the minimum number of images required was determined using the progressive mean test (Williams, 1977) according to Corral-Martínez et al. (2019). For each type of structure, the width of the intine and subintinal layer of the cell walls was measured using FIJI software (Schindelin et al., 2012). Statistically significant differences in cell wall and subintinal layer width were determined using a least significant difference (LSD) test with $p \leq 0.05$.

Immunogold Labeling

For callose detection, an anti-callose monoclonal antibody (mAb) from Biosupplies (Australia) was used that specifically recognizes linear (1→3)-β-oligosaccharide segments in (1→3)-β-glucan. For AGP detection, a JIM13 rat IgM mAb (PlantProbes, United Kingdom) was used that recognizes the AGP2 epitope present in different plant exudates like gum arabic and gum ghatti (Knox et al., 1991). For pectin detection, the following antibodies (PlantProbes) were used: JIM7, a rat IgA mAb that cross-reacts with highly methyl-esterified epitopes of the homogalacturonan domain of pectic polysaccharides (Knox et al., 1990; Willats et al., 2000) and JIM5, a rat IgG mAb that cross-reacts with low methyl-esterified epitopes of homogalacturonan (Knox et al., 1990; Willats et al., 2000). For immunolocalization of cell wall components, sections were hydrated with PBS for 1 min. Non-specific binding was prevented by incubation with 0.2% BSA and 3% skimmed milk in PBS for 30 min. For the anti-callose antibody, sections were incubated with the primary antibody diluted 1:5000 in 1% BSA in PBS for 1 h. For the remaining antibodies, sections were incubated with the primary antibody diluted 1:5 (JIM13) or 1:2 (JIM7 and JIM5) in 0.2% BSA in PBS for 1 h. For all antibodies, sections were then washed six times during 5 min with 0.2% BSA in PBS. Secondary antibodies (goat anti-mouse for anti-callose antibody and goat anti-rat for the rest) conjugated with 10 nm gold particles (BBI solutions, United Kingdom) were diluted 1:25 with 0.2% BSA in PBS (1% BSA for the anti-callose antibody) and incubated with the sections for 45 min. Finally, sections were washed five times with PBS, 5 min each, post-fixed with 2% glutaraldehyde in PBS for 10 min and washed again with PBS and distilled water as the last step. Samples were then counterstained with uranyl acetate in 70% methanol (6 min) and lead citrate (30 s). Controls excluding primary antibodies were performed to check for non-specific binding of the secondary antibody. All steps were performed at 25°C.

Quantification of Immunogold Labeling

Three different blocks were randomly selected and micrographs were taken systematically at the same magnification. Several micrographs were taken randomly from all the structures of interest on each grid. The minimum number of micrographs was determined using the progressive mean test (Williams, 1977), with a minimum confidence limit of $\alpha = 0.05$. In general, around 15–20 micrographs per antibody and type of structure were studied. The labeling density of each compartment under study was manually calculated by counting the number of particles and dividing this by the area where they were counted, being expressed as particles/μm^2. For all the structures studied in this work, the analyzed compartments were (1) Golgi stacks and cytoplasmic vesicles, (2) inner cell walls, and (3) outer cell walls (the intine and the subintinal layer formed in microspore-derived structures) but excluding the outermost exine layer. Particles over regions where the presence of the studied epitopes is not expected (the cytoplasm excluding Golgi stacks and vesicles, cytoplasmic organelles, nuclei, and the embedding resin outside cells), were considered as background noise, which was estimated as the particle density of these regions. The area in μm^2 was measured using a square lattice composed of 11 × 16 squares of 15 × 15 mm each. Labeling density was expressed as the average labeling density of all micrographs ± SD. Comparisons of mean labeling densities were performed by one-way ANOVA tests using StatGraphics software. In cases where data were not homoscedastic, Mood's median test was used. Means were separated using a LSD test with $p \leq 0.05$. Histograms of the same antibody in different subcellular compartments were built using the same *Y*-axis scale to facilitate comparisons.

RESULTS

DH4079 Microspore Cultures Comprise a Heterogeneous Population of Structures That Respond Differently to Embryogenesis Induction

During *B. napus* microspore culture, not all microspores are equally sensitive to heat stress and therefore follow different pathways. The majority of microspores either followed a gametophytic-like pathway and became pollen-like structures or arrested in development and eventually died. Depending on the genotype and culture conditions, microspore embryogenesis may occur in a variable percentage of microspores. Our study focused on the highly responsive DH4079 line, where the only embryogenic structures previously described were EE and suspensor-bearing (SUS) embryos (Telmer et al., 1995; Supena et al., 2008). These cell types together with CC and LC structures were described in the low responsive DH12075 genotype. As it was not clear whether the presence of CC and LC in microspore cultures is specifically associated with

the recalcitrance of this genotype, we reexamined the types of structures found in DH4079 cultures in quantitative (**Figure 1A**) and qualitative detail (**Figures 1B–E**). The starting point of this analysis, before embryo induction, was a population comprising mostly vacuolated microspores (**Figure 1B**) and some young pollen grains. After the heat stress treatment, 75% of the initial microspores/pollen died or arrested and 13% followed a pollen-like development. A third subset (12%) comprised four types of multicellular, proliferating and potentially embryogenic structures with different sizes, levels of cellular organization and adhesion, and degrees of exine coverage. EE structures (**Figure 1C** left; 3.85%) were highly compact and organized (defined as having straight cell walls and regular division patterns), fully covered by exine, with thin inner cell walls and closely adhered cells. CC structures (**Figure 1D**; 4.9%) were similar to EE but more disorganized, less compact, with thicker inner cell walls, less cellular adhesion and more extensive exine breakage. LC (**Figure 1E**; 2.97%) were very disorganized structures with weak cellular adhesion where the exine was either completely ruptured or absent. Finally, loose bicellular structures (LBS) (**Figure 1C** right; 0.16%) comprised 2–3 loosely connected cells surrounded by partially ruptured exine, but with a level of cell organization higher than LC and similar to EE. These structures strongly resembled the few-celled suspensors observed in DH4079 under milder heat stress treatment (Supena et al., 2008) or in DH12075 (Corral-Martinez et al., 2020). However, in the absence of cell fate tracking data, we refer to these as LBS.

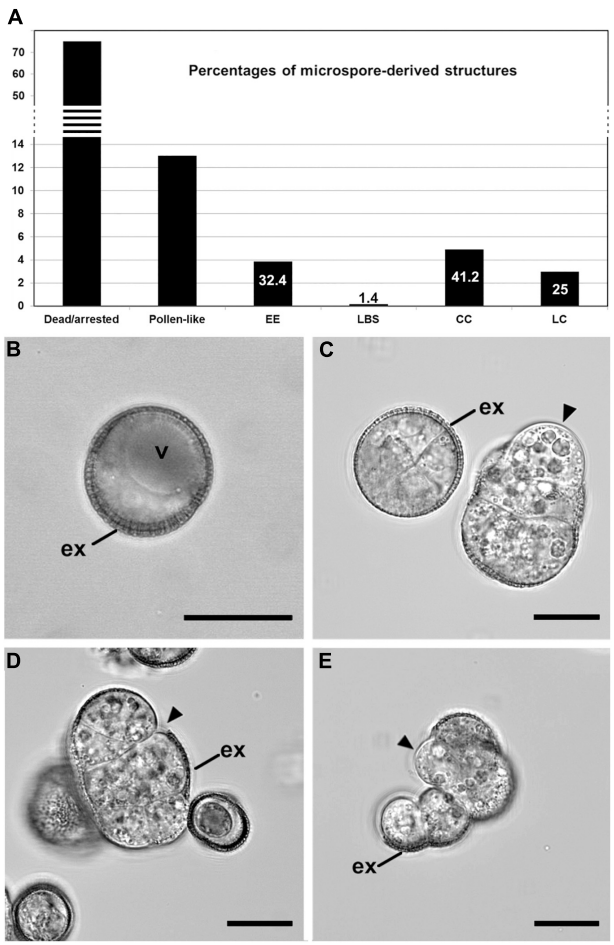

FIGURE 1 | Development of isolated microspore cultures. **(A)** Percentages of the different structures derived from *in vitro* cultured microspores, including dead or arrested microspores, pollen-like structures, exine-enclosed (EE) structures, loose bicellular structures (LBS), compact calli (CC), and loose calli (LC). Percentages were calculated from a total of 1245 randomly selected structures. The numbers in EE, LBS, CC, and LC represent the relative percentages of each type of potentially embryogenic structure, excluding non-embryogenic forms (dead/arrested and pollen-like). **(B–E)** Confocal microscopy images of a vacuolated microspore at the start of culture (day 0; **B**), an EE structure (**C** left), a LBS (**C** right), a CC **(D)**, and a LC **(E)**. Arrowheads point to areas devoid of exine (ex). Bars: 20 μm.

Our observations indicate that the same embryogenic cell types found in the low embryogenic DH12075 line are also found in the highly response DH4079 line and therefore, that the heterogeneity of embryogenic cell types in DH4079 has been previously underestimated. Given the extensive cell wall remodeling that takes place as microspores and pollen transition to embryos, we examined whether these four types of embryogenic structures also showed differences in their cell wall architectures.

External Cell Walls Have a Different Width in Different Types of Proliferating Structures

In DH12075, it was previously shown that callus-like structures (LC and CC) have thicker cell walls than EE (Corral-Martinez et al., 2020). We therefore used SCRI Renaissance Cell 2200 staining to examine cell wall thickness in the DH4079 proliferating structures, paying special attention to the two cell wall layers observed previously in embryogenic microspores, the subintinal layer and the intine (**Figure 2A**). Highly embryogenic EE structures (**Figure 2A**) and the young globular embryos derived from them (**Figure 2B**) had cell walls that were thinner than those of barely embryogenic structures (CC and LC, **Figures 2C,D**, respectively). To quantify cell wall thickness, we measured both the subintinal layer and the total cell wall width in TEM images. We observed that the cell wall of callus-like structures (CC and LC) was wider than that of highly embryogenic structures (EE and LBS; **Figure 2E**). Consistent with this, the width of the subintinal layer was also higher in barely embryogenic structures (**Figure 2F**), and proportional to the total cell wall width, which was always around 70–80%, with no significant differences among structures. In summary, there were significant differences between the cell wall widths of the different DH4079 microspore-derived structures, with barely embryogenic structures having thicker walls than highly embryogenic structures. By contrast, the percentage of subintinal layer relative to the entire cell wall was similar for the different structures, which suggested that the differences in cell wall dynamics between structures are not related to differences in the relative thickness of the subintinal layer.

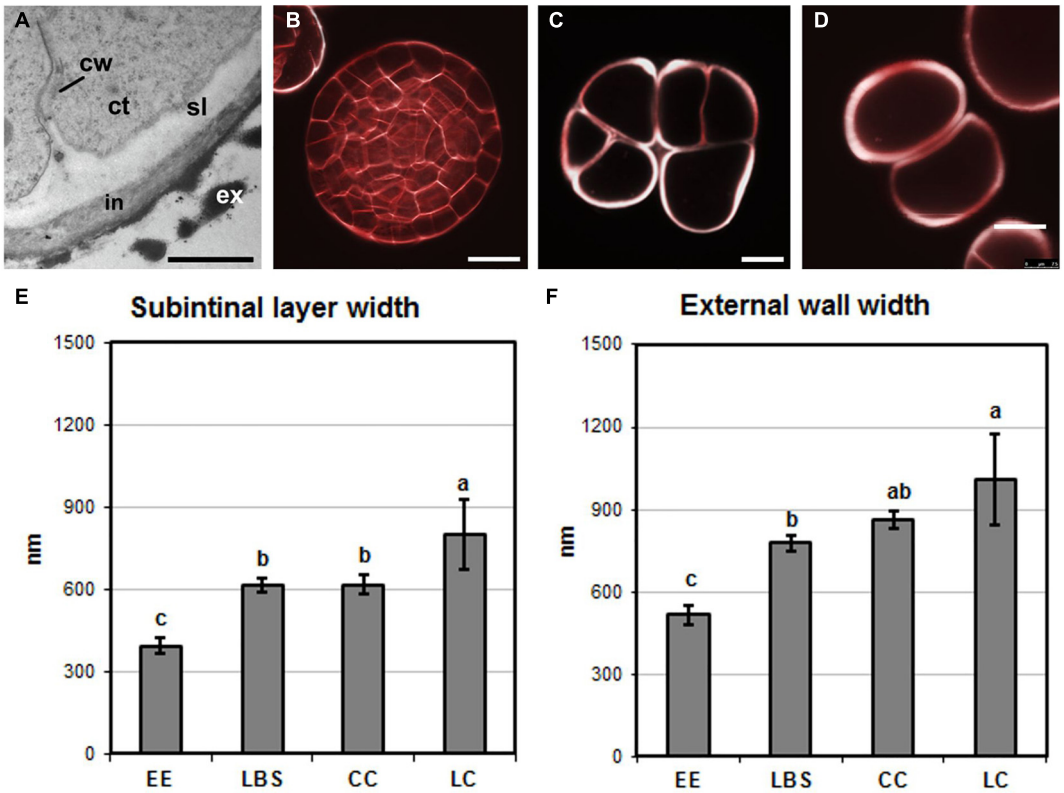

FIGURE 2 | Cell wall width. **(A)** Electron microscopy image of an exine-enclosed (EE) structure, showing the inner cell wall (cw), subintinal layer (sl), intine (in), and exine (ex). ct, cytoplasm. **(B–D)** Images of structures stained with SCRI Renaissance Cell 2200 observed by confocal microscopy. **(B)** Young, EE-derived embryo, **(C)** compact callus (CC), and **(D)** loose callus (LC). **(E)** Subintinal layer width (in nm) in each type of structure. **(F)** Width (in nm) of the intine + subintinal layer in each type of structure. Different letters represent significant differences according to the LSD test. Bars: **(A)**, 500 nm; **(B–D)**, 10 μm.

Exine-Enclosed and Loose Bicellular Structures Accumulate More Callose in Internal and External Cell Walls

Next, we examined the composition of the cell wall in the four different types of structures. In general, callose staining was present in large amounts in the walls of all structures during the first stages of embryogenesis, but was reduced upon culture progression (**Figures 3A–C**). Cellulose staining showed the opposite pattern, with faint wall staining during the first embryogenic stages, followed by increased staining at later stages, in parallel with a reduction in callose staining (**Figures 3A′–C′**). In the anti-callose immunogold labeling experiments, the unspecific labeling density observed in the cytoplasm and organelles (background noise) was consistently low compared with that of cell walls, as expected. No significant differences among structures were observed in cell walls between adjacent cells of the same structure. However, different structure types showed different levels of callose in their cell walls. In highly embryogenic structures (EE and LBS), anti-callose labeling was present in higher amounts than in barely embryogenic structures (LC and CC), in both internal (**Figures 4A–C**) and external walls (**Figures 4D–F**), although at different levels. In general, inner cell walls showed more anti-callose labeling than external walls in all types of structures (**Figures 4G,H**). Statistically significant differences among structure types were found in internal (**Figure 4G**) and external cell walls (**Figure 4H**). EE showed a significantly higher callose content in inner cell walls than the

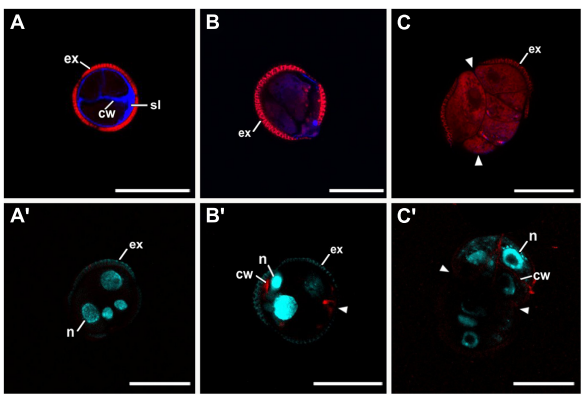

FIGURE 3 | Confocal microscopy images of EE structures at 2 **(A,A′)**, 5 **(B,B′)**, and 8 days of culture **(C,C′)**, stained with aniline blue for callose (blue in **A–C**) together with propidium iodide (red), and with Direct Red for cellulose (red in **A′–C′**) together with DAPI (blue). Arrowheads indicate regions of exine (ex) rupture or absence. cw, cell wall; n, nucleus; sl, subintinal layer. Bars: 20 μm.

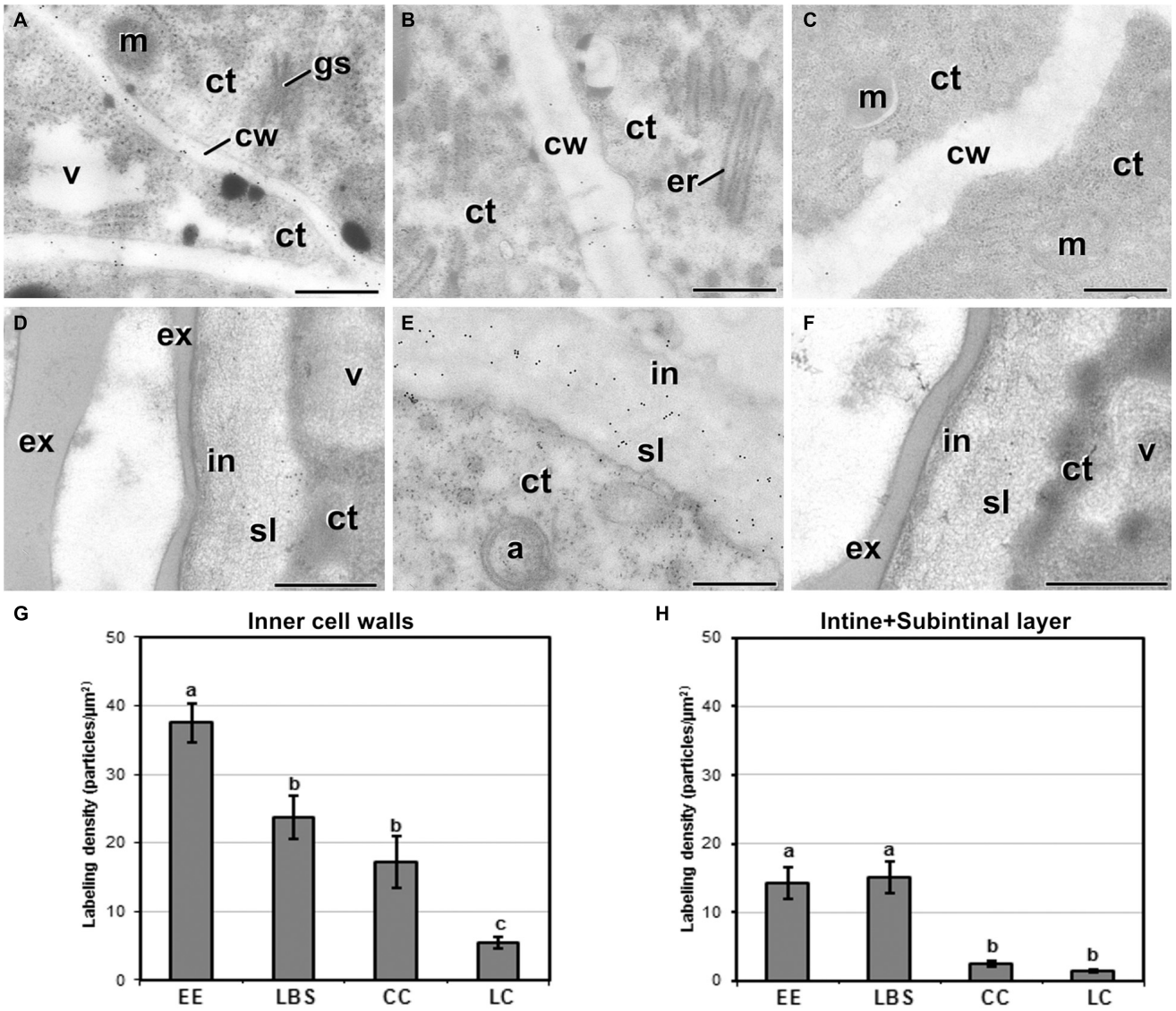

FIGURE 4 | Callose detection by immunogold labeling and quantification in TEM images of 5-day-old microspore cultures. Inner cell wall images from EE **(A)**, LBS **(B)**, and LC **(C)** structures. Outer cell wall images from EE **(D)**, LBS **(E)**, and CC **(F)** structures. **(G)** Callose labeling density in inner cell walls. **(H)** Callose labeling density in external cell walls. Different letters represent significant differences according to the LSD test. Labeling density is expressed in number of particles per μm^2. a, autophagosome; ct, cytoplasm; cw, cell wall; er, endoplasmic reticulum; ex, exine; gs, Golgi stack; in, intine; m, mitochondrion; v, vacuole. Bars: 500 nm.

rest of the structures, while in LC it was significantly lower than the rest. In external walls (intine + subintinal layer), two groups were observed according to callose labeling density: highly embryogenic structures (EE and LBS) presented higher labeling than barely embryogenic structures (CC and LC), where labeling density was close to zero. Upon embryogenesis induction, callose is known to accumulate only in the subintinal layer (Parra-Vega et al., 2015b), implying that the labeling we observed in outer cell walls can only be attributed to the subintinal layer. Together, our results showed remarkable differences in callose accumulation between the different embryogenic structures: abundant in highly embryogenic structures (EE and LBS) and very limited in barely embryogenic structures (CC and LC). This suggests that differences in callose accumulation in the subintinal layer are related to the level of cellular organization and embryogenic competence of the different structures.

The Cell Walls of Exine-Enclosed and Loose Bicellular Structures Accumulate More JIM13-Cross-Reacting Arabinogalactan Proteins Than Those of Compact Callus and Loose Callus Structures

We studied the differences in abundance and distribution of JIM13-cross-reacting AGPs in the different structures (**Figure 5**).

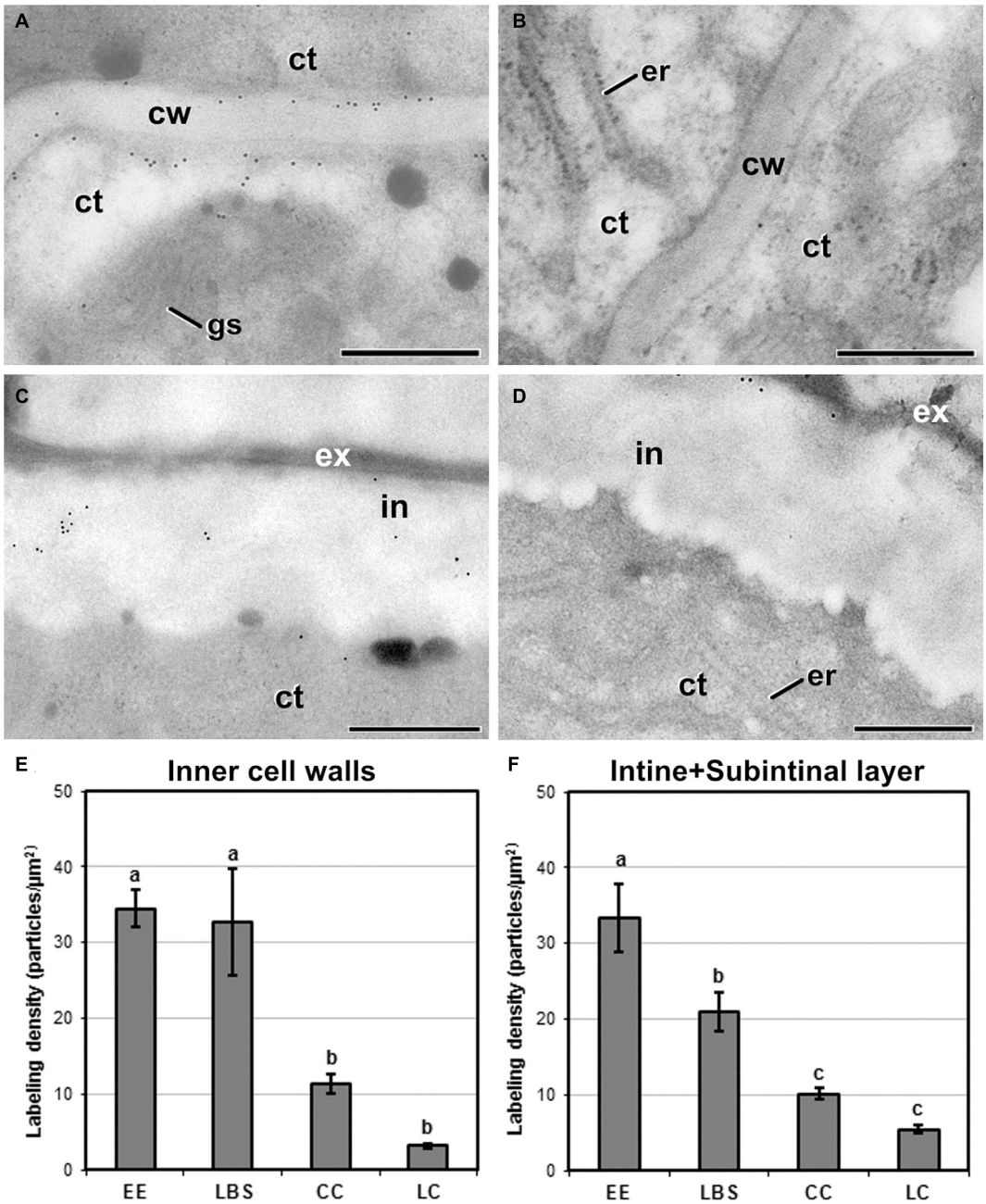

FIGURE 5 | Detection of JIM13 cross-reacting AGPs by immunogold labeling and quantification in TEM images of 5-day-old microspore cultures. Inner cell wall images of EE **(A)** and LC structures **(B)**. Outer cell wall (intine + subintinal layer) images of EE **(C)** and CC structures **(D)**. **(E)** Quantification of JIM13-cross-reacting AGPs in inner cell walls. **(F)** Quantification of JIM13-cross-reacting AGPs in outer cell walls (intine + subintinal layer). Labeling density is expressed as number of particles/μm^2. Different letters represent significant differences according to the LSD test. ct, cytoplasm; cw, cell wall; er, endoplasmic reticulum; ex, exine; gs, Golgi stack; in, intine; m, mitochondria; v, vacuole. Bars: 500 nm.

JIM13 epitopes were detected in Golgi stacks and cytoplasmic vesicles, although at much lower densities than in cell walls, and with no differences between structures (data not shown). Background noise was always negligible. In inner walls, EE (**Figure 5A**) and LBS showed higher JIM13 labeling density than CC and LC (**Figure 5B**). In outer walls, EE (**Figure 5C**) exhibited a significantly higher JIM13 labeling density than LBS, LC, and CC structures (**Figure 5D**). The distribution of JIM13 labeling in cell walls was similar to that of callose but, opposite to callose, the JIM13 levels in inner and outer walls of a given structure were similar (**Figures 5E,F**). Statistically significant differences among structures were found in inner (**Figure 5E**)

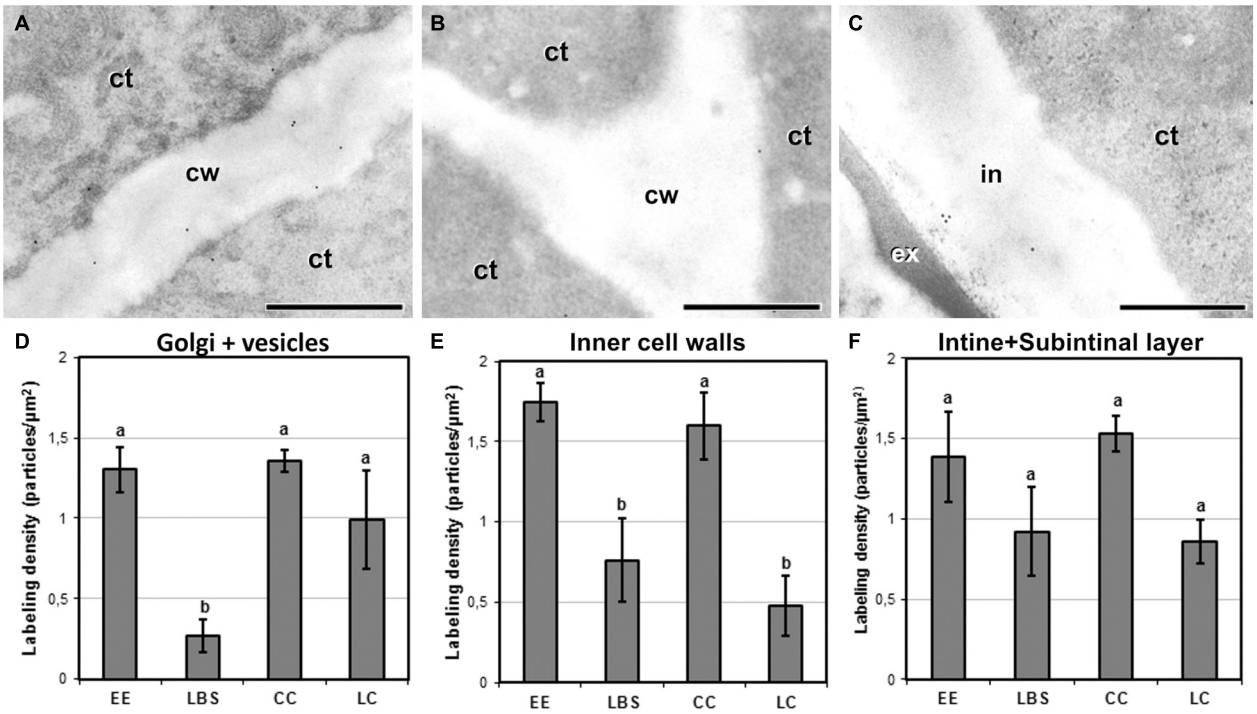

FIGURE 6 | Detection of JIM5 cross-reacting low methyl-esterified pectin by immunogold labeling and quantification in TEM images of 5-day-old microspore cultures. Inner cell wall images of EE **(A)** and LC **(B)**. **(C)** Outer cell wall image of EE. **(D)** Quantification of JIM5 cross-reacting low methyl-esterified pectin in cytoplasmic Golgi stacks and vesicles. **(E)** Quantification of JIM5 cross-reacting low methyl-esterified pectin in inner cell walls. **(F)** Quantification of JIM5 cross-reacting low methyl-esterified pectin in outer cell walls (intine + subintinal layer). Labeling density is expressed in number of particles per μm^2. Different letters represent statistically significant differences according to the LSD test. ct, cytoplasm; cw, cell wall; ex, exine; in, intine; m, mitochondrion. Bars: 500 nm.

and outer walls (**Figure 5F**), with barely embryogenic structures (LC and CC) having a significantly lower labeling density than highly embryogenic structures (EE and LBS). In summary, AGPs carrying the JIM13 epitope accumulated in a different manner in the cell walls of the different embryogenic structures, being more abundant in highly embryogenic and hardly detectable in barely embryogenic structures.

Structures With Less Intercellular Adhesion Have Reduced Levels of Low Methyl-Esterified Pectin

We performed immunogold labeling with JIM5 antibody to determine whether the four different embryogenic structures show differences among structures in the levels of low methyl-esterified pectin (**Figure 6**). For all the structures, JIM5 signal was present in inner walls and in both the intine and subintinal layer of outer walls, as well as in cytoplasmic Golgi stacks and transport vesicles. Background labeling density was always negligible, irrespective of the sample studied. In general, compact structures such as EE (**Figure 6A**) and CC presented more JIM5 labeling in inner cell walls than the loose LBS and LC (**Figure 6B**). This trend was also observed in outer walls (**Figure 6C**). Quantification of immunogold labeling confirmed these observations. Significant and structure-specific differences in labeling density were observed in the Golgi stacks and cytoplasmic vesicles (**Figure 6D**), and in the inner walls (**Figure 6E**). In outer walls (**Figure 6F**), the pattern observed was remarkably similar to that of inner walls, although the differences observed were not statistically significant. Considering all these results together, LBS showed the lowest density of low methyl-esterified pectin of all types of structures, followed by LC. These results pointed to a relationship between the level of low methyl-esterified pectin and the degree of adhesion between cells of the same structure. In particular, compact structures with higher cell adhesion (EE and CC) showed higher levels of low methyl-esterified pectin than loosely connected structures (LBS and LC).

Exine-Enclosed and Loose Bicellular Structures Accumulate More Highly Methyl-Esterified Pectin in Their Internal and External Cell Walls

JIM7 immunogold labeling revealed that highly methyl-esterified pectin was present in cytoplasmic Golgi stacks and transport vesicles, inner walls and the intine and subintinal layers. Background noise was negligible. Quantitatively, average labeling density in outer and inner walls was similar for each type of structure. Cell walls showed a pattern of JIM7 immunolocalization similar to that of JIM13 and anti-callose: highly embryogenic EE (**Figures 7A,C**) and LBS structures

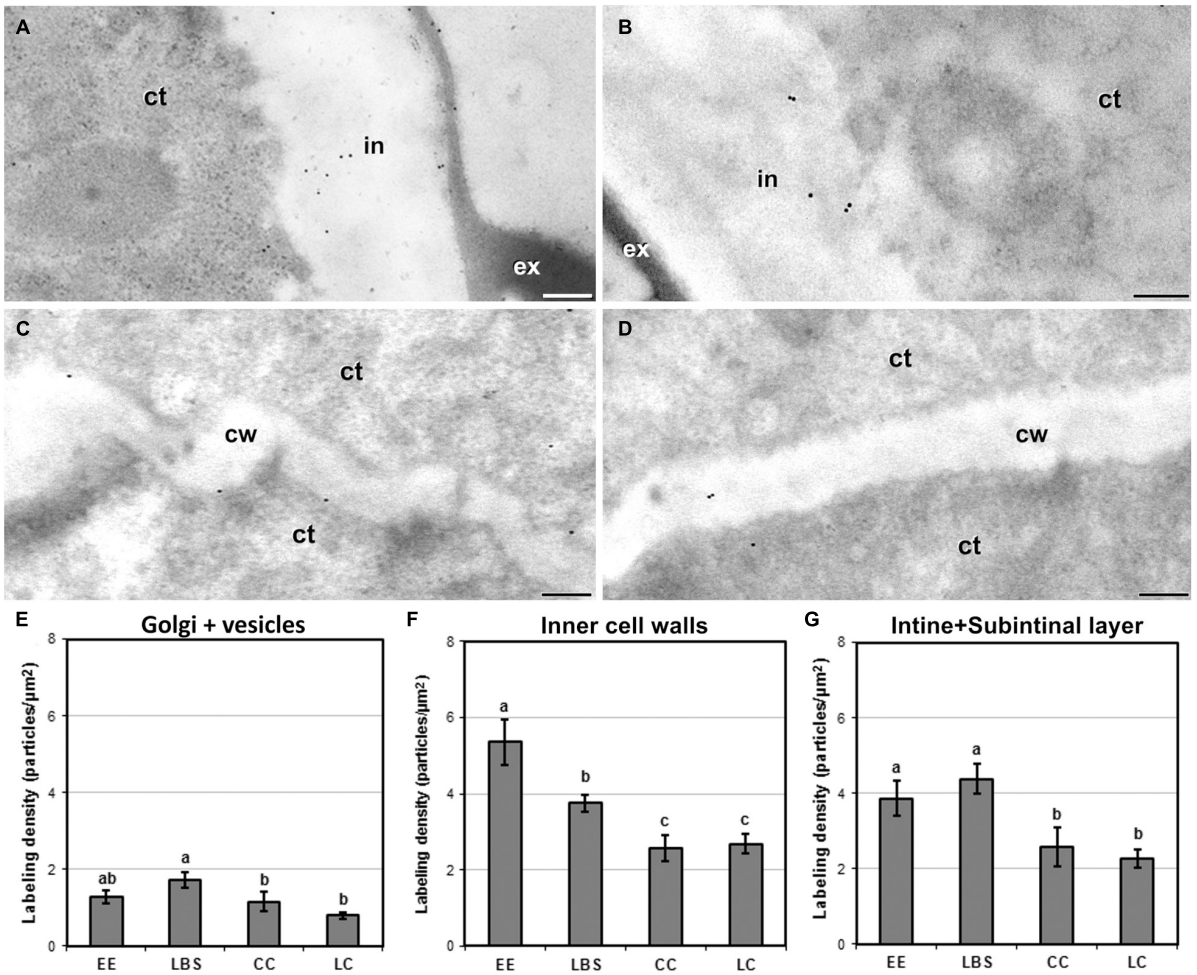

FIGURE 7 | Detection of JIM7-cross-reacting highly methyl-esterified pectin by immunogold labeling and quantification in TEM images of 5-day-old microspore cultures. External cell wall images of EE **(A)** and CC **(B)**. Inner cell wall images of EE **(C)** and CC **(D)**. **(E)** Quantification of JIM7-cross-reacting highly methyl-esterified pectin in cytoplasmic Golgi stacks and vesicles. **(F)** Quantification of JIM7-cross-reacting highly methyl-esterified pectin in inner cell walls. **(G)** Quantification of JIM7-cross-reacting highly methyl-esterified pectin in outer cell walls (intine + subintinal layer). Labeling density is expressed in number of particles per μm^2. Different letters represent statistically significant differences according to LSD test. ct, cytoplasm; cw, cell wall; ex, exine; in, intine; m, mitochondria. Bars: 200 nm.

showed higher labeling densities than barely embryogenic CC (**Figures 7B,D**) and LC structures. Differences were found between the four structures for both inner and outer walls, as well as for Golgi stacks and vesicles (**Figure 7E**), where labeling density was lower than in cell walls, showing a pattern similar to outer walls. In inner walls (**Figure 7F**), JIM7 epitopes were significantly more abundant in highly embryogenic (EE and LBS) structures than in barely embryogenic structures (CC and LC). No differences in JIM7 labeling density were found in outer walls between EE and LBS (**Figure 7G**), but labeling density in these structures was higher than in LC and CC.

In addition to the general patterns observed in the quantitative analysis and to the differences observed among different wall and layer types, we detected remarkable differences among structures in the cell walls separating adjacent cells, and in particular, in the outermost region where these walls connect with the subintinal layer and the intine. Depending on the presence or absence of exine covering these regions, the labeling density were dramatic. EE structures, which are completely covered by exine (**Figure 8A**), showed levels of JIM7 epitopes in these regions that were much higher than in equivalent regions of other structures devoid of exine (**Figure 8B**). In structures partially covered by exine (CC and LC), the regions covered by exine (**Figure 8C**) had a much higher labeling than the equivalent regions devoid of exine in the same structure (**Figure 8D**). Statistical analysis of labeling density (**Figure 8E**) confirmed these observations. These results suggest that the presence of exine in the regions where inner wall edges connect with outer walls, influences the accumulation of highly methyl-esterified pectin in these regions, being reduced in structures with lower levels of cell compaction and adhesion. Therefore, exine presence appears to play a role in the accumulation of highly methyl-esterified pectin and in the adhesion properties of cell wall edges.

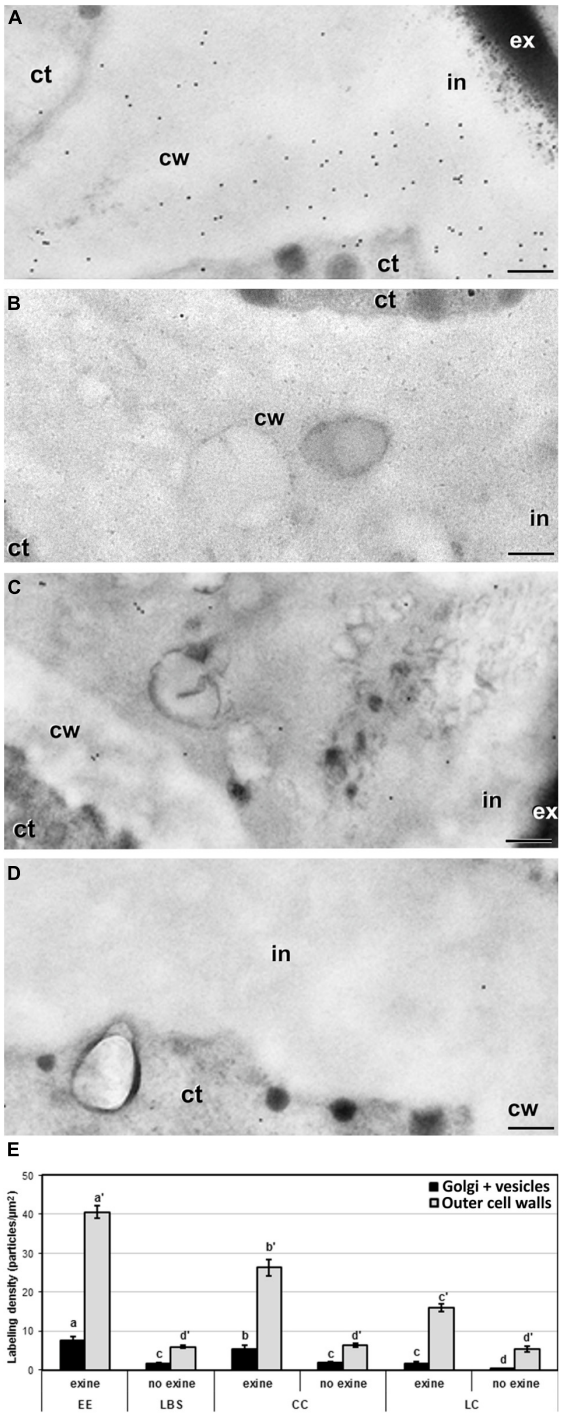

FIGURE 8 | Detection of JIM7 cross-reacting highly methyl-esterified by immunogold labeling and quantification in TEM images of cell wall regions connecting to outer walls from 5-day-old microspore cultures. Images of cell wall regions connecting with outer walls in EE **(A)**, LBS without exine **(B)**, and LC with **(C)** and without exine **(D)**. **(E)** Quantification of JIM7-cross-reacting highly methyl-esterified pectin in cytoplasmic Golgi stacks and vesicles and outer cell wall in different types of structures and in areas with or without exine. Labeling density is expressed in number of particles per μm^2. Different letters represent statistically significant differences obtained with LSD test. ct, cytoplasm; cw, cell wall; ex, exine; in, intine. Bars: 200 nm.

DISCUSSION

Brassica napus microspore cultures are heterogeneous systems where different populations with different developmental fates coexist. It was initially assumed that the subset of embryogenic microspores is homogeneous (Telmer et al., 1995) and follows the same pathway toward embryogenesis. This idea changed when two different types of structures, EE, suspensorless embryos (EE), and suspensor-bearing embryos (SUS) were found to coexist in DH4079 microspore cultures (Supena et al., 2008). This was further refined in *B. napus* DH12075 microspore cultures, where besides EE and SUS, embryogenic compact and loose calli (CC and LC) were also described (Corral-Martinez et al., 2020). Embryo identity and fate were unambiguously assigned to these multicellular structures using embryo fluorescent reporters and time-lapse imaging (Li et al., 2014; Soriano et al., 2014; Corral-Martinez et al., 2020). However, not all these structures are able to develop into embryos. EE and SUS are highly embryogenic, producing most of the embryos, whereas LC and in particular CC are barely embryogenic. In this work we showed that very similar structures are also induced in DH4079 microspore cultures, demonstrating that the range of embryogenic types in DH4079 is wider than previously assumed. We observed EE, CC, and LC, anatomically equivalent to the structures found in DH12075. We also identified LBS, which resemble the early stages of DH12075 suspensor-bearing embryos (SUS), but growing slightly slower, having less cells and a less prominent suspensor at day 5, when observations were made. Since we did not track the fate of each structure, we erred on the side of caution and first considered LBS as a different type of structure. However, after completion of our study, we can reasonably assume that DH4079 and DH12075 embryogenic structures are equivalent based on their similar anatomies, degrees of exine rupture, levels of cell adhesion, general cell wall characteristics, and developmental fate.

Our study revealed equivalent differences between compact (EE and CC) and loose structures (LC and LBS/SUS), as well as similarities between the highly embryogenic (EE and LBS/SUS) and the barely embryogenic structures (CC and LC). These differences and similarities and their significance in the context of *in vitro* morphogenesis are discussed below.

Different Microspore-Derived Structures Present Specific Cell Wall Profiles That Define Their Developmental Fate

Combining our data with that from previous studies (Li et al., 2014; Soriano et al., 2014; Corral-Martinez et al., 2020), we can conclude that the potential for differentiated embryo formation, even through different pathways (with or without a suspensor) correlates with the cell wall profile of the embryogenic structure. We examined these cell wall properties in detail by studying the thickness of outer cell walls (intine + subintinal layer), as well as the composition of inner and outer cell walls in terms of callose, cellulose, high and low methyl-esterified pectin, and AGPs. The most relevant differences are summarized in **Figure 9**. Our data indicate that EE structures, shown to be by far the most viable and embryo-producing structures in DH12075

	EE	LBS	CC	LC
Cell wall width	c	b	ab	a
Subintinal layer width	c	b	b	a
Callose				
Inner walls	a	b	b	c
Outer walls	a	a	b	b
JIM13 - AGPs				
Inner walls	a	a	b	b
Outer walls	a	b	c	c
Low methyl-esterified pectin				
Cytoplasm	a	b	a	a
Inner walls	a	b	a	b
Outer walls	a	a	a	a
Highly methyl-esterified pectin				
Cytoplasm	ab	a	b	b
Inner walls	a	b	c	c
Outer walls	a	a	b	b
Highly methyl-esterified pectin in inner wall edges				
Exine	a		b	c
No exine		d	d	d

FIGURE 9 | Summary of the cell wall composition characteristics of the different embryogenic microspore-derived structures. Different letters represent statistically significant differences in labeling density according to the LSD test, ranging from a (the highest labeling density) to d (the lowest labeling density). For a better comparison among structures, each letter is associated with a different background color.

(Corral-Martinez et al., 2020), had the thinnest walls of all the structures, but with the highest labeling density for almost all the antibodies used in this study. This suggests that this specific cell wall profile is the most favorable for cell proliferation and embryo progression. Conversely, CC, which produced almost no embryos and was the main source of calli (Corral-Martinez et al., 2020), had cell walls thicker than EE and an overall lower antibody signal, except for low methyl-esterified pectin, where a strong signal was observed in all cell walls. This cell wall profile, opposite to that of EE except for low methyl-esterified pectin, would confirm that embryo progression is favored by thin walls enriched in callose, AGPs, and high methyl-esterified pectin. It is interesting to note that the two compact structures, EE and CC, showed similarly high levels of low methyl-esterified pectin but completely different developmental fates. This assigns a role for low methyl-esterified pectin in the maintenance of cell adhesion and structural compactness, but not in the embryogenic competence.

Loose structures (LBS/SUS and LC), shown to have a very low viability in DH12075 (Corral-Martinez et al., 2020), showed the thickest cell walls and the lowest density of certain components in DH4079, especially in inner walls. It appears that these features accounted for the low levels of cell adhesion found between cells and eventually for their low viability. However, the few embryos they produced were all suspensor-bearing embryos (Corral-Martinez et al., 2020). It seems clear that this particular cell wall profile determined their developmental fate as barely viable structures, but with potential to become suspensor-bearing embryos. In particular, LC structures presented the widest cell walls and the lowest values for almost all the studied epitopes. They also have the lowest viability, with nearly 83% of them being arrested or undergoing only few cell divisions (Corral-Martinez et al., 2020). These cell wall properties, totally opposite to those of EE structures, could be defined as the less favorable for cell proliferation and embryo progression. In conclusion, we showed that each embryogenic structure has a specific cell wall profile that directly correlates with its ability to form embryos. The cell wall profile of each structure would define its developmental fate.

The Newly Formed Cell Walls That Support Embryo Formation Are Thin, Plastic, and Callose-Rich

The inner cell walls formed in DH4079 embryogenic microspores between neighboring cells just upon induction are known to be plastic, irregular, incomplete, and rich in callose, an amorphous polymer that confers flexibility and fluidity to nascent cell plates (Samuels et al., 1995) and also to the cell walls of embryogenic microspores when it is not replaced by cellulose (Parra-Vega et al., 2015b). This combination of properties allows for cell expansion and growth (Parra-Vega et al., 2015b) and is found in the thin inner walls of highly embryogenic structures (EE and LBS/SUS) in both DH4079 (this work) and DH12075 (Corral-Martinez et al., 2020). In turn, these properties markedly differ from the thick walls found in barely embryogenic structures (CC and LC). Cell wall width is a crucial characteristic of multicellular structures. It affects not only the compactness of the structure, but also intercellular communication (Parra-Vega et al., 2015b), required to organize and functionally coordinate the role of cells within the same tissue or organ. Cell-to-cell communication proceeds through plasmodesmata, through which cells share chemical signals and form symplastic domains of shared communication. In zygotic embryogenesis, the first divided cells form a single symplast where cells are connected up to the heart-shaped embryo stage, when different symplasts are formed to start with organ differentiation (Kim and Zambryski, 2005). Intercellular connections maintain the identity of the early zygotic embryo, and it can be assumed that also of the microspore-derived embryo. During *in vitro* embryogenesis from somatic explants, embryogenic cells are isolated symplasmically from non-embryogenic cells through callose deposition in plasmodesmata (Godel-Jedrychowska et al., 2020). Intercellular connections are easier to establish in cells with thin and incomplete walls, where in addition to plasmodesmata, gaps, and fenestrae permit the contact of neighboring cytoplasms (Parra-Vega et al., 2015b). If inner walls become excessively thick, as in barely embryogenic structures (LC and CC), plasmodesmata would collapse and wall gaps would occlude, thereby reducing or preventing cell-to-cell communication. It is not surprising that those structures with thinner and more tightly connected cell walls (EE and LBE/SUS) have a higher probability to form a differentiated embryo (Corral-Martinez et al., 2020).

Here, we also examined the biological significance of the subintinal layer. This callose-rich layer is a good predictor

for the ability to form differentiated embryos. It allows cells to create an impermeable layer underneath the intine and protects cells from osmotic changes in the *in vitro* culture environment, which has a positive impact on cell viability (Rivas-Sendra et al., 2019). In cell walls, callose tends to form highly hydrated but semipermeable gels, which are ideal physical and chemical barriers (Albersheim et al., 2011). During plant morphogenesis, callose is used by cells to isolate themselves from the surrounding environment, thereby preventing swelling or bursting and allowing them to express a new morphogenic program in isolation. Examples include natural processes such as the formation of male and female meiocytes (Heslop-Harrison and Mackenzie, 1967; Zhang et al., 2002; Abramova et al., 2003), *in vitro* organogenesis (Fortes et al., 2002), and somatic embryogenesis (Maheswaran and Williams, 1985; Dubois et al., 1991; Pedroso and Pais, 1992; You et al., 2006). Our observation that high levels of callose accumulated in the subintinal layer of outer cell walls of highly embryogenic structures (EE and LBS/SUS) is in line with these studies, and provides additional evidence in a different *in vitro* morphogenic system. Increased callose accumulation was observed even when the subintinal layer itself was not thicker than in barely embryogenic structures (LC and CC), which suggests that the level of callose accumulation rather than the thickness of the subintinal layer is the critical parameter of outer cell walls that supports microspore embryogenesis.

High Levels of Highly Methyl-Esterified Pectin Are Necessary for Cell Wall Flexibility and Growth of Highly Embryogenic Structures

Microspores and pollen are covered by a protective layer, the exine, a key determinant for survival outside the plant. The exine is a relatively rigid coat whose flexibility is largely determined by the number and type of pollen apertures. However, during microspore embryogenesis this layer must eventually break to allow the release of the developing embryo. The specific place where exine breaks is critical for the fate of the released structure (Tang et al., 2013; Corral-Martinez et al., 2020). We showed that exine rupture occurs earlier and to a larger extent in LBS/SUS, and later in CC, LC, and EE. EE and LBS/SUS structures are by far the most embryogenic (Corral-Martinez et al., 2020), which indicates that the timing of exine rupture is not critical for embryo production. However, EE structures produced only suspensorless embryos, whereas LBS/SUS produced only suspensor-bearing embryos (Corral-Martinez et al., 2020), which points to a critical role for exine presence in the developmental pathway adopted by the structure.

Highly methyl-esterified pectin is more abundant in the intine of embryogenic microspores than in pollen-like structures (Corral-Martínez et al., 2019). Here, we found that highly methyl-esterified pectin was present in both inner walls and the intine, being more abundant in organized, highly embryogenic structures (EE and LBS/SUS; **Figure 7**). During somatic-type cytokinesis, pectin is synthesized in the Golgi stacks in a methyl-esterified form, and delivered through the cytoplasm *via* vesicles to the growing cell wall where it is de-esterified by pectin methyl-esterases (PMEs) and cross-linked by calcium, becoming stiff and thereby providing rigidity to the cell wall (Bou Daher and Braybrook, 2015). A similar mechanism has been described for pollen tube formation (Palin and Geitmann, 2012). During the first stages of microspore embryogenesis in *B. napus*, the expression levels of pectin methyl-esterase are low in cultures, and the levels of highly methyl-esterified pectin are high (Solis et al., 2016). In line with this, our results point to highly embryogenic structures (EE and LBS/SUS) as the main contributors to the high levels of highly methyl-esterified pectin described previously. The higher levels of highly methyl-esterified pectin, not yet de-esterified and cross-linked, would suggest that these structures are actively growing.

Surprisingly, we also found that highly methyl-esterified pectin is more abundant at the region of the edges of inner cell walls that connect with outer walls, including the adjacent cytoplasm, but much more abundant where these regions are covered by exine (**Figure 8**), suggesting a relationship between the presence of exine and the deposition of highly methyl-esterified pectin. The cytoplasm adjacent to these cell wall regions also had high levels of highly methyl-esterified pectin immunogold labeling that was proportional in all cases to the labeling found in the corresponding cell wall regions, suggesting that highly methyl-esterified pectin is actively synthesized at this stage and selectively transported to exine-covered regions. In pollen tubes, methyl-esterified pectin promotes the formation of loose walls at the tube tip that are necessary for expansion and tip growth (Li et al., 1994). Away from the tip, pectin de-esterification generates rigid walls that provide stability to the pollen tube. Consistent with this, the high levels of highly methyl-esterified pectin in the inner cell wall edge regions implies that these regions are growing more actively to adapt cell wall width to the increasing size of these growing cells, and that their pectin is not yet de-esterified. Thus, it is reasonable to propose that this pectin composition, typical of growing walls, is what permits the cell walls to produce the expanding force necessary for exine rupture. Indeed, it is common to find points of exine rupture precisely at these regions where inner walls connect with outer walls (arrowhead in **Figure 1C**). In turn, the regions devoid of exine with corresponding lower amounts of highly methyl-esterified pectin would reflect cell wall regions where expansion has already taken place and walls are transitioning to a more stable, non-growing state. This notion is supported by the observation that loose structures (LBS and LC) are the structures where less exine remains attached to the walls and lower levels of highly methyl-esterified pectin were observed.

The Particular Combination of Pectin, Arabinogalactan Proteins, and Calcium Levels Determines the Developmental Fate of Exine-Enclosed and Loose Bicellular Structures/SUS Structures

The role of AGPs in microspore embryogenesis has been the object of study for many years. The AGP composition of

the microspore walls changes drastically when microspores enter the embryogenic pathway, becoming rich in certain AGPs (Corral-Martínez et al., 2019). AGPs are known to play a role in different microspore culture systems, since their addition to the culture medium promotes embryogenesis, whereas their depletion inhibits it (Borderies et al., 2004; Tang et al., 2006; Corral-Martínez and Seguí-Simarro, 2014; Makowska et al., 2017). However, their specific role is still not known. Calcium accumulation is involved in the embryogenic commitment of microspores/pollen (Rivas-Sendra et al., 2017) and the relationship between calcium and AGPs during cell wall growth is well known. In growing pollen tubes, AGP depletion inhibits growth, whereas calcium influx promotes the delivery of exocytosis vesicles (Gaffal et al., 2007). Periplasmic AGPs can act as calcium capacitors, releasing calcium when the apoplast changes by the activation of H^+-ATPs pumps due to the tensional force that occurs in the plasma membrane during cell growth (Lamport and Varnai, 2013; Lamport et al., 2018). Indeed, the ability of cell surface AGPs for binding and releasing apoplastic calcium was recently demonstrated (Lopez-Hernandez et al., 2020).

We showed that highly embryogenic structures (EE and LBS/SUS) have the highest density of JIM13-detected AGPs in both outer and inner cell walls and the highest levels of intracellular calcium soon after embryogenesis induction (Rivas-Sendra et al., 2017). According to the model of Lamport and Varnai (2013), AGPs would provide these structures with more capacity to release Ca^{+2} when needed for the microspore-to-embryo switch. When the plasma membrane stretches due to cell growth, calcium would be released by AGPs, thereby signaling the need for more cell wall synthesis and activating the delivery of exocytosis vesicles, as in pollen tube growth. This sets off a positive feedback loop that increases the amount of AGPs in the cell wall and in turn increases calcium. Calcium is also required for gelification of low methyl-esterified pectin to provide cellular adhesion (Palin and Geitmann, 2012; Bou Daher and Braybrook, 2015). In general, inner cell walls of compact structures (EE and CC) have a higher density of low methyl-esterified pectin, indicating their importance for cell adhesion. In addition, the combined high levels of AGPs, pectin, and calcium in EE structures would confer them unique properties to combine cell adhesion with high embryogenic potential.

Loose bicellular structures/SUS structures showed an unusual pattern of AGP accumulation. They have high amounts of AGPs in their inner walls and high amounts of both low and highly methyl-esterified pectin in their outer walls. The high degree of pectin esterification in outer walls and the detachment of the exine would provide flexibility to these walls, but the low degree of pectin esterification in inner cell walls would support cell adhesion. In other words, these structures are loose because the exine is not present to restrict their expansion and their outer walls allow for it, but the connection between cells is sufficient to maintain intercellular communication. This combination of cell wall properties provides the optimal conditions for their development as suspensor-bearing embryos, which would be nearly impossible with any other cell wall type. In support of this notion, LC structures, with similar pectin composition in inner and outer walls, were only able to produce suspensor-bearing embryos, although at a very low frequency (Corral-Martinez et al., 2020). In this case, the increased cell wall thickness and other differences in their cell wall components combined with their low viability would account for their low embryogenic response.

CONCLUSION

Here we demonstrate that each type of structure has a different cell wall composition and architecture. The structures with the highest probability to become embryos (EE) have thin walls that allow them to keep cells close and communicated, a callose-rich subintinal layer that allows them to isolate from the environment and to create their own embryo identity, and a specific pectin and AGP composition that determines their development as embryos. Other structures with different cell wall profiles are also able to become embryos, but through different pathways and with lower rates of success (Corral-Martinez et al., 2020). There seems to be an optimal cell wall profile to become an embryo, but such profile is not the only possible. Other profiles would allow for embryogenesis, but less efficiently. From a developmental perspective, each structure seems to find its way to progress toward embryogenesis, but its success would be determined by the cell wall profile. The next question would be why each embryogenic structure has a different cell wall profile. We previously showed that the first cell walls formed by embryogenic microspores are morphologically altered and have an abnormal composition, rich in callose and deficient in cellulose, due to the partial impairment of conventional cytokinesis during the heat shock stage (Parra-Vega et al., 2015b). These problems are undergone by each microspore to different extents, leading to different cell walls with different properties in terms of adhesion, stiffness and permeability, among others. Each microspore may manage the situation differently, trying to compensate the deficiencies through different ways. This has been demonstrated to occur during pollen tube growth, a similar system where cell walls have untypically low cellulose contents. In this system, when cellulose deposition is compromised, alternative compensatory mechanisms for increased pectin synthesis and/or deposition are activated (Aouar et al., 2010; Palin and Geitmann, 2012). This way, pollen tubes are able to adapt their cell wall properties to a new scenario. Since both pollen tubes and cell walls of embryogenic microspores are formed from the microspore/pollen plasma membrane and cell wall, their initial composition and chemical environment should be similar. Given the similarities between both cell walls, it is plausible to propose that similar, pectin-based compensatory mechanisms may operate in both cases. In conclusion, this study provides relevant data to further understand the role of cell wall during the initial stages of microspore embryogenesis, and how different cell wall profiles are related to different developmental fates.

DATA AVAILABILITY STATEMENT

The original contributions presented in the study are included in the article/supplementary material, further inquiries can be directed to the corresponding author.

AUTHOR CONTRIBUTIONS

PC-M, KB, and JS-S: conceptualization and methodology. PC-M, CC-F, and RM: data curation, formal analysis, and investigation. PC-M, CC-F, and JS-S: visualization. PC-M and JS-S: supervision. CC-F and JS-S: writing – original draft preparation. JS-S and KB: writing – review and editing. All authors contributed to the article and approved the submitted version.

FUNDING

This work was supported by grant PID2020-115763RB-I00 to JS-S from Spanish MICINN and by a Juan de la Cierva – Incorporación Fellowship and a Marie Skłodowska-Curie Individual Fellowship (656579) to PC-M. RM holds a CDEIGENT (2018/023) fellowship from Generalitat Valenciana.

ACKNOWLEDGMENTS

We thank the Electron Microscopy Service of Universitat Politècnica de València and to Marisol Gascón (IBMCP-CSIC Microscopy Service) for their excellent technical help.

REFERENCES

Abramova, L. I., Avalkina, N. A., Golubeva, E. A., Pyzhenkova, Z. S., and Golubovskaya, I. N. (2003). Synthesis and deposition of callose in anthers and ovules of meiotic mutants of maize (*Zea mays*). *Russ. J. Plant Physiol.* 50, 324–329. doi: 10.1023/a:1023866019102

Albersheim, P., Darvill, A., Roberts, K., Sederoff, R., and Staehelin, A. (2011). *Plant Cell Walls*. New York: Garland Science.

Aouar, L., Chebli, Y., and Geitmann, A. (2010). Morphogenesis of complex plant cell shapes: the mechanical role of crystalline cellulose in growing pollen tubes. *Sex. Plant. Reprod.* 23, 15–27. doi: 10.1007/s00497-009-0110-7

Borderies, G., Le Bechec, M., Rossignol, M., Lafitte, C., Le Deunff, E., Beckert, M., et al. (2004). Characterization of proteins secreted during maize microspore culture: arabinogalactan proteins (AGPs) stimulate embryo development. *Eur. J. Cell Biol.* 83, 205–212.

Bou Daher, F., and Braybrook, S. A. (2015). How to let go: pectin and plant cell adhesion. *Front. Plant Sci.* 6:523. doi: 10.3389/fpls.2015.00523

Camacho-Fernández, C., Hervás, D., Rivas-Sendra, A., Marín, M. P., and Seguí-Simarro, J. M. (2018). Comparison of six different methods to calculate cell densities. *Plant Methods* 14:30. doi: 10.1186/s13007-018-0297-4

Chebli, Y., Kaneda, M., Zerzour, R., and Geitmann, A. (2012). The cell wall of the arabidopsis pollen tube—Spatial distribution, recycling, and network formation of polysaccharides. *Plant Physiol.* 160, 1940–1955. doi: 10.1104/pp.112.199729

Chen, H.-W., Persson, S., Grebe, M., and Mcfarlane, H. E. (2018). Cellulose synthesis during cell plate assembly. *Physiol. Plant.* 164, 17–26. doi: 10.1111/ppl.12703

Cheung, A. Y., and Wu, H. M. (1999). Arabinogalactan proteins in plant sexual reproduction. *Protoplasma* 208, 87–98.

Corral-Martínez, P., Camacho-Fernández, C., Mir, R., and Seguí-Simarro, J. M. (2021). "Doubled haploid production in high- and low-response genotypes of rapeseed (*Brassica napus*) through isolated microspore culture," in *Doubled Haploid Technology II: Hot Topics, Apiaceae, Brassicaceae, Solanaceae*, ed. J. M. Seguí-Simarro (New York: Springer Science+Business Media), 129–144.

Corral-Martínez, P., Driouich, A., and Seguí-Simarro, J. M. (2019). Dynamic changes in arabinogalactan-protein, pectin, xyloglucan and xylan composition of the cell wall during microspore embryogenesis in *Brassica napus*. *Front. Plant Sci.* 10:332. doi: 10.3389/fpls.2019.00332

Corral-Martínez, P., Parra-Vega, V., and Seguí-Simarro, J. M. (2013). Novel features of *Brassica napus* embryogenic microspores revealed by high pressure freezing and freeze substitution: evidence for massive autophagy and excretion-based cytoplasmic cleaning. *J. Exp. Bot.* 64, 3061–3075. doi: 10.1093/jxb/ert151

Corral-Martínez, P., and Seguí-Simarro, J. M. (2014). Refining the method for eggplant microspore culture: effect of abscisic acid, epibrassinolide, polyethylene glycol, naphthaleneacetic acid, 6-benzylaminopurine and arabinogalactan proteins. *Euphytica* 195, 369–382. doi: 10.1007/s10681-013-1001-4

Corral-Martinez, P., Siemons, C., Horstman, A., Angenent, G. C., De Ruijter, N., and Boutilier, K. (2020). Live Imaging of embryogenic structures in *Brassica napus* microspore embryo cultures highlights the developmental plasticity of induced totipotent cells. *Plant Reprod.* 33, 143–158. doi: 10.1007/s00497-020-00391-z

Custers, J. (2003). "Microspore culture in rapeseed (*Brassica napus* L.)," in *Doubled Haploid Production in Crop Plants*, eds M. Maluszynski, K. J. Kasha, B. P. Forster, and I. Szarejko (Dordrecht: Kluwer Academic Publishers), 185–193.

Dong, X., Hong, Z., Sivaramakrishnan, M., Mahfouz, M., and Verma, D. P. S. (2005). Callose synthase (CalS5) is required for exine formation during microgametogenesis and for pollen viability in Arabidopsis. *Plant J.* 42, 315–328. doi: 10.1111/j.1365-313X.2005.02379.x

Dresselhaus, T., and Jürgens, G. (2021). Comparative embryogenesis in angiosperms: activation and patterning of embryonic cell lineages. *Ann. Rev. Plant. Biol.* 72, 641–676. doi: 10.1146/annurev-arplant-082520-094112

Dubois, T., Guedira, M., Dubois, J., and Vasseur, J. (1991). Direct somatic embryogenesis in leaves of *Cichorium*: a histological and SEM study of early stages. *Protoplasma* 162, 120–127.

Fortes, A. M., Testillano, P. S., Risueño, M. C., and Pais, M. S. (2002). Studies on callose and cutin during the expression of competence and determination for organogenic nodule formation from internodes of *Humulus lupulus* var. *Nugget*. *Physiol. Plant.* 116, 113–120.

Gaffal, K. P., Friedrichs, G. J., and El-Gammal, S. (2007). Ultrastructural evidence for a dual function of the phloem and programmed cell death in the floral nectary of *Digitalis purpurea*. *Ann. Bot.* 99, 593–607. doi: 10.1093/aob/mcm002

Gaspar, Y., Johnson, K., Mckenna, J., Bacic, A., and Schultz, C. (2001). The complex structures of arabinogalactan-proteins and the journey towards understanding function. *Plant Mol. Biol.* 47, 161–176. doi: 10.1023/a:1010683432529

Godel-Jedrychowska, K., Kulinska-Lukaszek, K., Horstman, A., Soriano, M., Li, M., Malota, K., et al. (2020). Symplasmic isolation marks cell fate changes during somatic embryogenesis. *J. Exp. Bot.* 71, 2612–2628. doi: 10.1093/jxb/eraa041

Gorska-Brylass, A. (1967). Transitory callose envelope surrounding the generative cell in pollen grains. *Acta Soc. Bot. Poloniae* 36, 419–422.

Heslop-Harrison, J., and Mackenzie, A. (1967). Autoradiography of soluble [2-I4C] thymidine derivatives during meiosis and microsporogenesis in *Lilium* anthers. *J. Cell. Sci.* 2, 387–400.

Jouannic, S., Champion, A., Seguí-Simarro, J. M., Salimova, E., Picaud, A., Tregear, J., et al. (2001). The protein kinases AtMAP3Kε1 and BnMAP3Kε1 are functional homologues of *S. pombe* cdc7p and may be involved in cell division. *Plant J.* 26, 637–649.

Karnovsky, M. J. (1965). A formaldehyde-glutaraldehyde fixative of high osmolality for use in electron microscopy. *J. Cell Biol.* 27, 137A–138A.

Kim, I., and Zambryski, P. C. (2005). Cell-to-cell communication via plasmodesmata during Arabidopsis embryogenesis. *Curr. Opin. Plant Biol.* 8, 593–599. doi: 10.1016/j.pbi.2005.09.013

Knox, J. P., Linstead, P. J., King, J., Cooper, C., and Roberts, K. (1990). Pectin esterification is spatially regulated both within cell walls and between developing tissues of root apices. *Planta* 181, 512–521. doi: 10.1007/bf00193004

Knox, J. P., Linstead, P. J., Peart, J., Cooper, C., and Roberts, K. (1991). Developmentally regulated epitopes of cell surface arabinogalactan proteins and their relation to root tissue pattern formation. *Plant J.* 1, 317–326.

Lamport, D. T., and Varnai, P. (2013). Periplasmic arabinogalactan glycoproteins act as a calcium capacitor that regulates plant growth and development. *New Phytol.* 197, 58–64. doi: 10.1111/nph.12005

Lamport, D. T. A., Tan, L., Held, M. A., and Kieliszewski, M. J. (2018). Pollen tube growth and guidance: occam's razor sharpened on a molecular arabinogalactan glycoprotein Rosetta Stone. *New Phytol.* 217, 491–500. doi: 10.1111/nph.14845

Li, H., Soriano, M., Cordewener, J., Muiño, J. M., Riksen, T., Fukuoka, H., et al. (2014). The histone deacetylase inhibitor Trichostatin A promotes totipotency in the male gametophyte. *Plant Cell* 26, 195–209. doi: 10.1105/tpc.113.116491

Li, Y. Q., Chen, F., Linskens, H. F., and Cresti, M. (1994). Distribution of unesterified and esterified pectins in cell walls of pollen tubes of flowering plants. *Sex. Plant. Reprod.* 7, 145–152. doi: 10.1007/bf00228487

Lopez-Hernandez, F., Tryfona, T., Rizza, A., Xiaolan, L. Y., Harris, M. O., Webb, A. A., et al. (2020). Calcium binding by arabinogalactan polysaccharides is important for normal plant development. *Plant Cell* 32, 3346–3369.

Maheswaran, G., and Williams, E. G. (1985). Origin and development of somatic embryoids formed directly on immature embryos of *Trifolium repens in vitro*. *Ann. Bot.* 56, 619–630.

Makowska, K., Kałużniak, M., Oleszczuk, S., Zimny, J., Czaplicki, A., and Konieczny, R. (2017). Arabinogalactan proteins improve plant regeneration in barley (*Hordeum vulgare* L.) anther culture. *Plant Cell Tissue Organ Cult.* 131, 247–257. doi: 10.1007/s11240-017-1280-x

Musielak, T. J., Schenkel, L., Kolb, M., Henschen, A., and Bayer, M. (2015). A simple and versatile cell wall staining protocol to study plant reproduction. *Plant Reprod.* 28, 161–169. doi: 10.1007/s00497-015-0267-1

Palin, R., and Geitmann, A. (2012). The role of pectin in plant morphogenesis. *Biosystems* 109, 397–402. doi: 10.1016/j.biosystems.2012.04.006

Parra-Vega, V., Corral-Martínez, P., Rivas-Sendra, A., and Seguí-Simarro, J. M. (2015a). Formation and excretion of autophagic plastids (plastolysomes) in *Brassica napus* embryogenic microspores. *Front. Plant Sci.* 6:94. doi: 10.3389/fpls.2015.00094

Parra-Vega, V., Corral-Martínez, P., Rivas-Sendra, A., and Seguí-Simarro, J. M. (2015b). Induction of embryogenesis in *Brassica napus* microspores produces a callosic subintinal layer and abnormal cell walls with altered levels of callose and cellulose. *Front. Plant Sci.* 6:1018. doi: 10.3389/fpls.2015.01018

Pedroso, M. C., and Pais, M. S. (1992). A scanning electron-microscopy and X-ray-microanalysis study during induction of morphogenesis in *Camellia japonica* L. *Plant Sci.* 87, 99–108. doi: 10.1016/0168-9452(92)90197-t

Pereira, A. M., Pereira, L. G., and Coimbra, S. (2015). Arabinogalactan proteins: rising attention from plant biologists. *Plant Reprod.* 28, 1–15. doi: 10.1007/s00497-015-0254-6

Rivas-Sendra, A., Calabuig-Serna, A., and Seguí-Simarro, J. M. (2017). Dynamics of calcium during *in vitro* microspore embryogenesis and *in vivo* microspore development in *Brassica napus* and *Solanum melongena*. *Front. Plant Sci.* 8:1177. doi: 10.3389/fpls.2017.01177

Rivas-Sendra, A., Corral-Martínez, P., Porcel, R., Camacho-Fernández, C., Calabuig-Serna, A., and Seguí-Simarro, J. M. (2019). Embryogenic competence of microspores is associated with their ability to form a callosic, osmoprotective subintinal layer. *J. Exp. Bot.* 70, 1267–1281. doi: 10.1093/jxb/ery458

Samuels, A. L., Giddings, T. H. Jr., and Staehelin, L. A. (1995). Cytokinesis in tobacco BY-2 and root tip cells: a new model of cell plate formation in higher plants. *J. Cell Biol.* 130, 1345–1357.

Satpute, G., Long, H., Seguí-Simarro, J. M., Risueño, M. C., and Testillano, P. S. (2005). Cell architecture during gametophytic and embryogenic microspore development in *Brassica napus*. *Acta Physiol. Plant.* 27, 665–674.

Schindelin, J., Arganda-Carreras, I., Frise, E., Kaynig, V., Longair, M., Pietzsch, T., et al. (2012). Fiji: an open-source platform for biological-image analysis. *Nat. Methods* 9, 676–682. doi: 10.1038/nmeth.2019

Seguí-Simarro, J. M., Corral-Martínez, P., Corredor, E., Raska, I., Testillano, P. S., and Risueño, M. C. (2011). A change of developmental program induces the remodeling of the interchromatin domain during microspore embryogenesis in *Brassica napus* L. *J. Plant Physiol.* 168, 746–757. doi: 10.1016/j.jplph.2010.10.014

Seguí-Simarro, J. M., Jacquier, N. M. A., and Widiez, T. (2021). "Overview of *in vitro* and *in vivo* doubled haploid technologies," in *Doubled Haploid Technology Vol. 1. General topics, Alliaceae, Cereals*, ed. J. M. Seguí-Simarro (New York: Springer Science+Business Media), 3–22.

Seguí-Simarro, J. M., and Nuez, F. (2007). Embryogenesis induction, callogenesis, and plant regeneration by *in vitro* culture of tomato isolated microspores and whole anthers. *J. Exp. Bot.* 58, 1119–1132. doi: 10.1093/jxb/erl271

Seguí-Simarro, J. M., and Nuez, F. (2008). How microspores transform into haploid embryos: changes associated with embryogenesis induction and microspore-derived embryogenesis. *Physiol. Plant.* 134, 1–12. doi: 10.1111/j.1399-3054.2008.01113.x

Seguí-Simarro, J. M., Otegui, M. S., Austin, J. R., and Staehelin, L. A. (2008). "Plant cytokinesis - Insights gained from electron tomography studies," in *Cell Division Control in Plants*, eds D. P. S. Verma and Z. Hong (Berlin: Springer), 251–287.

Seifert, G. J., and Roberts, K. (2007). The biology of arabinogalactan proteins. *Ann. Rev. Plant. Biol.* 58, 137–161. doi: 10.1146/annurev.arplant.58.032806.103801

Simmonds, D. H., and Keller, W. A. (1999). Significance of preprophase bands of microtubules in the induction of microspore embryogenesis of *Brassica napus*. *Planta* 208, 383–391.

Solis, M. T., Berenguer, E., Risueño, M. C., and Testillano, P. S. (2016). BnPME is progressively induced after microspore reprogramming to embryogenesis, correlating with pectin de-esterification and cell differentiation in *Brassica napus*. *BMC Plant Biol.* 16:176. doi: 10.1186/s12870-016-0863-8

Soriano, M., Li, H., and Boutilier, K. (2013). Microspore embryogenesis: establishment of embryo identity and pattern in culture. *Plant Reprod.* 26, 181–196. doi: 10.1007/s00497-013-0226-7

Soriano, M., Li, H., Jacquard, C., Angenent, G. C., Krochko, J., Offringa, R., et al. (2014). Plasticity in cell division patterns and auxin transport dependency during *in vitro* embryogenesis in *Brassica napus*. *Plant Cell* 26, 2568–2581. doi: 10.1105/tpc.114.126300

Supena, E. D. J., Winarto, B., Riksen, T., Dubas, E., Van Lammeren, A., Offringa, R., et al. (2008). Regeneration of zygotic-like microspore-derived embryos suggests an important role for the suspensor in early embryo patterning. *J. Exp. Bot.* 59, 803–814.

Tang, X., Liu, Y., He, Y., Ma, L., and Sun, M.-X. (2013). Exine dehiscing induces rape microspore polarity, which results in different daughter cell fate and fixes the apical–basal axis of the embryo. *J. Exp. Bot.* 64, 215–228. doi: 10.1093/jxb/ers327

Tang, X. C., He, Y. Q., Wang, Y., and Sun, M. X. (2006). The role of arabinogalactan proteins binding to Yariv reagents in the initiation, cell developmental fate, and maintenance of microspore embryogenesis in *Brassica napus* L. cv. Topas. *J. Exp. Bot.* 57, 2639–2650.

Telmer, C. A., Newcomb, W., and Simmonds, D. H. (1995). Cellular changes during heat shock induction and embryo development of cultured microspores of *Brassica napus* cv. Topas. *Protoplasma* 185, 106–112.

Willats, W. G. T., Limberg, G., Buchholt, H. C., Van Alebeek, G.-J., Benen, J., Christensen, T. M., et al. (2000). Analysis of pectic epitopes recognised by hybridoma and phage display monoclonal antibodies using defined oligosaccharides, polysaccharides, and enzymatic degradation. *Carbohydrate Res.* 327, 309–320. doi: 10.1016/S0008-6215(00)00039-2

Williams, M. A. (1977). *Quantitative Methods in Biology (Practical methods in electron microscopy, vol 6, part 2)*. Amsterdam: North Holland.

You, X. L., Yi, J. S., and Choi, Y. E. (2006). Cellular change and callose accumulation in zygotic embryos of *Eleutherococcus senticosus* caused by plasmolyzing pretreatment result in high frequency of single-cell-derived somatic embryogenesis. *Protoplasma* 227, 105–112. doi: 10.1007/s00709-006-0149-3

Zhang, C., Guinel, F. C., and Moffatt, B. A. (2002). A comparative ultrastructural study of pollen development in *Arabidopsis thaliana* ecotype Columbia and male-sterile mutant *apt1-3*. *Protoplasma* 219, 59–71.

Conflict of Interest: The authors declare that the research was conducted in the absence of any commercial or financial relationships that could be construed as a potential conflict of interest.

frontiers in Plant Science

ORIGINAL RESEARCH
published: 10 February 2022
doi: 10.3389/fpls.2021.802424

Forgotten Actors: Glycoside Hydrolases During Elongation Growth of Maize Primary Root

*Alsu Nazipova[1], Oleg Gorshkov[1], Elena Eneyskaya[2], Natalia Petrova[1], Anna Kulminskaya[2,3], Tatyana Gorshkova[1] and Liudmila Kozlova[1]**

[1] Kazan Institute of Biochemistry and Biophysics, FRC Kazan Scientific Center of RAS, Kazan, Russia, [2] Petersburg Nuclear Physics Institute Named by B.P. Konstantinov of National Research Center "Kurchatov Institute", Gatchina, Russia, [3] Kurchatov Genome Center - PNPI, Gatchina, Russia

Plant cell enlargement is coupled to dynamic changes in cell wall composition and properties. Such rearrangements are provided, besides the differential synthesis of individual cell wall components, by enzymes that modify polysaccharides *in muro*. To reveal enzymes that may contribute to these modifications and relate them to stages of elongation growth in grasses, we carried out a transcriptomic study of five zones of the primary maize root. In the initiation of elongation, significant changes occur with xyloglucan: once synthesized in the meristem, it can be linked to other polysaccharides through the action of hetero-specific xyloglucan endotransglycosidases, whose expression boosts at this stage. Later, genes for xyloglucan hydrolases are upregulated. Two different sets of enzymes capable of modifying glucuronoarabinoxylans, mainly bifunctional α-arabinofuranosidases/β-xylosidases and β-xylanases, are expressed in the maize root to treat the xylans of primary and secondary cell walls, respectively. The first set is highly pronounced in the stage of active elongation, while the second is at elongation termination. Genes encoding several glycoside hydrolases that are able to degrade mixed-linkage glucan are downregulated specifically at the active elongation. It indicates the significance of mixed-linkage glucans for the cell elongation process. The possibility that many glycoside hydrolases act as transglycosylases *in muro* is discussed.

Keywords: cell wall, elongation (growth), maize (*Zea mays* L.), root, glycoside hydrolase, RNA-seq

OPEN ACCESS

Edited by:
Simon Gilroy, University of Wisconsin-Madison, United States

Reviewed by:
Jozef Mravec, University of Copenhagen, Denmark
Oskar Jarosław Siemianowski, University of Warsaw, Poland

****Correspondence:***
Liudmila Kozlova
kozlova@kibb.knc.ru

Specialty section:
This article was submitted to Plant Cell Biology, a section of the journal Frontiers in Plant Science

Received: *26 October 2021*
Accepted: *30 December 2021*
Published: *10 February 2022*

Citation:
Nazipova A, Gorshkov O, Eneyskaya E, Petrova N, Kulminskaya A, Gorshkova T and Kozlova L (2022) Forgotten Actors: Glycoside Hydrolases During Elongation Growth of Maize Primary Root. Front. Plant Sci. 12:802424. doi: 10.3389/fpls.2021.802424

INTRODUCTION

Elongation or expansion growth of plant cells generally occurs between their division and specialization. During this process, they irreversibly elongate or expand many times compared to the meristematic initial (Cosgrove, 2005). Only cells that are surrounded by thin primary cell walls are able to increase their size, so primary cell walls have to be extensible and strong enough to withstand turgor pressure. Primary cell walls are mainly composed of polysaccharides and are classified into two types in angiosperms (Carpita, 1996). The dicots and non-commelinid monocots possess type I cell walls in contrast to type II cell walls of commelinid monocots including *Poales*. Cellulose is common for both types; xyloglucans (XyGs) and pectins are the basic matrix polysaccharides for cell walls of type I, and glucuronoarabinoxylans (GAXs) and mixed-linkage glucans (MLGs) are the main hemicelluloses in cell walls of type II (Carpita, 1996).

One of the early hypotheses of the cell wall expansion mechanism was that glycoside hydrolases (GHs) act on so-called load-bearing linkages within the cellulose-hemicellulose network, so as to promote an increase in cell size. This point of view was supported by several observations: (i) Cell walls are capable of autolysis. During growth, the cell walls of both dicots and monocots lose some sugars, mainly glucose (Matchett and Nance, 1962; Wada et al., 1968); (ii) Extracts of growing tissues show enzymatic activities toward hemicelluloses (Davies and Maclachlan, 1968; Johnson et al., 1974; Huber and Nevins, 1980); (iii) The elongation growth of maize coleoptiles induced by auxin is inhibited by the infiltration of polyclonal antibodies specific to endo- and exo-β-D-glucanases (Hoson and Nevins, 1989; Inouhe and Nevins, 1991). The schematic structure of matrix polysaccharides of primary cell walls and GH families that can modify these polymers are represented in **Figure 1**.

However, after the discovery of expansins (McQueen-Mason et al., 1992), the significance of plant GHs in the elongation process was subjected to a question. At present, GHs are thought to participate in cell wall polysaccharide turnover; although neither cause nor effect of this intensive metabolism is understood yet (Barnes and Anderson, 2018). For instance, MLG turnover is coupled to the day and night cycle in maize leaves *via* the expression of an MLG-specific hydrolase (Kraemer et al., 2021). GHs take part in cellulose microfibril formation (Nicol et al., 1998; Lane et al., 2001; Szyjanowicz et al., 2004) and control the angle of cellulose microfibrils (Derba-Maceluch et al., 2015). The importance of GHs in different physiological processes such as root aerenchyma formation (Grandis et al., 2019), proper cell wall deposition (Moneo-Sánchez et al., 2019, 2020), and xylem differentiation (Yu et al., 2013; Hu et al., 2020; Tu et al., 2020) was shown. Despite a wide variety of GHs acting during different processes has been described in several omics studies (Francin-Allami et al., 2015; Calderan-Rodrigues et al., 2017; Grandis et al., 2019), in many cases, the physiological significance of these GHs in plants has remained elusive.

Here, we report a comprehensive characterization of cell wall-related GHs in the maize genome. All genes encoding the representatives of these protein families were identified and characterized. Transcriptomics analysis of their expression, together with enzymatic activity determination in the apical zones of growing maize root, permitted to advance the understanding of occurring cell wall rearrangements and their timing through the stages of root cell development.

MATERIALS AND METHODS

Plant Material

Primary roots of 4-day old maize (*Zea mays* L., cv Mashuk) seedlings were used for this study. Maize grains were sterilized by 10-min incubation in 1% sodium hypochlorite solution and then washed three times in distilled water for 10 min. The seedlings were grown hydroponically in the dark at 27°C in distilled water. The primary root was subdivided into zones according to the following pattern: root cap, meristem (0-1 mm from the root cap junction), early elongation (1-2 mm), elongation (2-6 mm), and late elongation (7-11 mm), as described in Kozlova et al. (2020) and (**Figure 2**).

Glycoside Hydrolase Activity and Protein Content Assay

Primary roots from 30 to 40 plants were cut into the studied zones (**Figure 2**), and samples were fixed in liquid nitrogen. The plant material was ground using mortar and pestle in a 50-mM NaOAc buffer (pH 5.6) with 0.05% (w/w) sodium azide and 3 mM dithiothreitol at 4°C. Homogenates were clarified by 10-min centrifugation at 5,000 *g* and used for enzyme activity and protein content (Bradford, 1976) assays. Enzyme activities were measured using the following substrates: *p*-nitrophenyl β-D-glucopyranoside, *p*-nitrophenyl β-D-galactopyranoside, *p*-nitrophenyl β-D-xylopyranoside, *p*-nitrophenyl α-D-mannopyranoside, *p*-nitrophenyl-α-L-fucopyranoside, and β-N-acetyl glucopyranoside at 10 mM concentration. Reaction mixtures containing 20-50 μl of clarified homogenates and 50 μl of a substrate solution were incubated at 37°C in a water bath for 10 min – 1 h depending on the reaction rate. The reaction was stopped by adding 900 μl of 10% (w/w) Na_2CO_3 solution. The optical density at 400 nm was determined on a spectrophotometer (V-576, Jasco, Tokyo, Japan). The amount of 4-nitrophenol liberated as a result of glycosidase catalysis was determined using a reference extinction coefficient (Dawson, 1986). The lichenase (1,3;1,4-endo-β-D-glucan endohydrolase) and endo-β-xylanase assays were performed using K-MBG4 and K-XylX6 commercial kits, respectively (Megazyme, Bray, Ireland) according to the instructions of the manufacturer. The experiment was performed at least in three biological replicates for each type of activity.

β-D-Galactosidase and β-D-glucosidase activities were detected on cross sections of the primary root of maize seedlings using the resorufin-β-D-galactopyranose (Res-βDGal*p*) and resorufin-β-D-glucopyranose (Res-βDGlc*p*) substrates (Merck, Kenilworth, NJ, United States). The substrates were resolved in dimethyl sulfoxide and then diluted with 0.2 M phosphate-buffered saline (PBS, pH 7.4) to 100 μM concentration. Ten microliters of the substrate were added to each cross section. Twenty-five and 50 μm-thick sections were made on a vibratome (Leica Biosystems, Wetzlar, Germany) in the middle part of each analyzed maize root zone (**Figure 2**). Enzyme activity was detected by red fluorescence on a Leica DM1000 epifluorescence microscope (Leica Biosystems, Wetzlar, Germany) fitted with a mercury lamp and filter cube with excitation at 540-580 nm and extinction at 608-683 nm. Exposure time was maintained constant. The sections were observed after 10 min of reaction. The control sections were heated to 90°C for 5 min in a water drop and then treated with substrates. Images were obtained using a digital camera. The experiment was performed in three biological replicates.

RNA Extraction and Sequencing

In addition to the previously published data (Kozlova et al., 2020, BioProject: PRJNA639682), twenty more individual libraries of mRNAs were obtained from the same five zones of the maize

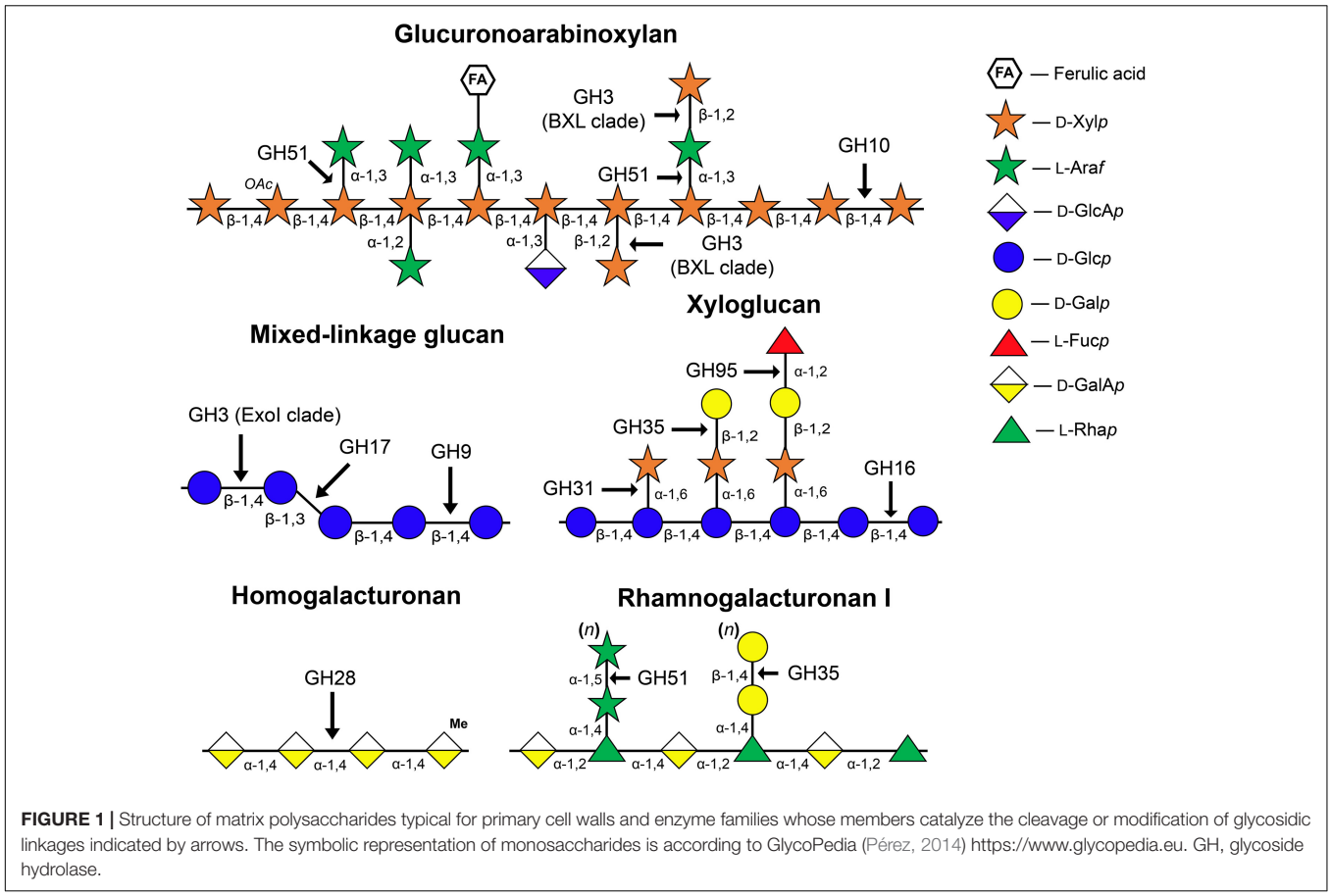

FIGURE 1 | Structure of matrix polysaccharides typical for primary cell walls and enzyme families whose members catalyze the cleavage or modification of glycosidic linkages indicated by arrows. The symbolic representation of monosaccharides is according to GlycoPedia (Pérez, 2014) https://www.glycopedia.eu. GH, glycoside hydrolase.

primary root in four biological replicates were analyzed using an Illumina sequencing technology. Root segments of ca. 30 plants were collected in plastic tubes with liquid nitrogen and stored in a freezer at −80°C until mRNA extraction. Total RNA was isolated from the plant samples using the TRIzol-based extraction method in combination with RNeasy Plant Mini Kit (Qiagen, Hilden, Germany) according to the instructions of the manufacturer. Residual DNA was removed by treating the samples with a Turbo DNA-free kit (Ambion, Austin, TX, United States). The quantity and quality of RNA were controlled using NanoPhotometer NP-80 Touch (Implen, Munich, Germany) and by electrophoresis in 1% (w/w) agarose gel. RNA integrity test (all samples had a RIN value higher than 7), cDNA library construction, and sequencing were performed by Novogene Company Limited (Cambridge, United Kingdom[1]). Data in the form of raw reads and sample preparation descriptions were added to BioProject number PRJNA639682[2] in the Sequence Read Archive (SRA).

Processing and Analysis of RNA-seq Data

Low-quality reads, reads containing adapters, and contaminating sequences were removed with the BBDuk utility of the BBToolsv38.73[3] tool to get clean read data. Paired-end clean reads for each sample were mapped onto the maize genome version B73 RefGen_v4 downloaded from Gramene[4] using HISAT2 v2.1.(Kim et al., 2015). The StringTie v2.0. software (Pertea et al., 2016) was employed to count the number of reads mapped to each gene. Normalized TGR (total gene read) values were used as input for differential expression analyses using R package DESeq2 v1.30.1 after normalization of the combined dataset (previously generated by us (Kozlova et al., 2020, BioProject: PRJNA639682) and in this study) in a DESeq2's statistical model (Love et al., 2014)[5]. A gene was considered as expressed if the average normalized TGR in at least one sample was > = 16 according to the recommendations of the sequencing quality control project (Su et al., 2014). The resulting dataset consisted of 28,888 genes. The transcriptomic data were combined with the results of the proteomic study performed on maize primary root by C. Marcon et al. (2015). Details of the maize root sampling in both studies can be found in **Figure 2**.

Cluster and Co-Expression Analyses

A set of expressed genes encoding maize GHs in the form of rlog-transformed values (the regularized-logarithm transformation

[1]https://en.novogene.com/

[2]http://www.ncbi.nlm.nih.gov/bioproject/639682

[3]https://jgi.doe.gov/data-and-tools/bbtools/bb-tools-user-guide/bbduk-guide/

[4]https://ensembl.gramene.org/Zea_mays/Info/Index

[5]https://www.R-project.org

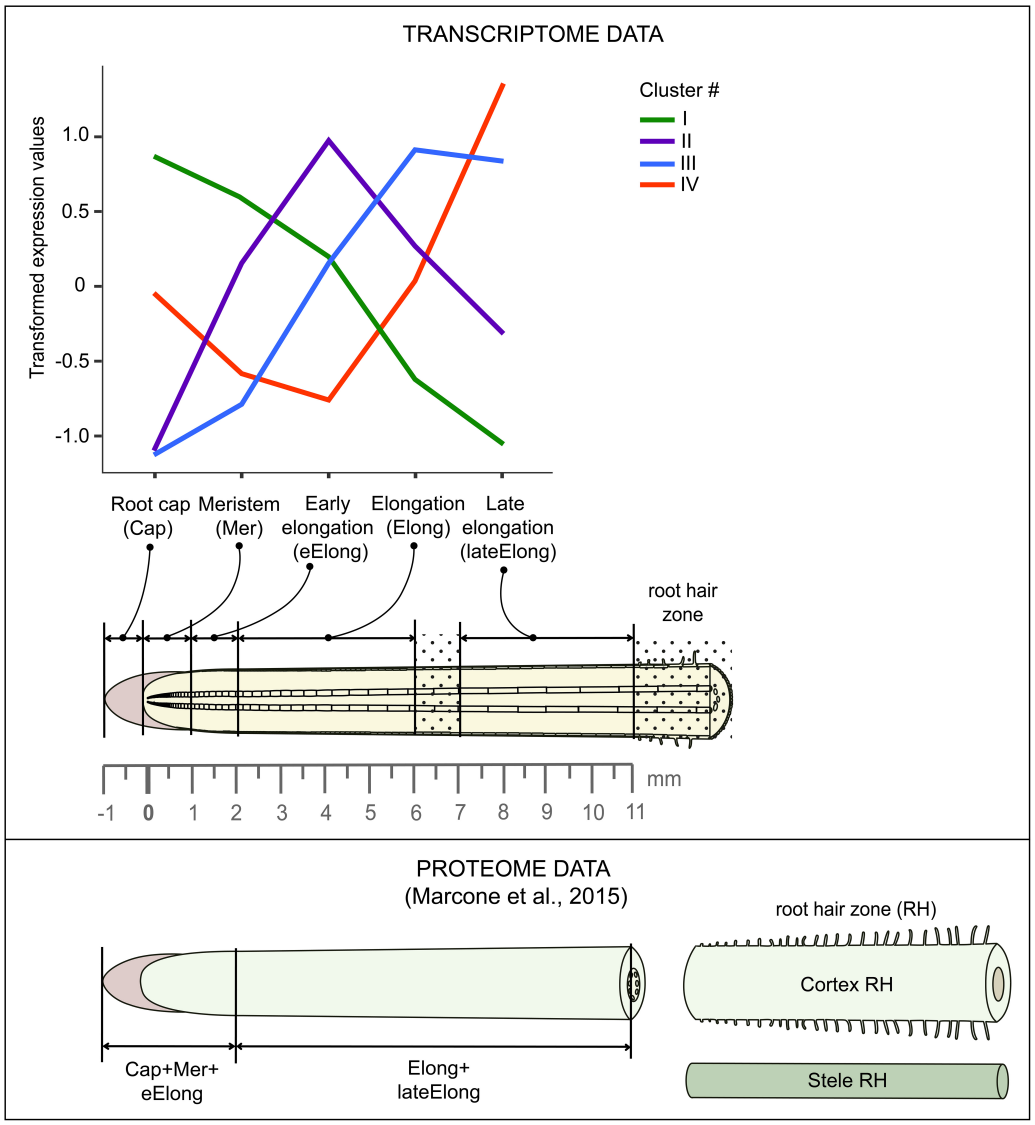

FIGURE 2 | Scheme of maize root sampling for transcriptome and proteome (Marcon et al., 2015) analyses and four clusters of GH transcript abundance obtained by cluster analysis. The dot painting indicates maize root zones that were not used for analyses in this study.

of count data; Love et al., 2014) was used as input for R packages (hclust, heatmap.2, gplots, dendextend) to generate clusters. The normalized expression matrix (TGR > = 16 in at least one sample) was used to generate the targeted co-expression networks by the Comparative Co-Expression Network Construction and Visualization tool (CoExpNetViz) using the Pearson correlation coefficient and "bait" genes that are supposed to be involved in the same biological process or pathway (Tzfadia et al., 2016). The following genes were used as baits: six genes encoding putative maize cellulose synthases of the primary cell wall (*Zm00001d019317*, *Zm00001d037636*, *Zm00001d005250*, *Zm00001d019149*, *Zm00001d009795*, and *Zm00001d005478*); four genes encoding putative maize cellulose synthases of the secondary cell wall (*Zm00001d043477*, *Zm00001d032776*, *Zm00001d020531*, and *Zm00001d005775*); maize homolog of main XyG backbone synthase of rice (*Zm00001d04933*) (Penning et al., 2019; Kozlova et al., 2020). The co-expression networks were visualized using Cytoscape version 3.8.1. (Shannon et al., 2003)[6].

Search for Genes Encoding Maize Polysaccharide Hydrolases and Phylogenetic Analysis

Putative GHs were recognized in the maize B73 genome (RefGen_AGPv4) by the presence of characteristic Pfam domains in the predicted full-length protein sequences. The protein sequences of the maize genome were downloaded from the

[6]http://www.cytoscape.org

Ensembl Plants database (release 47) (Bolser et al., 2016)[7]. Domain search was performed in the HMMer3.3 software using the following domain profiles: PF00232 – GH1; PF01915, PF00933 – GH3; PF00759 – GH9; PF00331 – GH10; PF00722 – GH16; PF00332 – GH17; PF00295 – GH28; PF01301 – GH35; PF06964 – GH51, PF14498 – GH95. The domain profiles were downloaded from Pfam32.0 (El-Gebali et al., 2019)[8]. Sequences with *E*-values higher than 1×10^{-6} were discarded. Protein sequences with high *E*-values were additionally checked in the InterProScan tool implemented in the InterPro database (Mitchell et al., 2019)[9] to confirm the presence of GH domains. Signal peptide presence was predicted with the SignalP tool (Armenteros et al., 2019)[10].

The obtained maize transcripts of GHs were aligned between each other within each GH family using ClustalW (Madeira et al., 2019)[11]. The longest transcripts encoding the sequence with catalytic acid/base residues (revealed by literature data) were used for further phylogenetic analysis. Genes with only one transcript encoding the sequence shorter than 150 amino acids were recognized as pseudogenes.

The protein sequences of *Arabidopsis thaliana* GHs were recognized by Pfam domain name or gene name search and downloaded from the Phytozome v12.1 database (Goodstein et al., 2012)[12] or from the Uniprot database (release 2020_05) (Consortium, 2019)[13]. The protein sequences of other plant genes were obtained from the Uniprot database and from the NCBI Protein database (GenPept) (Benson et al., 2012)[14]. Phylogenetic trees were built as described previously (Kozlova et al., 2020) using the IQ-TREE software (Nguyen et al., 2015). In the case when shortened gene names are used in the trees, corresponding locus IDs can be found in **Supplementary Table 1**.

RESULTS

Cluster analysis of gene expression performed on all investigated GHs revealed four major clusters (**Figure 2**). Cluster I was characterized by the highest levels of expression in root cap and meristem with further decrease. A similar expression pattern in maize root was shown by glycosyltransferases (GTs) putatively involved in the synthesis of XyG (Kozlova et al., 2020). Cluster II was composed of genes whose transcript abundance peaked in the zone of early elongation and was minimal in both root cap and late elongation zone. Similar dynamics of transcript levels in maize root were demonstrated by GTs related to homogalacturonan (HG) biosynthesis (Kozlova et al., 2020). Cluster III contained genes whose expression was highest in the stage of active elongation with a subsequent decrease in the late elongation zone. Such character of expression was typical for GTs involved in the synthesis of primary cell wall cellulose, MLGs, rhamnogalacturonans (RGs), and GAXs (Kozlova et al., 2020). These polysaccharides are abundant in the primary cell wall of grasses. Cluster IV was composed of genes whose transcription was low in the early elongation zone but increased in the active elongation and, especially, late elongation zones.

Expression of Genes Encoding Exo-β-Glucosidases and Endo-β-Glucanases

The glucose-containing polysaccharides of cell walls include only β-linked glucose residues. Thus, we have focused on exo-β-glucosidases (EC 3.2.1.21), which act on terminal glucose, and endo-β-glucanases (EC 3.2.1.4), which are supposed to cut β-glucan backbones. According to the CAZy database (Lombard et al., 2014)[15], plant β-glucosidases occur in the GH1 and GH3 families.

We identified 29 genes encoding proteins of the GH1 family in the maize genome of the fourth assembly (RefGen_B73 AGPv4). All of them possess catalytic nucleophiles and acid/base glutamic acids according to multiple alignments (data not shown). Twenty-two out of the 29 revealed that GH1 genes were expressed in the maize primary root (**Figure 3A**).

The genes encoding GH1 members are distributed over all four clusters. Cluster III (maximum of TGR values in the zone of active elongation) included *ZmBGLU1* that had extremely high TGR values and the highest content of corresponding protein among all the maize GT and GH genes studied (Kozlova et al., 2020; **Figure 3A**). The ZmBGLU1 enzyme is cytosolic and participates in anti-insect defense by releasing aromatic compound DIMBOA from its glucoside form (Babcock and Esen, 1994). The *ZmBGLU3* gene, a homolog of *ZmBGLU1* also expressed at a very high level, however, joined cluster II (**Figure 3A**). The other member of cluster III with a high level of transcripts and high abundance of corresponding protein was *ZmBGLU18*. The ZmBGLU18 homologs in *Arabidopsis* and tomato, AtBGLU43-44 (Xu et al., 2004) and LeMside1 (Mo and Bewley, 2002), were proven to serve as β-mannosidases (EC 3.2.1.25). In the phylogenetic dendrogram of the GH1 protein family, several other maize genes besides *ZmBGLU18* shear the clade with *AtBGLU43-44* (**Supplementary Figure 1**). They belong to clusters I, III, and IV, and some of them are characterized by considerable TGR values and protein content (**Figure 3A**). Thus, highly expressed in maize root isoforms of GH1 proteins are either cytosolic and defense-related or putative mannosidases, and barely contribute to MLG metabolism during growth.

Another protein family that contains putative exo-β-D-glucosidases is GH3. In the maize genome, we identified 17 maize genes encoding GH3 proteins by the simultaneous presence of PF00933 (Glyco_hydro_3, GH3 N-terminal domain) and PF01915 (Glyco_hydro_3_C, GH3 C-terminal domain) Pfam domains in their predicted protein sequences. The phylogenetic tree of GH3 diverges into two distant clades (**Figure 3B**). The ExoI clade was named after the characterized barley

[7]http://plants.ensembl.org/index.html
[8]http://pfam.xfam.org
[9]https://www.ebi.ac.uk/interpro
[10]http://www.cbs.dtu.dk/services/SignalP/
[11]https://www.ebi.ac.uk/Tools/msa/clustalo/
[12]https://phytozome.jgi.doe.gov/pz/portal.html
[13]https://www.uniprot.org/
[14]https://www.ncbi.nlm.nih.gov/protein/
[15]http://www.cazy.org

A

Locus ID	Gene name	Protein family	Cluster #	Cap	Mer	eElong	Elong	late Elong	Plant homologs	Function of homologs	References	Signal peptide	Matched GeneID (RefGen_AGPv3)	Cap+Mer+ eElong	Elong+ lElong	Cortex RH	Stele RH	Whole Root
Zm00001d021119	ZmBGLU14	GH1	I	1 979	1 950	2 265	1 104	1 093	AtBGLU1-11			1-24 aa	GRMZM2G108133	4	0	11	0	0
Zm00001d033651	-	GH1	I	1 658	2 266	2 835	1 880	727	AtBGLU43-44	Mannosidase	Xu et al., 2004	1-35 aa	AC217401.3_FG002	328	504	288	499	510
Zm00001d041173	ZmBGLU3	GH1	II	20 783	44 058	83 985	76 327	20 133	AtBGLU12-16	DIMBOA release	Babcock, Esen 1994	no	GRMZM2G120962	10477	19818	14762	796	4223
Zm00001d042507	-	GH1	II	1 592	2 206	2 864	2 204	1 923	AtBGLU42			no	GRMZM2G044092	112	202	230	44	73
Zm00001d023994	ZmBGLU1	GH1	III	36 838	76 652	150 603	187 424	188 222	AtBGLU12-16	DIMBOA release	Babcock, Esen 1994	no	GRMZM2G016890	12966	42862	53407	2536	51579
Zm00001d033649	ZmBGLU18	GH1	III	2 032	4 574	16 488	30 911	20 561	AtBGLU43-44	Mannosidase	Xu et al., 2004	1-22 aa	GRMZM2G118003	173	878	1313	3918	1417
Zm00001d048099	ZmBGLU26	GH1	III	87	322	3 369	18 596	13 587	AtBGLU40			1-22 aa	GRMZM5G828987	0	4	96	5	19
Zm00001d041168	ZmBGLU7	GH1	III	0	0	133	2 651	6 673	AtBGLU12-16			no	GRMZM2G426467	0	18	0	0	0
Zm00001d028199	ZmBGLU21	GH1	III	103	100	477	1 011	788	AtBGLU40			1-36 aa	GRMZM2G015804	0	0	0	0	0
Zm00001d008435	ZmBGLU15	GH1	III	3	5	25	136	208	AtBGLU44	Mannosidase	Xu et al., 2004	no	AC234160.1_FG003	0	0	4	0	0
Zm00001d012159	-	GH1	IV	169	236	330	714	2 024	AtBGLU42			1-36 aa	AC155376.2_FG005	0	0	0	0	0
Zm00001d025846	ZmBGLU23	GH1	IV	15	23	41	146	1 191	AtBGLU47	Lignification	Escamilla-Trevino et al., 2006	1-29 aa	GRMZM5G810727	0	0	14	0	0
Zm00001d022367	ZmBGLU16	GH1	IV	375	330	232	311	1 078	AtBGLU43	Mannosidase	Xu et al., 2004	1-18 aa	GRMZM2G148176	0	14	12	86	27
Zm00001d046210	ZmBGLU13	GH1	IV	52	18	34	290	990	AtBGLU1-11			1-33 aa	GRMZM2G376416	18	21	98	69	63
Zm00001d014489	ZmBGLU20	GH1	IV	170	159	101	147	819	AtBGLU41			1-19 aa	GRMZM2G163544	0	0	0	0	0
Zm00001d033650	ZmBGLU17	GH1	IV	315	262	108	79	243	AtBGLU43-44	Mannosidase	Xu et al., 2004	1-22 aa	AC217401.3_FG001	0	0	0	0	0
Zm00001d003044	ZmBGLU9	GH1	IV	31	17	12	67	109	AtBGLU45-47	Lignification	Escamilla-Trevino et al., 2006	1-27aa	GRMZM5G845736	0	0	0	0	0

Locus ID	Gene name	Protein family	Cluster #	Cap	Mer	eElong	Elong	late Elong	Plant homologs	Function of homologs	References	Signal peptide	Matched GeneID (RefGen_AGPv3)	Cap+Mer+ eElong	Elong+ lElong	Cortex RH	Stele RH	Whole Root
Zm00001d013268		GH3	I	4 528	6 464	2 183	759	1 552	HvExol / BdBGLC1	MLG degradation / XyG exo-glucosidase	Hrmova et al., 1998 / Rubaines et al., 2019	1-23 aa	GRMZM2G172043	2316	1947	659	1409	845
Zm00001d053982		GH3	I	2 593	2 514	728	27	17				1-32 aa	GRMZM2G023986	649	737	272	6	283
Zm00001d043309		GH3	I	1 182	999	985	689	590	AtBGLC1	XyG exo-glucosidase	Sampedro et al., 2017	1-40 aa	AC197578.4_FG001	no data	no data	no data	no data	no data
Zm00001d038271		GH3	I	150	104	44	19	25				no	GRMZM2G115065	0	0	0	0	0
Zm00001d034017		GH3	II	2 794	3 864	4 607	2 101	3 352	HvExol / AtBGLC1	MLG degradation / XyG exo-glucosidase	Hrmova et al., 1998 / Rubaines et al., 2019	no	GRMZM2G017186	6	58	209	32	18
Zm00001d038272		GH3	II	953	950	1 504	1 230	851				no	GRMZM2G181259	36	38	17	0	0
Zm00001d034015	ZmEXG1	GH3	IV	13 870	30 031	18 477	11 388	58 399	HvExoII	MLG degradation	Kim et al., 2001	no	GRMZM2G147687	2419	4447	7738	7684	3727

B

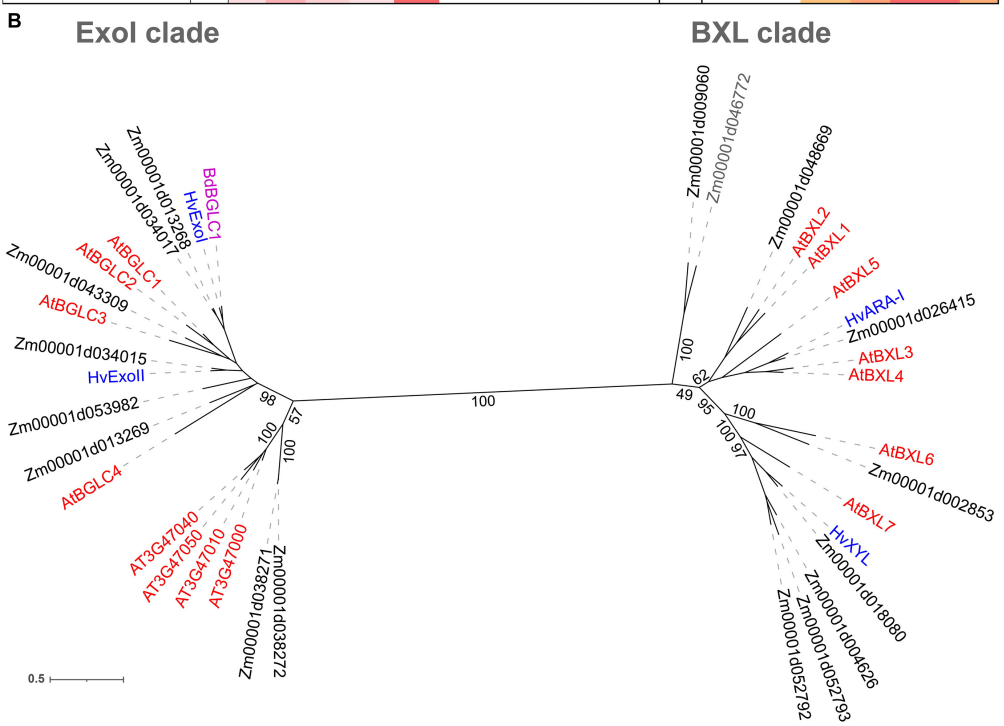

FIGURE 3 | Expression of maize genes encoding putative GH1 and GH3 β-D-glucosidases in maize roots and phylogenetic analysis of plant GH3 family members. **(A)** The level of transcripts (TGR, red-blue heat map) and abundance of corresponding protein (averaged and normalized total spectral counts (Marcon et al., 2015, red-green heat map) of genes encoding putative β-D-glucosidases of GH1 and GH3 protein families in analyzed zones of maize roots. Heat map color-coding was applied to each protein family separately. Genes with expression values below 100 in all the studied samples are not shown. TGR values are sorted from maximum to minimum within each cluster. Maize genes that co-expressed with primary and secondary cell wall cellulose-synthases, and with the XyG backbone synthase are given in blue, red, and green, respectively. Maize GH1 gene names are given according to Gómez-Anduro et al. (2011). ZmEXG1 is named after Kim et al. (2000). Cap, root cap; Mer, meristem; eElong, early elongation zone; Elong, zone of active elongation; lateElong, zone of late elongation before root hair initiation; RH, root hair zone; aa, amino acids; no data, no corresponding peptides were found by Marcon et al. (2015) proteomic analysis. **(B)** The unrooted maximum likelihood phylogenetic tree of plant GH3 members. Maize expressed genes are given in black, and unexpressed (TGR values lower than 16 in all the analyzed root samples) in gray, *Arabidopsis thaliana* genes in red, and barley in blue (only genes encoding enzymes with characterized enzymatic activity are shown (Hrmova et al., 1996; Hrmova and Fincher, 1997; Lee et al., 2003), *Brachypodium distachyon BdBGLC1* (*Bd1g08550*) (Rubianes et al., 2019) is given in purple. The *A. thaliana* gene names follow Minic et al. (2004) for the BXL clade and follow Sampedro et al. (2017) for the Exol clade. Numbers indicate ultrafast bootstrap support values for some branches.

β-glucosidase HvExoI (Hrmova et al., 1998). Besides this barley gene, the ExoI clade contains eight maize genes including *ZmEXG1*, whose product was characterized as β-glucosidase in maize coleoptiles (Kim et al., 2000), and *AtBGLC1-4* encoding β-glucosidases of *A. thaliana* attacking XyGs oligosaccharides (Sampedro et al., 2017; **Figure 3B**). The second clade, BXL, is formed by nine maize homologs of *A. thaliana AtBXL1-7* encoding β-xylosidases/arabinofuranosidases (Minic et al., 2004; **Figure 3B**).

Among all genes encoding GH3 members, *ZmEXG1* was characterized by the highest levels of mRNA in all the maize root zones studied (**Figure 3A**). The expression pattern of *ZmEXG1* demonstrated two peaks: one in the meristem zone with a subsequent decrease during initiation and active elongation growth, and then a dramatic increase in the late elongation stage (**Figure 3A**). The protein content of ZmEXG1 was found to be very high in the elongating part of the root (Marcon et al., 2015). Two maize homologs of *HvExoI* (*Zm00001d034017* and *Zm00001d013268*) displayed similar two-peak dynamics of transcript abundance along the maize root (**Figure 3A**). The amount of protein for the *Zm00001d013268* gene was at a very high level in maize root (Marcon et al., 2015).

Another GH3 member characterized by a considerable amount of detected proteins was *Zm00001d053982*. It belonged to cluster I, with the peak of TGR values in the root cap and meristem zone with a gradual decrease in subsequent zones. *Zm00001d053982* co-expressed with the *Zm00001d049336* gene, which encodes the putative maize XyG backbone synthase. The *Zm00001d049336* gene is a close homolog (Kozlova et al., 2020) of rice *OsCslC3* (Liu et al., 2015).

Besides exo-glucosidases, glucans can be utilized *in planta* by endo-glucanases, which act on non-terminal bonds releasing oligo- or polymer products but not monosaccharides. Plant endo-glucanases are thought to belong to the GH9 and GH17 families.

We identified 27 genes encoding GH9 family proteins in the maize genome by the presence of the PF00759 (Glyco_hydro_9) domain in their predicted amino acid sequences. The gene *Zm00001d002943* is annotated as methyltransferase (Methyltransf_29). However, three out of forty transcripts of this gene encoded sequences with the Glyco_hydro_9 domain instead of the Methyltransf_29 domain. Thus, in our study, it was included in the GH9 family (**Supplementary Figure 2**). Twenty-three out of the 27 identified GH9 genes were expressed in maize root with TGR values higher than 16 in at least one root zone (**Supplementary Figure 2A**). The highest expression level was displayed by maize genes (*Zm00001d002943*, *Zm00001d026712*, *Zm00001d021304*, *Zm00001d033917*, and *Zm00001d013319*) homologous to *KORRIGAN1-3* (*KOR1-3*) of *A. thaliana* (**Supplementary Figure 2**). KORRIGANs are parts of the cellulose synthase complex in many plants starting from the earliest taxa (Lampugnani et al., 2019). Maize homologs of KORRIGANs belonged to the third cluster demonstrating an increasing level of transcript abundance from root cap to the active or late elongation zone. Cluster III also contained maize genes that are homologous to *AtEG11 (At2g32990)* of *A. thaliana* (*Zm00001d044744*, *Zm00001d017978*, *Zm00001d015292*, *Zm00001d020371*, and *Zm00001d051814*) (**Supplementary Figure 2**). Three of them were co-expressed with secondary cell wall cellulose synthases (**Supplementary Figure 2A**). Corresponding proteins for many of these genes were found in the proteomics study by Marcon et al. (2015) mainly in the root hair zone (**Supplementary Figure 2**).

Maize homologs of *AtCEL1*, the gene whose protein product was found to be important for cell wall relaxation during growth in *A. thaliana* (Tsabary et al., 2003), and maize homologs of the related *AtCEL2,3,5* genes transcribed at a significant level only in the root cap falling into cluster I (**Supplementary Figure 2**). Their proteins were detected mainly in the root segment combining root cap, meristem, and early elongation zone (Marcon et al., 2015). This well agrees with the root cap-specific expression of *AtCEL5* and its redundancy in the *Arabidopsis* genome reported by Del Campillo et al. (2004). Maize homologs of *OsGLU1*, a rice gene encoding an enzyme able to cleave β-1,4-glucans and graminaceous hemicelluloses (Yoshida and Komae, 2006), transcribed at a very low level, and no protein products for them were found along the maize root (**Supplementary Figure 2**). Cluster IV was represented by genes having low levels of transcript and protein abundance (**Supplementary Figure 2**). It seems feasible that maize homologs of KORRIGANs, AtEG11, and AtCEL1-5 participate in cellulose biosynthesis in different cell types.

Maize cell walls are capable of autolysis during growth. Hatfield and Nevins purified endoglucanase from maize coleoptiles and characterized it as an enzyme able to cleave MLG, carboxymethylcellulose, and XyG (Hatfield and Nevins, 1986, 1987). The sequence of more than three β-1,4-linked glucose is required for recognition and hydrolysis by this endoglucanase (Hatfield and Nevins, 1987). A BLAST search using the N-terminal amino acid sequence of endoglucanase as query (Inouhe et al., 1999) revealed two corresponding maize *Zm00001d050196* and *Zm00001d050198* genes. Transcript levels of these genes in maize roots were high and significantly increased during elongation growth (**Supplementary Figure 2**). *Zm00001d050198* was co-expressed with primary cell wall-related cellulose-synthases and MLG-synthases, and corresponding proteins were detected at a very high level (Marcon et al., 2015; **Supplementary Figure 2**). However, protein sequences encoded by the *Zm00001d050196* and *Zm00001d050198* genes do not possess any known glycoside hydrolase domains. They are annotated as alpha/beta hydrolases and possess an Abhydrolase_5 (PF12695) Pfam domain.

In the maize genome, 58 genes encoding proteins that possess a Glyco_hydro_17 (PF00332) Pfam domain were identified. The list was reduced to 51 genes by the presence of catalytic glutamic acids that were established by multiple alignments with protein sequences of barley HvEII and HvGII endo-hydrolases. Their crystal structures and catalytic mechanisms were resolved (Varghese et al., 1994; Müller et al., 1998). Forty genes of GH17 were transcribed with TGR values higher than 16 in at least one analyzed root zone (**Supplementary Figure 3**).

In maize root, all the four main clusters of gene expression were represented by genes encoding GH17 proteins. In cluster I, which joins genes with the peak of TGR values in the root cap and meristem, for almost all genes, corresponding peptides were

detected (**Supplementary Figure 3**). The two maize homologs (*Zm00001d028243* and *Zm00001d048055*) of *Arabidopsis PdBG3* also joined cluster I. *PdBG3* was shown to be involved in lateral root formation by the control of callose accumulation (Benitez-Alfonso et al., 2013). Cluster II that included genes with a peak of TGR values in the early elongation zone was highly populated by the GH17 genes. No homologs of any characterized plant enzymes were among them. Clusters III and IV included many genes that were co-expressed with secondary cell wall cellulose-synthases. The corresponding proteins were found predominantly in the stele of the root hair zone (Marcon et al., 2015; **Supplementary Figure 3**). Cluster IV also joined the maize homolog (*Zm00001d038049*) of barley *HvEI-HvEII* (**Supplementary Figure 3**). Barley *HvEI-HvEII* enzymes are 1,3;1,4-β-D-glucan endohydrolases (Varghese et al., 1994). The *Zm00001d038049* gene matches the maize *GRMZM2G137535* gene, which was demonstrated to be an MLG-degrading enzyme in maize leaves (Kraemer et al., 2021). The protein content of *Zm00001d038049* in roots was negligible (**Supplementary Figure 3**).

Expression of Genes Encoding β-D-Galactosidases

β-D-Galactosidases (EC 3.2.1.23) are enzymes that cleave off terminal β-D-galactose. In higher plants, β-D-galactosidases can act on the side chains of XyG, pectins, and other galactose-containing substrates. Plant β-D-galactosidases belong exclusively to the GH35 protein family according to the CAZy database and possess the Glyco_hydro_35 (PF01301) domain. Two glutamic acids in conserved motifs Q-x-E-N-**E**- and W-T-**E**-x-W serve as the proton donor and nucleophile of GH35, respectively (Chandrasekar and van der Hoorn, 2016), so sequences lacking one of these motifs were excluded from further analysis. We identified 14 putative maize β-D-galactosidases, and 11 of them were transcribed in the maize root samples with TGR values higher than 100 in at least one root zone (**Figure 4**).

The expression of about half of the GH35 maize genes corresponded to cluster I with the highest TGR values in the root cap and meristem zones of maize roots (**Figure 4A**). All of them join the same clade as *A. thaliana* pectin-related β-galactosidases *AtBGAL1* and *AtBGAL5* (Gantulga et al., 2008) in the phylogenetic tree except for *Zm00001d022621* (**Figure 4B**). However, these genes were characterized by moderate protein content.

The sole maize β-galactosidase (*Zm00001d028474*) resides in cluster II. It is a homolog for *AtBGAL8* and radish *RsBGAL1*. The latter was characterized as β-galactosidase with specificity to 1,3- and 1,6-linked galactose, but not to 1,4-linked galactose (Kotake et al., 2005). Interestingly, the transcript abundance of this maize gene sharply decreased in the active elongation zone in a way similar to *ZmEXG1* expression (**Figure 3A**). Despite moderate gene expression, the protein products of *Zm00001d028474* accumulated in the elongation zone at a very high level (**Figure 4A**). The *Zm00001d046357* gene demonstrated the highest TGR values among GH35 members in maize root with the peak of expression in the active elongation zone. *Zm00001d046357* joined cluster III and is one of the closest maize homologs for *Arabidopsis AtBGAL1,2,4,12* and flax *LusBGAL* (**Figure 4B**). AtBGAL1, 2, 3, 5, and LusBGAL are involved in the trimming of β-1,4-galactan side chains of RGs-I in *Arabidopsis* and flax, respectively (Gantulga et al., 2008; Roach et al., 2011; Moneo-Sánchez et al., 2018). *Zm00001d046357* joined the co-expression network based on primary cell wall cellulose synthases that also included *ZmGALS1*, the predicted maize β-1,4-galactan synthase (Kozlova et al., 2020).

The cluster IV joined *Zm00001d041880* and *Zm00001d042654* homologs of *AtBGAL9* and *AtBGAL10*, respectively. They displayed considerable levels of transcripts and proteins along the maize root (**Figure 4**) and co-expressed with secondary cell wall-related cellulose synthases. AtGAL10 is the main β-galactosidase of *A. thaliana* with specificity against XyG. This gene is highly expressed in elongating tissues. The insertional mutation of *AtGAL10* resulted in an unusual pattern of side chain distribution along the XyG molecule and growth defects (Sampedro et al., 2012).

Expression of Genes Encoding Pectinases

Plant pectin-related GHs include exo- (EC 3.2.1.67) and endo-polygalacturonases (EC 3.2.1.15) belonging to the GH28 family. The maize genome contains 53 genes encoding GH28 members, although only 27 of them had TGR values over 16 in at least one studied root zone (**Supplementary Figure 4**). All maize genes whose transcript and protein abundance in maize root varied significantly during growth belonged to one divergent clade of the GH28 phylogenetic tree (**Supplementary Figure 4B**). In *Arabidopsis*, this clade was defined by Cao (2012) as the group V of polygalacturonases. This clade still has no characterized representatives. Genes encoding maize genes homologous to studied plant enzymes had relatively low transcript levels, and no proteins were detected (**Supplementary Figure 4**).

Expression of Genes Encoding Enzymes Degrading Xylose- and Arabinose-Containing Substrates

Plant β-xylosidases (EC 3.2.1.37) belong to the GH3 family. They occupy one of the two clades of GH3, which is designated as the BXL clade (**Figure 3B**). Nine maize genes occupy the BXL clade, and eight of them were expressed in maize root (**Figure 5**). Besides maize genes, the BXL clade includes *Arabidopsis* genes encoding β-xylosidases and bifunctional arabinofuranosidase/β-xylosidase *AtBXL1-7* (Minic et al., 2004), and barley *HvARA-I* and *HvXYL* (Lee et al., 2003).

The highest transcript and protein levels among maize GH3 BXL clade members were shown by the *Zm00001d018080* and *Zm00001d026415* genes (**Figure 5A**). According to the phylogenetic dendrogram of GH3, the *Zm00001d018080* and *Zm00001d026415* genes are homologs of *HvXYL* and *HvARA-I,* respectively (**Figure 3B**). HvXYL and HvARA-I are β-xylosidase and bifunctional α-L-arabinofuranosidase/β-D-xylosidase, respectively, that were purified from barley seedlings (Lee et al., 2003). Their maize homologs had peak TGR values in the

A

Min Max

Min 50 Max

Gene ID	Protein family	Cluster #	Cap	Mer	eElong	Elong	late Elong	Plant homologs	Function of homologs	References	Signal peptide	Matched GeneID (RefGen_AGPv3)	Cap+Mer+ eElong	Elong+ lElong	Cortex RH	Stele RH	Whole Root
Zm00001d027803	GH35	I	2 718	2 324	1 955	1 144	947	AtBGAL3, 5	Removes 1,4 and 1,3-linked Gal from pectins	Gantulga et al., 2008	1-21 aa	GRMZM2G417455	56	28	2	16	8
Zm00001d048440	GH35	I	1 695	2 283	2 677	857	496	AtBGAL3, 5	Removes 1,4 and 1,3-linked Gal from pectins	Gantulga et al., 2008	1-22 aa	GRMZM2G178106	45	116	2	0	0
Zm00001d044290	GH35	I	1 334	1 890	2 760	1 566	738	AtBGAL1, 2, 4, 12	β-1,4-galactan degradation	Moneo-Sanchez et al., 2019	1-27 aa	GRMZM2G130375	23	24	14	0	8
Zm00001d022621	GH35	I	900	770	841	846	364	AtBGAL11,13-14			1-25 aa	GRMZM2G386824	0	0	0	0	0
Zm00001d053585	GH35	I	614	484	356	63	90	AtBGAL1, 2, 4, 12	β-1,4-galactan degradation	Moneo-Sanchez et al., 2019	1-38 aa	GRMZM2G121495	0	0	0	3	0
Zm00001d048783	GH35	I	398	201	139	135	167	AtBGAL3,5	Removes 1,4 and 1,3-linked Gal from pectins	Gantulga et al., 2008	no	GRMZM5G891430	no data	no data	no data	no data	no data
Zm00001d028474	GH35	II	905	3 794	6 665	2 806	4 568	RsBGAL1	Removes 1,3-, 1,6-linked Gal	Kotake et al., 2005	1-27 aa	GRMZM2G127123	219	1030	859	1187	1231
Zm00001d046357	GH35	III	128	1 655	8 986	15 121	10 619	AtBGAL1, 2, 4, 12	β-1,4-galactan degradation	Moneo-Sanchez et al., 2019	1-26 aa	GRMZM2G027385	0	342	464	1494	646
Zm00001d041880	GH35	IV	472	628	932	2 616	8 397	AtBGAL9			1-37 aa	GRMZM2G073584	11	6	251	76	107
Zm00001d042654	GH35	IV	1 275	1 364	1 319	1 977	3 103	AtBGAL10	XyG β-galactosidase	Sampedro et al., 2012	1-25 aa	GRMZM2G038281	232	155	140	301	164
Zm00001d010212	GH35	IV	308	7	6	37	30	AtBGAL6			1-23 aa	AC234152.1_FG005	0	0	0	0	0

B

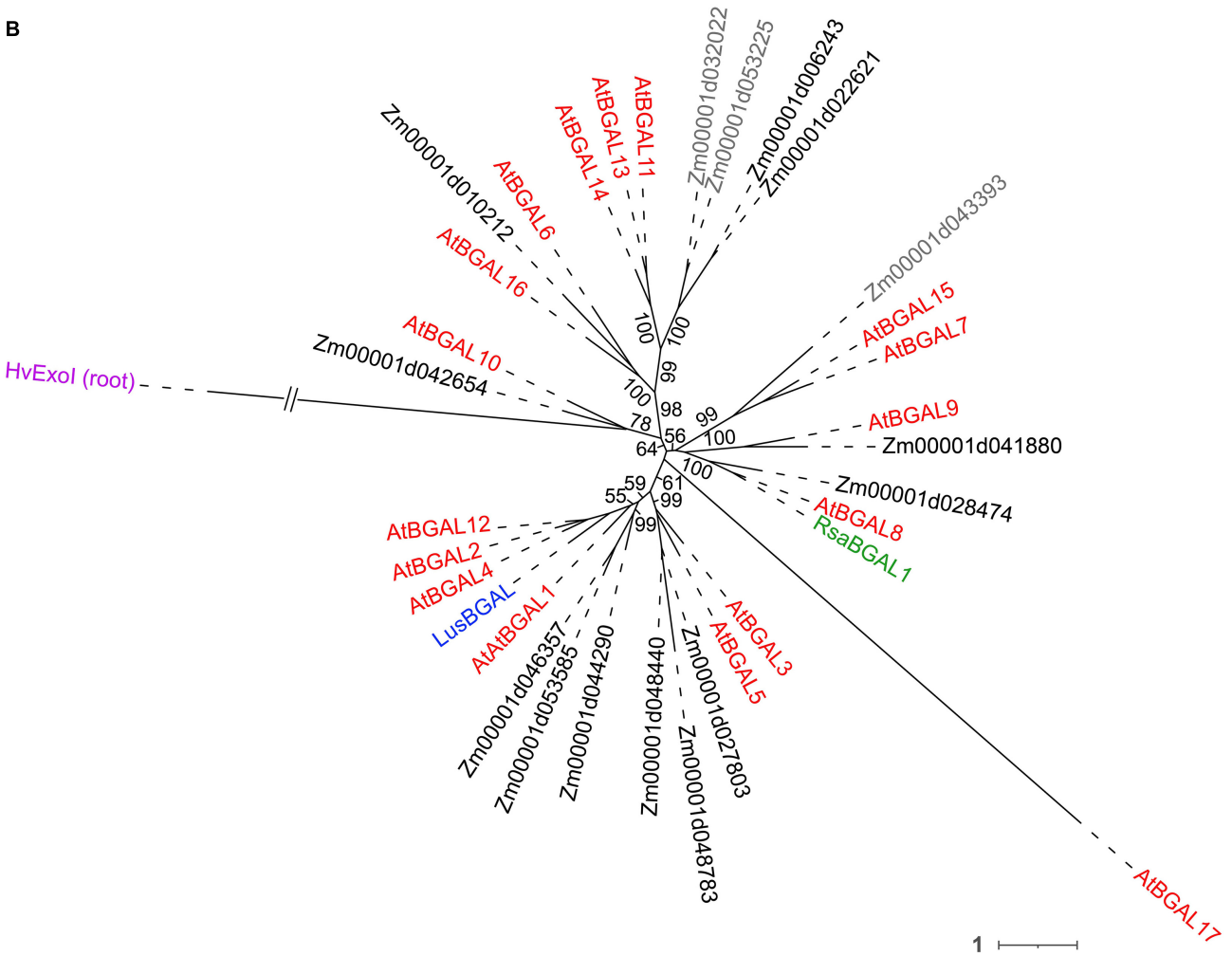

FIGURE 4 | Expression of maize genes encoding putative GH35 β-D-galactosidases in maize roots and phylogenetic analysis of plant GH35 family. **(A)** The level of transcripts (TGR, red-blue heat map) and abundance of corresponding proteins (averaged and normalized total spectral counts (Marcon et al., 2015), red-green heat map) of genes encoding putative β-D-galactosidases of the GH35 protein family in various zones of maize roots. Genes with expression values below 100 in all the studied samples are not shown. TGR values are sorted from maximum to minimum within each cluster. Maize genes co-expressed with primary and secondary cell wall cellulose-synthases, and with the XyG backbone synthase are given in blue, red, and green, respectively. XyG, xyloglucan; Gal, galactose; aa, amino acids; Cap, root cap; Mer, meristem; eElong, early elongation zone; Elong, zone of active elongation; lateElong, zone of late elongation before root hair initiation; RH, root hair zone; no data, no corresponding peptides were found by Marcon et al. (2015) proteomic analysis. **(B)** Unrooted maximum likelihood phylogenetic tree of GH35 protein family members. Maize expressed genes are given in black, and unexpressed (TGR values lower than 16 in all the analyzed root samples) in gray, *Arabidopsis thaliana* genes in red, flax *LusBGAL* (Roach et al., 2011) in blue, and radish *RsBGAL1* (Kotake et al., 2005) in green. *Arabidopsis* gene names follow Chandrasekar and van der Hoorn (2016). *HvExoI* was used as outgroup, and branch length was shortened. Numbers indicate ultrafast bootstrap support values for some branches.

A

Min Max

Gene ID	Gene name	Protein family	Cluster #	Cap	Mer	eElong	Elong	late Elong	Plant homologs	Signal peptide	Matched GeneID (RefGen_AGPv3)	Cap+Mer+ eElong	Elong+ lElong	Cortex RH	Stele RH	Whole Root
Zm00001d048669		GH3	I	680	538	477	330	307	AtBXL1-2	no	GRMZM2G146192	13	0	2	17	43
Zm00001d009060		GH3	II	764	1 589	4 373	4 122	954		1-39 aa	GRMZM2G111998	38	155	184	47	253
Zm00001d052792		GH3	II	261	570	737	468	1 378	AtBXL7 / HvXYL	1-24 aa	GRMZM2G044107	0	28	59	362	49
Zm00001d018080		GH3	III	20	725	6 440	10 257	6 064	AtBXL7 / HvXYL	1-30 aa	GRMZM2G035503	0	313	269	2814	869
Zm00001d026415		GH3	III	1 684	2 675	7 659	7 658	5 896	AtBXL3-4 / HvARA-I	no	GRMZM2G136895	116	391	484	815	717
Zm00001d052793		GH3	III	25	176	689	1 151	968	AtBXL7 / HvXYL	no	GRMZM2G343828	0	0	6	161	42
Zm00001d004626		GH3	III	2	0	16	116	203	AtBXL7 / HvXYL	1-25 aa	AC234091.1_FG001	0	0	0	0	0
Zm00001d002853		GH3	IV	1 241	1 159	949	1 443	5 093	AtBXL6	1-17 aa	GRMZM2G177923	2	11	110	131	5

Gene ID	Gene name	Protein family	Cluster #	Cap	Mer	eElong	Elong	late Elong	Plant homologs	Signal peptide	Matched GeneID (RefGen_AGPv3)	Cap+Mer+ eElong	Elong+ lElong	Cortex RH	Stele RH	Whole Root
Zm00001d030468	Zmxyl7	GH10	II	6	79	155	20	0	AtXYN4-5	1-25 aa	GRMZM2G170839	0	0	0	0	0
Zm00001d028398	Zmxyl5	GH10	III	439	159	916	1 986	1 045		no	GRMZM2G108032	7	8	0	19	6
Zm00001d019586	Zmxyl1	GH10	III	915	961	1 383	1 869	1 471	AtXYN1-3	no	GRMZM2G058128	13	18	12	31	11
Zm00001d039946	Zmxyl3	GH10	III	0	1	45	734	1 907	AtXYN1-3	no	GRMZM2G003794	0	0	19	608	30
Zm00001d039958	Zmxyl2	GH10	III	29	4	15	61	42	AtXYN1-3	no	GRMZM2G031004	0	0	0	0	0
Zm00001d013561	WI5	GH10	IV	0	0	0	57	757	AtXYN1-3	no	GRMZM2G002260	0	0	0	555	7
Zm00001d016558	Zmxyl4	GH10	IV	27	8	20	58	100	AtXYN1-3	no	GRMZM2G004856	no data	no data	no data	no data	no data

Gene ID	Gene name	Protein family	Cluster #	Cap	Mer	eElong	Elong	late Elong	Plant homologs	Signal peptide	Matched GeneID (RefGen_AGPv3)	Cap+Mer+ eElong	Elong+ lElong	Cortex RH	Stele RH	Whole Root
Zm00001d052425	ZmaABF2	GH51	I	490	399	145	71	99		no	GRMZM2G077299	0	0	46	0	0
Zm00001d028952	ZmaABF5	GH51	III	197	126	185	1 530	3 868		no	GRMZM2G180889	0	0	0	0	0
Zm00001d044648	ZmaABF1	GH51	IV	1 058	737	556	1 920	6 726		1-24 aa	GRMZM2G006130	0	0	38	218	74
Zm00001d007195	ZmaABF4	GH51	IV	236	136	115	288	1 276		1-29 aa	GRMZM2G097277	0	0	0	6	0
Zm00001d048993	ZmaABF3	GH51	IV	0	0	0	40	384		1-24 aa	GRMZM2G393002	3	0	0	0	0

B

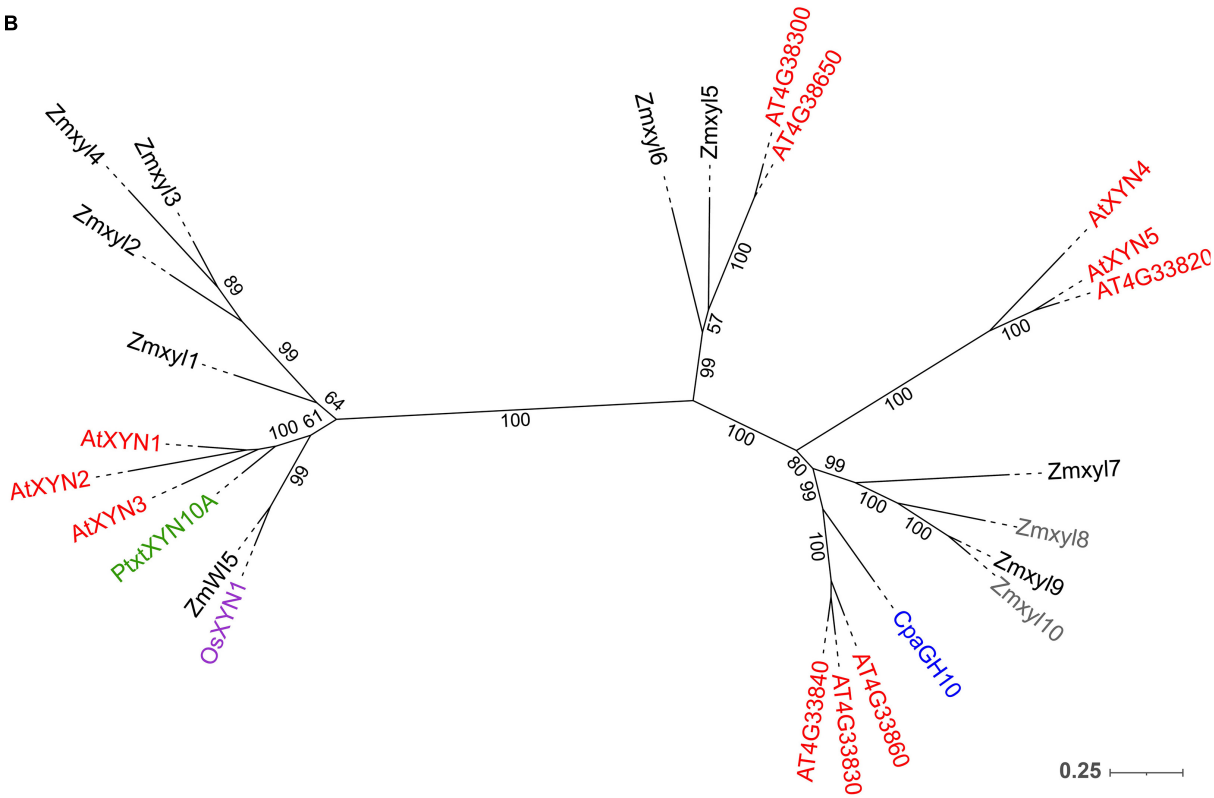

FIGURE 5 | Expression of maize genes encoding putative β-D-xylosidases, xylanases, and α-L-arabinofuranosidases of the GH3, GH10, and GH51 families in maize roots and phylogenetic analysis of plant GH10 family. **(A)** The level of transcripts (TGR, red-blue heat map) and abundance of corresponding proteins (averaged and normalized total spectral counts (Marcon et al., 2015), red-green heat map) of genes encoding putative β-D-xylosidases, xylanases, and α-L-arabinofuranosidases in various zones of maize roots. Genes with expression values below 100 in all the studied samples are not shown. TGR values are sorted from maximum to minimum within each cluster. Maize genes co-expressed with primary and secondary cell wall cellulose-synthases are given in blue and red, respectively. Maize gene names

(Continued)

FIGURE 5 | for GH10 follow Hu et al. (2020). Maize gene names for GH51 follow Kozlova et al. (2015). Cap, root cap; Mer, meristem; eElong, early elongation zone; Elong, zone of active elongation; lateElong, zone of late elongation before root hair initiation; RH, root hair zone; aa, amino acids; no data, no corresponding peptides were found in any of the studied samples. **(B)** Unrooted maximum likelihood phylogenetic dendrogram of plant GH10 family members. Maize expressed genes are given in black, and unexpressed (TGR values lower than 16 in all the analyzed root samples) in gray, *Arabidopsis thaliana* in red, poplar (Derba-Maceluch et al., 2015), rice (Tu et al., 2020), and papaya (Johnston et al., 2013) genes are given in green, pink, and purple, respectively. *Arabidopsis thaliana* gene names follow Suzuki et al. (2002), and maize gene names follow Hu et al. (2020). Numbers indicate ultrafast bootstrap support values.

active elongation stage and significant protein content in maize root (Marcon et al., 2015; **Figure 5A**). Relatively low levels of transcript and protein abundances were displayed by maize BXL clade members representing clusters I and IV (**Figure 5A**). Cluster II (TGR values are highest in the early elongation zone) included two other members of this clade. One of them (*Zm00001d052792*) is also a homolog of *HvXYL*, while the other (*Zm00001d009060*) is located in the remote branch of the GH3 phylogenetic tree rather distant from any of its characterized members (**Figure 3B**).

Enzymes called xylanases (EC 3.2.1.8) cleave the backbone of xylan chains and act as endo-hydrolases. Seventeen GH families contain endo-xylanases according to the CAZy database; however, plant endo-xylanases reside only in the GH10 protein family (Hu et al., 2020). The phylogenetic tree of the plant GH10 family splits into two clades (**Figure 5B**). One clade includes the majority of plant xylanases characterized to date, *Arabidopsis* AtXYN-1, *Populus* PtxtXYN10A, maize WI5, and rice OsXYN1 (**Figure 5B**). For all of them, roles in secondary cell wall formation and vascular system differentiation have been shown (Suzuki et al., 2002; Derba-Maceluch et al., 2015; Hu et al., 2020; Tu et al., 2020). The other clade of GH10 has only two characterized members. One of them, ZmXYL, was described as the most abundant enzyme on the surface of maize pollen grains (Bih et al., 1999). This enzyme operates as xylanase, which facilitates pollen tube penetration through the silk by means of xylan degradation (Suen and Huang, 2007). We designated it as *Zmxyl7* following Hu et al. (2020). Another characterized member of this clade is papaya *CpaEXY1* (*CpaGH10*), the xylanase that acts during fruit softening (Johnston et al., 2013; **Figure 5B**).

Eleven maize genes encoding putative xylanases were identified in the maize genome by Hu et al. (2020). Nine of them were transcribed in primary maize root (**Figure 5A**). The *Zmxyl1* and *Zmxyl5* genes displayed the highest transcript levels in the elongation zone, but their protein content was low (**Figure 5A**). *Zmxyl3* had its highest TGR value in the late elongation zone similar to *ZmWI5*. The corresponding proteins for both these genes were found exclusively in the stele of the root hair zone (Marcon et al., 2015; **Figure 5A**).

Plant α-L-arabinofuranosidases (EC 3.2.1.55) were classified into the GH3 and GH51 families (CAZy database). Putative maize GH51 α-L-arabinofuranosidases were identified by the presence of characteristic PF06964 domain and named following our previous study (Kozlova et al., 2015). Five out of six predicted GH51 genes were transcribed in maize root. *ZmaABF5* and *ZmaABF1* were expressed at high levels in the late elongation zone and co-expressed with maize secondary cell wall cellulose synthases. Proteins of α-L-arabinofuranosidases were detected only in the root hair zone of maize root (**Figure 5A**).

Expression of Genes Encoding Xyloglucan Endotransglycosylases/Hydrolases

Xyloglucan (XyGs) can be modified *in planta* by xyloglucan endotransglucosylases/hydrolases (XTHs) belonging to the GH16 protein family. This group is composed of XyG endohydrolases (EC 3.2.1.151, XEHs) and XyG endotransglycosylases (EC 2.4.1.207, XETs). XEHs cleave the backbone of XyGs as usual β-1,4-endoglucanases, releasing two parts of an initial polymer as individual molecules. In the case of XETs, the first step of catalysis is the same but the non-reducing terminus of a cleaved XyG is retained in the catalytic site and serves as donor substrate for further stage. In the second step, the XET enzyme transfers the bound portion of XyG into another XyG molecule (acceptor). This type of reaction is called homo-transglycosylation. When either a donor or an acceptor substrate is presented by a polysaccharide other than XyG, the reaction is described as hetero-transglycosylation (Stratilova et al., 2020).

Xyloglucan endotransglucosylases/hydrolases (XTHs) were recognized in the maize genome by the presence of the PF00722 domain and conserved motif E-x-D-x-E. A total of 36 putative XTH genes were identified in the maize genome, and 31 of them were expressed in maize primary root (**Figures 6**, **7**).

Maize genes that demonstrate peak of transcription in the root cap and meristem joined cluster I. Most of them represented the *Poaceae*-specific subclade in the plant GH16 phylogenetic tree together with barley hetero-transglycosylases *HvXET3, 4*, and *6* (Hrmova et al., 2009; Stratilova et al., 2020). Despite moderate TGR values of cluster I members, the content of corresponding proteins was extremely high in the elongating part of the root (Marcon et al., 2015; **Figure 6**). Two members of cluster I (*Zm00001d050201* and *Zm00001d002409*) were co-expressed with the putative XyG backbone synthase of maize (**Figure 6**).

Cluster II contained the *Zm00001d052651*gene that displayed the highest TGR values among all the maize XTHs (**Figure 6**). The *Zm00001d052651* gene is the sole homolog to *Arabidopsis AtXTH4*, and *5*, and barley *HvXET5* (**Figure 7**). AtXTH4 is involved in cell wall remodeling during fiber expansion and intrusive growth (Kushwah et al., 2020) in *Arabidopsis*. HvXET5 was described as a hetero-transglycosylase, which mediates XyGs tailoring to MLG and cellulose (Hrmova et al., 2007) in barley. The protein abundance of *Zm00001d052651* increased 10 times between the maize root tip and root hair zone (**Figure 6**). Two more putative hetero-XETs of maize, homologous to *BdXTH8* of *Brachypodium* and *HvXET3,4* of barley, belonged to cluster II (**Figure 6**). BdXTH8 connects XyG and MLG (Fan et al., 2018),

Gene ID	Protein family	Cluster #	Cap	Mer	eElong	Elong	late Elong	Plant homologs	Function of homologs	References	Signal peptide	Matched GeneID (RefGen_AGPv3)	Cap+Mer +eElong	Elong+ lElong	Cortex RH	Stele RH	Whole Root
Zm00001d050201	GH16	I	2 065	2 351	1 020	50	9				1-32 aa	GRMZM2G104651	1391	1876	383	14	520
Zm00001d027368	GH16	I	1 132	1 394	1 628	1 024	220				no	GRMZM2G030173	792	1044	1055	602	1123
Zm00001d026251	GH16	I	380	1 183	1 508	305	38				1-24 aa	GRMZM2G091303	348	1964	685	0	42
Zm00001d002409	GH16	I	447	402	284	57	8				1-31 aa	GRMZM2G091118	261	259	101	0	104
Zm00001d020392	GH16	I	751	197	48	12	19				1-30 aa	GRMZM2G319798	no data	no data	no data	no data	no data
Zm00001d002412	GH16	I	384	20	0	3	1				1-26 aa	GRMZM2G091191	7	0	0	0	0
Zm00001d026250	GH16	I	130	9	2	1	4				1-27 aa	GRMZM2G142857	no data	no data	no data	no data	no data
Zm00001d052651	GH16	II	1 934	9 075	36 731	52 695	12 227	HvXET5 / AtXTH4-5	Transglycosylation of XyG/MLG/cellulose / Fiber expansion and intrusive growth	Hrmova et al., 2007 / Kushwah et al., 2020	1-23 aa	GRMZM2G004699	243	2040	1401	930	2224
Zm00001d024071	GH16	II	489	1 187	4 385	5 903	1 934	BdXTH8 / EfHTG	Transglycosylation of XyG/MLG/cellulose	Herburger et al., 2021 / Fan et al., 2018	1-29 aa	GRMZM2G128876	32	120	4	180	30
Zm00001d014613	GH16	II	788	1 882	2 643	2 570	1 456	HvXET3-4	Transglycosylation of XyG/MLG/$(\alpha\text{-GalAp})_5$	Stratilová et al., 2020	1-22 aa	GRMZM2G413006	87	161	0	50	0
Zm00001d021667	GH16	II	1 219	2 489	2 638	971	876	AtXTH8			1-39 aa	GRMZM2G174855	377	741	176	475	217
Zm00001d024382	GH16	III	7	47	3 031	33 079	18 755	BdXTH8 / EfHTG	Transglycosylation of XyG/MLG/cellulose	Herburger et al., 2021 / Fan et al., 2018	1-23 aa	GRMZM2G063566	7	416	752	2991	743
Zm00001d024379	GH16	III	1 293	1 870	4 767	16 878	16 714	BdXTH8 / EfHTG	Transglycosylation of XyG/MLG/cellulose	Herburger et al., 2021 / Fan et al., 2018	1-26 aa	GRMZM2G364748	52	439	40	550	303
Zm00001d024386	GH16	III	7	6	441	10 375	15 436	BdXTH8 / EfHTG	Transglycosylation of XyG/MLG/cellulose	Herburger et al., 2021 / Fan et al., 2018	1-24 aa	GRMZM2G119783	0	20	1391	4604	1330
Zm00001d017699	GH16	III	269	242	683	4 999	3 708	AtXTH29-30			1-28 aa	GRMZM2G060837	no data	no data	no data	no data	no data
Zm00001d009309	GH16	III	194	596	1 605	3 432	2 728	HvXET3-4	Transglycosylation of XyG/MLG/$(\alpha\text{-GalAp})_5$	Stratilová et al., 2020	1-24 aa	AC210669.3_FG001	no data	no data	no data	no data	no data
Zm00001d014617	GH16	III	22	64	273	2 050	4 494	HvXET3-4	Transglycosylation of XyG/MLG/$(\alpha\text{-GalAp})_5$	Stratilová et al., 2020	1-24 aa	GRMZM2G166944	0	0	24	274	24
Zm00001d002410	GH16	III	32	54	172	2 042	2 512				1-26 aa	GRMZM2G392125	14	378	337	76	26
Zm00001d015977	GH16	III	501	958	922	1 563	1 527	AtXTH26	Transglucosylation of XyG:XyG only, RH zone specific, reduced growth when applicated to Elong zone	Maris et al., 2009	1-36 aa	GRMZM5G886185	6	24	99	44	231
Zm00001d053320	GH16	III	0	4	91	467	779	AtXTH26	Transglucosylation of XyG:XyG only, RH zone specific, reduced growth when applicated to Elong zone	Maris et al., 2009	1-25 aa	GRMZM2G112619	0	0	172	0	165
Zm00001d047970	GH16	III	119	112	131	197	126				1-23 aa	GRMZM2G039919	0	0	0	0	0
Zm00001d046007	GH16	III	0	5	45	150	113	AtXTH26	Transglucosylation of XyG:XyG only, RH zone specific, reduced growth when applicated to Elong zone	Maris et al., 2009	1-27 aa	GRMZM2G143473	0	0	14	0	25
Zm00001d030103	GH16	III	4	0	4	77	349	AtXTH29-30			1-22 aa	GRMZM2G070271	no data	no data	no data	no data	no data
Zm00001d027313	GH16	IV	0	0	2	116	1 792	AtXTH31-32	Hydrolysis of XyG	Kaewthai et al., 2013	1-23 aa	GRMZM2G388684	0	0	605	178	627
Zm00001d029814	GH16	IV	6	13	84	151	928	AtXTH31-32	Hydrolysis of XyG	Kaewthai et al., 2013	1-34 aa	GRMZM2G113761	0	0	822	181	466
Zm00001d002192	GH16	IV	662	426	82	345	763	AtXTH9	Involved in SCW formation	Kushwah et al., 2020	no	GRMZM2G180870	17	0	0	0	0
Zm00001d002193	GH16	IV	989	417	204	667	748	AtXTH9	Involved in SCW formation	Kushwah et al., 2020	1-34 aa	GRMZM2G180870	17	0	0	0	0

Gene ID	Protein family	Cluster #	Cap	Mer	eElong	Elong	late Elong	Plant homologs	Function of homologs	References	Signal peptide	Matched GeneID (RefGen_AGPv3)	Cap+Mer +eElong	Elong+ lElong	Cortex RH	Stele RH	Whole Root
Zm00001d030471	GH95	IV	406	697	1 645	2 736	2 980	AtAXY8	Removes Fuc from XXFG XyG	Günl et al., 2011	no	GRMZM2G019673	29	84	67	131	106

Gene ID	Protein family	Cluster #	Cap	Mer	eElong	Elong	late Elong	Plant homologs	Function of homologs	References	Signal peptide	Matched GeneID (RefGen_AGPv3)	Cap+Mer +eElong	Elong+ lElong	Cortex RH	Stele RH	Whole Root
Zm00001d039994	GH31		2062	893	510	311	1995	AtXYL1	Removes Xyl from XyG	Sampedro et al., 2010		GRMZM2G009282	252	202	204	174	152

FIGURE 6 | Expression of maize genes encoding putative xyloglucan endotransglucosylases/hydrolases (XTHs) of GH16 in maize roots. The level of transcripts (TGR, red-blue heat map) and abundance of corresponding proteins (averaged and normalized total spectral counts (Marcon et al., 2015), red-green heat map) of genes encoding putative XyG endotransglycosylases/hydrolases of the GH16 protein family in various zones of maize roots. Genes with expression values below 100 in all the studied samples are not shown. TGR values are sorted from maximum to minimum within each cluster. Maize genes co-expressed with primary and secondary cell wall cellulose-synthases, and the XyG backbone synthase are labeled in blue, red, and green, respectively. XyG, xyloglucan; MLG, mixed-linkage glucan; SCW, secondary cell wall, Cap, root cap; Mer, meristem; eElong, early elongation zone; Elong, zone of active elongation; lateElong, zone of late elongation before root hair initiation; RH, root hair zone; no data, no corresponding peptides were found by Marcon et al. (2015) proteomics analysis.

and HvXET3-4 are able to join XyG and HG pentasaccharides (Stratilova et al., 2020). Corresponding proteins were abundant in the elongating part of the maize root (**Figure 6**).

The highest TGR values and protein content in cluster III (expression is maximum at active elongation) were also displayed by maize homologs of *Brachypodium BdXTH8* and barley *HvXET3-4* (**Figure 6**). The transcript and protein abundance of putative maize hetero-transglycosylases of clusters II and III indicates the importance of reactions of this type for elongation growth initiation and realization. Putative maize homo-transglycosylases [homologs of *AtXTH26* that were characterized by Maris et al. (2009)] were also present in cluster III. Their TGR values and protein levels were lower than those of hetero-transglycosylases of the same cluster

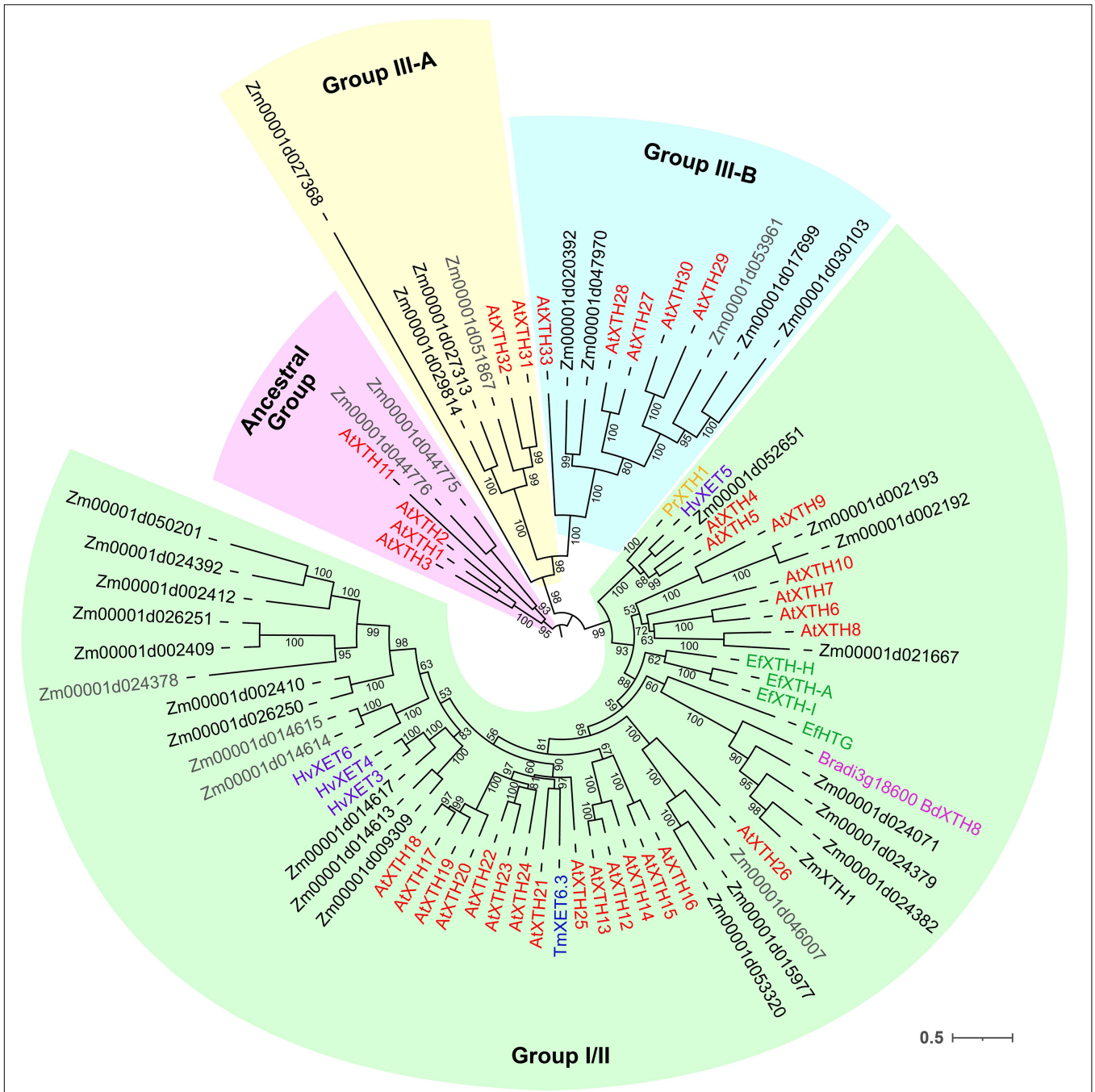

FIGURE 7 | Unrooted maximum likelihood phylogenetic analysis of the plant GH16 family. Maize genes are given in black font for expressed genes and gray for those having TGR values lower than 16 in all the analyzed root samples, and *Arabidopsis thaliana* genes are given in red. Characterized XTHs of barley (Hrmova et al., 2007, 2009), *Equisetum* (Herburger et al., 2021), nasturtium (Crombie et al., 1998), and *Brachypodium* (Fan et al., 2018) are shown in purple, green, blue, and magenta, respectively. Numbers indicate ultrafast bootstrap support values for some branches.

(**Figure 6**). The highest transcription levels in cluster IV (late elongation zone-specific) were demonstrated by maize homologs of *AtXTH31* and *32* (**Figure 7**). These genes encode XEHs in *Arabidopsis* (Kaewthai et al., 2013). Proteins of their maize homologs appeared only in the root hair zone of maize primary root (**Figure 6**).

Glycoside Hydrolase Activities Along Maize Root

Glycoside hydrolase (GH) activities in clarified homogenates of maize root segments were assayed by the rate of hydrolysis of corresponding synthetic substrates. The β-glucosidase activity was highest among all the studied enzymatic activities in all

root zones (**Figure 8A**). It was followed by β-D-galactosidase, α-L-arabinofuranosidase (Kozlova et al., 2015), and β-D-xylosidase activities (**Figure 8B**). The activities of β-glucosidase, β-galactosidase, and β-xylosidase significantly increased from the meristem to the elongation zone and remained at the same level in the late elongation zone (**Figures 8A,B**). The activity of 1,3;1,4-β-D-glucan endohydrolase (lichenase), in contrast, was constant in all the analyzed root zones except for the active elongation zone where it was significantly reduced (**Figure 8B**). In clarified homogenates, endo-β-xylanase activity was detected using linear xylopentaose as a substrate being undetectable with xylobiose and xylotriose substrates. Xylanase activity was higher in the active elongation and late elongation zones than in meristem (**Figure 8B**). We were unable to detect α-L-fucosidase activity in clarified homogenates using *p*-nitrophenyl-α-L-fucopyranoside as a substrate.

β-D-Glucosidase and β-D-galactosidase activities were also analyzed on cross-sections of maize primary root using Res-βDGlc*p* and Res-βDGal*p*, respectively (**Figure 8C**). In contrast to measurements on clarified homogenates, rates of resorufin release from these two substrates on maize root sections were similar (**Figure 8C**). For both probes, the highest intensity of fluorescence was observed in meristem and the early elongation zone, and especially in root mucilage. Tissues of the central cylinder displayed lower staining than the cortical part of the maize root (**Figure 8C**). In contrast to the results of assays with *p*-nitrophenyl glycosides, a visible decrease in staining by resorufin glycosides was observed in the active and late elongation zones. There are two possible explanations for this discrepancy. First, the contribution of cytoplasmic enzymes to total measured activity may grow during the course of elongation growth. Second, the section of the meristem zone included several layers of cells because of their small size, while the elongation and late elongation zone sections contained only one layer where all cells were dissected. Thus, the signal produced by the meristem section was generated by a higher amount of cell walls and cytoplasm than one of elongation and late elongation zones sections. Nevertheless, the high fluorescent signal observed in cell walls after treatment with Res-βDGal*p* and Res-βDGlc*p* indicates that some β-D-galactosidases and β-D-glucosidases are localized in cell walls.

DISCUSSION

Metabolic Paths Paved for Different Polysaccharides by GT and GH Expression

Xyloglucan

Enzymes involved in the synthesis of XyGs are actively expressed in the root cap and meristem zone of maize primary root, and the intensity of their transcription is largely reduced in the active and late elongation zones (**Figure 9**; Kozlova et al., 2020). Transcriptomics and proteomics data on maize primary root suggest that active XyG biosynthesis is followed by intensive rearrangement mediated by XETs in stages of early and active elongation (**Figure 9**). An exceptionally high level of transcripts in these zones was observed for maize genes homologous to *AtXTH4-5/HvXTH5* and *BdXTH8* (**Figure 6**). The content of corresponding proteins was also significant. The BdXTH8 protein exhibits predominantly MLG:XyG endotransglucosylase activity and can, thus, produce MLG:XyG covalent bonds (Fan et al., 2018). Moreover, in *Brachypodium*, BdXTH8 accumulates in elongating tissues characterized by high amounts of MLG (Fan et al., 2018). The *Equisetum* homolog of BdXTH8 (EfHTG) is able to use cellulose as the donor substrate and exhibits the dominance of cellulose:XyG endotransglucosylase activity over XyG:XyG homo-transglucosylation activity (Herburger et al., 2021). *HvXTH5* also encodes an XTH capable of using cellulose as the donor substrate although with a rate lower than that for XyG:XyG endotransglycosylation (Hrmova et al., 2007). Homologs of *HvXTH5* in *Arabidopsis* and poplar (*AtXTH4* and *PtxtXTH34*) positively affect the intrusive and expansion growth of fibers and vessels (Nishikubo et al., 2011; Kushwah et al., 2020). The immunolabeling of XyGs was intensive in meristem and the early elongation zone of maize root and gradually decreased in the active and late elongation zones (Kozlova et al., 2020). Because of the high level of gene expression and corresponding protein abundance (Marcon et al., 2015) of putative hetero-transglycosylases in maize primary root, one can suggest that XyG fragments may integrate into the cell wall through covalent linkages with cellulose and MLG during active elongation and, hence, become unrecognizable for antibodies.

Levels of transcripts and proteins for enzymes able to degrade XyGs were much lower than those for XETs (**Figures 6**, **4**). A XEG (GH16), xylan α-L-fucosidase (GH95), and XyG-specific β-D-galactosidase (GH35) were shown to attack XyGs in *Arabidopsis* and *Brachypodium* (Günl et al., 2011; Sampedro et al., 2012; Kaewthai et al., 2013; Rubianes et al., 2019). Maize homologs of these genes had the peak of TGR values in the late elongation zone of maize primary root, and their proteins were accumulated in the late elongation and root hair zones (**Figures 4**, **6**, **9**). Thus, we can suggest that after elongation growth is finished XyG molecules can undergo a decrease in molecular weight and backbone decoration.

Arabinoxylan

Previously, it has been shown that two sets of GTs putatively involved in GAX synthesis were expressed in maize primary root with different profiles. One of the sets was co-expressed with cellulose-synthases of primary cell walls, while the other was co-expressed with cellulose-synthases for secondary cell walls (**Figure 9**; Kozlova et al., 2020). Similarly, the two sets of genes encoding AX modifying enzymes can be identified by their expression levels in growing maize roots (**Figures 5**, **9**). One set included genes of GH3 and GH10 enzymes that were co-expressed with genes of primary cell wall biosynthetic machinery (**Figure 5A**) and similar genes with the highest levels of transcription in early and active elongation zones. Homologs of these genes encode β-D-xylosidases, bifunctional α-L-arabinofuranosidases/β-D-xylosidases, and endo-xylanases in different plants (**Figures 3B**, **5B**). Corresponding activities were detected in clarified homogenates of maize root zones (**Figure 8**;

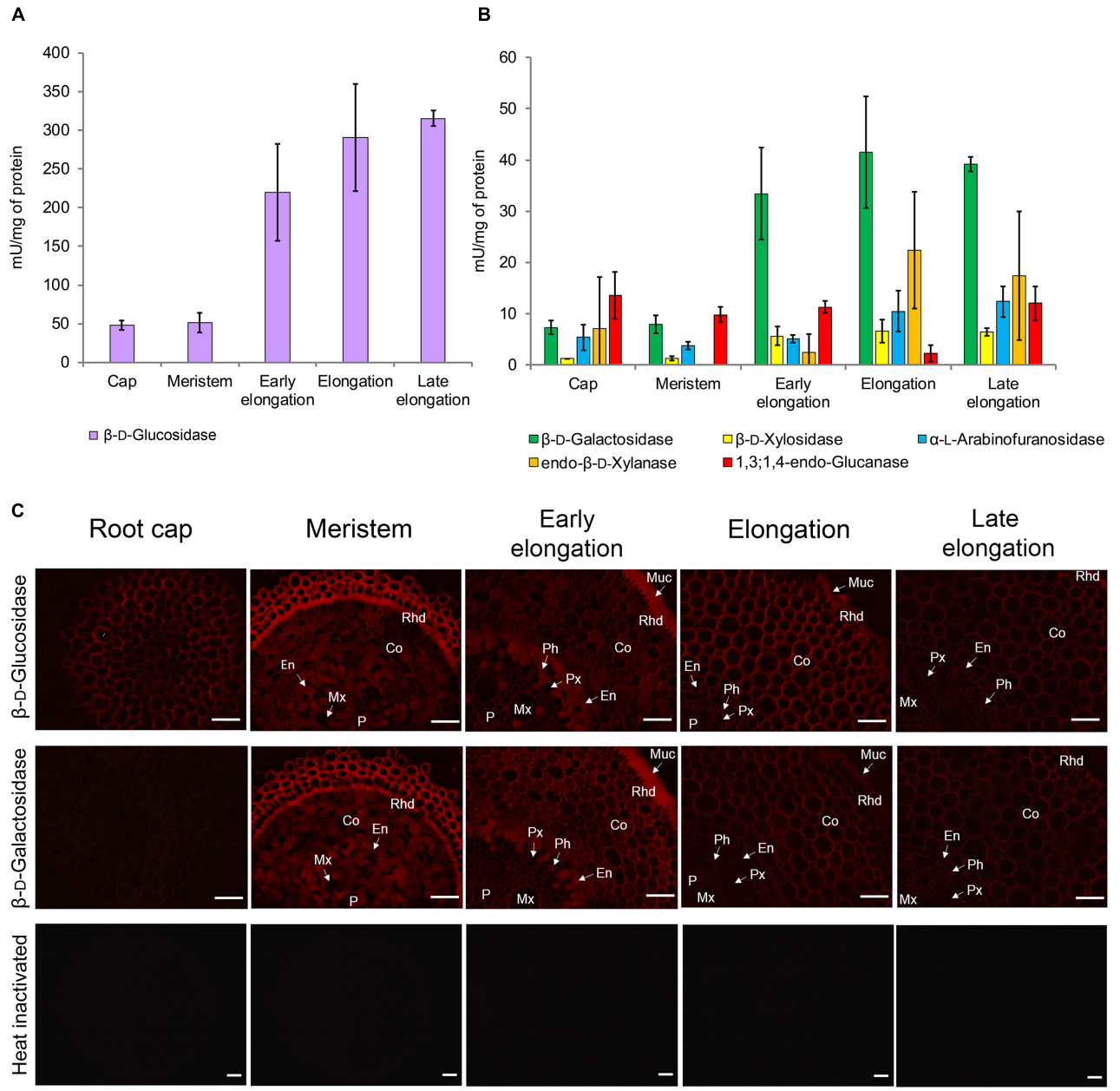

FIGURE 8 | Glycoside hydrolase activities in different zones of maize primary roots assayed *in vitro* and *in situ*. **(A)** The β-D-glucosidase, **(B)** β-D-galactosidase, β-D-xylosidase, α-L-arabinofuranosidase, xylanase, and 1,3;1,4-β-D-glucan endohydrolase activities measured in clarified homogenates. Values are given as mean (n = 3) ± SE. **(C)** The β-D-glucosidase and β-D-galactosidase activities of non-fixed maize primary root cross sections. Co, cortex; En, endodermis; Mx, metaxylem; Muc, mucilage; P, pith; Px, protoxylem; Rhd, rhizodermis. Bars are 50 μm.

Kozlova et al., 2015). Thus, it is possible that the action of GHs that remove arabinose as well as xylose substitution is more prominent in the active elongation stage and can be targeted on primary cell wall AXs.

The second set included genes of GH10 and GH51 members that were co-expressed with genes of secondary cell wall biosynthetic machinery (**Figures 5A**, **9**). These genes encode putative xylanases and arabinofuranosidases. Their proteins were found almost exclusively in the stele of the root hair region (Marcon et al., 2015; **Figure 5A**), suggesting their importance for vascular tissue formation. The maize *WI5* gene, whose significance for this process had already been established in stems (Hu et al., 2020), belonged to the second set. AXs of secondary cell walls may serve as a target for these enzymes.

At least two characterized plant β-xylanases, poplar PtxtXYN10A and papaya CaEXY1, are xylanases-endotransglycosylases (Derba-Maceluch et al., 2015; Johnston et al., 2013) catalyzing both hydrolysis and ligation

FIGURE 9 | Expression patterns of genes encoding enzymes that can mediate the synthesis, transglycosylation, and hydrolysis of cell wall matrix polysaccharides observed in growing maize roots. Only one gene representing a particular clade or family with the typical dynamics of transcript abundance is shown. The closest characterized homolog for each maize gene is indicated in parenthesis. All profiles are normalized to maximum. Cap, root cap; Mer, meristem; eElong, early elongation zone; Elong, elongation zone; lateElong, late elongation zone; PW, primary cell wall; SW, secondary cell wall.

of xylan chains. It was suggested that the secondary cell wall β-xylanase of poplar acted as transglycosylase and allowed for the release of tensional stress that arises during wall deposition (Derba-Maceluch et al., 2015). Trans-xylosylating activity exceeding the hydrolytic one was reported earlier for *Poacea* seedlings (Johnston et al., 2013) and some other species (Franková and Fry, 2011). The maize roots were characterized by higher endo-trans-xylosylating activity than coleoptiles and leaves (Franková and Fry, 2011). We also found β-xylanase activity in clarified maize homogenates (**Figure 8B**) but did not test its transglycosylation potential. β-Xylosidases often possess trans-xylosylating activity (Franková and Fry, 2011). Consequently, it is possible that the BXL clade members of GH3 as well as GH10 representatives mediate both degradation and rearrangement of AXs during elongation growth of cells with type II cell walls.

Mixed-Linkage Glucan

The dynamics of MLGs during elongation of different cereal organs and features of glucan-degrading enzymes were the most important arguments in favor of the glycoside hydrolase theory of plant cell growth. The β-glucosidase activity of clarified homogenates was at least six times higher than any other one measured within this study (**Figures 8A,B**). However, most likely, it was provided by cytosolic members of the GH1 family. These enzymes were characterized by an extraordinary transcript and protein abundance (**Figure 3**). These proteins are accumulated to guarantee the fast release of protective substance DIMBOA from its glucosylated form in case of herbivore attack (Babcock and Esen, 1994). According to the resorufin release from Res-βDGlc by unfixed cross-sections of maize root, the β-glucosidase activity in cell walls was comparable with the β-galactosidase one (**Figure 8C**). Other members of GH1 with high expression are putative exo-β-mannosidases (**Figure 3**).

Representatives of the ExoI clade of the GH3 family are more promising candidates for participation in the active turnover of MLGs in cell walls of cereals than GH1 members. J.-B. Kim et al. (2000) purified and characterized ZmEXG1 as the main exo-glucosidase degrading MLGs in maize coleoptiles. We have found a high level of *ZmEXG1* transcripts in maize primary root (**Figure 3**). Its dynamics were characterized by two peaks, in the meristem and in the late elongation zone, with a significant decrease of transcript abundance in the active elongation zone (**Figures 3**, **9**). Interestingly, the reduction of *ZmEXG1* mRNA abundance in the stage of the most rapid coleoptile growth was also noted by Kim et al. (2000). A similar dynamics of transcript levels were found for two maize homologs

of barley ExoI (**Figure 3**). HvExoI was characterized as the MLG-targeted β-glucosidase in barley seedlings and endosperm (Hrmova et al., 1996, 1998). However, the *Arabidopsis* homolog of *HvExoI* (*AtBGLC1*) was shown to encode the enzyme involved in XyG metabolism. Loss of function of this gene resulted in the accumulation of partially digested XyG fragments in plant tissues (Sampedro et al., 2017). The use of the *Brachypodium* homolog (*BdBGLC1*) of *AtBGLC1* complemented the *Arabidopsis bglc1* mutant (Rubianes et al., 2019). Thus, it remains unclear what polysaccharide is the main target for the GH3 glucosidase activity in maize root cell walls. Moreover, glucosidases of GH3 generally have broad substrate specificity because of their spatial structure (Hrmova et al., 2002). However, it is clear that maize roots have at least three isoforms of exo-β-glucosidases of GH3, which can modify cell wall polysaccharides during the elongation growth of cells. Their specific expression pattern with a decrease of transcript abundance in the zone of the most active elongation requires further studies.

Besides exo-glucosidases, MLGs can be degraded by endo-β-glucanases (**Figure 1**). We have screened the expression of genes encoding predicted members of the GH9 and GH17 families. In spite of the fact that some known GH9 family members are able to cleave grass hemicelluloses (Yoshida and Komae, 2006), their activity as cellulases or hemicellulases has never been shown *in planta*. Numerous growth defects were described for plants with suppressed gene expression or gene knockout of various GH9 members (Tsabary et al., 2003; Szyjanowicz et al., 2004; Yu et al., 2013); however, no excessive accumulation of any cell wall component in their cell walls were shown. The most extensively studied representative of GH9, KORIGAN, is supposed to serve as part of the cellulose biosynthetic complex (Lampugnani et al., 2019). Genes encoding other proteins of GH9 display a cell-type specific expression (Del Campillo et al., 2004). Their homologs in maize roots were also predominantly expressed in the zones containing these cell types (**Supplementary Figure 2**). We suggest that in maize, like in many other plant species, GH9 members are rather important for proper assembly of cell walls than associated with the hydrolysis of MLGs.

The other plant protein family of endo-β-glucanases is GH17. It is a huge family that especially develops in grasses (Minic, 2008). Plant proteomes display a wide variety of GH17 members in any physiological state (Nguyen-Kim et al., 2016; Calderan-Rodrigues et al., 2018; Grandis et al., 2019). However, only a few of its representatives were characterized. Some isoforms degrade callose (Benitez-Alfonso et al., 2013), others have antifungal properties and are able to cleave 1,3;1,6-glucans, and some are known to operate with MLGs (Hrmova et al., 2009). However, due to the huge size of the family and the high homology of its members between each other, it is difficult to assume which type of reaction can be catalyzed by a particular isoform. Many representatives of the GH17 family are diversely expressed during the elongation growth of maize roots (**Supplementary Figure 3**), but their roles in this process require further studies. Nevertheless, the presence of lichenase (endo-β-1,3;1,4-glucanase) activity in clarified homogenates of maize root was established (**Figure 8B**). Being at the same basic level in all the studied root zones, it was considerably lower in the zone of active elongation. In the same zone, the expression of putative MLG exo-hydrolases also decreased, while the transcript abundance of MLG synthases peaked (**Figure 9**; Kozlova et al., 2020). MLG degradation accompanies the cessation of elongation growth in maize coleoptiles and internodes (Kim et al., 2000; Zhang et al., 2014) but not in roots (Kozlova et al., 2012, 2020). Proteins for MLG synthases continue to accumulate after the cessation of growth, and their content in the root hair region is higher than that in the elongating part of maize roots (Kozlova et al., 2020). It seems that there are several mechanisms recruited by maize to enhance MLG deposition in cell walls during the stage of the most active elongation.

Galactans

Among all tested GH activities, β-galactosidase was the second by its intensity in clarified homogenates after β-glucosidase, though in each zone of maize root, it was at least six times lower than the latter (**Figures 8A,B**). At the same time, these two activities had comparable intensities while being tested on the maize root cross-sections (**Figure 8C**). The β-galactosidase activity was found in elongating *Avena* coleoptiles in the 1970s (Johnson et al., 1974). There were also some reports on the reduction of galactan and galactose content in barley and wheat seedlings, oat coleoptiles, and maize roots during elongation growth (Ray, 1963; Dever et al., 1968; Obel et al., 2002; Gibeaut et al., 2005). However, other studies on growing cereal plants reported no significant reduction of 1,4-linked galactose during elongation (Carpita, 1984; Zhang et al., 2014).

Cereal cell walls are thought to have much lower pectin content than cell walls of dicots or non-commelinid monocots (Carpita, 1996). Cell walls in all zones of maize primary roots were labeled by an antibody recognizing β-1,4-galactans (Kozlova et al., 2020), and the maize homolog of *Arabidopsis* galactan-synthase GALS1 was co-expressed with primary cell wall cellulose-synthases (**Figure 9**; Kozlova et al., 2020). The maize β-galactosidase putatively active toward β-1,4-galactan was also co-expressed with these cellulose-synthases and was characterized by the highest TGR values among all other genes encoding GH35 members (**Figure 4**). However, several other isoforms of putative pectin-targeted maize BGALs were expressed predominantly in the root cap and early elongation zone (**Figure 4**). Their homologs in *Arabidopsis* were characterized as galactosidases able to cleave off β-1,4- and β-1,3- but not β-1,6-linked galactose (Gantulga et al., 2008). Interestingly, labeling by the antibody recognizing 1,6-branched 1,4-galactan was much stronger in all zones of maize roots than that of linear galactan (Petrova et al., 2021), and 1,6-branching could serve as the protection for galactan chains against the action of the vast majority of β-galactosidases expressed in maize roots. However, there is another galactosidase of maize whose homolog in radish was shown to degrade 1,6- and 1,3-linked galactosides (Kotake et al., 2005). Its transcript abundance had two peaks: in the early elongation zone and the late elongation zone (**Figures 4**, **9**). In summary, any zone of maize root expresses at least a couple of putative galactosidases able to cleave off any type of terminal galactose residue (**Figure 9**). The

persistence of galactans in maize root cell walls simultaneously with high β-galactosidase activities of homogenates and on sections may be explained by the high rate of galactan turnover during the elongation growth of maize primary roots. Another explanation could be based on the fact that trans-galactosylation reaction often accompanies galactoside hydrolysis (Franková and Fry, 2012). Thus, it is possible that galactans in maize roots are remodeled *in muro* rather than be degraded, assimilated, activated, and returned back to the cell wall.

The importance of galactans for the proper assembly of other polysaccharides has been shown previously for both primary and secondary cell walls on dicots (Moneo-Sánchez et al., 2019, 2020). The mechanisms of this involvement are yet to be studied; however, basic principles can be similar for both type I and type II cell walls.

Do Glycoside Hydrolases Act as Trans-Glycosylases *in muro*?

Despite a huge pool of information on the existence of various GHs catalyzing the hydrolysis of plant polysaccharides, we suggest that their role is not so straightforward. There are several lines of evidence in support of the activation of transglycosylation reactions catalyzed by GHs *in muro*.

(1) Some GHs, which operate by retaining the substrate anomeric center configuration in the resulting product, can catalyze both hydrolysis and transglycosylation to synthesize oligosaccharides (Davies and Henrissat, 1995). Numerous plant representatives of various GH families able to catalyze the transfer of a glycosyl donor to other than water OH-containing acceptor have been described (GH3: Kim et al., 2000; GH10: Derba-Maceluch et al., 2015; GH35: Franková and Fry, 2012, etc.). The vast amount of plant enzymes, especially cell wall-related, are retaining GHs (Minic, 2008). In this study, the majority of GHs are retaining enzymes; representatives of only three GH families (GH9, GH28, and GH95) operate *via* the inverting mechanism (CAZy database).

(2) In general, the analyzed GHs were characterized by a higher amount of protein than the corresponding GTs. For example, the total protein abundance for two MLG synthases (ZmCslF2 and ZmCslF4) in the elongation zone of maize roots was 498 spectral counts (Kozlova et al., 2020). The abundance of a protein of the known GH3 β-glucosidase (ZmEXG1) active toward MLG (Kim et al., 2000) was 10 times higher and amounted to 4,447 total spectral counts (**Figure 3**). If we add to this value the protein abundance of numerous endo-β-glucanases expressed in maize roots (**Supplementary Figures 2, 3**), the lifespan of MLG molecules in the cell wall should be estimated as short. Moreover, many GHs demonstrating higher transcript and protein abundances than their GTs counterparts were found to be co-expressed with them. This can be exemplified by maize homologs of AtGALS1 (Kozlova et al., 2020) and AtBGAL1 (**Figures 4**, **9**), which are supposed to synthesize and degrade, respectively, β-1,4-galactan and belong to one co-expression network. Genes encoding β-xylosidases of GH3, xylanases of GH10, and arabinofuranosidases of GH51 are co-expressed with genes for GTs involved in the synthesis of AXs (Kozlova et al., 2020; **Figures 5**, **9**). Overall, polysaccharide synthesis is a highly demanding process (Barnes and Anderson, 2018). Thus, it seems irrational to break apart (to hydrolyze) the structure immediately after its construction (synthesis).

(3) It is well-documented that GHs catalyze transglycosylation reactions under conditions of high concentration of saccharide substrates (Hrmova and Fincher, 1997; Kim et al., 2000; Franková and Fry, 2012; Derba-Maceluch et al., 2015). In supersaturated solutions of saccharides, transglycosylation reactions catalyzed by glycosidases proceed with higher efficiency because of saccharides competing with water molecules for accommodation in the enzyme active center (MacManus et al., 2001). One can assume that the enzymatic reaction conditions *in muro* and *in vitro* differ in the ratio of sugar and water molecules and, accordingly, in the viscosity of the medium. These are the parameters on which the shift of the thermodynamic equilibrium of hydrolysis:transglycosylation reactions directly depends. Indeed, the water content in plant primary cell walls has been reported to be 60 (Gaff and Carr, 1961) or 80% (Hardegree, 1989). If one assumes that the cell wall contains approximately 30% of saccharides, then, in terms of glucose residues, their content is approximately 1.5 moles, which is obviously higher than the concentration of saccharide substrates in the study on enzymatic catalysis of hydrolysis reaction *in vitro*. For example, all characterized GH3 β-glucosidases catalyzed transglycosylation reactions at substrate concentrations that varied between 2 and 20 mM (Hrmova and Fincher, 1997; Crombie et al., 1998; Kim et al., 2000).

(4) The transglycosylation:hydrolysis ratio with the same substrates varies in different plant organs and species (Franková and Fry, 2011). This indicates that transglycosylation is not just an inevitable side reaction accompanying hydrolysis. The degree of its expression depends on particular enzymes produced by the plant and, hence, can be regulated as being more or less pronounced when it is beneficial for the plant.

The results obtained in this study support the previously suggested physiological importance of GH-mediated transglycosylation for plants (Franková and Fry, 2011). However, the occurrence and details of this process in plants remain to be studied.

DATA AVAILABILITY STATEMENT

The datasets presented in this study can be found in the BioProject online repository under the accession number PRJNA639682 or using the following link https://www.ncbi.nlm.nih.gov/bioproject/PRJNA639682.

AUTHOR CONTRIBUTIONS

LK and TG conceived the study. AN, OG, NP, EE, and LK carried out the experiments and analyzed the results. AN and LK wrote the original draft and prepared all the illustrations, tables, and **Supplementary Material**. AN, LK, AK, and TG edited the manuscript. All authors reviewed and approved the final version.

FUNDING

This study was partially supported by the Russian Science Foundation (project number 18-14-00168, AN, OG, NP, and LK). A part of the study was performed with financial support from the government assignment for the FRC Kazan Scientific Center of RAS (TG).

ACKNOWLEDGMENTS

We would like to express our gratitude to Dmitry Suslov (Saint-Petersburg State University) for providing the maize seeds.

SUPPLEMENTARY MATERIAL

The Supplementary Material for this article can be found online at: https://www.frontiersin.org/articles/10.3389/fpls.2021.802424/full#supplementary-material

REFERENCES

Armenteros, J. J. A., Tsirigos, K. D., Sønderby, C. K., Petersen, T. N., Winther, O., Brunak, S., et al. (2019). SignalP 5.0 improves signal peptide predictions using deep neural networks. *Nat. Biotechnol.* 37, 420–423. doi: 10.1038/s41587-019-0036-z

Babcock, G. D., and Esen, A. (1994). Substrate specificity of maize β-glucosidase. *Plant Sci.* 101, 31–39. doi: 10.1016/0168-9452(94)90162-7

Barnes, W. J., and Anderson, C. T. (2018). Release, recycle, rebuild: cell-wall remodeling, autodegradation, and sugar salvage for new wall biosynthesis during plant development. *Mol. Plant* 11, 31–46. doi: 10.1016/j.molp.2017.08.011

Benitez-Alfonso, Y., Faulkner, C., Pendle, A., Miyashima, S., Helariutta, Y., and Maule, A. (2013). Symplastic intercellular connectivity regulates lateral root patterning. *Dev. Cell* 26, 136–147. doi: 10.1016/j.devcel.2013.06.010

Benson, D. A., Cavanaugh, M., Clark, K., Karsch-Mizrachi, I., Lipman, D. J., Ostell, J., et al. (2012). GenBank. *Nucleic Acids Res.* 41, D36–D42.

Bih, F. Y., Wu, S. S. H., Ratnayake, C., Walling, L. L., Nothnagel, E. A., and Huang, A. H. C. (1999). The predominant protein on the surface of maize pollen is an endoxylanase synthesized by a tapetum mRNA with a long 5 ' leader. *J. Biol. Chem.* 274, 22884–22894. doi: 10.1074/jbc.274.32.22884

Bolser, D., Staines, D. M., Pritchard, E., and Kersey, P. (2016). Ensembl Plants: Integrating Tools for Visualizing, Mining, and Analyzing Plant Genomics Data. *Plant Bioinforma. Methods Protoc. 2nd Ed.* 1374, 115–140. doi: 10.1007/978-1-4939-3167-5_6

Bradford, M. M. (1976). A rapid and sensitive method for the quantitation of microgram quantities of protein utilizing the principle of protein-dye binding. *Anal. Biochem.* 72, 248–254. doi: 10.1006/abio.1976.9999

Calderan-Rodrigues, M. J., Fonseca, J. G., Clemente, H. S., Labate, C. A., and Jamet, E. (2018). Glycoside hydrolases in plant cell wall proteomes: Predicting functions that could be relevant for improving biomass transformation processes. *Adv. Biofuels Bioenergy* 1, 165–182. doi: 10.5772/intechopen.73181

Calderan-Rodrigues, M. J., Fonseca, J. G., Labate, C. A., and Jamet, E. (2017). Cell wall proteomics as a means to identify target genes to improve second-generation biofuel production. *Front. Bioenergy Biofuels* 5:66189. doi: 10.5772/66189

Cao, J. (2012). The pectin lyases in Arabidopsis thaliana: evolution, selection and expression profiles. *PLoS One* 7:e46944. doi: 10.1371/journal.pone.0046944

Carpita, N. C. (1984). Cell-Wall Development in Maize Coleoptiles. *Plant Physiol.* 76, 205–212. doi: 10.1104/pp.76.1.205

Carpita, N. C. (1996). Structure and biogenesis of the cell walls of grasses. *Annu. Rev. Plant Biol.* 47, 445–476. doi: 10.1146/annurev.arplant.47.1.445

Chandrasekar, B., and van der Hoorn, R. A. L. (2016). Beta galactosidases in *Arabidopsis* and tomato–a mini review. *Biochem. Soc. Trans.* 44, 150–158. doi: 10.1042/BST20150217

Consortium, T. U. (2019). UniProt: a worldwide hub of protein knowledge. *Nucleic Acids Res.* 47, D506–D515. doi: 10.1093/nar/gky1049

Cosgrove, D. J. (2005). Growth of the plant cell wall. *Nat. Rev. Mol. Cell Biol.* 2005:nrm1746. doi: 10.1038/nrm1746

Crombie, H. J., Chengappa, S., Hellyer, A., and Reid, J. S. G. (1998). A xyloglucan oligosaccharide-active, transglycosylating-D-glucosidase from the cotyledons of nasturtium (*Tropaeolum majus* L.) seedlings–purification, properties and characterization of a cDNA clone. *Plant J.* 15, 27–38. doi: 10.1046/j.1365-313x.1998.00182.x

Davies, E., and Maclachlan, G. A. (1968). Effects of indoleacetic acid on intracellular distribution of β-glucanase activities in the pea epicotyl. *Arch. Biochem. Biophys.* 128, 595–600. doi: 10.1016/0003-9861(68)90068-4

Davies, G., and Henrissat, B. (1995). Structures and mechanisms of glycosyl hydrolases. *Structure* 3, 853–859. doi: 10.1016/S0969-2126(01)00220-9

Dawson, R. M. C. (1986). *Data for Biochemical Research*, 3rd Edn. Oxford: Oxford Science Publications.

Del Campillo, E., Abdel-Aziz, A., Crawford, D., and Patterson, S. E. (2004). Root cap specific expression of an endo-β-1, 4-glucanase (cellulase): a new marker to study root development in *Arabidopsis*. *Plant Mol. Biol.* 56, 309–323. doi: 10.1007/s11103-004-3380-3

Derba-Maceluch, M., Awano, T., Takahashi, J., Lucenius, J., Ratke, C., Kontro, I., et al. (2015). Suppression of xylan endotransglycosylase PtxtXyn10A affects cellulose microfibril angle in secondary wall in aspen wood. *New Phytol.* 205, 666–681. doi: 10.1111/nph.13099

Dever, J. E., Bandurski, R. S., and Kivilaan, A. (1968). Partial chemical characterization of corn root cell walls. *Plant Physiol.* 43, 50–56. doi: 10.1104/pp.43.1.50

El-Gebali, S., Mistry, J., Bateman, A., Eddy, S. R., Luciani, A., Potter, S. C., et al. (2019). The Pfam protein families database in 2019. *Nucleic Acids Res.* 47, D427–D432. doi: 10.1093/nar/gky995

Fan, M. Z., Herburger, K., Jensen, J. K., Zemelis-Durfee, S., Brandizzi, F., Fry, S. C., et al. (2018). A trihelix family transcription factor is associated with key genes in mixed-linkage glucan accumulation. *Plant Physiol.* 178, 1207–1221. doi: 10.1104/pp.18.00978

Francin-Allami, M., Merah, K., Albenne, C., Rogniaux, H., Pavlovic, M., Lollier, V., et al. (2015). Cell wall proteomic of *Brachypodium distachyon* grains: A focus on cell wall remodeling proteins. *Proteomics* 15, 2296–2306. doi: 10.1002/pmic.201400485

Franková, L., and Fry, S. C. (2011). Phylogenetic variation in glycosidases and glycanases acting on plant cell wall polysaccharides, and the detection of transglycosidase and trans-β-xylanase activities. *Plant J.* 67, 662–681. doi: 10.1111/j.1365-313X.2011.04625.x

Franková, L., and Fry, S. C. (2012). Trans-α-xylosidase and trans-β-galactosidase activities, widespread in plants, modify and stabilize xyloglucan structures. *Plant J.* 71, 45–60. doi: 10.1111/j.1365-313X.2012.04966.x

Gaff, D. F., and Carr, D. T. (1961). The quantity of water in the cell wall and its significance. *Aust. J. Biol. Sci.* 14, 299–311. doi: 10.1071/bi9610299

Gantulga, D., Turan, Y., Bevan, D. R., and Esen, A. (2008). The *ArabidopsisAt1g45130* and *At3g52840* genes encode β-galactosidases with

activity toward cell wall polysaccharides. *Phytochemistry* 69, 1661–1670. doi: 10.1016/j.phytochem.2008.01.023

Gibeaut, D. M., Pauly, M., Bacic, A., and Fincher, G. B. (2005). Changes in cell wall polysaccharides in developing barley (*Hordeum vulgare*) coleoptiles. *Planta* 221, 729–738. doi: 10.1007/s00425-005-1481-0

Gómez-Anduro, G., Ceniceros-Ojeda, E. A., Casados-Vázquez, L. E., Bencivenni, C., Sierra-Beltrán, A., Murillo-Amador, B., et al. (2011). Genome-wide analysis of the beta-glucosidase gene family in maize (*Zea mays* L. var B73). *Plant Mol. Biol.* 77, 159–183. doi: 10.1007/s11103-011-9800-2

Goodstein, D. M., Shu, S., Howson, R., Neupane, R., Hayes, R. D., Fazo, J., et al. (2012). Phytozome: a comparative platform for green plant genomics. *Nucleic Acids Res.* 40, D1178–D1186. doi: 10.1093/nar/gkr944

Grandis, A., Leite, D. C. C., Tavares, E. Q. P., Arenque-Musa, B. C., Gaiarsa, J. W., Martins, M. C. M., et al. (2019). Cell wall hydrolases act in concert during aerenchyma development in sugarcane roots. *Ann. Bot.* 124, 1067–1089. doi: 10.1093/aob/mcz099

Günl, M., Neumetzler, L., Kraemer, F., de Souza, A., Schultink, A., Pena, M., et al. (2011). AXY8 encodes an α-fucosidase, underscoring the importance of apoplastic metabolism on the fine structure of *Arabidopsis* cell wall polysaccharides. *Plant Cell* 23, 4025–4040. doi: 10.1105/tpc.111.089193

Hardegree, S. P. (1989). Derivation of plant cell wall water content by examination of the water-holding capacity of membrane-disrupted tissues. *J. Exp. Bot.* 40, 1099–1104. doi: 10.1093/jxb/40.10.1099

Hatfield, R. D., and Nevins, D. J. (1987). Hydrolytic activity and substrate specificity of an endoglucanase from *Zea mays* seedling cell walls. *Plant Physiol.* 83, 203–207. doi: 10.1104/pp.83.1.203

Hatfield, R., and Nevins, D. J. (1986). Purification and properties of an endoglucanase isolated from the cell walls of *Zea mays* seedlings. *Carbohydr. Res.* 148, 265–278. doi: 10.1016/s0008-6215(00)90394-x

Herburger, K., Frankova, L., Pièmanová, M., Xin, A., Meulewaeter, F., Hudson, A., et al. (2021). Defining natural factors that stimulate and inhibit cellulose: xyloglucan hetero-transglucosylation. *Plant J.* 105, 1549–1565. doi: 10.1111/tpj.15131

Hoson, T., and Nevins, D. J. (1989). Effect of anti-wall protein antibodies on auxin-induced elongation, cell-wall loosening, and beta-D-glucan degradation in maize coleoptile segments. *Physiol. Plant.* 77, 208–215. doi: 10.1111/j.1399-3054.1989.tb04971.x

Hrmova, M., and Fincher, G. B. (1997). Barley beta-D-glucan exohydrolases. Substrate specificity and kinetic properties. *Carbohydr. Res.* 305, 209–221. doi: 10.1016/S0008-6215(97)00257-7

Hrmova, M., De Gori, R., Smith, B. J., Fairweather, J. K., Driguez, H., Varghese, J. N., et al. (2002). Structural basis for broad substrate specificity in higher plant beta-D-glucan glucohydrolases. *Plant Cell* 14, 1033–1052. doi: 10.1105/tpc.010442

Hrmova, M., Farkas, V., Harvey, A. J., Lahnstein, J., Wischmann, B., Kaewthai, N., et al. (2009). Substrate specificity and catalytic mechanism of a xyloglucan xyloglucosyl transferase HvXET6 from barley (*Hordeum vulgare* L.). *FEBS J.* 276, 437–456. doi: 10.1111/j.1742-4658.2008.06791.x

Hrmova, M., Farkas, V., Lahnstein, J., and Fincher, G. B. (2007). A barley xyloglucan xyloglucosyl transferase covalently links xyloglucan, cellulosic substrates, and (1,3;1,4)-beta-D-glucans. *J. Biol. Chem.* 282, 12951–12962. doi: 10.1074/jbc.M611487200

Hrmova, M., Harvey, A. J., Wang, J., Shirley, N. J., Jones, G. P., Stone, B. A., et al. (1996). Barley beta-D-glucan exohydrolases with beta-D-glucosidase activity-Purification, characterization, and determination of primary structure from a cDNA clone. *J. Biol. Chem.* 271, 5277–5286. doi: 10.1074/jbc.271.9.5277

Hrmova, M., Varghese, J. N., Hoj, P. B., and Fincher, G. B. (1998). Crystallization and preliminary X-ray analysis of beta-glucan exohydrolase isoenzyme ExoI from barley (*Hordeum vulgare*). *Acta Crystallogr. D Biol. Crystallogr.* 54, 687–689. doi: 10.1107/s0907444997018866

Hu, X., Cui, Y., Lu, X., Song, W., Lei, L., Zhu, J., et al. (2020). Maize WI5 encodes an endo-1, 4-β-xylanase required for secondary cell wall synthesis and water transport in xylem. *J. Integr. Plant Biol.* 62, 1607–1624. doi: 10.1111/jipb.12923

Huber, D. J., and Nevins, D. J. (1980). β-D-glucan hydrolase activity in *Zea* coleoptile cell walls. *Plant Physiol.* 65, 768–773.

Inouhe, M., and Nevins, D. J. (1991). Inhibition of auxin-induced cell elongation of maize coleoptiles by antibodies specific for cell-wall glucanases. *Plant Physiol.* 96, 426–431. doi: 10.1104/pp.96.2.426

Inouhe, M., Hayashi, K., and Nevins, D. J. (1999). Polypeptide characteristics and immunological properties of exo-and endoglucanases purified from maize coleoptile cell walls. *J. Plant Physiol.* 154, 334–340. doi: 10.1016/s0176-1617(99)80176-x

Johnson, K. D., Daniels, D., Dowler, M. J., and Rayle, D. L. (1974). Activation of *Avena* coleoptile cell wall glycosidases by hydrogen ions and auxin. *Plant Physiol.* 53, 224–228. doi: 10.1104/pp.53.2.224

Johnston, S. L., Prakash, R., Chen, N. J., Kumagai, M. H., Turano, H. M., Cooney, J. M., et al. (2013). An enzyme activity capable of endotransglycosylation of heteroxylan polysaccharides is present in plant primary cell walls. *Planta* 237, 173–187. doi: 10.1007/s00425-012-1766-z

Kaewthai, N., Gendre, D., Eklöf, J. M., Ibatullin, F. M., Ezcurra, I., Bhalerao, R. P., et al. (2013). Group III-A XTH genes of *Arabidopsis* encode predominant xyloglucan endohydrolases that are dispensable for normal growth. *Plant Physiol.* 161, 440–454. doi: 10.1104/pp.112.207308

Kim, D., Landmead, B., and Salzberg, S. L. (2015). HISAT: a fast spliced aligner with low memory requirements. *Nat. Methods* 12, 357–U121. doi: 10.1038/Nmeth.3317

Kim, J. B., Olek, A. T., and Carpita, N. C. (2000). Cell wall and membrane-associated exo-beta-D-glucanases from developing maize seedlings. *Plant Physiol.* 123, 471–486. doi: 10.1104/pp.123.2.471

Kotake, T., Dina, S., Konishi, T., Kaneko, S., Igarashi, K., Samejima, M., et al. (2005). Molecular cloning of a β-galactosidase from radish that specifically hydrolyzes β-(1 → 3)-and β-(1 → 6)-galactosyl residues of arabinogalactan protein. *Plant Physiol.* 138, 1563–1576. doi: 10.1104/pp.105.062562

Kozlova, L. V., Gorshkov, O. V., Mokshina, N. E., and Gorshkova, T. A. (2015). Differential expression of alpha-L-arabinofuranosidases during maize (*Zea mays* L.) root elongation. *Planta* 241, 1159–1172. doi: 10.1007/s00425-015-2244-1

Kozlova, L. V., Nazipova, A. R., Gorshkov, O. V., Petrova, A. A., and Gorshkova, T. A. (2020). Elongating maize root: zone-specific combinations of polysaccharides from type I and type II primary cell walls. *Sci. Rep.* 10, 1–20. doi: 10.1038/s41598-020-67782-0

Kozlova, L. V., Snegireva, A. V., and Gorshkova, T. A. (2012). Distribution and structure of mixed linkage glucan at different stages of elongation of maize root cells. *Russ. J. Plant Physiol.* 59, 339–347. doi: 10.1134/s1021443712030090

Kraemer, F. J., Lunde, C., Koch, M., Kuhn, B. M., Ruehl, C., Brown, P. J., et al. (2021). A mixed-linkage (1, 3; 1, 4)-β-D-glucan specific hydrolase mediates dark-triggered degradation of this plant cell wall polysaccharide. *Plant Physiol.* 185, 1559–1573. doi: 10.1093/plphys/kiab009

Kushwah, S., Banasiak, A., Nishikubo, N., Derba-Maceluch, M., Majda, M., Endo, S., et al. (2020). *Arabidopsis* XTH4 and XTH9 contribute to wood cell expansion and secondary wall formation. *Plant Physiol.* 182, 1946–1965. doi: 10.1104/pp.19.01529

Lampugnani, E. R., Flores-Sandoval, E., Tan, Q. W., Mutwil, M., Bowman, J. L., and Persson, S. (2019). Cellulose synthesis–central components and their evolutionary relationships. *Trends Plant Sci.* 24, 402–412. doi: 10.1016/j.tplants.2019.02.011

Lane, D. R., Wiedemeier, A., Peng, L., Höfte, H., Vernhettes, S., Desprez, T., et al. (2001). Temperature-sensitive alleles of RSW2 link the KORRIGAN endo-1, 4-β-glucanase to cellulose synthesis and cytokinesis in *Arabidopsis*. *Plant Physiol.* 126, 278–288. doi: 10.1104/pp.126.1.278

Lee, R. C., Hrmova, M., Burton, R. A., Lahnstein, J., and Fincher, G. B. (2003). Bifunctional family 3 glycoside hydrolases from barley with alpha-L-arabinofuranosidase and beta-D-xylosidase activity - Characterization, primary structures, and COOH-terminal processing. *J. Biol. Chem.* 278, 5377–5387. doi: 10.1074/jbc.M210627200

Liu, L., Paulitz, J., and Pauly, M. (2015). The presence of fucogalactoxyloglucan and its synthesis in rice indicates conserved functional importance in plants. *Plant Physiol.* 168, 549–560. doi: 10.1104/pp.15.00441

Lombard, V., Golaconda Ramulu, H., Drula, E., Coutinho, P. M., and Henrissat, B. (2014). The carbohydrate-active enzymes database (CAZy) in 2013. *Nucleic Acids Res.* 42, D490–D495. doi: 10.1093/nar/gkt1178

Love, M. I., Huber, W., and Anders, S. (2014). Moderated estimation of fold change and dispersion for RNA-seq data with DESeq2. *Genome Biol.* 15:8. doi: 55010.1186/s13059-014-0550-8

MacManus, D. A., Millqvist-Fureby, A., and Vulfson, E. N. (2001). Biotransformations in Supersaturated Solutions. *Enzymes*

Nonaqueous Solvents 2001, 545–552. doi: 10.1385/1-59259-112-4:545

Madeira, F., Park, Y. M., Lee, J., Buso, N., Gur, T., Madhusoodanan, N., et al. (2019). The EMBL-EBI search and sequence analysis tools APIs in 2019. *Nucleic Acids Res.* 47, W636–W641. doi: 10.1093/nar/gkz268

Marcon, C., Malik, W. A., Walley, J. W., Shen, Z. X., Paschold, A., Smith, L. G., et al. (2015). A high-resolution tissue-specific proteome and phosphoproteome atlas of maize primary roots reveals functional gradients along the root axes. *Plant Physiol.* 168, 233–246. doi: 10.1104/pp.15.00138

Maris, A., Suslov, D., Fry, S. C., Verbelen, J.-P., and Vissenberg, K. (2009). Enzymic characterization of two recombinant xyloglucan endotransglucosylase/hydrolase (XTH) proteins of *Arabidopsis* and their effect on root growth and cell wall extension. *J. Exp. Bot.* 60, 3959–3972. doi: 10.1093/jxb/erp229

Matchett, W. H., and Nance, J. F. (1962). Cell wall breakdown and growth in pea seedling stems. *Am. J. Bot.* 49, 311–319. doi: 10.1002/j.1537-2197.1962.tb14943.x

McQueen-Mason, S., Durachko, D. M., and Cosgrove, D. J. (1992). Two endogenous proteins that induce cell wall extension in plants. *Plant Cell* 4, 1425–1433. doi: 10.1105/tpc.4.11.1425

Minic, Z. (2008). Physiological roles of plant glycoside hydrolases. *Planta* 227, 723–740. doi: 10.1007/s00425-007-0668-y

Minic, Z., Rihouey, C., Do, C. T., Lerouge, P., and Jouanin, L. (2004). Purification and characterization of enzymes exhibiting beta-D-xylosidase activities in stem tissues of *Arabidopsis*. *Plant Physiol* 135, 867–878. doi: 10.1104/pp.104.041269

Mitchell, A. L., Attwood, T. K., Babbitt, P. C., Blum, M., Bork, P., Bridge, A., et al. (2019). InterPro in 2019: improving coverage, classification and access to protein sequence annotations. *Nucleic Acids Res.* 47, D351–D360. doi: 10.1093/nar/gky1100

Mo, B., and Bewley, D. J. (2002). β-Mannosidase (EC 3.2. 1.25) activity during and following germination of tomato (Lycopersicon esculentum Mill.) seeds. Purification, cloning and characterization. *Planta* 215, 141–152. doi: 10.1007/s00425-001-0725-x

Moneo-Sánchez, M., Alonso-Chico, A., Knox, J. P., Dopico, B., Labrador, E., and Martín, I. (2019). β-(1, 4)-Galactan remodelling in *Arabidopsis* cell walls affects the xyloglucan structure during elongation. *Planta* 249, 351–362. doi: 10.1007/s00425-018-3008-5

Moneo-Sánchez, M., Izquierdo, L., Martín, I., Hernández-Nistal, J., Albornos, L., Dopico, B., et al. (2018). Knockout mutants of *Arabidopsis thaliana* β-galactosidase. Modifications in the cell wall saccharides and enzymatic activities. *Biol. Plant.* 62, 80–88.

Moneo-Sánchez, M., Vaquero-Rodríguez, A., Hernández-Nistal, J., Albornos, L., Knox, P., Dopico, B., et al. (2020). Pectic galactan affects cell wall architecture during secondary cell wall deposition. *Planta* 251, 1–15. doi: 10.1007/s00425-020-03394-2

Müller, J. J., Thomsen, K. K., and Heinemann, U. (1998). Crystal structure of barley 1, 3–1, 4-β-glucanase at 2.0-Å resolution and comparison with *Bacillus*1, 3–1, 4-β-glucanase. *J. Biol. Chem.* 273, 3438–3446. doi: 10.1074/jbc.273.6.3438

Nguyen, L.-T., Schmidt, H. A., Von Haeseler, A., and Minh, B. Q. (2015). IQ-TREE: a fast and effective stochastic algorithm for estimating maximum-likelihood phylogenies. *Mol. Biol. Evol.* 32, 268–274. doi: 10.1093/molbev/msu300

Nguyen-Kim, H., San Clemente, H., Balliau, T., Zivy, M., Dunand, C., Albenne, C., et al. (2016). *Arabidopsis thaliana* root cell wall proteomics: Increasing the proteome coverage using a combinatorial peptide ligand library and description of unexpected Hyp in peroxidase amino acid sequences. *Proteomics* 16, 491–503. doi: 10.1002/pmic.201500129

Nicol, F., His, I., Jauneau, A., Vernhettes, S., Canut, H., and Höfte, H. (1998). A plasma membrane-bound putative endo-1, 4-β-d-glucanase is required for normal wall assembly and cell elongation in *Arabidopsis*. *EMBO J.* 17, 5563–5576. doi: 10.1093/emboj/17.19.5563

Nishikubo, N., Takahashi, J., Roos, A. A., Derba-Maceluch, M., Piens, K., Brumer, H., et al. (2011). Xyloglucan endo-transglycosylase-mediated xyloglucan rearrangements in developing wood of hybrid aspen. *Plant Physiol.* 155, 399–413. doi: 10.1104/pp.110.166934

Obel, N., Porchia, A. C., and Scheller, H. V. (2002). Dynamic changes in cell wall polysaccharides during wheat seedling development. *Phytochemistry* 60, 603–610. doi: 10.1016/s0031-9422(02)00148-6

Penning, B. W., McCann, M. C., and Carpita, N. C. (2019). Evolution of the Cell Wall Gene Families of Grasses. *Front. Plant Sci.* 10:1205. doi: 10.3389/fpls.2019.01205

Pérez, S. (2014). The symbolic representation of monosaccharides in the age of glycobiology. *Glycopedia. EU* 2014, 1–19.

Pertea, M., Kim, D., Pertea, G. M., Leek, J. T., and Salzberg, S. L. (2016). Transcript-level expression analysis of RNA-seq experiments with HISAT, StringTie and Ballgown. *Nat. Protoc.* 11, 1650–1667. doi: 10.1038/nprot.2016.095

Petrova, A., Gorshkova, T., and Kozlova, L. (2021). Gradients of cell wall nano-mechanical properties along and across elongating primary roots of maize. *J. Exp. Bot.* 72, 1764–1781.

Ray, P. M. (1963). Sugar composition of oat-coleoptile cell walls. *Biochem. J.* 89, 144–150. doi: 10.1042/bj0890144

Roach, M. J., Mokshina, N. Y., Badhan, A., Snegireva, A. V., Hobson, N., Deyholos, M. K., et al. (2011). Development of cellulosic secondary walls in flax fibers requires β-galactosidase. *Plant Physiol.* 156, 1351–1363. doi: 10.1104/pp.111.172676

Rubianes, D., Valdivia, E. R., Revilla, G., Zarra, I., and Sampedro, J. (2019). Xyloglucan exoglycosidases in the monocot model Brachypodium distachyon and the conservation of xyloglucan disassembly in angiosperms. *Plant Mol. Biol.* 100, 495–509. doi: 10.1007/s11103-019-00875-1

Sampedro, J., Gianzo, C., Iglesias, N., Guitián, E., Revilla, G., and Zarra, I. (2012). AtBGAL10 is the main xyloglucan β-galactosidase in *Arabidopsis*, and its absence results in unusual xyloglucan subunits and growth defects. *Plant Physiol.* 158, 1146–1157. doi: 10.1104/pp.111.192195

Sampedro, J., Valdivia, E. R., Fraga, P., Iglesias, N., Revilla, G., and Zarra, I. (2017). Soluble and membrane-bound β-glucosidases are involved in trimming the xyloglucan backbone. *Plant Physiol.* 173, 1017–1030. doi: 10.1104/pp.16.01713

Shannon, P., Markiel, A., Ozier, O., Baliga, N. S., Wang, J. T., Ramage, D., et al. (2003). Cytoscape: A software environment for integrated models of biomolecular interaction networks. *Genome Res.* 13, 2498–2504. doi: 10.1101/gr.1239303

Stratilova, B., Sestak, S., Mravec, J., Garajova, S., Pakanova, Z., Vadinova, K., et al. (2020). Another building block in the plant cell wall: Barley xyloglucan xyloglucosyl transferases link covalently xyloglucan and anionic oligosaccharides derived from pectin. *Plant J.* 104, 752–767. doi: 10.1111/tpj.14964

Su, Z. Q., Labaj, P. P., Li, S., Thierry-Mieg, J., Thierry-Mieg, D., Shi, W., et al. (2014). A comprehensive assessment of RNA-seq accuracy, reproducibility and information content by the Sequencing Quality Control Consortium. *Nat. Biotechnol.* 32, 903–914. doi: 10.1038/nbt.2957

Suen, D. F., and Huang, A. H. C. (2007). Maize pollen coat xylanase facilitates pollen tube penetration into silk during sexual reproduction. *J. Biol. Chem.* 282, 625–636. doi: 10.1074/jbc.M608567200

Suzuki, M., Kato, A., Nagata, N., and Komeda, Y. (2002). A xylanase, AtXyn1, is predominantly expressed in vascular bundles, and four putative xylanase genes were identified in the Arabidopsis thaliana genome. *Plant Cell Physiol.* 43, 759–767. doi: 10.1093/pcp/pcf088

Szyjanowicz, P. M. J., McKinnon, I., Taylor, N. G., Gardiner, J., Jarvis, M. C., and Turner, S. R. (2004). The irregular xylem 2 mutant is an allele of korrigan that affects the secondary cell wall of Arabidopsis thaliana. *Plant J.* 37, 730–740. doi: 10.1111/j.1365-313x.2003.02000.x

Tsabary, G., Shani, Z., Roiz, L., Levy, I., Riov, J., and Shoseyov, O. (2003). Abnormalwrinkled′cell walls and retarded development of transgenic *Arabidopsis thaliana* plants expressing endo-1, 4-β-glucanase (cell) antisense. *Plant Mol. Biol.* 51, 213–224. doi: 10.1023/a:1021162321527

Tu, B., Zhang, T., Wang, Y., Hu, L., Li, J., Zheng, L., et al. (2020). Membrane-associated xylanase-like protein OsXYN1 is required for normal cell wall deposition and plant development in rice. *J. Exp. Bot.* 71, 4797–4811. doi: 10.1093/jxb/eraa200

Tzfadia, O., Diels, T., De Meyer, S., Vandepoele, K., Aharoni, A., and Van de Peer, Y. (2016). CoExpNetViz: comparative co-expression networks construction and visualization tool. *Front. Plant Sci.* 6:1194. doi: 10.3389/fpls.2015.01194

Varghese, J. N., Garrett, T. P., Colman, P. M., Chen, L., Høj, P. B., and Fincher, G. B. (1994). Three-dimensional structures of two plant beta-glucan endohydrolases with distinct substrate specificities. *Proc. Natl. Acad. Sci.* 91, 2785–2789. doi: 10.1073/pnas.91.7.2785

Wada, S., Tanimoto, E., and Masuda, Y. (1968). Cell elongation and metabolic turnover of the cell wall as affected by auxin and cell wall degrading enzymes. *Plant Cell Physiol.* 9, 369–376. doi: 10.1007/BF00202963

Xu, Z., Escamilla-Treviño, L., Zeng, L., Lalgondar, M., Bevan, D., Winkel, B., et al. (2004). Functional genomic analysis of *Arabidopsis thaliana* glycoside hydrolase family 1. *Plant Mol. Biol.* 55, 343–367. doi: 10.1007/s11103-004-0790-1

Yoshida, K., and Komae, K. (2006). A rice family 9 glycoside hydrolase isozyme with broad substrate specificity for hemicelluloses in type II cell walls. *Plant cell Physiol.* 47, 1541–1554. doi: 10.1093/pcp/pcl020

Yu, L., Sun, J., and Li, L. (2013). PtrCel9A6, an endo-1, 4-β-glucanase, is required for cell wall formation during xylem differentiation in Populus. *Mol. Plant* 6, 1904–1917. doi: 10.1093/mp/sst104

Zhang, Q. S., Cheetamun, R., Dhugga, K. S., Rafalski, J. A., Tingey, S. V., Shirley, N. J., et al. (2014). Spatial gradients in cell wall composition and transcriptional profiles along elongating maize internodes. *BMC Plant Biol.* 14:27. doi: 10.1186/1471-2229-14-27

Conflict of Interest: The authors declare that the research was conducted in the absence of any commercial or financial relationships that could be construed as a potential conflict of interest.

frontiers in Plant Science

ORIGINAL RESEARCH
published: 11 March 2022
doi: 10.3389/fpls.2022.821947

CmNDB1 and a Specific Domain of CmMYB1 Negatively Regulate CmMYB1-Dependent Transcription of Nitrate Assimilation Genes Under Nitrogen-Repleted Condition in a Unicellular Red Alga

*Baifeng Zhou[1,2], Hiroki Shima[3], Kazuhiko Igarashi[3], Kan Tanaka[2] and Sousuke Imamura[2,4]**

[1] School of Life Science and Technology, Tokyo Institute of Technology, Yokohama, Japan, [2] Laboratory for Chemistry and Life Science, Institute of Innovative Research, Tokyo Institute of Technology, Yokohama, Japan, [3] Department of Biochemistry, Tohoku University Graduate School of Medicine, Sendai, Japan, [4] NTT Space Environment and Energy Laboratories, Nippon Telegraph and Telephone Corporation, Tokyo, Japan

OPEN ACCESS

Edited by:
Julian Eaton-Rye, University of Otago, New Zealand

Reviewed by:
Hiroyoshi Takano, Kumamoto University Hospital, Japan
Yoshiaki Ueda, Japan International Research Center for Agricultural Sciences (JIRCAS), Japan

***Correspondence:**
Sousuke Imamura
sousuke.imamura.hp@hco.ntt.co.jp

Specialty section:
This article was submitted to Plant Cell Biology, a section of the journal Frontiers in Plant Science

Received: *25 November 2021*
Accepted: *07 February 2022*
Published: *11 March 2022*

Citation:
Zhou B, Shima H, Igarashi K, Tanaka K and Imamura S (2022) CmNDB1 and a Specific Domain of CmMYB1 Negatively Regulate CmMYB1-Dependent Transcription of Nitrate Assimilation Genes Under Nitrogen-Repleted Condition in a Unicellular Red Alga. Front. Plant Sci. 13:821947. doi: 10.3389/fpls.2022.821947

Nitrogen assimilation is an essential process that controls plant growth and development. Plant cells adjust the transcription of nitrogen assimilation genes through transcription factors (TFs) to acclimatize to changing nitrogen levels in nature. However, the regulatory mechanisms of these TFs under nitrogen-repleted (+N) conditions in plant lineages remain largely unknown. Here, we identified a negative domain (ND) of CmMYB1, the nitrogen-depleted (−N)-activated TF, in a unicellular red alga *Cyanidioschyzon merolae*. The ND deletion changed the localization of CmMYB1 from the cytoplasm to the nucleus, enhanced the binding efficiency of CmMYB1 to promoters of nitrate assimilation genes, and increased the transcripts of nitrate assimilation genes under +N condition. A pull-down assay using an ND-overexpressing strain combined with liquid chromatography-tandem mass spectrometry (LC-MS/MS) analysis helped us to screen and identify an unknown-function protein, the CmNDB1. Yeast two-hybrid analysis demonstrated that CmNDB1 interacts with ND. Similar to ND deletion, *CmNDB1* deletion also led to the nucleus localization of CmMYB1, enhanced the promoter-binding ratio of CmMYB1 to the promoter regions of nitrate assimilation genes, and increased transcript levels of nitrate assimilation genes under +N condition. Thus, these presented results indicated that ND and CmNDB1 negatively regulate CmMYB1 functions under the +N condition in *C. merolae*.

Keywords: transcription factor, nitrogen, nitrogen-repleted, red alga, nitrate assimilation

INTRODUCTION

Nitrogen is a component of most basic macromolecules, including proteins and nucleic acids. Thus, it is an essential element for all living organisms. Plants uptake nitrogen sources, mainly ammonium and nitrate through ammonium transporter (AMT) and nitrate transporter (NRT), respectively, from their growing environments. These nitrogen sources are then assimilated into amino

acids through nitrogen assimilation enzymes, and these amino acids would be further utilized (Crawford and Forde, 2002).

Plants alter their gene expression to acclimate to the changing nitrogen level in the environment. Several studies have reported that transcription factors (TFs) positively regulate in controlling the expressions of nitrogen assimilation genes under nitrogen-deficient or −N conditions. In *Arabidopsis*, recent studies have uncovered that the Nodule INception (NIN)-Like Protein 6 and 7 (NLP6, NLP7), could positively regulate the transcripts of *AtNRT1.1*, as well as the gene-encoding nitrate reductase (NR), *AtNIA1* and *AtNIA2,* under −N conditions through forming a complex with TCP20 in the nucleus (Marchive et al., 2013; Guan et al., 2017). Although NLP6 and NLP7 have been originally identified as TFs that are involved in the regulation of primary nitrate response (Konishi and Yanagisawa, 2013; Marchive et al., 2013), the inactivation mechanism of −N-activated TFs under +N condition is not well studied. In rice, through the gene expression analysis, recent research has demonstrated that bZIP-type TFs, bZIP11 and bZIP41, positively regulate expression of *OsNRT2.3* and gene-encoding glutamine synthetase (GS), *OsGS1;1*, under nitrogen-deficient condition but not +N condition in roots (Ueda et al., 2020). The mechanism underlying the low transcription of bZIP11&41-mediated *OsNRT2.3* and *OsGS1;1* under +N condition remains unknown. Although functions of specific regions of the −N-activated TFs must be important for understanding the regulatory mechanism of these TFs under +N conditions, this point is unclear, so far. Furthermore, the regulators affecting the −N-activated TFs function under +N conditions in the plant kingdom are largely unknown.

Cyanidioschyzon merolae is a unicellular red alga, which was isolated from a hot spring in Italy (Kuroiwa, 1998). *C. merolae* has extremely simple cellular architectures and a minimally redundant small genome. *C. merolae* could be used as an excellent model of photosynthetic eukaryote for various research studies (Ohta et al., 1998, 2003; Matsuzaki et al., 2004; Nozaki et al., 2007). In our previous study, we have identified an R2R3-type MYB TF, CmMYB1, which is indispensable for −N-responsible transcription of nitrogen assimilation genes (Imamura et al., 2009). However, the mechanism underlying the regulation of CmMYB1 under the +N condition remains to be uncovered. Based on the advantage of *C. merolae* and the clear evidence of the −N-activated central player, CmMYB1, it is reasonable to use *C. merolae* for investigating the regulatory mechanism of CmMYB1.

In the present study, we revealed a critical region of CmMYB1, which negatively controls CmMYB1 functions under the +N condition. Furthermore, we identified and characterized an unknown-function protein, CMR469C (named CmNDB1 in this study), which negatively controls the function of CmMYB1 under the +N condition in *C. merolae*.

MATERIALS AND METHODS

Strain and Growth Conditions

C. merolae T1, BZU1, BZ1, CmMYB1 partially truncated transformants (pPD1–310, pPD1–380, pPD1–460, pPD1–99, 201–523, pPD1–523, and pPD1–310, 381–523), MΔ95a and BZ6 strains were grown at 40°C under continuous white light (50 μmol m^{-2} s^{-1}) in a liquid MA2 medium [containing 40 mM $(NH_4)_2SO_4$; Imamura et al., 2010] at pH 2.5 bubbling with air supplemented with 2% CO_2. For cultivation of T1, BZ1, and MΔ95a, about 0.5-mg ml^{-1} uracil and 0.8-mg ml^{-1} 5-fluoroorotic acid (5-FOA) were added to the MA2 medium.

Construction of *CmMYB1* Knockout Strain, BZU1, and BZ1

Using the primer sets MYB1pro_F (listed in **Supplementary Table 1**), MYB1pro_R and MYB1ter_F, MYB1ter_R and KOD One Master Mix (Toyobo, Osaka, Japan), –1499 to +0 bp of *CmMYB1* promoter (+1 indicates the site of the start codon), and +1,570 to +3,070 bp of *CmMYB1* terminator were amplified with *C. merolae* genomic DNA as templates and purified by Wizard® SV Gel and PCR Clean-up System (Promega, Madison, WI, United States). Purified *CmMYB1* promoter and terminator DNAs were then cloned into *Stu*I (Takara, Shiga, Japan)-digested pMKTf (Takemura et al., 2018) to create pMKT_CmMYB1_KO plasmid using the Gibson Assembly Master Mix (New England Biolabs, Ipswich, MA, United States). The DNA for *CmMYB1* knockout transformation was amplified using the primer set MYB1tf_F and MYB1tf_R and purified as mentioned above. The transformation using *C. merolae* T1 strain (Taki et al., 2015) was performed as described previously (Takemura et al., 2018). To get the uracil auxotrophy strain of BZU1, BZ1, approximately 1×10^8 BZU1 strain cells were mixed with 1-ml 50% m/v cornstarch solution and spread on an MA2 Gellan Gum plate containing 0.5-mg ml^{-1} uracil and 0.8 mg ml^{-1} 5-FOA. The plate was incubated in a bag with Aneropack CO_2 (Mitsubishi Gas Chemical Co., Inc., Tokyo, Japan) for 4 weeks, and colonies were picked up into a 2-ml MA2 medium supplemented with 0.5-mg ml^{-1} uracil and 0.8-mg ml^{-1} 5-FOA for 2 weeks further. The PCR analysis was performed to select the desired transformants using the primers listed in **Supplementary Table 1**.

RNA Preparation and Northern Blot Analysis

Total RNA preparation and Northern blot analysis were performed as described previously (Imamura et al., 2008). Gene-specific probes for Northern blot analyses were generated with specific primers (listed in **Supplementary Table 2**) and the *C. merolae*-genomic DNA as templates.

Construction of CmMYB1 Amino Acids Truncated Strains

Plasmids expressing truncated types of CmMYB1 were constructed using primers listed in **Supplementary Table 1**. −1,499 to +0 bp of the *CmMYB1* promoter together with *CmMYB1* ORF and +1,570 to +3,070 bp of the *CmMYB1* terminator were first amplified using the primer sets MYB1pro_F2 (listed in **Supplementary Table 1**), MYB1orf_R, MYB1ter_F, and MYB1ter_R, respectively, with KOD One Master Mix (Toyobo, Osaka, Japan) with *C. merolae*-genomic DNA as templates. Then, they were purified by Wizard® SV Gel and PCR Clean-up System (Promega, Madison, WI,

United States). Two fragments: the *CmMYB1* promoter together with ORF and the *CmMYB1* terminator were cloned into separate two *Stu*I sites of pMKTf (Takemura et al., 2018) to construct pMKT_CmMYB1 plasmid. Plasmids—pMKT_1-310 (TEV_F, 1_310_R), pMKT_1-380 (TEV_F, 1_380_R), pMKT_1-460 (TEV_F, 1_460_R), pMKT_1-99, 201-523 (MYB1db_F, MYB1db_R), pMKT_1-310, 381-523 (MYB1ne_F, MYB1ne_R)—were constructed using the pMKT_CmMYB1 plasmid as templates and primer sets indicated in the individual brackets above. The BZ1 strain was cultured under normal culture conditions supplemented with 0.5-mg ml^{-1} uracil and 0.8-mg ml^{-1} 5-FOA to reach OD_{750} above 3. Then, BZ1 cells were diluted into a 50-ml MA2 medium supplemented with 0.5-mg ml^{-1} uracil and 0.8-mg ml^{-1} 5-FOA to give an OD_{750} to 0.4 and cultured in the same culture condition as mentioned above until OD_{750} reached 0.5 to 0.7. BZ1 cells were centrifuged and resuspended in a 180-μl MA2 medium containing 0.5-mg ml^{-1} uracil in a 1.5-ml microtube. The transformation using *C. merolae* BZ1 strain was performed as described previously (Takemura et al., 2018).

Protein Extraction and Immunoblot Analysis

C. merolae logarithmic growth cells (25 ml at OD_{750} = 0.5) were collected, and a 250-μl lysis buffer [50-mM Tris-HCl, pH 7.5, 150-mM NaCl, 10% v/v Glycerol, a complete protease inhibitor EDTA-free cocktail (Roche, Basel, Switzerland), a phosphatase inhibitor cocktail (Nacalai Tesque, Inc., Kyoto, Japan)] was added into the cell pellet followed by 0.15-g glass beads (Ø ≤ 106 μm, Sigma-Aldrich, MA, United States). Cells were disrupted by vortexing (scale 10, 5 min, TurboMix attached to Vortex Genie 2, Scientific Industries, New York, NY, United States), and supernatant (hereafter, a total soluble protein fraction) was collected by centrifuging at 15,000 rpm for 20 min at 4°C and stored at −80°C until use. Protein samples were boiled at 95°C for 5 min and later cooled on ice for 2 min. The proteins were separated by 10% SDS-PAGE and transferred to a polyvinylidene fluoride (PVDF, Millipore) membrane (0.45-μm pore size, Millipore, Burlington, MA, United States). The membrane was blocked with 5% w/v skim milk in 0.1% TBS-Tween at 4°C overnight. In case of detecting FLAG-fused CmMYB1, the membrane was briefly washed three times with 0.1% TBS-Tween before being incubated with an anti-FLAG antibody (Wako, Osaka, Japan, dilution rate: 1/5,000) for 1 h at room temperature. Next, the membrane was washed as mentioned above and incubated with antimouse IgG (H + L) and an HRP conjugate antibody (Promega, Madison, WI, United States, dilution rate: 1/5,000) for 1 h at room temperature. The washing step was repeated before visualization using the ImmunoStar Zeta (Fujifilm, Tokyo, Japan).

Dot Blot Analysis

A total soluble protein fraction was collected as described in section "Protein extraction and immunoblot analysis." PVDF membrane was firstly treated with methanol for 60 s and washed with RO water two times. Then, a blotting buffer (25-mM Tris base, 192-mM glycine, 20% v/v methanol) was used for PVDF membrane incubation for 5 min; a 16.6-μg/sample total soluble protein fraction was used. The membrane was dried for 10 min and incubated in a blocking solution (5% w/v skim milk in 0.1% TBS-Tween) at 4°C overnight. The remaining steps were the same as mentioned in *immunoblot analysis*.

cDNA Synthesis and Quantitative Real-Time PCR Analysis

Total RNA was prepared as described previously (Imamura et al., 2008). Genome DNA was removed, and cDNA was synthesized by ReverTra Ace® qPCR RT Master Mix with gDNA Remover (Toyobo, Osaka, Japan) using 500 ng RNA of each sample as input. Synthesized cDNA was then subjected to Quantitative Real-Time PCR (qRT-PCR) analysis. qRT-PCR analysis was performed as described previously (Imamura et al., 2008). Primers used for qRT-PCR analyses are listed in **Supplementary Table 2**.

Immunostaining Analysis

C. merolae logarithmic growth cells (10 ml at OD_{750} = 0.5) were collected and fixed with a cold fixation buffer (Ohnuma et al., 2008) and incubated at −30°C for 5 min. Fixed cells were then collected and resuspended in methanol and stored at −30°C until use. The cells were washed with 1 × PBS and blocked with 5% v/v, blocking one solution (hereafter, blocking solution, Nacalai Tesque, Inc., Kyoto, Japan) for 30 min at room temperature. The cells were washed with blocking solution and incubated with an anti-FLAG antibody (Wako, Osaka, Japan, a dilution rate: 1/100) in blocking solution at 4°C overnight. The cells were washed with blocking solution and incubated with an Alexa Fluor 488 donkey antimouse antibody (Thermo Fisher Scientific, Waltham, MA, United States, a dilution rate: 1/100) in blocking solution at room temperature for 1 h while avoiding light. The cells were then washed with blocking solution, and the fluorescence signal was captured by fluorescence microscopy (BX-51, Olympus, Tokyo, Japan). Data were treated by Adobe Photoshop 2021 to enhance the contrast and light intensity of the fluorescence from the sample cells.

Chromatin Immunoprecipitation Analysis

C. merolae logarithmic growth cells (25 ml at OD_{750} = 0.5) were collected and fixed as described previously (Imamura et al., 2008). The fixed cells were resuspended in a 1-ml ChIP lysis buffer [50-mM Tris-HCl, 1-mM EDTA, pH 8.0, 140-mM NaCl, 0.1% SDS, 1% Triton X-100, 0.1% sodium deoxycholate, Complete Mini, EDTA-free, a protease inhibitor (Roche, Basel, Switzerland)] and disrupted by sonication (Sonifier 250 advanced, Branson, Emerson, Tokyo, Japan) with output 3, 50% duty for 18 cycles. The supernatant (chromatin solution) was collected by centrifugation and stored at −80°C until use. About 175-μl Slurry protein G Sepharose 4 Fast Flow (Roche, Basel, Switzerland) with a 900-μl ChIP lysis buffer was added to 100-μl chromatin solution, and the samples were rotated at 4°C overnight. The supernatant was

collected by removing protein G Sepharose 4 Fast Flow using Poly-Prep Chromatography Columns (Bio-Rad, Hercules, CA, United States) and incubated with a 2.5-μg/sample anti-FLAG antibody (Wako, Osaka, Japan) at 4°C overnight. The samples were further incubated for 5 h at 4°C after adding 30-μl/sample Dynabeads protein G (Thermo Fisher Scientific, Waltham, MA, United States). Dynabeads were collected by a magnetic stand and sequentially washed as described previously (Imamura et al., 2008). Together with 20-μg/sample RNase A (Nippon Gene, Tokyo, Japan), a 500-μl/sample ChIP direct elution buffer (Imamura et al., 2008) was added to Dynabeads, and the samples were incubated at 65°C overnight. The samples were further incubated at 37°C for 1 h after adding 40-μg/sample proteinase K (Thermo Fisher Scientific, Waltham, MA, United States). The supernatant was collected, and DNA was extracted using phenol:chloroform:isoamyl alcohol (25:24:1) followed by ethanol precipitation. Finally, the pellet was dissolved in 25-μl Milli-Q^{TM} (Millipore, Burlington, MA, United States) water and used for qRT-PCR analyses. Primers used for qRT-PCR analyses are listed in **Supplementary Table 2**.

Construction of Negative Domain-Overexpressing Strain and Control Strain (TFc)

The pSUGA_CmMYB1_1-380 was first created with primer set MYB1OE380_F (listed in **Supplementary Table 1**), MYB1OE380_R with pO250-CmMYB1 (Zhou et al., 2021) as a template using the Gibson Assembly Master Mix (New England Biolabs, Ipswich, MA, United States). Then, primer sets MYB1TFc_F, MYB1TFc_R, and MYB1ND_OE_F, MYB1ND_OE_R were used to create pSUGA_CmMYB1_1−9, pSUGA_CmMYB1_1−9, and 311−380 with pSUGA_CmMYB1_1−380 as templates, respectively. The T1 strain was transformed with pSUGA_CmMYB1_1−9 and pSUGA_MYB1_1−9, 311−380, as described previously (Takemura et al., 2018), and transformants were spread and grown on an MA2 gellan gum plate. The PCR using in the primer set listed in **Supplementary Table 1** was performed to get the correct transformants. Each cloned protein was fused with a FLAG-tag, and the expression was regulated by the strong *APCC* promoter (Fujii et al., 2013).

Pull-Down Assay and Liquid Chromatography-Tandem Mass Spectrometry Analysis

Proteins from Negative Domain-Overexpressing Strain (ND_OE) and TFc were extracted as described in section "Protein extraction and immunoblot analysis." From each sample, the 750-μg protein was subjected to the pull-down assay with 50-μl/sample anti-FLAG antibody magnetic beads (Wako, Osaka, Japan). The beads were washed six times with a lysis buffer (see section "Protein extraction and immunoblot analysis") and were boiled for 5 min in an SDS sample buffer. The eluted proteins were separated by SDS-PAGE using a 5–20% polyacrylamide gradient gel (Oriental Instruments, Kanagawa, Japan) and were visualized by Coomassie brilliant blue staining. Each lane in the gel was entirely cut out, was transferred to a 14-ml round-bottom tube, and was shaken sequentially in 30, 50, and 100% acetonitrile solutions for destaining and dehydration. The gel strips were incubated in 25-mM ammonium bicarbonate containing 10-mM dithiothreitol (DTT) at 56°C for 1 h and then in 25-mM ammonium bicarbonate containing 55-mM acrylamide at room temperature for 1 h for reduction and alkylation of the sulfhydryl groups. The samples were washed in water and were then dehydrated in the acetonitrile solutions before tryptic digestion. The dried gel strips were reconstituted by a solution containing 90-ng Trypsin Gold (Promega, Madison, WI, United States), 50-mM ammonium bicarbonate, and 10% acetonitrile, and were incubated overnight at 37°C. The resulting tryptic peptides were eluted three times in 75% acetonitrile and 1% formic acid. After concentration in a speedvac, the samples were finally dissolved in 45 μl of 0.5% formic acid. From each sample, 15 μl was subjected to liquid chromatography-tandem mass spectrometry (LC-MS/MS) using an Orbitrap Fusion mass spectrometer equipped with an Easy-nLC 1,000 high-performance liquid chromatography (HPLC) system (Thermo Fisher Scientific, Waltham, MA, United States). The peptides were separated on a C18 tip column (a 75-μm inner diameter and 10-cm length, Nikkyo Technos, Tokyo, Japan) at a 300-ml min^{-1} flow rate with a linear gradient generated by aqueous solvent A (0.1% formic acid in water) and organic solvent B (0.1% formic acid in acetonitrile): 5% B to 35% B in 40 min, to 45% B in 46 min, to 95% B in 48 min, 95% B from 48 to 49 min, and, finally, to 5% B in 50 min. MS^1 scans from m/z = 321–1,500 were performed in the Orbitrap mass spectrometer with the resolution set to 120,000 with lock masses at m/z = 445.12003 and 391.28429, which was followed by the acquisition of higher energy collisional dissociation (HCD)-MS^2 using the ion trap. The settings for the MS^2 scans were as follows: an intensity threshold = 1,000, charge states = + 2 to + 6, isolation width = 1.2 m/z, AGC target = 5,000, maximum ion injection time = 50 ms, normalized collision energy = 35%, and dynamic exclusion enabled with 50-s exclusion duration. The MS/MS cycle time was set to 4 s. The MS/MS data were acquired over 55 min after the LC gradient was started. Peptide identification was done by searching the *C. merolae* protein database[1] and a common contaminating protein list using a MASCOT search engine (version 2.6.0, Matrix Science, Mount Prospect, IL, United States). A maximum of four trypsin miscleavages were allowed. The peptide mass tolerance and MS/MS tolerance were set at 5 ppm and 0.5 Da, respectively. Propionamidated cysteine (+71.0371) was set as a fixed modification. Protein N-terminal acetylation (+42.0106 Da) and oxidation of methionine (+15.9949 Da) were considered as variable modifications. The Mascot ion score threshold was set to 0.05. Obtained MS/MS data are presented in **Supplementary Table 3**.

Yeast Two-Hybrid Analysis

The open-reading frames (ORFs) of the top 15 candidates' encoded genes picked up from LC-MS/MS analysis were amplified with the primer sets listed in **Supplementary Table 4**

[1]http://merolae.biol.s.u-tokyo.ac.jp/download/orf.fasta

[For Y2H activation domain (AD) vector construction] and *C. merolae* genomic DNA as templates. The PCR-amplified genes were then cloned into *Sma*I-digested pGADT7, respectively, using the Gibson Assembly Master Mix (New England Biolabs, Ipswich, MA, United States) to create each AD vector. To create the BD plasmid, the *CmMYB1* ORF was firstly amplified with the primer set MYB1y2h_F, MYB1y2h_R listed in **Supplementary Table 4** [For Y2H-binding domain (BD) vector construction] and *C. merolae* genomic DNA as a template. The PCR-amplified *CmMYB1* ORF was then cloned into *Sma*I-digested pGBT9 using the same method mentioned above to create the pGBT9_CmMYB1 vector. The pGBT9_CmMYB1_1–380 plasmid was then created using the same method mentioned above with primer set MYB1y2h_381_F, MYB1y2h_381_R listed in **Supplementary Table 4**, and pGBT9_CmMYB1 was used as a template. Finally, BD plasmid pGBT9_ND was created using primer set MYB1ND_OE_F, MYB1ND_OE_R listed in Table S4, and pGBT9_CmMYB1_1–380 as a template. All the vectors (15 AD vectors and 1 BD vector) were transformed to yeast gold competent cells (Takara, Shiga, Japan) using Frozen-EZ Yeast Transformation II Kit (Zymo Research, Irvine, CA, United States) according to the manufacturer's instructions. Transformants were incubated at 30°C for 1 week, and transformants containing AD vectors were mated with transformants containing BD vector, respectively, and spread on SD−LW [synthetic dextrose (SD), leucine (L), and tryptophan (W) lacking] plates. Resulted transformants were further diluted and spotted on SD−LWH (L, W, and histidine (H) lacking) with 5-Bromo-4-chloro-3-indolyl-α-D-galactopyranoside [(X-α-Gal) (Wako, Osaka, Japan) and Aureobasidin A (AbA) (Takara, Shiga, Japan) being added] and SD−LWHA (L, W, H, and alanine (A) lacking with X-α-Gal and AbA being added) plates and SD−LW plates and incubated at 30°C for 1 week. Photos of SD−LW plates were taken on the second incubation day. Photos of SD−LWH and SD−LWHA plates were taken on the 7th incubation day.

Construction of FLAG-Fused CmMYB1 Strain, WM1

The DNA fragment used for transformation was constructed through three steps. Firstly, the primer set CAT_MCS_F (listed in **Supplementary Table 1**), NOS_ter_R was used to amplify Fragment_1 using KOD Plus NEO (Toyobo, Osaka, Japan), and pMKTf (Takemura et al., 2018) plasmid as a template. Secondly, primer set NOS_ter_CAT_F, URA_CAT_R was used to amplify Fragment_2 using KOD Plus NEO (Toyobo, Osaka, Japan) and pD-184 CAT plasmid (given by Dr. Fujiwara) as a template. Thirdly, primer sets MCS_J282C_orf_F, MCS_J282C_orf_R, and MCS_J282C_ter_F, MCS_J282C_ter_R were used to amplify CmMYB1_ORF DNA and CmMYB1_ter DNA, respectively, using KOD Plus NEO (Toyobo, Osaka, Japan) and *C. merolae* genomic DNA as templates, respectively. Then, Fragment_1 and Fragment_2 were used to create pMKT_CAT plasmid using the Gibson Assembly Master Mix (New England Biolabs, Ipswich, MA, United States). Restriction enzyme *Hpa*I was used to cut the pMKT_CAT plasmid, and two linear DNA fragments, "pMKT" DNA fragment and "CAT" DNA fragment, were obtained. Finally, "pMKT" DNA, "CAT" DNA, CmMYB1_ORF DNA, and CmMYB1_ter DNA were used to create pMKT_CAT_CmMYB1 plasmid using the Gibson Assembly Master Mix (New England Biolabs, Ipswich, MA, United States). The primer set MCS_J282C_orf_F, MCS_J282C_ter_R was used to amplify CmMYB1_CAT DNA using KOD Plus NEO (Toyobo, Osaka, Japan). The CmMYB1_CAT DNA was then transformed into a WT strain as described previously (Takemura et al., 2018), and transformants were cultured in an MA2 medium for 1 week and spread on an MA2 gellan gum plate containing 300 μg ml^{-1} chloramphenicol (Fujiwara et al., 2017). The PCR using primer sets listed in **Supplementary Table 1** was performed to get correct transformants.

Construction of Uracil Auxotrophy Strain of WM1, MΔ95a

The DNA fragment used for transformation was constructed through four steps. Firstly, the primer set URA5.3pro_KS_F (listed in **Supplementary Table 1**), URA5.3ter_SK_R was used to amplify Fragment_1, using KOD Plus NEO (Toyobo, Osaka, Japan) and *C. merolae* genomic DNA as a template. Secondly, Fragment_1 was inserted into the *Sma*I-digested pBluescript SK plasmid to create the pBluescript _URA5.3 plasmid. Thirdly, inverse PCR was performed using primer set URA5.3ORFdel_F, URA5.3ORFdel_R with pBluescript _URA5.3 plasmid as a template, and the amplified DNA fragment was directly used for creating the pBluescript _URA5.3KO plasmid with the Gibson Assembly Master Mix (New England Biolabs, Ipswich, MA, United States). Finally, the DNA fragment used for transformation was amplified using the primer set URA5.3pro_F, URA5.3ter_R with pBluescript _URA5.3KO plasmid as a template. The amplified DNA fragment was then transformed into the WM1 strain as described previously (Takemura et al., 2018), and transformants were spread and grown on an MA2 gellan gum plate supplied with 0.5-mg ml^{-1} uracil and 0.8-mg ml^{-1} 5-FOA. Sequencing analysis was performed using URA5.3_seq_F primer listed in **Supplementary Table 1** to get the correct transformants.

Construction of *CmNDB1* Knockout Strain, BZ6

The DNA fragment used for transformation was constructed through three steps. Firstly, the primer sets pCmNDB1pro_F (listed in **Supplementary Table 1**), pCmNDB1pro_R, and pCmNDB1ter_F, pCmNDB1ter_R were used to amplify Fragment_1 and Fragment_2, using KOD Plus NEO (Toyobo, Osaka, Japan) and *C. merolae* genomic DNA as templates, respectively. Secondly, Fragment_1 and Fragment_2 were inserted into the *Stu*I-digested pMKTm (Takemura et al., 2018) plasmid to create the pMKT_CmNDB1_KO plasmid. Thirdly, the DNA fragment used for transformation was amplified using the primer set CmNDB1_879pro_F, CmNDB1_651ter_R with pMKT_CmNDB1_KO plasmid as a template. The amplified DNA fragment was then transformed into the MΔ95a strain as described previously (Takemura et al., 2018), and transformants were spread and grown on an MA2 gellan gum plate. The

PCR using primer sets listed in **Supplementary Table 1** was performed to get the correct transformants.

Construction of Myc-Fused CmNDB1 Strain, MR66

The DNA fragment used for transformation was constructed through three steps. Firstly, the primer sets CmNDB1orf_F (listed in Table S1), CmNDB1orf_R, and CmNDB1ter_F, CmNDB1ter_R were used to amplify Fragment_1 and Fragment_2, using KOD Plus NEO (Toyobo, Osaka, Japan) and *C. merolae* genomic DNA as templates, respectively. Secondly, Fragment_1 and Fragment_2 were inserted into the *Stu*I-digested pMKTm (Takemura et al., 2018) plasmid to create the pMKT_NDB1myc plasmid. Thirdly, the DNA fragment used for transformation was amplified using the primer set CmNDB1tf_F, CmNDB1tf_R with pMKT_NDB1myc plasmid as a template. The amplified DNA fragment was then transformed into the MΔ95a strain as described previously (Takemura et al., 2018), and transformants were spread and grown on an MA2 gellan gum plate. The PCR using primer sets listed in **Supplementary Table 1** was performed to get the correct transformants.

RESULTS

Identification of the Negative Element of CmMYB1 for Its Function

Functions of TFs are usually modulated by their regulatory elements that bind to cofactors and metabolite molecules (Xie et al., 2006; Puga et al., 2014; Le et al., 2016; Qi et al., 2017; Zhu et al., 2019; Wang et al., 2020) or by post-translational modifications (Gill, 2003; Tootle and Rebay, 2005; Schütze et al., 2008). Therefore, we hypothesized that the underlying mechanism related to nitrogen status-dependent CmMYB1 function could be revealed by the identification of the CmMYB1 regulatory element. To test this hypothesis, using a non-*CmMYB1* background strain combined with a plasmid series expressing partially truncated CmMYB1s would be a good strategy. Since CmMYB1 would only be expressed exogenously; different phenotypes among the strains must be caused by the different CmMYB1 sequences. Firstly, we designed and obtained a *CmMYB1* knockout strain named BZ1 (**Supplementary Figure 1**), which shows uracil auxotrophy and 5-FOA resistance (**Figures 1A,B**) as a host strain for the analysis. We constructed a series of plasmids expressing FLAG-fused CmMYB1 in different amino acid sequence patterns from the carboxyl-terminus, which is regulated by *CmMYB1* own promoter. After transforming each plasmid into BZ1, we succeeded in obtaining all five types of CmMYB1 transformants (**Supplementary Figures 2, 3**): pPD1–310, which expresses +1 to +310 amino acids of CmMYB1 (+1 indicates the start position of translation), pPD1–380, pPD1–460, pPD1–99, 201–523, and pPD1–523 (**Figure 1C**).

A previous study showed that the *CmNRT* transcript was completely CmMYB1 dependent. It was increased under −N conditions and came to a peak at the fourth hour after −N treatment (Imamura et al., 2009). Thus, the transcript level of *CmNRT* at the fourth hour after −N could well represent the functional status of CmMYB1 in the cell. We first investigated the transcripts before (+N) and after the −N condition in each constructed strain by Northern blot analysis (**Figure 1D**). We evaluated *CmNRT* transcript levels after normalizing with CmMYB1 protein levels in each strain since the CmMYB1 protein level could affect the transcripts. Our recent work has demonstrated that overexpressing *CmMYB1* in *C. merolae* significantly increased *CmNRT* transcripts under the +N condition (Zhou et al., 2021). To monitor CmMYB1 protein levels, we conducted dot blot analysis since different sizes of proteins could cause distinct membrane transfer efficiencies during immunoblot analysis (**Figure 1E** and **Supplementary Figure 3**). Eventually, we got the transcript accumulation of *CmNRT*, and the results showed that the *CmNRT* transcript level was higher in pPD1–310 than in pPD1–523 under the +N condition (**Figure 1F**). No *CmNRT* transcripts were observed in pPD1–380, pPD1–460, or pPD1–99, 201–523, same as in pPD1–523 (**Figure 1D**). On the contrary, *CmNRT* transcripts showed no difference in pPD1–310 as opposed to pPD1–523 under the −N condition, whereas it was lower in pPD1–380, pPD1–460, and pPD1–99, 201–523 (**Figure 1F**). These results clearly suggested that +311 to +380 amino acids of CmMYB1 negatively regulate the transcripts of *CmNRT* under the +N condition.

Next, we wondered whether this regulation could also be observed in other nitrogen assimilation genes expression. Therefore, we checked these transcripts under the same condition shown in **Figure 1D** by quantitative real-time PCR (qRT-PCR) analysis using specific primer sets (**Supplementary Table 2**). The results showed that transcript accumulation of nitrate assimilation genes, *CmNRT*, *CmNR,* and *CmNIR* (encoding nitrite reductase, NIR), was higher in pPD1–310 but lower or no change in pPD1–380, pPD1–460, and pPD1–99, 201–523 than in pPD1–523 under the +N condition (**Figure 1G** and **Supplementary Figures 4A–C**). In the case of the transcript accumulation of *CmNRT* and *CmNR* under the −N condition, a significant decrease was observed in pPD1–380, pPD1–99, 201–523 compared with pPD1–523, whereas there was no difference in pPD1–310 (**Figure 1G** and **Supplementary Figures 4A,B**). Contrarily, transcript accumulation of *CmAMT* and *CmGS* was lower in pPD1–310 and other transformants than in pPD1–523 under + N and −N conditions, respectively (**Figure 1G** and **Supplementary Figures 4D,E**). These data clearly revealed that the +311 to +380 amino acid region of CmMYB1 functions as a negative domain for CmMYB1 (hereafter ND) and specifically regulates transcription of nitrate assimilation genes under the +N condition.

Effects of Subcellular Localization and the Promoter-Binding Ratio of CmMYB1 by Negative Domain

Given the evidence that ND negatively regulates transcription of nitrate assimilation genes under the +N condition, we considered two possibilities regarding the regulation, namely localization and the DNA-binding ratio of CmMYB1. We first investigated the effect of ND on the intracellular localization

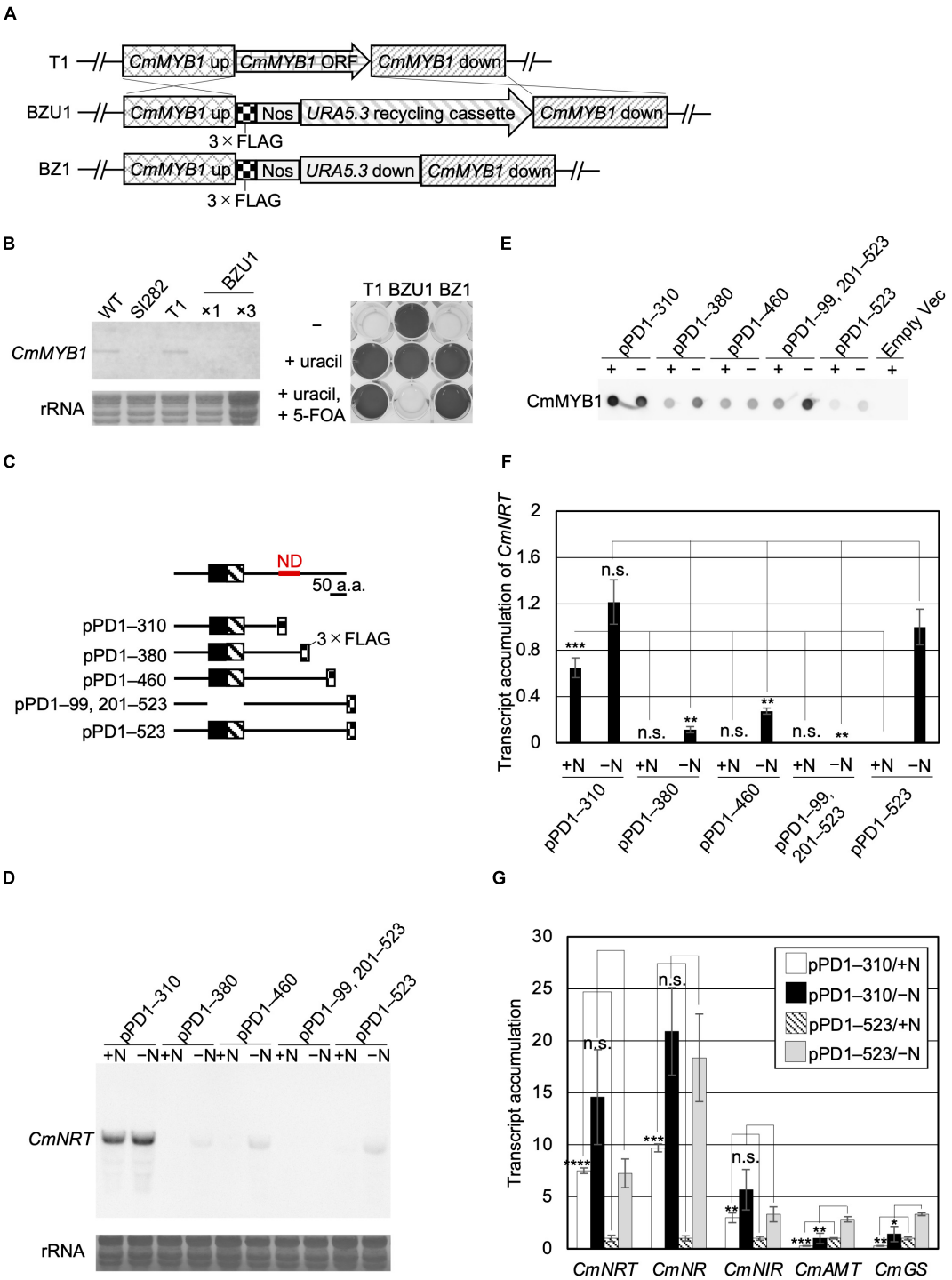

FIGURE 1 | Acquisition of CmMYB1 partially truncated transformants and expression of nitrogen assimilation genes under nitrogen-repleted (+N)/nitrogen-depleted (−N) conditions. **(A)** Schematic representation of the *CmMYB1* ORF locus in the T1 (top panel), BZU1 (middle panel), and BZ1 (bottom panel) strains. "*CmMYB1* up" and "*CmMYB1* down" indicate the 1,500-bp upstream and downstream regions of *CmMYB1*, respectively, used for homologous recombination. "*CmMYB1* ORF" indicates the 1,569-bp open-reading frame of *CmMYB1*. "Nos" indicates the nopaline synthase (NOS) terminator. "Uracil recycling cassette" indicates a 3,234-bp fragment used for uracil auxotrophic transformant selection. "*URA5.3* down" indicates a 483-bp downstream region of *URA5.3*. **(B)** Confirmation of the transcript level of *CmMYB1* in BZU1 strain (left panel) and uracil auxotrophy of BZ1 strain (right panel). Left panel, BZU1, and T1 cells were harvested under normal culture condition, and total RNAs were prepared from the cells. Total RNAs (2.8 μg, ×1) were then subjected to Northern blot analysis with a specific probe for *CmMYB1*. Total RNAs (8.4 μg) from BZU1 cells were used as an overloaded sample (×3) in the analysis. rRNA-stained with methylene blue is shown as the loading control (bottom panel). SI282 strain is a *CmMYB1*-null strain whose host strain is M4, a uracil auxotrophy strain. T1, which was generated from WT, contains no *URA5.3*

(Continued)

FIGURE 1 | ORF. The right panel, stationary phase T1, BZU1, and BZ1 cells were diluted into OD_{750} = 0.1 and incubated for 7 days prior to photography. "-" represents an MA2 medium. "+uracil" represents an MA2 medium containing 0.5-mg ml^{-1} uracil. "+uracil, +5-FOA" represents an MA2 medium containing 0.5-mg ml^{-1} uracil and 0.8-mg ml^{-1} 5-fluoroorotic acid (5-FOA). **(C)** Schematic representation of the CmMYB1 partially truncated transformants. Black and hatched boxes indicate the R2- and R3-type MYB domain, respectively. As an example, pPD1–310 represents the transformant, which expresses +1 to +310 amino acids (+1 indicates the start position of translation) of CmMYB1 with three-time repeats of the FLAG epitope tag (3 × FLAG). ND is short for "negative domain." **(D)** Transcript levels of *CmNRT* under the +N/−N conditions in CmMYB1 partially truncated transformants. Cells were treated under the +N/−N conditions for 4 h, and total RNAs were prepared from the cells. Total RNAs (4.5 μg) were used in Northern blot analysis with a specific probe for *CmNRT*. Same experiments were performed three times, independently. **(E)** Protein levels of FLAG-fused CmMYB1 under the +N/−N conditions in CmMYB1 partially truncated transformants. Aliquots containing 16.6 μg of total proteins harvested from the *C. merolae* cells under the same condition as in **(D)** were dropped on a hydrophilized PVDF membrane and analyzed with an anti-FLAG antibody (Wako, Osaka, Japan). Proteins extracted from empty vector transformants (Empty Vec) were used as a negative control. Same experiments were performed three times, independently. **(F)** Transcript accumulation of *CmNRT* in CmMYB1 partially truncated transformants. ImageJ (Schneider et al., 2012) was used for determining the signal strength of *CmNRT* and CmMYB1 from **(D,E)**. Transcript accumulation of *CmNRT* was calculated by dividing the strength of *CmNRT* transcript levels into the strength of CmMYB1 protein levels. Values represent the average transcript accumulation of *CmNRT* in three independent experiments. Error bars indicate the standard deviation (SD). Significant differences were determined using one-way ANOVA (for the +N condition, $p = 0.0000012$; for the −N condition, $p = 0.000056$) followed by *post hoc* tests. The asterisks denote the difference between the "pPD1–523/ + N" sample *vs.* other +N condition samples, the "pPD1–523/−N" sample *vs.* other −N condition samples, respectively (***$p \leq 0.001$, **$p \leq 0.01$, n.s., $p > 0.0125$). **(G)** Quantitative real-time PCR (qRT-PCR) analysis of the transcript accumulation of nitrogen assimilation genes. Of the total RNAs per condition of pPD1–310 and pPD1–523 from **(D)**, 500 ng was used for genome DNA re-movement and cDNA synthesis. Results were from three independent experiments, and data represent transcript accumulation of each gene. Asterisks indicate the statistical significance of differences between the pPD1–310/+N sample and the pPD1–523/+N sample, the pPD1–310/−N sample and the pPD1–523/−N sample, respectively (*$p < 0.05$, **$p < 0.01$, ***$p < 0.001$, ****$p < 0.0001$, n.s., $p > 0.05$; Student's *T*-test).

of CmMYB1 by immunostaining analysis before (+N) and after the −N condition. In addition to the strains used in **Figure 1**, to investigate the impact of only the ND region, we further constructed a transformant expressing +1 to +310, +381 to +523 amino acids of CmMYB1 and named it pPD1–310, 381–523 (**Supplementary Figure 2**). The results showed that CmMYB1 in pPD1–523 and pPD1–99, 201–523 was localized in the cytoplasm under the +N condition (**Figure 2A**). Contrarily, ND truncated CmMYB1 in pPD1–310, 381–523, and pPD1–310 showed nucleus and cytoplasm localizations that were similarly observed in pPD1–523 under the −N condition (**Figure 2A**). Besides, localization data from over 110 cells per strain under the +N/−N condition were subjected to statistical analysis. Results showed that CmMYB1 in about 4% of cells was localized in the cytoplasm and nucleus in pPD1–523 under the +N condition, whereas CmMYB1 in over 63% of cells exhibited the same distribution in pPD1–310 and pPD1–310, 381–523 (**Figure 2B**). On the other hand, CmMYB1 in about 58% of cells was localized in the cytoplasm and nucleus in pPD1–523 under the −N condition. Results of immunostaining analysis and statistical analysis implied that ND maintains CmMYB1 in the cytoplasm under the +N condition.

Next, we checked the other possibility, namely, the effect of ND on the DNA-binding efficiency of CmMYB1. The previous study has shown that CmMYB1 specifically binds to the proximal promoter region of *CmNRT* under the −N condition but not the distinct region (Imamura et al., 2009). Therefore, we tested the promoter-binding ratio of several truncated CmMYB1s at these two regions under the +N condition through chromatin immunoprecipitation (ChIP) analysis. We normalized the values from ChIP analysis with CmMYB1 protein levels from dot blot analysis (**Figure 2C**). The results showed that ND-truncated CmMYB1 in pPD1–310, 381–523, and pPD1–310 exhibited a specifically higher promoter-binding ratio to the #2 region of *CmNRT* (**Figure 2D**, up panel) than the full length of CmMYB1 in pPD1–523 under the +N condition (**Figure 2D**). In contrast, the similar high-binding ratio of CmMYB1 detected in the #2 region was not observed in the #4 region (**Figure 2D**). We also performed ChIP analysis under the −N condition using pPD1–310, pPD1–99, 201–523, and pPD1–523. We normalized the values from ChIP analysis with CmMYB1 protein levels from dot blot analysis (**Figure 2E**). The results showed that the promoter-binding ratio to the #2 region of *CmNRT* showed no difference between ND-truncated CmMYB1 in pPD1–310 and the full length of CmMYB1 in pPD1–523 (**Figure 2F**). These results exhibited that ND inhibits the promoter-binding ratio of CmMYB1 under the +N condition, but not the −N condition.

Identification of Negative Domain-Interacting Proteins

Since ND regulates CmMYB1 localization and the promoter-binding ratio under the +N condition, we decided to further investigate the underlying mechanism. We assumed ND is controlled by its binding protein(s), because, in *Saccharomyces cerevisiae*, transcriptional regulator Ure2 binds to Gln3 and maintains Gln3 in the cytoplasm under the +N condition (Blinder et al., 1996; Beck and Hall, 1999; Carvalho and Zheng, 2003). To investigate the possibility, we first constructed a FLAG-fused ND-overexpressing strain (ND_OE) and its control strain (TFc) (**Supplementary Figure 5**). We performed a pull-down assay using ND_OE and TFc grown under the +N condition, and the resultant pull-down products were subjected to LC-MS/MS. After analyzing the data, we eventually obtained a list of potential ND-interacting proteins (**Supplementary Table 3**). Among them, based on the setting rule that the protein score is higher than 130, we picked up the top 15 candidates for further analysis (**Figure 3A**).

To confirm the interaction between ND and those candidates, we performed a yeast two-hybrid (Y2H) analysis. Results showed that transformants coexpressing ND and CMR469C (protein number in the *C. merolae* database[2]), annotated as a hypothetical protein with a comment as a "cyanobacterial protein," could grow on SD−LWH media and SD−LWHA, stronger selection media than SD−LWH (**Figure 3B**). These data, together with

[2]http://czon.jp

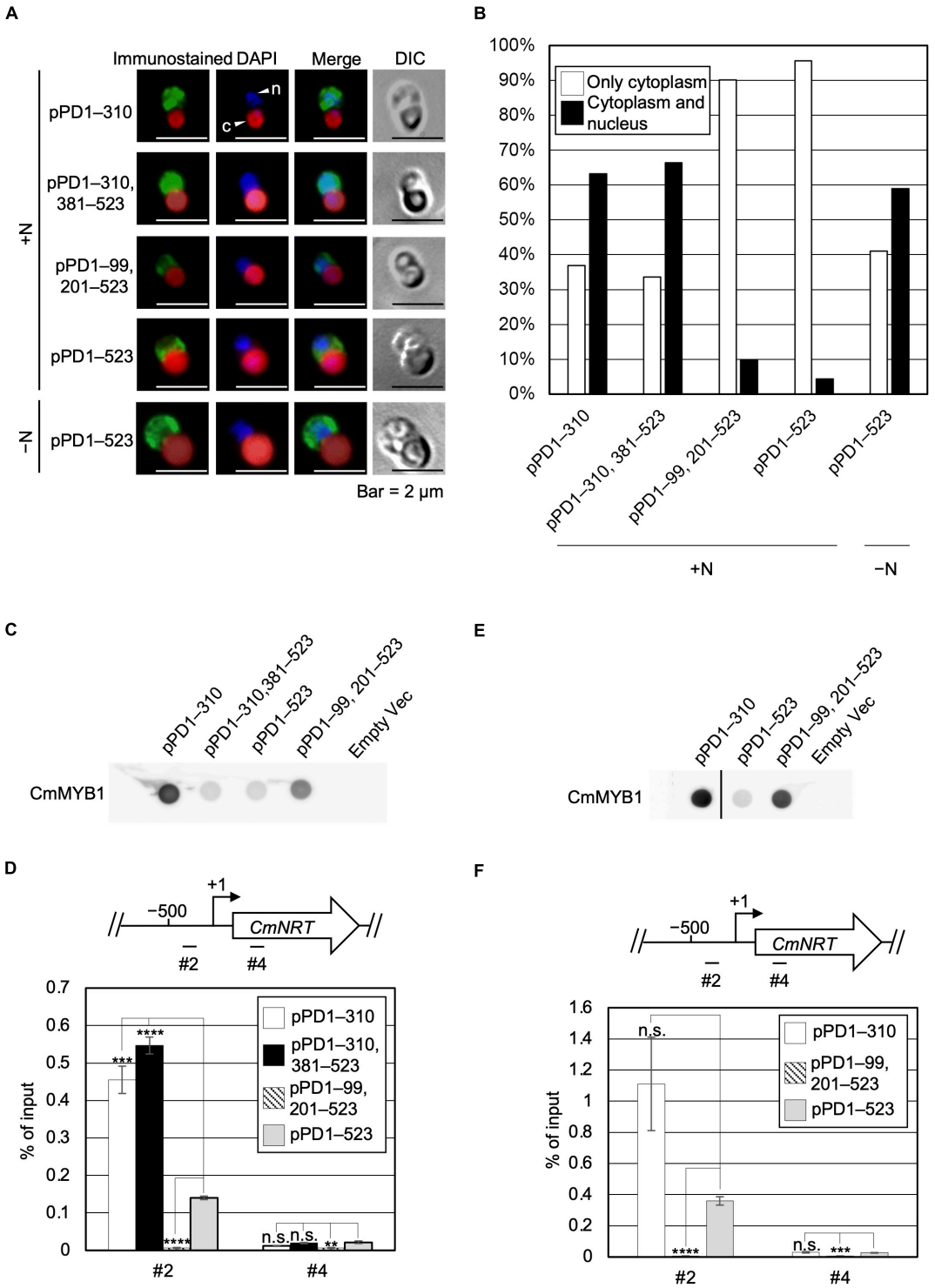

FIGURE 2 | Subcellular localization and a promoter-binding ratio of CmMYB1 under the +N/−N conditions. **(A)** Subcellular localization of CmMYB1 in CmMYB1 partially truncated transformants. Fixed cells under the +N/−N conditions for 4 h were reacted with an anti-FLAG antibody (Wako, Osaka, Japan), and the localization of FLAG-fused CmMYB1 was detected with an Alexa Fluor 488-conjugated donkey anti-mouse antibody (Thermo Fisher Scientific, Waltham, MA, United States, a green signal from "immunostained" pictures). DAPI staining of nucleus DNA (a blue signal from "DAPI" pictures), merged image of immunostaining and DAPI staining (Merge), and differential interference contrast image (DIC) are shown. Positions of nucleus (n) and chloroplast (c) were indicated with arrowheads (a scale bar, 2 μm). **(B)** Statistical analysis of CmMYB1 localization in CmMYB1 partially truncated transformants. Over 110 cells per strain under the +N condition were used in this analysis. Photos of fluorescence of CmMYB1 and the nucleus were treated with the same parameter, and colocalization of CmMYB1 with the nucleus was determined by covering CmMYB1 fluorescence with the nucleus fluorescence. **(C)** Protein levels of FLAG-fused CmMYB1 under the +N condition in CmMYB1

(Continued)

FIGURE 2 | partially truncated transformants. Aliquots containing 16.6 μg of total proteins from the *C. merolae* cells harvested under the +N condition for 4 h were dropped on a hydrophilized PVDF membrane and analyzed with an anti-FLAG antibody (Wako, Osaka, Japan). Proteins extracted from empty vector transformants (Empty Vec) were used as a negative control. Same experiments were performed three times, independently. **(D)** Determination of the CmMYB1 promoter-binding ratio to *CmNRT in vivo* under the +N condition. CmMYB1 partially truncated transformant cells were treated under the +N condition for 4 h and subsequently fixed for ChIP analysis. The schematic diagram above the image indicates the analyzed gene *CmNRT* and positions that were amplified by qRT-PCR following ChIP (+1 indicates the transcription start site). The anti-FLAG antibody (Wako, Osaka, Japan) was used in this ChIP analysis. Values are averages of three independent experiments, and % of input was calculated by dividing percentage recovery from ChIP analysis into CmMYB1 protein levels. Error bars indicate the standard deviation (SD). Significant differences were determined using one-way ANOVA (for position #2 of *CmNRT*, $p = 0.00000029$; for position #4 of *CmNRT*, $p = 0.0034$), followed by *post hoc* tests. The asterisks denote the difference between the pPD1–523 +N sample vs. the other samples in position #2 or #4 of *CmNRT*, respectively. (****$p \leq 0.0001$, ***$p \leq 0.001$, **$p \leq 0.01$, n.s., $p > 0.0167$). **(E)** Protein levels of FLAG-fused CmMYB1 under the −N condition in CmMYB1 partially truncated transformants. Aliquots containing 16.6 μg of total proteins from the *C. merolae* cells harvested under the −N condition for 4 h were dropped on a hydrophilized PVDF membrane and analyzed with an anti-FLAG antibody (Wako, Osaka, Japan). Proteins extracted from empty vector transformants (Empty Vec) were used as a negative control. The pPD1–310 +N lane and the right membrane are on the same membrane. A straight line was added between the pPD1–310 +N lane and the pPD1–523 +N lane since we removed some additional signal between these two lanes. Same experiments were performed three times, independently. **(F)** Determination of the CmMYB1 promoter-binding ratio to *CmNRT in vivo* under the −N condition. CmMYB1 partially truncated transformant cells were treated under the −N condition for 4 h and subsequently fixed for ChIP analysis. The schematic diagram above the image indicates the analyzed gene *CmNRT* and positions that were amplified by qRT-PCR following ChIP (+1 indicates the transcription start site). The anti-FLAG antibody was used in this ChIP analysis. Values are averages of three independent experiments, and % of input was calculated by dividing percentage recovery from ChIP analysis into CmMYB1 protein levels. Error bars indicate the standard deviation (SD). Significant differences were determined using one-way ANOVA (for position #2 of *CmNRT*, $p = 0.0021$; for position #4 of *CmNRT*, $p = 0.000059$), followed by *post hoc* tests. The asterisks denote the difference between the pPD1–523 −N sample *vs.* the other samples in position #2 or #4 of *CmNRT*, respectively. (****$p \leq 0.0001$, ***$p \leq 0.001$, n.s., $p > 0.025$).

the pull-down assay, showed that CMR469C interacts with the ND of CmMYB1. We named CMR469C as CmNDB1, short for *C. merolae* Negative Domain Binding Protein 1.

Effect of Subcellular Localization and the Promoter-Binding Ratio of CmMYB1 by Deletion of *CmNDB1*

Based on the results observed from the Y2H analysis, we investigated whether CmNDB1 interacts with CmMYB1 in the *C. merolae* cell. Thus, we investigated the possibility by co-immunoprecipitation (Co-IP) analysis using a strain in which Myc-fused CmNDB1 and FLAG-fused CmMYB1 were expressed. We could not observe the interaction between CmNDB1 and CmMYB1 in *C. merolae* cells under many experimental conditions (see section "Discussion").

Therefore, we tried to reveal the effect of CmNDB1 on the regulation of CmMYB1 functions through the genetic analysis approach. To examine this, we first constructed a strain named WM1 (**Supplementary Figure 6**), in which FLAG-fused CmMYB1 was expressed. Using WM1, we then obtained a strain named MΔ95a (**Supplementary Figure 7**), which was used as a parent strain for constructing a *CmNDB1* knockout strain named BZ6 (**Supplementary Figure 8**). We investigated CmMYB1 localization by immunostaining analysis before (+N) and after the −N condition using MΔ95a and BZ6. The results showed that CmMYB1 was localized in the cytoplasm in MΔ95a, a parent strain of BZ6, whereas it was localized in both the cytoplasm and nucleus in BZ6 under the +N condition (**Figure 4A**, a green signal from the first and third rows). Contrarily, CmMYB1 exhibited cytoplasm and nucleus distribution in both MΔ95a and BZ6 under the −N condition (**Figure 4A**, a green signal from the second and fourth rows). Besides, localization data from over 110 cells per strain under the +N or −N condition were subjected to statistical analysis. Results showed that CmMYB1 in about 18% of cells was localized in the cytoplasm and nucleus in MΔ95a under the +N condition, whereas CmMYB1 in over 65% of cells exhibited the same distribution in BZ6 (**Figure 4B**). On the contrary, cytoplasm and nucleus localization of CmMYB1 was observed in over 70% MΔ95a cells, 73% BZ6 cells, under the −N condition, respectively (**Figure 4B**). Results of immunostaining analysis and statistical analysis indicated that CmNDB1 contributes to maintaining CmMYB1 in the cytoplasm under the +N condition.

Since localization of CmMYB1 was altered in the *CmNDB1* deletion strain, we wondered whether the promoter-binding ratio of CmMYB1 was also influenced by deleting *CmNDB1*. To this end, we examined this possibility by ChIP analysis and normalized the values with CmMYB1 protein levels from dot blot analysis (**Figure 4C**). Results showed that CmMYB1 exhibited a specifically higher promoter-binding ratio to the #2 region of *CmNRT* in BZ6 than in MΔ95a under the +N condition (**Figure 4D**). In contrast, the promoter-binding ratio of CmMYB1 to the #2 region showed no difference under the −N condition between the two strains (**Figure 4D**). In both strains, reduced promoter-binding ratios of CmMYB1 were observed under the −N condition than under the +N condition, which is inconsistent with our previous result observed in WT (Imamura et al., 2009). The reason that caused these different change patterns of CmMYB1 promoter-binding ratios between WT and MΔ95a is still unknown. One possibility could be the chromatin architecture change around *CmMYB1* due to the insertion of construction for FLAG epitope tag expression. These results suggested that CmNDB1 reduces the CmMYB1 promoter-binding ratio under the +N condition.

Effect on Transcription of Nitrate Assimilation Genes by Deletion of *CmNDB1*

Subcellular localization and ChIP analysis data above showed that *CmNDB1* deletion caused cytoplasmic and nuclear localization of CmMYB1 and a higher promoter-binding ratio of CmMYB1 under the +N condition. Does *CmNDB1* deletion also influence

A

Gene number[1]	Annotation	Ratio (ND_OE vs. TFc)	
		Protein scores[2]	Peptide matches[3]
CMT579C	Luminal binding protein BiP	8.1	3.7
CMC180C	Probable protein disulfide-isomerase	26.8	22.7
CMQ089C	Probable protease	16.8	9.1
CMR469C	Hypothetical protein, conserved	11.0	10.3
CMR380C	Fusion protein of glyoxysomal fatty acid oxidation tetrafunctional protein, and acetyl-CoA acyltransferase	8.9	9.3
CMP227C	Probable ferritin, chloroplast precursor	10.1	4.0
CMA009C	NAD-dependent sorbitol dehydrogenase	17.2	10.0
CMG039C	Aspartyl aminopeptidase	-	-
CMR125C	Similar to nucleoporin complex subunit	4.4	5.0
CMP337C	Similar to desmoplakin	-	-
CMI268C	Hypothetical protein, conserved	-	-
CMM285C	Hypothetical protein, conserved	7.6	7.0
CMM226C	Hypothetical protein, conserved	5.8	2.0
CMN113C	Cullin 4	-	-
CMH109C	Raptor	-	-

[1] Gene number in *C. merolae* database, http://czon.jp accessed on 22 November 2021.
[2] Protein scores were given by MASCOT search engine (version 2.6.0, Matrix Science).
[3] Peptide matches indicate the detected number of unique peptides generated from the MS analysis.

B

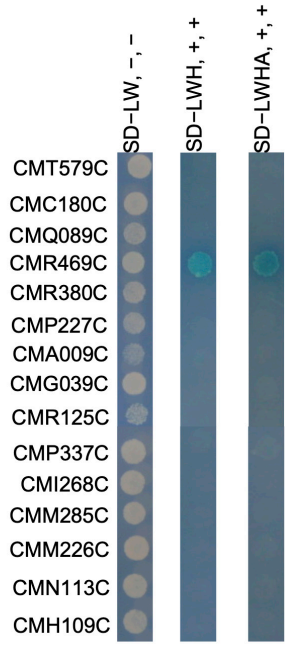

FIGURE 3 | A list of ND-binding proteins from LC-MS/MS analysis and confirmation of ND-binding proteins by yeast two-hybrid analysis. **(A)** A list of potential ND-binding proteins. ND-overexpressing and control samples were used in LC-MS/MS analysis. The ND-binding protein list was conducted depending on the rate of protein scores and the rate of peptide matches. The proteins whose protein scores ratio and peptide matches ratio were both below 5.0. were cut off, and the remaining top 15 candidates were listed up. "–" denotes that a signal from the control sample was not detected. **(B)** Confirmation of ND-binding proteins in yeast. DNA sequence of the ND region was used to construct BD plasmid. Each ORF of the top 15 candidates from LC-MS/MS analysis was used to construct AD plasmids. Each AD plasmid was cotransformed into yeast gold competent cells with BD plasmid, respectively, and spread on leucine (L) and tryptophan (W)-lacking (SD−LW) plates. Resulted transformants were further diluted and spotted on SD−LW plates without adding 5-Bromo-4-chloro-3-indolyl-α-D-galactopyranoside [X-α-Gal], [Wako, Osaka, Japan] and Aureobasidin A [AbA], [Takara, Shiga, Japan] (SD−LW, -, -, left lane), L, W, and histidine (H) lacking but with X-α-Gal and AbA plates (SD−LWH, +, +, middle lane), and L, W, H and alanine (A) lacking but with X-α-Gal and AbA plates (SD−LWHA, +, +, right lane), and incubated at 30°C for 1 day (SD−LW plates) or 1 week (SD−LWH, SD−LWHA plates) prior to photography.

the transcription of nitrogen assimilation genes? To answer this, we first investigated the *CmNRT* transcripts in MΔ95a and BZ6 (**Figure 4E**) by Northern blot analysis. We normalized *CmNRT* transcript levels using CmMYB1 protein levels (**Figure 4C**). The result showed that the transcript accumulation of *CmNRT* was higher in BZ6 than in MΔ95a under the +N condition, whereas there was no difference under the −N condition (**Figure 4F**). Furthermore, we examined the *CmNRT* transcripts by adding ammonium into MΔ95a and BZ6 cells after −N treatment. Results showed that *CmNRT* transcripts in BZ6 reduced to 17.3 and 7.5% after adding ammonium for 0.5 and 1 h, respectively (**Supplementary Figure 9**). A much more severe reduction of *CmNRT* transcripts was observed in MΔ95a (0.5 and 0% at the indicated time shown above) (**Supplementary Figure 9**). These results indicated that *CmNDB1* deletion increases *CmNRT* transcripts under the +N condition.

Next, we checked the transcripts of other nitrogen assimilation genes under the same condition shown in **Figure 4E** by qRT-PCR analysis. The results showed that transcript accumulation of nitrate assimilation genes, *CmNRT*, *CmNR*, and *CmNIR*, was significantly increased in BZ6 against in MΔ95a under the +N condition (**Figure 4G**). Contrarily, the transcript levels of *CmAMT* and *CmGS* showed no difference between the two strains (**Figure 4G**). In the case of the −N condition, transcript accumulation of all nitrogen assimilation genes showed no significant difference between the two strains (**Figure 4G**).

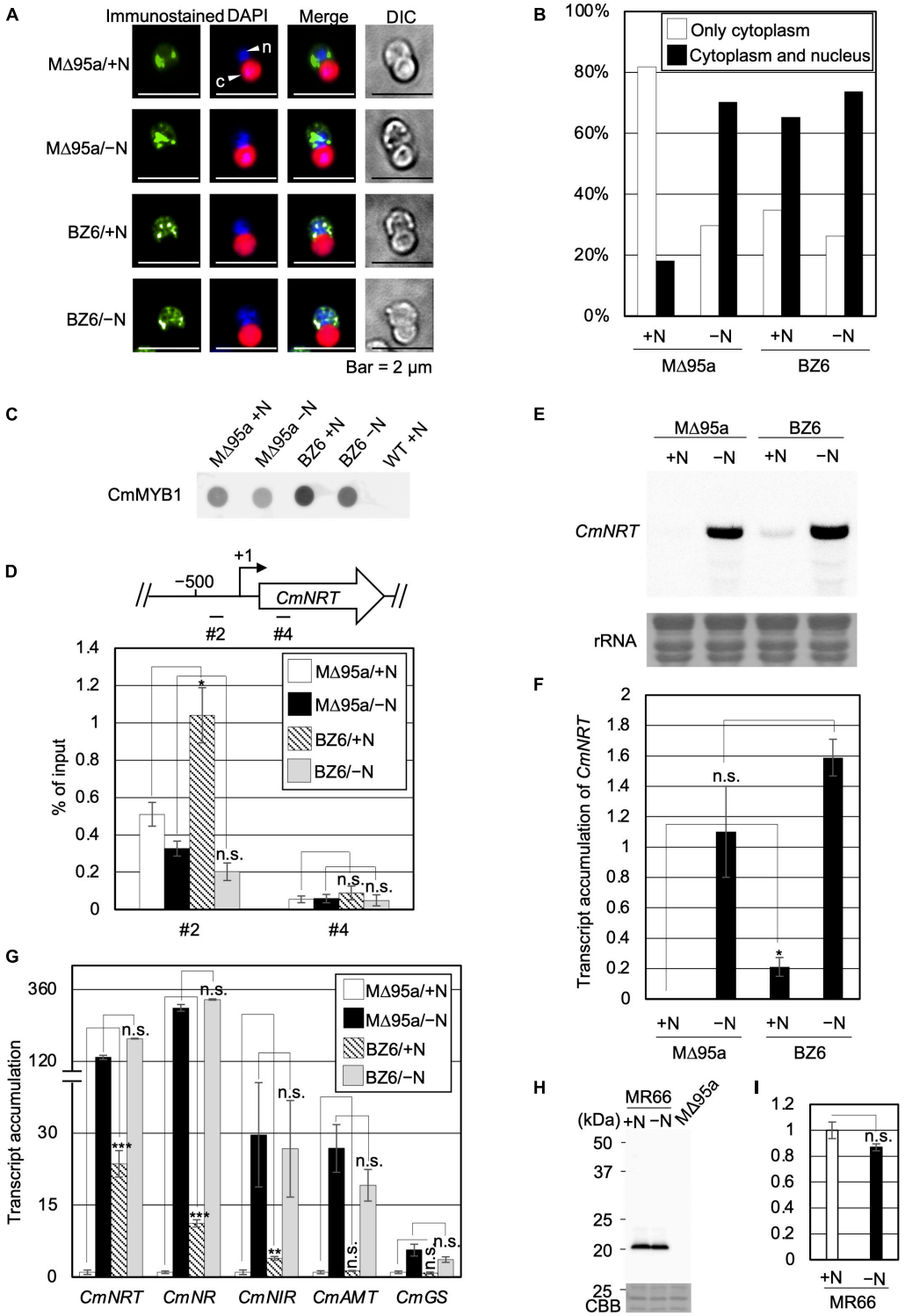

FIGURE 4 | Subcellular localization, the promoter-binding ratio of CmMYB1 and expression of nitrogen-assimilation genes in MΔ95a and BZ6 under the +N/−N conditions. **(A)** Subcellular localization of CmMYB1 in MΔ95a and BZ6 cells under the +N/−N conditions. Cells were fixed and reacted with an anti-FLAG antibody (Wako, Osaka, Japan), and the localization of FLAG-fused CmMYB1 was detected with an Alexa Fluor 488-conjugated donkey anti-mouse antibody (Thermo Fisher Scientific, Waltham, MA, United States, a green signal from "immunostained" pictures). DAPI staining of nucleus DNA (a blue signal from "DAPI" pictures), merged image of immunostaining and DAPI staining (Merge), and differential interference contrast image (DIC) are shown. Positions of the nucleus (n) and chloroplast (c) were indicated with arrowheads (a scale bar, 2 μm). **(B)** Statistical analysis of CmMYB1 localization in MΔ95a and BZ6 cells treated under +N/−N for 4 h. Over 110 cells per strain under the +N/−N conditions were used in this analysis. Photos of fluorescence of CmMYB1 and the nucleus were treated with the same parameter, and

(Continued)

FIGURE 4 | colocalization of CmMYB1 with the nucleus was determined by covering CmMYB1 fluorescence with the nucleus fluorescence. **(C)** Protein levels of FLAG-fused CmMYB1 in MΔ95a and BZ6 under the +N/−N conditions. Aliquots containing 16.6 μg of total proteins from the *C. merolae* cells harvested under the same condition as in **(A)** were dropped on a hydrophilized PVDF membrane and analyzed with an anti-FLAG antibody (Wako, Osaka, Japan). Proteins extracted from WT were used as a negative control. Same experiments were performed 3 times, independently. **(D)** Determination of the CmMYB1 promoter-binding ratio to *CmNRT in vivo*. MΔ95a and BZ6 cells were treated under the +N/−N conditions for 4 h as in **(A)**, and the cells were subsequently fixed for ChIP analysis. The schematic diagram above the image indicates the analyzed gene *CmNRT* and positions that were amplified by qRT-PCR following ChIP (+1 indicates the transcription start site). The anti-FLAG antibody was used in this ChIP analysis. Values are averages of three independent experiments, and % of input was calculated by dividing percentage recovery from ChIP analysis into CmMYB1 protein levels. Error bars indicate the standard deviation (SD). Asterisks indicate the statistical significance of differences between the MΔ95a + N sample *vs.* the BZ6+N sample, the MΔ95a −N sample *vs.* the BZ6 −N sample in position #2 or #4 of *CmNRT*, respectively (*$p < 0.05$, n.s., $p > 0.05$; Student's *T*-test). **(E)** Transcript levels of *CmNRT* in MΔ95a and BZ6 under the +N/−N conditions. Cells treated under +N/−N for 4 h were harvested, and total RNAs were prepared from the cells. Northern blot analysis was performed with total RNAs (3 μg) using a specific probe for *CmNRT*. The bottom panel shows rRNA stained with methylene blue as a loading control. **(F)** Transcript accumulation of *CmNRT* in MΔ95a and BZ6. The signal strength of *CmNRT* and CmMYB1 from **(C,E)** was determined by ImageJ, same as in **Figure 1F**, respectively. Transcript accumulation of *CmNRT* was calculated by dividing the strength of *CmNRT* transcript levels into the strength of CmMYB1 protein levels. Values represent the average transcript accumulation of *CmNRT* in three independent experiments. Error bars indicate the standard deviation (SD). Asterisks indicate the statistical significance of differences between the +N samples (*$p < 0.05$, n.s., $p > 0.05$; Student's *T*-test). **(G)** qRT-PCR analysis of the transcript accumulation of nitrogen assimilation genes. Of the total RNAs per condition of MΔ95a and BZ6 from **(E)**, 500 ng was used for genome DNA removement and cDNA synthesis. Results were from three independent experiments, and data represent transcript accumulation of each gene. Asterisks indicate the statistical significance of differences between the MΔ95a/+N sample *vs*. the BZ6/+N sample, the MΔ95a/−N sample *vs.* the BZ6/−N sample, respectively (**$p < 0.01$, ***$p < 0.001$, n.s., $p > 0.05$; Student's *T*-test). **(H)** Protein levels of CmNDB1 under the +N/−N conditions. Aliquots containing 12 μg of total proteins from the *C. merolae* cells harvested under the +N/−N conditions were separated by 12% SDS-PAGE and analyzed by immunoblot analysis with an anti-Myc antibody (MBL, Tokyo, Japan). Protein extracted from the MΔ95a cells was used as a negative control. The positions of molecular size markers are indicated in kilodaltons (kDa) at the left. Same experiments were performed 3 times, independently. **(I)** Statistical analysis of CmNDB1 protein levels. Data from **(H)** were used in this analysis. n.s., $p > 0.05$; Student's *T*-test.

Altogether, these results clearly showed that *CmNDB1* deletion specifically increases the transcription of nitrate assimilation genes under the +N condition.

The Expression Level of CmNDB1 Under the +N/−N Condition

Finally, we investigated the protein expression level of CmNDB1 under the +N/−N condition. To achieve this, we constructed a Myc-tagged CmNDB1 strain, MR66 (**Supplementary Figure 10**), using MΔ95a as the host strain. The result of immunoblot analysis using proteins extracted from MR66 cells under the +N/−N condition for 4 h showed that CmNDB1 exhibited no significant change between the +N and −N conditions (**Figures 4H,I**). The immunoblot analysis result indicated that CmNDB1 regulates the function of CmMYB1 without changing the CmNDB1 protein level.

DISCUSSION

Given the evidence shown above, we proposed a working model of the regulatory mechanism of CmMYB1 in *C. merolae* (**Figure 5**). The ND and CmNDB1 contribute to maintaining CmMYB1 in the cytoplasm (**Figures 2A,B**, **4A,B**) under the +N condition. The ND or *CmNDB1* deletion results in CmMYB1 nuclear localization and an increased CmMYB1 promoter-binding ratio (**Figures 2D**, **4D**), which, in turn, induces transcription of nitrate assimilation genes (**Figures 1F,G**, **4F,G**). The ND may function synergistically with CmNDB1 due to two observations: one is the interaction between two proteins from the Y2H analysis; the other is the same upregulation pattern of nitrate assimilation genes transcription in ND or *CmNDB1* deletion transformant under the +N condition.

Since CmNDB1 interacts with ND of CmMYB1 in Y2H analysis (**Figure 3B**), we investigated the interaction between CmNDB1 and CmMYB1 in the cells by co-IP analysis. Besides, we applied dithiobis [succinimidyl propionate] (DSP), a membrane-permeable crosslinker, to fix the interaction between protein complexes. However, we could not get any positive binding evidence from both analyses at least under the examined conditions so far. One possibility is that the interaction between CmMYB1 and CmNDB1 is not rigid and hard to be monitored by IP in the cells. The other possibility that must be considered is post-translational modifications of CmMYB1 and/or CmNDB1. Our previous study showed that the target of rapamycin (TOR) inhibition resulted in increased transcripts of nitrate assimilation genes under the +N condition (Imamura et al., 2015), implying that phosphorylation of CmMYB1 or its partner protein(s) is involved in regulating transcription of nitrate assimilation genes under the +N condition. In rice, it has been revealed that exogenous Cry1Ab/c protein binds to endogenous CP43 or DnaJ in Y2H analysis. Although a weak interaction was observed between Cry1Ab/c and CP43 in bimolecular fluorescence complementation analysis, no interaction between these proteins was observed in co-IP analysis in the cells (Fu and Liu, 2020). This observed difference may be caused by the detection limitations of these technologies or could also be possible due to the ubiquitination of DnaJ (Zhong et al., 2018). Similarly, investigation of the post-translational modifications of CmMYB1 and/or CmNDB1 for their interaction in the cells would be required to solve the regulation mechanism between those proteins *in vivo* as a future project.

Our previous studies have shown that transcription of nitrate assimilation genes is regulated by the CmMYB1-dependent nitrogen catabolite repression (NCR) mechanism (Imamura et al., 2009, 2010). Transcripts of *CmNRT*, *CmNR*, and *CmNIR* were increased after shifting from an ammonium medium

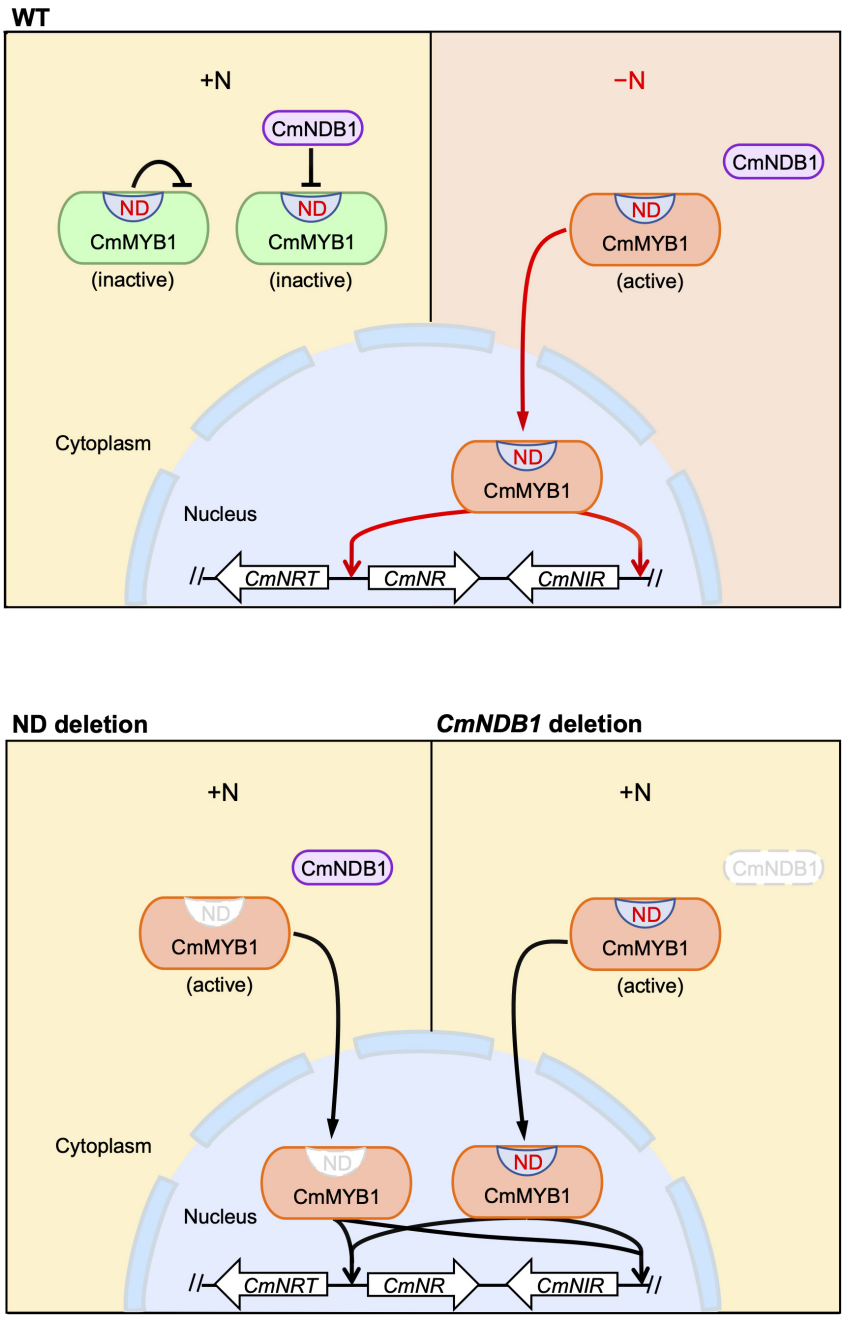

FIGURE 5 | A predicted model of an activation mechanism of CmMYB1 in *C. merolae*. "ND" is short for negative domain of CmMYB1. In case of WT, under the +N condition, ND and CmNDB1 maintain CmMYB1 in the cytoplasm and repress its ability of induction of CmMYB1-dependent transcription. Under the −N condition, repression from ND and CmNDB1 is resolved, which results in nucleus localization of CmMYB1. Finally, CmMYB1 specifically induces the transcription of nitrate assimilation genes. In case of ND or *CmNDB1* deletion, under the +N condition, CmMYB1 is translocated from cytoplasm to nucleus, where it starts to induce the transcription of nitrate assimilation genes.

to a nitrate medium. This increase was completely abolished in the *CmMYB1* null strain (Imamura et al., 2010). In the present study, increased transcripts of the nitrate assimilation genes were observed from ND or *CmNDB1* deletion mutants cultured in the ammonium medium (**Figures 1F,G**, **4F,G**), where CmMYB1-dependent NCR was working. This raises the possibility that CmNDB1 and/or ND are involved in the NCR mechanism. Interestingly, deletion of ND or *CmNDB1* did not result in an increase of *CmAMT* and *CmGS* transcripts under the +N condition (**Figures 1G**, **4G**). This could be due to the predominant role of additional regulators, including TF(s) other than CmMYB1 for *CmAMT* and *CmGS* transcripts since

these transcripts were still presented in the *CmMYB1* null strain under the +N condition (Imamura et al., 2009). The other possibility could be the different promoter architectures between nitrate assimilation genes and *CmAMT* and *CmGS*. The nitrate assimilation genes are located next to each other and form clusters on the chromosome (Imamura et al., 2010), suggesting that the expression of nitrate assimilation genes could be controlled by identical regulators, such as CmNDB1, and regulatory pathway(s) that are not involved in C*mAMT* and *CmGS* transcription. Genome-wide effect/regulation of CmMYB1 by ND and CmNDB1 needs further research.

The ND or *CmNDB1* deletion resulted in CmMYB1 localization change (**Figures 2A,B**, **4A,B**). How do these two factors regulate the localization under the +N condition? One possibility could be the post-translational phosphorylation of ND. Phosphorylation prediction analysis using NETPhos 3.1 (Blom et al., 2004) reported 56 sites among 523 amino acids of CmMYB1 (10.7%) that were predicted to be phosphorylated. Interestingly, phosphorylation sites were highly enriched in ND. Among 70 amino acids of ND, 18 sites (25.7%) were predicted to be phosphorylated (**Supplementary Figure 11**). The MS analysis that we performed supported the prediction since we detected 12 phosphorylation sites among NDs under the +N condition (**Supplementary Figure 11**). In *Saccharomyces cerevisiae*, it has been revealed that Gln3 was phosphorylated under the +N condition (Cox et al., 2004). A recent study has shown that Gln3 nuclear localization was abolished by substituting serine to aspartate in the sites of +505 to +594 (Tate et al., 2021). Further investigation focusing on *in vivo* phosphorylation modification would help in understanding the underlying mechanism of CmMYB1 localization changes.

DATA AVAILABILITY STATEMENT

The datasets presented in this study can be found in online repositories. The names of the repository/repositories and accession number(s) can be found in the article/ **Supplementary Material**.

AUTHOR CONTRIBUTIONS

BZ and SI designed the research. BZ, HS, and SI performed the research and wrote the manuscript. BZ, HS, KI, KT, and SI analyzed the data. All the authors contributed to the article and approved the submitted version.

FUNDING

This work was supported by Ohsumi Frontier Science Foundation, Iwatani Naoji Foundation, Takeda Science Foundation, and Sasakawa Scientific Research Grant from the Japan Science Society for providing financial support.

ACKNOWLEDGMENTS

We thank Drs. Takayuki Fujiwara and Shin-ya Miyagishima for generously gifting the plasmid "pD-184 CAT," which contained the chloramphenicol resistance cassette. We would also like to thank Ohsumi Frontier Science Foundation, Iwatani Naoji Foundation, Takeda Science Foundation, and Sasakawa Scientific Research Grant from The Japan Science Society for providing financial support.

SUPPLEMENTARY MATERIAL

The Supplementary Material for this article can be found online at: https://www.frontiersin.org/articles/10.3389/fpls.2022.821947/full#supplementary-material

REFERENCES

Beck, T., and Hall, M. N. (1999). The TOR signalling pathway controls nuclear localization of nutrient-regulated transcription factors. *Nature* 402, 689–692. doi: 10.1038/45287

Blinder, D., Coschigano, P. W., and Magasanik, B. (1996). Interaction of the GATA factor Gln3p with the nitrogen regulator Ure2p in *Saccharomyces cerevisiae*. *J. Bacteriol.* 178, 4734–4736. doi: 10.1128/jb.178.15.4734-4736.1996

Blom, N., Sicheritz-Pontén, T., Gupta, R., Gammeltoft, S., and Brunak, S. (2004). Prediction of post-translational glycosylation and phosphorylation of proteins from the amino acid sequence. *Proteomics* 4, 1633–1649. doi: 10.1002/pmic.200300771

Carvalho, J., and Zheng, X. F. (2003). Domains of Gln3p interacting with karyopherins, Ure2p, and the target of rapamycin protein. *J. Biol. Chem.* 278, 16878–16886. doi: 10.1074/jbc.M300429200

Cox, K. H., Kulkarni, A. A., Tate, J. J., and Cooper, T. G. (2004). Gln3 phosphorylation and intracellular localization in nutrient limitation and starvation differ from those generated by rapamycin inhibition of Tor1/2 in *Saccharomyces cerevisiae*. *J. Biol. Chem.* 279, 10270–10278. doi: 10.1074/jbc.M312023200

Crawford, N. M., and Forde, B. G. (2002). Molecular and developmental biology of inorganic nitrogen nutrition. *Arabidopsis Book* 1:e0011. doi: 10.1199/tab.0011

Fu, J., and Liu, B. (2020). Exogenous Cry1Ab/c protein recruits different endogenous proteins for its function in plant growth and development. *Front. Bioeng. Biotechnol.* 8:685. doi: 10.3389/fbioe.2020.00685

Fujii, G., Imamura, S., Hanaoka, M., and Tanaka, K. (2013). Nuclear-encoded chloroplast RNA polymerase sigma factor SIG2 activates chloroplast-encoded phycobilisome genes in a red alga, *Cyanidioschyzon merolae*. *FEBS Lett.* 587, 3354–3359. doi: 10.1016/j.febslet.2013.08.031

Fujiwara, T., Ohnuma, M., Kuroiwa, T., Ohbayashi, R., Hirooka, S., and Miyagishima, S. Y. (2017). Development of a double nuclear gene-targeting method by two-step transformation based on a newly established chloramphenicol-selection system in the red alga *Cyanidioschyzon merolae*. *Front. Plant Sci.* 8:343. doi: 10.3389/fpls.2017.00343

Gill, G. (2003). Post-translational modification by the small ubiquitin-related modifier SUMO has big effects on transcription factor activity. *Curr. Opin. Genet. Dev.* 13, 108–113. doi: 10.1016/s0959-437x(03)00021-2

Guan, P., Ripoll, J. J., Wang, R., Vuong, L., Bailey-Steinitz, L. J., Ye, D., et al. (2017). Interacting TCP and NLP transcription factors control plant responses

to nitrate availability. *Proc. Natl. Acad. Sci. U.S.A.* 114, 2419–2424. doi: 10.1073/pnas.1615676114

Imamura, S., Hanaoka, M., and Tanaka, K. (2008). The plant-specific TFIIB-related protein, pBrp, is a general transcription factor for RNA polymerase I. *EMBO J.* 27, 2317–2327. doi: 10.1038/emboj.2008.151

Imamura, S., Kanesaki, Y., Ohnuma, M., Inouye, T., Sekine, Y., Fujiwara, T., et al. (2009). R2R3-type MYB transcription factor, CmMYB1, is a central nitrogen assimilation regulator in *Cyanidioschyzon merolae*. *Proc. Natl. Acad. Sci. U.S.A.* 106, 12548–12553. doi: 10.1073/pnas.0902790106

Imamura, S., Kawase, Y., Kobayashi, I., Sone, T., Era, A., Miyagishima, S. Y., et al. (2015). Target of rapamycin (TOR) plays a critical role in triacylglycerol accumulation in microalgae. *Plant Mol. Biol.* 89, 309–318. doi: 10.1007/s11103-015-0370-6

Imamura, S., Terashita, M., Ohnuma, M., Maruyama, S., Minoda, A., Weber, A. P. M., et al. (2010). Nitrate assimilatory genes and their transcriptional regulation in a unicellular red alga *Cyanidioschyzon merolae*: genetic evidence for nitrite reduction by a sulfite reductase-like enzyme. *Plant Cell Physiol.* 51, 707–717. doi: 10.1093/pcp/pcq043

Konishi, M., and Yanagisawa, S. (2013). Arabidopsis NIN-like transcription factors have a central role in nitrate signalling. *Nat. Commun.* 4:1617. doi: 10.1038/ncomms2621

Kuroiwa, T. (1998). The primitive red algae *Cyanidium caldarium* and *Cyanidioschyzon merolae* as model system for investigating the dividing apparatus of mitochondria and plastids. *Bioessays* 20, 344–354.

Le, C. T. T., Brumbarova, T., Ivanov, R., Stoof, C., Weber, E., Mohrbacher, J., et al. (2016). Zinc finger of *Arabidopsis thaliana* 12 (ZAT12) interacts with fer-like Iron deficiency-induced transcription factor (FIT) linking iron deficiency and oxidative stress responses. *Plant Physiol.* 170, 540–557. doi: 10.1104/pp.15.01589

Marchive, C., Roudier, F., Castaings, L., Bréhaut, V., Blondet, E., Colot, V., et al. (2013). Nuclear retention of the transcription factor NLP7 orchestrates the early response to nitrate in plants. *Nat. Commun.* 4:1713. doi: 10.1038/ncomms2650

Matsuzaki, M., Misumi, O., Shin-i, T., Maruyama, S., Takahara, M., Miyagishima, S. Y., et al. (2004). Genome sequence of the ultrasmall unicellular red alga *Cyanidioschyzon merolae* 10D. *Nature* 428, 653–657. doi: 10.1038/nature02398

Nozaki, H., Takano, H., Misumi, O., Terasawa, K., Matsuzaki, M., Maruyama, S., et al. (2007). A 100%-complete sequence reveals unusually simple genomic features in the hot-spring red alga *Cyanidioschyzon merolae*. *BMC Biol.* 5:28. doi: 10.1186/1741-7007-5-28

Ohnuma, M., Yokoyama, T., Inouye, T., Sekine, Y., and Tanaka, K. (2008). Polyethylene glycol (PEG)-mediated transient gene expression in a red alga, *Cyanidioschyzon merolae* 10D. *Plant Cell Physiol.* 49, 117–120. doi: 10.1093/pcp/pcm157

Ohta, N., Matsuzaki, M., Misumi, O., Miyagishima, S. Y., Nozaki, H., Tanaka, K., et al. (2003). Complete sequence and analysis of the plastid genome of the unicellular red alga *Cyanidioschyzon merolae*. *DNA Res.* 10, 67–77. doi: 10.1093/dnares/10.2.67

Ohta, N., Sato, N., and Kuroiwa, T. (1998). Structure and organization of the mitochondrial genome of the unicellular red alga *Cyanidioschyzon merolae* deduced from the complete nucleotide sequence. *Nucleic Acids Res.* 26, 5190–5198. doi: 10.1093/nar/26.22.5190

Puga, M. I., Mateos, I., Charukesi, R., Wang, Z., Franco-Zorrilla, J. M., de Lorenzo, L., et al. (2014). SPX1 is a phosphate-dependent inhibitor of phosphate starvation response 1 in *Arabidopsis*. *Proc. Natl. Acad. Sci. U.S.A.* 111, 14947–14952. doi: 10.1073/pnas.1404654111

Qi, W., Manfield, I. W., Muench, S. P., and Baker, A. (2017). AtSPX1 affects the AtPHR1–DNA-binding equilibrium by binding monomeric AtPHR1 in solution. *Biochem. J.* 474, 3675–3687. doi: 10.1042/BCJ20170522

Schneider, C. A., Rasband, W. S., and Eliceiri, K. W. (2012). NIH image to imageJ: 25 years of image analysis. *Nat. Methods* 9, 671–675. doi: 10.1038/nmeth.2089

Schütze, K., Harter, K., and Chaban, C. (2008). Post-translational regulation of plant bZIP factors. *Trends Plant Sci.* 13, 247–255. doi: 10.1016/j.tplants.2008.03.002

Takemura, T., Imamura, S., Kobayashi, Y., and Tanaka, K. (2018). Construction a selectable marker recycling system and the use in epitope tagging of multiple nuclear genes in the unicellular red alga *Cyanidioschyzon merolae*. *Plant Cell Physiol.* 59, 2308–2316. doi: 10.1093/pcp/pcy156

Taki, K., Sone, T., Kobayashi, Y., Watanabe, S., Imamura, S., and Tanaka, K. (2015). Construction of a *URA*5.3 deletion strain of the unicellular red alga *Cyanidioschyzon merolae*: a backgroundless host strain for transformation experiments. *J. Gen. Appl. Microbiol.* 61, 211–214. doi: 10.2323/jgam.61.211

Tate, J. J., Rai, R., De Virgilio, C., and Cooper, T. G. (2021). N- and C-terminal Gln3–Tor1 interaction sites: one acting negatively and the other positively to regulate nuclear Gln3 localization. *Genetics* 217:iyab017. doi: 10.1093/genetics/iyab017

Tootle, T. L., and Rebay, I. (2005). Post-translational modifications influence transcription factor activity: a view from the ETS superfamily. *Bioessays* 27, 285–298. doi: 10.1002/bies.20198

Ueda, Y., Ohtsuki, N., Kadota, K., Tezuka, A., Nagano, A. J., Kadowaki, T., et al. (2020). Gene regulatory network and its constituent transcription factors that control nitrogen-deficiency responses in rice. *New Phytol.* 227, 1434–1452. doi: 10.1111/nph.16627

Wang, S., Li, L., Ying, Y., Wang, J., Shao, J. F., Yamaji, N., et al. (2020). A transcription factor OsbHLH156 regulates strategy II iron acquisition through localising IRO2 to the nucleus in rice. *New Phytol.* 225, 1247–1260. doi: 10.1111/nph.16232

Xie, Z., Zhang, Z. L., Zou, X., Yang, G., Komatsu, S., and Shen, Q. J. (2006). Interactions of two abscisic-acid induced WRKY genes in repressing gibberellin signaling in aleurone cells. *Plant J.* 46, 231–242. doi: 10.1111/j.1365-313X.2006.02694.x

Zhong, X., Yang, J., Shi, Y., Wang, X., and Wang, G. L. (2018). The DnaJ protein OsDjA6 negatively regulates rice innate immunity to the blast fungus *Magnaporthe oryzae*. *Mol. Plant Pathol.* 19, 607–614. doi: 10.1111/mpp.12546

Zhou, B., Takahashi, S., Takemura, T., Tanaka, K., and Imamura, S. (2021). Establishment of a firefly luciferase reporter assay system in the unicellular red alga *Cyanidioschyzon merolae*. *J. Gen. Appl. Microbiol.* 67, 42–46. doi: 10.2323/JGAM.2020.02.003

Zhu, J., Lau, K., Puschmann, R., Harmel, R. K., Zhang, Y., Pries, V., et al. (2019). Two bifunctional inositol pyrophosphate kinases/phosphatases control plant phosphate homeostasis. *Elife* 8:e43582. doi: 10.7554/eLife.43582.001

Conflict of Interest: SI was employed by Nippon Telegraph and Telephone Corporation.

The remaining authors declare that the research was conducted in the absence of any commercial or financial relationships that could be construed as a potential conflict of interest.

Publisher's Note: All claims expressed in this article are solely those of the authors and do not necessarily represent those of their affiliated organizations, or those of the publisher, the editors and the reviewers. Any product that may be evaluated in this article, or claim that may be made by its manufacturer, is not guaranteed or endorsed by the publisher.

frontiers in Plant Science

ORIGINAL RESEARCH
published: 25 March 2022
doi: 10.3389/fpls.2022.846970

The ER Is a Common Mediator for the Behavior and Interactions of Other Organelles

Jaideep Mathur, Olivia Friesen Kroeker, Mariann Lobbezoo and Neeta Mathur*

Laboratory of Plant Development and Interaction, Department of Molecular and Cellular Biology, University of Guelph, Guelph, ON, Canada

Optimal functioning of a plant cell depends upon the efficient exchange of genetic information, ions, proteins and metabolites between the different organelles. Intuitively, increased proximity between organelles would be expected to play an important role in facilitating exchanges between them. However, it remains to be seen whether under normal, relatively non-stressed conditions organelles maintain close proximity at all. Moreover, does interactivity involve direct and frequent physical contact between the different organelles? Further, many organelles transition between spherical and tubular forms or sporadically produce thin tubular extensions, but it remains unclear whether changes in organelle morphology play a role in increasing their interactivity. Here, using targeted multicolored fluorescent fusion proteins, we report observations on the spatiotemporal relationship between plastids, mitochondria, peroxisomes and the endoplasmic reticulum in living plant cells. Under normal conditions of growth, we observe that the smaller organelles do not establish direct, physical contacts with each other but, irrespective of their individual form they all maintain intimate connectivity with the ER. Proximity between organelles does increase in response to stress through concomitant alterations in ER dynamics. Significantly, even under increased proximity the ER still remains sandwiched between the different organelles. Our observations provide strong live-imaging-based evidence for the ER acting as a common mediator in interactions between other organelles.

Keywords: ER, organelle extensions, fluorescent proteins (FPs), chloroplasts, peroxisomes, mitochondria

OPEN ACCESS

Edited by:
Simon Gilroy,
University of Wisconsin-Madison,
United States

Reviewed by:
Verena Kriechbaumer,
Oxford Brookes University,
United Kingdom
Byung-Ho Kang,
The Chinese University of Hong Kong,
China

****Correspondence:***
Jaideep Mathur
jmathur@uoguelph.ca

Specialty section:
This article was submitted to Plant Cell Biology, a section of the journal Frontiers in Plant Science

Received: *31 December 2021*
Accepted: *02 March 2022*
Published: *25 March 2022*

Citation:
Mathur J, Kroeker OF, Lobbezoo M and Mathur N (2022) The ER Is a Common Mediator for the Behavior and Interactions of Other Organelles. Front. Plant Sci. 13:846970. doi: 10.3389/fpls.2022.846970

INTRODUCTION

The eukaryotic cell is characterized by the presence of functionally discrete domains called organelles. The mitochondria and chloroplasts are distinguished by the presence of an envelope and postulated to be of endo-symbiogenic origins (Mereschkowsky, 1905; Sagan, 1967; Margulis et al., 2006; Martin et al., 2015). By contrast, organelles such as peroxisomes, Golgi bodies, lipid droplets, vacuoles, and assorted vesicles are *de novo* derivatives of the endomembrane system and the bounding plasma-membrane. While each organelle creates a biochemically independent domain within the cell, it is clear that the optimal functioning of the cell as a unit relies upon the combined activities of all constituent organelles. Organelle interactions provide succinct explanations for the extensive biochemical and genetic exchanges known to occur between organelles. However, from a cell biological perspective it is not always clear whether the interactions involve direct

physical contacts between the different organelles or are only possible in an indirect manner through mediation of vesicles, protein complexes and acyl-lipids. In recent years it has become increasingly clear that discrete membrane contact sites (MCS) between organelles facilitate inter-organelle trafficking (Prinz, 2014; Michaud et al., 2016; Michaud and Jouhet, 2019). Notably, MCS form between closely appressed membranes, typically less than 30 nm apart (Helle et al., 2013; Prinz, 2014). Thus, a key requirement for membrane interactions to occur is for two organelles to be very close to each other. In plants, organelle proximity leading to direct interactivity has been best documented for the fusion of independent mitochondria (Schattat et al., 2012) and is considered common for membrane vesicles fusing together or fusing with other organelle membranes (reviewed by Perico and Sparkes, 2018; Oikawa et al., 2019). Similarly, membrane fusion and detachment form the underlying basis for the dynamic behavior of the endoplasmic reticulum (ER; Staehelin, 1997; Stefano et al., 2014). It is worth noting that while molecular exchanges between endomembrane derivatives may generally involve two membrane bilayers, for endosymbiont organelles the presence of a two-layered envelope necessitates the crossing of four bi-layered membranes. Although the presence of ion channels and gated pores, specific transporters and dedicated translocons facilitates inter-organelle exchanges physical proximity between organelles is believed to play an important role in their interactions (Helle et al., 2013; Mehrshahi et al., 2013, 2014).

However, a critical assessment of published literature suggests that in many cases the so called "interactions" between organelles are not built on actual data involving physical connectivity between organelles. Instead, they are inferences drawn from correlated biochemical findings that rely on clean preparations obtained by efficiently separating the different organelles from the cellular milieu. Consequently, actual physical contacts between organelle pairs such as chloroplasts and mitochondria, mitochondria and peroxisomes, and chloroplasts and peroxisomes have not been unequivocally demonstrated.

Nevertheless, the close proximity of chloroplasts, mitochondria and peroxisomes, three biochemically linked organelles (Bauwe et al., 2010), is succinctly depicted through several classic transmission electron microscopic images such as those presented in Frederick and Newcomb (1969) and Frederick et al. (1975). These images depict mitochondria and cytosomes (later identified as peroxisomes) appressed to chloroplasts and are annotated by definitive statements such as "mitochondria are abundant around the chloroplasts. The cytosomes are similarly distributed but show a greater tendency to lie wedged tightly between adjacent chloroplasts" (Frederick and Newcomb, 1969). While noting a lack of ER membranes between the three organelles, the authors cautioned that the images of mesophyll cells in photo-respiring plants might not be representative for other parts of plants and other plant species (Frederick and Newcomb, 1969). Several other TEM based studies have pointed to membrane continuities between chloroplasts and different organelles (Gibbs, 1962; Diers, 1966; Cran and Dyer, 1973; Crotty and Ledbetter, 1973). In more recent times comparative observations on the proximity between chloroplasts, peroxisomes, and mitochondria in wild type Arabidopsis and photorespiration defective mutants of the Arabidopsis PEROXIN10 (PEX10) gene (Schumann et al., 2007) have further strengthened the idea of organelle juxtaposition as a major factor in facilitating organelle interactions. Similarly, the implications of organelle proximity have been used for insights on the functional anatomy of rice leaves (Sage and Sage, 2009). TEM based interpretations of closely appressed membranes have also been made for glyoxysomes and lipid droplets (Hayashi et al., 2001). Notably, all TEM images are obtained from fixed, dead plant tissue and therefore do not portray the dynamic nature of living plant cells. Whether organelle proximity is a common occurrence in living plant cells under normal conditions of growth and development has thus remained unclear.

Advances in the imaging of living cells and analyzing subcellular dynamics using video rate -cinephotomicrography (Wildman et al., 1962; Gunning, 2005) and time-lapse movies of fluorescently highlighted organelles have shown the continuous movement of different organelles in living plant cells. However, in this dynamic subcellular milieu it is unclear as to how close two organelles should be, and for how long they should remain together, for an interaction to occur. Upon observing living plant cells, our attention is readily drawn to organelle clusters and to sporadic occurrences of two or more organelles remaining near each other over relatively long periods even though the majority of organelles around the clusters may continue moving independently. Studies that take the majority behavior into account and provide relevant comparative data are largely missing. Moreover, light microscopy-based imaging does not provide the ultrastructural resolution afforded by TEM images. The limits on image resolution become very relevant in fluorescence-based microscopy since the blooming effect of fluorescent probes can often create a false impression of organelle proximity and not allow an estimation of the true distance between them. Nevertheless, imaging of living cells has provided strong correlations between organelle motility, cytoskeletal elements, and motor proteins (Nebenführ et al., 1999; Logan and Leaver, 2000; Brandizzi et al., 2002; Mano et al., 2002; Mathur et al., 2002; Sparkes et al., 2011; Stefano et al., 2014; Oikawa et al., 2015). In addition, it has become clear that organelle morphology and behavior in plant cells are not fixed traits and can change transiently during rapid organelle responses to environmental cues (Mathur, 2020). The sporadic changes in organelle shape may involve the formation of thin, tubular, dynamic extensions named stromules, matrixules, and peroxules from plastids, mitochondria, and peroxisomes, respectively (Köhler and Hanson, 2000; Scott et al., 2007; Sinclair et al., 2009; Mathur, 2021). Plastids are known to aggregate around the nucleus in expanding as well as wounded plant cells, and observations on stromules extended from the plastids aggregated around nuclei have been used to suggest their interactions (Kwok and Hanson, 2004a; Caplan et al., 2015). Proximity-based conclusions have been used to suggest that stromules interact with mitochondria (Kwok and Hanson, 2004b) and other organelles (Natesan et al., 2009; Sage and Sage, 2009). In a similar manner, under high light stress peroxisomal extensions have been shown to interact with mitochondria (Jaipargas et al., 2016).

Many of the spatiotemporal correlations have been drawn from cells that are transiently expressing a particular construct or placed under some kind of stress. The most common, unintended stress is the use of excised leaf sections that can quickly bias observations through wound induced artifacts. Whether similar correlations can be made in unstressed cells remain unclear. In recent years the presence of organelle extensions and tubular organelles has become well established and clearly extends the interactive surface of an organelle beyond the diameter of the main body (Mathur, 2021). Whether plastid extensions interact with matrixules or peroxules, or if the tubular forms of organelles interact more with each other than when they are present in a spheroidal form, remains unclear.

Here we have investigated whether it is common for chloroplasts, mitochondria, and peroxisomes to come in direct physical contact with each other in living plant cells under normal conditions of growth and development. Our investigations have utilized several stable transgenic lines of Arabidopsis expressing fluorescent proteins targeted to the different organelles (**Table 1**). As our investigations progressed, the need for considering another organelle that may act as a mediator between all other organelles was felt, thus fluorescent probes highlighting the ER lumen and membrane were added. Several Arabidopsis mutants with aberrant morphologies and behavior for the different organelles were also utilized in our investigations.

Combining these various resources have resulted in a comprehensive investigation that provides fresh insights on organelle interactivity in the plant cell.

RESULTS

Establishing Baseline Imaging Considerations

When considering the proximity between organelles and trying to link it to possible interactivity and exchanges between them, an important consideration was maintained. Both plastids and mitochondria have envelopes consisting of two membrane bilayers separated by an intermembrane region. Thus, any direct interactions between mitochondria and chloroplasts would be expected to involve at least four membrane bilayers. In comparison, the peroxisome is bounded by a single bilayer membrane only. Therefore, peroxisome interactions with the other two organelles would involve three bilayer membranes. Since earlier studies on organelle interactions have not adequately acknowledged the presence of several membrane layers between organelles most suggestions of their direct interactivity become debatable. Given the scarcity of information, the published TEM images depicting proximity between chloroplasts, mitochondria, and peroxisomes (Frederick and Newcomb, 1969; Schumann et al., 2007; Sage and Sage, 2009) became baseline criterion for organelle interactivity even in our live-imaging based investigations. We looked for instances where two or three of the organelles could be observed together. An implicit bias in our observations became apparent quickly as our eyes readily picked out organelle clusters within the dynamic cytoplasmic strands while ignoring the non-clustered organelles.

The bias was minimized by considering "dwell time", which denoted the time spent by two organelles in close proximity to each other. The dwell time estimations were made by recording the time that two organelles actually spent with each other within a region circumscribed by the length of the long axis of the smaller organelle (more details in "Materials and Methods" Section).

Using these considerations, we used well-characterized fluorescent protein probes targeted to the plastid stroma, mitochondrial outer envelope membrane and matrix, and the peroxisomal matrix (**Table 1**). However, stroma-targeted fluorescent probes for plastids do not highlight the outer envelope membrane (OEM), which constitutes the outermost boundary of the plastid and the actual interactor with the rest of the cytoplasm. Therefore, a new probe, proCaMV-35S-SFR2mRFP was created. Stable transgenic plants of SFR2mRFP in the Columbia wild type background showed all plastids with a red fluorescent OEM (**Figure 1A**). Several double and triple transgenic Arabidopsis plants were developed for observing the spatiotemporal relationship between the three key organelles in living cells (**Table 1**).

Chloroplasts, Mitochondria, and Peroxisomes Do Not Maintain Proximity Under Normal Growth Conditions

Experiments reported in this section were aimed at establishing the dynamic behavior of the three organelles and carried out on unwounded, living plant cells of the cotyledon and hypocotyl in 8 to 10-day old soil-grown seedlings of the different transgenic lines (**Table 1**). Cytoplasmic streaming with organelles moving freely was observed in all the cells. In elongated hypocotyl cells (length 100 $\pm$ 30 μm; width 18 $\pm$ 8 μm), two distinct organelle behaviors and relationships were observed due to the differences in cytoplasmic flow characteristics. Conspicuous transvacuolar strands contained rapidly flowing and continuously splitting and merging cytoplasmic strands wherein organelles with diameters of 0.5 to 1.5 μm moved at velocities ranging from 1.5 up to 3 μm s^{-1}. The positions of organelles within these cytoplasmic strands changed continuously. In double transgenic plants for peroxisomes and mitochondria we observed both organelles moving independently and also in clusters of up to 5 μm diameter. Based on counts from 35 hypocotyl epidermal cells and a total of 350 each of peroxisomes and mitochondria we found that 47% of these organelles moved in tandem. Occasionally both organelles clustered transiently (<10 s) around small epidermal chloroplasts of 2.5 $\pm$ 1.2 μm diameter (Barton et al., 2018) which also moved as part of the general cytoplasmic stream. While a case could be made that organelles in a cluster are close to each other and therefore maintain the required proximity for direct interactions, we were unable to uncover a pattern for the formation of the clusters or arrive at a specific number of organelles within each cluster. Moreover, judging from the fluorescent color, many clusters contained organelles of one kind only, and thus could include organelles that might be undergoing division. Alternatively, clusters that contained all three organelles under consideration here were also observed. Since organelles

TABLE 1 | Transgenic Arabidopsis plants and mutants used in the study.

Targeted Organelle(s)	Name used for fluorescent fusion protein/color	Characteristic feature(s) of transgenic line	References
Single transgenic			
Plastid (stroma)	tpFNR-EGFP/G	Stroma and stromules green	Schattat et al., 2011a
Plastid (stroma)	Pt-YK/Y	ABRC stock CS16267; pea RUBISCO small subunit fused to EYFP, stroma – stromules yellow	Nelson et al., 2007
Plastid (OEM)	SFR2-mRFP/R	Highlights plastid OEM in red fluorescence	• This study
Peroxisome matrix	YPeroxi/Y	Yellow fluorescent peroxisomes and peroxules YFP-SKL	Mathur et al., 2002
Peroxisome matrix	GPeroxi/G	Green fluorescent peroxisomes due to GFP-SKL	Mano et al., 2002
Mitochondrion matrix	mitoGFP/G	Green fluorescent mitochondria and matrixules due to targeting using a tpßATPase- GFP fusion protein	Logan and Leaver, 2000
Mitochondrion matrix	Mt-YK = Ymito/Y	ABRC stock CS16264; mitochondrial targeting sequence from yeast ScCOX4 fused to EYFP	Nelson et al., 2007
Endoplasmic reticulum (ER) lumen	GER/G	Green ER with GFP filled lumen due to ER targeting signal sequence appended to mGFP-HDEL	Haseloff et al., 1997
Endoplasmic reticulum (ER) lumen	RER/R	Red fluorescent ER with mRFP filled lumen by fusion of ss-mRFP-HDEL	Sinclair et al., 2009
Double and Triple transgenic			
Plastid stroma + mitochondrion	tpFNR-EGFP – mtyk/G, Y	Plastids appear green, mitochondria yellow	• This study
Plastid OEM + mitochondrion	SFR2mRFP – mitoGFP/R, G	Plastid OEM fluoresces red, mitochondria green	• This study
Plastid stroma + peroxisome	tpFNR-EGFP – Yperoxi/G/Y	Plastids appear green peroxisomes yellow	Barton et al., 2013
Plastid stroma + ER	tpFNR-EGFP- RER/G, R	Plastids appear green, ER lumen red fluorescent	Schattat et al., 2011a
Plastid OEM + ER	SFR2mRFP-GER/R, G	Plastid OEM red, ER lumen green fluorescent	• This study
Plastid OEM + peroxisome + mitochondrion	SFR2mRFP- GPeroxi – Ymito/R, G,Y	Plastid OEM red, peroxisomes yellow, mitochondria green fluorescent	• This study
Plastid + peroxisome + ER	tpFNR-EGFP - Yperoxi – RER/G, Y,R	Plastid stroma green, peroxisomes yellow, ER red fluorescent	Barton et al., 2013, 2014
Peroxisomes + ER	YPeroxi-GER/Y, G	Normal peroxisomes yellow, ER green fluorescent	Barton et al., 2013, 2014
Mitochondrion + ER	mitoGFP-RER/G, R	Normal mitochondria green, ER red fluorescent	Jaipargas et al., 2015, 2016
Mitochondrion - peroxisomes	mtYK -GPeroxi	Yellow fluorescent mitochondria and green peroxisomes	Jaipargas et al., 2015, 2016
Peroxisomes – mitochondrion - ER	GPeroxi-YMito-RER/Y, G, R	Normal peroxisomes Green, mitochondria yellow, ER red fluorescent	Jaipargas et al., 2015; Delfosse et al., 2016
Mitochondrion-Peroxisome - ER	Gmito-Yperoxi-RER/G, Y, R	Normal mitochondria Green, peroxisomes yellow, ER red fluorescent	Barton et al., 2013; Jaipargas et al., 2015
Mutation and transgene			
apm1	*At4g33650; aberrant peroxisome morphology1/G*	Green fluorescent, elongated peroxisomes and mitochondria due to impaired fission	Mano et al., 2004; Arimura et al., 2004
apm1-RER	/G, R	Elongated peroxisomes and red ER lumen	Sinclair et al., 2009; Barton et al., 2013, 2014
apm1-MtYK	/G, Y	Green elongated peroxisomes, yellow elongated mitochondria	• This study
apm1-MtYK – SFR2mRFP	/G, Y, R	Elongated Green peroxisomes and yellow mitochondria, red plastid OEM	• This study

(Continued)

TABLE 1 | (Continued)

Targeted Organelle(s)	Name used for fluorescent fusion protein/color	Characteristic feature(s) of transgenic line	References
apm1-MtYK – RER	/G, Y, R	Green elongated peroxisomes, yellow elongated mitochondria, red ER lumen	• This study
arc6	*At5g42480 accumulation and replication of chloroplasts1/-*	Enlarged mesophyll chloroplasts, detected by chlorophyll autofluorescence	Pyke et al., 1994
arc6-tpFNR EGFP	/G	Green stroma in large plastids, many stroma-filled extensions	Delfosse et al., 2016
arc6 tpFNREGFP-RER	/G, R	Green stroma in large plastids and red ER lumen	Mathur, 2021
arc6 tpFNREGFP-RER – YPeroxi	/G, R, Y	Green stroma in large plastids, red ER lumen and yellow peroxisomes	• This study
elm1	*At5g22350 elongated mitochondria1/G*	Elongated, green tubular mitochondria	Arimura et al., 2008
elm1-RER	/G, R	Tubular mitochondria and red ER lumen	Jaipargas et al., 2015

EGFP, G- enhanced green fluorescent protein; YFP, Y -enhanced yellow fluorescent protein; ER, endoplasmic reticulum; mRFP, R- monomeric red fluorescent protein; OEM, plastid outer envelope membrane; tp, transit peptide.

continuously joined a cluster or moved away from it, dwell time measurement was applied to clusters with only two different organelles (**Figure 1A** and **Supplementary Movie 1**). On the basis of 100 peroxisome and mitochondrial clusters a dwell time of less than 10 s (ca. 5 frames of our confocal scans) was arrived at for 83 clusters while the rest exhibited dwell time longer than 10 s (**Figure 1B**). Considering that many organelles did not remain clustered we considered transient proximity-dependent interactivity and possible direct connectivity between organelles in the cytoplasmic strands to be coincidental.

The second pattern of organelle movement observed in hypocotyl cells was different from the rapid cytoplasmic flow and was confined to the shallow cortical cytoplasmic sleeve pressing against the plasma-membrane and cell wall. As also documented in earlier studies on peroxisomes (Barton et al., 2013, 2014), mitochondria (Jaipargas et al., 2015), and chloroplasts (Barton et al., 2018) present in this cortical domain exhibited a relatively slow and erratic movement with an average velocity of 0.75 $\mu m\ s^{-1}$ for mitochondria and peroxisomes (**Supplementary Figure 1**). Chloroplasts in the epidermal cell cortex generally moved very slowly with occasional stops of up to several minutes before their position shifted again. Our earlier work has shown that such slow-moving chloroplasts are often located within pockets created by the subtending and closely appressed tonoplast (Barton et al., 2018).

Observations on the cortical regions of 375 un-stressed hypocotyl epidermal cells (5 cells/tissue × 25 seedlings) each from double transgenic (exhibiting combinations of chloroplast and mitochondria, chloroplasts and peroxisomes, and peroxisomes and mitochondria) and triple transgenic plants with fluorescently highlighted chloroplasts-mitochondria and peroxisomes showed that the three organelles were most often localized away from each other and exhibited independent movements. Time lapse imaging showed occasional cases where a mitochondrion or a peroxisome remained for 5–7 frames (10–14 s) around an epidermal chloroplast. However, observations of clear distances between the three different organelles did not suggest their sustained proximity within the cortical regions.

Nevertheless, a different impression was obtained when the three organelles were observed in cotyledon and leaf mesophyll cells of ten to twelve days old plants after an overnight period. In a top-down view both peroxisomes and mitochondria, ranging in diameters from 0.5 to 1.2 μm appeared packed between chloroplasts of 5 to 8 μm diameter. Notably, chloroplast movement was minimal in mesophyll cells taken after the dark period but resumed within 5 min of illumination with 120 ± 10 $\mu mol\ m^{-2}\ s^{-2}$ light.

Based on observations on 50 cotyledon cells from 10 plants double transgenic for mitoGFP-Yperoxi, each cell showing between 12 to 16 chloroplasts in the top-down view, 1 to 3 of the small organelles were observed maintaining a dwell time higher than 20 s around a total of 196 chloroplasts (representing about 28% of the total number of chloroplasts observed). Within the same population only mitochondria were observed around 29 (ca. 13% of the total) of the chloroplasts, while 33 chloroplasts (ca. 17%) were surrounded only by peroxisomes and the rest

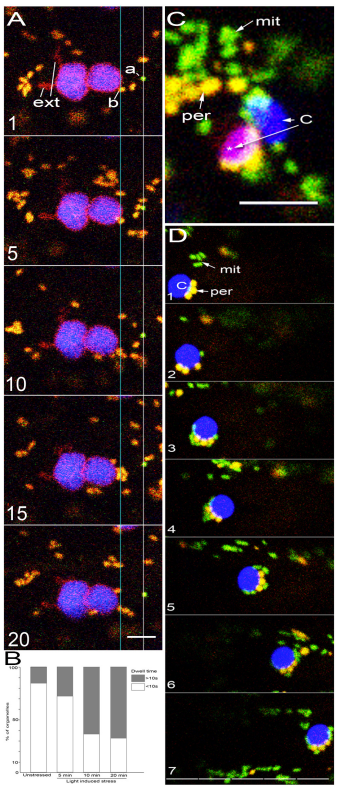

FIGURE 1 | Several different possibilities for organelle interactions are observed in living cells. **(A)** Five snapshots used to illustrate the ideas of coincidental interactions, sustained proximity based on long dwell time and no possible direct interactions when chloroplasts, peroxisomes and mitochondria clearly remain at a distance from each other. The consecutive images are from 100 frames representing about 200 s of imaging (**Supplementary Movie 1**). A peroxisome labeled "a" maintains its position at a distance from the two chloroplasts observed for 100 frames. A mitochondrion labeled "b" maintains a position at or within 500 nm of the plastid OEM for 100 frames or a total dwell time of 200 s. During this time up to 6 other mitochondria cluster near it but the cluster is maintained only for a maximum of 45 frames or dwell time of 90 s. Other than one mitochondrion that is present close to the plastid OEM during the 200 s, the rest do not exhibit sustained proximity with the plastid or with a peroxisome. The single instance of a peroxisome and mitochondria appearing in frame 15 and the several frames with mitochondrial clusters are considered coincidental occurrences. Notably, two extensions (ext) are present in the chloroplast (C) but neither mitochondria or peroxisomes exhibit sustained proximity with them. **(B)** In unstressed plants, on the basis of 100 peroxisome and mitochondrial clusters with chloroplasts a dwell-time of less than 10 s (ca. 5 frames of our confocal scans) was arrived at for 83 clusters while the rest exhibited dwell time longer than 10 s. High light intensity induced stress by exposing plants for 5 min to light of 450 ± 25 μmol $m^{-2}s^{-2}$ resulted in the three organelle clusters with a dwell-time greater than 10 s to 29% Longer exposures of 10 and 20 min resulted the three-organelle cluster with dwell-time longer than 10 s to increase to 64 and 67%, respectively. **(C)** Organelles clustered after a 20-min exposure to high light intensity also contain chloroplasts that based on the loss of chlorophyll autofluorescence appear bleached (pink *) compared to an unbleached chloroplast (blue -c). Plastids with degraded chlorophyll often maintained peroxisome clusters for long dwell time. **(D)** Seven consecutive images illustrating high light induced stress for 10 min that leads to increased proximity between the chloroplasts (blue -C), peroxisomes (per – yellow) and mitochondria (mit – green). A split scale bar with each unit representing 10 μm shows that the clustered organelles remained together as they moved for at least 50 μm. Scale bars – A = 5; C, D = 10 μm.

exhibited both small organelles. Notably, as with the composition of the peri-plastid organelle cluster the relative positions of the small organelles continuously changed and conveyed the impression of their moving around a chloroplast.

Based on observations made on the cortical region of hypocotyl and cotyledon cells it was concluded that under normal conditions of growth, unstressed plants do not exhibit sustained proximity between chloroplasts, peroxisomes, and mitochondria. Whether this changed under stress was assessed next.

Exposure to High Light Intensity Increases Clustering of Peroxisomes and Mitochondria Around Chloroplasts

Earlier our lab had reported increased peroxisome and mitochondrial interactions in response to high light stress (Jaipargas et al., 2016). Here we took 8–10 day old seedlings of a double transgenic (mitoGFP-Yperoxi) line after an overnight dark period and exposed them to high light intensity of 450 ± 25 μmol $m^{-2}s^{-2}$ for 5, 10 and 20 min before observations. Different from our earlier observations on plants growing under normal light conditions, exposing hypocotyl cells to 5 min to high light resulted in peroxisomes or mitochondria or both organelles clustering for more than 10 s around 36% of the larger mesophyll cell chloroplasts (MCC; n = 100) and 22% of pavement cell chloroplasts (PCC; n = 100). Increasing the exposure time to 10 min increased small organelle clustering to 78 and 50% around MCC and PCC, respectively (**Figure 1B**). A 20-min exposure increased clustering only slightly to about 55% around PCC (**Figure 1B**) but also resulted in 12–17% PCC displaying signs of chlorophyll bleaching (**Figure 1C**). Based on twelve separate instances of observing the three organelles moving together around the cell for up to 4 min, after 10 min of exposure it was concluded that high light induced stress increases proximity between the three organelles (**Figure 1D**).

Upon comparing the number of peroxisomes and mitochondria clustered around MCC and PCC in hypocotyl cells, it was found that more of the small organelles had appeared around MCC. While not experimentally assessed further, this observation might be due to the relatively large size (5–8 μm diameter) and high chlorophyll content of closely packed MCC, compared to the nearly-half sized (long axis approximately 2.5 μm), 9 to 12 PCC dispersed in a large epidermal cell (Barton et al., 2016).

Mesophyll cell chloroplasts, as the major organelles responsible for oxygenic photosynthesis in response to light are also active producers of reactive oxygen species (ROS; Foyer and Noctor, 2003; Noctor et al., 2018). The presence of peroxisomes around MCC in response to high light stress thus matches our earlier observations (Jaipargas et al., 2016). An increase in subcellular ROS results in the formation of peroxules, thin tubular extensions from peroxisomes (Sinclair et al., 2009). Similar tubular extensions called stromules and matrixules have been described from plastids and mitochondria, respectively (Scott et al., 2007; Mathur, 2021). Indeed, illuminating a triple transgenic SFR2mRFP-GPerox–Ymito line with 450 ± 25 μmol

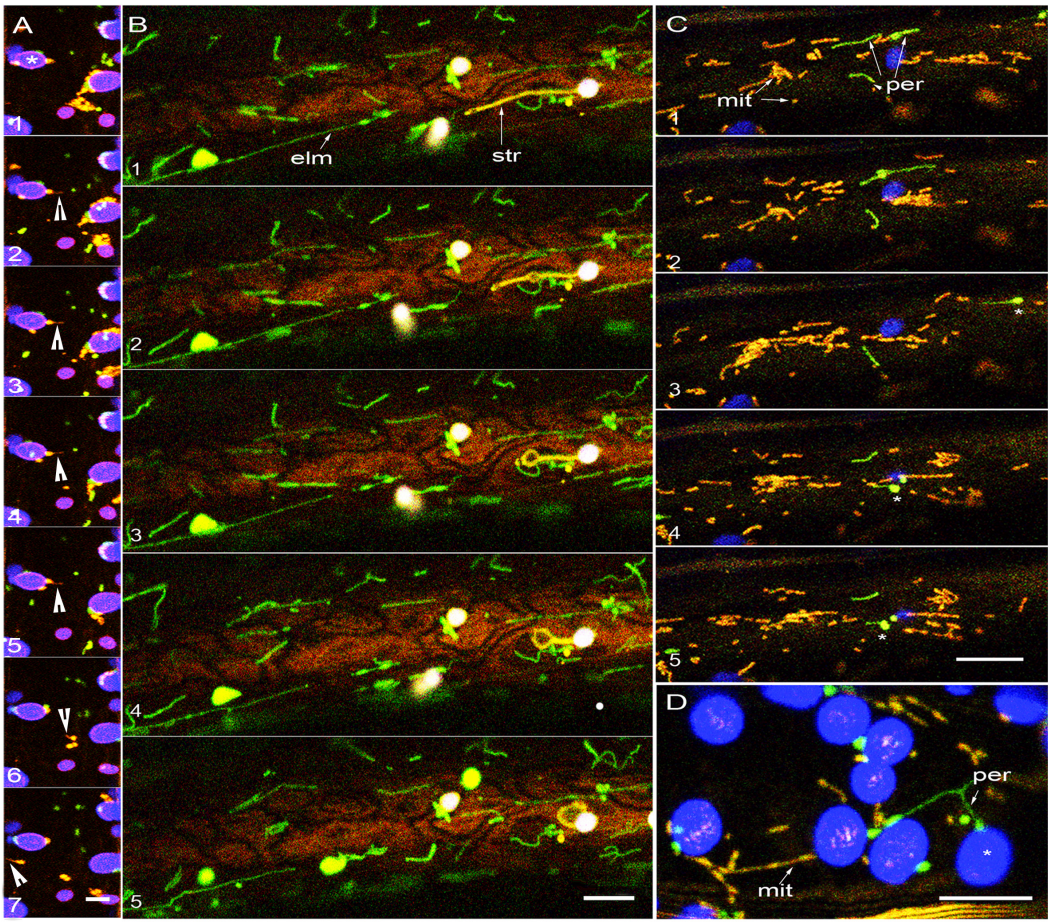

FIGURE 2 | Tubular forms do not increase proximity between plastids, mitochondria and peroxisomes. **(A)** Sequential images taken after 5 min of exposure to about 450 μmol $m^{-2}s^{-2}$ of light show mild organelle clustering and a quick matrixule (arrowhead) extension response by a mitochondrion in apparent proximity to a chloroplast (*). Panel 7 and 8 show other mitochondria extending matrixules independently (arrowheads). While mitochondria and peroxisome remain around the lower chloroplast (*) the cluster around the other chloroplasts disperse over time suggesting that dwell time and organelle dynamics can vary considerably even in neighboring regions of the cell (see **Supplementary Movies 2**, **3**). **(B)** Five sequential images from a single hypocotyl cell from a non-stressed double transgenic *elm1* mutant with elongated green fluorescent mitochondria (elm- arrow) and stroma targeted YFP. The elongated mitochondria do not interact with the extended stromule (str- arrow) that exhibits independent dynamic behavior (**Supplementary Movie 4**). **(C)** In non-stressed double transgenic *apm1* mutant elongated mitochondria (yellow -mit) and peroxisomes (per- green) pass by each other without showing sustained proximity. Peroxules (*) seen in panels 3, 4, 5 do not exhibit sustained proximity with the elongated mitochondria streaming around them (**Supplementary Movie 5**). **(D)** Representative snapshot from a double transgenic *apm1* mutant cell stressed by exposing to 450 ± 25 μmol $m^{-2}s^{-2}$ for 10 min suggests increased proximity between chloroplasts (* blue) elongated peroxisomes (per-green) and mitochondria (mit- yellow). Scale bars – A = 5; B, C, D = 10 microns.

$m^{-2}s^{-2}$ for 5 min is sufficient to induce organelle clustering and the extension of matrixules (**Figure 2A** and **Supplementary Movie 2**). It has been suggested that since organelle extensions transiently change the shape of a spheroidal organelle into a more tubular form (Mathur, 2020) they may serve to increase interactivity between organelles (Mathur, 2021). While most of the observations on organelle extensions have used some form of stress to achieve their increased frequency (Mathur, 2021) a low number of tubular organelle forms is found under relatively non-stressed and normal growth conditions too (Barton et al., 2018). In light of our observations that the spheroidal forms of chloroplasts, peroxisomes, and mitochondria do not exhibit sustained proximity under non-stressed conditions we wondered if the presence of a tubular organelle form could increase its interactivity even under normal growth conditions.This idea was explored next using *Arabidopsis thaliana* plants with constitutively elongated organelles.

Tubular Forms Do Not Increase Proximity Between Plastids, Mitochondria, and Peroxisomes

After an overnight period, chloroplasts in hypocotyl epidermal cells form long extensions within 2 h of illumination. A stable double transgenic line (mtyk-GPeroxi) that shows YFP-targeted to mitochondria and GFP-targeted to peroxisomes was crossed with another transgenic line expressing SFR2mRFP that labels the plastid outer envelope membrane (OEM) (**Figure 2A** and

Supplementary Movie 3). The triple transgenic SFR2mRFP-GPerox–Ymito line showed long red fluorescent plastid extensions, green peroxisomes, and yellow mitochondria. Based on observations from 25 chloroplasts with extensions, we found that the smaller organelles formed transient clusters around the chlorophyll-containing plastid body with the longest dwell time of 270 s exhibited by a mitochondrion. By contrast, the longest dwell time for mitochondria and peroxisomes moving past plastid extensions of up to 30 μm was between 12–20 s. We concluded that the two small organelles did not exhibit prolonged proximity with plastid extensions. Whether two tubules would have increased proximity was investigated next.

The Arabidopsis *elongated mitochondria1 (elm1/nmt1)* mutant is impaired in mitochondrial fission and shows greatly elongated GFP-highlighted mitochondria (Arimura et al., 2008; Logan, 2010). The mutant was crossed with the PtYK line that carries a YFP targeted to the plastid stroma (Nelson et al., 2007). As depicted in **Figure 2B** and time lapse **Supplementary Movie 4**, observations on this double transgenic line established that 5 to 25 μm long yellow fluorescent plastid extensions were present within a few micrometers of the 5 to 50 μm long green fluorescent tubular mitochondria. As these elongated forms did not exhibit any intertwining or alignment we concluded that organelle tubulation does not necessarily increase organelle proximity.

A third probe was considered to observe the behavior of elongated peroxisomes and elongated mitochondria simultaneously. The Arabidopsis *apm1/drp3a* mutant is impaired in the fission of both peroxisomes and mitochondria and consequently both organelles appear abnormally elongated (Arimura et al., 2004; Mano et al., 2004). A double transgenic line called *apm1*-mtYK showed green fluorescent peroxisomes (Mano et al., 2004) and yellow fluorescent mitochondria (**Figure 2**). As demonstrated earlier (Jaipargas et al., 2016) peroxules interact with small, punctate mitochondria in response to high light induced stress. However, we did not observe tubular peroxisomes interacting with tubular mitochondria in the hypocotyl cells of 80 non-stressed *apm1*-mtyk plants ranging in age from 8 to 10 days. Although 12 independent instances were recorded in the cell cortex where both tubular forms appeared within a few μm of each other, they maintained independent dynamic behavior in a manner similar to their considerably smaller, non-tubular forms. Independent tubule behavior was further underscored by the non-synchronous extension and retraction of the tubules and the sporadic appearance of dilations along the tubule length (**Figure 2C** and **Supplementary Movie 5**).

Exposing the *apm1*-mtYK plants to 450 ± 25 μmol $m^{-2}s^{-2}$ for 10 min resulted in peroxisome and mitochondrial clustering around chloroplasts (**Figure 2D**) and occasional intertwining of the tubules. However, as demonstrated by us earlier (Schattat et al., 2012) the intertwining and close interaction of tubular mitochondria results in their fusion and exchange of matrix proteins. Here, instead of suggesting increased proximity leading to interactions, the dynamic folds and loops formed asynchronously by the tubular organelles only served to reinforce their independent behavior.

A triple transgenic line expressing yellow fluorescent mitochondria (Ymito/mt-Yk; Nelson et al., 2007), and *SFR2*mRFP that highlights the plastid OEM in red was created in the *apm1* mutant background that already possesses elongated green fluorescent peroxisomes (Mano et al., 2004). Although all three organelles showed tubules, and four instances of elongated peroxisomes and mitochondria moving in tandem within a cytoplasmic strand were noted, two or three tubules representing the different organelles remaining in close proximity were not observed. As noted earlier in the *apm1*-mtYk line, hypoxia resulted in mitochondrial expansion into assorted shapes but there was only a decrease in the extension-retraction of plastid extensions and the dynamic movement of tubular peroxisomes.

We concluded that under normal conditions of growth both the spherical-oblong as well as the tubular forms of chloroplasts, mitochondria and peroxisomes maintain their spatiotemporal independence. Increased proximity that could suggest their high interactivity was not observed. While high light intensity-induced stress reduced the distance between the three organelles, hypoxia did not change their separate localization but largely affected their dynamic behavior.

The conundrum facing us at this stage was that our observations on the three key organelles in living cells contradicted the proximity-based suggestions used to underscore their biochemical interactivity. Although their increased interactivity was observed in response to photorespiratory stress, it seemed implausible to consider that chloroplasts, mitochondria and peroxisomes do not come close to each other under non-stressed conditions. An additional question was about the mechanism by which their spatial relationship changed quickly in response to stress. Therefore, we considered the possibility that instead of relying upon direct contacts with each other the interactions between these organelles involved a common mediator.

Irrespective of Their Shapes Plastids, Mitochondria, and Peroxisomes Are Closely Appressed to the Endoplasmic Reticulum Membranes

We have reported earlier on the independent alignments between the endoplasmic reticulum (ER) and peroxisomes (Sinclair et al., 2009; Barton et al., 2013, 2014), the ER and plastids (Schattat et al., 2011a,b; Barton et al., 2018) and the ER and mitochondria (Jaipargas et al., 2015, 2016). Observations made using different double transgenic lines, GPeroxi-RER that showed peroxisomes in green and the ER tubules in red, (mitoGFP)-RER that showed green mitochondria and red fluorescent ER lumen and (tpFNRG-EGFP)-RER where plastid extensions appeared green and the ER lumen appeared red, reconfirmed that each of the three key organelles is independently enmeshed in the ER (**Figures 3A–E**). While the mesh around mitochondria and peroxisomes is observed in **Figures 3B,C** shows peroxisomes and mitochondria at a distance from the chloroplast. A cluster of mitochondria (**Figure 3D**) and of mitochondria and peroxisomes (**Figure 3E**) is observed around separate chloroplasts. While showing the ER sandwiched between

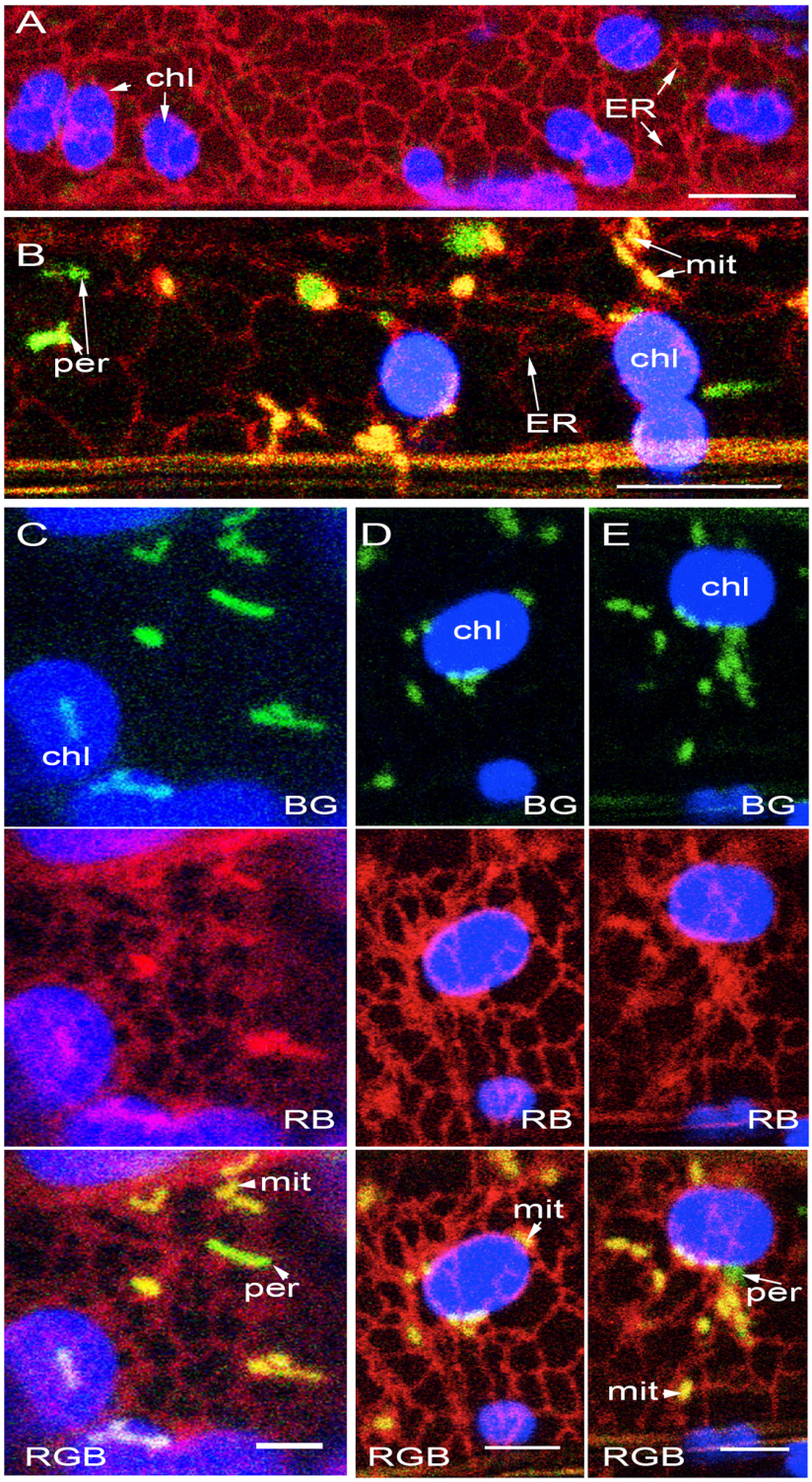

FIGURE 3 | Plastids, mitochondria and peroxisomes are individually surrounded by the ER. **(A)** Representative image showing the general ER mesh(red) and the loose ER-cage formed around chloroplasts (chl). **(B)** A representative image from GPeroxi-YMito-RER plants showing chloroplasts (chl in blue), mitochondria (mit in yellow) and peroxisomes (per in green) individually enmeshed in the ER (red). **(C)** Representative snapshot showing the independent spatial relationship that the ER (red) maintains with chloroplasts (chl-blue), mitochondria (mit- yellow) and peroxisomes (per -green). **(D)** Mitochondrial clusters in the peri-chloroplastidic ER and neighboring regions with each mitochondrion encased in its own ER. **(E)** Mitochondrial (mito – yellow) and peroxisomal (per- green) clusters in the peri-chloroplastidic ER (red)and neighboring regions with each of the smaller organelles encased in its own ER pocket (Based on **Supplementary Movie 6**). Scale bars- A, B = 10; C, D, E = 5 μm.

the different organelles, the observations also established that each cluster of small organelles around chloroplasts could be different from the other.

The ER mesh around chloroplast extensions (**Figure 4A**), tubular mitochondria (**Figure 4B**), and tubular peroxisomes (**Figure 4C**) reinforced the idea that the ER formed the most extensive membrane network around the different organelles. Additional observations came from a triple transgenic line in the Arabidopsis *accumulation and replication of chloroplasts 6* (*arc6*; Pyke et al., 1994) mutant background. Compared to chloroplasts in wild type Arabidopsis plants, the 2–3 mesophyll chloroplasts in the *arc6* mutant may show an enlarged size of up to 25 times and have a higher frequency of long plastid extensions (Pyke et al., 1994; Holzinger et al., 2008). The triple transgenic *arc6* tpFNREGFP-RER – Yperoxi line allowed simultaneous assessment of the spatial relationship between individual peroxisomes and the long plastid extensions with the surrounding ER (**Figure 4D**). Time lapse movies established that ER-enmeshed peroxisomes could occasionally align over a few μm with the tubular extensions or move past the extensions following a different trajectory. However, even when they appeared near each other, both the plastid extensions and the peroxisomes remained encaged independently by the ER.

Further evidence on the close alignment between the ER and tubular forms came from several other transgenic lines: the *apm1*-RER that showed elongated peroxisomes in green and the ER tubules in red (**Figure 4E**), *elm1*-RER that exhibited elongated green mitochondria and ER in red (**Figure 4F**). Since the *apm1* and the *elm1* mutants have elongated green fluorescent peroxisomes and mitochondria, respectively, time lapse image sequences showed how ER rearrangement affected the enmeshed organelles and their relation with the chloroplasts (**Figures 4E,F**). For both organelles, observations based on GFP and chlorophyll autofluorescence (e.g., top panels in **Figures 4E,F**) only showed the close alignment of the tubular organelles around the chloroplasts. Visualization of the ER created a different impression as it filled in the ER membranes present between the organelles.

We concluded that the ER is sandwiched between and in contact with each of the organelles considered here. The intimate association with the ER suggested that a change in ER-dynamics could directly impact the spatiotemporal behavior of the organelles embedded in it.

Conditions That Alter ER Membranes Also Affect Plastids, Peroxisomes, and Mitochondria

As shown earlier (**Figure 1**) exposure to high light intensity had increased the proximity between chloroplasts, mitochondria, and peroxisomes, although each organelle was in a separate ER pocket (**Figures 3**, **4**). Observations on 28 cells in 7 plants of the Gmito-Yperoxi-RER triple transgenic line showed that exposure to high light intensity for 10 min significantly altered the size of ER polygons around the different organelles. In an earlier publication we have reported that ER polygon sizes change in response to dark and light conditions and correlate with the fission of mitochondria (Jaipargas et al., 2015). Here, we observed that peroxisomes and mitochondria became confined within small ER polygons that developed around chloroplasts (**Figures 3D,E**). While this phenomenon requires further detailed investigations at the ultrastructural level, it suggested that closer contacts could occur between the membranes of the ER and the enmeshed organelles.

An opposite effect on the ER membranes was observed in seedlings placed in water under a glass coverslip for 45 min. This treatment creates hypoxic conditions for the plant cells (Van Gestel and Verbelen, 2002; Jaipargas et al., 2015). As observed here, the movement of organelles showed a general slowing down from ca. 1.5 $\mu m\ s^{-1}$ to between 0.75–0.5 $\mu m\ s^{-1}$. The most pronounced effect was observed on mitochondria which, during their slow movement, also expanded and fused to form giant mitochondria (**Figures 5A,B**). Concomitantly, the ER membranes expanded and thin cisternae became more prominent than the tubules. We concluded that ER membrane expansion was the reason for the reduced organelle motility. Notably the slowed down motility of all organelles allowed their independent behaviors to be maintained (**Figure 5B**) and did not increase their proximity.

In plant cells, it is well established that the cytoskeleton provides the tracks for movement of all organelles including the endomembrane system (Boevink et al., 1998; Nebenführ et al., 1999; Mathur et al., 2002). While an impaired actin cytoskeleton results in a general collapse of organelle movement (Mathur et al., 2002, 2003) we wished to assess whether peroxisomes and mitochondria came closer to chloroplasts during this process. The effects of Latrunculin B, a well-established inhibitor of actin polymerization (Spector et al., 1989) on organelle proximity were investigated. Treatment of the triple transgenic line (Gmito-Yperoxi-RER), with 100 nM of Latrunculin B for an hour resulted in a disruption of ER tubules, the formation of large diffuse globules, the development of a diffuse red fluorescence in the cell, and a general cessation of organelle motility. The effects of a general collapse of actin organization and the clumping of organelles were similar to earlier reported observations (Mathur et al., 2002; Barton et al., 2013) and have therefore not been shown here. Notably, mitochondrial expansion that formed a prominent feature of the response to hypoxia was not observed. It was concluded that while the other two treatments directly seemed to affect ER membranes the change in organelle proximity due to impaired actin cytoskeleton was a non-specific effect reflecting a totally collapsed subcellular activity.

Taken together, our observations reaffirmed that organelle movement, including the dynamic organization of the ER are actin dependent processes. Nevertheless, compared to the phenomenon of organelle motility the decrease in ER polygon size under high light as well as the expansion of ER membranes under hypoxia might be more directly linked to rapid alterations in organelle membranes. While these observations require more detailed investigations, it was concluded here that changes that result in the swelling or fusion of ER membrane have a direct effect on the distance between enmeshed organelles.

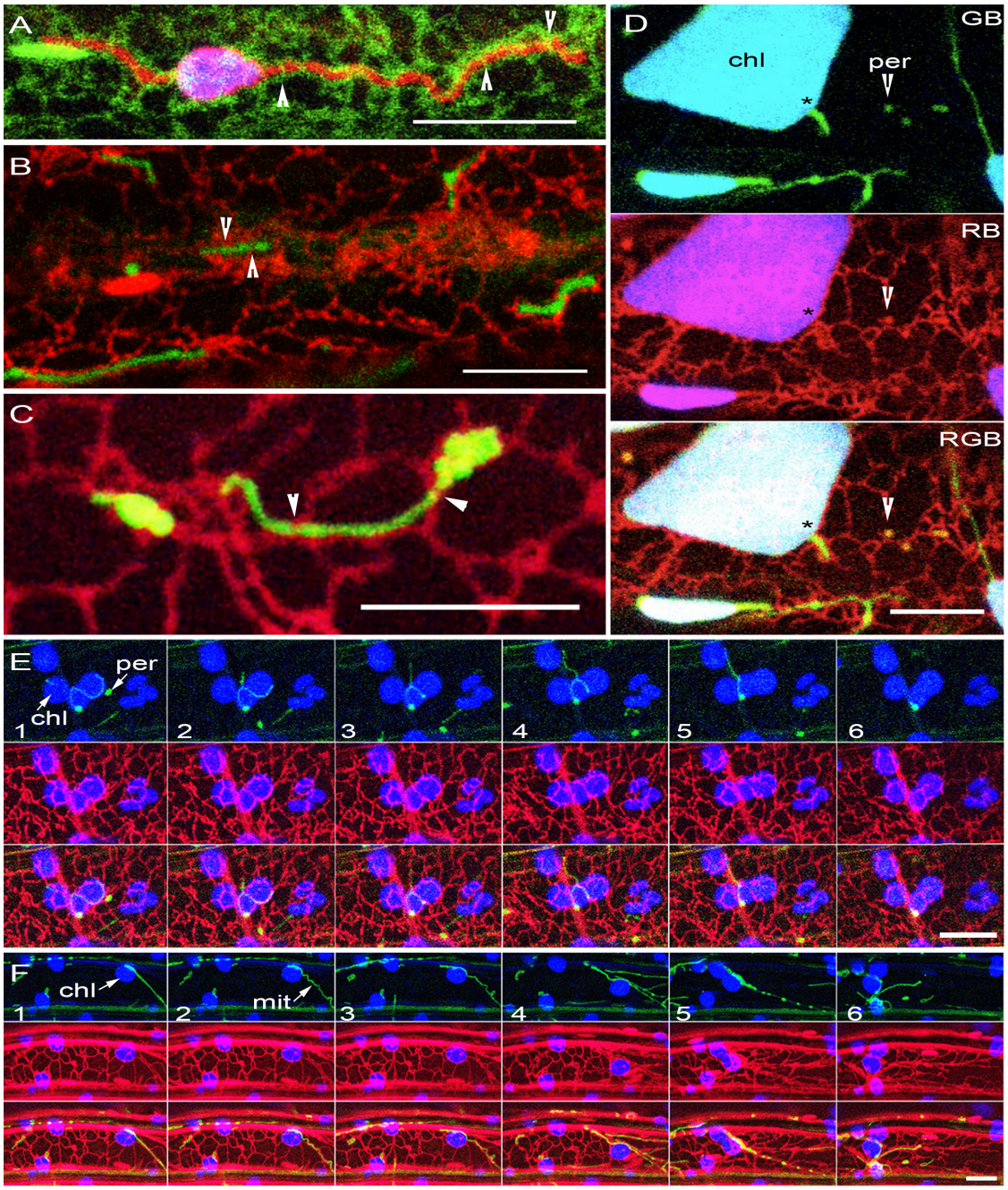

FIGURE 4 | Organelle extensions and tubular forms maintain connectivity only with the ER. **(A)** Plastid extension highlighted by OEM targeted expression of SFR2mRFP (red) enmeshed in the ER (green). Note the ER bands encircling the tubular extension (arrowheads). **(B)** Elongated mitochondria (green) in the Arabidopsis *elm1* mutant enmeshed in the ER (red) through the ER encircling the tubules at different points (arrowheads). **(C)** GFP-labeled peroxisomes in the Arabidopsis *apm1* mutant enmeshed in the ER (red) with main contact points indicated by arrowheads. **(D)** A single snapshot from image series shows large chloroplasts in the Arabidopsis *arc6* mutant with extensions (*), highlighted using a stroma targeted tpFNR-EGFP and observed with peroxisomes (yellow -arrowheads), both enmeshed independently by the ER (red). Chlorophyll depicted in blue (B), GFP in green (G), RFP in red (R); Yellow color of peroxisomes detected by overlapping R and G fluorescence. **(E)** Six sequential images showing an elongated green fluorescent peroxisome (per) in the Arabidopsis *apm1* mutant along with red fluorescent ER and chloroplasts (chl- blue). Note the close association between the peroxisome and the peri-plastid ER which allows the peroxisome to appear close to and molded around the chloroplasts. **(F)** Six sequential images from a time lapse series (**Supplementary Movie 7**) of elongated mitochondria (mit) in Arabidopsis *elm1* mutant appearing closely appressed to the chloroplast (chl- blue) as both organelles relocate in tandem with changing ER (red) organization. Scale bars = 10 μm.

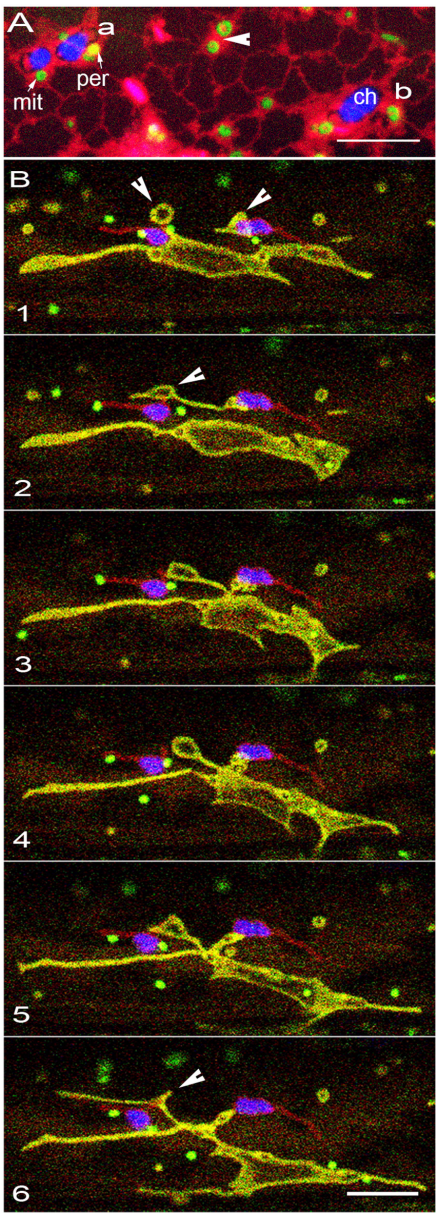

FIGURE 5 | Changes in ER membranes coincide with alterations in the morphology and behavior of other organelles. **(A)** Representative image of organelles in GPeroxi-YMito-RER triple transgenic plants under hypoxia after 45 min under water. While the ER-tubules (red) have not disappeared completely, chloroplasts (blue – chlorophyll; ch), peroxisomes (yellow – per) and mitochondria (mit – green) become surrounded separately by expanded, thin ER membranes (red). Whereas some regions of the expanded ER may not exhibit entrapped organelles, in other locations such as, "a" three organelles are trapped, "b" shows only a chloroplast and a mitochondrion while an arrowhead indicates two swollen, donut -shaped mitochondria (arrowheads). The phenomenon is reversible. **(B)** Six sequential snapshots from a time-lapse series (**Supplementary Movie 8**) illustrate the pleomorphy of expanded dynamic mitochondria while peroxisomes (green) and plastids (red OEM) retain their shapes and motility. While some donut-shaped mitochondria remain independent, other mitochondria indicated by arrowheads (panels 1, 2) fuse over time (arrowhead panel 6) to form a single large mitochondrion. Scale bars = 10 μm.

DISCUSSION

Our investigations started as an innocuous attempt to understand the routinely used words, 'organelle interactivity.' The words often create a useful backdrop for explaining the numerous biochemical interactions and pathways necessary for cell survival and proliferation. For many biologists, the words also evoke an image of the interacting organelles being close to each other. Despite the widely held belief in organelle interactivity being linked to proximity, the actual evidence behind the idea was traceable to only a few high-resolution ultrastructural snapshots of plant cells [e.g., Frederick and Newcomb (1969); Frederick et al. (1975); Hayashi et al., 2001; Sage and Sage, 2009]. Observations from studies using fluorescent fusion proteins to look at living plant cells have also contributed to the belief. Many of the studies use transient protein over-expression systems over incredibly long durations and frequently employ excised, wounded tissue for drawing conclusions about protein localizations and organelle interactions. Nevertheless, even with their accompanying artifacts, observations on stressed plant cells have been relevant in building up our ideas about subcellular interactions in the plant cell. One of the insights from observing living plant cells is that the cell continues to respond to the stimulus and consequently organelle behavior changes very quickly.

In order to add more insights to the body of knowledge on organelle interactions this study took a purely observational approach to find out about the actual proximity between different key organelles in living, intact plant cells under normal conditions of growth and development.

We considered that our baseline observations would lay down the foundation for more detailed studies leading to the discovery of proteins involved in creating MCS and exchange channels between organelles. Unexpectedly, our observations on non-stressed cells did not show close associations between chloroplasts, mitochondria, and peroxisomes, the three key organelles implicated in myriad aspects of plant metabolism. Whereas even transient stress can bring some of these organelles closer to each other and maintain proximity for several minutes it became clear that the majority of organelles exhibit a rather individualistic behavior. What allows a few chloroplasts, mitochondria, and peroxisomes to come together while others remain at a distance from each other?

We found that each of the three organelles investigated by us, irrespective of the form that they transiently adopted, did not interact directly with each other. Instead, each of them remained in close connectivity with the ER. Notably, exposure to high light intensity affects all the organelles and results in an increase in subcellular ROS. A short random diffusion distance of 1 μm is attributed to H_2O_2 and other ROS (Hallwell and Gutteridge, 1989) and one of the responses to increased cellular ROS is the expansion of membranes (Margittai et al., 2008). Based on our observations in response to high light intensity and hypoxia we suggest that changes in ER membrane dynamics are responsible for changes in the proximity of enmeshed organelles. Most significantly, even when the organelles appear close to each other

and form clusters that move around the cell, the ER membranes were always present between them.

This study only observed the relationship between the ER and chloroplasts, mitochondria, and peroxisomes. Within the limitations imposed by light microscopy, but with confidence due to the clear distance maintained between the majority of organelles observed, we surmised that the three key organelles do not interact physically with each other. Whether the ER is also involved in creating peri-nuclear clusters of chloroplasts (Erickson et al., 2017; Ding et al., 2019) remains an open question at present. For a similar reason, a more detailed investigation is underway for exploring the intimate relationship between peroxisomes and lipid droplets (LD; Thazar-Poulot et al., 2015; Cui et al., 2016). It is possible that similar to the relationship between the ER and Golgi bodies (Brandizzi et al., 2002; Sparkes et al., 2009; Stefano et al., 2012) peroxisomes and LD and other *de novo* generated endomembrane derived organelles and vesicles do exhibit direct interactivity with each other.

While our findings do not challenge the biochemical interactivity known to exist between different organelles, they do introduce some additional membrane layers that need to be accounted for during the exchanges.

Perhaps a key to assimilating our new insights into existing knowledge would lie in understanding the general redox state of a cell but then also breaking it down into multiple localized events so that the formation of small, transient redox domains may also be considered.

As already well established for mitochondria (Rizzuto et al., 1998; Kornmann et al., 2009; Csordás et al., 2010) MCS between the ER and the different enmeshed organelles might be the norm. Consequently, the specific output from an organelle (for example different forms of ROS; Exposito-Rodriguez et al., 2017) in response to a stimulus would affect the contiguous ER to produce an ER-microdomain. The continuous reorganization of ER tubules and cisternae would facilitate interactions between such *de novo* generated ER-microdomains. Thus, we suggest that instead of direct physical interactions occurring between the membranes of functionally discrete organelles, it is the membranes of ER-microdomains that interact with each other. The cumulative response output of a plant cell would still reflect the activities of all the different organelles but its dispersal and dissemination would involve interactions of ER-microdomains.

CONCLUSION

Although a compelling number of TEM images in published literature suggest direct interactions between different organelles our imaging of living plant cells using a variety of mutants and double and triple transgenic lines expressing targeted fluorescent probes did not convince us of their direct connectivity. Under non-stressed conditions a majority of organelles did not even come near each other. However, our observations clearly established that irrespective of their form at any given time, all plastids, mitochondria and peroxisomes remained in intimate connectivity with ER membranes. Whether ER mediation is a global phenomenon applicable to the interactivity of all organelles in a cell remains to be established. The use of mutants such as *ermo1/gnl1* (Nakano et al., 2009), *gom8* and *rhd3-7* (Stefano et al., 2012) that are impaired in ER morphology and dynamics should provide interesting insights on the role played by the ER in dictating the behavior and interactions of other organelles. Since many more insights might be obtained by using the robust set of new cell biological tools generated during this study we invite other investigators to undertake more detailed investigations on subcellular interactions in the plant cell.

MATERIALS AND METHODS

Gene Cloning

PCR primers for cloning the outer envelope localized gene SENSITIVE TO FREEZING2 (SFR2; Moellering et al., 2010) AT3G06510 gene were based on the coding sequence available in the Arabidopsis Information resource <TAIR; https://www.arabidopsis.org/> (Forward primer JM698 5′GTC TAGAATGGAATTATTCGCATTGTTAATT 3′carrying an *Xba*I site and the reverse primer with *Bam*HI site introduced – JM 699 5′GGATCCGTCAAAGGGTGAGGCTAAAGCA 3′. The resultant CDS was ligated in frame to create a C-terminal fusion with a monomeric RFP (mRFP; Campbell et al., 2002) and placed in a binary pCAMBIA 1300 vector backbone to which a proCaMV-35S and a nos-terminator sequence had been added earlier.

Creation of Transgenic Plants and Growth Conditions

Single and double transgenic lines of *Arabidopsis thaliana* were created through *Agrobacterium tumefaciens* mediated floral dip transformation (Clough and Bent, 1998) or through crossing of already selected stable transgenic lines. The proCaMV35S-SFR2mRFP transgenic lines were created in the Columbia ecotype of *Arabidopsis thaliana*. Other lines used have been published earlier and used for double or triple transgenic plants as detailed in **Table 1**. All seeds were stratified for 2 days at 4°C. For investigating soil-grown plants Sunshine mix LA4 (Sun Gro Horticulture, United States) soil in sealed Magenta boxes was used. Alternatively, if specified, plants were grown in plastic petri dishes containing Murashige and Skoog basal medium (Murashige and Skoog, 1962; Sigma M404) with B5 vitamins, 0.75% sucrose and 3 g/L phytagel (Sigma-Aldrich) (pH adjusted to 5.8 before autoclaving). Plants were grown for 7–14 days under a long-day light regime (16-h-light–8-h- dark) under light intensity of 120 $\pm$ 20 μmol m^{-2} s^{-1} light and an ambient temperature of 21 $\pm$ 2°C.

Microscopy

Entire seedlings were lifted from the soil, mounted in deionized water (pH 6.9 $\pm$ 0.2) on a glass depression slide and placed under a coverslip for observation using a 40X (numerical aperture 0.80) water immersion ceramic lens. A three channel Leica TCS-SP5 confocal laser- scanning unit equipped with 488 nm Ar and 543 nm He-Ne lasers was used for simultaneous imaging of

GFP, YFP, RFP, and chlorophyll. The emission spectra acquired were: GFP—503 to 515 nm (green); RFP- 555 to 630 nm (red); chlorophyll—650 to 710 nm (false colored blue). In double and triple transgenic plants with a YFP probe the yellow fluorescence was detected by extending the Red channel acquisition (525 to 630 nm) to create an overlap with GFP emission spectrum. The merged regions in images appeared yellow and were confirmed separately by using a YFP-dedicated 514 nm excitation laser line.

The x,y,z series used for 3-D projections maintained a 0.99 μm distance between sections. Time-lapse image capture (x, y, t) used a 1024 × 512-pixel box size and a line averaging of three in the bi-directional mode to obtain a frame every 1.935 s. All images were captured at a color depth of 24-bit RGB, cropped and processed for brightness/contrast as complete montages or image stacks using either Adobe Photoshop CS3[1] or the ImageJ/Fiji platform[2]. Adobe Photoshop was used for annotation of images and movies.

Measurement of Lipid Droplets Dwell Time Around Chloroplasts

In our experiments the idea of measuring "dwell time" was to establish the time that two organelles stayed together within a close distance. For measuring the dwell time at least ten independent time-lapse series ranging from 120 to 240 s (about 60 to 120 frames of 1024 × 512 pixels each) were used. Recognizing that in living cells the relative velocity of organelles is not constant (Mathur et al., 2002), it was assumed that a 1 μm diameter organelle, moving at a low velocity of 0.5 μm s^{-1} would require 20 s to move past a relatively immotile 8 μm diameter organelle and a buffer zone of 1 μm on each side (total path length of 10 μm). The Leica TCS SP5 point scanning laser confocal system used by us requires nearly 20 s for 10 x, y, t scans of a 1024 × 512 pixels rectangle with each scan an averaging of 3 lines. A "dwell time" longer than expected by the relative dimensions of the organelles was considered as being beyond a coincidental occurrence where the two organelles just happened to be in the same cytoplasmic neighborhood at the same time. While dwell time does not inform about whether an interaction has taken place or not it provides a likelihood for interaction with the chances of organelle interactions increasing with longer dwell time.

Stress and Inhibitor Treatments

High light stress was created on the microscope stage using the incandescent lap used routinely for bright field imaging an intensity of 450 ± 25 μmol m^{-2} s^{-2} for varying amounts of time. Mild hypoxic conditions were routinely obtained within 45 min of seedlings being placed in water under a 24 × 60 mm glass cover slip (Fisher Sci. 12-548-5P) and were characterized by the appearance of swollen mitochondria. Actin polymerization inhibition was achieved by treating the different seedlings for 1 h with 100 nM Latrunculin B (CAS 76343-94-7- Calbiochem) and observing them while still in the inhibitor solution.

[1]http://www.adobe.com

[2]http://fiji.sc/Fiji

DATA AVAILABILITY STATEMENT

The raw data supporting the conclusions of this article will be made available by the authors, without undue reservation.

AUTHOR CONTRIBUTIONS

JM initiated the study and designed the experiments. OK helped with the imaging. ML cloned the SFR2 gene. NM did all the plant transformations and growth experiments. All authors contributed to the article and approved the submitted version.

ACKNOWLEDGMENTS

We thank Shoji Mano and M. Nishimura for the *apm1*, S. Arimura for *elm1* mutant and David Logan for the GFP-mitochondria transgenic line. Research in the Mathur lab is funded by a Discovery grant to JM by the Natural Sciences and Engineering Research Council of Canada (NSERC).

SUPPLEMENTARY MATERIAL

The Supplementary Material for this article can be found online at: https://www.frontiersin.org/articles/10.3389/fpls.2022.846970/full#supplementary-material

Supplementary Figure 1 | Nine successive frames taken at intervals of 3 s from one of the 25 independent time-lapse x,y,t series taken on transgenic mtYK-Gperoxi plants that were used to observe differences in the rate of organelle movement in transvacuolar cytoplasmic strands (indicated by white arrow) compared to the cortical cytoplasmic sleeve. Small organelles often cluster in the linear cytoplasmic strands (arrowheads in different panels) and move at nearly twice the speed in comparison to the random and erratic movements of organelles in the cortical regions (peroxisome, red circle, mitochondrion white square). However, transvacuolar strands undergo rearrangements ly and small organelles are frequently drawn into the flow to move at a faster rate. Size bar = 10 μ m.

Supplementary Movie 1 | A representative time lapse (x,y,t) series comprising of 135 frames representing about 270 s of imaging time played at 3 fps. The series was captured from a single hypocotyl cell from a non-stressed triple transgenic Arabidopsis exhibiting the plastid OEM labeled by SFR2mRFP, peroxisomes targeted using GFP-SKL (Mathur et al., 2002) and mitochondria targeted with a YFP (Nelson et al., 2007). The chloroplasts, with chlorophyll false colored blue, exhibit OEM extensions. Numerous mitochondria and peroxisomes pass by the extensions and in a few frames appear to cluster around the chloroplast body. However, the subcellular motility presented in these images do not convey an impression of sustained proximity.

Supplementary Movie 2 | A representative x,y,t series depicting 60 frames and a collective time of about 120 s shows mild organelle clustering after a 5 min exposure to about 450 μmol m^{-2} s^{-2} of light. The number of mitochondria and peroxisomes that appear to cluster around chloroplasts and elsewhere in the cytoplasm keeps on changing over time. The small organelles maintain proximity near a single chloroplast in the lower part of the images for the duration of the image series collection. The movie illustrates that the response of different organelles with respect to each other including the dwell time between them can vary organelles considerably within a small subcellular locale. It also demonstrates that matrixules may be extended by independent mitochondria and do not necessarily interact with chloroplasts or peroxisomes in the neighborhood.

Supplementary Movie 3 | A time lapse series acquired over 140 s on a hypocotyl cell with plastid extensions (red), mitochondria and peroxisomes shows that the smaller organelles have a higher likelihood of interacting with the plastid body than with the long tubular extensions. Sustained proximity between mitochondria (yellow) and peroxisomes (green) is not concluded.

Supplementary Movie 4 | A 1:05 min x,y,t series of elongated peroxisomes (green) and mitochondria (yellow) in a hypocotyl cell of double transgenic *apm1* mutant establishes that the tubulation of both organelles does not prolong their proximity with each other. As seen for their non-elongated forms both organelles maintain independent behavior, including the sporadic formation of loops, constrictions and dilations along tubule length.

Supplementary Movie 5 | A 76 s time lapse representing 228 s of acquisition time from a double transgenic line in the *elm1* mutants shows green mitochondria and yellow plastid extensions. Despite both organelles presenting tubules within a few micrometers of each other, the tubules behave independently and do not exhibit increased proximity with each other. The plastid extension changes its shape considerably during the image acquisition time but this does not have an influence on its interactivity with elongated mitochondria.

Supplementary Movie 6 | A x,y,t series of 39 s representing about 118 frames shows a single cell from a triple transgenic plant expressing ER in red, mitochondria in green and mitochondria in yellow. Chlorophyl autofluorescence has been depicted in blue. Peroxisomes and mitochondria appear around the chloroplast but occupy separate pockets of the ER present within the peri-plastidic ER cage. Thus, their proximity to the chloroplasts results in ER being sandwiched between the three different organelles.

Supplementary Movie 7 | Time lapse series capturing about 387 s of elongated mitochondria (green) and ER (red) behavior in relation to chloroplasts (depicted blue) in a hypocotyl cell of the *elm1* mutant. The long mitochondria appear to wind around a chloroplast and faithfully move during its translocation. However, the time lapse sequence reveals that it is the intimate association of both chloroplasts and mitochondria with the ER that is responsible for their proximity and coordinated movement.

Supplementary Movie 8 | A time-lapse series captured over 225 s shows the differing effects of hypoxia on mitochondria (yellow) that expand considerably into assorted shapes that fuse and extend or retract. Plastid extensions (red) do not change while all organelles including peroxisomes (green) continue moving independently.

REFERENCES

Arimura, S. I., Aida, G. P., Fujimoto, M., Nakazono, M., and Tsutsumi, N. (2004). *Arabidopsis* dynamin-like protein 2a (ADL2a), like ADL2b, is involved in plant mitochondrial division. *Plant Cell Physiol.* 45, 236–242. doi: 10.1093/pcp/pch024

Arimura, S. I., Fujimoto, M., Doniwa, Y., Kadoya, N., Nakazono, M., Sakamoto, W., et al. (2008). *Arabidopsis* ELONGATED MITOCHONDRIA1 is required for localization of DYNAMIN- RELATED PROTEIN3A to mitochondrial fission sites. *Plant Cell* 20, 1555–1566. doi: 10.1105/tpc.108.058578

Barton, K., Mathur, N., and Mathur, J. (2013). Simultaneous live-imaging of peroxisomes and the ER in plant cells suggests contiguity but no luminal continuity between the two organelles. *Front. Physiol.* 4:196. doi: 10.3389/fphys.2013.00196

Barton, K. A., Jaipargas, E.-A., Griffiths, N., and Mathur, J. (2014). "Live imaging of peroxisomes and peroxules in plants," in *Molecular Machines Involved in Peroxisome Biogenesis and Maintenance*, eds C. Brocard and A. Hartig (Vienna: Springer), 233–253. doi: 10.1007/978-3-7091-1788-0

Barton, K. A., Schattat, M. H., Jakob, T., Hause, G., Wilhelm, C., McKenna, J. F., et al. (2016). Epidermal pavement cells of *Arabidopsis* have chloroplasts. *Plant Physiol.* 171, 723–726. doi: 10.1104/pp.16.00608

Barton, K. A., Wozny, M. R., Mathur, N., Jaipargas, E.-A., and Mathur, J. (2018). Chloroplast behaviour and interactions with other organelles in *Arabidopsis thaliana* pavement cells. *J. Cell Sci.* 131:jcs202275. doi: 10.1242/jcs.202275

Bauwe, H., Hagemann, M., and Fernie, A. R. (2010). Photorespiration: players, partners and origin. *Trends Plant Sci.* 15, 330–336. doi: 10.1016/j.tplants.2010.03.006

Boevink, P., Oparka, K., Cruz, S. S., Martin, B., Betteridge, A., and Hawes, C. (1998). Stacks on tracks: the plant Golgi apparatus traffics on an actin/ER network. *Plant J.* 15, 441–447. doi: 10.1046/j.1365-313X.1998.00208.x

Brandizzi, F., Snapp, E. L., Roberts, A. G., Lippincott-Schwartz, J., and Hawes, C. (2002). Membrane protein transport between the endoplasmic reticulum and the Golgi in tobacco leaves is energy dependent but cytoskeleton independent: evidence from selective photobleaching. *Plant Cell* 14, 1293–1309. doi: 10.1105/tpc.001586

Campbell, R. E., Tour, O., Palmer, A. E., Steinbach, P. A., Baird, G. S., Zacharias, D. A., et al. (2002). A monomeric red fluorescent protein. *Proc. Natl. Acad. Sci. U.S.A.* 99, 7877–7882. doi: 10.1073/pnas.082243699

Caplan, J. L., Kumar, A. S., Park, E., Padmanabhan, M. S., Hoban, K., Modla, S., et al. (2015). Chloroplast stromules function during innate immunity. *Dev. Cell* 34, 45–57. doi: 10.1016/j.devcel.2015.05.011

Clough, S. J., and Bent, A. F. (1998). Floral dip: a simplified method for *Agrobacterium*-mediated transformation of *Arabidopsis thaliana*. *Plant J.* 16, 735–743. doi: 10.1046/j.1365-313X.1998.00343.x

Cran, D. G., and Dyer, A. F. (1973). Membrane continuity and associations in the fern *Dryopteris borreri*. *Protoplasma* 76, 103–108. doi: 10.1007/bf01279676

Crotty, W. J., and Ledbetter, M. C. (1973). Membrane continuities involving chloroplasts and other organelles in plant cells. *Science* 182, 839–841. doi: 10.1126/science.182.4114.839

Csordás, G., Várnai, P., Golenár, T., Roy, S., Purkins, G., Schneider, T. G., et al. (2010). Imaging Interorganelle contacts and local calcium dynamics at the ER-mitochondrial interface. *Mol. Cell* 39, 121–132. doi: 10.1016/j.molcel.2010.06.029

Cui, S., Hayashi, Y., Otomo, M., Mano, S., Oikawa, K., Hayashi, M., et al. (2016). Sucrose production mediated by lipid metabolism suppresses the physical interaction of peroxisomes and oil bodies during germination of *Arabidopsis thaliana*. *J. Biol. Chem.* 291, 19734–19745. doi: 10.1074/jbc.M116.748814

Delfosse, K., Wozny, M. R., Jaipargas, E. A., Barton, K. A., Anderson, C., and Mathur, J. (2016). Fluorescent protein aided insights on plastids and their extensions: a critical appraisal. *Front. Plant Sci.* 6:1253. doi: 10.3389/fpls.2015.01253

Diers, L. (1966). On the plastids, mitochondria, and other cell constituents during oogenesis of a plant. *J. Cell Biol.* 28, 527–543. doi: 10.1083/jcb.28.3.527

Ding, X., Jimenez-Gongora, T., Krenz, B., and Lozano-Duran, R. (2019). Chloroplast clustering around the nucleus is a general response to pathogen perception in *Nicotiana benthamiana*. *Mol. Plant Pathol.* 20, 1298–1306. doi: 10.1111/mpp.12840

Erickson, J. L., Kantek, M., and Schattat, M. H. (2017). Plastid-nucleus distance alters the behavior of stromules. *Front. Plant Sci.* 8:1135. doi: 10.3389/fpls.2017.01135

Exposito-Rodriguez, M., Laissue, P. P., Yvon-Durocher, G., Smirnoff, N., and Mullineaux, P. M. (2017). Photosynthesis-dependent H_2O_2 transfer from chloroplasts to nuclei provides a high-light signalling mechanism. *Nat. Commun.* 8:49. doi: 10.1038/s41467-017-00074-w

Foyer, C. H., and Noctor, G. (2003). Redox sensing and signalling associated with reactive oxygen in chloroplasts, peroxisomes and mitochondria. *Physiol. Plant.* 119, 355–364. doi: 10.1034/j.1399-3054.2003.00223.x

Frederick, S. E., Gruber, P. J., and Newcomb, E. H. (1975). Plant microbodies. *Protoplasma* 84, 1–29. doi: 10.1007/BF02075940

Frederick, S. E., and Newcomb, E. H. (1969). Microbody-like organelles in leaf cells. *Science* 163, 1353–1355. doi: 10.1126/science.163.3873.1353

Gibbs, S. P. (1962). Nuclear envelope-chloroplast relationships in algae. *J. Cell Biol.* 14, 433–444. doi: 10.1083/jcb.14.3.433

Gunning, B. E. S. (2005). Plastid stromules: video microscopy of their outgrowth, retraction, tensioning, anchoring, branching, bridging, and tip-shedding. *Protoplasma* 225, 33–42. doi: 10.1007/s00709-004-0073-3

Hallwell, B., and Gutteridge, J. M. C. (1989). *Free Radicals in Biology and Medicine*, 2nd Edn. Oxford: Clarendon Press.

Haseloff, J., Siemering, K. R., Prasher, D. C., and Hodge, S. (1997). Removal of a cryptic intron and subcellular localization of green fluorescent protein are

required to mark transgenic *Arabidopsis* plants brightly. *Proc. Natl. Acad. Sci. U.S.A.* 94, 2122–2127. doi: 10.1073/pnas.94.6.2122

Hayashi, Y., Hayashi, M., Hayashi, H., Hara-Nishimura, I., and Nishimura, M. (2001). Direct interaction between glyoxysomes and lipid bodies in cotyledons of the *Arabidopsis thaliana ped1* mutant. *Protoplasma* 218, 83–94. doi: 10.1007/BF01288364

Helle, S. C. J., Kanfer, G., Kolar, K., Lang, A., Michel, A. H., and Kornmann, B. (2013). Organization and function of membrane contact sites. *Biochim. Biophys. Acta* 1833, 2526–2541. doi: 10.1016/j.bbamcr.2013.01.028

Holzinger, A., Kwok, E. Y., and Hanson, M. R. (2008). Effects of *arc3*, *arc5* and *arc6* mutations on plastid morphology and stromule formation in green and nongreen tissues of *Arabidopsis thaliana*. *Photochem. Photobiol.* 84, 1324–1335. doi: 10.1111/j.1751-1097.2008.00437.x

Jaipargas, E. A., Barton, K. A., Mathur, N., and Mathur, J. (2015). Mitochondrial pleomorphy in plant cells is driven by contiguous ER dynamics. *Front. Plant Sci.* 6:783. doi: 10.3389/fpls.2015.00783

Jaipargas, E. A., Mathur, N., Daher, F. B., Wasteneys, G. O., and Mathur, J. (2016). High light intensity leads to increased peroxule-mitochondria interactions in plants. *Front. Cell Dev. Biol.* 4:6. doi: 10.3389/fcell.2016.00006

Köhler, R. H., and Hanson, M. R. (2000). Plastid tubules of higher plants are tissue-specific and developmentally regulated. *J. Cell Sci.* 113, 81–89. doi: 10.1242/jcs.113.1.81

Kornmann, B., Currie, E., Collins, S. R., Schuldiner, M., Nunnari, J., Weissman, J. S., et al. (2009). An ER-mitochondria tethering complex revealed by a synthetic biology screen. *Science* 325, 477–481. doi: 10.1126/science.1175088

Kwok, E. Y., and Hanson, M. R. (2004a). *In vivo* analysis of interactions between GFP-labeled microfilaments and plastid stromules. *BMC Plant Biol.* 4:2. doi: 10.1186/1471-2229-4-2

Kwok, E. Y., and Hanson, M. R. (2004b). Plastids and stromules interact with the nucleus and cell membrane in vascular plants. *Plant Cell Rep.* 23, 188–195. doi: 10.1007/s00299-004-0824-9

Logan, D. C. (2010). Mitochondrial fusion, division and positioning in plants. *Biochem. Soc. Trans.* 38, 789–795. doi: 10.1042/BST0380789

Logan, D. C., and Leaver, C. J. (2000). Mitochondria-targeted GFP highlights the heterogeneity of mitochondrial shape, size and movement within living plant cells. *J. Exp. Bot.* 51, 865–871. doi: 10.1093/jxb/51.346.865

Mano, S., Nakamori, C., Hayashi, M., Kato, A., Kondo, M., and Nishimura, M. (2002). Distribution and characterization of peroxisomes in *Arabidopsis* by visualization with GFP: dynamic morphology and actin-dependent movement. *Plant Cell Physiol.* 43, 331–341. doi: 10.1093/pcp/pcf037

Mano, S., Nakamori, C., Kondo, M., Hayashi, M., and Nishimura, M. (2004). An *Arabidopsis* dynamin-related protein, DRP3A, controls both peroxisomal and mitochondrial division. *Plant J.* 38, 487–498. doi: 10.1111/j.1365-313X.2004.02063.x

Margittai, É, Löw, P., Szarka, A., Csala, M., Benedetti, A., and Bánhegyi, G. (2008). Intraluminal hydrogen peroxide induces a permeability change of the endoplasmic reticulum membrane. *FEBS Lett.* 582, 4131–4136. doi: 10.1016/j.febslet.2008.11.012

Margulis, L., Chapman, M., Guerrero, R., and Hall, J. (2006). The last eukaryotic common ancestor (LECA): acquisition of cytoskeletal motility from aerotolerant spirochetes in the Proterozoic Eon. *Proc. Natl. Acad. Sci. U.S.A.* 103, 13080–13085. doi: 10.1073/pnas.0604985103

Martin, W. F., Garg, S., and Zimorski, V. (2015). Endosymbiotic theories for eukaryote origin. *Philos. Trans. R. Soc. B Biol. Sci.* 370:20140330. doi: 10.1098/rstb.2014.0330

Mathur, J. (2020). Morphology, behaviour and interactions of organelles. *Plant Sci.* 301:110662. doi: 10.1016/j.plantsci.2020.110662

Mathur, J. (2021). Organelle extensions in plant cells. *Plant Physiol.* 185, 593–607. doi: 10.1093/PLPHYS/KIAA055

Mathur, J., Mathur, N., and Hülskamp, M. (2002). Simultaneous visualization of peroxisomes and cytoskeletal elements reveals actin and not microtubule-based peroxisome motility in plants. *Plant Physiol.* 128, 1031–1045. doi: 10.1104/pp.011018

Mathur, J., Mathur, N., Kirik, V., Kernebeck, B., Srinivas, B. P., and Hülskamp M. (2003) *Arabidopsis CROOKED* encodes for the smallest subunit of the ARP2/3 complex and controls cell shape by region specific fine F-actin formation. *Development* 130, 3137–3146. doi: 10.1242/dev.00549

Mehrshahi, P., Johnny, C., and DellaPenna, D. (2014). Redefining the metabolic continuity of chloroplasts and ER. *Trends Plant Sci.* 19, 501–507. doi: 10.1016/j.tplants.2014.02.013

Mehrshahi, P., Stefano, G., Andaloro, J. M., Brandizzi, F., Froehlich, J. E., and DellaPenna, D. (2013). Transorganellar complementation redefines the biochemical continuity of endoplasmic reticulum and chloroplasts. *Proc. Natl. Acad. Sci. U.S.A.* 110, 12126–12131. doi: 10.1073/pnas.1306331110

Mereschkowsky, C. (1905). Über natur und ursprung der chromatophoren im pflanzenreiche. *Biol. Cent.* 25, 593–604.

Michaud, M., Gros, V., Tardif, M., Brugière, S., Ferro, M., Prinz, W. A., et al. (2016). *AtMic60* is involved in plant mitochondria lipid trafficking and is part of a large complex. *Curr. Biol.* 26, 627–639. doi: 10.1016/j.cub.2016.01.011

Michaud, M., and Jouhet, J. (2019). Lipid trafficking at membrane contact sites during plant development and stress response. *Front. Plant Sci.* 10:2. doi: 10.3389/fpls.2019.00002

Moellering, E. R., Muthan, B., and Benning, C. (2010). Freezing tolerance in plants requires lipid remodeling at the outer chloroplast membrane. *Science* 330, 226–228. doi: 10.1126/science.1191803

Murashige, T., and Skoog, F. (1962). A revised medium for rapid growth and bio assays with tobacco tissue cultures. *Physiol. Plant.* 15, 473–497. doi: 10.1111/j.1399-3054.1962.tb08052.x

Nakano, R. T., Matsushima, R., Ueda, H., Tamura, K., Shimada, T., Li, L., et al. (2009). GNOM-LIKE1/ERMO1 and SEC24a/ERMO2 are required for maintenance of endoplasmic reticulum morphology in *Arabidopsis thaliana*. *Plant Cell* 21, 3672–3685. doi: 10.1105/tpc.109.068270

Natesan, S. K. A., Sullivan, J. A., and Gray, J. C. (2009). Myosin XI is required for actin-associated movement of plastid stromules. *Mol. Plant* 2, 1262–1272. doi: 10.1093/mp/ssp078

Nebenführ, A., Gallagher, L. A., Dunahay, T. G., Frohlick, J. A., Mazurkiewicz, A. M., Meehl, J. B., et al. (1999). Stop-and-go movements of plant Golgi stacks are mediated by the acto-myosin system. *Plant Physiol.* 121, 1127–1141. doi: 10.1104/pp.121.4.1127

Nelson, B. K., Cai, X., and Nebenführ, A. (2007). A multicolored set of in vivo organelle markers for co-localization studies in *Arabidopsis* and other plants. *Plant J.* 51, 1126–1136. doi: 10.1111/j.1365-313X.2007.03212.x

Noctor, G., Reichheld, J. P., and Foyer, C. H. (2018). ROS-related redox regulation and signaling in plants. *Semin. Cell Dev. Biol.* 80, 3–12. doi: 10.1016/j.semcdb.2017.07.013

Oikawa, K., Hayashi, M., Hayashi, Y., and Nishimura, M. (2019). Re-evaluation of physical interaction between plant peroxisomes and other organelles using live-cell imaging techniques. *J. Integr. Plant Biol.* 61, 836–852. doi: 10.1111/jipb.12805

Oikawa, K., Matsunaga, S., Mano, S., Kondo, M., Yamada, K., Hayashi, M., et al. (2015). Physical interaction between peroxisomes and chloroplasts elucidated by *in situ* laser analysis. *Nat. Plants* 1:15035. doi: 10.1038/nplants.2015.35

Perico, C., and Sparkes, I. (2018). Plant organelle dynamics: cytoskeletal control and membrane contact sites. *New Phytol.* 220, 381–394. doi: 10.1111/nph.15365

Prinz, W. A. (2014). Bridging the gap: membrane contact sites in signaling, metabolism, and organelle dynamics. *J. Cell Biol.* 205, 759–769. doi: 10.1083/jcb.201401126

Pyke, K. A., Rutherford, S. M., Robertson, E. J., and Leech, R. M. (1994). *arc6*, a fertile *Arabidopsis* mutant with only two mesophyll cell chloroplasts. *Plant Physiol.* 106, 1169–1177. doi: 10.1104/pp.106.3.1169

Rizzuto, R., Pinton, P., Carrington, W., Fay, F. S., Fogarty, K. E., Lifshitz, L. M., et al. (1998). Close contacts with the endoplasmic reticulum as determinants of mitochondrial Ca^{2+} responses. *Science* 280, 1763–1766. doi: 10.1126/science.280.5370.1763

Sagan, L. (1967). On the origin of mitosing cells. *J. Theor. Biol.* 14, 225–274. doi: 10.1016/0022-5193(67)90079-3

Sage, T. L., and Sage, R. F. (2009). The functional anatomy of rice leaves: implications for refixation of photorespiratory CO_2 and efforts to engineer C_4 photosynthesis into rice. *Plant Cell Physiol.* 50, 756–772. doi: 10.1093/pcp/pcp033

Schattat, M., Barton, K., Baudisch, B., Klösgen, R. B., and Mathur, J. (2011a). Plastid stromule branching coincides with contiguous endoplasmic reticulum dynamics. *Plant Physiol.* 155, 1667–1677. doi: 10.1104/pp.110.170480

Schattat, M., Barton, K., and Mathur, J. (2011b). Correlated behavior implicates stromules in increasing the interactive surface between plastids and ER tubules. *Plant Signal. Behav.* 6, 715–718. doi: 10.4161/psb.6.5.15085

Schattat, M. H., Griffiths, S., Mathur, N., Barton, K., Wozny, M. R., Dunn, N., et al. (2012). Differential coloring reveals that plastids do not form networks for exchanging macromolecules. *Plant Cell* 24, 1465–1477. doi: 10.1105/tpc.111.095398

Schumann, U., Prestele, J., O'Geen, H., Brueggeman, R., Wanner, G., and Gietl, C. (2007). Requirement of the C_3HC_4 zinc RING finger of the *Arabidopsis* PEX10 for photorespiration and leaf peroxisome contact with chloroplasts. *Proc. Natl. Acad. Sci. U.S.A.* 104, 1069–1074. doi: 10.1073/pnas.0610402104

Scott, I., Sparkes, I. A., and Logan, D. C. (2007). The missing link: inter-organellar connections in mitochondria and peroxisomes? *Trends Plant Sci.* 12, 380–381. doi: 10.1016/j.tplants.2007.07.001

Sinclair, A. M., Trobacher, C. P., Mathur, N., Greenwood, J. S., and Mathur, J. (2009). Peroxule extension over ER-defined paths constitutes a rapid subcellular response to hydroxyl stress. *Plant J.* 59, 231–242. doi: 10.1111/j.1365-313X.2009.03863.x

Sparkes, I., Hawes, C., and Frigerio, L. (2011). FrontiERs: movers and shapers of the higher plant cortical endoplasmic reticulum. *Curr. Opin. Plant Biol.* 14, 658–665. doi: 10.1016/j.pbi.2011.07.006

Sparkes, I. A., Ketelaar, T., De Ruijter, N. C. A., and Hawes, C. (2009). Grab a Golgi: laser trapping of Golgi bodies reveals in vivo interactions with the endoplasmic reticulum. *Traffic* 10, 567–571. doi: 10.1111/j.1600-0854.2009.00891.x

Spector, I., Shorlet, N. R., Blasberger, D., and Kashman, Y. (1989). Latrunculins – novel marine macrolides that disrupt microfilament organization and affert cell growth: I. Comparison with cytochalasin D. *Cell Motil. Cytoskeleton* 13, 127–144. doi: 10.1002/cm.970130302

Staehelin, A. L. (1997). The plant ER: a dynamic organelle composed of a large number of discrete functional domains. *Plant J.* 11, 1151–1165. doi: 10.1046/j.1365-313x.1997.11061151.x

Stefano, G., Renna, L., and Brandizzi, F. (2014). The endoplasmic reticulum exerts control over organelle streaming during cell expansion. *J. Cell Sci.* 127, 947–953. doi: 10.1242/jcs.139907

Stefano, G., Renna, L., Moss, T., McNew, J. A., and Brandizzi, F. (2012). In *Arabidopsis*, the spatial and dynamic organization of the endoplasmic reticulum and Golgi apparatus is influenced by the integrity of the C-terminal domain of RHD3, a non-essential GTPase. *Plant J.* 69, 957–966. doi: 10.1111/j.1365-313X.2011.04846.x

Thazar-Poulot, N., Miquel, M., Fobis-Loisy, I., and Gaude, T. (2015). Peroxisome extensions deliver the *Arabidopsis* SDP1 lipase to oil bodies. *Proc. Natl. Acad. Sci. U.S.A.* 112, 4158–4163. doi: 10.1073/pnas.1403322112

Van Gestel, K., and Verbelen, J. P. (2002). Giant mitochondria are a response to low oxygen pressure in cells of tobacco (*Nicotiana tabacum* L.). *J. Exp. Bot.* 53, 1215–1218. doi: 10.1093/jexbot/53.371.1215

Wildman, S., Hongladarom, T., and Honda, S. (1962). Chloroplasts and mitochondria in living plant cells: cinephotomicrographic studies. *Science* 138, 434–436. doi: 10.1126/science.138.3538.434

Conflict of Interest: The authors declare that the research was conducted in the absence of any commercial or financial relationships that could be construed as a potential conflict of interest.

Publisher's Note: All claims expressed in this article are solely those of the authors and do not necessarily represent those of their affiliated organizations, or those of the publisher, the editors and the reviewers. Any product that may be evaluated in this article, or claim that may be made by its manufacturer, is not guaranteed or endorsed by the publisher.

frontiers | Frontiers in Plant Science

ORIGINAL RESEARCH
published: 04 April 2022
doi: 10.3389/fpls.2022.857745

Edited by:
Francisco Javier Medina, Margarita Salas Center for Biological Research (CSIC), Spain

Reviewed by:
Elena Ramirez-Parra, National Institute of Agricultural and Food Research and Technology, Spain
Cristina Ferrandiz, Polytechnic University of Valencia, Spain

***Correspondence:**
Maria Helena S. Goldman
mgoldman@ffclrp.usp.br
orcid.org/0000-0002-6786-9320
Matteo Barberis
matteo@barberislab.com;
m.barberis@surrey.ac.uk
orcid.org/0000-0001-5640-7422

†Present addresses:
Juca A. B. San Martin, Instituto de Botánica Darwinion (Consejo Nacional de Investigaciones Científicas y Técnicas, Academia Nacional de Ciencias Exactas, Físicas y Naturales), San Isidro, Argentina
Henrique C. De Paoli, Biological Systems and Engineering Division, Lawrence Berkeley National Laboratory, Berkeley, CA, United States

‡These authors have contributed equally to this work and share first authorship

§These authors share senior authorship

Specialty section:
This article was submitted to Plant Cell Biology, a section of the journal Frontiers in Plant Science

Received: *19 January 2022*
Accepted: *14 March 2022*
Published: *04 April 2022*

Citation:
Strini EJ, Bertolino LT, San Martin JAB, Souza HAO, Pessotti F, Pinoti VF, Ferreira PB, De Paoli HC, Lubini G, Del-Bem L-E, Quiapim AC, Mondin M, Araujo APU, Eloy NB, Barberis M and Goldman MHS (2022) Stigma/Style Cell-Cycle Inhibitor 1, a Regulator of Cell Proliferation, Interacts With a Specific 14-3-3 Protein and Is Degraded During Cell Division. Front. Plant Sci. 13:857745. doi: 10.3389/fpls.2022.857745

Stigma/Style Cell-Cycle Inhibitor 1, a Regulator of Cell Proliferation, Interacts With a Specific 14-3-3 Protein and Is Degraded During Cell Division

Edward J. Strini[1,2‡], Lígia T. Bertolino[1,2‡], Juca A. B. San Martin[1†], Hebréia A. O. Souza[1], Francine Pessotti[1,2], Vitor F. Pinoti[1,2], Pedro B. Ferreira[1,2], Henrique C. De Paoli[1,2†], Greice Lubini[1,2], Luiz-Eduardo Del-Bem[3], Andréa C. Quiapim[1], Mateus Mondin[4], Ana Paula U. Araujo[5], Nubia B. Eloy[6], Matteo Barberis[7,8,9*§] and Maria Helena S. Goldman[1,2*§]

[1]Departamento de Biologia, Faculdade de Filosofia, Ciências e Letras de Ribeirão Preto, University of São Paulo, Ribeirão Preto, Brazil, [2]PPG-Genética, Faculdade de Medicina de Ribeirão Preto, University of São Paulo, Ribeirão Preto, Brazil, [3]Departamento de Botânica, Instituto de Ciências Biológicas, Universidade Federal de Minas Gerais, Belo Horizonte, Brazil, [4]Departamento de Genética, Escola Superior de Agricultura Luiz de Queiroz, University of São Paulo, Piracicaba, Brazil, [5]São Carlos Institute of Physics, University of São Paulo, São Carlos, Brazil, [6]Departamento de Ciências Biológicas, Escola Superior de Agricultura Luiz de Queiroz, University of São Paulo, Piracicaba, Brazil, [7]Systems Biology, School of Biosciences and Medicine, Faculty of Health and Medical Sciences, University of Surrey, Guildford, United Kingdom, [8]Centre for Mathematical and Computational Biology, CMCB, University of Surrey, Guildford, United Kingdom, [9]Synthetic Systems Biology and Nuclear Organization, Swammerdam Institute for Life Sciences, University of Amsterdam, Amsterdam, Netherlands

The final shape and size of plant organs are determined by a network of genes that modulate cell proliferation and expansion. Among those, *SCI1 (Stigma/style Cell-cycle Inhibitor 1)* functions by inhibiting cell proliferation during pistil development. Alterations in *SCI1* expression levels can lead to remarkable stigma/style size changes. Recently, we demonstrated that *SCI1* starts to be expressed at the specification of the *Nicotiana tabacum* floral meristem and is expressed at all floral meristematic cells. To elucidate how SCI1 regulates cell proliferation, we screened a stigma/style cDNA library through the yeast two-hybrid (Y2H) system, using SCI1 as bait. Among the interaction partners, we identified the 14-3-3D protein of the Non-Epsilon group. The interaction between SCI1 and 14-3-3D was confirmed by pulldown and co-immunoprecipitation experiments. 14-3-3D forms homo- and heterodimers in the cytoplasm of plant cells and interacts with SCI1 in the nucleus, as demonstrated by Bimolecular Fluorescence Complementation (BiFC). Analyses of SCI1-GFP fluorescence through the cell-cycle progression revealed its presence in the nucleoli during interphase and prophase. At metaphase, SCI1-GFP fluorescence faded and was no longer detected at anaphase, reappearing at telophase. Upon treatment with the 26S proteasome inhibitor MG132, SCI1-GFP was stabilized during cell division. Site-directed mutagenesis of seven serines into alanines in the predicted 14-3-3 binding sites on the SCI1 sequence prevented its degradation during mitosis. Our results demonstrate that SCI1 degradation at the beginning of metaphase

is dependent on the phosphorylation of serine residues and on the action of the 26S proteasome. We concluded that SCI1 stability/degradation is cell-cycle regulated, consistent with its role in fine-tuning cell proliferation.

Keywords: cell division regulator, early mitosis, 14-3-3 interaction, nuclear shuttling, proteasome degradation, SCI1

INTRODUCTION

Successful sexual plant reproduction depends on the proper development of the male and female reproductive organs, stamens, and pistil, respectively. The upper pistil, comprised of style and stigma, is responsible for receiving the pollen grains and providing the appropriate conditions for compatible pollen tube germination and directional growth (Goldman et al., 1994). Pistil organogenesis relies on the tight control of cell proliferation and differentiation, achieved through complex gene regulatory networks that are not fully understood. The identification and characterization of *SCI1* showed that this gene has a role in the network controlling cell proliferation in the upper pistil of *Nicotiana tabacum* (DePaoli et al., 2011) and *Arabidopsis thaliana* (DePaoli et al., 2014). Knockdown transgenic tobacco plants and Arabidopsis mutants display enlarged stigmas and elongated styles that contain more cells than plants with normal SCI1 transcript levels (DePaoli et al., 2011, 2014). Based on the evidence, we proposed that SCI1 is a tissue-specific regulator of cell proliferation (DePaoli et al., 2012). Recently, SCI1 was demonstrated to be specifically expressed in the proliferative cells of the *N. tabacum* floral meristem, which is terminated after style and stigma development (Cruz et al., 2021).

Stigma/style cell-cycle inhibitor 1 is a small protein (154 amino acids) containing 15 putative phosphorylation sites (NetPhos, ≥96%), suggesting that it may be regulated in a signal transduction pathway (DePaoli et al., 2011). To elucidate how SCI1 engages with the cell-cycle machinery, we have undertaken different approaches to identify SCI1 interaction partners. By analyzing the SCI1 interactome in tobacco stigmas/styles, we identified, among many other proteins, two 14-3-3 proteins of the Non-Epsilon group. 14-3-3s are conserved eukaryotic proteins that usually recognize proteins containing phosphoserine and/or phosphothreonine residues within specific sequence motifs (de Boer et al., 2012; Wilson et al., 2016). They are regulatory proteins with signaling roles in various cellular processes, such as regulation of hormonal signal transduction processes (Roberts, 2000; Aducci et al., 2002; Schoonheim et al., 2007; Chevalier et al., 2009; Denison et al., 2011; Keicher et al., 2017; Camoni et al., 2018; Lee et al., 2020), plant growth dependent on sugar signaling (Chen et al., 2019), and flowering transition (Mayfield et al., 2007; Paul et al., 2008; Jaspert et al., 2011; Collani et al., 2019). Their involvement in cell-cycle control (Laronga et al., 2000; van Hemert et al., 2001; Usui and Petrini, 2007; Grandin and Charbonneau, 2008; Gardino and Yaffe, 2011; Bokros et al., 2016; Gryaznova et al., 2016; Pennington et al., 2018) is well studied in yeast, animals and cancer research, but largely unknown in plants. In budding yeast, there are only two genes encoding 14-3-3s, BMH1 and BMH2. Mutants lacking both genes, which are involved in regulating cell division, are lethal. Interestingly, these mutants can be rescued by expressing the 14-3-3 counterparts from Arabidopsis, among which the isoforms At14-3-3 Phi and At14-3-3 Upsilon (van Heusden et al., 1996), both from the Non-Epsilon group (see below). This suggests that 14-3-3 proteins may be involved in regulating cell division also in plants.

Phylogenetically, plant 14-3-3 protein family can be divided into the Epsilon and the Non-Epsilon groups (Ferl et al., 2002), based on their amino acid sequences and gene structures. The Epsilon group is considered to contain the ancestral 14-3-3s undertaking essential functions, while the 14-3-3s from the Non-Epsilon group would assume more specialized roles (Jaspert et al., 2011; Hloušková et al., 2019). 14-3-3 proteins can form homo and heterodimers (Jones et al., 1995; Chaudhri et al., 2003), and it has been suggested that each type of dimer could undertake diverse functions (Paul et al., 2012). There is certain specificity in 14-3-3 dimerization and not all homodimers and possible heterodimers are formed (Pallucca et al., 2014; Lin et al., 2021). The 14-3-3 dimer can interact with two different sites of a single protein or simultaneously interact with two distinct proteins (Yaffe, 2002; Chevalier et al., 2009). At the genomic level, 13 genes encode 14-3-3 proteins in tomato (Cao et al., 2016) and Arabidopsis, in addition to two pseudogenes in the latter genome (DeLille et al., 2001; Rosenquist et al., 2001). In *N. tabacum*, 17 transcript sequences encoding 14-3-3 proteins were identified (Konagaya et al., 2004; Lozano-Durán and Robatzek, 2015), and two of these correspond to alternative transcripts of the same gene. Considering the number of genes encoding the monomeric subunits and the possibility of forming different combinations of homo- and heterodimers, 14-3-3 proteins can assume many functions and specificities of client proteins. The binding of 14-3-3 dimers can cause a conformational change of the client proteins, stimulating or inhibiting their activity or modifying their stability (Ferl et al., 2002). Additionally, 14-3-3 binding can facilitate the interaction between two proteins or change their subcellular localization (van Heusden, 2009; reviewed in Chevalier et al., 2009; Gökirmak et al., 2010). Thus, plant 14-3-3 proteins can be considered nodes in signaling networks and establish a crosstalk platform in diverse pathways (Ferl, 2004; Oecking and Jaspert, 2009).

Here, we investigated the cellular and molecular mechanisms through which SCI1 may engage in cell-cycle control and regulate cell proliferation. We report the identification and characterization of SCI1 interaction with 14-3-3D from *N. tabacum*. We show that when chromatin starts condensation (G2/prophase), 14-3-3D moves from the cytoplasm to the nucleus, where it interacts with SCI1. SCI1 is degraded by the proteasome at late prophase/prometaphase, possibly due

to its interaction with 14-3-3D, since mutations at key serine residues of SCI1 stabilize the protein during metaphase. This behavior is consistent with a role for SCI1 as an inhibitor of cell proliferation, which must be degraded at mitosis to allow proper cell division.

MATERIALS AND METHODS

Plant Material

Nicotiana tabacum L. cv. Petit Havana SR-1 and *Nicotiana benthamiana* seeds were sown on Bioplant® substrate with vermiculite, irrigated from below, and cultivated in an environmental growth chamber Weiss-Gallenkamp (55% humidity, 16-h day/8-h night regime, and 22°C). In addition, wild-type and transgenic *N. tabacum* plants were also grown in a greenhouse under standard conditions in Ribeirão Preto—SP, BRAZIL (Latitude—21° 10′24″ S, Longitude—47° 48′24″ W, with an average temperature of 22°C in winter and 27°C in summer; the difference in day length between summer and winter is less than 2 h) for collecting floral tissues (for protein and RNA extractions). Samples were immediately used or frozen in liquid nitrogen and stored at −70°C.

Y2H cDNA Library Construction

Total RNA was extracted from stigmas/styles of *N. tabacum* flowers at stages 1–11 (Koltunow et al., 1990) with Trizol reagent (Invitrogen). mRNA was purified with GenElute mRNA Miniprep (Sigma), and cDNA synthesis was performed with CloneMiner II cDNA Library Construction (Invitrogen) following the manufacturer's instructions. Briefly, biotin-attB2-Oligo(dT) primer was used for reverse transcription reaction followed by second-strand synthesis and attB1 adapter ligation to the 5′ end of double-stranded cDNAs. The resulting cDNAs were size-fractionated by column chromatography, cloned in pDONR™222 (Invitrogen) with BP Clonase II enzyme mix (Invitrogen), and transformed into DH10B cells. The quality and the average insert cDNA size were estimated based on electrophoresis analyses of DNA from 24 transformants. Then, BP reactions were performed until 5×10^6 clones were obtained. The plasmid DNA of the pDONR™ 222 clones (clone library) was purified, subcloned in pDEST22 (Invitrogen) vector with LR Clonase II Enzyme Mix (Invitrogen), and transformed into DH10B cells. The average insert cDNA size and the library quality were estimated, and LR reactions were performed until 5×10^6 clones were obtained. Finally, plasmid DNA from the pDEST22 clones was extracted as a pool, composing the final yeast two-hybrid (Y2H) cDNA library.

Screening of Y2H cDNA Library and Binary Assays of Candidate Clones

The screening of the Y2H cDNA library was carried out using ProQuest™ Two-Hybrid System and Gateway Technology kit (Invitrogen). Yeast strain PJ69-4a (MATa; trp1-901 leu2-3,112 ura3-52 his3-200 gal4 (deleted) gal80 (deleted) LYS2::GAL1-HIS3 GAL2-ADE2 met2::GAL7-lacZ) cells, previously transformed with pDEST32-SCI1 plasmid and tested for self-activation, were transformed with 1 μg of DNA of the Y2H library. The transformation procedure was repeated 30 times to achieve approximately $1–2 \times 10^6$ yeast transformants. The transformed yeast cells were plated on selective Synthetic Complete (SC) medium (lacking leucine, tryptophan, and histidine) and incubated for 2 days at 30°C followed by 1–2 days at room temperature. During that period, the appearing colonies were scored and labeled. The HIS3 positive yeast colonies were organized in 96 well microtiter plates, used for glycerol stock preparation and LacZ reporter gene assay. Plasmid DNA from each positive yeast colony was extracted and individually transformed into DH10B cells. Plasmid DNA from *Escherichia coli* transformants was analyzed by restriction digestion. Distinct AD plasmids from a single *E. coli* transformation were individually introduced in PJ69-4a cells bearing pDEST32-SCI1 or pDEST32-empty vector and tested for histidine auxotrophy (binary assay). Different concentrations of 3′AT (3-Amino-1,2,4-triazole) were added on a selective medium in the case of self-activation. All plates of Y2H binary assays were performed in 96-well format (for an example, see **Supplementary Figure S1**), which included a set of the negative and positive controls of the ProQuestTM Two-Hybrid System and Gateway Technology kit (Invitrogen). Finally, the AD plasmids presenting growth along with pDEST32-SCI1, but not with empty vector (self-activation control), were sequenced, analyzed by the BLAST program,[1] and annotated as positive interactors.

Cloning Procedures

The complete coding sequences (CDSs) of 14-3-3A1 (accession number AB119466) and 14-3-3D2AS (AB119473) were amplified by PCR from the Y2H cDNA library clones H6.1 and D9.4, respectively. *Nicotiana tabacum* Wee1 coding sequence was amplified by PCR from stigma/style cDNAs. All primers used for amplification and cloning are listed in **Table 1**. CDSs were cloned into the pDONR221 entry vector using BP Clonase (Invitrogen). pENTRY-SCI1 was produced in previous work (DePaoli et al., 2011). *Escherichia coli* DH10B electrocompetent cells were used for all cloning procedures. The CDSs were transferred to the appropriate destination vectors: pK7FWG2 for GFP fusion in plants (Karimi et al., 2002); pDEST32 and pDEST22 (Invitrogen) for Y2H; and pDEST15 and pDEST17 (Invitrogen) for *E. coli* expression with appropriate tags, using LR clonase (Invitrogen). The construction of the Bimolecular Fluorescence Complementation (BiFC) vectors, based on pK7m34GW and pH7m34GW and building blocks (Karimi et al., 2007), was done using LR Clonase II Plus (Invitrogen). Site-directed mutagenesis in SCI1 serines (shown in **Supplementary Figure S2**) was done in two steps, using the QuikChange™ Site-Directed Mutagenesis kit (Stratagene), according to manufacturer's instructions, and the primers listed in **Table 1**. All constructions were sequenced to verify undesired PCR or cloning errors and confirmed the correct reading frame in the translational fusions.

[1]http://www.ncbi.nlm.nih.gov/BLAST/

TABLE 1 | Primers used to amplify the coding regions of *N. tabacum* genes used in this work.

Primer names	Primer Sequences (5′–3′)
attB1SDK-14-3-3D-FW	gca ggc ttc gaa gga gat aga acc ATG GCC GTA CCG GAA AAT TTA AC
attB2-14-3-3D-RV	aag ctg ggt cTC AAG CCT CGT CCA TCT GC
attB2-14-3-3Dss-RV	aag ctg ggt cAG CCT CGT CCA TCT GCT CC
14–3-3A-FW	gca ggc ttc gaa gga gat aga acc ATG GCA TCG CCG CGC GAG
14–3-3A-RV	aag ctg ggt cTT ACT GCT GCT CCT CCG CTT
14–3-3Ass-RV	aag ctg ggt cCT GCT GCT CCT CCG CTT TT
SCI1(Ct11)Mut1NewFW	G AGG AAG CAT AAG AGA *GC*T *G*CG CCT *G*CT *G*CT CCA CGA GAT GAA G
SCI1(Ct11)Mut1NewRV	C TTC ATC TCG TGG AG*C* AG*C* AGG CG*C* A*GC* TCT CTT ATG CTT CCT C
SCI1mut2-FW	G AAG GAG AAG CAC AAA *G*CC CAT *G*CT *GC*T GAA GAG AAG AAG TCA GG
SCI1mut2-RV	CC TGA CTT CTT CTC TTC A*GC* AG*C* ATG GG*C* TTT GTG CTT CTC CTT C
attB1-NtWee1-FW	gca ggc ttc gaa gga gat aga acc ATG AAG AGG AAA ACC CTA AAT C
attB2-NtWee1-RV	aag ctg ggt cTT ACT TGT TAG CAT TTC TTT G
BP1	ggg gac aag ttt gta caa aaa agc agg ctt c
BP2	ggc gac cac ttt gta caa gaa agc tgg gtc

Capital letters indicate the gene-specific sequences of each primer. Small letters are part of the attB1 and attB2 recombination sites. Underlined and italic letters show the mutations introduced in the SCI1 sequence.

In vitro Pulldown

Recombinant proteins HIS-14-3-3D2, GST-SCI1, and GST alone were expressed in *E. coli* BL21(DE3) Rosetta cells after induction with 0.1 mM IPTG for 2 h. Total soluble proteins were extracted with PBS Buffer [140 mM KCl, 10 mM Na_2HPO_4, 1.8 mM KH_2PO_4, 1 mM PMSF, 50 µg/ml lysozyme, and 1% protease inhibitor cocktail for general use (Roche), pH 7.3], sonication, and centrifugation. Soluble proteins from the indicated extracts were mixed and incubated overnight at 4°C with equilibrated 100% Glutathione Sepharose 4 FastFlow bead slurry (GE Healthcare). Beads were washed three times with PBS supplemented with 1 mM PMSF. Bound proteins were eluted with 100 µl of 2x Laemmli Sample Buffer and boiled. The different fractions were resolved in 12% bis-acrylamide gel, immunoblotted with anti-GST (Sigma SAB4200055), or anti-HIS primary antibody (Sigma H1029), and visualized by enhanced chemiluminescence reaction (ECL) reaction.

Co-immunoprecipitation

Soluble proteins were obtained from *N. tabacum* $35S_{prom}$::SCI1-GFP stigmas/styles in extraction buffer (50 mM Tris-HCl pH7.5, 75 mM NaCl, 1% Triton X-100, 5% glycerol, 2 mM EDTA, 5 mM Na_3VO_4, 5 mM NaF e 20 mM β-glycerolphosphate, and cOmplete™, EDTA-free Protease Inhibitor Cocktail—Roche). The material was vortexed for 10 min on ice, submitted to sonication (six pulses of 30 s) at 30% Branson Sonifier™ (S-450 digital ultrasonic cell disruptor/homogenizer, Fisher Scientific), and centrifuged at 18,500 × *g* for 20 min, and the supernatant was collected. HIS-14-3-3D2 protein was expressed on *E. coli* BL21(DE3) Rosetta strain and extracted with sonication (five pulses of 30 s) in lysis buffer [Tris-HCl 50 mM pH 7.4, NaCl 75 mM, 1 mM Protease Inhibitor Cocktail for General Use (Sigma), and 50 µg/ml lysozyme]. Both soluble protein extracts were mixed and incubated with monoclonal anti-GFP antibody (Sigma G6539) at 4°C for 2 h, under gentle agitation. Then, Protein G Sepharose beads four-fast flow (GE Healthcare) was added, followed by incubation at 4°C for 2 h and centrifugation. The precipitated immunocomplexes were washed six times with extraction buffer, eluted from the beads by boiling in SDS-PAGE sample buffer, and resolved on 12.5% acrylamide gels. Immunoblots were carried out using anti-HIS primary antibody (Sigma H1029) or anti-HIS-SCI1-polyclonal antibody (produced in chicken by IgY Biotech—Brazil, against the recombinant HIS-SCI1 protein produced in *E. coli*).

Subcellular Localization and Bimolecular Fluorescence Complementation in *Nicotiana benthamiana* Leaves

The recombinant plasmids ($35S_{prom}$::SCI1-GFP and the nuclear markers AtFibrillarin-mRFP and AtCoilin-mRFP—Koroleva et al., 2009) were transformed into *A. tumefaciens* strain C58C1(pGV2260) and infiltrated on leaves of 5–6 weeks old *N. benthamiana* plants, as previously described (Bracha et al., 2002). Fluorescence detection was observed 24–72 h following infiltration. Cells were stained with DAPI (4′,6-diamidino-2-phenylindole) and examined under a Leica TCS SP5 confocal laser scanning microscope (Leica Microsystems—Germany). GFP excitation was done with an argon laser at 488 nm, and the spectral detector was set between 500 and 550 nm, while RFP excitation was done with a laser at 543 nm and a spectral detector set between 630 and 680 nm. The fluorescence of DAPI was obtained with excitation at 340–380 nm and captured at 425–450 nm. Image analysis was carried out with Leica LCS, ImageJ, and Illustrator CS6.

To verify interaction partners *in planta*, the coding sequences of SCI1, 14-3-3A1 and 14-3-3D2 were subcloned into pK7m34GW or pH7m34GW vectors with nGFP or cGFP fragments, under the control of 35S promoter (Karimi et al., 2007). These split-GFP Gateway-based vectors were infiltrated in *N. benthamiana* leaves and used for BiFC analysis, as Bracha-Drori et al. (2004) described.

Stable Transgenic BY-2 Cell Lines

Nicotiana tabacum BY-2 cells were cultivated and stably transformed, as described by Nagata et al. (1992) and Nocarova and Fischer (2009), with constructions $35S_{prom}$::SCI1-GFP and

$35S_{prom}$::SCI1mut3-GFP. Samples were stained with Hoechst 33342 (Sigma) or DAPI, analyzed, and photographed at confocal microscope Leica TCS SP5. Treatment with MG132 (50 μM in DMSO) was used to block the proteolytic activity of the 26S proteasome complex. The fluorescence intensity emitted by SCI1-GFP, SCI1mut3-GFP, and DAPI was quantified, and graphs were obtained using the ImageJ software histogram tool.

Accession Numbers

SCI1 (GQ272329), 14-3-3D2AS (AB119473), 14-3-3A1 (AB119466), 14-3-3G1 (AB119477), 14-3-3H1 (AB119478), SKP1 (JN793550), CSN6a (XM002267120), BTB/POZ (XP016450235), and Wee1 (AM408785).

RESULTS

SCI1 Interacts With 14-3-3D From the Non-Epsilon Group

To study the molecular mechanisms underlying the control of cell proliferation by SCI1, we constructed a tobacco stigma/style cDNA library through the Y2H system and screened it for SCI1-interacting proteins. The entire SCI1 coding sequence was used as bait (BD-SCI1), and approximately 1×10^6 virtual transformants were screened. Among the yeast colonies able to grow on the selective medium lacking histidine (His), we identified two clones encoding 14-3-3D2 and one encoding the 14-3-3A1 protein, both from the Non-Epsilon group (**Supplementary Figure S3**). Consistently, three putative 14-3-3 mode I (RSX-pS/pT-XP) binding motifs were found by MotifScan software (Pagni et al., 2004) on the SCI1 amino acid sequence (**Supplementary Figure S2**). After verification by Y2H binary assay, the interaction between SCI1 and 14-3-3D2 was confirmed, but not between SCI1 and 14-3-3A1 (**Figure 1A**). For simplicity, from this point on, these sequences will be referred to as 14-3-3A and 14-3-3D.

The interaction between SCI1 and 14-3-3D was further verified by an *in vitro* pulldown assay (**Figure 1B**). The binding of HIS-14-3-3D to glutathione beads in the presence of GST-SCI1, but not of GST alone, showed the specific interaction of 14-3-3D with SCI1 (**Figure 1B**—bottom panel). We also assayed the interaction of SCI1 and 14-3-3D by immunoprecipitation of stigma/style proteins from a transgenic tobacco plant expressing $35S_{prom}$::SCI1-GFP mixed with an extract of *E. coli* expressing HIS-14-3-3D. A band corresponding to the expected size of HIS-14-3-3D (33.6 kDa) was detected, confirming its interaction with SCI1 (**Figure 1C**). Of note, two bands were revealed with the anti-SCI1 antibody, consistent with SCI1 protein being modified, possibly phosphorylated by the stigma/style proteins as proposed previously (DePaoli et al., 2011). Altogether, these results confirm the interaction between SCI1 and 14-3-3D.

14-3-3A and 14-3-3D Form Homo- and Heterodimers in the Cytoplasm of Cells in Interphase

Expression analysis shows that both 14-3-3A and 14-3-3D (**Supplementary Figure S4**) are well expressed in different tobacco organs (roots, stems, young leaves, mature leaves, young flowers, young stigmas/styles, mature flowers, and dry capsules). Meanwhile, some other 14-3-3 isoforms (14-3-3E and 14-3-3F) have low expression levels (**Supplementary Figure S4**). It is worth mentioning that 14-3-3A and 14-3-3D are not the 14-3-3 proteins with the highest expression levels in stigmas/styles (**Supplementary Figure S5**), the organs used to construct the Y2H cDNA library.

Although 14-3-3A interaction with SCI1 was not confirmed, we chose to investigate whether 14-3-3A and 14-3-3D can form homo and/or heterodimers, taking 14-3-3A as a representative member of the distant and larger subclade within the 14-3-3 family (**Supplementary Figure S3**). Therefore, we performed Y2H and BiFC assay with split GFP. For the Y2H, yeast cells were co-transformed with combinations of the four constructions (AD-14-3-3A; BD-14-3-3A; AD-14-3-3D; and BD-14-3-3D) and assayed for their ability to grow on the selective medium lacking histidine. The Y2H results have demonstrated the formation of homodimers of 14-3-3A, homodimers of 14-3-3D, and the heterodimers of 14-3-3A and 14-3-3D (**Figure 2A**).

Transient expression of 14-3-3A-GFP in *N. benthamiana* leaves demonstrated its localization in both nucleus and cytoplasm (**Figures 2Ba,c**), while 14-3-3D-GFP is cytoplasm restricted (**Figures 2Bb,d**). BiFC assays confirmed the *in planta* formation of homo- and heterodimers and established their subcellular localization. 14-3-3A homodimers were detected in both the nucleus and cytoplasm (**Figures 2Ca–d**), whereas 14-3-3D homodimers (**Figures 2Ce–h**) and the 14-3-3D/14-3-3A heterodimers (**Figures 2Ci–l**) were found only in the cytoplasm.

SCI1 Interacts With the 14-3-3D Protein in the Nucleus in Early Mitosis

Transient expression of SCI1-GFP in *N. benthamiana* leaves shows it is localized in the nucleus (DePaoli et al., 2011, 2014), while 14-3-3D was found only in the cytoplasm (above), and yet we have demonstrated their interaction (**Figure 1**). We ruled out possible mislocalization of SCI1-GFP due to lack/need of tissue-specific factors in leaves by confirming that SCI1-GFP has the same subcellular localization in both stigma/style cells of *SCI1prom::SCI1-GFP* transgenic plants (Cruz et al., 2021) and cells of transiently transformed leaves of *N. tabacum* and *N. benthamiana*. Furthermore, SCI1-GFP co-localizes with fibrillarin-RFP (nucleoli marker) and not with coilin-RFP (Cajal bodies marker), demonstrating that it is contained in the nucleolus (**Figure 3A**).

Our previous approaches evaluated the interaction between SCI1 and 14-3-3D by either heterologous or cell disruptive methods; then, we performed subsequent interaction analysis in intact plant cells. BiFC assays, performed in *N. benthamiana* leaves, revealed that SCI1 and 14-3-3D interact in the nucleus (**Figure 3B**), more specifically, in areas interspersed with early-condensing chromatin (**Figures 3Ba–i**), which occurs at the transition G2/prophase as evaluated by the DAPI staining (Li et al., 2005; San Martin et al., unpublished results).

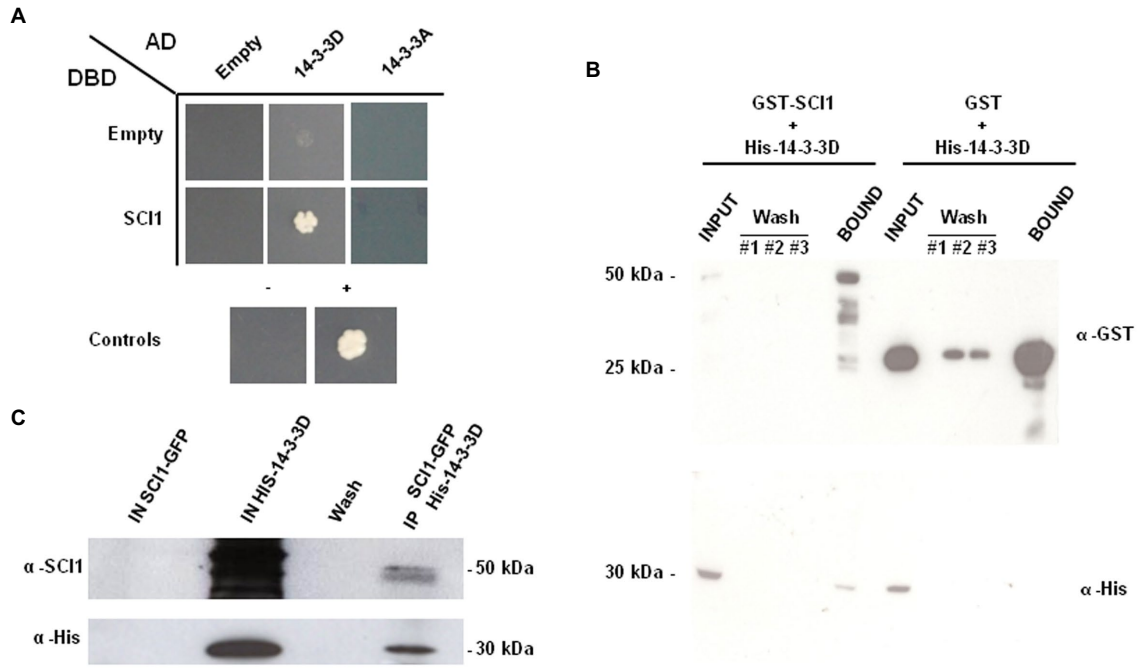

FIGURE 1 | (A) Yeast two-hybrid (Y2H) binary assays of the interaction of BD-SCI1 with AD-14-3-3D and AD-14-3-3A proteins. Yeast PJ69-4a cells with empty vectors are unable to grow on a selective medium without histidine. The self-activation of BD-SCI1, AD-14-3-3D, and AD-14-3-3A were negative. Cells could only grow when BD-SCI1 and AD-14-3-3D proteins were present, showing HIS3 reporter gene expression and confirming the interaction between these proteins. **(B)** *In vitro* pulldown with recombinant GST-SCI1, GST, and HIS-14-3-3D produced in *Escherichia coli*. **(C)** Co-immunoprecipitation of HIS-14-3-3D protein using an extract of stigmas/styles from *Nicotiana tabacum* $35S_{prom}$::SCI1-GFP plants. The smear observed at the input HIS-14-3-3D lane is due to background recognition of *E. coli* proteins by the anti-HIS-SCI1 polyclonal antibody.

SCI1 Is Degraded by the 26S Proteasome During Cell Division

To explore SCI1 protein behavior during cell-cycle progression, *N. tabacum* BY-2 cells were stably transformed to express *35S*$_{prom}$*::SCI1-GFP*. During interphase and prophase, the chimeric protein was clearly observed in nucleoli (**Figures 4A–F**). However, at metaphase, SCI1-GFP was hardly visible (**Figures 4G–I**), and it was no longer detected at anaphase (**Figures 4J–L**; see also **Supplementary Figure S6**). At the end of mitosis (telophase), SCI1-GFP became visible again into the reassembling nascent nucleoli (**Figures 4M–O**). To test the hypothesis that SCI1 is degraded at early mitosis by the 26S proteasome pathway, an important mechanism to regulate cell-cycle phase transitions (Genschik et al., 2014), we treated the tobacco BY-2 cells stably expressing SCI1-GFP with the 26S proteasome inhibitor MG132. This treatment significantly minimized SCI1 degradation during cell division, which is detected spread on the cell after nuclear envelope breakdown (**Figure 5**). Notably, under MG132 treatment, SCI1 protein also accumulated in several specific positions of the condensed metaphase chromosomes. A detailed analysis was performed in different MG132 treated cells, revealing that the number and position of the SCI1-spots on the chromosomes (**Supplementary Figure S7**) are consistent with SCI1 being associated with the tobacco nucleolar organizer regions—NOR (Parokonny and Kenton, 1995).

Altogether, these data indicate that SCI1 interacts with 14-3-3D in the nucleus, is ultimately degraded at a specific time during cell division (late prophase/metaphase), preceding the separation of chromosomes, and reappears at telophase. Thus, SCI1 stability is dependent on the cell-cycle phase, showing similar behavior to other cell-cycle regulators (Genschik et al., 2014; Koepp, 2014), further supporting our claim of SCI1 as a molecular regulator of cell proliferation.

SCI1 Degradation by the 26S Proteasome Is Dependent on Serine Residues

To further investigate SCI1 stability and cellular behavior, we mutated seven conserved serine residues of SCI1 (S17, 18, 20, 21, 54, 56, and 57) to alanine (SCI1mut3), which lay within the predicted 14-3-3 binding sites in the N-terminal region (as shown in **Supplementary Figure S2**). Then, SCI1mut3 was fused to GFP, and the chimeric gene construction was introduced into BY-2 cells. Stably transformed BY-2 cells demonstrated that, at interphase, SCI1mut3-GFP and SCI1-GFP have the same localization, in the nucleoli. On the other hand, at cell division, while SCI1-GFP is degraded before metaphase and still undetected in anaphase, SCI1mut3-GFP is stable at these different phases (**Figure 6**; note fluorescence quantification and comparison for SCI1-GFP and SCI1mut3-GFP). Notably, SCI1mut3-GFP is associated with chromosomes at metaphase (**Figure 6** and **Supplementary Figures S8**, **S9**). Therefore, SCI1 proteasomal degradation during mitosis may rely on the (phospho)-serine residues present at the putative 14-3-3 binding sites. Additionally, we identified different proteins related to the ubiquitin-proteasome

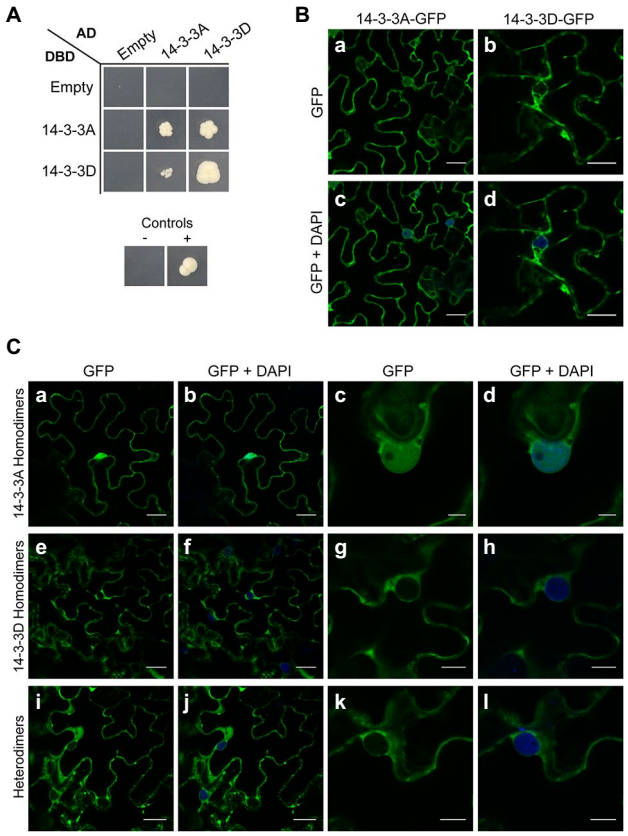

FIGURE 2 | Dimerization and subcellular localization of 14-3-3A and 14-3-3D. **(A)** Y2H assay testing the dimerization of 14-3-3A and 14-3-3D proteins. Selective medium: SC-Leu-Trp-His +1 mM 3AT. C−: Negative interaction control; C+: positive interaction control. AD—Activation domain; DBD—DNA binding domain. **(B)** Subcellular localization of 14-3-3A-GFP and 14-3-3D-GFP. **(Ba)** Cytosolic and nuclear localization of 14-3-3A-GFP, bar 20 μm. **(Bc)** Merged image of 14-3-3A-GFP localization and nuclear DAPI staining, bar 20 μm. **(Bb)** Cytosolic localization of 14-3-3D-GFP, bar 15 μm. **(Bd)** Merged image of 14-3-3D-GFP localization and nuclear DAPI staining, bar 15 μm. **(C)** Bimolecular Fluorescence Complementation (BiFC) assay showing the dimerization of 14-3-3A and 14-3-3D. **(Ca,D)** 14-3-3A-nGFP × 14-3-3A-cGFP, showing 14-3-3A homodimers formation in cytosol and nucleus, bars 20 and 5 μm. **(Cb,D)** Merged images of 14-3-3A homodimers and DAPI staining, bars 20 and 5 μm. **(Ce,G)** 14-3-3D-nGFP × 14-3-3D-cGFP, showing 14-3-3D homodimers formation in cytosol, bars 20 and 10 μm. **(Cf,H)** Merged images of 14-3-3D homodimers and DAPI staining, bars 20 and 10 μm. **(Ci,K)** 14-3-3A-nGFP × 14-3-3D-cGFP, showing heterodimers formation in cytosol, bars 40 and 10 μm. **(Cj,L)** Merged images of heterodimers and DAPI staining. Subcellular localization and BiFC experiments were performed as transient expressions in *N. benthamiana* leaves.

pathway using 14-3-3D as a bait on a new Y2H screening: CSN6A, a subunit of the COP9 signalosome (homologous to At5g56280); a BTB/POZ domain-containing protein (homolog of At1g03010); and SKP1, a core component of the SCF family of E3 ubiquitin ligases (homologous to At1g75950). Furthermore, 14-3-3D, 14-3-3G, and 14-3-3H were found in the screening as interaction partners of 14-3-3D, which was confirmed by a binary Y2H assay (**Supplementary Figure S10**). The interaction of 14-3-3D with components mediating proteasomal-dependent degradation supports the role of 14-3-3D as a docking degron for SCI1 in mitosis.

DISCUSSION

SCI1 Interacts With a Specific 14-3-3 Protein

The Y2H screening used to search for SCI1-interacting proteins has identified only 14-3-3A and 14-3-3D and no other 14-3-3 protein. As Y2H screenings are hardly exhaustive, we cannot ruled out the possibility that SCI1 interacts with other 14-3-3 proteins expressed in stigmas/styles (**Supplementary Figure S5**). On the other hand, 14-3-3C1 has the highest expression in these organs and should be well represented among the clones available at the Y2H library. Nonetheless, no clone encoding 14-3-3C1 was found in the screening, suggesting specificity in the interaction of SCI1 with members of the 14-3-3 family.

We could not confirm the interaction between SCI1 and 14-3-3A in the Y2H binary assay (**Figure 1A**). If 14-3-3A interacts with SCI1, it may depend on additional factors or protein modifications that rarely occur in yeast or are challenging to be detected. The screening of the stigma/style Y2H cDNA library using 14-3-3D as bait has identified only 14-3-3D, 14-3-3G, and 14-3-3H as its partners within the 14-3-3 family, despite the expression of other 14-3-3s (**Supplementary Figure S5**). Although 14-3-3D may form a heterodimer with 14-3-3G and 14-3-3H (**Supplementary Figure S10**), it is unlikely that these other 14-3-3 proteins directly interact with SCI1 as homodimers, since they were not recovered during the screening using SCI1 as bait. Conversely, heterodimers of 14-3-3D may be important for SCI1 regulation and were not thoroughly investigated here. Nevertheless, it seems that a functional specialization may exist among the 14-3-3 proteins, in which not all heterodimers are formed or are functionally interchangeable, as already observed in other plant systems (Paul et al., 2012; Pallucca et al., 2014). Future experiments may shed some light on the patterns of dimerization that actually occur *in vivo* to regulate SCI1.

14-3-3A and 14-3-3H belong to the same phylogenetic subgroup, while 14-3-3D and 14-3-3G are placed together in another subgroup within the Non-Epsilon group (**Supplementary Figure S3**). The interactions of 14-3-3D found in our Y2H screening were restricted to these two phylogenetic branches. Similarly, the 14-3-3s from other branches were not identified as SCI1 interactors in this study. Such a 14-3-3 interaction specificity is not always the case in plants. For example, several Arabidopsis 14-3-3 proteins (14-3-3 Lambda, Kappa, Epsilon, Phi, and Omega) interact with the transcription factors BZR1 (BRASSINAZOLE-RESISTANT 1) and BES1 (BRI1-EMS-SUPPRESSOR 1) from the brassinosteroid signaling pathway (de Boer et al., 2012).

SCI1 Proteasomal Degradation Occurs in Early Mitosis and Is Possibly Mediated by 14-3-3D

Stigma/style cell-cycle inhibitor 1 mutated in seven serines (SCI1mut3; **Supplementary Figure S2**) is not degraded during mitosis, as it occurs for the non-mutated SCI1 protein (**Figure 6**; **Supplementary Figures S8**, **S9**). Interestingly, SCI1mut3-GFP is associated with the condensed chromatin and with microtubules during cell division (metaphase and anaphase), localizations

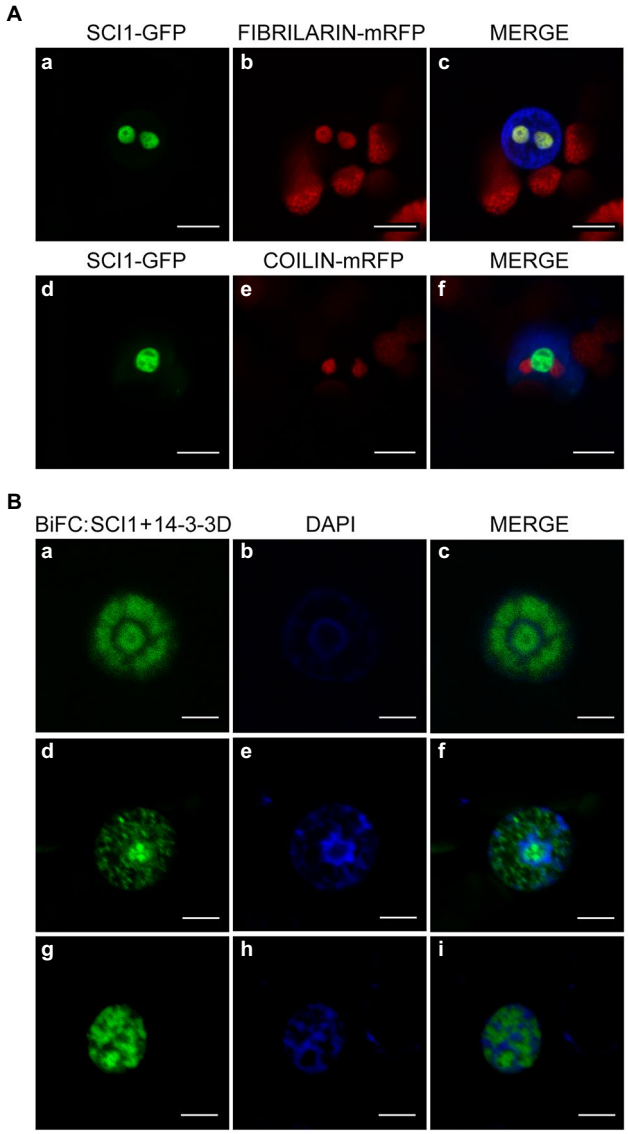

FIGURE 3 | (A) Co-localization of SCI1-GFP with the nuclear markers AtFibrillarin-mRFP for nucleoli and AtCoilin-mRFP for Cajal bodies (Koroleva et al., 2009), in transiently transformed *N. benthamiana* leaf cells. The red color organelles observed outside of the nucleus correspond to chloroplasts (auto-fluorescence). **(B)** BiFC assays indicating that SCI1 interacts *in vivo* with 14-3-3D protein in the nucleus of epidermal cells of *N. benthamiana* leaves. This interaction was observed only in cells at G2/prophase (early mitosis). Three different cells are shown in each line **(Ba,d,g)**. Blue indicates DAPI stained DNA. Green indicates the interaction of SCI1-nGFP and 14-3-3D-cGFP **(a–i)**. nGFP, N-terminal fragment of GFP (amino-acid residues 1–149); cGFP, C-terminal GFP fragment (amino-acid residues 150–238). Scale bars—5 μm.

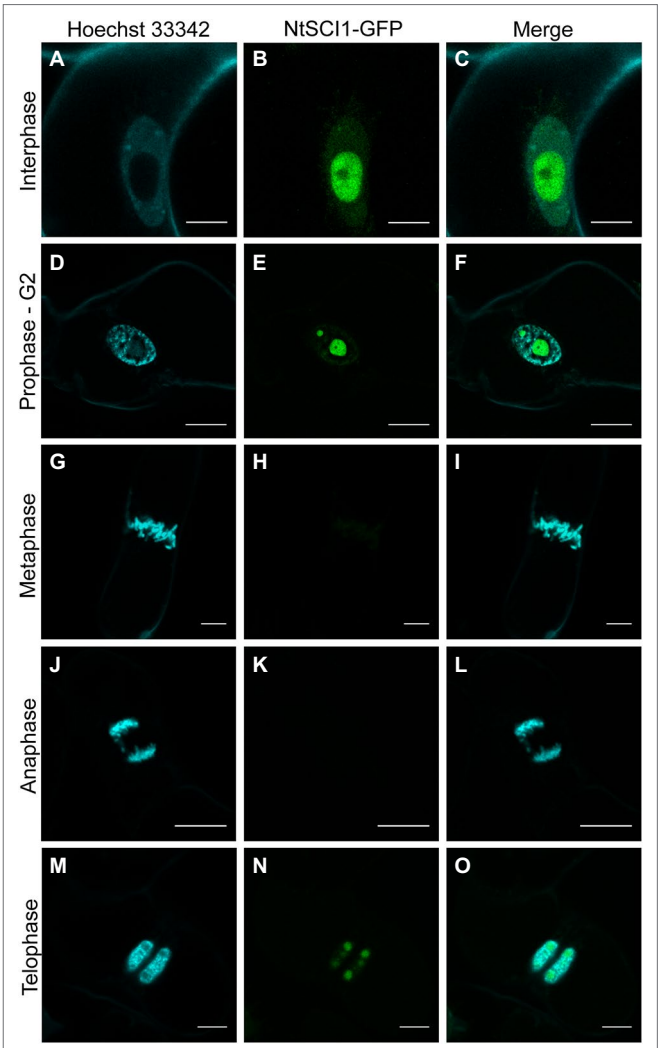

FIGURE 4 | Stigma/Style Cell-Cycle Inhibitor 1 (SCI1) dynamics throughout cell-cycle progression. Confocal microscopy images showing SCI1-GFP subcellular localization in each cell-cycle phase. Tobacco BY-2 cells stably transformed with $35S_{prom}$::SCI1-GFP were stained with Hoechst 33342. Images were captured using Leica TCS SP5 (Leica Microsystems). Scale bars—10 μm **(A–C)** and 20 μm **(D–O)**.

never observed for the non-mutated version. At these cell division stages, SCI1mut3-GFP is spread all over the entire length of the chromosomes (**Figure 6; Supplementary Figures S8**, **S9**). On the other hand, SCI1-GFP in cells treated with MG132 concentrates on chromosomes' specific spots (**Figure 5; Supplementary Figure S7**), besides being dispersed throughout the cell. The different behaviors observed may be explained by the fact that proteasome inhibition by MG132 does not affect SCI1 only, but many other proteins that should be degraded during cell division.

Previous studies in other systems have demonstrated the importance of 14-3-3 proteins as signaling integrators for cell-cycle control (Peng et al., 1997; Laronga et al., 2000; van Hemert et al., 2001; Gardino and Yaffe, 2011). In plants, some of the Arabidopsis Non-Epsilon 14-3-3 proteins can bind to the CDC25 phosphatase, as well as to rescue cell-cycle defects in fission yeast mutants (Sorrell et al., 2003) and to contribute to the robustness of the DNA damage and spindle checkpoints in budding yeast (Usui and Petrini, 2007; Grandin and Charbonneau, 2008; Engels et al., 2011; Caydasi et al., 2014; Bokros et al., 2016; Gryaznova et al., 2016; Chappidi et al., 2019). Additionally,

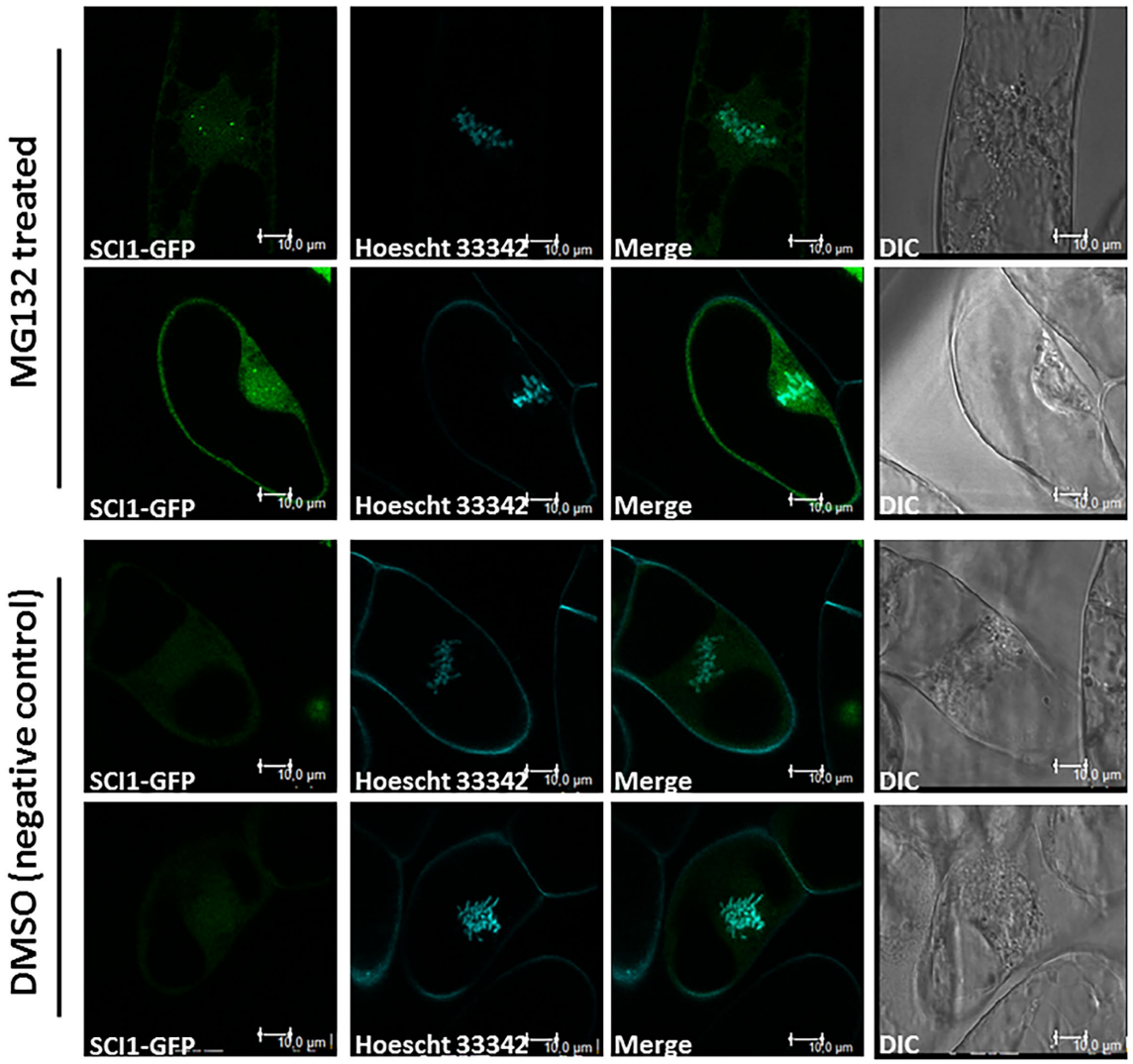

FIGURE 5 | Stigma/Style Cell-Cycle Inhibitor 1 is stabilized upon treatment with MG132, an inhibitor of 26S proteasome. Confocal microscopy images showing SCI1-GFP in metaphase cells after treatment with MG132 (50 µM in DMSO) and control (DMSO). Tobacco BY-2 cells stably transformed with $35S_{prom}$::SCI1-GFP were stained with Hoechst 33342. Images were captured using Leica TCS SP5 (Leica Microsystems). DIC—Differential interference contrast microscopy. Scale bars—10 µm.

Non-Epsilon Arabidopsis 14-3-3 proteins were shown to interact with Wee1, a kinase that inhibits the cell-cycle in the nucleus of interphase cells (Grønlund et al., 2009 and references therein). Wee1 degradation has been observed in yeast and animals occurring in G2/M and is important for mitotic progression (Owens et al., 2010). Indeed, 14-3-3 proteins have been shown to interact with Wee1 in yeast and animals (Honda et al., 1997; Wang et al., 2000) and regulate its stability and kinase activity in G2/M (Wang et al., 2000). Interestingly, 14-3-3D, but not 14-3-3A, can interact with the tobacco Wee1 (**Supplementary Figure S11**), supporting a role for 14-3-3D in the cell division signaling pathway.

It is known that 14-3-3 proteins may act as adaptors or "chaperone molecules" that can move freely from cytoplasm to the nucleus and *vice-versa* (Mhawech, 2005). During interphase, 14-3-3D is cytoplasm localized (**Figure 2**) and moves to the nucleus in early mitosis, where and when it interacts with SCI1 (**Figure 3**). It is possible that the nuclear shuttling of 14-3-3D is influenced by PTMs in its own amino acid sequence. PTMs, such as phosphorylation, have already been identified in 14-3-3 proteins (Wilson et al., 2016). Therefore, we suggest that cell division signaling promotes 14-3-3D PTM(s) in the cytoplasm and, consequently, modifies its subcellular localization. Alternatively, cell division signaling could promote PTM(s) of other protein(s), which would then interact with 14-3-3D in the cytoplasm and translocate it to the nucleus, as already described to some Arabidopsis 14-3-3 proteins (Paul et al., 2005). In the nucleus, the interaction between SCI1 and 14-3-3D could be facilitated by PTM(s) on SCI1 (**Figure 7**), most likely by phosphorylation. The presence of SCI1 differentially migrating bands in the 1D western blot of the co-immunoprecipitation

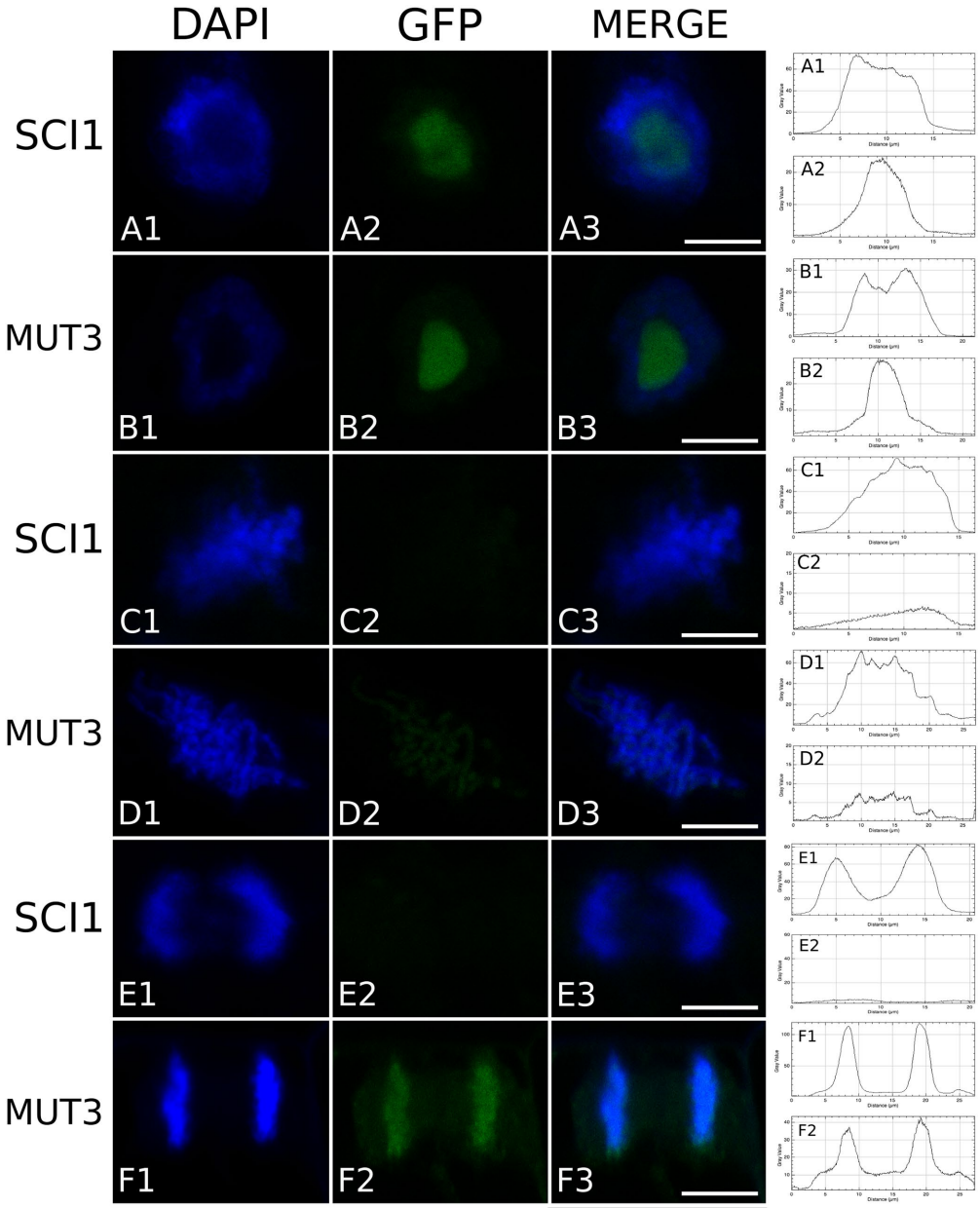

FIGURE 6 | A mutated version of SCI1 lacking seven serine residues is not degraded during cell division. Confocal microscopy images showing SCI1-GFP and SCI1mut3-GFP in different cell-cycle phases: interphase, metaphase, and anaphase. Tobacco BY-2 cells stably transformed with $35S_{prom}$::SCI1-GFP and $35S_{prom}$::SCI1mut3-GFP were stained with DAPI. Images were captured using Leica TCS SP5 (Leica Microsystems). Identical settings were used to compare fluorescence intensity, which was quantified and is shown on the graphics at right (two graphics for each line of cells). The first graphic (above) refers to the DAPI image's fluorescence, while the second graphic (below) represents the GFP fluorescence. Scale bars 7.5 μm.

with 14-3-3D (**Figure 1C**) and three spots (with higher molecular weights and lower isoelectric points than the unmodified protein) in a 2D western blot (**Supplementary Figure S12**) strengthens the idea that PTMs may be relevant for SCI1 function and/or degradation.

Using a mutagenesis strategy, through which serines of the predicted 14-3-3 binding sites of SCI1 were mutated into alanines to prevent phosphorylation, we have shown that these serines have a role in the SCI1 cell-cycle-regulated degradation. Interestingly, five out of the seven mutated serines are conserved in the Arabidopsis SCI1 sequence (**Supplementary Figure S2B**). Phosphorylation-mediated signaling and the role of 14-3-3 proteins in the nucleocytoplasmic shuttling have already been demonstrated in some processes in plants, such as in the gibberellin signaling pathway (Igarashi et al., 2001) and on the shade response of PIF7 (PHYTOCHROME-INTERACTING FACTOR 7; Huang et al., 2018). 14-3-3 proteins have also been demonstrated to promote client protein degradation. For

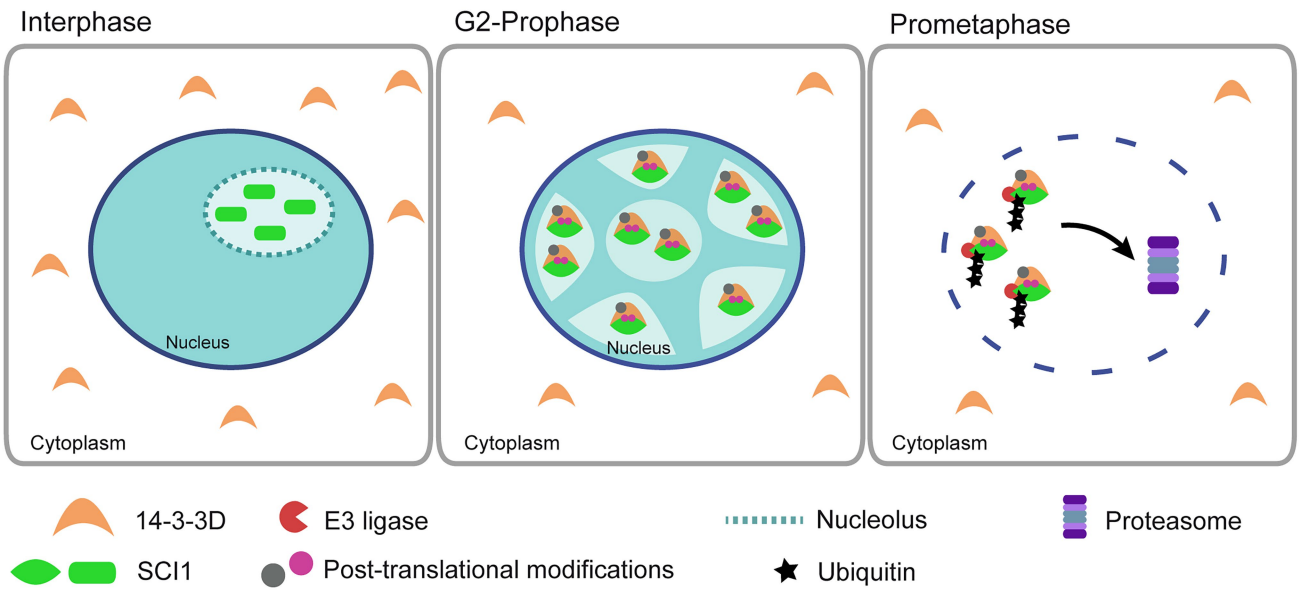

FIGURE 7 | A proposed model illustrates the interaction of SCI1 and 14-3-3D during early mitosis. During interphase (DAPI staining, in blue, is well spread in the nucleus), SCI1 is in the nucleolus, and 14-3-3D is in the cytoplasm. Signals to start cell division promote the movement of 14-3-3D to the nucleus. In parallel, cell division signals cause SCI1 post-translational modifications (possibly phosphorylation by a still unknown kinase). At G2/prophase, chromatin is starting its condensation (shown in blue), and SCI1 and 14-3-3D interact at the nucleoplasm. At prometaphase, 14-3-3D mediates SCI1 26S proteasome degradation, which allows cell division to progress.

example, 14-3-3 downregulates the stability of the ETO1/EOL E3 ligase components of the ethylene signaling pathway in Arabidopsis (Yoon and Kieber, 2013). 14-3-3 proteins are also responsible for exporting phosphorylated BRZ1 and BES1 from the nucleus to the cytoplasm for proteasomal degradation (de Boer et al., 2012). Additionally, 14-3-3 proteins shuttle from the cytosol to the nucleus, where they interact with and destabilize the key cold-responsive C-repeat-binding factor (CBF) proteins (Liu et al., 2017), a mechanism similar to what we are proposing for SCI1 and 14-3-3D.

We have shown that 14-3-3D interacts with SKP1, a core component of the SCF family of E3 ubiquitin ligases (see **Supplementary Figure S10**). Remarkably, At14-3-3-Phi (GRF4) and At14-3-3-Upsilon (GRF5) proteins, that belong to the same Non-Epsilon group of 14-3-3D (**Supplementary Figure S3**), can rescue the lethality of budding yeast cells that lack the Bmh1 and Bmh2 14-3-3 proteins (van Heusden et al., 1996). Of note, Bmh1 and Bmh2 physically interact with Skp1 that, together with the SCF ubiquitin ligase complex, promotes ubiquitination and degradation of the cell-cycle inhibitor of yeast cell proliferation called Sic1 (Barberis, 2012), *in vitro* and *in vivo* (Feldman et al., 1997; Verma et al., 1997).

Evidence from budding yeast indicates that the Bmh1 and Bmh2 14-3-3 proteins are involved in regulating the spindle checkpoint (Grandin and Charbonneau, 2008; Bokros et al., 2016; Gryaznova et al., 2016). Intriguingly, the cell-cycle inhibitor Sic1 inhibits spindle pole separation (Chee and Haase, 2010) through binding and inhibiting the mitotic cyclin/Cdk1 kinases that regulate a timely cell division in budding yeast (Barberis et al., 2012; Schreiber et al., 2012). We can speculate that SCI1 may be involved in similar events by regulating mitosis in floral meristematic cells. In this hypothesis, SCI1 could interact with a protein(s) necessary for spindle-related events, inhibiting its function. Phosphorylation of SCI1 serines would release this protein, allowing its association with chromosomes and cell division to progress. However, the unphosphorylated SCI1 would remain bound to this protein and, therefore, be driven to its target site of action during cell division, explaining SCI1mut3 association with chromosomes at metaphase (**Figure 6** and **Supplementary Figures S8**, **S9**).

CONCLUSION AND FINAL REMARKS

The nucleoli have demonstrated roles in regulating mitosis, cell-cycle progression, and cell proliferation (Boisvert et al., 2007; Shaw and Brown, 2012). The physical containment of SCI1 in the nucleoli during interphase (**Figure 3A**) suggests that it may sequester and regulate the availability of cell-cycle effectors, which are necessary for cell division to progress. A similar role has been shown for Sic1, an inhibitor of the Cdk1/Clb cyclin that controls cell-cycle progression in budding yeast (Barberis, 2012; Barberis et al., 2012).

Two molecular mechanisms known to coordinate cell proliferation are phosphorylation and ubiquitin/proteasome-mediated protein degradation. Regulatory modules have evolved to integrate these two control systems at crucial decision points in the cell division cycle to manage plant development (Holt, 2012). Based on our results, we conclude that SCI1 stability is cell-cycle regulated. Its proteasomal degradation before

metaphase depends on the serine residues at the predicted 14-3-3 binding sites. Therefore, we propose a model (**Figure 7**) in which cell division signals promote 14-3-3D translocation from the cytoplasm to the nucleus through a yet unknown mechanism. In the nucleus, 14-3-3D interacts with SCI1 and mediates its proteasomal degradation at early mitosis. SCI1, as an inhibitor of cell proliferation, would be degraded for cell division to progress appropriately. Further experiments will be required to test our proposed model.

Stigma/style cell-cycle inhibitor 1 is a regulator of cell division specifically expressed in the proliferative cells of the floral meristem (Cruz et al., 2021). So why would floral meristems have additional regulators of cell division? The development of plant organs is largely post-embryonic. However, it has already been shown that plants minimize the number of divisions of the meristematic cells that give rise to flowers and seeds to avoid passing on new mutations to their offspring (Burian et al., 2016; Watson et al., 2016). Thus, it is reasonable to assume that *SCI1* is expressed in floral meristem to allow the precise regulation (fine-tuning) of proliferation rates of the flower meristematic cells. This additional control mechanism would ensure DNA integrity passed on to the descendants, including an extra level of checking to those already existing in the other plant cells.

DATA AVAILABILITY STATEMENT

The datasets presented in this study can be found in online repositories. The names of the repository/repositories and accession number(s) can be found in the article/ **Supplementary Material**.

AUTHOR CONTRIBUTIONS

ES, LB, JS, HS, FP, VP, PF, GL, and AQ conducted the research and participated in the drafting of the manuscript. Data were analyzed with the assistance of HP, L-ED-B, MM, and AA, which also revised the manuscript critically providing important intellectual contributions. NE, MB, and MG conceived the research, designed the experiments, analyzed the data, and drafted the manuscript. All authors contributed to the article and approved the submitted version.

FUNDING

This work was supported by grants 2012/50562-2, 2016/20486-3, and 2019/24774-1, São Paulo Research Foundation (FAPESP)—Brazil to MG and by the Systems Biology Grant of the University of Surrey to MB. The authors are also grateful to the Brazilian agencies that financed their fellowships: CNPq to LB (130159/2012-3), JS (435447/2016-5), and VP (141909/2016-1); HS—FAPESP (2011/51844-9), and CAPES to ES, PF, and GL. Therefore, this study was financed in part by the Coordenação de Aperfeiçoamento de Pessoal de Nível Superior—Brazil (CAPES)—Finance Code 001. MG is indebted to CNPq—Brazil for her Research fellowship. MM is the PET-Ministry of Education-Brazil fellowship.

ACKNOWLEDGMENTS

The authors are grateful to Elizabete Rosa Milani and Roberta Ribeiro Costa (FMRP/USP, Brazil) for their support and advice during the confocal microscopy work; to Matheus E. Bianconi (University of Sheffield, Department of Animal and Plant Sciences—the United Kingdom) for advice with the phylogenetic analysis; to VIB-UGent (Belgium) for the plant expression vectors of the Gateway system; and to Peter Shaw and Ali Pendle (John Innes Centre, Norwich, United Kingdom) for providing the nuclear markers AtFibrillarin-mRFP and AtCoilin-mRFP. We also thank David Smyth (Monash University—Australia) for fruitful discussions.

SUPPLEMENTARY MATERIAL

The Supplementary Material for this article can be found online at: https://www.frontiersin.org/articles/10.3389/fpls.2022.857745/full#supplementary-material

REFERENCES

Aducci, P., Camoni, L., Marra, M., and Visconti, S. (2002). From cytosol to organelles: 14-3-3 proteins as multifunctional regulators of plant cell. *IUBMB Life* 53, 49–55. doi: 10.1080/15216540210813

Barberis, M. (2012). Sic1 as a timer of Clb cyclin waves in the yeast cell-cycle design principle of not just an inhibitor. *FEBS J.* 279, 3386–3410. doi: 10.1111/j.1742-4658.2012.08542.x

Barberis, M., Linke, C., Adrover, M. À., González-Novo, A., Lehrach, H., Krobitsch, S., et al. (2012). Sic1 plays a role in timing and oscillatory behaviour of B-type cyclins. *Biotechnol. Adv.* 30, 108–130. doi: 10.1016/j.biotechadv.2011.09.004

Boisvert, F. M., van Koningsbruggen, S., Navascués, J., and Lamond, A. I. (2007). The multifunctional nucleolus. *Nat. Rev. Mol. Cell Biol.* 8, 574–585. doi: 10.1038/nrm2184

Bokros, M., Gravenmier, C., Jin, F., Richmond, D., and Wang, Y. (2016). Fin1-PP1 helps clear spindle assembly checkpoint protein Bub1 from kinetochores in anaphase. *Cell Rep.* 14, 1074–1085. doi: 10.1016/j.celrep.2016.01.007

Bracha, K., Lavy, M., and Yalovsky, S. (2002). The Arabidopsis AtSTE24 is a CAAX protease with broad substrate specificity. *J. Biol. Chem.* 277, 29856–29864. doi: 10.1074/jbc.M202916200

Bracha-Drori, K., Shichrur, K., Katz, A., Oliva, M., Angelovici, R., Yalovsky, S., et al. (2004). Detection of protein–protein interactions in plants using bimolecular fluorescence complementation. *Plant J.* 40, 419–427. doi: 10.1111/j.1365-313X.2004.02206.x

Burian, A., Reuille, P. B., and Kuhlemeier, C. (2016). Patterns of stem cell divisions contribute to plant longevity. *Curr. Biol.* 26, 1385–1394. doi: 10.1016/j.cub.2016.03.067

Camoni, L., Visconti, S., Aducci, P., and Marra, M. (2018). 14-3-3 proteins in plant hormone signaling: doing several things at once. *Front. Plant Sci.* 9:297. doi: 10.3389/fpls.2018.00297

Cao, H., Xu, Y., Yuan, L., Bian, Y., Wang, L., Zhen, S., et al. (2016). Molecular characterization of the 14-3-3 gene family in *Brachypodium distachyon* L.

reveals high evolutionary conservation and diverse responses to abiotic stresses. *Front. Plant Sci.* 7:1099. doi: 10.3389/fpls.2016.01099

Caydasi, A. K., Micoogullari, Y., Kurtulmus, B., Palani, S., and Pereira, G. (2014). The 14-3-3 protein Bmh1 functions in the spindle position checkpoint by breaking Bfa1 asymmetry at yeast centrosomes. *Mol. Biol. Cell* 25, 2143–2151. doi: 10.1091/mbc.E14-04-0890

Chappidi, N., De Gregorio, G., and Ferrari, S. (2019). Replication stress-induced Exo1 phosphorylation is mediated by Rad53/Pph3 and Exo1 nuclear localization is controlled by 14-3-3 proteins. *Cell Div* 14:1. doi: 10.1186/s13008-018-0044-2

Chaudhri, M., Scarabel, M., and Aitken, A. (2003). Mammalian and yeast 14-3-3 isoforms form distinct patterns of dimers in vivo. *Biochem. Biophys. Res. Commun.* 300, 679–685. doi: 10.1016/S0006-291X(02)02902-9

Chee, M. K., and Haase, S. B. (2010). B-cyclin/CDKs regulate mitotic spindle assembly by phosphorylating kinesins-5 in budding yeast. *PLoS Genet.* 6:e1000935. doi: 10.1371/journal.pgen.1000935

Chen, Y. S., Ho, T. D., Liu, L., Lee, D. H., Lee, C. H., Chen, Y. R., et al. (2019). Sugar starvation-regulated MYBS2 and 14-3-3 protein interactions enhance plant growth, stress tolerance, and grain weight in rice. *Proc. Natl. Acad. Sci. U. S. A.* 116, 21925–21935. doi: 10.1073/pnas.1904818116

Chevalier, D., Morris, E. R., and Walker, J. C. (2009). 14-3-3 and FHA domains mediate phosphoprotein interactions. *Annu. Rev. Plant Biol.* 60, 67–91. doi: 10.1146/annurev.arplant.59.032607.092844

Collani, S., Neumann, M., Yant, L., and Schmid, M. (2019). FT modulates genome-wide DNA-binding of the bZIP transcription factor FD. *Plant Physiol.* 180, 367–380. doi: 10.1104/pp.18.01505

Cruz, J. O., San Martin, J. A. B., Lubini, G., Strini, E. J., Sobral, R., Pinoti, V. F., et al. (2021). SCI1 is a direct target of AGAMOUS and WUSCHEL and is specifically expressed in the floral meristematic cells. *Front. Plant Sci.* 12:642879. doi: 10.3389/fpls.2021.642879

de Boer, A. H., van Kleeff, P. J., and Gao, J. (2012). Plant 14-3-3 proteins as spiders in a web of phosphorylation. *Protoplasma* 250, 425–440. doi: 10.1007/s00709-012-0437-z

DeLille, J. M., Sehnke, P. C., and Ferl, R. J. (2001). The *Arabidopsis* 14-3-3 family of signaling regulators. *Plant Physiol.* 126, 35–38. doi: 10.1104/pp.126.1.35

Denison, F. C., Paul, A.-L., Zupanska, A. K., and Ferl, R. J. (2011). 14-3-3 proteins in plant physiology. *Semin. Cell Dev. Biol.* 22, 720–727. doi: 10.1016/j.semcdb.2011.08.006

DePaoli, H. C., Brito, M. S., Quiapim, A. C., Teixeira, S. P., Goldman, G. H., Dornelas, M. C., et al. (2011). Stigma/style cell-cycle inhibitor 1 (SCI1), a tissue-specific cell-cycle regulator that controls upper pistil development. *New Phytol.* 190, 882–895. doi: 10.1111/j.1469-8137.2011.03660.x

DePaoli, H. C., Dornelas, M. C., and Goldman, M. H. (2014). SCI1 is a component of the auxin-dependent control of cell proliferation in Arabidopsis upper pistil. *Plant Sci.* 229, 122–130. doi: 10.1016/j.plantsci.2014.09.003

DePaoli, H. C., Goldman, G. H., and Goldman, M. H. (2012). SCI1, the first member of the tissue-specific inhibitors of CDK (TIC) class, is probably connected to the auxin signaling pathway. *Plant Signal. Behav.* 7, 53–58. doi: 10.4161/psb.7.1.18525

Engels, K., Giannattasio, M., Muzi-Falconi, M., Lopes, M., and Ferrari, S. (2011). 14-3-3 proteins regulate exonuclease 1-dependent processing of stalled replication forks. *PLoS Genet.* 7:e1001367. doi: 10.1371/journal.pgen.1001367

Feldman, R. M., Correll, C. C., Kaplan, K. B., and Deshaies, R. J. (1997). A complex of Cdc4p, Skp1p, and Cdc53p/cullin catalyzes ubiquitination of the phosphorylated CDK inhibitor Sic1p. *Cell* 91, 221–230. doi: 10.1016/S0092-8674(00)80404-3

Ferl, R. J. (2004). 14-3-3 proteins: regulation of signal-induced events. *Physiol. Plant.* 120, 173–178. doi: 10.1111/j.0031-9317.2004.0239.x

Ferl, R. J., Manak, M. S., and Reyes, M. F. (2002). The 14-3-3s. *Genome Biol.* 3, 3010.1–3010.7. doi: 10.1186/gb-2002-3-7-reviews3010

Gardino, A. K., and Yaffe, M. B. (2011). 14-3-3 proteins as signaling integration points for cell-cycle control and apoptosis. *Semin. Cell Dev. Biol.* 22, 688–695. doi: 10.1016/j.semcdb.2011.09.008

Genschik, P., Marrocco, K., Bach, L., Noir, S., and Criqui, M.-C. (2014). Selective protein degradation: a rheostat to modulate cell-cycle phase transitions. *J. Exp. Bot.* 65, 2603–2615. doi: 10.1093/jxb/ert426

Gökirmak, T., Paul, A. L., and Ferl, R. J. (2010). Plant phosphopeptide-binding proteins as signaling mediators. *Curr. Opin. Plant Biol.* 13, 527–532. doi: 10.1016/j.pbi.2010.06.001

Goldman, M. H., Goldberg, R. B., and Mariani, C. (1994). Female sterile tobacco plants are produced by stigma-specific cell ablation. *EMBO J.* 13, 2976–2984. doi: 10.1002/j.1460-2075.1994.tb06596.x

Grandin, N., and Charbonneau, M. (2008). Budding yeast 14-3-3 proteins contribute to the robustness of the DNA damage and spindle checkpoints. *Cell* 7, 2749–2761. doi: 10.4161/cc.7.17.6592

Grønlund, A. L., Dickinson, J. R., Kille, P., Harwood, J. L., Herbert, R. J., Francis, D., et al. (2009). Plant WEE1 kinase interacts with a 14-3-3 protein, GF14 omega but a mutation of WEE1 at S485 alters their spatial interaction. *Open Plant Sci. J.* 3, 40–48. doi: 10.2174/1874294700903010040

Gryaznova, Y., Koca Caydasi, A., Malengo, G., Sourjik, V., and Pereira, G. (2016). A FRET-based study reveals site-specific regulation of spindle position checkpoint proteins at yeast centrosomes. *elife* 5:e14029. doi: 10.7554/eLife.14029

Hloušková, P., Černý, M., Kořínková, N., Luklová, M., Minguet, E. G., Brzobohatý, B., et al. (2019). Affinity chromatography revealed 14-3-3 interactome of tomato (*Solanum lycopersicum* L.) during blue light-induced de-etiolation. *J. Proteome* 193, 44–61. doi: 10.1016/j.jprot.2018.12.017

Holt, L. J. (2012). Regulatory modules: coupling protein stability to phosphoregulation during cell division. *FEBS Lett.* 586, 2773–2777. doi: 10.1016/j.febslet.2012.05.045

Honda, R., Ohba, Y., and Yasuda, H. (1997). 14-3-3 zeta protein binds to the carboxyl half of mouse wee1 kinase. *Biochem. Biophys. Res. Commun.* 230, 262–265. doi: 10.1006/bbrc.1996.5933

Huang, X., Zhang, Q., Jiang, Y., Yang, C., Wang, Q., and Li, L. (2018). Shade-induced nuclear localization of PIF7 is regulated by phosphorylation and 14-3-3 proteins in Arabidopsis. *elife* 7:e31636. doi: 10.7554/eLife.31636

Igarashi, D., Ishida, S., Fukazawa, J., and Takahashi, Y. (2001). 14-3-3 proteins regulate intracellular localization of the bZIP transcriptional activator RSG. *Plant Cell* 13, 2483–2497. doi: 10.1105/tpc.010188

Jaspert, N., Throm, C., and Oecking, C. (2011). Arabidopsis 14-3-3 proteins: fascinating and less fascinating aspects. *Front. Plant Sci.* 2:96. doi: 10.3389/fpls.2011.00096

Jones, D. H., Ley, S., and Aitken, A. (1995). Isoforms of 14-3-3 protein can form homo- and heterodimers in vivo and in vitro: implications for function as adapter proteins. *FEBS Lett.* 368, 55–58. doi: 10.1016/0014-5793(95)00598-4

Karimi, M., Bleys, A., Vanderhaeghen, R., and Hilson, P. (2007). Building blocks for plant gene assembly. *Plant Physiol.* 145, 1183–1191. doi: 10.1104/pp.107.110411

Karimi, M., Inzé, D., and Depicker, A. (2002). GATEWAY™ vectors for *agrobacterium*-mediated plant transformation. *Trends Plant Sci.* 7, 193–195. doi: 10.1016/S1360-1385(02)02251-3

Keicher, J., Jaspert, N., Weckermann, K., Möller, C., Throm, C., Kintzi, A., et al. (2017). Arabidopsis 14-3-3 epsilon members contribute to polarity of PIN auxin carrier and auxin transport-related development. *elife* 6:e24336. doi: 10.7554/eLife.24336

Koepp, D. M. (2014). "Cell-cycle regulation by protein degradation," in *Cell-Cycle Control. Methods in Molecular Biology (Methods and Protocols)*. *Vol. 1170*. eds. E. Noguchi and M. Gadaleta (New York, NY: Humana Press).

Koltunow, A. M., Truettner, J., Cox, K. H., Wallroth, M., and Goldberg, R. B. (1990). Different temporal and spatial gene expression patterns occur during anther development. *Plant Cell* 2, 1201–1224. doi: 10.2307/3869340

Konagaya, K.-I., Matsushita, Y., Kasahara, M., and Nyunoya, H. (2004). Members of 14-3-3 protein isoforms interacting with the resistance gene product N and the elicitor of tobacco mosaic virus. *J. Gen. Plant Pathol.* 70, 221–231. doi: 10.1007/s10327-003-0113-4

Koroleva, O. A., Calder, G., Pendle, A. F., Kim, S. H., Lewandowska, D., SimpsonCG, J. I. M., et al. (2009). Dynamic behavior of Arabidopsis eIF4A-III, putative core protein of exon junction complex: fast relocation to nucleolus and splicing speckles under hypoxia. *Plant Cell* 21, 1592–1606. doi: 10.1105/tpc.108.060434

Laronga, C., Yang, H. Y., Neal, C., and Lee, M. H. (2000). Association of the cyclin-dependent kinases and 14-3-3 sigma negatively regulates cell-cycle progression. *J. Biol. Chem.* 275, 23106–23112. doi: 10.1074/jbc.M905616199

Lee, J. H., Kwak, G., Lim, Y. P., and Oh, M. H. (2020). 14-3-3 proteins contribute to leaf and root development via brassinosteroid insensitive 1 in *Arabidopsis thaliana*. *Genes Genomics* 42, 347–354. doi: 10.1007/s13258-019-00909-4

Li, Y., Butenko, Y., and Grafi, G. (2005). Histone deacetylation is required for progression through mitosis in tobacco cells. *Plant J.* 41, 346–352. doi: 10.1111/j.1365-313X.2004.02301.x

Lin, X., Huang, S., Huang, G., Chen, Y., Wang, X., and Wang, Y. (2021). 14-3-3 proteins are involved in BR-induced ray petal elongation in Gerbera hybrida. *Front. Plant Sci.* 12:718091. doi: 10.3389/fpls.2021.718091

Liu, Z., Jia, Y., Ding, Y., Shi, Y., Li, Z., Guo, Y., et al. (2017). Plasma membrane CRPK1-mediated phosphorylation of 14-3-3 proteins induce their nuclear import to fine-tune CBF signaling during cold response. *Mol. Cell* 66, 117–128. doi: 10.1016/j.molcel.2017.02.016

Lozano-Durán, R., and Robatzek, S. (2015). 14-3-3 proteins in plant-pathogen interactions. *Mol. Plant-Microbe Interact.* 28, 511–518. doi: 10.1094/MPMI-10-14-0322-CR

Mayfield, J. D., Folta, K. M., Paul, A.-L., and Ferl, R. J. (2007). The 14-3-3 proteins mu and upsilon influence transition to flowering and early phytochrome response. *Plant Physiol.* 145, 1692–1702. doi: 10.1104/pp.107.108654

Mhawech, P. (2005). 14-3-3 proteins—an update. *Cell Res.* 15, 228–236. doi: 10.1038/sj.cr.7290291

Nagata, T., Nemoto, Y., and Hasezawa, S. (1992). Tobacco BY-2 cell line as the "HeLa" cells in the biology of higher plants. *Int. Rev. Cytol.* 132, 1–30.

Nocarova, E., and Fischer, L. (2009). Cloning of transgenic tobacco BY-2 cells; an efficient method to analyse and reduce high natural heterogeneity of transgene expression. *BMC Plant Biol.* 22:44. doi: 10.1186/1471-2229-9-44

Oecking, C., and Jaspert, N. (2009). Plant 14-3-3 proteins catch up with their mammalian orthologs. *Curr. Opin. Plant Biol.* 12, 760–765. doi: 10.1016/j.pbi.2009.08.003

Owens, L., Simanski, S., Squire, C., Smith, A., Cartzendafner, J., Cavett, V., et al. (2010). Activation domain-dependent degradation of somatic Wee1 kinase. *J. Biol. Chem.* 285, 6761–6769. doi: 10.1074/jbc.M109.093237

Pagni, M., Ioannidis, V., Cerutti, L., Zahn-Zabal, M., Jongeneel, C. V., and Falquet, L. (2004). MyHits: a new interactive resource for protein annotation and domain identification. *Nucleic Acids Res.* 32, W332–W335. doi: 10.1093/nar/gkh479

Pallucca, R., Visconti, S., Camoni, L., Cesareni, G., Melino, S., Panni, S., et al. (2014). Specificity of ε and non-ε isoforms of Arabidopsis 14-3-3 proteins towards the H+-ATPase and other targets. *PLoS One* 9:e90764. doi: 10.1371/journal.pone.0090764

Parokonny, A. S., and Kenton, A. Y. (1995). "Comparative physical mapping and evolution of the *Nicotiana tabacum* L. karyotype." in *Kew Chromosome Conference IV*. eds. P. E. Brandham and M. D. Bennett (Kew: Royal Botanic Gardens), 301–320.

Paul, A.-L., Denison, F. C., Schultz, E. R., Zupanska, A. K., and Ferl, R. J. (2012). 14-3-3 phosphoprotein interaction networks—does isoform diversity present functional interaction specification? *Front. Plant Sci.* 3:190. doi: 10.3389/fpls.2012.00190

Paul, A.-L., Folta, K. M., and Ferl, R. J. (2008). 14-3-3 proteins, red light and photoperiodic flowering. *Plant Signal. Behav.* 3, 511–515. doi: 10.4161/psb.3.8.5717

Paul, A.-L., Sehnke, P. C., and Ferl, R. J. (2005). Isoform-specific subcellular localization among 14-3-3 proteins in Arabidopsis seems to be driven by client interactions. *Mol. Biol. Cell* 16, 1735–1743. doi: 10.1091/mbc.e04-09-0839

Peng, C.-Y., Graves, P. R., Thoma, R. S., Wu, Z., Shaw, A. S., and Piwnica-Worms, H. (1997). Mitotic and G2 checkpoint control: regulation of 14-3-3 protein binding by phosphorylation of Cdc25C on serine-216. *Science* 277, 1501–1505. doi: 10.1126/science.277.5331.1501

Pennington, K. L., Chan, T. Y., Torres, M. P., and Andersen, J. L. (2018). The dynamic and stress-adaptive signaling hub of 14-3-3: emerging mechanisms of regulation and context-dependent protein-protein interactions. *Oncogene* 37, 5587–5604. doi: 10.1038/s41388-018-0348-3

Roberts, M. R. (2000). Regulatory 14-3-3 protein–protein interactions in plant cells. *Curr. Opin. Plant Biol.* 3, 400–405. doi: 10.1016/S1369-5266(00)00103-5

Rosenquist, M., Alsterfjord, M., Larsson, C., and Sommarin, M. (2001). Data mining the Arabidopsis genome reveals fifteen 14-3-3 genes. Expression is demonstrated for two out of five novel genes. *Plant Physiol.* 127, 142–149. doi: 10.1104/pp.127.1.142

Schoonheim, P. J., Veiga, H., Pereira, D. C., Friso, G., van Wijk, K. J., and de Boer, A. H. (2007). A comprehensive analysis of the 14-3-3 interactome in barley leaves using a complementary proteomics and two hybrid approach. *Plant Physiol.* 143, 670–683. doi: 10.1104/pp.106.090159

Schreiber, G., Barberis, M., Scolari, S., Klaus, C., Herrmann, A., and Klipp, E. (2012). Unraveling interactions of cell-cycle-regulating proteins Sic1 and B-type cyclins in living yeast cells: a FLIM-FRET approach. *FASEB J.* 26, 546–554. doi: 10.1096/fj.11-192518

Shaw, P., and Brown, J. (2012). Nucleoli: composition, function, and dynamics. *Plant Physiol.* 158, 44–51. doi: 10.1104/pp.111.188052

Sorrell, D. A., Marchbank, A. M., Chrimes, D. A., Dickinson, J. R., Rogers, H. J., Francis, D., et al. (2003). The Arabidopsis 14-3-3 protein, GF14ω, binds to the *Schizosaccharomyces pombe* Cdc25 phosphatase and rescues checkpoint defects in the rad24− mutant. *Planta* 218, 50–57. doi: 10.1007/s00425-003-1083-7

Usui, T., and Petrini, J. H. (2007). The Saccharomyces cerevisiae 14-3-3 proteins Bmh1 and Bmh2 directly influence the DNA damage-dependent functions of Rad53. *Proc. Natl. Acad. Sci. U. S. A.* 104, 2797–2802. doi: 10.1073/pnas.0611259104

van Hemert, M. J., Steensma, H. Y., and van Heusden, G. P. (2001). 14-3-3 proteins: key regulators of cell division, signalling and apoptosis. *BioEssays* 23, 936–946. doi: 10.1002/bies.1134

van Heusden, G. P., van der Zanden, A. L., Ferl, R. J., and Steensma, H. Y. (1996). Four Arabidopsis thaliana 14-3-3 protein isoforms can complement the lethal yeast Bmh1 Bmh2 double disruption. *FEBS Lett.* 391, 252–256. doi: 10.1016/0014-5793(96)00746-6

van Heusden, G. P. H. (2009). 14-3-3 proteins: Insights from genome-wide studies in yeast. *Genomics* 94, 287–293. doi: 10.1016/j.ygeno.2009.07.004

Verma, R., Feldman, R. M., and Deshaies, R. J. (1997). SIC1 is ubiquitinated in vitro by a pathway that requires CDC4, CDC34, and cyclin/CDK activities. *Mol. Biol. Cell* 8, 1427–1437.

Wang, Y., Jacobs, C., Hook, K. E., Duan, H., Booher, R. N., and Sun, Y. (2000). Binding of 14-3-3beta to the carboxyl terminus of Wee1 increases Wee1 stability, kinase activity, and G2-M cell population. *Cell Growth Differ.* 11, 211–219.

Watson, J. M., Platzera, A., Kazdaa, A., Akimchevaa, S., Valuchovab, S., Nizhynskaa, V., et al. (2016). Germline replications and somatic mutation accumulation are independent of vegetative life span in Arabidopsis. *Proc. Natl. Acad. Sci. U. S. A.* 113, 12226–12231. doi: 10.1073/pnas.1609686113

Wilson, R. S., Swatek, K. N., and Thelen, J. J. (2016). Regulation of the regulators: post-translational modifications, subcellular, and spatiotemporal distribution of plant 14-3-3 proteins. *Front. Plant Sci.* 7:611. doi: 10.3389/fpls.2016.00611

Yaffe, M. B. (2002). How do 14-3-3 proteins work?-- Gatekeeper phosphorylation and the molecular anvil hypothesis. *FEBS Lett.* 513, 53–57. doi: 10.1016/s0014-5793(01)03288-4

Yoon, G. M., and Kieber, J. J. (2013). 14-3-3 regulates 1-aminocyclopropane-1-carboxylate synthase protein turnover in Arabidopsis. *Plant Cell* 25, 1016–1028. doi: 10.1105/tpc.113.110106

Conflict of Interest: The authors declare that the research was conducted in the absence of any commercial or financial relationships that could be construed as a potential conflict of interest.

Publisher's Note: All claims expressed in this article are solely those of the authors and do not necessarily represent those of their affiliated organizations, or those of the publisher, the editors and the reviewers. Any product that may be evaluated in this article, or claim that may be made by its manufacturer, is not guaranteed or endorsed by the publisher.

frontiers | Frontiers in Plant Science

REVIEW
published: 06 April 2022
doi: 10.3389/fpls.2022.837528

Recent Advances in Understanding the Structural and Functional Evolution of FtsH Proteases

Lanbo Yi[1,2,3], Bin Liu[2,3], Peter J. Nixon[4], Jianfeng Yu[2,4]* and Feng Chen[2,3]**

[1] Institute for Food and Bioresource Engineering, College of Engineering, Peking University, Beijing, China, [2] Shenzhen Key Laboratory of Marine Microbiome Engineering, Institute for Advanced Study, Shenzhen University, Shenzhen, China, [3] Institute for Innovative Development of Food Industry, Shenzhen University, Shenzhen, China, [4] Sir Ernst Chain Building-Wolfson Laboratories, Department of Life Sciences, Imperial College London, London, United Kingdom

The FtsH family of proteases are membrane-anchored, ATP-dependent, zinc metalloproteases. They are universally present in prokaryotes and the mitochondria and chloroplasts of eukaryotic cells. Most bacteria bear a single *ftsH* gene that produces hexameric homocomplexes with diverse house-keeping roles. However, in mitochondria, chloroplasts and cyanobacteria, multiple FtsH homologs form homo- and heterocomplexes with specialized functions in maintaining photosynthesis and respiration. The diversification of FtsH homologs combined with selective pairing of FtsH isomers is a versatile strategy to enable functional adaptation. In this article we summarize recent progress in understanding the evolution, structure and function of FtsH proteases with a focus on the role of FtsH in photosynthesis and respiration.

Keywords: FtsH protease, mitochondria, protein engineering, functional adaptation, evolution, chloroplasts, photosystem II repair

OPEN ACCESS

Edited by:
Simon Gilroy, University of Wisconsin–Madison, United States

Reviewed by:
Jean-David Rochaix, Université de Genève, Switzerland
Yusuke Kato, Setsunan University, Japan

****Correspondence:***
Peter J. Nixon
p.nixon@imperial.ac.uk
orcid.org/0000-0003-1952-6937
Jianfeng Yu
j.yu@imperial.ac.uk
orcid.org/0000-0001-7174-3803
Feng Chen
sfchen@szu.edu.cn
orcid.org/0000-0002-9054-943X

Specialty section:
This article was submitted to Plant Cell Biology, a section of the journal Frontiers in Plant Science

Received: *16 December 2021*
Accepted: *24 February 2022*
Published: *06 April 2022*

Citation:
Yi L, Liu B, Nixon PJ, Yu J and Chen F (2022) Recent Advances in Understanding the Structural and Functional Evolution of FtsH Proteases. Front. Plant Sci. 13:837528. doi: 10.3389/fpls.2022.837528

THE BASICS OF FtsH PROTEASES

Discovery of FtsH

FtsH proteases belong to the ATPase Associated with diverse cellular Activities (AAA+) super family. FtsH was first identified by Santos and De Almeida following the isolation of a mutant of *Escherichia coli* that displayed elongated cells and was sensitive to heat-shock, and hence named *filamentous temperature sensitive H* (*ftsH*) (Santos and De Almeida, 1975). However, later studies demonstrated that the *ftsH* mutation was only responsible for heat-induced growth arrest and not the filamentation defect (Ogura et al., 1991). FtsH orthologs were later identified in almost all cellular organisms except for some archaebacteria (Summer et al., 2006; Wagner et al., 2012; Giménez et al., 2015). For a period of time, *E. coli* FtsH was also designated as HflB until it was confirmed to be encoded by the same gene (Herman et al., 1993). FtsH proteases have been found to target a broad-range of proteins, both membrane-bound and soluble, and to participate in the regulation of diverse pathways (Ogura et al., 1999; Ito and Akiyama, 2005; Janska et al., 2013; Kato and Sakamoto, 2018).

The Layout of Domains in the FtsH Primary Structure

FtsH proteases are present in prokaryotes, and mitochondria and chloroplasts of eukaryotic cells (Adam et al., 2005; Tatsuta and Langer, 2009). The typical bioinformatic features of FtsH (**Figure 1**) include an N-terminal transmembrane domain consisting of one or two transmembrane helices,

followed by a highly conserved AAA+ ATPase domain containing Walker A and B structural elements, a second region of homology motif that is responsible for the binding and hydrolysis of ATP (Ito and Akiyama, 2005; Suno et al., 2006), and a downstream M41 peptidase domain featuring a zinc-binding proteolytic site capable of digesting unfolded proteins into ∼12 amino-acid long oligopeptides (Suno et al., 2006). The ATPase domain is highly conserved across species, while the C-terminal tail of the protease domain and the regions connecting the transmembrane domains are less conserved (Langer, 2000; Suno et al., 2006; Graef et al., 2007).

Formation of FtsH Complexes

Both *in vivo* and *in vitro* studies suggest that the proteolytic activity of FtsH requires the formation of oligomeric complexes (Akiyama et al., 1995; Krzywda et al., 2002; Suno et al., 2006; Lee et al., 2011; Boehm et al., 2012). Structural data reveal that an FtsH complex consists of six protomers, with the soluble ATPase and protease domains interacting with the neighboring protomers to form a hexagonal particle (**Figure 2**; Suno et al., 2006; Lee et al., 2011; Boehm et al., 2012). In organisms containing multiple FtsH homologs, the pairing of protomers is strictly regulated, resulting in the formation of distinctive FtsH homo- and heterocomplexes conferring specialized functions (Lee et al., 2011; Boehm et al., 2012; Gerdes et al., 2012; Wagner et al., 2012; Scharfenberg et al., 2015; Kato and Sakamoto, 2018). In most cases, FtsH homologs form either homohexamers or heterohexamers. Exceptions include Afg312, a human mitochondrial FtsH, that can form both homocomplexes and heterocomplexes with paraplegin (Casari et al., 1998; Karlberg et al., 2009; Gerdes et al., 2012; Patron et al., 2018) and FtsH3 and FtsH10 in *Arabidopsis* mitochondria which form both homo- and heterocomplexes (Piechota et al., 2010). A variety of experimental data suggest that FtsH heterocomplexes in diverse organisms contain two types of FtsH protomer in a 1:1 stoichiometry (Lee et al., 2011; Boehm et al., 2012; Langklotz et al., 2012; Kato and Sakamoto, 2018; Steele and Glynn, 2019). However, possible exceptions are some type A/type B FtsH heterocomplexes isolated from *Arabidopsis* which have been suggested to contain the two forms in a 1:2 ratio (Moldavski et al., 2012) although a recent study supports a 1:1 ratio (Kato et al., 2018).

Studies on FtsH heterocomplexes show that the pairing of FtsH isomers is highly specific, hence the formation of hexamers requires a selective matching mechanism. Early research suggested that the transmembrane domain helps homo-oligomerization of *E. coli* FtsH (Makino et al., 1999). However, later studies on FtsH from *Thermophilus maritima* and *Thermus thermophilus* demonstrated that heterologous expression of the ATPase domain, protease domain, or the complete cytosolic domain, can still form hexamers (Langklotz et al., 2012). Therefore, the tendency to form hexameric oligomers is determined by the soluble domains. Mutations in the protease domain have been shown to convert yeast Yta10/Yta12 FtsH heterocomplexes into Yta12 homocomplexes (Lee et al., 2011). This work implies that the structure of the protease domain plays a key role in selecting the appropriate FtsH protomer. However, the residues responsible for determining specificity are not totally conserved in FtsH sequences, and the resolution of the yeast FtsH structure is still too low to identify specific interactions for these residues in the complex. Therefore, the underlying mechanism requires further investigation.

The Molecular Mechanism of FtsH Complexes

It is widely accepted that FtsH complexes conduct ATP-dependent proteolysis by unfolding and translocating the target substrate through the central pore of the ATPase complex to the protease domain for degradation (Yamada-Inagawa et al., 2003; Okuno et al., 2006; Suno et al., 2006; Carvalho et al., 2021). However, the detailed molecular mechanism for substrate recognition and proteolysis is still under investigation. Current models suggest a ∼20 amino acid flexible linker between the transmembrane and ATPase domains creates space for substrates to gain access to the protease (Lee et al., 2011; Puchades et al., 2017; Carvalho et al., 2021). A phenylalanine residue positioned on the top surface near the central pore of ATPase domain (in the FVG motif) is responsible for substrate binding (Bieniossek et al., 2006; Narberhaus et al., 2009). ATP hydrolysis induces conformational changes in the ATPase domain so that the phenylalanine slides into the central pore with the substrate (Suno et al., 2006). For each ATP-driven movement, the substrate can be translocated ∼35 Å in distance with the unfolded peptide chain translocated via internal channels to the protease catalytic site for degradation. From an energy perspective, 8 ATP molecules are consumed for each peptide cleavage reaction based on experimental data (Murata and Nishiyama, 2018). Theoretical considerations suggest 6 ATP molecules per cleavage event is the minimum requirement (Suno et al., 2006).

Multiple atomic-resolution structures of FtsH, mostly of the soluble domains of homocomplexes from bacteria, are available in the protein databank (Bieniossek et al., 2006; Suno et al., 2006; Puchades et al., 2017; Carvalho et al., 2021). The structures reveal that the protease domains form a rigid hexameric "disk" underneath the ATPase domains; whereas the ATPase "disk" is flexible (Bieniossek et al., 2006; Suno et al., 2006). The structural symmetry of the ATPase domains is inconsistent across species. Early works on *E. coli* FtsH (PDB: 1LV7) suggested a sixfold symmetry for the ATPase domains (Krzywda et al., 2002; Scharfenberg et al., 2015). FtsH structures from *Aquifex aeolicus* (PDB: 4WW0) and *Thermotoga maritima* (PDB: 2CE7 and 2CEA) suggest that the ATPase domains display a twofold symmetry in the ADP-bound state (Bieniossek et al., 2006, 2009; Vostrukhina et al., 2015). Two protomers on the opposite side of the central pore display an identical interdomain angle that is different to the other four protomers. In a separate study, the crystal structure of an ADP-bound FtsH complex from *T. thermophilus* (PDB:2DHR) revealed a threefold symmetry (Suno et al., 2006) so that the ATPase domain displays alternating "open" or "closed" conformations in the ring. In contrast, analysis of a cryo-EM structure of the yeast mitochondrial Yme1 mitochondrial homocomplex has revealed a spiral staircase conformation of the ATPase domains which has led to the

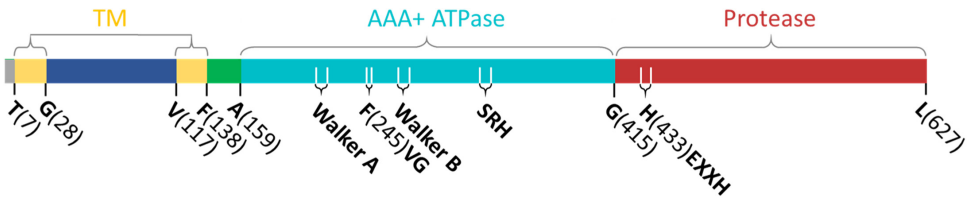

FIGURE 1 | Schematic representation of domains of FtsH2 from *Synechocystis* sp. PCC 6803. Annotations: transmembrane domain (TM), ATPase domain (AAA + ATPase) and protease domain (Protease) are illustrated as colored boxes. The TM domain includes two transmembrane helices (yellow) and a soluble linker exposed to the thylakoid lumen (blue). The soluble regions exposed to the cytoplasm include a flexible linker (green), ATPase (cyan), and protease domains (red). The amino-acid residues that separate each domain are labeled below the colored boxes. Annotated functional motifs include the proposed substrate entry point (FVG); ATP hydrolysis motifs Walker A and B, and the second region of homology (SRH); and the zinc-binding proteolytic site (HEXXH, X represents any amino acid).

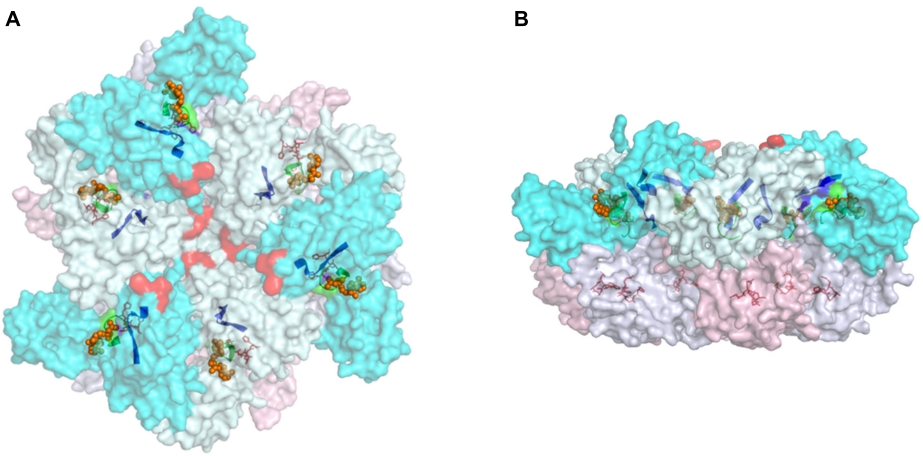

FIGURE 2 | Top **(A)** and side **(B)** views of the cytoplasmic region of hexameric FtsH complex from *T. thermophilus* (PDB:2DHR). Annotations: protomers are defined according to the status of its ATPase domains ("open" confirmation in cyan and "closed" confirmation in pale-cyan). The protease domains of "open" protomers are labeled pink, and the "closed" counterparts are in blue-white. Selected motifs presented in a non-translucent color include Walker A (green ribbon) and B (blue ribbon), and the zinc coordinates of the protease site (red sticks). The proposed FVG motif responsible for substrate binding is displayed as a red sphere, and ADP molecules are shown as orange spheres.

suggestion that ATP hydrolysis leads to progressive rotary conformational changes (Puchades et al., 2017).

We speculate that the differences in symmetry among FtsH structures might be artifacts of crystallization and cryo-EM, as the sequence identity and structure of the ATPase domains are highly conserved and hence likely to operate in a similar fashion. In addition, the "staircase" structure of Yme1 was obtained from an ATPase-inactivated mutant. On the flipside, it is plausible that FtsH orthologs have adopted different ATP hydrolysis strategies during evolution to improve energy efficiency. Depending on the nature of the substrates and reaction conditions, energy-dependent enzymatic activities require optimization of power and efficiency. For example, the number of c-subunits of ATP synthases in each species is adjusted to achieve a specific proton per ATP ratio for balanced performance (Kramer and Evans, 2011).

The gap between the ATPase domain and membrane is considered a limiting factor for substrates to gain access to the protease (Lee et al., 2011; Carvalho et al., 2021). Structural studies on native FtsH from yeast determined the gap to be ∼13 Å, which would suggest that only unfolded substrates can reach the central pore (Lee et al., 2011). However, recent structural and mutagenesis work suggests that the gap can be enlarged via tilting of the linker region (Carvalho et al., 2021). Therefore, the width of the gap may not be a strict gatekeeper element for substrate specificity.

FtsH Supercomplexes

In vivo FtsH activities are regulated by members of the band 7 (or SPFH) protein family that includes the stomatins, prohibitins, flotillins and HflK/C (Tavernarakis et al., 1999; Gehl and Sweetlove, 2014). In *E. coli*, FtsH activity is negatively regulated through the action of a large complex consisting of the HflK and HflC subunits (Kihara et al., 1996, 1997, 1998; Akiyama, 2009). A recent cryo-EM structure of a HflK/C-FtsH super-complex has revealed that the HflK and HflC subunits assemble within the membrane to form a ring with a large dome in a "hat-like" structure (Ma et al., 2022). Up to four FtsH complexes can be contained within the HflK/C complex. The transmembrane helices of HlfK and HflC form a circular barrier that prevents the FtsH complexes from moving out into the surrounding membrane thereby potentially preventing unwanted degradation of proteins. The work also showed that FtsH activity is negatively correlated with the abundance of HflK/C. The related prohibitin

complexes might play a similar role in regulating FtsH activity in mitochondria (Steglich et al., 1999) and cyanobacteria (Boehm et al., 2012; Bečková et al., 2017; Zhang et al., 2021), and more generally members of the SPFH family could form ring-like structures in the membrane and have scaffolding functions (Gehl and Sweetlove, 2014; Wai et al., 2016).

The Cellular Locations and Functions of FtsH Proteases

In *E. coli,* there are five proteases (ClpXP, ClpAP, HslUV, Lon and FtsH) of the AAA+ protease family involved in ATP-dependent proteolysis (Langklotz et al., 2012). Of these, FtsH and Lon proteases are membrane-anchored, and FtsH is essential for cell viability (Ogura et al., 1999). In most prokaryotes, FtsH is encoded by a single gene, and localized in the cytoplasmic membrane (Tomoyasu et al., 1995). In cyanobacteria, typically 4 FtsH homologs are present which form specialized complexes in the cytoplasmic and thylakoid membranes (Boehm et al., 2012; Sacharz et al., 2015). In eukaryotes, FtsHs are exclusive to mitochondria and chloroplasts in accordance with the prokaryotic origin of FtsH proteases (Wagner et al., 2012). However, all FtsH homologs in eukaryotes are encoded by nuclear genes, implicating gene transfer during endosymbiosis.

FtsH proteases perform both protease and chaperone roles to maintain cellular homeostasis (Wagner et al., 2012). Previous studies revealed that FtsH in *E. coli* cells regulates heat-stress response via degradation of heat-shock transcription factor σ^{32} (Tomoyasu et al., 1995). FtsH is also required to balance the turnover rate of LpxC deacetylase, an important regulatory mechanism to maintain the lipopolysaccharide/phospholipid ratio (Ogura et al., 1999). FtsH plays a crucial role in removing inactive membrane-bound Sec translocons (Kihara et al., 1995; Akiyama et al., 1996). Interestingly, rapid removal of Sec translocons by FtsH can be a greater risk to cell viability than allowing inactivated Sec translocons to accumulate (Kihara et al., 1995). Chaperone activities of FtsH have been reported from studies on bacteria, mitochondria and chloroplasts (Ogura et al., 1991; Bailey et al., 2001; Wagner et al., 2012; Li et al., 2013; Mishra et al., 2019). FtsH is essential in *E. coli*, *Bradyrhizobium japonicum*, *Helicobacter pylori* and *Borrelia burgdorferi* (Wang et al., 2021); whereas, it is dispensable in *Bacillus subtilis*, *Lactococcus lactis*, *Caulobacter crescentus*, *Staphylococcus aureus,* and *Pseudomonas aeruginosa* (Kamal et al., 2019). However, the lack of FtsH reduces their cell fitness (Chu et al., 2016).

FtsH proteases are safeguards of photosynthesis and respiration and are found in the thylakoid and the mitochondrial inner membranes, where the major photosynthetic and respiratory electron transport machineries are located. Both photosynthesis and respiration are subject to oxidative stress, hence the proteins involved are often short-lived due to damage by reactive oxygen species (ROS) (Krynická et al., 2014; Steele and Glynn, 2019). Spatially coordinated FtsH complexes can efficiently recognize and remove damaged proteins, thus leave room for *de novo* produced replacements to be incorporated to reactivate the pathway (Janska et al., 2010; Nixon et al., 2010; Kato and Sakamoto, 2018). In the case of photosynthesis, efficient FtsH-mediated repair of damaged photosystem II (PSII) is an important determinant of primary productivity (Nixon et al., 2005; Boehm et al., 2012; Wagner et al., 2012).

PHOTOSYNTHESIS AND FtsH

Photosynthesis and Photosystem II Repair

Oxygenic photosynthesis is the primary energy harnessing process on Earth and a prominent source of oxygen for the atmosphere (Nelson and Ben-Shem, 2004). Water photolysis catalyzed by PSII generates molecular oxygen and reducing power to produce organic matter. The process is chemically challenging due to the high redox potentials generated in the reaction center, which leads to protein damage (Vass et al., 2007; Vass, 2012; Bricker et al., 2015). Nature's solution to mitigate photodamage is to restrict hazardous reactions to a single subunit, namely the D1 protein, to enable rapid replacement of inactivated D1. The PSII repair strategy is energy efficient as it enables recycling of nearly all the subunits and cofactors of PSII (Nixon et al., 2010; Nickelsen and Rengstl, 2013).

Maintaining photosynthetic activity requires the PSII repair rate to match the rate of damage to D1. When D1 damage exceeds repair, inactivated PSII accumulates, and net photosynthetic rate falls. This phenomenon, termed chronic photoinhibition, can be lethal if prolonged (Aro et al., 1993; Edelman and Mattoo, 2008; Nixon et al., 2010; Nickelsen and Rengstl, 2013). Removal of damaged D1 is a crucial step that leads to reassembly and reactivation of PSII. The current view is that upon photodamage, PSII undergoes partial disassembly which allows D1 to be exposed for replacement (Krynicka et al., 2015). Specialized FtsH complexes extract D1 from the membrane which allows the replacement copy to be assembled into the PSII chassis (Bailey et al., 2001; Silva et al., 2003; Nixon et al., 2005).

Efficient D1 replacement is vital to maintain photosynthetic activity. D1 is the most conserved protein known to date (Cardona et al., 2019; Sánchez-Baracaldo and Cardona, 2020), and consists of 5 transmembrane helices with a peripheral N-terminal tail that is crucial to initiate degradation (Komenda et al., 2007), and a C-terminal post-translational cleavage site for controlled assembly of the inorganic oxygen-evolving complex (Nixon et al., 1992; Anbudurai et al., 1994; Oelmüller et al., 1996; Suorsa and Aro, 2007). Under strong illumination, D1 is among the fastest turned-over proteins in cells, with a half-life as short as 15–20 min (Jansen et al., 1996, 1999; Yao et al., 2012; Kale et al., 2017). It is reported that the biosynthesis rate of D1 in mature chloroplasts accounts for 50% of net protein synthesis, however, the abundance of D1 is only ∼0.1% of protein content (Nelson and Ben-Shem, 2004). Hence the rate and efficiency of D1 replacement are important metrics to evaluate the productivity and light tolerance of a photoautotroph.

Role of FtsH in Photosystem II Repair

Thylakoid FtsH has been shown to selectively remove damaged D1 in both cyanobacterial and plant models. Initial suggestions

for a role for FtsH came in 1999, when Spetea et al. (1999) reported that D1 degradation was a multi-stage, ATP- and zinc-dependent process using an *in vitro* proteolysis assay; and suggested multiple proteases including thylakoid FtsH could be involved. Since then, extensive mutagenesis works have been conducted to evaluate the significance of each protease candidate (Bailey et al., 2002; Silva et al., 2003; Huesgen et al., 2006; Kapri-Pardes et al., 2007). In both plants and cyanobacteria, only FtsH complexes are essential for efficient PSII repair (Nixon et al., 2005).

The molecular mechanism of FtsH-mediated D1 degradation remains elusive. Pulse-chase labeling experiments show that newly synthesized D1 accumulates as an unassembled membrane protein in an FtsH2-deficient *Synechocystis* mutant, indicating FtsH-mediated proteolysis of damaged D1 is vital for D1 incorporation (Silva et al., 2003; Komenda et al., 2006). FtsH complexes co-purify with PSII complexes (Silva et al., 2003) but the direct interaction between FtsH and D1 has yet to be observed, possibly due to rapid D1 degradation. D1 mutants lacking 20 amino-acids of the N-terminal tail display an FtsH null-like phenotype in cyanobacteria (Komenda et al., 2007) which would suggest that the N-terminal tail of D1 exposed on the membrane surface is crucial to initiate proteolysis. Hence in the current D1 degradation model (**Figure 3**), the N-terminus of D1 facilitates the initial contact with the FVG motif of an FtsH complex and is then pulled into the central pore of FtsH for degradation. FtsH complexes involved in PSII repair are heterohexameric and composed of type A and type B FtsH subunits (Sakamoto et al., 2003; Boehm et al., 2012). Site-directed mutagenesis of type B FtsH protomers has revealed that inactivation of ATPase activity compromises PSII repair, but that inactivation of the protease activity does not (Zhang et al., 2010; Yu, 2013). Hence only one functional protease domain might be needed for FtsH function. The hypothesis is also in agreement with the structural model proposed from a *T. thermophilus* FtsH study (Suno et al., 2006).

Cells lacking thylakoid FtsH can maintain photosynthesis under low light intensity. Photodamage is inevitable even under low irradiance, which indicates the presence of auxiliary D1 degradation routes (Silva et al., 2003; Adam et al., 2005; Nixon et al., 2005). Increased accumulation of truncated D1 fragments is observed in the *Arabidopsis* and *Chlamydomonas reinhardtii* FtsH mutants, highlighting the involvement of other proteases, although cleavage by ROS cannot be ruled out (Kato et al., 2012; Malnoë et al., 2014).

In vitro biochemical analyses indicate Deg proteases, a class of ATP-independent serine proteases, as responsible for the cleavage of D1 in the lumenal loop region between transmembrane helix C and D (Sun et al., 2007; Kato et al., 2012). 16 Deg proteases are found in *Arabidopsis thaliana*, of which Deg2 and Deg7 are localized in the stroma (Sun et al., 2010; Luciński et al., 2011); whereas, Deg1, Deg5 and Deg8 reside in the thylakoid lumen (Kapri-Pardes et al., 2007; Sun et al., 2007). The potential benefit from Deg cleavage is that once D1 is

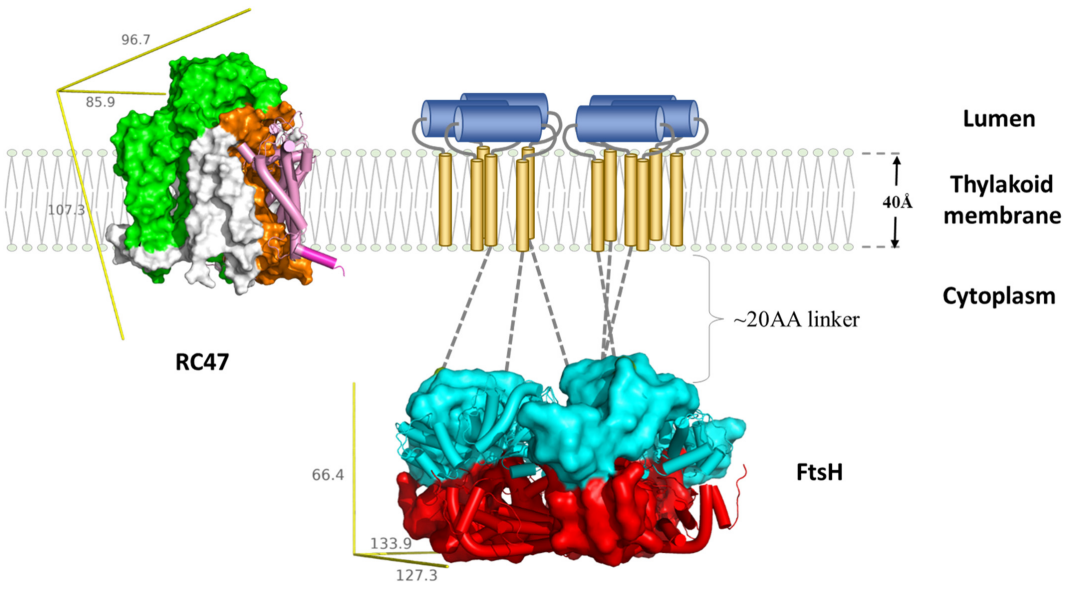

FIGURE 3 | Schematic representation of FtsH-mediated D1 degradation. Upon inactivation, PSII undergo partial disassembly, resulting in transient complex RC47 (PDB:4V62) containing inactivated D1 (pink and purple), D2 (orange), CP47 (green), and small chlorophyll-binding subunits (white). The N-terminal loop of D1 (purple cylinder) is exposed for degradation. The thylakoid FtsH complex (adapted using crystal structure of the whole cytosolic domains of FtsH from *T. thermophilus*, PDB:2DHR) participates in D1 removal. In the current model, the N-terminal D1 loop feeds through the FtsH linker region (gray dotted lines) and is pulled by the ATPase domains (cyan) down the central pore, and translocated to the protease domain (red). Both RC47 and FtsH complexes are plotted to scale using the lipid membrane as size reference. The missing transmembrane region of FtsH is illustrated as a cartoon: transmembrane helices (gold cylinders) and lumenal region (blue cylinders). The yellow reference rulers represent the dimension (unit: Å) of the Inertia Axis Aligned Bounding Box (IAAB) for the respective protein, which are calculated by Guardado-Calvo's Python scripts for pymol (https://pymolwiki.org/index.php/Draw_Protein_Dimensions).

broken into multiple smaller degradants, additional proteases, such as Clp can be involved to accelerate D1 replacement (Kato et al., 2012). Several studies on *Arabidopsis* mutants lacking Deg protease subunits observed reduced D1 repair rate under strong illumination, hence the involvement of Deg proteases in D1 repair is physiologically relevant, too (Kapri-Pardes et al., 2007; Sun et al., 2007, 2010; Schuhmann and Adamska, 2012). However, an *Arabidopsis* mutant lacking Deg1, 5, and 8 is still able to grow photoautotrophically unless challenged with strong abiotic stress (Butenko et al., 2018). In contrast, mutants lacking all type A or type B FtsH subunits abolish autotrophic growth and are embryo lethal (Yu et al., 2004, 2005; Zaltsman et al., 2005a). Therefore, Deg proteases play a more minor role in PSII repair (Yu et al., 2004, 2005; Zaltsman et al., 2005a).

However, in the *Synechocystis* model, mutants lacking all three annotated Deg proteases do not display measurable defects in PSII repair, which casts doubt over the universality of Deg-mediated cleavage (Barker et al., 2006). It is possible that D1 turnover in viridiplantae is more sophisticated as they possess more complex thylakoid structures and are typically exposed to stronger light irradiance. Overall, current models suggest that FtsH complexes are the main proteases involved in D1 degradation in both cyanobacteria (Silva et al., 2003) and chloroplasts (Kato et al., 2009) and that the Deg and Clp proteases play a supplementary role (Kato and Sakamoto, 2018).

Regulation of FtsH Involved in Photosystem II Repair

Several proteins associated with the thylakoid membranes are reported to regulate FtsH activity. Psb29 from *Synechocystis* plays an important role in the accumulation of FtsH. Psb29 is a "pin" shaped protein that is needed for formation of the FtsH2/FtsH3 complex (Bečková et al., 2017). *Synechocystis* mutants lacking Psb29 are more susceptible to light stress, although not as severe as that of the FtsH2 deletion mutant. Psb29 interacts with FtsH2/FtsH3 complexes *in vivo*, however, the regulatory mechanism requires further investigation. THF1, which is the ortholog of Psb29 in plants, appears to play an equivalent role as levels of FtsH in *Arabidopsis* mutants lacking THF1 are also repressed, and the plants exhibit defective thylakoid formation and leaf variegation (Wang et al., 2004; Huang et al., 2013).

EngA is a GTPase that directly interacts with FtsH complexes. Its abundance negatively correlates with FtsH activities (Kato et al., 2018) so that *Arabidopsis* mutants over-expressing EngA display a leaf-variegation phenotype that is comparable to the FtsH-deficient *var* mutants (Chen et al., 2000; Takechi et al., 2000). Thylakoid FtsH exhibits a high turnover rate, especially under strong light (Zaltsman et al., 2005a; Li et al., 2017). EngA is therefore postulated to be a negative regulator acting on FtsH turnover (Kato et al., 2018).

FIP is a small thylakoid-anchored protein carrying a zinc-finger domain at the C-terminus (Lopes et al., 2018). It interacts with type A FtsH subunits in *Arabidopsis*, and possibly plays a role in assembly. The expression of FIP is downregulated when plants are exposed to abiotic stress, including excessive light, salt, oxidative agents and osmotic pressure. FIP knockdown mutants also display greater resilience to stress conditions. Hence, FIP negatively regulates FtsH activity. Unlike EngA mutants, over-expression of FIP does not result in aberrant plant development (Wang et al., 2017). Therefore, the impact of FIP on FtsH could be weaker. Further proteomic analysis on FIP mutants would help to clarify the role of FIP, as the initial report largely focused on a transcriptional analysis (Lopes et al., 2018).

The Potential Co-evolution of Photosystem II and FtsH

The FtsH-mediated PSII repair cycle is a conserved feature for efficient oxygenic photosynthesis (Shao et al., 2018). Thus, understanding the co-evolution of PSII and FtsH might provide insights into the origin of oxygenic photosynthesis. A recent phylogenetic analysis has revealed that the FtsH protease complex involved in PSII repair forms a separate clade and is independent of the clade of FtsH protease subunits found in extant anoxygenic photosynthetic bacteria (Shao et al., 2018). Hence, the evolution timeline of the FtsH protease involved in PSII repair seems to match the early origin of PSII (Shao et al., 2018). In addition, the branching of the phylogenetic tree for FtsH in phototrophic bacteria closely resembles that of the type I and type II reaction centers, supporting the gene duplication hypothesis of oxygenic photosynthesis instead of horizontal gene transfer (Shao et al., 2018).

RESPIRATION AND FtsH

FtsH Proteases Maintain Protein Quality in Mitochondria

Like chloroplasts, mitochondria are also organelles of prokaryotic origin that were acquired by a eukaryotic host via endosymbiosis (Osteryoung and Nunnari, 2003). Mitochondria are cellular powerhouses dedicated to the supply of cellular ATP through aerobic respiration (Bertram et al., 2006). The respiratory reactions, also known as oxidative phosphorylation (OXPHOS), take place in the inner membrane of mitochondria (Chaban et al., 2014). Respiratory complexes embedded in the mitochondrial inner membrane perform a series of redox reactions that lead to the reduction of molecular oxygen to water and the formation of a proton motive force across the membrane which is then used to produce ATP via the ATP synthase (Hatefi, 1985; Chaban et al., 2014). Respiratory complexes are also prone to oxidative stress and require maintenance (Remmen and Richardson, 2001; Sweetlove et al., 2002; Augustin et al., 2005).

FtsH proteases are found on both sides of the mitochondrial inner membrane, namely *m*-AAA and *i*-AAA, originally identified in studies on yeast (Thorsness et al., 1993; Guelin et al., 1994; Tzagoloff et al., 1994; Leonhard et al., 1996). The soluble domains of *m*-AAA are exposed to the inner matrix, whereas that of *i*-AAA face the intermembrane space (**Figure 4**; Leonhard et al., 1996; Steele and Glynn, 2019). Mitochondrial FtsH complexes target diverse substrates and exhibit functional overlap with other proteases. The maintenance

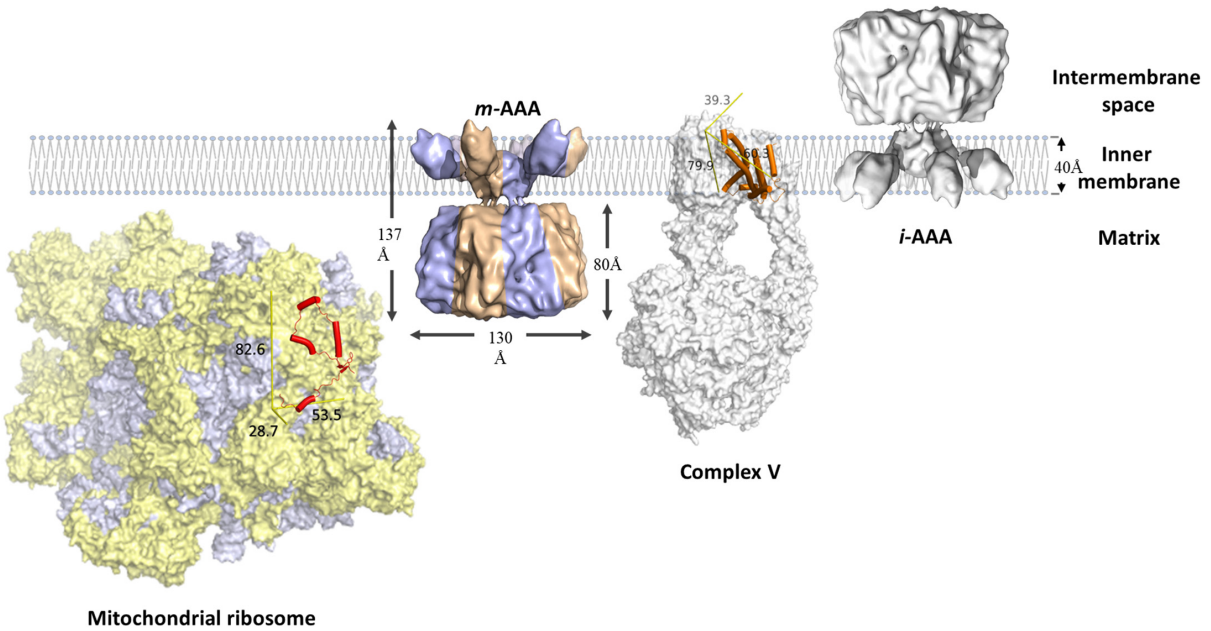

FIGURE 4 | Schematic representation of mitochondrial FtsH complexes. The *i*-AAA is a homocomplex facing the intermembrane space, the *m*-AAA is a heterocomplex (blue and bronze) facing the mitochondrial matrix. Both complexes are modeled using the cryo-EM structure of yeast *m*-AAA (Lee et al., 2011). The unassembled F_Oa (orange cylinders) subunit of respiratory complex V (PDB: 6CP6) is a membrane protein substrate of *m*-AAA. MrpL32 (red cylinders) is a subunit of the mitochondrial ribosome (PDB: 5MRC), which consists of protein (yellow) and RNA (purple-gray) components. MrpL32 is a soluble substrate that requires post-translational modification by *m*-AAA. The proteins are scaled using the membrane width as reference. The yellow reference rulers represent the dimension (unit: Å) of the Inertia Axis Aligned Bounding Box (IAAB) for the respective protein, which are calculated by Guardado-Calvo's Python scripts for pymol (https://pymolwiki.org/index.php/Draw_Protein_Dimensions).

of some respiratory complexes requires the participation of both *m*-AAA and *i*-AAA. For example, the stability of ATP synthase is reduced in *Arabidopsis* and yeast mutants lacking either *m*-AAA or *i*-AAA. However, *Arabidopsis* mutants lacking *i*-AAA retain the ability to degrade the unassembled *a* subunit of the ATP synthase (Marta et al., 2007). These results indicate that both FtsH complexes are involved in the assembly of ATP synthase, but *m*-AAA might be crucial for removal of damaged or unassembled ATP synthase subunits. Other respiratory proteins that require *m*-AAA-mediated maintenance include cytochrome bc_1 and cytochrome *c* oxidase (Guélin et al., 1996; Stiburek et al., 2012). The *m*-AAA protease also plays a crucial role in ribosomal protein biosynthesis. It facilitates post-translational maturation of MrpL32, a subunit of the mitochondrial ribosome that is essential to assemble functional ribosomes (Nolden et al., 2005).

i-AAA on the opposite side plays a crucial role in maintaining lipid metabolism in mitochondria. Phosphatidylethanolamine and cardiolipin constitute up to 50% of the phospholipid in the inner membrane (Calzada et al., 2016; Schlame and Greenberg, 2017; Tatsuta and Langer, 2017). However, their biosynthesis requires the phosphatidylserine and phosphatidic acid precursors to be transported across the intermembrane space (Calzada et al., 2016; Schlame and Greenberg, 2017; Tatsuta and Langer, 2017). *i*-AAA regulates membrane biogenesis via restricting the number of lipid transfer proteins, e.g., PRELID1 and STARD7 (Potting et al., 2010; Wai et al., 2016; Saita et al., 2018). *i*-AAA also regulates protein transport between the cytoplasm and mitochondria by selective removal of the TIM translocase (Baker et al., 2012; Spiller et al., 2015). The release of cytochrome *c* from mitochondria during cell apoptosis is also regulated by *i*-AAA (Jiang et al., 2014; Saita et al., 2017).

Functions and Regulation of Mitochondrial FtsH Complexes

Mitochondrial FtsH complexes are thought to have functional overlaps with other mitochondrial proteases, hence it is challenging to pinpoint the molecular targets of FtsH complexes (Patron et al., 2018). However, many links between FtsH mutations and diseases are well established through medical research (Karlberg et al., 2009; Gerdes et al., 2012; Patron et al., 2018). Human *i*-AAA mutations that destabilize complex formation lead to neuromuscular disorders including intellectual disability, motor developmental delay, optic atrophy, ataxia and movement deficiencies (Hartmann et al., 2016; Sprenger et al., 2019). Two types of *m*-AAA proteases are present in human: the AFG3L2 homocomplex and the AFG3L2/SPG7 heterocomplex (Martinelli et al., 2009; Tatsuta and Langer, 2009; Pierson et al., 2011). Recessive mutations in SPG7 (paraplegin) cause hereditary spastic paraplegia (HSP7) (Casari et al., 1998). The clinical features include weakness and spasticity of the lower limbs, loss of vibratory sense and urinary urgency (Patron et al., 2018). Mutations in AFG3L2 cause spinocerebellar ataxia type 28 (SCA28), a juvenile-onset disease featuring progressive gait

and limb ataxia with abnormal eye movement (Cagnoli et al., 2006; Di Bella et al., 2010). A potential explanation for these FtsH-related diseases is that impaired FtsH activities destabilize respiration performance, leading to reduced energy output. The development and operation of the nervous system is particularly energy dependent, hence mitochondrial FtsH dysfunction causes severe neurodegenerative diseases (Tymianski and Tator, 1996; Adamo et al., 1999; Langer, 2000; Lee and Bendayan, 2004).

In plants, several mitochondrial FtsH subunits are crucial to mitigate heat stress. For example, *Arabidopsis* mutants lacking FtsH11 fail to grow at 30°C (Janska et al., 2010). A similar phenomenon is observed in the maize *ndl-1* mutants (Liu et al., 2019). A striking discrepancy is that a phylogenetic analysis suggests Ndl-1 is an *m*-AAA protease closely related to FtsH3 and FtsH10 in *Arabidopsis*. However, *Arabidopsis* mutants lacking FtsH3 or FtsH10 display a wild-type-like phenotype, and the mutants lacking both proteins only exhibit a minor growth defect, i.e., smaller size and shorter roots (Kolodziejczak et al., 2018; Liu et al., 2019). FtsH11 in *Arabidopsis* belongs to the *i*-AAA group, therefore, Ndl-1 and FtsH11 should be localized on the opposite side of the mitochondrial inner membrane. This apparent inconsistency in phenotype between the two plant species might reflect functional divergence of the FtsH proteases during evolution.

Prohibitins and stomatins are prominent modulators of the activities of mitochondrial FtsH proteases. As membrane scaffolding proteins, they act on the ultrastructure and dynamics of mitochondrial inner membranes (Artal-Sanz and Tavernarakis, 2009; Ikon and Ryan, 2017). Mutagenesis studies show that the activity of *m*-AAA is negatively correlated to the abundance of prohibitins (Koppen et al., 2007; Piechota et al., 2010). On the opposite side of the membrane, *i*-AAA complexes form super-complexes with stomatins (Wai et al., 2016). It is postulated that stomatins play a similar modulator role to prohibitins in regulating *i*-AAA activity in the intermembrane space (Wai et al., 2016). The molecular interactions between mitochondrial FtsH complexes and prohibitins or stomatins could be similar to that recently described for the interaction between *E. coli* HflK/C and FtsH (Yokoyama and Matsui, 2020; Ma et al., 2022).

EVOLUTION AND DIVERGENCE OF FtsH IN OXYGENIC PHOTOSYNTHETIC ORGANISMS

Photosynthetic Organisms Contain Diverse FtsH Complexes

Phylogeny mapping of 6,028 FtsH orthologs from 3,100 species has revealed that cyanobacteria carry ∼4 FtsH homologs per genome, the highest number among prokaryotes. Whereas the average number of FtsH homologs in fungal genomes is 2; that of animals is 4 and that of photosynthetic eukaryotes is 8 (Shao et al., 2018). This phylogenetic analysis concluded that FtsH orthologs cluster into three groups, Group 1 contains most bacterial and photosynthesis-related FtsH, Group 2 contains *m*-AAA forming homologs, Group 3 contains *i*-AAA-related FtsH and FtsHi (**Figure 5**). However, there are exceptions, e.g., FtsHi3 from *Arabidopsis* belongs to Group 2. Therefore, the FtsHi proteases in plants have a mixed ancestry.

FtsH in Cyanobacteria

Cyanobacteria are a phylum of prokaryotes that perform oxygenic photosynthesis. It is widely accepted that chloroplasts in algae and plants are derived from an ancient cyanobacterium via endosymbiosis (Raven and Allen, 2003; Sakamoto et al., 2004; Kutschera and Niklas, 2005; Ayuso-Tejedor et al., 2010; Falcón et al., 2010). Like chloroplasts, cyanobacteria feature a thylakoid membrane system where photosynthesis takes place. Three classes of FtsH complexes are present in the *Synechocystis* model, the FtsH1/FtsH3 complex is present in cytoplasmic membranes and regulates iron acquisition (Boehm et al., 2012; Krynická et al., 2014, 2019); FtsH2/FtsH3 is anchored in the thylakoid membranes and is involved in PSII repair, osmoregulation and inorganic carbon assimilation (Stirnberg et al., 2007; Zhang et al., 2007; Boehm et al., 2012); the FtsH4 homocomplex is also located in the thylakoid membranes but its function is not yet clear (Silva et al., 2003; Boehm et al., 2012; Krynická et al., 2014; Sacharz et al., 2015).

In spite of different cellular localizations, FtsH1 and FtsH2 share the highest sequence identity and are both categorized as type B FtsH; while their partner FtsH3 resembles the type A FtsH subunits described for *Arabidopsis* (Sakamoto et al., 2003; Bečková et al., 2017). In both cyanobacteria and plants, disruption of type B FtsH leads to a dramatic reduction in levels of the thylakoid type A subunit (Sakamoto et al., 2003; Boehm et al., 2012). The speculation is that unassembled FtsH subunits are prone to degradation, hence unable to accumulate in the thylakoid membranes (Boehm et al., 2012). This hypothesis is further strengthened by the work on the FtsH1/FtsH3 complex, in which controlled repression of FtsH3 also led to a reduction in FtsH1 levels in *Synechocystis* (Krynická et al., 2014).

The physiological function of FtsH4 is not yet clear. Confocal microscopy of mutants expressing GFP-tagged FtsH4 revealed that FtsH4 is exclusively localized in the thylakoid membranes (Krynická et al., 2014; Sacharz et al., 2015). However, deletion of FtsH4 has not yet yielded a distinctive phenotype (Mann et al., 2000; Bailey et al., 2001). We speculate that FtsH4 could be a "failsafe" option for a broad range of degradants, which are predominantly removed via other proteases than the AAA + family of proteases. Hence probing the function of FtsH4 might require disruption of multiple proteases. Biochemical analysis shows that although the thylakoid membranes contain FtsH2, FtsH3, and FtsH4 subunits, the pairing of the protomers to produce hexameric complexes is strictly controlled by the FtsH type; no FtsH4 heterocomplexes have been reported.

FtsH in Algae and Plants

Photosynthetic eukaryotes contain increased numbers of FtsH subunits. Green algae are the evolutionary link between cyanobacteria and plants, hence it is unsurprising that the number of FtsH homologs in algae is more than that of

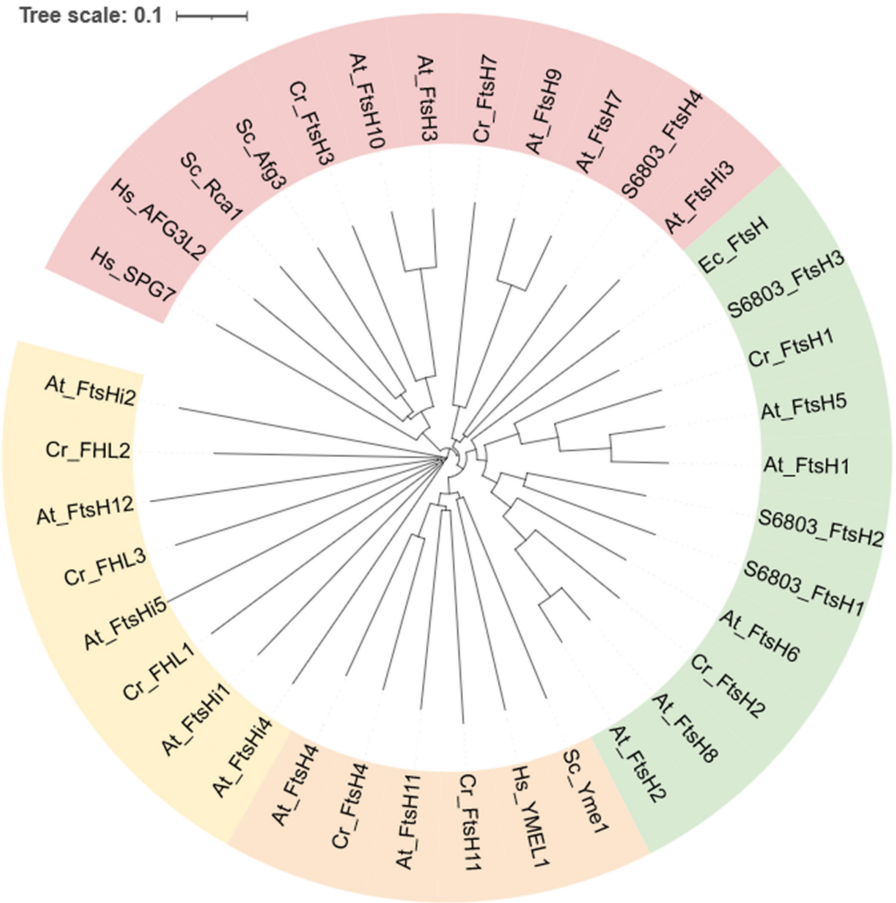

FIGURE 5 | Phylogenetic analysis of FtsH orthologs from selected species. Annotations are: FtsH from *Escherichia coli* (begins with "Ec"), *Synechocystis* sp. PCC 6803 (begins with "S6803"), *Saccharomyces cerevisiae* S288C (begins with "Sc"), *Homo sapiens* (begins with "Hs"), *Chlamydomonas reinhardtii* (begins with "Cr"), and *Arabidopsis thaliana* (begins with "At"). Homologs with pale-green background correspond to Group1, that of pink correspond to Group2, orange and yellow correspond to Group3 as designated in the Shao et al. (2018) article. The tree was generated using MUSCLE (https://www.ebi.ac.uk/Tools/msa/muscle/). The sequences of At_FtsH were obtained from Tair (https://www.arabidopsis.org/index.jsp), and that of Cr_FtsH were collected from Phytozome *Chlamydomonas reinhardtii* v5.6 (https://phytozome-next.jgi.doe.gov). The remaining sequences were collected from NCBI (https://www.ncbi.nlm.nih.gov/protein/). The information was accessed on November 10, 2021.

cyanobacteria and fewer than plants. For instance, the model green alga *C. reinhardtii* encodes six FtsH and three FtsHi homologs (Malnoë et al., 2014; Mishra and Funk, 2021; Zou and Bozhkov, 2021). FtsHi (recently reviewed by Mishra and Funk, 2021) represents a clade of FtsH with inactivated proteolytic capacity. Among the six homologs, CrFtsH1 and CrFtsH2 are involved in the quality control of thylakoid membrane proteins, such as the repair of PSII and the removal of cytochrome b_6f (Malnoë et al., 2014; Bujaldon et al., 2017; Wang et al., 2017).

In *A. thaliana*, 12 FtsH and 5 FtsHi homologs have been identified (Wagner et al., 2012). They form five paired branches in the phylogram: AtFtsH1/5, AtFtsH2/8, AtFtsH7/9, AtFtsH3/10, and AtFtsH4/11 (**Figure 5**). The FtsH isoforms of each pair are functionally redundant and structurally interchangeable, except for the AtFtsH4/11 pair (Janska et al., 2010; Wagner et al., 2012; Mishra and Funk, 2021). Numerous studies have been conducted to elucidate the functions of each FtsH homolog (results summarized in **Table 1**).

Five FtsH homologs are localized on the thylakoid membrane. AtFtsH1 and 5 belong to type A FtsH and AtFtsH2 and 8 are type B (Wagner et al., 2012). Together, they form heterocomplexes responsible for PSII repair (Kato and Sakamoto, 2018). AtFtsH2 and AtFtsH5 are the dominant isoforms in thylakoid membranes; disruption of either homolog leads to leaf-variegation phenotypes (Chen et al., 2000; Takechi et al., 2000; Sakamoto et al., 2002; Zaltsman et al., 2005b). Mutants lacking AtFtsH1 and AtFtsH8 do not display a clear change in phenotype to WT, however, dual disruption of AtFtsH1/5 or AtFtsH2/8 produces mutants with severe albino-like leaves. Hence, AtFtsH1 and 8 contribute to activity, but are insufficient to substitute for the dominant isoform (Wagner et al., 2012). Over-expression of AtFtsH8 can complement the loss of functional AtFtsH2, indicating the physiological impact of AtFtsH8 is restricted by its quantity in the wild-type plants (Yu et al., 2004).

The import of FtsH into the chloroplast and insertion into the thylakoid membrane is determined by the N-terminal

TABLE 1 | Summary of the phenotypes from FtsH mutants of *Arabidopsis thaliana*.

Genotype	FtsH location	Phenotype	Reference(s)
ftsH1 (typeA) null	Thylakoid membrane	WT-like phenotype	Sakamoto et al., 2003; Zaltsman et al., 2005b
ftsH5 (type A) null	Thylakoid membrane	Weak leaf variegation (var1)	Sakamoto et al., 2002; Wagner et al., 2011
ftsH1, *ftsH5* null	Thylakoid membrane	Albino-like, embryo lethality, loss of photoautotrophic growth	Yu et al., 2004, 2005; Zaltsman et al., 2005b
ftsH2 (type B) null	Thylakoid membrane	Yellow variegated 2 (var2) severe leaf variegation	Chen et al., 2000; Takechi et al., 2000; Bailey et al., 2002; Wagner et al., 2011
ftsH8 (type B) null	Thylakoid membrane	WT-like phenotype	Sakamoto et al., 2003; Zaltsman et al., 2005b; Wagner et al., 2011
ftsH2, *ftsH8* null	Thylakoid membrane	Albino-like, embryo lethality, loss of photoautotrophic growth	Yu et al., 2004, 2005; Zaltsman et al., 2005b
ftsH1, *ftsH8* null	Thylakoid membrane	WT-like phenotype	Zaltsman et al., 2005b
ftsH6 null	Thylakoid membrane	Enhanced heat-tolerance and thermomemory	Sedaghatmehr et al., 2016
ftsH7 null	Chloroplast envelope	WT-like phenotype	Wagner et al., 2011
ftsH9 null	Chloroplast envelope	Unknown	Ferro et al., 2010; Wagner et al., 2011
ftsH12 null	Chloroplast envelope	Embryo lethality	Ferro et al., 2010
ftsHi1 null	Chloroplast envelope	Embryo lethality	Kadirjan-Kalbach et al., 2012; Mishra et al., 2019
ftsHi1 missense mutant	Chloroplast envelope	Pale seedling	Kadirjan-Kalbach et al., 2012; Mishra et al., 2019
ftsHi2 null	Chloroplast envelope	Embryo lethality	Schreier et al., 2018; Mishra et al., 2019
ftsHi3 null	Chloroplast envelope	Residual albino growth	Kikuchi et al., 2018
ftsHi4 null	Chloroplast envelope or thylakoid membrane	Embryo lethality	Lu et al., 2014; Mishra et al., 2019
ftsHi5 null	Chloroplast envelope	Embryo lethality	Wang et al., 2018; Mishra et al., 2019
ftsH11 (*i*-AAA) null	Chloroplast envelope	Reduced heat-tolerance	Urantowka et al., 2005; Chen et al., 2006; Wagner et al., 2011, 2016
ftsH4 (*i*-AAA) null	Mitochondrial inner membrane	Abnormal leaf morphology in late rosette development under short-day conditions	Gibala et al., 2009; Wagner et al., 2011
ftsH3 (*m*-AAA) null	Mitochondrial inner membrane	WT-like phenotype	Piechota et al., 2010; Wagner et al., 2011
ftsH10 (*m*-AAA) null	Mitochondrial inner membrane	WT-like phenotype	Piechota et al., 2010; Wagner et al., 2011
ftsH3, *ftsH10* null	Mitochondrial inner membrane	Decreased size of seedlings and developmental delay	Kolodziejczak et al., 2018

sequence. Type A FtsH subunits are inserted via the secretion pathway (Sec), which inserts unfolded proteins into the membrane; however, type B FtsH subunits are inserted via the twin-arginine translocation pathway (TAT), which transports fully folded protein across the membrane (Rodrigues et al., 2011). *In vitro* import studies suggest that the mature thylakoid FtsH subunits from *Arabidopsis* might contain a single transmembrane alpha helix (Rodrigues et al., 2011) rather than the two transmembrane helices predicted for cyanobacterial FtsH subunits based on N-terminal sequencing of the protein subunits (Boehm et al., 2012).

The role of thylakoid AtFtsH6 remain elusive, despite its wide conservation in plants (Sun et al., 2006; Johnson et al., 2014; Yu et al., 2014; Xue et al., 2015). AtFtsH6 is rapidly induced under heat stress, and is involved in the degradation of heat-shock protein HSP21 (Sedaghatmehr et al., 2016). Mutants lacking AtFtsH6 are reported to display stronger thermomemory and thermotolerance, but the phenotype is weak (Sedaghatmehr et al., 2016).

In *Arabidopsis*, the following FtsH isoforms are anchored in the chloroplast envelope membrane: FtsH7, 9, 12 and FtsHi1-i5 (Kadirjan-Kalbach et al., 2012; Wagner et al., 2012; Mishra et al., 2019). Notably, FtsH7, 9 and i3 are members of the Group 2 clade (**Figure 5**). Both FtsH7 and FtsH9 contain an additional protease domain between the second transmembrane helix and the ATPase domain. FtsHi3 also contains a protease domain upstream of the ATPase domain, however, its zinc-binding catalytic site is missing, and the C-terminal protease domain is also lost (Mishra and Funk, 2021). Mutants lacking AtFtsH7 retain a wild-type-like phenotype and the function of AtFtsH9 is unclear (Wagner et al., 2011). In contrast, the remaining FtsH homologs found in the chloroplast envelope membrane are essential for embryogenesis (Wagner et al., 2012; Mishra and Funk, 2021).

In *Arabidopsis*, FtsHi1, 2, 4, and 5 lack the HEXXH motif necessary for substrate degradation (**Figure 1**); whereas the entire protease-inactive domain of FtsHi3 is relocated upstream of the ATPase domain (Wagner et al., 2012; Mishra and Funk, 2021).

FtsH12 and FtsHi have been speculated to form complexes, because the mortality rate of a FtsH12 knockout mutant is comparable to that of FtsHi2, 4, and 5 single mutants (Ferro et al., 2010; Wagner et al., 2012). Four FtsHi (FtsHi1, 2, 4, and 5) have been confirmed to form complexes with Ycf2 and AtFtsH12 on the stroma-side of the chloroplast envelope and are thought to be involved in substrate transport (Kikuchi et al., 2018). Interestingly, Ycf2 is a distant relative of FtsH that has remained encoded by the chloroplast genome (Downie et al., 1994; Bungard, 2004). A phylogenetic analysis of Ycf2 suggests the gradual loss of the protease catalytic site during evolution, and the enlargement of the soluble region between the two transmembrane helices (Kikuchi et al., 2018).

AtFtsH3/4/10 are found in mitochondria. AtFtsH3 and AtFtsH10 are *m*-AAA proteases that form both homo- and heterocomplexes (Janska et al., 2010). Surprisingly, neither of them is essential for growth under optimal conditions (Wagner et al., 2012). AtFtsH4 and AtFtsH11 are related to *i*-AAA, and are present as homocomplexes in mitochondria (Janska et al., 2010). AtFtsH4-deficient mutants develop a distinct asymmetric shape and irregular serration of expanding leaf blades (Gibala et al., 2009). Despite being paired with AtFtsH4, AtFtsH11 was thought to be targeted to both mitochondria and chloroplasts (Urantowka et al., 2005), however, recent work suggests that AtFtsH11 is exclusively targeted to the chloroplast envelope (Ferro et al., 2010; Wagner et al., 2016). Mutants lacking AtFtsH11 are sensitive to high temperature with growth arrested at 30°C (Janska et al., 2010).

In summary, FtsH homologs in plants preserve genetic redundancy, functional overlap, and structural plasticity to deliver diverse functions. The functional redundancy among isoforms enables FtsH homologs to adapt to emerging environmental demands, resulting in a robust and flexible system to maintain cellular homeostasis through evolution.

OUTLOOK

The FtsH family of proteases are versatile tools to regulate diverse pathways by removing both soluble and membrane-bound proteins (Kihara et al., 1995; Tomoyasu et al., 1995; Silva et al., 2003; Krynická et al., 2014). FtsH is proficient in maintaining membrane protein quality, hence plays a crucial role in energy metabolism, including photosynthesis and respiration. FtsH functions as a hexameric complex, with the type of protomer defining substrate specificity. The proteolytic activities can be further adjusted by modulator proteins. The molecular mechanisms that regulate FtsH activities at multiple levels make the FtsH-mediated proteolysis system reliable and adaptable.

The cellular localization and subunit composition of many FtsH complexes have been determined. However, we think the following questions could be important to address in the future. The first question is how the composition of FtsH complexes is controlled. Mutagenesis studies have revealed that the protease domain is important to prevent formation of undesirable protomer pairing, however, the protease domain is also variable across species. The high-resolution structures of intact FtsH complexes have not yet been determined but will be crucial for understanding how specific protomers are selected for assembly into heterocomplexes.

The second question is how substrates are targeted for degradation. Although a structure of a FtsH complex has been determined with a target protein stuck in the proteolytic chamber (Puchades et al., 2017), there is still no structural information regarding the entry of substrates through the central pore of the ATPase domain.

The third question is how the proteolytic activity of FtsH complexes is regulated. Despite recent advances in the structural analysis of the HflK/C-FtsH super-complex (Ma et al., 2022), the molecular mechanisms that modulate FtsH activities in the thylakoid and mitochondrial inner membrane remain unclear. In particular, further investigations are required to verify the role of prohibitins in photosynthetic and eukaryotic organisms.

AUTHOR CONTRIBUTIONS

LY participated in drafting the manuscript and offered first authorship. BL helped with project management and data analysis, offered second authorship. PN was an expert in this field, and gave guidance and support and helped draft the manuscript. JY supervised LY, worked together to craft the manuscript. FC was the team leader that brought all resources together for this project. PN, JY, and FC agreed to share correspondence. All authors contributed to the article and approved the submitted version.

FUNDING

This work was funded by the National Natural Science Foundation of China (Grant No. 31901624), Natural Science Foundation of Shandong Province (Grant No. ZR2019BC068), Guangdong Province Zhujiang Talent Program (Grant No. 2019ZT08H476), Shenzhen Science and Technology Program (Grant No. KQTD20180412181334790), the Innovation Team Project of Universities in Guangdong Province (Grant No. 2020KCXTD023), and the Biotechnology and Biological Sciences Research Council (Grant Nos. BB/R003211/1 and BB/N016807/1).

REFERENCES

Adam, Z., Zaltsman, A., Sinvany-Villalobo, G., and Sakamoto, W. (2005). FtsH proteases in chloroplasts and cyanobacteria. *Physiol. Plant.* 123, 386–390. doi: 10.1111/j.1399-3054.2004.00436.x

Adamo, A. M., Pasquini, L. A., Moreno, M. B., Oteiza, P. I., Soto, E. F., and Pasquini, J. M. (1999). Effect of oxidant systems on the ubiquitylation of proteins in the central nervous system. *J. Neurosci. Res.* 55, 523–531. doi: 10.1002/(SICI)1097-4547(19990215)55:4<523::AID-JNR12<3.0.CO;2-Q

Akiyama, Y. (2009). Quality Control of Cytoplasmic Membrane Proteins in *Escherichia coli*. *J. Biochem.* 146, 449–454. doi: 10.1093/jb/mvp071

Akiyama, Y., Kihara, A., Tokuda, H., and Ito, K. (1996). FtsH (HflB) Is an ATP-dependent Protease Selectively Acting on SecY and Some Other Membrane Proteins*. *J. Biol. Chem.* 271, 31196–31201. doi: 10.1074/jbc.271.49.31196

Akiyama, Y., Yoshihisa, T., and Ito, K. (1995). FtsH, a Membrane-bound ATPase, Forms a Complex in the Cytoplasmic Membrane of *Escherichia coli*(*). *J. Biol. Chem.* 270, 23485–23490. doi: 10.1074/jbc.270.40.23485

Anbudurai, P., Mor, T. S., Ohad, I., Shestakov, S. V., and Pakrasi, H. B. (1994). The ctpA gene encodes the C-terminal processing protease for the D1 protein of the photosystem II reaction center complex. *Proc. Natl. Acad. Sci. U S A.* 91, 8082–8086. doi: 10.1073/pnas.91.17.8082

Aro, E.-M., Virgin, I., and Andersson, B. (1993). Photoinhibition of photosystem II. Inactivation, protein damage and turnover. *Biochim. Biophys. Acta Bioenerg.* 1143, 113–134. doi: 10.1016/0005-2728(93)90134-2

Artal-Sanz, M., and Tavernarakis, N. (2009). Prohibitin and mitochondrial biology. *Trends Endocrinol. Metab.* 20, 394–401. doi: 10.1016/j.tem.2009.04.004

Augustin, S., Nolden, M., Müller, S., Hardt, O., Arnold, I., and Langer, T. (2005). Characterization of Peptides Released from Mitochondria: EVIDENCE FOR CONSTANT PROTEOLYSIS AND PEPTIDE EFFLUX*. *J. Biol. Chem.* 280, 2691–2699. doi: 10.1074/jbc.M410609200

Ayuso-Tejedor, S., Nishikori, S., Okuno, T., Ogura, T., and Sancho, J. (2010). FtsH cleavage of non-native conformations of proteins. *J. Struct. Biol.* 171, 117–124. doi: 10.1016/j.jsb.2010.05.001

Bailey, S., Silva, P., Nixon, P., Mullineaux, C., Robinson, C., and Mann, N. (2001). Auxiliary functions in photosynthesis: the role of the FtsH protease. *Biochem. Soc. Trans.* 29, 455–459. doi: 10.1042/bst0290455

Bailey, S., Thompson, E., Nixon, P. J., Horton, P., Mullineaux, C. W., Robinson, C., et al. (2002). A Critical Role for the Var2 FtsH Homologue of *Arabidopsis thaliana* in the Photosystem II Repair Cycle in *Vivo*. *J. Biol. Chem.* 277, 2006–2011. doi: 10.1074/jbc.M105878200

Baker, M. J., Mooga, V. P., Guiard, B., Langer, T., Ryan, M. T., and Stojanovski, D. (2012). Impaired folding of the mitochondrial small TIM chaperones induces clearance by the *i*-AAA protease. *J. Mol. Biol.* 424, 227–239. doi: 10.1016/j.jmb.2012.09.019

Barker, M., de Vries, R., Nield, J., Komenda, J., and Nixon, P. J. (2006). The deg proteases protect *Synechocystis* sp. PCC 6803 during heat and light stresses but are not essential for removal of damaged D1 protein during the photosystem two repair cycle. *J. Biol. Chem.* 281, 30347–30355. doi: 10.1074/jbc.M601064200

Bečková, M., Yu, J., Krynická, V., Kozlo, A., Shao, S., Koník, P., et al. (2017). Structure of Psb29/Thf1 and its association with the FtsH protease complex involved in photosystem II repair in cyanobacteria. *Philos. Trans. R. Soc. Lond. B. Biol. Sci.* 372:20160394. doi: 10.1098/rstb.2016.0394

Bertram, R., Pedersen, M. G., Luciani, D. S., and Sherman, A. (2006). A simplified model for mitochondrial ATP production. *J. Theor. Biol.* 243, 575–586. doi: 10.1016/j.jtbi.2006.07.019

Bieniossek, C., Niederhauser, B., and Baumann, U. M. (2009). The crystal structure of *apo*-FtsH reveals domain movements necessary for substrate unfolding and translocation. *Proc. Natl. Acad. Sci. U S A.* 106, 21579–21584. doi: 10.1073/pnas.0910708106

Bieniossek, C., Schalch, T., Bumann, M., Meister, M., Meier, R., and Baumann, U. (2006). The molecular architecture of the metalloprotease FtsH. *Proc. Natl. Acad. Sci. U S A.* 103, 3066–3071. doi: 10.1073/pnas.0600031103

Boehm, M., Yu, J., Krynicka, V., Barker, M., Tichy, M., Komenda, J., et al. (2012). Subunit organization of a *Synechocystis* hetero-oligomeric thylakoid FtsH complex involved in photosystem II repair. *Plant Cell* 24, 3669–3683. doi: 10.1105/tpc.112.100891

Bricker, T. M., Mummadisetti, M. P., and Frankel, L. K. (2015). Recent advances in the use of mass spectrometry to examine structure/function relationships in photosystem II. *J. Photochem. Photobiol. B Biol.* 152, 227–246. doi: 10.1016/j.jphotobiol.2015.08.031

Bujaldon, S., Kodama, N., Rappaport, F., Subramanyam, R., de Vitry, C., Takahashi, Y., et al. (2017). Functional accumulation of antenna proteins in chlorophyll b-less mutants of *Chlamydomonas reinhardtii*. *Mol. Plant* 10, 115–130. doi: 10.1016/j.molp.2016.10.001

Bungard, R. A. (2004). Photosynthetic evolution in parasitic plants: insight from the chloroplast genome. *Bioessays* 26, 235–247. doi: 10.1002/bies.10405

Butenko, Y., Lin, A., Naveh, L., Kupervaser, M., Levin, Y., Reich, Z., et al. (2018). Differential Roles of the Thylakoid Lumenal Deg Protease Homologs in Chloroplast Proteostasis. *Plant Physiol.* 178, 1065–1080. doi: 10.1104/pp.18.00912

Cagnoli, C., Mariotti, C., Taroni, F., Seri, M., Brussino, A., Michielotto, C., et al. (2006). SCA28, a novel form of autosomal dominant cerebellar ataxia on chromosome 18p11.22-q11.2. *Brain* 129, 235–242. doi: 10.1093/brain/awh651

Calzada, E., Onguka, O., and Claypool, S. M. (2016). Phosphatidylethanolamine Metabolism in Health and Disease. *Int. Rev. Cell Mol. Biol.* 321, 29–88. doi: 10.1016/bs.ircmb.2015.10.001

Cardona, T., Sánchez-Baracaldo, P., Rutherford, A. W., and Larkum, A. W. (2019). Early Archean origin of photosystem II. *Geobiology* 17, 127–150. doi: 10.1111/gbi.12322

Carvalho, V., Prabudiansyah, I., Kovacik, L., Chami, M., Kieffer, R., van der Valk, R., et al. (2021). The cytoplasmic domain of the AAA+ protease FtsH is tilted with respect to the membrane to facilitate substrate entry. *J. Biol. Chem.* 296:100029. doi: 10.1074/jbc.RA120.014739

Casari, G., De Fusco, M., Ciarmatori, S., Zeviani, M., Mora, M., Fernandez, P., et al. (1998). Spastic paraplegia and OXPHOS impairment caused by mutations in paraplegin, a nuclear-encoded mitochondrial metalloprotease. *Cell* 93, 973–983. doi: 10.1016/s0092-8674(00)81203-9

Chaban, Y., Boekema, E. J., and Dudkina, N. V. (2014). Structures of mitochondrial oxidative phosphorylation supercomplexes and mechanisms for their stabilisation. *Biochim. Biophys. Acta Bioenerg.* 1837, 418–426. doi: 10.1016/j.bbabio.2013.10.004

Chen, J., Burke, J. J., Velten, J., and Xin, Z. (2006). FtsH11 protease plays a critical role in Arabidopsis thermotolerance. *Plant J.* 48, 73–84. doi: 10.1111/j.1365-313X.2006.02855.x

Chen, M., Choi, Y., Voytas, D. F., and Rodermel, S. (2000). Mutations in the Arabidopsis VAR2 locus cause leaf variegation due to the loss of a chloroplast FtsH protease. *Plant J.* 22, 303–313. doi: 10.1046/j.1365-313x.2000.00738.x

Chu, C.-Y., Stewart, P. E., Bestor, A., Hansen, B., Lin, T., Gao, L., et al. (2016). Function of the *Borrelia burgdorferi* FtsH homolog is essential for viability both in vitro and in vivo and independent of HflK/C. *MBio* 7, e00404–e00416. doi: 10.1128/mBio.00404-16

Di Bella, D., Lazzaro, F., Brusco, A., Plumari, M., Battaglia, G., Pastore, A., et al. (2010). Mutations in the mitochondrial protease gene AFG3L2 cause dominant hereditary ataxia SCA28. *Nat. Genet.* 42, 313–321. doi: 10.1038/ng.544

Downie, S. R., Katz-Downie, D. S., Wolfe, K. H., Calie, P. J., and Palmer, J. D. (1994). Structure and evolution of the largest chloroplast gene (ORF2280): internal plasticity and multiple gene loss during angiosperm evolution. *Curr. Genet.* 25, 367–378. doi: 10.1007/BF00351492

Edelman, M., and Mattoo, A. K. (2008). D1-protein dynamics in photosystem II: the lingering enigma. *Photosynthesis Res.* 98, 609–620. doi: 10.1007/s11120-008-9342-x

Falcón, L. I., Magallón, S., and Castillo, A. (2010). Dating the cyanobacterial ancestor of the chloroplast. *ISME J.* 4, 777–783. doi: 10.1038/ismej.2010.2

Ferro, M., Brugière, S., Salvi, D., Seigneurin-Berny, D., Court, M., Moyet, L., et al. (2010). AT_CHLORO, a comprehensive chloroplast proteome database with subplastidial localization and curated information on envelope proteins. *Mol. Cell. Proteomics* 9, 1063–1084. doi: 10.1074/mcp.M900325-MCP200

Gehl, B., and Sweetlove, L. J. (2014). Mitochondrial Band-7 family proteins: scaffolds for respiratory chain assembly? *Front. Plant Sci.* 5:141. doi: 10.3389/fpls.2014.00141

Gerdes, F., Tatsuta, T., and Langer, T. (2012). Mitochondrial AAA proteases—towards a molecular understanding of membrane-bound proteolytic machines. *Biochim. Biophys. Acta Mol. Cell. Res.* 1823, 49–55. doi: 10.1016/j.bbamcr.2011.09.015

Gibala, M., Kicia, M., Sakamoto, W., Gola, E. M., Kubrakiewicz, J., Smakowska, E., et al. (2009). The lack of mitochondrial AtFtsH4 protease alters Arabidopsis leaf morphology at the late stage of rosette development under short-day photoperiod. *Plant J.* 59, 685–699. doi: 10.1111/j.1365-313X.2009.03907.x

Giménez, M. I., Cerletti, M., and De Castro, R. E. (2015). Archaeal membrane-associated proteases: insights on *Haloferax volcanii* and other haloarchaea. *Front. Microbiol.* 6:39. doi: 10.3389/fmicb.2015.00039

Graef, M., Seewald, G., and Langer, T. (2007). Substrate Recognition by AAA+ ATPases: Distinct Substrate Binding Modes in ATP-Dependent Protease Yme1

of the Mitochondrial Intermembrane Space. *Mol. Cell. Biol.* 27, 2476–2485. doi: 10.1128/MCB.01721-06

Guelin, E., Rep, M., and Grivell, L. A. (1994). Yeast sequencing reports. Sequence of the *AFG3* gene encoding a new member of the FtsH/Yme1/Tma subfamily of the AAA-protein family. *Yeast* 10, 1389–1394. doi: 10.1002/yea.320101016

Guélin, E., Rep, M., and Grivell, L. A. (1996). Afg3p, a mitochondrial ATP-dependent metalloprotease, is involved in degradation of mitochondrially-encoded Cox1, Cox3, Cob, Su6, Su8 and Su9 subunits of the inner membrane complexes III, IV and V. *FEBS Lett.* 381, 42–46. doi: 10.1016/0014-5793(96)00074-9

Hartmann, B., Wai, T., Hu, H., MacVicar, T., Musante, L., Fischer-Zirnsak, B., et al. (2016). Homozygous YME1L1 mutation causes mitochondriopathy with optic atrophy and mitochondrial network fragmentation. *Elife* 5:e16078. doi: 10.7554/eLife.16078

Hatefi, Y. (1985). The mitochondrial electron transport and oxidative phosphorylation system. *Annu. Rev. Biochem.* 54, 1015–1069. doi: 10.1146/annurev.bi.54.070185.005055

Herman, C., Ogura, T., Tomoyasu, T., Hiraga, S., Akiyama, Y., Ito, K., et al. (1993). Cell growth and lambda phage development controlled by the same essential *Escherichia coli* gene, *fts*H/*hfl*B. *Proc. Natl. Acad. Sci. U S A.* 90:10861. doi: 10.1073/pnas.90.22.10861

Huang, W., Chen, Q., Zhu, Y., Hu, F., Zhang, L., Ma, Z., et al. (2013). *Arabidopsis thylakoid* formation 1 is a critical regulator for dynamics of PSII–LHCII complexes in leaf senescence and excess light. *Mol. Plant* 6, 1673–1691. doi: 10.1093/mp/sst069

Huesgen, P. F., Schuhmann, H., and Adamska, I. (2006). Photodamaged D1 protein is degraded in *Arabidopsis* mutants lacking the Deg2 protease. *FEBS Lett.* 580, 6929–6932. doi: 10.1016/j.febslet.2006.11.058

Ikon, N., and Ryan, R. O. (2017). Cardiolipin and mitochondrial cristae organization. *Biochim. Biophys. Acta Biomembr.* 1859, 1156–1163. doi: 10.1016/j.bbamem.2017.03.013

Ito, K., and Akiyama, Y. (2005). Cellular functions, mechanism of action, and regulation of FtsH protease. *Annu. Rev. Microbiol.* 59, 211–231. doi: 10.1146/annurev.micro.59.030804.121316

Jansen, M. A., Gaba, V., Greenberg, B. M., Mattoo, A. K., and Edelman, M. (1996). Low threshold levels of ultraviolet-B in a background of photosynthetically active radiation trigger rapid degradation of the D2 protein of photosystem-II. *Plant J.* 9, 693–699. doi: 10.1046/j.1365-313X.1996.9050693.x

Jansen, M. A., Mattoo, A. K., and Edelman, M. (1999). D1-D2 protein degradation in the chloroplast: Complex light saturation kinetics. *Eur. J. Biochem.* 260, 527–532. doi: 10.1046/j.1432-1327.1999.00196.x

Janska, H., Kwasniak, M., and Szczepanowska, J. (2013). Protein quality control in organelles — AAA/FtsH story. *Biochim. Biophys. Acta Mol. Cell. Res.* 1833, 381–387. doi: 10.1016/j.bbamcr.2012.03.016

Janska, H., Piechota, J., and Kwasniak, M. (2010). ATP-dependent proteases in biogenesis and maintenance of plant mitochondria. *Biochim. Biophys. Acta Bioenerg.* 1797, 1071–1075. doi: 10.1016/j.bbabio.2010.02.027

Jiang, X., Jiang, H., Shen, Z., and Wang, X. (2014). Activation of mitochondrial protease OMA1 by Bax and Bak promotes cytochrome c release during apoptosis. *Proc. Natl. Acad. Sci. U S A.* 111, 14782–14787. doi: 10.1073/pnas.1417253111

Johnson, S. M., Lim, F.-L., Finkler, A., Fromm, H., Slabas, A. R., and Knight, M. R. (2014). Transcriptomic analysis of Sorghum bicolor responding to combined heat and drought stress. *BMC Genomics* 15:456–456. doi: 10.1186/1471-2164-15-456

Kadirjan-Kalbach, D. K., Yoder, D. W., Ruckle, M. E., Larkin, R. M., and Osteryoung, K. W. (2012). FtsHi1/ARC1 is an essential gene in Arabidopsis that links chloroplast biogenesis and division. *Plant J.* 72, 856–867. doi: 10.1111/tpj.12001

Kale, R., Hebert, A. E., Frankel, L. K., Sallans, L., Bricker, T. M., and Pospíšil, P. (2017). Amino acid oxidation of the D1 and D2 proteins by oxygen radicals during photoinhibition of Photosystem II. *Proc. Natl. Acad. Sci. U S A.* 114, 2988–2993. doi: 10.1073/pnas.1618922114

Kamal, S. M., Rybtke, M. L., Nimtz, M., Sperlein, S., Giske, C., Trček, J., et al. (2019). Two FtsH proteases contribute to fitness and adaptation of *Pseudomonas aeruginosa* clone C strains. *Front. Microbiol.* 10:1372. doi: 10.3389/fmicb.2019.01372

Kapri-Pardes, E., Naveh, L., and Adam, Z. (2007). The thylakoid lumen protease Deg1 is involved in the repair of photosystem II from photoinhibition in Arabidopsis. *Plant Cell* 19, 1039–1047. doi: 10.1105/tpc.106.046573

Karlberg, T., van den Berg, S., Hammarström, M., Sagemark, J., Johansson, I., Holmberg-Schiavone, L., et al. (2009). Crystal structure of the ATPase domain of the human AAA+ protein paraplegin/SPG7. *PLoS One* 4:e6975. doi: 10.1371/journal.pone.0006975

Kato, Y., and Sakamoto, W. (2018). FtsH protease in the thylakoid membrane: physiological functions and the regulation of protease activity. *Front. Plant Sci.* 9:855. doi: 10.3389/fpls.2018.00855

Kato, Y., Hyodo, K., and Sakamoto, W. (2018). The photosystem II repair cycle requires FtsH turnover through the EngA GTPase. *Plant Physiol.* 178, 596–611. doi: 10.1104/pp.18.00652

Kato, Y., Miura, E., Ido, K., Ifuku, K., and Sakamoto, W. (2009). The variegated mutants lacking chloroplastic FtsHs are defective in D1 degradation and accumulate reactive oxygen species. *Plant Physiol.* 151, 1790–1801. doi: 10.1104/pp.109.146589

Kato, Y., Sun, X., Zhang, L., and Sakamoto, W. (2012). Cooperative D1 degradation in the photosystem II repair mediated by chloroplastic proteases in Arabidopsis. *Plant Physiol.* 159, 1428–1439. doi: 10.1104/pp.112.199042

Kihara, A., Akiyama, Y., and Ito, K. (1995). FtsH is required for proteolytic elimination of uncomplexed forms of SecY, an essential protein translocase subunit. *Proc. Natl. Acad. Sci. U S A.* 92:4532. doi: 10.1073/pnas.92.10.4532

Kihara, A., Akiyama, Y., and Ito, K. (1996). A protease complex in the *Escherichia coli* plasma membrane: HflKC (HflA) forms a complex with FtsH (HflB), regulating its proteolytic activity against SecY. *EMBO J.* 15, 6122–6131. doi: 10.1002/j.1460-2075.1996.tb01000.x

Kihara, A., Akiyama, Y., and Ito, K. (1997). Host regulation of lysogenic decision in bacteriophage λ: Transmembrane modulation of FtsH (HflB), the cII degrading protease, by HflKC?(HflA). *Proc. Natl. Acad. Sci. U S A.* 94:5544. doi: 10.1073/pnas.94.11.5544

Kihara, A., Akiyama, Y., and Ito, K. (1998). Different pathways for protein degradation by the FtsH/HflKC membrane-embedded protease complex: an implication from the interference by a mutant form of a new substrate protein, YccA. *J. Mol. Biol.* 279, 175–188. doi: 10.1006/jmbi.1998.1781

Kikuchi, S., Asakura, Y., Imai, M., Nakahira, Y., Kotani, Y., Hashiguchi, Y., et al. (2018). A Ycf2-FtsHi heteromeric AAA-ATPase complex is required for chloroplast protein import. *Plant Cell* 30, 2677–2703. doi: 10.1105/tpc.18.00357

Kolodziejczak, M., Skibior-Blaszczyk, R., and Janska, H. (2018). *m*-AAA Complexes Are Not Crucial for the Survival of Arabidopsis Under Optimal Growth Conditions Despite Their Importance for Mitochondrial Translation. *Plant Cell Physiol.* 59, 1006–1016. doi: 10.1093/pcp/pcy041

Komenda, J., Barker, M., Kuviková, S., de Vries, R., Mullineaux, C. W., Tichy, M., et al. (2006). The FtsH protease slr0228 is important for quality control of photosystem II in the thylakoid membrane of *Synechocystis* sp. PCC 6803. *J. Biol. Chem.* 281, 1145–1151. doi: 10.1074/jbc.M503852200

Komenda, J., Tichy, M., Prasil, O., Knoppová, J., Kuviková, S., de Vries, R., et al. (2007). The exposed N-terminal tail of the D1 subunit is required for rapid D1 degradation during photosystem II repair in *Synechocystis* sp PCC 6803. *Plant Cell* 19, 2839–2854. doi: 10.1105/tpc.107.053868

Koppen, M., Metodiev, M. D., Casari, G., Rugarli, E. I., and Langer, T. (2007). Variable and tissue-specific subunit composition of mitochondrial *m*-AAA protease complexes linked to hereditary spastic paraplegia. *Mol. Cell. Biol.* 27, 758–767. doi: 10.1128/MCB.01470-06

Kramer, D. M., and Evans, J. R. (2011). The Importance of Energy Balance in Improving Photosynthetic Productivity. *Plant Physiol.* 155, 70–78. doi: 10.1104/pp.110.166652

Krynická, V., Georg, J., Jackson, P. J., Dickman, M. J., Hunter, C. N., Futschik, M. E., et al. (2019). Depletion of the FtsH1/3 Proteolytic complex suppresses the nutrient stress response in the cyanobacterium *Synechocystis* sp strain PCC 6803. *Plant Cell* 31, 2912–2928. doi: 10.1105/tpc.19.00411

Krynicka, V., Shao, S., Nixon, P. J., and Komenda, J. (2015). Accessibility controls selective degradation of photosystem II subunits by FtsH protease. *Nat. Plants* 1, 1–6. doi: 10.1038/nplants.2015.168

Krynická, V., Tichý, M., Krafl, J., Yu, J., Kaňa, R., Boehm, M., et al. (2014). Two essential FtsH proteases control the level of the Fur repressor during iron deficiency in the cyanobacterium *Synechocystis* sp. PCC 6803. *Mol. Microbiol.* 94, 609–624. doi: 10.1111/mmi.12782

Krzywda, S., Brzozowski, A. M., Verma, C., Karata, K., Ogura, T., and Wilkinson, A. J. (2002). The Crystal Structure of the AAA Domain of the ATP-Dependent Protease FtsH of *Escherichia coli* at 1.5 Å Resolution. *Structure* 10, 1073–1083. doi: 10.1016/S0969-2126(02)00806-7

Kutschera, U., and Niklas, K. J. (2005). Endosymbiosis, cell evolution, and speciation. *Theory Biosci.* 124, 1–24. doi: 10.1016/j.thbio.2005.04.001

Langer, T. (2000). AAA proteases: cellular machines for degrading membrane proteins. *Trends Biochem. Sci* 25, 247–251. doi: 10.1016/S0968-0004(99)01541-8

Langklotz, S., Baumann, U., and Narberhaus, F. (2012). Structure and function of the bacterial AAA protease FtsH. *Biochim. Biophys. Acta Mol. Cell. Res.* 1823, 40–48. doi: 10.1016/j.bbamcr.2011.08.015

Lee, G., and Bendayan, R. (2004). Functional expression and localization of P-glycoprotein in the central nervous system: relevance to the pathogenesis and treatment of neurological disorders. *Pharm. Res.* 21, 1313–1330. doi: 10.1023/b:pham.0000036905.82914.8e

Lee, S., Augustin, S., Tatsuta, T., Gerdes, F., Langer, T., and Tsai, F. T. (2011). Electron cryomicroscopy structure of a membrane-anchored mitochondrial AAA protease. *J. Biol. Chem.* 286, 4404–4411. doi: 10.1074/jbc.M110.158741

Leonhard, K., Herrmann, J., Stuart, R., Mannhaupt, G., Neupert, W., and Langer, T. (1996). AAA proteases with catalytic sites on opposite membrane surfaces comprise a proteolytic system for the ATP-dependent degradation of inner membrane proteins in mitochondria. *EMBO J.* 15, 4218–4229. doi: 10.1002/j.1460-2075.1996.tb00796.x

Li, L., Nelson, C. J., Trösch, J., Castleden, I., Huang, S., and Millar, A. H. (2017). Protein Degradation Rate in *Arabidopsis thaliana* Leaf Growth and Development. *Plant Cell* 29, 207–228. doi: 10.1105/tpc.16.00768

Li, W., Rao, D. K., and Kaur, P. (2013). Dual role of the metalloprotease FtsH in biogenesis of the DrrAB drug transporter. *J. Biol. Chem.* 288, 11854–11864. doi: 10.1074/jbc.M112.441915

Liu, Q., Galli, M., Liu, X., Federici, S., Buck, A., Cody, J., et al. (2019). NEEDLE1 encodes a mitochondria localized ATP-dependent metalloprotease required for thermotolerant maize growth. *Proc. Natl. Acad. Sci. U S A.* 116, 19736–19742. doi: 10.1073/pnas.1907071116

Lopes, K. L., Rodrigues, R. A. O., Silva, M. C., Braga, W. G. S., and Silva-Filho, M. C. (2018). The Zinc-Finger Thylakoid-Membrane Protein FIP Is Involved With Abiotic Stress Response in *Arabidopsis thaliana*. *Front. Plant Sci.* 9:504–504. doi: 10.3389/fpls.2018.00504

Lu, X., Zhang, D., Li, S., Su, Y., Liang, Q., Meng, H., et al. (2014). FtsHi4 is essential for embryogenesis due to its influence on chloroplast development in Arabidopsis. *PLoS One* 9:e99741. doi: 10.1371/journal.pone.0099741

Luciński, R., Misztal, L., Samardakiewicz, S., and Jackowski, G. (2011). The thylakoid protease Deg2 is involved in stress-related degradation of the photosystem II light-harvesting protein Lhcb6 in *Arabidopsis thaliana*. *New Phytol.* 192, 74–86. doi: 10.1111/j.1469-8137.2011.03782.x

Ma, C., Wang, C., Luo, D., Yan, L., Yang, W., Li, N., et al. (2022). Structural insights into the membrane microdomain organization by SPFH family proteins. *Cell Res.* 2022:3. doi: 10.1038/s41422-021-00598-3

Makino, S.-I., Makinoa, T., Abe, K., Hashimoto, J., Tatsuta, T., Kitagawa, M., et al. (1999). Second transmembrane segment of FtsH plays a role in its proteolytic activity and homo-oligomerization. *FEBS Lett.* 460, 554–558. doi: 10.1016/s0014-5793(99)01411-8

Malnoë, A., Wang, F., Girard-Bascou, J., Wollman, F.-A., and de Vitry, C. (2014). Thylakoid FtsH protease contributes to photosystem II and cytochrome b_6f remodeling in *Chlamydomonas reinhardtii* under stress conditions. *Plant Cell* 26, 373–390. doi: 10.1105/tpc.113.120113

Mann, N. H., Novac, N., Mullineaux, C. W., Newman, J., Bailey, S., and Robinson, C. (2000). Involvement of an FtsH homologue in the assembly of functional photosystem I in the cyanobacterium *Synechocystis* sp. PCC 6803. *FEBS Lett.* 479, 72–77. doi: 10.1016/s0014-5793(00)01871-8

Marta, K., Marta, G., Adam, U., and Hanna, J. (2007). The significance of Arabidopsis AAA proteases for activity and assembly/stability of mitochondrial OXPHOS complexes. *Physiol. Plant.* 129, 135–142. doi: 10.1111/j.1399-3054.2006.00835.x

Martinelli, P., La Mattina, V., Bernacchia, A., Magnoni, R., Cerri, F., Cox, G., et al. (2009). Genetic interaction between the *m*-AAA protease isoenzymes reveals novel roles in cerebellar degeneration. *Hum. Mol. Genet.* 18, 2001–2013. doi: 10.1093/hmg/ddp124

Mishra, L. S., and Funk, C. (2021). The FtsHi Enzymes of Arabidopsis thaliana: Pseudo-Proteases with an Important Function. *Int. J. Mol. Sci.* 22:5917. doi: 10.3390/ijms22115917

Mishra, L. S., Mielke, K., Wagner, R., and Funk, C. (2019). Reduced expression of the proteolytically inactive FtsH members has impacts on the Darwinian fitness of *Arabidopsis thaliana*. *J. Exp. Bot.* 70, 2173–2184. doi: 10.1093/jxb/erz004

Moldavski, O., Levin-Kravets, O., Ziv, T., Adam, Z., and Prag, G. (2012). The Hetero-Hexameric Nature of a Chloroplast AAA+ FtsH Protease Contributes to Its Thermodynamic Stability. *PLoS One* 7:e36008. doi: 10.1371/journal.pone.0036008

Murata, N., and Nishiyama, Y. (2018). ATP is a driving force in the repair of photosystem II during photoinhibition. *Plant Cell Environ.* 41, 285–299. doi: 10.1111/pce.13108

Narberhaus, F., Obrist, M., Führer, F., and Langklotz, S. (2009). Degradation of cytoplasmic substrates by FtsH, a membrane-anchored protease with many talents. *Res. Microbiol.* 160, 652–659. doi: 10.1016/j.resmic.2009.08.011

Nelson, N., and Ben-Shem, A. (2004). The complex architecture of oxygenic photosynthesis. *Nat. Rev. Mol. Cell Biol.* 5, 971–982. doi: 10.1038/nrm1525

Nickelsen, J., and Rengstl, B. (2013). Photosystem II assembly: from cyanobacteria to plants. *Annu. Rev. Plant Biol.* 64, 609–635. doi: 10.1146/annurev-arplant-050312-120124

Nixon, P. J., Barker, M., Boehm, M., de Vries, R., and Komenda, J. (2005). FtsH-mediated repair of the photosystem II complex in response to light stress. *J. Exp. Bot.* 56, 357–363. doi: 10.1093/jxb/eri021

Nixon, P. J., Michoux, F., Yu, J., Boehm, M., and Komenda, J. (2010). Recent advances in understanding the assembly and repair of photosystem II. *Ann. Bot.* 106, 1–16. doi: 10.1093/aob/mcq059

Nixon, P. J., Trost, J. T., and Diner, B. A. (1992). Role of the carboxy-terminus of polypeptide D1 in the assembly of a functional water-oxidizing manganese cluster in photosystem II of the cyanobacterium *Synechocystis* sp. PCC 6803: assembly requires a free carboxyl group at C-terminal position 344. *Biochemistry* 31, 10859–10871. doi: 10.1021/bi00159a029

Nolden, M., Ehses, S., Koppen, M., Bernacchia, A., Rugarli, E. I., and Langer, T. (2005). The *m*-AAA protease defective in hereditary spastic paraplegia controls ribosome assembly in mitochondria. *Cell* 123, 277–289. doi: 10.1016/j.cell.2005.08.003

Oelmüller, R., Herrmann, R. G., and Pakrasi, H. B. (1996). Molecular studies of CtpA, the carboxyl-terminal processing protease for the D1 protein of the photosystem II reaction center in higher plants. *J. Biol. Chem.* 271, 21848–21852. doi: 10.1074/jbc.271.36.21848

Ogura, T., Inoue, K., Tatsuta, T., Suzaki, T., Karata, K., Young, K., et al. (1999). Balanced biosynthesis of major membrane components through regulated degradation of the committed enzyme of lipid A biosynthesis by the AAA protease FtsH (HflB) in *Escherichia coli*. *Mol. Microbiol.* 31, 833–844. doi: 10.1046/j.1365-2958.1999.01221.x

Ogura, T., Tomoyasu, T., Yuki, T., Morimura, S., Begg, K. J., Donachie, W. D., et al. (1991). Structure and function of the *ftsH* gene in *Escherichia coli*. *Res. Microbiol.* 142, 279–282. doi: 10.1016/0923-2508(91)90041-8

Okuno, T., Yamanaka, K., and Ogura, T. (2006). Characterization of mutants of the *Escherichia coli* AAA protease, FtsH, carrying a mutation in the central pore region. *J. Struct. Biol.* 156, 109–114. doi: 10.1016/j.jsb.2006.02.003

Osteryoung, K. W., and Nunnari, J. (2003). The division of endosymbiotic organelles. *Science* 302, 1698–1704. doi: 10.1126/science.1082192

Patron, M., Sprenger, H.-G., and Langer, T. (2018). *m*-AAA proteases, mitochondrial calcium homeostasis and neurodegeneration. *Cell Res.* 28, 296–306. doi: 10.1038/cr.2018.17

Piechota, J., Kolodziejczak, M., Juszczak, I., Sakamoto, W., and Janska, H. (2010). Identification and characterization of high molecular weight complexes formed by matrix AAA proteases and prohibitins in mitochondria of *Arabidopsis thaliana*. *J. Biol. Chem.* 285, 12512–12521. doi: 10.1074/jbc.M109.063644

Pierson, T. M., Adams, D., Bonn, F., Martinelli, P., Cherukuri, P. F., Teer, J. K., et al. (2011). Whole-exome sequencing identifies homozygous AFG3L2 mutations in a spastic ataxia-neuropathy syndrome linked to mitochondrial *m*-AAA proteases. *PLoS Genet.* 7:e1002325. doi: 10.1371/journal.pgen.1002325

Potting, C., Wilmes, C., Engmann, T., Osman, C., and Langer, T. (2010). Regulation of mitochondrial phospholipids by Ups1/PRELI-like proteins depends on proteolysis and Mdm35. *EMBO J.* 29, 2888–2898. doi: 10.1038/emboj.2010.169

Puchades, C., Rampello, A. J., Shin, M., Giuliano, C. J., Wiseman, R. L., Glynn, S. E., et al. (2017). Structure of the mitochondrial inner membrane AAA+ protease YME1 gives insight into substrate processing. *Science* 358:eaao0464. doi: 10.1126/science.aao0464

Raven, J. A., and Allen, J. F. (2003). Genomics and chloroplast evolution: what did cyanobacteria do for plants? *Genome Biol.* 4:209. doi: 10.1186/gb-2003-4-3-209

Remmen, H. V., and Richardson, A. (2001). Oxidative damage to mitochondria and aging. *Exp. Gerontol.* 36, 957–968. doi: 10.1016/S0531-5565(01)00093-6

Rodrigues, R. A., Silva-Filho, M. C., and Cline, K. (2011). FtsH2 and FtsH5: two homologous subunits use different integration mechanisms leading to the same thylakoid multimeric complex. *Plant J.* 65, 600–609. doi: 10.1111/j.1365-313X.2010.04448.x

Sacharz, J., Bryan, S. J., Yu, J., Burroughs, N. J., Spence, E. M., Nixon, P. J., et al. (2015). Sub-cellular location of FtsH proteases in the cyanobacterium *Synechocystis* sp. PCC 6803 suggests localised PSII repair zones in the thylakoid membranes. *Mol. Microbiol.* 96, 448–462. doi: 10.1111/mmi.12940

Saita, S., Nolte, H., Fiedler, K. U., Kashkar, H., Venne, A. S., Zahedi, R. P., et al. (2017). PARL mediates Smac proteolytic maturation in mitochondria to promote apoptosis. *Nat. Cell Biol.* 19, 318–328. doi: 10.1038/ncb3488

Saita, S., Tatsuta, T., Lampe, P. A., König, T., Ohba, Y., and Langer, T. (2018). PARL partitions the lipid transfer protein STARD7 between the cytosol and mitochondria. *EMBO J.* 37:e97909. doi: 10.15252/embj.201797909

Sakamoto, W., Miura, E., Kaji, Y., Okuno, T., Nishizono, M., and Ogura, T. (2004). Allelic characterization of the leaf-variegated mutation var2 identifies the conserved amino acid residues of FtsH that are important for ATP hydrolysis and proteolysis. *Plant Mol. Biol.* 56, 705–716. doi: 10.1007/s11103-004-4561-9

Sakamoto, W., Tamura, T., Hanba-Tomita, Y., Sodmergen, and Murata, M. (2002). The VAR1 locus of Arabidopsis encodes a chloroplastic FtsH and is responsible for leaf variegation in the mutant alleles. *Genes Cells* 7, 769–780. doi: 10.1046/j.1365-2443.2002.00558.x

Sakamoto, W., Zaltsman, A., Adam, Z., and Takahashi, Y. (2003). Coordinated regulation and complex formation of YELLOW VARIEGATED1 and YELLOW VARIEGATED2, chloroplastic FtsH metalloproteases involved in the repair cycle of photosystem II in Arabidopsis thylakoid membranes. *Plant Cell* 15, 2843–2855. doi: 10.1105/tpc.017319

Sánchez-Baracaldo, P., and Cardona, T. (2020). On the origin of oxygenic photosynthesis and Cyanobacteria. *New Phytol.* 225, 1440–1446. doi: 10.1111/nph.16249

Santos, D., and De Almeida, D. F. (1975). Isolation and characterization of a new temperature-sensitive cell division mutant of *Escherichia coli* K-12. *J. Bacteriol.* 124, 1502–1507. doi: 10.1128/jb.124.3.1502-1507.1975

Scharfenberg, F., Serek-Heuberger, J., Coles, M., Hartmann, M. D., Habeck, M., Martin, J., et al. (2015). Structure and Evolution of N-domains in AAA Metalloproteases. *J. Mol. Biol.* 427, 910–923. doi: 10.1016/j.jmb.2014.12.024

Schlame, M., and Greenberg, M. L. (2017). Biosynthesis, remodeling and turnover of mitochondrial cardiolipin. *Biochim. Biophys. Acta Mol. Cell. Biol. Lipids* 1862, 3–7. doi: 10.1016/j.bbalip.2016.08.010

Schreier, T. B., Cléry, A., Schläfli, M., Galbier, F., Stadler, M., Demarsy, E., et al. (2018). Plastidial NAD-Dependent Malate Dehydrogenase: A Moonlighting Protein Involved in Early Chloroplast Development through Its Interaction with an FtsH12-FtsHi Protease Complex. *Plant Cell* 30, 1745–1769. doi: 10.1105/tpc.18.00121

Schuhmann, H., and Adamska, I. (2012). Deg proteases and their role in protein quality control and processing in different subcellular compartments of the plant cell. *Physiol. Plant.* 145, 224–234. doi: 10.1111/j.1399-3054.2011.01533.x

Sedaghatmehr, M., Mueller-Roeber, B., and Balazadeh, S. (2016). The plastid metalloprotease FtsH6 and small heat shock protein HSP21 jointly regulate thermomemory in Arabidopsis. *Nat. Commun.* 7, 1–14. doi: 10.1038/ncomms12439

Shao, S., Cardona, T., and Nixon, P. (2018). Early emergence of the FtsH proteases involved in photosystem II repair. *Photosynthetica* 56, 163–177. doi: 10.1007/s11099-018-0769-9

Silva, P., Thompson, E., Bailey, S., Kruse, O., Mullineaux, C. W., Robinson, C., et al. (2003). FtsH is involved in the early stages of repair of photosystem II in *Synechocystis* sp PCC 6803. *Plant Cell* 15, 2152–2164. doi: 10.1105/tpc.012609

Spetea, C., Hundal, T., Lohmann, F., and Andersson, B. (1999). GTP bound to chloroplast thylakoid membranes is required for light-induced, multienzyme degradation of the photosystem II D1 protein. *Proc. Natl. Acad. Sci. U S A.* 96, 6547–6552. doi: 10.1073/pnas.96.11.6547

Spiller, M. P., Guo, L., Wang, Q., Tran, P., and Lu, H. (2015). Mitochondrial Tim9 protects Tim10 from degradation by the protease Yme1. *Biosci. Rep.* 35:e00193. doi: 10.1042/BSR20150038

Sprenger, H. G., Wani, G., Hesseling, A., König, T., Patron, M., MacVicar, T., et al. (2019). Loss of the mitochondrial *i*-AAA protease YME 1L leads to ocular dysfunction and spinal axonopathy. *EMBO Mol. Med.* 11:e9288. doi: 10.15252/emmm.201809288

Steele, T. E., and Glynn, S. E. (2019). Mitochondrial AAA proteases: a stairway to degradation. *Mitochondrion* 49, 121–127. doi: 10.1016/j.mito.2019.07.012

Steglich, G., Neupert, W., and Langer, T. (1999). Prohibitins regulate membrane protein degradation by the *m*-AAA protease in mitochondria. *Mol. Cell. Biol.* 19, 3435–3442. doi: 10.1128/MCB.19.5.3435

Stiburek, L., Cesnekova, J., Kostkova, O., Fornuskova, D., Vinsova, K., Wenchich, L., et al. (2012). YME1L controls the accumulation of respiratory chain subunits and is required for apoptotic resistance, cristae morphogenesis, and cell proliferation. *Mol. Biol. Cell* 23, 1010–1023. doi: 10.1091/mbc.E11-08-0674

Stirnberg, M., Fulda, S., Huckauf, J., Hagemann, M., Krämer, R., and Marin, K. (2007). A membrane-bound FtsH protease is involved in osmoregulation in *Synechocystis* sp. PCC 6803: the compatible solute synthesizing enzyme GgpS is one of the targets for proteolysis. *Mol. Microbiol.* 63, 86–102. doi: 10.1111/j.1365-2958.2006.05495.x

Summer, H., Bruderer, R., and Weber-Ban, E. (2006). Characterization of a new AAA+ protein from archaea. *J. Struct. Biol.* 156, 120–129. doi: 10.1016/j.jsb.2006.01.010

Sun, A.-Q., Yi, S.-Y., Yang, J.-Y., Zhao, C.-M., and Liu, J. (2006). Identification and characterization of a heat-inducible *fts*H gene from tomato (*Lycopersicon esculentum* Mill.). *Plant Sci.* 170, 551–562. doi: 10.1016/j.plantsci.2005.10.010

Sun, X., Fu, T., Chen, N., Guo, J., Ma, J., Zou, M., et al. (2010). The stromal chloroplast Deg7 protease participates in the repair of photosystem II after photoinhibition in Arabidopsis. *Plant Physiol.* 152, 1263–1273. doi: 10.1104/pp.109.150722

Sun, X., Peng, L., Guo, J., Chi, W., Ma, J., Lu, C., et al. (2007). Formation of DEG5 and DEG8 complexes and their involvement in the degradation of photodamaged photosystem II reaction center D1 protein in Arabidopsis. *Plant Cell* 19, 1347–1361. doi: 10.1105/tpc.106.049510

Suno, R., Niwa, H., Tsuchiya, D., Zhang, X., Yoshida, M., and Morikawa, K. (2006). Structure of the whole cytosolic region of ATP-dependent protease FtsH. *Mol. Cell* 22, 575–585. doi: 10.1016/j.molcel.2006.04.020

Suorsa, M., and Aro, E.-M. (2007). Expression, assembly and auxiliary functions of photosystem II oxygen-evolving proteins in higher plants. *Photosynthesis Res.* 93, 89–100. doi: 10.1007/s11120-007-9154-4

Sweetlove, L. J., Heazlewood, J. L., Herald, V., Holtzapffel, R., Day, D. A., Leaver, C. J., et al. (2002). The impact of oxidative stress on *Arabidopsis* mitochondria. *Plant J.* 32, 891–904. doi: 10.1046/j.1365-313X.2002.01474.x

Takechi, K., Murata, M., Motoyoshi, F., and Sakamoto, W. (2000). The YELLOW VARIEGATED (VAR2) locus encodes a homologue of FtsH, an ATP-dependent protease in Arabidopsis. *Plant Cell Physiol.* 41, 1334–1346. doi: 10.1093/pcp/pcd067

Tatsuta, T., and Langer, T. (2009). AAA proteases in mitochondria: diverse functions of membrane-bound proteolytic machines. *Res. Microbiol.* 160, 711–717. doi: 10.1016/j.resmic.2009.09.005

Tatsuta, T., and Langer, T. (2017). Prohibitins. *Curr. Biol.* 27, R629–R631. doi: 10.1016/j.cub.2017.04.030

Tavernarakis, N., Driscoll, M., and Kyrpides, N. C. (1999). The SPFH domain: implicated in regulating targeted protein turnover in stomatins and other membrane-associated proteins. *Trends Biochem. Sci* 24, 425–427. doi: 10.1016/S0968-0004(99)01467-X

Thorsness, P. E., White, K. H., and Fox, T. D. (1993). Inactivation of *YME1*, a member of the *ftsH-SEC18-PAS1-CDC48* family of putative ATPase-encoding genes, causes increased escape of DNA from mitochondria in *Saccharomyces cerevisiae*. *Mol. Cell. Biol.* 13, 5418–5426. doi: 10.1128/mcb.13.9.5418-5426.1993

Tomoyasu, T., Gamer, J., Bukau, B., Kanemori, M., Mori, H., Rutman, A., et al. (1995). *Escherichia coli* FtsH is a membrane-bound, ATP-dependent protease

which degrades the heat-shock transcription factor sigma 32. *EMBO J.* 14, 2551–2560. doi: 10.1002/j.1460-2075.1995.tb07253.x

Tymianski, M., and Tator, C. H. (1996). Normal and abnormal calcium homeostasis in neurons: a basis for the pathophysiology of traumatic and ischemic central nervous system injury. *Neurosurgery* 38, 1176–1195. doi: 10.1097/00006123-199606000-00028

Tzagoloff, A., Yue, J., Jang, J., and Paul, M. F. (1994). A new member of a family of ATPases is essential for assembly of mitochondrial respiratory chain and ATP synthetase complexes in *Saccharomyces cerevisiae*. *J. Biol. Chem.* 269, 26144–26151. doi: 10.1016/S0021-9258(18)47170-0

Urantowka, A., Knorpp, C., Olczak, T., Kolodziejczak, M., and Janska, H. (2005). Plant mitochondria contain at least two *i*-AAA-like complexes. *Plant Mol. Biol.* 59, 239–252. doi: 10.1007/s11103-005-8766-3

Vass, I. (2012). Molecular mechanisms of photodamage in the Photosystem II complex. *Biochim. Biophys. Acta, Bioenerg.* 1817, 209–217. doi: 10.1016/j.bbabio.2011.04.014

Vass, I., Cser, K., and Cheregi, O. (2007). Molecular Mechanisms of Light Stress of Photosynthesis. *Proc. Natl. Acad. Sci. U S A.* 1113, 114–122. doi: 10.1196/annals.1391.017

Vostrukhina, M., Popov, A., Brunstein, E., Lanz, M. A., Baumgartner, R., Bieniossek, C., et al. (2015). The structure of *Aquifex aeolicus* FtsH in the ADP-bound state reveals a C2-symmetric hexamer. *Acta Crystallogr. Sect. D Biol. Crystallogr.* 71, 1307–1318. doi: 10.1107/S1399004715005945

Wagner, R., Aigner, H., and Funk, C. (2012). FtsH proteases located in the plant chloroplast. *Physiol. Plant.* 145, 203–214. doi: 10.1111/j.1399-3054.2011.01548.x

Wagner, R., Aigner, H., Pružinská, A., Jänkänpää, H. J., Jansson, S., and Funk, C. (2011). Fitness analyses of *Arabidopsis thaliana* mutants depleted of FtsH metalloproteases and characterization of three FtsH6 deletion mutants exposed to high light stress, senescence and chilling. *New Phytol.* 191, 449–458. doi: 10.1111/j.1469-8137.2011.03684.x

Wagner, R., Von Sydow, L., Aigner, H., Netotea, S., Brugière, S., Sjögren, L., et al. (2016). Deletion of FtsH11 protease has impact on chloroplast structure and function in *Arabidopsis thaliana* when grown under continuous light. *Plant Cell Environ.* 39, 2530–2544. doi: 10.1111/pce.12808

Wai, T., Saita, S., Nolte, H., Müller, S., König, T., Richter-Dennerlein, R., et al. (2016). The membrane scaffold SLP2 anchors a proteolytic hub in mitochondria containing PARL and the *i*-AAA protease YME1L. *EMBO Rep.* 17, 1844–1856. doi: 10.15252/embr.201642698

Wang, F., Qi, Y., Malnoë, A., Choquet, Y., Wollman, F.-A., and de Vitry, C. (2017). The high light response and redox control of thylakoid FtsH protease in *Chlamydomonas reinhardtii*. *Mol. Plant* 10, 99–114. doi: 10.1016/j.molp.2016.09.012

Wang, Q., Sullivan, R. W., Kight, A., Henry, R. L., Huang, J., Jones, A. M., et al. (2004). Deletion of the chloroplast-localized Thylakoid formation1 gene product in Arabidopsis leads to deficient thylakoid formation and variegated leaves. *Plant Physiol.* 136, 3594–3604. doi: 10.1104/pp.104.049841

Wang, T., Li, S., Chen, D., Xi, Y., Xu, X., Ye, N., et al. (2018). Impairment of FtsHi5 Function Affects Cellular Redox Balance and Photorespiratory Metabolism in Arabidopsis. *Plant Cell Physiol.* 59, 2526–2535. doi: 10.1093/pcp/pcy174

Wang, Y., Cao, W., Merritt, J., Xie, Z., and Liu, H. (2021). Characterization of FtsH essentiality in Streptococcus mutans via genetic suppression. *Front. Genet.* 12:659220. doi: 10.3389/fgene.2021.659220

Xue, G.-P., Drenth, J., and McIntyre, C. L. (2015). TaHsfA6f is a transcriptional activator that regulates a suite of heat stress protection genes in wheat (*Triticum aestivum* L.) including previously unknown Hsf targets. *J. Exp. Bot.* 66, 1025–1039. doi: 10.1093/jxb/eru462

Yamada-Inagawa, T., Okuno, T., Karata, K., Yamanaka, K., and Ogura, T. (2003). Conserved Pore Residues in the AAA Protease FtsH Are Important for Proteolysis and Its Coupling to ATP Hydrolysis*. *J. Biol. Chem.* 278, 50182–50187. doi: 10.1074/jbc.M308327200

Yao, D. C., Brune, D. C., and Vermaas, W. F. (2012). Lifetimes of photosystem I and II proteins in the cyanobacterium *Synechocystis* sp. PCC 6803. *FEBS Lett.* 586, 169–173. doi: 10.1016/j.febslet.2011.12.010

Yokoyama, H., and Matsui, I. (2020). The lipid raft markers stomatin, prohibitin, flotillin, and HflK/C (SPFH)-domain proteins form an operon with NfeD proteins and function with apolar polyisoprenoid lipids. *Crit. Rev. Microbiol.* 46, 38–48. doi: 10.1080/1040841X.2020.1716682

Yu, E., Fan, C., Yang, Q., Li, X., Wan, B., Dong, Y., et al. (2014). Identification of heat responsive genes in *Brassica napus* siliques at the seed-filling stage through transcriptional profiling. *PLoS One* 9:e101914–e101914. doi: 10.1371/journal.pone.0101914

Yu, F., Park, S., and Rodermel, S. R. (2004). The Arabidopsis FtsH metalloprotease gene family: interchangeability of subunits in chloroplast oligomeric complexes. *Plant J.* 37, 864–876. doi: 10.1111/j.1365-313x.2003.02014.x

Yu, F., Park, S., and Rodermel, S. R. (2005). Functional redundancy of AtFtsH metalloproteases in thylakoid membrane complexes. *Plant Physiol.* 138, 1957–1966. doi: 10.1104/pp.105.061234

Yu, J. (2013). *Investigating the Structure and Function of the FtsH Protease Family in Synechocystis* sp. PCC 6803. Ph. D. thesis. London: Imperial College London.

Zaltsman, A., Feder, A., and Adam, Z. (2005a). Developmental and light effects on the accumulation of FtsH protease in Arabidopsis chloroplasts – implications for thylakoid formation and photosystem II maintenance. *Plant J.* 42, 609–617. doi: 10.1111/j.1365-313X.2005.02401.x

Zaltsman, A., Ori, N., and Adam, Z. (2005b). Two types of FtsH protease subunits are required for chloroplast biogenesis and photosystem II repair in Arabidopsis. *Plant Cell* 17, 2782–2790. doi: 10.1105/tpc.105.035071

Zhang, D., Kato, Y., Zhang, L., Fujimoto, M., Tsutsumi, N., and Sakamoto, W. (2010). The FtsH protease heterocomplex in Arabidopsis: dispensability of type-B protease activity for proper chloroplast development. *Plant Cell* 22, 3710–3725. doi: 10.1105/tpc.110.079202

Zhang, P., Sicora, C. I., Vorontsova, N., Allahverdiyeva, Y., Battchikova, N., Nixon, P. J., et al. (2007). FtsH protease is required for induction of inorganic carbon acquisition complexes in *Synechocystis* sp. PCC 6803. *Mol. Microbiol.* 65, 728–740. doi: 10.1111/j.1365-2958.2007.05822.x

Zhang, Z., Zhao, L.-S., and Liu, L.-N. (2021). Characterizing the supercomplex association of photosynthetic complexes in cyanobacteria. *R. Soc. Open Sci.* 8:202142. doi: 10.1098/rsos.202142

Zou, Y., and Bozhkov, P. V. (2021). Chlamydomonas proteases: classification, phylogeny, and molecular mechanisms. *J. Exp. Bot.* 72, 7680–7693. doi: 10.1093/jxb/erab383

Conflict of Interest: The authors declare that the research was conducted in the absence of any commercial or financial relationships that could be construed as a potential conflict of interest.

Publisher's Note: All claims expressed in this article are solely those of the authors and do not necessarily represent those of their affiliated organizations, or those of the publisher, the editors and the reviewers. Any product that may be evaluated in this article, or claim that may be made by its manufacturer, is not guaranteed or endorsed by the publisher.

frontiers | Frontiers in Plant Science

ORIGINAL RESEARCH
published: 15 April 2022
doi: 10.3389/fpls.2022.830140

Alternative Splicing Regulation of *Glycine-Rich Proteins via* Target of Rapamycin-Reactive Oxygen Species Pathway in Arabidopsis Seedlings Upon Glucose Stress

*Chang Du, Hai-yan Bai, Jing-jing Chen, Jia-hui Wang, Zhi-feng Wang and Zhong-hui Zhang**

Guangdong Provincial Key Laboratory of Biotechnology for Plant Development, School of Life Sciences, South China Normal University, Guangzhou, China

OPEN ACCESS

Edited by:
Simon Gilroy, University of Wisconsin-Madison, United States

Reviewed by:
Liuyin Ma, Fujian Agriculture and Forestry University, China
Richard John Barker, University of Wisconsin-Madison, United States

***Correspondence:**
Zhong-hui Zhang
zhzhang@m.scnu.edu.cn

Specialty section:
This article was submitted to Plant Cell Biology, a section of the journal Frontiers in Plant Science

Received: *06 December 2021*
Accepted: *16 March 2022*
Published: *15 April 2022*

Citation:
Du C, Bai H-y, Chen J-j, Wang J-h, Wang Z-f and Zhang Z-h (2022) Alternative Splicing Regulation of Glycine-Rich Proteins via Target of Rapamycin-Reactive Oxygen Species Pathway in Arabidopsis Seedlings Upon Glucose Stress. Front. Plant Sci. 13:830140. doi: 10.3389/fpls.2022.830140

Glucose can serve as both the source of energy and regulatory signaling molecule in plant. Due to the environmental and metabolic change, sugar levels could affect various developmental processes. High glucose environment is hardly conductive to the plant growth but cause development arrest. Increasing evidence indicate that alternative splicing (AS) plays a pivotal role in sugar signaling. However, the regulatory mechanism upon glucose stress remains unclear. The full-length transcriptomes were obtained from the samples of Arabidopsis seedlings with 3% glucose and mock treatment, using Oxford Nanopore sequencing technologies. Further analysis indicated that many genes involved in photosynthesis were significantly repressed and many genes involved in glycolysis, mitochondrial function, and the response to oxidative stress were activated. In total, 1,220 significantly differential alternative splicing (DAS) events related to 619 genes were identified, among which 75.74% belong to intron retention (IR). Notably, more than 20% of DAS events come from a large set of glycine-rich protein (*GRP*) family genes, such as *GRP7*, whose AS types mostly belong to IR. Besides the known productive *GRP* transcript isoforms, we identified a lot of splicing variants with diverse introns spliced in messenger RNA (mRNA) region coding the glycine-rich (GR) domain. The AS pattern of *GRP*s changed and particularly, the productive *GRP*s increased upon glucose stress. These ASs of *GRP* pre-mRNAs triggered by glucose stress could be abolished by AZD-8055, which is an ATP competitive inhibitor for the target of rapamycin (TOR) kinase but could be mimicked by H_2O_2. Additionally, AS pattern change of *arginine/serine-rich splicing factor 31*(*RS31*) *via* TOR pathway, which was previously described in response to light and sucrose signaling, was also induced in a similar manner by both glucose stress and reactive oxygen species (ROS). Here we

conclude that (i) glucose stress suppresses photosynthesis and activates the glycolysis-mitochondria energy relay and ROS scavenging system; (ii) glucose stress triggers transcriptome-wide AS pattern changes including a large set of splicing factors, such as *GRP*s and *RS31*; (iii) high sugars regulate AS pattern change of both *GRP*s and *RS31 via* TOR-ROS pathway. The results from this study will deepen our understanding of the AS regulation mechanism in sugar signaling.

Keywords: glucose stress, alternative splicing, glycine-rich proteins/GRPs, RS31, TOR pathway, ROS, Arabidopsis

INTRODUCTION

In eukaryotes, such as yeast, animals, and plants, sugar not only supplies carbon and energy sources, but also plays a crucial role in the signaling pathway to regulate carbon distribution and energy utilization (Smeekens et al., 2010; Chantranupong et al., 2015; Efeyan et al., 2015). However, both sugar starvation and high sugar supply are harmful to the growth of plants and human health (Moore et al., 2003; Couee et al., 2006; Aragno and Mastrocola, 2017; Huang et al., 2019). Thus, it is essential to elucidate the mechanism for sensing sugar and regulating the sugar homeostasis. In the perception of light, photosynthetic plants produce sugar, and utilize the complex sugar metabolism and signaling networks to regulate plant growth and development. Although sucrose is the major sugar for systemic transport and storage in plants, glucose, which could be converted from sucrose, is still the pivotal signaling molecule to trigger downstream signaling transduction *via* various sugar sensors and/or energy sensors. Up to date, several glucose sensing and signaling pathway have been identified in plants (Chen et al., 2021). Hexokinases 1(HXK1) in Arabidopsis is the first identified plant sugar sensor with dual functions in metabolism and glucose signaling (Moore et al., 2003). Regulator of G-protein signaling 1(RGS1), a plasma-membrane protein with seven-transmembrane domain, functions as an external glucose sensor (Johnston et al., 2007; Urano et al., 2012; Fu et al., 2014). Besides, the intracellular sugar levels could also be indirectly perceived by some evolutionarily conserved energy sensors, such as the homolog of SNF1 kinase homolog 10/11 (KIN10/11) and target of rapamycin (TOR) (Xiong et al., 2013; Crozet et al., 2014; Sheen, 2014). KIN10/KIN11, inactivated by sugars, orchestrate and integrate transcriptional network in the energy and stress signaling, promoting catabolism but repressing anabolism (Baena-Gonzalez et al., 2007; Baena-Gonzalez and Sheen, 2008). In contrast, glucose-activated TOR determines transcriptional reprogramming of large gene sets involved in the central and secondary metabolism, cell cycle, transcription, signaling, transport, and protein folding (Xiong et al., 2013). Notably, TOR kinase activated by photosynthesis-derived glucose signaling relies on the glycolysis-mitochondria energy and metabolic relay. Hypoxia condition, which inhibits the mitochondrial function, could reduce the action of TOR kinase in response to photosynthesis-derived sugar signaling (Riegler et al., 2021). Xiong et al. (2013) showed that the treatment with low exogenous glucose (15 mM) was sufficient to substitute for photosynthetic support in triggering glucose-TOR signaling and for accelerating the root growth. Instead, high glucose stress would lead to developmental arrest for Arabidopsis seedlings, such as the inhibition of root elongation, cotyledon greening, and expansion (Jang et al., 1997; Huang et al., 2019). Overexpression of glucose sensor, HXK1, and energy sensor KIN10, respectively, were both hypersensitive to 3% glucose treatment.

In plant, sugar metabolism and oxidative stress have a complicated link between each other. Photosynthesis can produce both soluble sugars and reactive oxygen species (ROS), which are maintained in a delicate balance. Soluble sugars appear to play a dual role with ROS production. On the one hand, soluble sugars are involved in ROS-producing pathways. For example, high sugars could feed the mitochondria and promote ROS production by normal mitochondrial respiration (Couee et al., 2006). On the other hand, high sugars could suppress photosynthesis and fatty acid β-oxidation to further inhibit ROS production; in addition, sugar can also feed nicotinamide adenine dinucleotide phosphate (NADPH)-producing metabolic pathway to enhance NADPH production for further ROS scavenging (Couee et al., 2006). Recently, Huang et al. (2019) showed that high glucose induces ROS accumulation in the root through autophagy pathway, which is positively and negatively regulated by KIN10 and TOR kinase, respectively.

The splicing of precursor messenger RNA (pre-mRNA) is a relevant mechanism in the post-transcriptional regulation of gene expression. Alternative splicing (AS) of pre-mRNA generates multiple transcripts from the same gene, which either provides extra manners of post-transcriptional regulation, or increases the protein diversity even though the eukaryotic genomes have limited gene numbers. AS was also regulated by some auxiliary proteins, such as serine/arginine-rich (SR) proteins and heterogenous nuclear ribonucleoprotein particle (hnRNP) proteins, in addition to spliceosome-consisting small nuclear ribonucleoproteins (Kathare and Huq, 2021). SR proteins generally interact with splicing enhancers in pre-mRNA to promote splicing, while hnRNP proteins generally interact with splicing silencers in pre-mRNA to inhibit splicing (Lee and Rio, 2015). In plants, AS plays an important regulatory role in various

Abbreviations: AS, Alternative splicing; DAS, Differential alternative splicing; DEGs, Differentially expressed genes; DSGs, Differentially alternatively spliced genes; GR, Glycine-rich; GRP, Glycine-rich protein; hnRNP, heterogenous nuclear ribonucleoprotein particle proteins; HXK, Hexokinase; NMD, non-sense-mediated decay; PRP, pre-mRNA processing factor; RGS1, regulator of G-protein signaling 1; ROS, Reactive oxygen species; RS31, arginine/serine-rich splicing factor 31; SI, Splicing index; SR, arginine/serine-rich; TOR, target of rapamycin.

biological processes, such as ovule development, circadian, and responses to light and temperature (Cucinotta et al., 2021; Dikaya et al., 2021; Kathare and Huq, 2021; Paajanen et al., 2021). Increasing evidences support that AS is also involved in the regulation of sugar signaling. SR45, a highly conserved plant-specific SR protein, was reported to negatively regulate glucose and ABA signaling (Carvalho et al., 2010). The seedlings of *sr45-1* null mutant were hypersensitive to 3 and 4.5% glucose, displaying impaired cotyledon greening and expansion as well as reduced hypocotyl elongation when growing in dark (Carvalho et al., 2010). Further study demonstrated that SR45 regulates AS of Arabidopsis *5PTase13* pre-mRNA, which promotes the proteasomal degradation of SnRK1 protein (Carvalho et al., 2016). Glucose sensitive mutant 1 (GSM1) is a homolog of yeast Prp2, which catalyzes the last step of spliceosome activation (Wahl et al., 2009; Zheng et al., 2019). The absence of *GSM1* led to hypersensitive phenotype upon 3% of glucose stress (Zheng et al., 2019). Two research groups independently demonstrated that different light condition could regulate the AS pattern of some genes encoding SR-type splicing factors, such as *arginine/serine-rich splicing factor 31* (*RS31*), *arginine/serine-rich splicing factor 30* (*RS30*), and *U2 snRNP auxiliary factor* (*U2AF65A*) in seed germination and seedling root establishment process, respectively (Petrillo et al., 2014; Tognacca et al., 2019). Further, recent study revealed that light is triggered as regulation in the roots is indeed driven *via* TOR kinase pathway by sugars (Riegler et al., 2021). Glycine-rich protein 7 (GRP7) and glycine-rich protein 8 (GRP8), as their names suggest, have high contents of glycine and function as components in hnRNP involved in the regulation of AS (Wang and Brendel, 2004; Streitner et al., 2012). Both *GRP7* and *GRP8* have similar gene structures and redundant function. However, they use an interlocked feedback mechanism of AS for negative autoregulation and reciprocal regulation: rising productive protein levels enhance AS by binding to *GRP7/8* pre-mRNA, and the alternatively spliced unproductive transcripts of *GRP7/8* are destructed *via* the non-sense-mediated decay (NMD) pathway (Staiger et al., 2003; Schoning et al., 2008). GRP7 and GRP8 have been implicated to be involved in diverse biological processes, such as flowering, circadian clock, innate immunity, and responses to various abiotic stresses and plant hormones (Staiger et al., 2003; Cao et al., 2006; Fu et al., 2007; Kim et al., 2010; Lohr et al., 2014; Steffen et al., 2019; Wang et al., 2020). However, their roles in the post-transcriptional regulation upon glucose stress are yet to be known.

The application of Oxford Nanopore Technologies (ONT) for transcriptome sequencing could generate much longer raw reads with better quality and provide more accurate estimation of AS manner and transcription level for each transcription isoforms. We therefore generated 6 full-length transcriptomes from Arabidopsis seedlings treated with 3% glucose and non-glucose control using Nanopore sequencing. We first analyzed the differentially expressed genes (DEGs) upon glucose stress and compared the DEGs with previous transcriptome data from low glucose treatment. Then we analyzed the genome-wide AS pattern and the differential alternative splicing (DAS) events upon glucose stress. Interestingly, here we showed that glucose stress-triggered AS pattern change for a large set of genes, including the genes encoding a series of splicing factors, *GRP*s, and *SR*s. Finally, we conclude that AS pattern changes of both *GRP7* and *RS31* are mediated by TOR-ROS pathway, which might be of relevance for post-transcriptional regulation upon glucose signaling.

MATERIALS AND METHODS

Plant Materials and Treatment

The seeds of Arabidopsis ecotype Col-0 were surface-sterilized by 1% of sodium hypochlorite and sown on the horizontal full-strength MS medium (MS salt, 2.5 mM MES, pH 5.8, 0.5 mM myoinositol, and 0.8% agar) after stratification at 4°C for 3 days. The 7-day-old seedlings were grown under long-day condition (16 h light/8 h dark) with a continuous temperature of 22°C. At 30 days after flowering, the seeds were harvested from more than 10 plants. After air-drying in fume hood at room temperature for 2 weeks, the sterilized seeds after 3-day stratification at 4°C were sown and grown on full-strength MS medium supplemented with 0% of glucose (control), 3% of glucose, 3% of sucrose, and 3% of mannitol, respectively, and then 7-day-old seedlings were harvested after 4-h illumination. For TOR inhibition treatment, 2 μM of AZD-8055 was added to full-strength MS medium supplemented with 0 or 3% of glucose, respectively, and then 7-day-old seedlings under long-day condition were harvested after 4-h illumination. For H_2O_2 treatment, 7-day-old seedlings under long-day condition were transferred after 8-h darkness and immersed in full-strength MS medium with 0 or 20 μM AZD-8055. After 1-h treatment under illumination, 30% of H_2O_2 was directly added into the respective medium by a pipette to a final concentration of 50 μM for another 3 h.

Complementary DNA Library Preparation and Nanopore Sequencing

The RNA of Arabidopsis seedlings was extracted by RNAprep Pure Plant Kit (DP441, Tiangen). The cDNA-PCR Barcoding Kit (SQK-PCS109 with SQK-PBK004, Oxford Nanopore Technologies) was used for quality control of total RNA and construction of complementary DNA (cDNA) library. Briefly, the RNA with polyA was reverse transcribed. The cDNA product was amplified for 14 cycles with LongAmp Tag (NEB). Then, adapter addition of cDNA samples was catalyzed by T4 DNA ligase (NEB) and the final cDNA library was purified with Agencourt AMPure XP beads. After the addition of cDNA library to FLO-MIN109 flow cell, sequencing was proceeded by the PromethION platform at Biomarker Technology Company (Beijing, China).

Raw Data Processing and Genome Mapping

The low-quality reads (Qscore < 7, length < 500 bp) were filtered and ribosomal RNAs were discarded after mapping to rRNA database.[1] The full-length, non-chemiric transcripts

[1]https://www.arb-silva.de

after trimming of adaptor primer, were mapped to Arabidopsis TAIR10 reference genome by minmap2 (Li, 2018) and further polished to be consensus sequences by pinfish.[2]

Alternative Splicing Analysis and Differentially Expressed Gene Analysis

Transcripts were validated against known reference transcript annotations (TAIR.10.48) with gffcompare. AS events were identified by the AStalavista tool (Foissac and Sammeth, 2007) and DAS events were analyzed by PSI-sigma tools (Lin and Krainer, 2019). Differential expression analysis of control and glucose-treated samples was performed using the DESeq2 R package 1.6.3 (Love et al., 2014). A model based on the negative binomial distribution was used to analyze differential expression in digital gene expression data. For controlling the false discovery rate, the resulting *P*-values were adjusted using the Benjamini and Hochberg's approach. Genes with a foldchange ≥ 2 and *P*-value < 0.01 found by DESeq2 were assigned as differentially expressed.

Gene Ontology Analysis

Gene ontology (GO) enrichment of DEGs upon low and high glucose was analyzed and visualized by Tbtools (Chen et al., 2020). GO terms of DAS genes were obtained using the agriGO tools (Tian et al., 2017). All categories with *p*-value lower than 0.01 in at least one dataset were visualized by R language to generate the air bubble plots.[3] GO terms was set as *Y*-axis and the ratio of genes in each term was set as *x*-axis. The color bar from blue (low) to red (high) indicated the logarithm (base 10) of *p*-value. The counts of genes in each term were set as bubble size.

Reverse Transcriptase PCR and Real-Time Quantitative PCR

The RNA was reverse transcribed using PrimeScript™ 1st Strand cDNA Synthesis Kit (6110A, Takara). Fivefold diluted cDNA was normalized into the same concentration by internal reference *ACTIN2* at the 22 cycles of amplification. The PCR products, which refers to the mentioned genes, were amplified for 27–31 cycles and then run in 1.5–3% agarose, respectively. The splicing index (SI) calculated from DNA level in agarose lane, which was analyzed by Image J. Primers, are listed in **Supplementary Table 1**.

The RNA was reverse-transcribed using PrimeScript™ RT reagent Kit with gDNA Eraser (PR047A, Takara). Bio-Rad CFX96 was used for qPCR proceeding by reorganizing SYBR Green. Three replicates from each sample were analyzed by $\Delta\Delta$ct methods using *ACTIN2* as internal reference. Primers are listed in **Supplementary Table 1**. The significant differences of SI and expression level in various samples were analyzed by ANOVA univariate analysis in SPSS.

3,3′-Diaminobenzidine Staining

Under long-day condition, the 7-day-old seedlings grown on the full-strength MS medium (MS salt, 2.5 mM of MES, pH 5.7, 0.5 mM of myoinositol, and 0.8% of agar) supplemented with 0 or 3% glucose were harvested after 4-h illumination and stained by 1 mg/ml of 3,3′-diaminobenzidine (DAB, Amresco, E733-50TABS, pH = 3.8) for 8 h at 22°C in the dark and destained by 75% of alcohol.

[2]https://github.com/nanoporetech/pinfish

[3]https://hiplot.com.cn/basic

RESULTS

Transcriptome Analysis by Nanopore Sequencing for Arabidopsis Seedlings Upon Glucose Stress

To investigate the defined transcriptional regulation in Arabidopsis upon glucose stress, with special focus on AS, three replicates of Columbia-0 (Col-0) wild type grown on MS non-sugar medium (WT_Ctr1/2/3) and MS + 3% of glucose medium (WT_Glc1/2/3) for 7 days, respectively, were sampled for RNA isolation and further Nanopore sequencing. Around 5 million clean reads were generated for each sample using Nanopore sequencing, which had a mean length ranging between 951 and 1,155 nt (**Supplementary Table 2**). Full-length reads account for more than 87% of total clean reads after filtering rRNAs in each sample (**Supplementary Table 3**). Among full-length reads, a high proportion of more than 99% reads in each sample were mapped transcripts (**Supplementary Table 4**). All these reads were subjected for further differential gene expression and AS analysis. In total, 3,438 differentially expressed genes (DEGs, $|\log2FC| > 1$, $P < 0.01$) were identified, in which 2,246 genes were upregulated and 1,192 genes were downregulated upon glucose stress treatment (**Figure 1A** and **Supplementary Table 5**). To dissect the expression profile and find out the difference of expression pattern between Arabidopsis seedlings in low and high glucose treatments, DEGs induced by low glucose treatment (15 mM of glucose; Xiong et al., 2013) were compared with the ones in our samples (**Figure 1B**). Among the downregulated DEGs, only 231 genes are overlapped between low glucose and glucose stress treatment, which are mainly involved in response to stimulus, stress, and oxygen level (**Figure 1B** and **Supplementary Figure 1A**). About 961 genes were uniquely downregulated by glucose stress treatment but not by low glucose treatment (**Figure 1B**), which were mainly related to photosynthesis (**Figure 1C**). A series of genes encoding the subunits of photosystem I (PSI) and photosystem II (PSII) were significantly downregulated upon glucose stress (**Figure 1D**). Meanwhile, among the upregulated DEGs, only 302 genes are overlapped between glucose signaling and glucose stress treatment, which are mainly involved in glycolysis and carbon metabolism (**Figure 1B** and **Supplementary Figure 1B**). About 1,944 genes were uniquely upregulated by glucose stress treatment (**Figure 1B**), which were mainly involved in response to stimulus/chemical/stress, including a series of *peroxidase* (*PER*) genes involved in scavenging of ROS (**Figure 1E**). All these results were also confirmed by quantitative real-time PCR (qRT-PCR) (**Figures 1F,G**). As cytoplasmic glucose needs to be maintained at a steady low level for normal cellular function, it is not surprising that glucose stress also triggered

the transcriptional regulation for those enzymes involved in the glucose homeostasis in the cytosol. Upon glucose stress, plant cells not only control the production of glucose through the suppression of photosynthesis, but also regulate the glucose metabolism and signaling. Sucrose-phosphate synthase (SPS) and sucrose-phosphate phosphatase (SPP), the two key enzymes for sucrose biosynthesis from UDP-glucose and fructose-6-phosphate (F-6-P) (Ruan, 2014), were significantly upregulated upon glucose stress (**Supplementary Figure 2**). In contrast, the expression of the cytoplasmic invertase, CINV1, which hydrolyzed sucrose into glucose and fructose, is downregulated upon glucose stress (**Supplementary Figure 2**). Although the key glucose sensor hexokinase HXK1 was only slightly upregulated upon glucose stress, those encoding a large set of key enzymes function downstream of glucose-6-phosphate (G-6-P) were mostly upregulated, e.g., the sucrose synthetase (*AtSS3*) and starch branching enzyme (*SBE2.1*) for starch biosynthesis, phosphoglucomutases (*PGM*) for the conversion from G-6-P to F-6-P, 6-phosphategluconate dehydrogenases (*PGD*) in pentose phosphate pathway, and target of rapamycin (TOR) kinase (**Supplementary Figure 2**). Additionally, a series of genes involved in tricarboxylic acid (TCA) cycle that occurred in mitochondria, were also upregulated (**Supplementary Figure 2**). Taken together, high glucose stress gives rise to the suppression of photosynthesis and the promotion of glycolysis and TCA cycle in mitochondria, probably resulting in the accumulation and further scavenging of ROS.

Glucose Stress Modulates Alternative Splicing Pattern Changes of 619 Genes in Arabidopsis Seedlings

The RNA splicing is a crucial step of RNA processing and plays a pivotal role in posttranscriptional regulation of gene expression. Increasing evidence indicated that sugar signaling could regulate AS and further affect plant growth and development (Carvalho et al., 2010, 2016; Zheng et al., 2019; Riegler et al., 2021). In response to glucose stress, a set of genes encoding pre-mRNA processing factors (PRPs) and heterogeneous nuclear ribonucleoproteins (hnRNPs) were significantly upregulated, while several genes encoding SR proteins were downregulated (**Figure 2A**). The expression level of these genes, such as *PRP1*, *PRP3*, *GRP3*, *GRP7*, *RS31,* and *SR45a*, were selected and confirmed by qRT-PCR (**Figure 2B**). To explore the regulatory mechanism of AS triggered by glucose stress, the AS events of each sample were evaluated by AStalavista tool (Foissac and Sammeth, 2007). In total, 2,094, 2,084, and 1,939 AS events were identified in each sample of control seedlings, respectively, whereas 1,177, 1,395, and 1,452 AS events were identified in each sample of seedlings upon glucose stress, respectively (**Figure 2C** and **Supplementary Figure 3A**). Notably, total AS events, intron retention (IR), exon skipping (ES), and alternative 3′ splicing site (A3SS) types in particular, dramatically decrease in response to glucose stress (**Figure 2C**). A total of 1,220 significant DAS events corresponding to 619 genes were identified ($|\Delta PSI| > 5\%$, p-value < 0.05) between glucose stress-treated and control samples (**Supplementary Table 6**). Notably, 75.74% of DAS events belong to IR type, while the other three AS types—A3SS, alternative 5′ splicing site (A5SS), and ES account for 10.98, 8.44, and 4.84%, respectively (**Figure 2D**). Many DAS events in the AS types mentioned above could be further confirmed by reverse transcriptase PCR (RT-PCR) (**Supplementary Figure 4**). Among the 619 differentially alternatively spliced genes (DSGs), only 76 and 43 genes were overlapped with upregulated and downregulated DEGs, respectively (**Supplementary Figure 3B**), suggesting that the effect of glucose stress on most of DEGs and DSGs are relatively exclusive. GO analysis of DSGs showed us a strong enrichment in GO categories related to mRNA processing, and mRNA metabolic process (**Figure 2E**), suggesting that glucose stress regulates AS patterns not only through gene expression level but also through its effect on the AS of splicing factors themselves.

Glucose Stress Regulates Alternative Splicing Pattern of Glycine-Rich Protein Family Genes

Previous studies have shown that different light conditions could regulate AS pattern of many genes including a series of splicing factors during different developmental stages, such as seed germination and seedling establishment in Arabidopsis (Petrillo et al., 2014; Hartmann et al., 2016; Tognacca et al., 2019; Riegler et al., 2021). Hartmann et al. (2016) reported that light and sucrose modulate comparable AS shifts in etiolated seedlings. Recently, Riegler et al. (2021) showed that light could regulate AS pattern in the root, and sugar could mimic its effect. Here, we also found that AS pattern of a variety of splicing factors are modulated by glucose stress during seedling establishment (**Supplementary Table 6**). Interestingly, more than 20% of DAS events come from a large set of *GRP* family genes, whose AS types mostly belong to IR (**Supplementary Table 7**). In particular, up to 91 DAS events were identified in the AS of *GRP7* transcripts, 79 of which belong to the IR type. Nanopore sequencing allowed us to identify the full-length sequence and calculate the expression level of different splicing variants for each gene more precisely. The gene annotation of *GRP7* from TAIR indicates that *GRP7* has at least two transcript variants, *GRP7.1* and *GRP7.2*. The *GRP7.1* is the productive and functional splicing variant, while *GRP7.2* is a splicing variant encoding GRP7 protein with a short truncation in the GR domain (**Figure 3A**). Previous studies reported another unproductive splicing variant due to A5SS type splicing in the first intron, which would be subjected to NMD (Staiger et al., 2003; Schoning et al., 2007, 2008). According to the full-length reads obtained by deep Nanopore sequencing, we could identify not only these three transcript variants mentioned above, but also many other splicing variants with diverse expression levels (**Figures 3A,B**). *GRP7.NT.7* is probably the previous reported A5SS-type splicing variant in the first intron which is hardly expressed in plant as mentioned in previous studies (Staiger et al., 2003; Schoning et al., 2008). Similar to *GRP7.NT.7*, some transcript variants with the first retained intron, such as *GRP7.NT.25* contain in-frame stop codon in the retained part of the first intron (**Figures 3A,B**). They could not generate a full-length protein

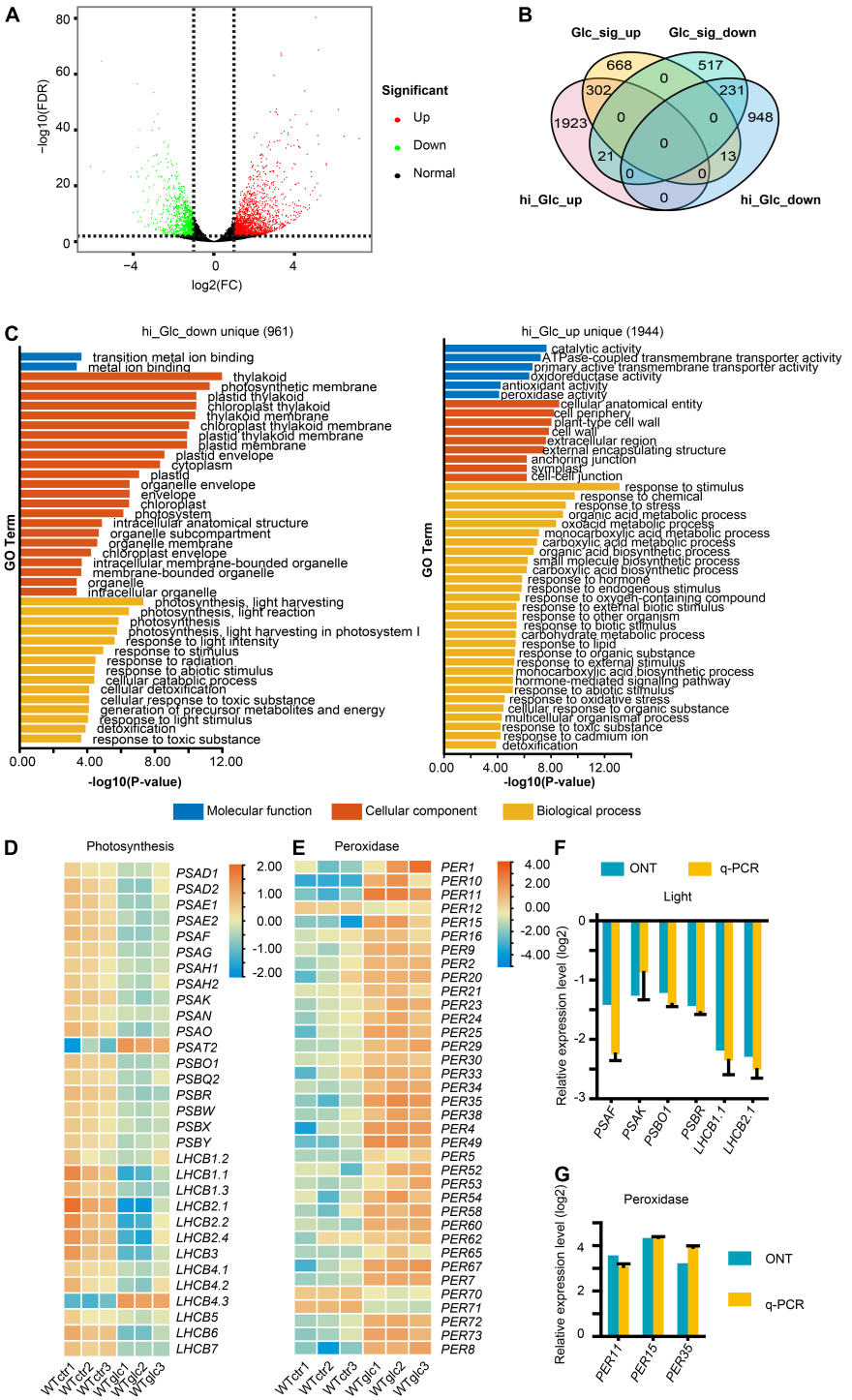

FIGURE 1 | High glucose suppresses the photosynthesis and activates the response to oxidative stress. **(A)** Volcano plot showing the differentially expressed genes (DEGs, | Log2FC| > 1, FDR < 0.01) regulated by 3% glucose treatment. **(B)** Venn diagram showing an overlap between DEGs regulated by 3% glucose and DEGs regulated by 15 mM glucose/glucose signaling (Xiong et al., 2013), hi_Glc_up, DEGs upregulated by 3% glucose, hi_Glc_down, DEGs downregulated by 3% glucose, Glc_sig_up, DEGs upregulated by 15 mM of glucose, Glc_sig_down, DEGs downregulated by 15 mM of glucose. **(C)** Gene ontology (GO) enrichment analysis of the DEGs uniquely upregulated by 3% glucose (1,944 genes) and uniquely downregulated by 3% glucose (961 genes) in comparison to DEGs. **(D)** Heatmap for the relative expression level of genes involved in photosynthesis. **(E)** Heatmap for the relative expression level of genes encoding peroxidases. **(F)** Nanopore sequencing (ONT) and quantitative real-time PCR (q-PCR) results for the relative expression of representative genes involved in photosynthesis. **(G)** Nanopore sequencing and q-PCR results for the relative expression of representative genes encoding peroxidases. *Actin* serves as an internal control for the q-PCR in both **(F,G)**.

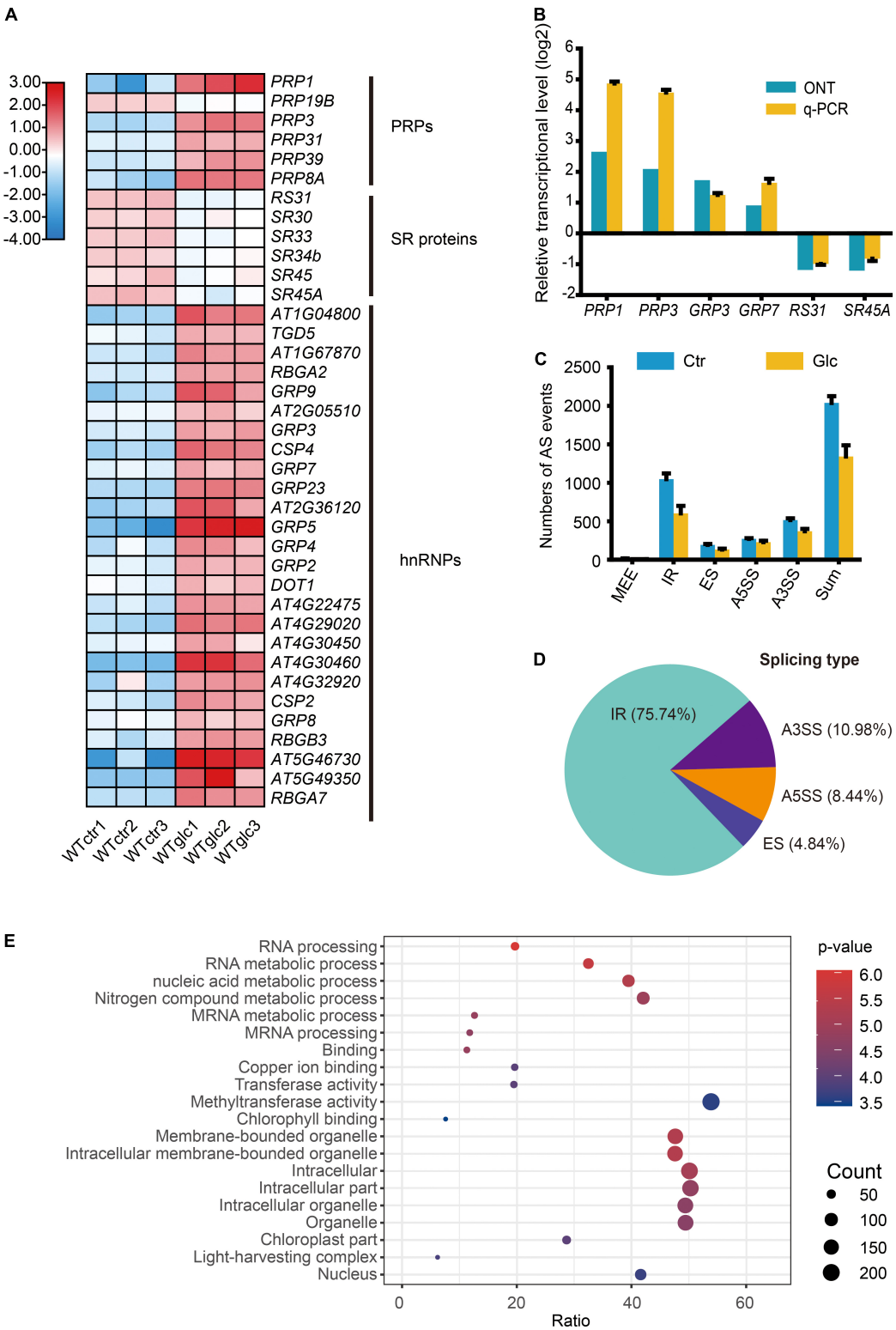

FIGURE 2 | Glucose stress regulates alternative splicing (AS) in Arabidopsis seedling. **(A)** Heatmap for the differentially expressed splicing factors regulated by 3% glucose treatment. **(B)** Nanopore sequencing and q-PCR results for representative splicing factors induced by 3% glucose treatment. **(C)** The numbers of AS events in different types in WT_Ctr and WT_Glc samples. **(D)** The type distribution of the differential alternative splicing (DAS) events between WT_Ctr and WT_Glc. IR, intron retention; A5SS, alternative 5′ splicing site; A3SS, alternative 3′ splicing site; ES, exon skipping. **(E)** The air bubble graph showing GO enrichments in differentially alternative spliced genes (DSGs) between WT_Ctr and WT_Glc. Gene numbers (circle size) and enrichment *q*-value (circle color) are shown.

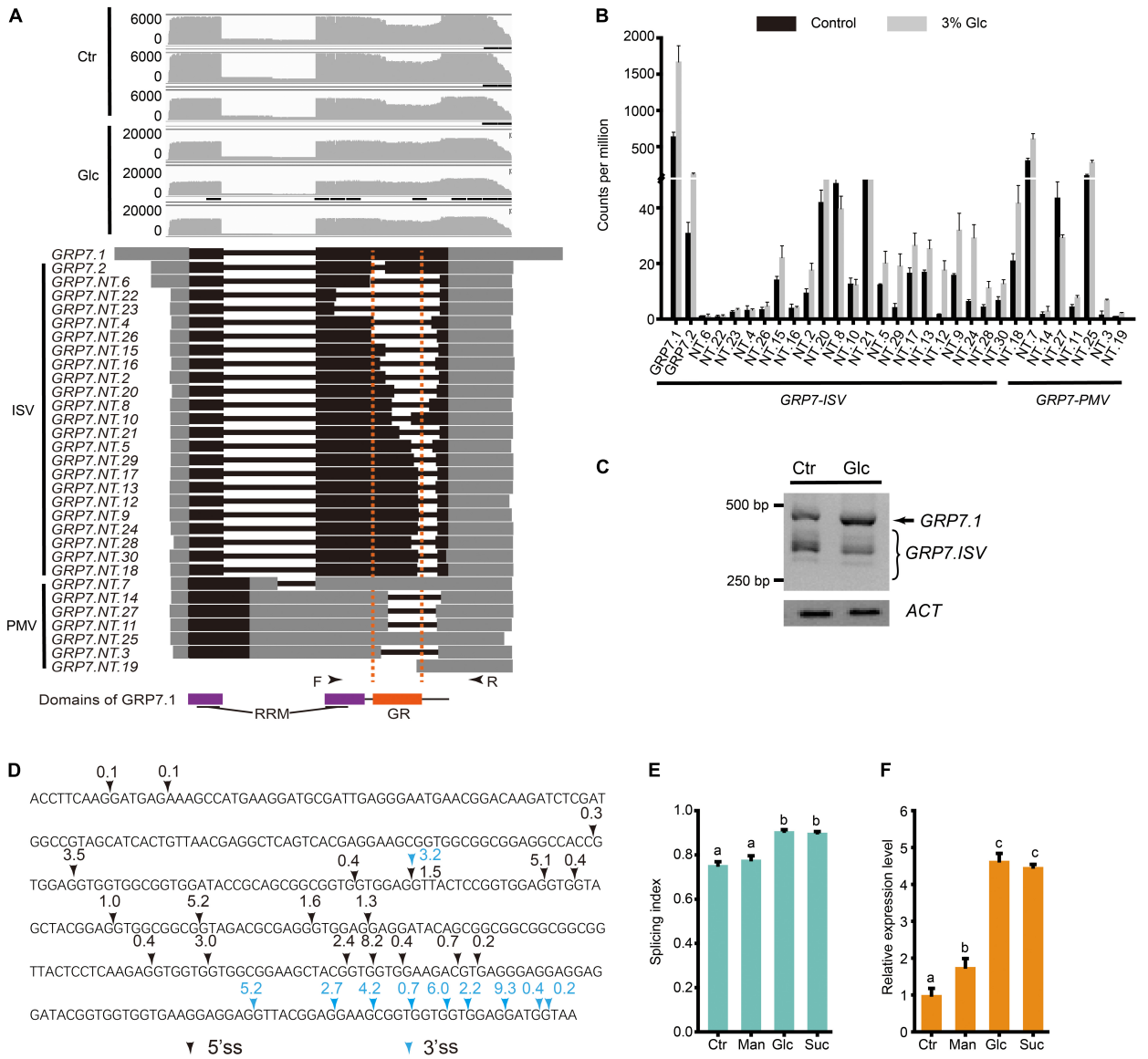

FIGURE 3 | Glucose stress regulates AS pattern change of *GRP7* in Arabidopsis seedling. **(A)** Gene model, AS isoforms, and IGV coverage diagrams of *GRP7*. Black arrows represent the binding sites of the primers of RT-PCR in **(C)**. Dotted lines indicate the pre-mRNA regions coding for GR domain in GRP7. **(B)** Transcription level of *GRP7* transcript variants by Nanopore sequencing. **(C)** RT-PCR result for *GRP7* transcript variants. *ACTIN* (*ACT*) serves as the internal control. **(D)** The splicing sites of the cryptic intron in *GRP7* pre-mRNA sequence. Black arrows represent the 5′ splicing sites, and blue arrows represent the 3′ splicing sites. The numbers above the arrows represents the percentage of the transcripts with the corresponding splicing site among total transcripts. **(E)** The SI of *GRP7* transcripts upon control treatment and different high soluble sugar treatments, respectively. The SI of *GRP7* was calculated by the ratio of *GRP7.1*/(*GRP7.1* + *GRP7* using the fluorescence intensity of PCR products in RT-PCR). **(F)** The expression levels of *GRP7* upon different treatments. Ctr, 0% glucose; Glc, 3% glucose; Man, 3% mannitol; Suc, 3% sucrose; ISV, intron spliced variant; PMV, pre-mature variant.

but a short premature peptide. By coincidence, like *GRP7.2*, most of *GRP7* splicing variants undergo various intron splicing in the mRNA region coding the GR domain in GRP7 protein (**Figures 3A,D**). Here, we named these intron-spliced transcript variants of *GRP7* as *GRP7.ISV*. The results from RT-PCR could detect a lot of truncated fragments corresponding to *GRP7.ISV*s smaller than the one from *GRP7.1* and further indicated that the ratio of *GRP7.1* and *GRP7.ISV*s increased upon glucose stress (**Figures 3A,C**). Besides, a variety of 5′ splicing site (5′SS) and 3′ splicing site (3′SS) are distributed in *GRP7.ISV* pre-mRNAs with diverse frequency, mostly generating introns with the canonical feature of 5′-GU and 3′-AG (**Figure 3D**). Different combination of 5′SS and 3′SS generated various DAS events for *GRP7* (**Figures 3A,D**). Similarly, many other *GRP*s, such as *GRP3S*, *GRP8*, *GRP9*, *CSP2*, and *CSP4*, also had various intron-spliced variants and coincidently, all these intron splicing events

would interrupt their GR domains of proteins (**Supplementary Table 7** and **Supplementary Figure 5**). Meanwhile, the ratios of functional *GRP* variants and *GRP.ISV*s also consistently increased upon glucose stress (**Supplementary Figure 5**). To evaluate the effect of glucose stress on AS change of *GRP7*, here we define *GRP7.1*/(*GRP7.1* + *GRP7.ISV*s) as the splicing index (SI) for *GRP7*, which is positively correlated with the ratio of functional *GRP7.1* in transcript variants. To figure out whether these AS pattern regulation of *GRP*s are specifically induced by glucose stress, experiments with the treatments of glucose, sucrose, and mannitol, respectively, were done and AS patterns of *GRP7* in each sample were compared. In consistent with the treatment of 3% of glucose, both the SI and the expression level of *GRP7* could be dramatically induced by the treatment of 3% sucrose (**Figures 3E,F**). In contrast, the SI of *GRP7* could not be induced by the treatment of 3% of mannitol, while the expression level of *GRP7* could only be mildly induced by the treatment of 3% of mannitol (**Figures 3E,F**). All these results suggest that both high sucrose and glucose stress, but not equivalent osmotic stress, could trigger the AS pattern shift of *GRP*s.

Glucose Stress Regulates Alternative Splicing Pattern of Glycine-Rich Proteins *via* Target of Rapamycin Pathway

Glucose is a central signaling molecule in plant which plays a pivotal regulatory role in plant growth and developmental process. Glucose signaling can be directly sensed by the key glucose sensor, hexokinase 1 (HXK1) and indirectly sensed by another two master energy sensor kinases, SNF1-related protein kinase 1 (SnRK1) and TOR kinase (Li and Sheen, 2016). Recent study has shown that TOR kinase could mediate the light-triggered AS pattern regulation of some splicing factors, such as *RS31* (Riegler et al., 2021). Here, we liked to find whether TOR pathway is also involved in the AS pattern regulation of *GRP*s upon glucose stress. First, our DEGs, upon glucose stress were compared with the TOR-regulated gene sets from the transcriptomic data from low glucose treatment (Xiong et al., 2013; **Figure 4A**). We found that glucose stress-induced genes considerably overlapped with TOR upregulated genes, but rarely overlapped with TOR downregulated genes. Moreover, glucose stress-repressed genes also considerably overlapped with TOR downregulated genes, but rarely overlapped with TOR upregulated genes (**Figure 4A**). These results suggest that glucose stress positively regulates TOR pathway, in reminiscence of the effect of glucose stress on the expression level of TOR (**Supplementary Figure 2**). Second, when 2 μM AZD-8055, an ATP competitive TOR kinase inhibitor (Montane and Menand, 2013) was applied in the 3% of glucose and 0% of glucose control treatment for Arabidopsis seedlings, glucose stress-induced AS pattern change was blocked (**Figure 4B**). However, it is notable that AZD-8055 could not block the upregulation of *GRP7* mRNA level upon glucose stress, suggesting that the transcription level of *GRP7* is regulated in a TOR kinase-independent manner (**Figure 4C**). All these results confirm that TOR kinase mediates the AS pattern regulation but not the expression level of *GRP*s upon glucose stress.

Reactive Oxygen Species Mimics the Effect of Glucose Stress on Alternative Splicing of Glycine-Rich Proteins Downstream of Target of Rapamycin Kinase

Two previous studies for glucose-TOR pathway supported that chloroplasts activate the TOR pathway in the root *via* the photosynthesized sugars that feed the mitochondria (Xiong et al., 2013; Riegler et al., 2021). Hypoxia condition treatment reduced the AS changes of splicing factor, *RS31* in response to sucrose (Riegler et al., 2021), suggesting that ROS might play a role in TOR pathway activated by sugar signaling. Our transcriptomic data have shown that high glucose treatment inhibits the transcription of many genes involved in photosynthesis and enhances the transcription of many genes involved in glycolysis, TCA cycles, and mitochondria function, supporting that high sugar has effect on the suppression of photosynthesis and promotion of mitochondrial respiration. The upregulated expression of peroxidase family genes, upon glucose stress, suggest that ROS might increase upon glucose stress. Indeed, we found that 3% glucose treatment could promote the accumulation of H_2O_2 in both the root and shoot by DAB staining (**Figure 5A**), in consistent with the previous results from Arabidopsis root with 3% glucose treatment (Huang et al., 2019), supporting that glucose stress triggers the accumulation of ROS, in general. To figure out whether ROS would affect the glucose stress-triggered AS pattern change of *GRP*s, we performed a treatment with H_2O_2 for the Arabidopsis seedlings and found that H_2O_2 could mimic the effect of glucose stress on the AS pattern of *GRP7* in Arabidopsis seedlings (**Figure 5B**). However, additional treatment with AZD-8055 for H_2O_2-treated and control samples, respectively, could not impact the AS pattern change of *GRP7* (**Figure 5B**). Besides, similar to the effect of glucose stress, H_2O_2 could increase the transcription level of *GRP7*, which could not be blocked by AZD-8055, either (**Figure 5C**). These results suggest that ROS regulates the AS pattern change of *GRP*s, downstream of TOR kinase upon glucose stress.

High Sugar Regulates Alternative Splicing Pattern of *RS31 via* Target of Rapamycin-Reactive Oxygen Species Pathway

Petrillo et al. (2014) have established that light could regulate the AS pattern of *RS31* through retrograde signals arising from chloroplasts, and they further proved that this AS is regulated by sugars but not directly by light (Petrillo et al., 2014; Riegler et al., 2021). Tognacca et al. (2019) have shown that red light also could modulate the AS pattern of *RS31* during light-induced germination in Arabidopsis. Here, we also noticed that glucose stress could regulate the A3SS and ES-type AS of *RS31* in our Nanopore sequencing data (**Supplementary Table 6**). Previously, at least three transcript isoforms including *RS31.1*, *RS31.2*, and *RS31.3*, have been reported (Petrillo et al., 2014; Riegler et al., 2021). In our Nanopore sequencing data, we identified limited

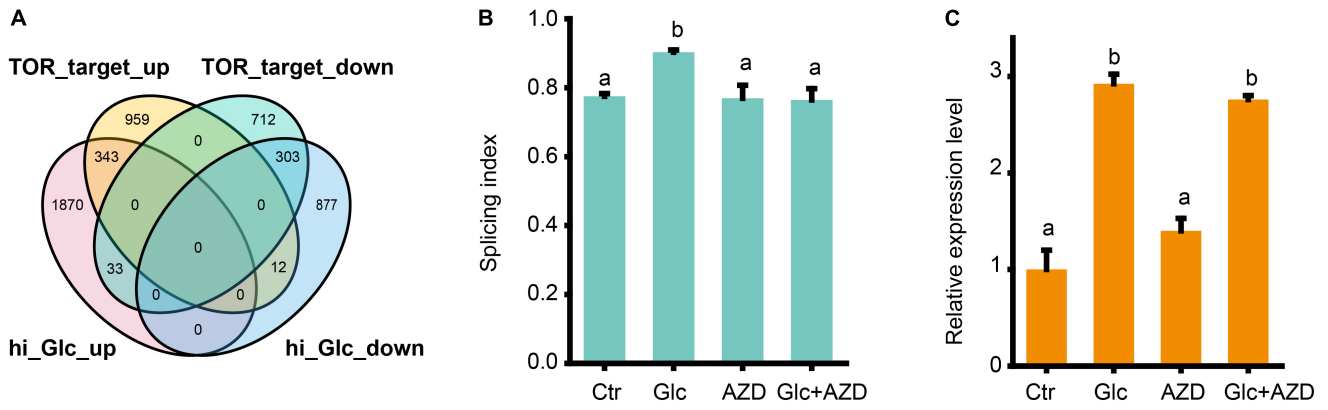

FIGURE 4 | Glucose stress regulates AS pattern change of *GRP7 via* TOR pathway. **(A)** Venn diagram showing an overlap between DEGs upon 3% glucose and DEGs regulated by TOR kinase in glucose signaling. hi_Glc_up: DEGs upregulated by 3% glucose; hi_Glc_down: DEGs down-regulated by 3% glucose; TOR_target_up: DEGs upregulated by TOR; TOR_target_down: DEGs down-regulated by TOR. **(B)** The SI of *GRP7* transcripts upon different treatments. **(C)** The expression levels of *GRP7* upon different treatments. Ctr, 0% glucose; Glc, 3% glucose; AZD, 0% glucose + 2 μM AZD-8055; Glc + AZD, 3% glucose + 2 μM AZD-8055.

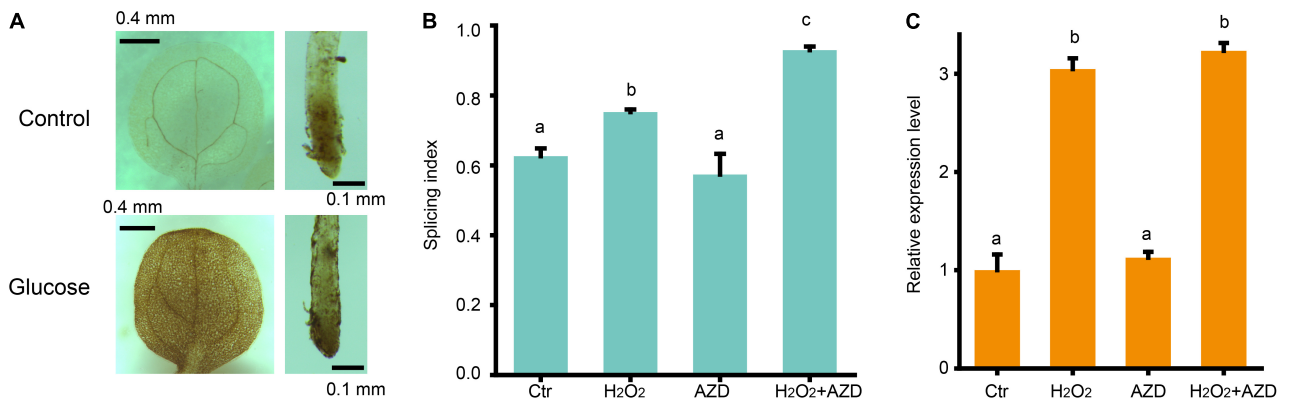

FIGURE 5 | ROS regulates AS pattern change of *GRP7* downstream of TOR. **(A)** DAB staining for the leaves and roots of 7-day-old seedlings upon glucose stress. **(B)** The SI of *GRP7* transcripts upon different treatments. **(C)** The expression levels of *GRP7* upon different treatment. Ctr, 0% glucose; H_2O_2, 50 μM H_2O_2; AZD, 0% glucose + 20 μM AZD-8055; H_2O_2 + AZD, 50 μM H_2O_2 + 20 μM AZD-8055.

full-length reads corresponding to another transcript isoform called, *RS31.4* with a retained intron (**Figures 6A,B**). Both the expression level of *RS31.2* and *RS31.4* were very low, and no significant change was detected upon glucose stress (**Figure 6B**). Both sucrose and glucose, together with mannitol, were tested for the effect of treatments on the AS pattern of *RS31*. In consistent with the effect on AS pattern of *GRP7*, the AS pattern of *RS31* could be regulated by sugar signals including sucrose and glucose, but not mannitol (**Figure 6C**). Similar to the effect of sucrose on the AS pattern of *RS31* in leaf (Riegler et al., 2021), AZD-8055 could reduce the AS pattern change of *RS31* upon glucose stress as well (**Figure 6D**). In addition, we also found that H_2O_2 could mimic the effect of glucose stress on the AS pattern of *RS31* in Arabidopsis seedlings, while additional treatment with AZD-8055 for H_2O_2-treated and control samples, respectively, could not impact the AS pattern change of *RS31* (**Figure 6E**). Taken together, high sugars also regulate the AS pattern of *RS31 via* TOR-ROS pathway.

DISCUSSION

As glucose has dual roles as the energy source and key signaling molecule, the glucose homeostasis is essential in the plant cells. Both sugar starvation and high glucose concentrations can lead to retardation and impairment of plant growth and development. Xiong et al. (2013) used Arabidopsis seedlings growing 3 days after germination in sugar-free medium with 2-h low glucose (15 mM) treatment for transcriptome analysis, and this minimal endogenous glucose level enlarged the detection sensitivity upon glucose induction. In consequence, they provide us global transcriptional reprogramming profile in response to glucose signaling in low glucose level. However, the transcriptional regulation upon high glucose stress remains unclear. Huang et al. (2019) have revealed that wild type 7-day-old seedlings of Arabidopsis showed gradually enhanced attenuation in the root growth on 1/2 MS medium with glucose concentration from 1 to 6%, and 3% glucose treatment could significantly

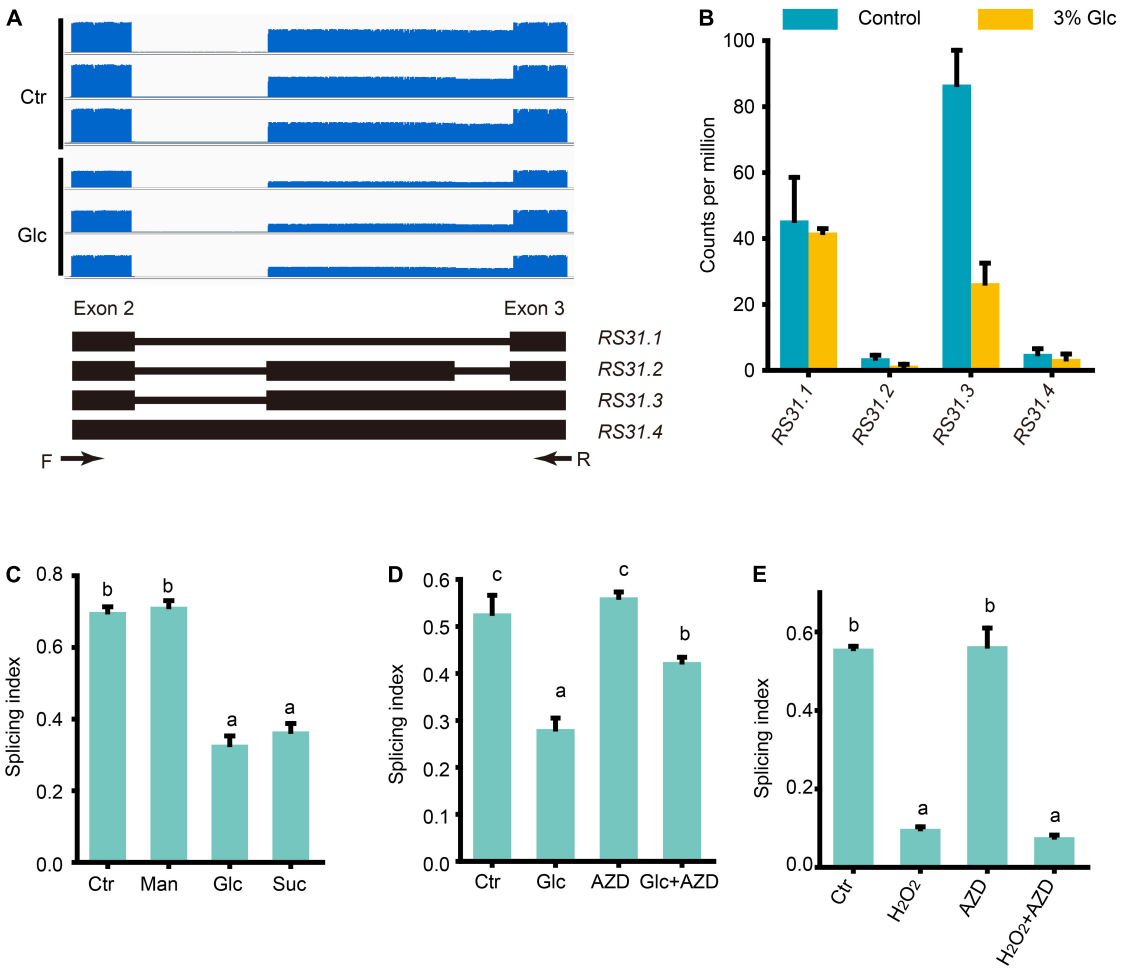

FIGURE 6 | Glucose stress regulates AS pattern change of *RS31 via* TOR pathway. **(A)** Gene model, AS isoforms and IGV coverage diagrams of *RS31*. Black arrows represent the binding sites of the primers of RT-PCR in **(C–E)**. **(B)** Transcription level of *RS31* transcript variants by Nanopore sequencing. **(C)** The splicing index (SI) of *RS31* transcripts upon different sugar treatments. **(D)** The SI of *RS31* transcripts upon glucose and AZD treatments. **(E)** The SI of *RS31* transcripts upon H_2O_2 and AZD treatments. Ctr, 0% glucose; Glc, 3% glucose; Man, 3% mannitol; Suc, 3% sucrose; AZD, 0% glucose + 20 μM AZD-8055; Glc + AZD, 3% glucose + 20 μM AZD-8055; H_2O_2, 50 μM H_2O_2; AZD, 0% glucose + 20 μM AZD-8055; H_2O_2 + AZD, 50 μM H_2O_2 + 20 μM AZD-8055.

suppress the root meristem activity. By analyzing the weight of 7-day-old seedlings grown on MS with 0, 1, 2, and 3% glucose treatment, we found that the biomass of seedlings exhibited stepwise increase upon 0, 1, and 2% glucose. However, 3% glucose treatment led to a significant decrease in the biomass of the whole plants, compared to the 2% glucose treatment (**Supplementary Figure 7**). These results suggested that 3% glucose may be high enough as a stress threshold for the inhibition of Arabidopsis seedling growth. Taking 7-day-old seedling samples of Arabidopsis with 0 and 3% glucose treatment for comparative transcriptome analysis, we identified 2,246 upregulated DEGs and 1,192 downregulated DEGs from our transcriptome data by Nanopore sequencing, which provide us full insight of the transcriptional regulation upon glucose stress. On the one hand, glucose stress turns out to suppress the expression of those genes encoding subunits of PSI and PSII complex, and cytoplasmic invertase CINV1 (**Supplementary Figure 2**), leading to limit the production of photosynthetic sugar and the conversion from sucrose to glucose. On the other hand, glucose stress also activates a series of genes encoding some metabolic enzymes involved in the conversion of glucose to sucrose and some other downstream metabolites, such as F-6-P, 6-PGL, and starch (**Supplementary Figure 2**), resulting in the depletion of endogenous glucose level. In comparison to the transcriptome data from the low glucose treatment, we have shown that, upon both low and high glucose treatment, many genes, mainly involved in glycolysis and carbon metabolism in mitochondria, were activated (**Supplementary Figure 1B**), supporting the important role of the glycolysis-mitochondria energy and metabolic relay in glucose signaling. Meanwhile, a large set of genes involved in response to stimulus, stress, and oxygen level, were commonly repressed (**Supplementary Figure 1A**), suggesting that both low and high glucose would trigger some stress-related responses, in particular, the oscillation of oxygen and ROS level in cells. Many

genes encoding peroxidases for ROS scavenging were uniquely upregulated upon glucose stress, implying that ROS burst might happen when glucose level is too high (**Figure 1C**). In contrast, many genes encoding ribosomal proteins and protein synthesis machineries were uniquely activated upon low glucose treatment (**Supplementary Figure 1D**), suggesting that protein synthesis could be promoted by appropriate glucose level and inhibited or restored to a regular level by excessive high glucose level. Many genes involved in photosynthesis are uniquely downregulated upon glucose stress in support of the suppressive effect of high glucose against photosynthesis (**Figure 1C**), while many genes involved in response to plant hormones were uniquely downregulated upon low glucose treatment (**Supplementary Figure 1C**), suggesting that some endogenous plant hormones might be involved in the regulation of plant growth and development while certain appropriate glucose level is available. In general, a large amount of unique DEGs upon glucose stress suggest a dynamic change of global expression profile along with the variation of endogenous glucose level.

Due to advantages of Nanopore sequencing for transcriptome analysis, we could identify a large set of novel transcripts including the unannotated transcript variants from known coding genes, long non-coding RNAs, and/or coding RNAs from putative intergenic regions, and in advance, calculate their transcription level in a more precise way. Therefore, Nanopore sequencing-based transcriptome also turns out to be a better way for the study on RNA splicing. Although the annotation for Arabidopsis genome is well-established and tons of transcriptome data and expressed sequence tags were done, here we still identified more than 17,453 novel transcripts from our samples. For example, in *GRP7* and *RS31*, besides the reported splicing isoforms, we identified novel splicing isoforms of these two genes from our transcriptome data. Meanwhile, we also identified 1,220 significantly DAS events corresponding to 619 genes upon glucose stress, most of which belong to IR type AS. Many of DSGs encode proteins related to RNA splicing, in particular, GR proteins and SR proteins, supporting the idea that splicing factors usually have autoregulation loop to regulate its own AS. It is notable that AS pattern of many genes encoding GR proteins were regulated by glucose stress, and these DAS types mostly belong to IR. *GRP7* is the most representative example, in which there are up to 91 DAS events identified. Here, we identified not only the previously reported transcript variants including *GRP7.1*, *GRP7.2*, and the A5SS-type splicing variant, named *GRP7.NT.7* in our data, but also dozens of other isoforms yet to be reported (**Figure 3**). Most of these isoforms, which are named *GRP7.ISV*s, undergo intron splicing in the mRNA region encoding the GR domain in the GRP7 protein, so that they might produce truncated GRP7 protein and become unproductive (**Figure 3A**). In Arabidopsis seedling with 0% glucose control treatment, both productive *GRP7.1* and unproductive *GRP7.ISV*s exist, while the SI of *GRP7* increased upon glucose stress (**Figure 3**), indicating that glucose stress triggers the retention of cryptic intron in the second exon of *GRP7* and probably produces more functional GRP7.

Indeed, *GRP7* is not a unique case here. A series of *GRP*s, such as *GRP3S*, *GRP8*, *GRP9*, *CSP2*, and *CSP4*, have similar AS pattern change upon glucose stress (**Supplementary Table 7** and **Supplementary Figure 5**). Plant GRPs, a superfamily of proteins with high content of glycine (20–70%) and conserved glycine-containing structural motif with repetitive amino acid residues, could be classified into five main classes (Czolpinska and Rurek, 2018). GRPs of class IV, also called glycine-rich RNA-binding proteins (GR-RBPs), can be further divided into four subclasses (denoted IVa–IVd) (Czolpinska and Rurek, 2018; Ma et al., 2021). Only members of subclass IVd, such as Arabidopsis GRP7, GRP8, and RZ-1C, share homology with the subunits of hnRNPs and are involved in the regulation of AS (Wang and Brendel, 2004). Those *GRP*s with AS pattern change in response to glucose stress, are widely distributed in different classes of *GRP*s. Only *GRP7*, *GRP8*, and *RZ-1C* belong to the subclass IVd and have been reported to be involved in the splicing of pre-mRNAs (Staiger et al., 2003; Wang and Brendel, 2004; Schoning et al., 2008; Wu et al., 2016; Wang et al., 2020). Therefore, it seems to be a general regulatory strategy for all these referred *GRP*s, at least. Interestingly, we noticed that due to a frequent usage of GGT/GGA codon for continuous glycines in GR domain (**Figure 3D**), the cryptic intron region of *GRP* pre-mRNA encoding the GR domain might be a hotspot region and provide many of 5′-GU and 3′-AG for potential 5′ and 3′SS, respectively. This may provide us an explanation for the highly diverse transcript variants for *GRP* genes. However, not all genes in *GRP* superfamily are subjected to this AS regulation, probably due to the different spatio-temporal expression pattern of individual *GRP* gene. Both *GRP7* and *GRP8* have been reported to use an interlocked feedback mechanism of AS for negative autoregulation and reciprocal regulation (Staiger et al., 2003; Schoning et al., 2008). GRP7/8 protein can bind to *GRP7/8* pre-mRNAs and inhibit the productive intron splicing to generate *GRP7.1/GRP8.1*, consequently forming a negative feedback loop (Schoning et al., 2008). Considering that glucose stress could trigger the retention of cryptic intron in the second exon of *GRP7/8* and produce more functional GRP7/8, how GRP7/8 finely regulate the first productive intron splicing and the second unproductive cryptic intron splicing to accomplish autoregulation remain elusive.

Recently, GRP7 has been identified as an RNA-binding protein that regulates AS *via* RALF1-FER-GRP7 regulatory module (Wang et al., 2020). Nearly 4,000 DAS events were detected in the *GRP7* loss-of-function mutant *grp7-1 8i* compared to the wild-type control. Meyer et al. (2017) applied individual nucleotide-resolution crosslinking and immunoprecipitation (iCLIP) and RNA immunoprecipitation (RIP) to identify more than 2,800 transcripts in AtGRP7-GFP expressing plants, indicating that GRP7 could bind to all transcript regions with a preference for 3′ untranslated regions. These results suggested that GRP7 is involved in the global regulation of AS events. Glucose stress could trigger AS change for a large set of genes including *GRP7*; here, we would like to know whether glucose stress-induced global AS change is regulated *via* GRP7. Glucose-induced DAS were compared with the DAS induced by loss function of *GRP7* in *grp7 8i* and GRP7 targets identified by RIP/iCLIP (Meyer et al., 2017; Wang et al., 2020; **Supplementary Figure 8A**). The 125 genes were commonly induced by glucose stress and *grp7 8i*. At the same time, 101 genes bound by GRP7 were

also regulated by glucose stress. GRP7-bound 12 genes with DAS concurrently controlled by glucose stress and *grp7 8i* were identified, suggesting that they might be the downstream targets of GRP7 upon glucose stress. Interestingly, among these 12 genes, *long after far-red light 3* (*LAF3*) encoded a factor required for normal PhyA signaling (Hare et al., 2003). PhyA, together with PhyB have been shown to be involved in the accumulation of starch and many other primary metabolites in response to light (Han et al., 2017). Upon glucose stress, the intron that retained *LAF3.3* and *LAF3.4* transcripts increased, whereas the intron-spliced *LAF3.NT.2* transcripts decreased (**Supplementary Figure 8B**). Considering the IR transcripts lead to shortened protein N-termini (Hare et al., 2003), the AS change of *LAF3* upon glucose stress might result in a decline of LAF3 function. Therefore, a feedback regulation might happen through glucose-GRP7-LAF3 regulatory module. Besides, another one of the 12 target genes, *AT5G51620* encoding an unknown function protein (UPF0172), was also identified to exhibit AS change upon glucose stress by RT-PCR (**Supplementary Figure 8C**). Its biological function and its correlation with glucose-GFP7 regulatory module remain elusive. However, these genes might not be the only targets for GRP7 upon glucose stress, as DAS genes in *grp7 8i* and GRP7 target genes identified by RIP/iCLIP were not identified upon high glucose treatment. Moreover, it is notable that not only GRP7, but also other GRP family proteins and other splicing factors, were dynamically regulated during this process.

Previous studies revealed the central role for TOR kinase in AS regulation by light-triggered photosynthesized sugar in both the root and shoot (Riegler et al., 2021). In our study, we provided a series of evidence: (1) both low and high glucose activated glycolysis and carbon metabolism in mitochondria, which is the key relay for the transition of chloroplast retrograde sugar signaling to TOR kinase; (2) TOR kinase was mildly induced by glucose stress; (3) In comparison to glucose stress-regulated DEGs with TOR-regulated DEGs, considerable overlap supported that glucose stress positively regulates the TOR pathway; (4) most importantly, the application of a TOR kinase inhibitor, AZD-8055, could block the AS pattern change upon glucose stress. Therefore, we concluded that glucose stress regulates AS pattern change of *GRP*s *via* TOR pathway, in consistent with the effect of light-triggered photosynthesized sugar on AS regulation of *RS31 via* TOR pathway. Treatment with the same concentration of sucrose but not mannitol could mimic the effect of glucose stress on AS pattern changes of *GRPs* and *RS31*, suggesting that sucrose might regulate these AS pattern changes through its conversion to glucose. Either the chloroplast retrogrades sugar signal or external sugar signal appears to activate TOR kinase pathway after glycolysis-mitochondria energy and metabolic relay. Hypoxia condition, which inhibits the mitochondrial function, could reduce the action of TOR kinase in response to photosynthesized sugar signaling (Riegler et al., 2021). Our transcriptome data support that high sugar promotes mitochondrial respiration and activate the expression of peroxidase family genes. These results imply that ROS might increase upon glucose stress and in turn affect AS regulation, which were further supported by our experimental results and the results from a previous study (Huang et al., 2019). Treatment of external H_2O_2 could mimic the effect of glucose stress on AS pattern change of *GRP*s, suggesting that ROS might regulate AS downstream of TOR kinase. Moreover, both glucose and H_2O_2 could regulate the AS pattern change of those genes encoding SR-rich type of splicing factors, such as *SR31*, in a similar manner. However, according to the Nanopore sequencing data and our RT-PCR results, glucose stress induced the productive transcript variants of *GRP*s with retained intron but repressed the unproductive transcript variants of *RS31* with retained intron. How does glucose stress coordinate these two types of AS regulation and consequent AS regulation of downstream target genes? Are AS pattern changes of *GRP*s and *RS31* simultaneously or hierarchically regulated *via* TOR-ROS pathway by glucose stress? These two key questions still need to be further investigated and answered.

In summary, here, we used Nanopore sequencing technology and designed experiments to analyze the transcriptional gene expression and AS events in Arabidopsis seedlings upon glucose stress, and we now have a more clear picture about how AS is regulated by high glucose stress (**Supplementary Figure 6**): (1) high glucose stress could suppress photosynthesis and activate glycolysis-mitochondria energy relay; (2) after glycolysis and sugars feed mitochondria, TOR kinase is activated and the level of ROS is further elevated; (3) TOR-ROS pathway regulates the AS pattern change of both *GRP*s and *RS31*, probably leading to the AS pattern change of downstream glucose-stress responsive genes.

DATA AVAILABILITY STATEMENT

The original contributions presented in the study are publicly available. This data can be found here: All datasets for this study are included in the manuscript and the **Supplementary Material**. The RNA-seq sequencing data is available at the Sequence Read Archive with the accession PRJNA785179.

AUTHOR CONTRIBUTIONS

Z-HZ and CD conceived, designed the research, performed the bioinformatics analysis, interpreted the data, and drafted the manuscript. CD, H-YB, J-JC, J-HW, and Z-FW performed the experiments. All authors have read and approved the final version of the manuscript.

FUNDING

This research was supported by the National Natural Science Foundation of China (Grant Nos. 31771349, 32170593), the Guangdong Provincial Pearl River Talents Program (Grant No. 2019QN01N108) provided to Z-HZ and the China Postdoctoral Science Foundation (Grant No. 2020M672673), and the

Guangdong Basic and Applied Basic Research Foundation (Grant No. 2021A1515110451) to CD.

ACKNOWLEDGMENTS

We thank the technical assistance from Guanshen Liu (Biomarker Technologies, Beijing, China). We would like to appreciate the reviewers' comments and helpful suggestions.

SUPPLEMENTARY MATERIAL

The Supplementary Material for this article can be found online at: https://www.frontiersin.org/articles/10.3389/fpls.2022.830140/full#supplementary-material

Supplementary Figure 1 | Comparison of the DEGs between the transcriptome data from the samples upon low- and high-glucose treatments. Comparation of the DEGs between our transcriptome data and previous transcriptome data (Xiong et al., 2013). **(A)** GO enrichment analysis of the DEGs commonly downregulated by 15 mM glucose and 3% glucose (231 genes). **(B)** GO enrichment analysis of the DEGs commonly upregulated by 15 mM glucose and 3% glucose (302 genes). **(C)** GO enrichment analysis of the DEGs uniquely downregulated by 15 mM glucose (517 genes). **(D)** GO enrichment analysis of the DEGs uniquely upregulated DEGs by 15 mM glucose (668 genes).

Supplementary Figure 2 | DEGs associated pathway induced by glucose stress. **(A)** Heatmap for the relative expression level of genes involved in the mentioned pathway. **(B)** The diagram of the regulatory gene network related to the mentioned DEGs. SPS, sucrose phosphate synthase; SPP, sucrose phosphatase; INV, invertase; SS, starch synthase; SBE, starch branching enzyme; HXK, Hexokinase; PGM, Phosphoglucomutase; PGD, Glucose 6-phosphatedehydrogenase; MDH, Malate dehydrogenase; IDH, Isocitrate dehydrogenase; MLS, Malate synthase; PPC, Phosphoenolpyruvate carboxylase; TCA cycle, Tricarboxylic acid cycle; RGS, Regulator of G-protein signaling; SnRK1, SNF1-related protein kinase 1; TOR, Target of rapamycin; G-6-P, Glucose-6-phosphate; G-1-P, Glucose-1-phosphate; 6-PGL, 6-Phosphogluconolactonase; PPP, Pentose phosphate pathway. Green downward arrows represent downregulation; red upward arrows represent upregulation.

Supplementary Figure 3 | AS events and genes (DSGs) upon glucose stress. **(A)** The numbers of AS events in WT_Ctr and WT_Glc samples. **(B)** Venn diagram showing the overlap between DEGs and DSGs upon glucose stress. DEG_up, differentially upregulated genes (FC > 2, FDR < 0.01); DSGs, differential alternative splicing genes ($|\Delta PSI| > 5\%$, $p < 0.05$); DEG_down, differentially down-regulated genes (FC < 1/2, FDR < 0.01).

Supplementary Figure 4 | Identification of DSGs genes upon glucose stress. **(A–E)** Alternative splicing events of *RNU1*, *AT5G48220*, *LUH*, *MED26B*, and *UGT76E4* in WT_Ctr and WT_Glc samples. The left panels shows the gene model, AS isoforms, and IGV coverage diagrams for each tested gene; the middle panel shows the transcription level of transcript variants for each tested gene; the right panel shows the confirmation results of AS events by RT-PCR with the primers shown as black arrows in the left panel. NT, novel transcripts.

Supplementary Figure 5 | Glucose stress regulates the AS events of *GRP*s upon glucose stress. **(A–E)** Identification of AS events of *GRP3S*, *GRP8*, *GRP9*, *CSP2*, and *CSP4* in WT_Ctr and WT_Glc samples. The left panels showed the gene model and IGV coverage diagrams for each tested gene, the yellow bars represent the mRNA region encoding glycine-rich (GR) domain; the right panel showed the confirmation results of AS events by RT-PCR with the primers shown as black arrows in the left panels.

Supplementary Figure 6 | Glucose stress regulates the AS events of *GRP*s and *RS31 via* TOR-ROS pathway upon glucose stress. Working model for the AS regulation upon glucose stress. High sugar inhibits the photosynthesis and promotes the glycolysis-mitochondria function; both the photosynthetic sugars and external high sugars are transmitted to mitochondria relay, further leading to the activation of TOR kinase; TOR kinase promotes the accumulation of ROS, such as H_2O_2, which results in the increase of productive transcript variants of *GRP*s and the decrease of unproductive transcript variants of *RS31*, consequently affecting the downstream AS-associated transcriptional regulation.

Supplementary Figure 7 | The biomass of the whole 7-day-old seedlings upon glucose treatment in different concentrations. The weight of wild type Arabidopsis 7-day-old seedlings grown upon glucose treatment in different concentration of 0 (Ctr), 1, 2, and 3%, respectively, were measured and the average weight of each seedling were compared.

Supplementary Figure 8 | The overlapping analysis of differential alternative splicing (DAS) genes induced by high glucose treatment, by loss of function of *GRP7* in *grp7-1 8i*, and GRP7 target genes identified by RIP/iCLIP. **(A)** Venn diagram showing an overlap between DSGs regulated by high glucose treatment, target genes of GRP7 identified by RIP/iCLIP and DSGs controlled by *grp7 8i*. **(B,C)** AS events of *LAF3* and *AT5G51620* in WT_Ctr and WT_Glc samples. The left panels show the gene model, AS isoforms, and IGV coverage diagrams for each tested gene; the right panel shows the confirmation results of AS events by RT-PCR with the primers shown as black arrows in the left panels. NT, novel transcripts.

REFERENCES

Aragno, M., and Mastrocola, R. (2017). Dietary sugars and endogenous formation of advanced glycation endproducts: emerging mechanisms of disease. *Nutrients* 9:385. doi: 10.3390/nu9040385

Baena-Gonzalez, E., and Sheen, J. (2008). Convergent energy and stress signaling. *Trends Plant Sci.* 13, 474–482. doi: 10.1016/j.tplants.2008.06.006

Baena-Gonzalez, E., Rolland, F., Thevelein, J. M., and Sheen, J. (2007). A central integrator of transcription networks in plant stress and energy signalling. *Nature* 448, 938–942. doi: 10.1038/nature06069

Cao, S., Jiang, L., Song, S., Jing, R., and Xu, G. (2006). AtGRP7 is involved in the regulation of abscisic acid and stress responses in *Arabidopsis*. *Cell Mol. Biol. Lett.* 11, 526–535. doi: 10.2478/s11658-006-0042-2

Carvalho, R. F., Carvalho, S. D., and Duque, P. (2010). The plant-specific SR45 protein negatively regulates glucose and ABA signaling during early seedling development in *Arabidopsis*. *Plant Physiol.* 154, 772–783. doi: 10.1104/pp.110.155523

Carvalho, R. F., Szakonyi, D., Simpson, C. G., Barbosa, I. C. R., Brown, J. W. S., Baena-González, E., et al. (2016). The *Arabidopsis* SR45 splicing factor, a negative regulator of sugar signaling, modulates SNF1-related protein kinase 1 stability. *Plant Cell* 28, 1910–1925. doi: 10.1105/tpc.16.00301

Chantranupong, L., Wolfson, R. L., and Sabatini, D. M. (2015). Nutrient-sensing mechanisms across evolution. *Cell* 161, 67–83. doi: 10.1016/j.cell.2015.02.041

Chen, C., Chen, H., Zhang, Y., Thomas, H. R., Frank, M. H., He, Y., et al. (2020). TBtools: an integrative toolkit developed for interactive analyses of big biological data. *Mol. Plant* 13, 1194–1202. doi: 10.1016/j.molp.2020.06.009

Chen, Q., Zhang, J., and Li, G. (2021). Dynamic epigenetic modifications in plant sugar signal transduction. *Trends Plant Sci.* 27, 379–390. doi: 10.1016/j.tplants.2021.10.009

Couee, I., Sulmon, C., Gouesbet, G., and El Amrani, A. (2006). Involvement of soluble sugars in reactive oxygen species balance and responses to oxidative stress in plants. *J. Exp. Bot.* 57, 449–459. doi: 10.1093/jxb/erj027

Crozet, P., Margalha, L., Confraria, A., Rodrigues, A., Martinho, C., Adamo, M., et al. (2014). Mechanisms of regulation of SNF1/AMPK/SnRK1 protein kinases. *Front. Plant Sci.* 5:190. doi: 10.3389/fpls.2014.00190

Cucinotta, M., Cavalleri, A., Guazzotti, A., Astori, C., Manrique, S., Bombarely, A., et al. (2021). Alternative splicing generates a MONOPTEROS isoform required for ovule development. *Curr. Biol.* 31, 892–899. doi: 10.1016/j.cub.2020.11.026

Czolpinska, M., and Rurek, M. (2018). Plant glycine-rich proteins in stress response: an emerging, still prospective story. *Front. Plant Sci.* 9:302. doi: 10.3389/fpls.2018.00302

Dikaya, V., El Arbi, N., Rojas-Murcia, N., Nardeli, S. M., Goretti, D., and Schmid, M. (2021). Insights into the role of alternative splicing in plant temperature response. *J. Exp. Bot.* 72, 7384–7403. doi: 10.1093/jxb/erab234

Efeyan, A., Comb, W. C., and Sabatini, D. M. (2015). Nutrient-sensing mechanisms and pathways. *Nature* 517, 302–310. doi: 10.1038/nature14190

Foissac, S., and Sammeth, M. (2007). ASTALAVISTA: dynamic and flexible analysis of alternative splicing events in custom gene datasets. *Nucleic Acids Res.* 35, W297–W299. doi: 10.1093/nar/gkm311

Fu, Y., Lim, S., Urano, D., Tunc-Ozdemir, M., Phan, N. G., Elston, T. C., et al. (2014). Reciprocal encoding of signal intensity and duration in a glucose-sensing circuit. *Cell* 156, 1084–1095. doi: 10.1016/j.cell.2014.01.013

Fu, Z. Q., Guo, M., Jeong, B. R., Tian, F., Elthon, T. E., Cerny, R. L., et al. (2007). A type III effector ADP-ribosylates RNA-binding proteins and quells plant immunity. *Nature* 447, 284–288. doi: 10.1038/nature05737

Han, X., Tohge, T., Lalor, P., Dockery, P., Devaney, N., Esteves-Ferreira, A. A., et al. (2017). Phytochrome A and B regulate primary metabolism in *Arabidopsis* leaves in response to light. *Front. Plant Sci.* 8:1394. doi: 10.3389/fpls.2017.01394

Hare, P. D., Moller, S. G., Huang, L. F., and Chua, N. H. (2003). LAF3, a novel factor required for normal phytochrome A signaling. *Plant Physiol.* 133, 1592–1604. doi: 10.1104/pp.103.028480

Hartmann, L., Drewe-Boss, P., Wiessner, T., Wagner, G., Geue, S., Lee, H. C., et al. (2016). Alternative splicing substantially diversifies the transcriptome during early photomorphogenesis and correlates with the energy availability in *Arabidopsis*. *Plant Cell* 28, 2715–2734. doi: 10.1105/tpc.16.00508

Huang, L., Yu, L. J., Zhang, X., Fan, B., Wang, F. Z., Dai, Y. S., et al. (2019). Autophagy regulates glucose-mediated root meristem activity by modulating ROS production in *Arabidopsis*. *Autophagy* 15, 407–422. doi: 10.1080/15548627.2018.1520547

Jang, J. C., Leon, P., Zhou, L., and Sheen, J. (1997). Hexokinase as a sugar sensor in higher plants. *Plant Cell* 9, 5–19. doi: 10.1105/tpc.9.1.5

Johnston, C. A., Taylor, J. P., Gao, Y., Kimple, A. J., Grigston, J. C., Chen, J. G., et al. (2007). GTPase acceleration as the rate-limiting step in *Arabidopsis* G protein-coupled sugar signaling. *Proc. Natl. Acad. Sci. U.S.A.* 104, 17317–17322. doi: 10.1073/pnas.0704751104

Kathare, P. K., and Huq, E. (2021). Light-regulated pre-mRNA splicing in plants. *Curr. Opin. Plant Biol.* 63, 102037. doi: 10.1016/j.pbi.2021.102037

Kim, J. Y., Kim, W. Y., Kwak, K. J., Oh, S. H., Han, Y. S., and Kang, H. (2010). Glycine-rich RNA-binding proteins are functionally conserved in *Arabidopsis thaliana* and *Oryza sativa* during cold adaptation process. *J. Exp. Bot.* 61, 2317–2325. doi: 10.1093/jxb/erq058

Lee, Y., and Rio, D. C. (2015). Mechanisms and regulation of alternative pre-mrna splicing. *Annu. Rev. Biochem.* 84, 291–323. doi: 10.1146/annurev-biochem-060614-034316

Li, H. (2018). Minimap2: pairwise alignment for nucleotide sequences. *Bioinformatics* 34, 3094–3100. doi: 10.1093/bioinformatics/bty191

Li, L., and Sheen, J. (2016). Dynamic and diverse sugar signaling. *Curr. Opin. Plant Biol.* 33, 116–125. doi: 10.1016/j.pbi.2016.06.018

Lin, K. T., and Krainer, A. R. (2019). PSI-Sigma: a comprehensive splicing-detection method for short-read and long-read RNA-seq analysis. *Bioinformatics* 35, 5048–5054. doi: 10.1093/bioinformatics/btz438

Lohr, B., Streitner, C., Steffen, A., Lange, T., and Staiger, D. (2014). A glycine-rich RNA-binding protein affects gibberellin biosynthesis in *Arabidopsis*. *Mol. Biol. Rep.* 41, 439–445. doi: 10.1007/s11033-013-2878-7

Love, M. I., Huber, W., and Anders, S. (2014). Moderated estimation of fold change and dispersion for RNA-seq data with DESeq2. *Genome Biol.* 15:550. doi: 10.1186/s13059-014-0550-8

Ma, L., Cheng, K., Li, J., Deng, Z., Zhang, C., and Zhu, H. (2021). Roles of plant glycine-rich rna-binding proteins in development and stress responses. *Int. J. Mol. Sci.* 22:5849. doi: 10.3390/ijms22115849

Meyer, K., Koster, T., Nolte, C., Weinholdt, C., Lewinski, M., Grosse, I., et al. (2017). Adaptation of iCLIP to plants determines the binding landscape of the clock-regulated RNA-binding protein AtGRP7. *Genome Biol.* 18:204. doi: 10.1186/s13059-017-1332-x

Montane, M. H., and Menand, B. (2013). ATP-competitive mTOR kinase inhibitors delay plant growth by triggering early differentiation of meristematic cells but no developmental patterning change. *J. Exp. Bot.* 64, 4361–4374. doi: 10.1093/jxb/ert242

Moore, B., Zhou, L., Rolland, F., Hall, Q., Cheng, W.-H., Liu, Y.-X., et al. (2003). Role of the *Arabidopsis* glucose sensor HXK1 in nutrient, light, and hormonal signaling. *Science* 300:332. doi: 10.1126/science.1080585

Paajanen, P., Lane de Barros Dantas, L., and Dodd, A. N. (2021). Layers of crosstalk between circadian regulation and environmental signalling in plants. *Curr. Biol.* 31, R399–R413. doi: 10.1016/j.cub.2021.03.046

Petrillo, E., Godoy Herz, M. A., Fuchs, A., Reifer, D., Fuller, J., Yanovsky, M. J., et al. (2014). A chloroplast retrograde signal regulates nuclear alternative splicing. *Science* 344, 427–430. doi: 10.1126/science.1250322

Riegler, S., Servi, L., Scarpin, M. R., Godoy Herz, M. A., Kubaczka, M. G., Venhuizen, P., et al. (2021). Light regulates alternative splicing outcomes via the TOR kinase pathway. *Cell Rep.* 36:109676. doi: 10.1016/j.celrep.2021.109676

Ruan, Y. L. (2014). Sucrose metabolism: gateway to diverse carbon use and sugar signaling. *Annu. Rev. Plant Biol.* 65, 33–67. doi: 10.1146/annurev-arplant-050213-040251

Schoning, J. C., Streitner, C., Meyer, I. M., Gao, Y., and Staiger, D. (2008). Reciprocal regulation of glycine-rich RNA-binding proteins via an interlocked feedback loop coupling alternative splicing to nonsense-mediated decay in *Arabidopsis*. *Nucleic Acids Res.* 36, 6977–6987. doi: 10.1093/nar/gkn847

Schoning, J. C., Streitner, C., Page, D. R., Hennig, S., Uchida, K., Wolf, E., et al. (2007). Auto-regulation of the circadian slave oscillator component AtGRP7 and regulation of its targets is impaired by a single RNA recognition motif point mutation. *Plant J.* 52, 1119–1130. doi: 10.1111/j.1365-313X.2007.03302.x

Sheen, J. (2014). Master regulators in plant glucose signaling networks. *J. Plant Biol.* 57, 67–79. doi: 10.1007/s12374-014-0902-7

Smeekens, S., Ma, J., Hanson, J., and Rolland, F. (2010). Sugar signals and molecular networks controlling plant growth. *Curr. Opin. Plant Biol.* 13, 273–278. doi: 10.1016/j.pbi.2009.12.002

Staiger, D., Zecca, L., Wieczorek Kirk, D. A., Apel, K., and Eckstein, L. (2003). The circadian clock regulated RNA-binding protein AtGRP7 autoregulates its expression by influencing alternative splicing of its own pre-mRNA. *Plant J.* 33, 361–371. doi: 10.1046/j.1365-313x.2003.01629.x

Steffen, A., Elgner, M., and Staiger, D. (2019). Regulation of flowering time by the rna-binding proteins AtGRP7 and AtGRP8. *Plant Cell Physiol.* 60, 2040–2050. doi: 10.1093/pcp/pcz124

Streitner, C., Koster, T., Simpson, C. G., Shaw, P., Danisman, S., Brown, J. W., et al. (2012). An hnRNP-like RNA-binding protein affects alternative splicing by *in vivo* interaction with transcripts in *Arabidopsis thaliana*. *Nucleic Acids Res.* 40, 11240–11255. doi: 10.1093/nar/gks873

Tian, T., Liu, Y., Yan, H., You, Q., Yi, X., Du, Z., et al. (2017). agriGO v2.0: a GO analysis toolkit for the agricultural community, 2017 update. *Nucleic Acids Res.* 45, W122–W129. doi: 10.1093/nar/gkx382

Tognacca, R. S., Servi, L., Hernando, C. E., Saura-Sanchez, M., Yanovsky, M. J., Petrillo, E., et al. (2019). Alternative splicing regulation during light-induced germination of *Arabidopsis thaliana* seeds. *Front. Plant Sci.* 10:1076. doi: 10.3389/fpls.2019.01076

Urano, D., Phan, N., Jones, J. C., Yang, J., Huang, J., Grigston, J., et al. (2012). Endocytosis of the seven-transmembrane RGS1 protein activates G-protein-coupled signalling in *Arabidopsis*. *Nat. Cell. Biol.* 14, 1079–1088. doi: 10.1038/ncb2568

Wahl, M. C., Will, C. L., and Lührmann, R. (2009). The spliceosome: design principles of a dynamic rnp machine. *Cell* 136, 701–718. doi: 10.1016/j.cell.2009.02.009

Wang, B. B., and Brendel, V. (2004). The ASRG database: identification and survey of *Arabidopsis thaliana* genes involved in pre-mRNA splicing. *Genome Biol.* 5:R102. doi: 10.1186/gb-2004-5-12-r102

Wang, L., Yang, T., Wang, B., Lin, Q., Zhu, S., Li, C., et al. (2020). RALF1-FERONIA complex affects splicing dynamics to modulate stress responses and growth in plants. *Sci. Adv.* 6:eaaz1622. doi: 10.1126/sciadv.aaz1622

Wu, Z., Zhu, D., Lin, X., Miao, J., Gu, L., Deng, X., et al. (2016). RNA Binding Proteins RZ-1B and RZ-1C Play critical roles in regulating pre-mrna splicing and gene expression during development in *Arabidopsis*. *Plant Cell* 28, 55–73. doi: 10.1105/tpc.15.00949

Xiong, Y., McCormack, M., Li, L., Hall, Q., Xiang, C., and Sheen, J. (2013). Glucose-TOR signalling reprograms the transcriptome and activates meristems. *Nature* 496, 181–186. doi: 10.1038/nature12030

Zheng, M., Yang, T., Tao, P., Zhu, C., Fu, Y., and Hsu, Y. F. (2019). Arabidopsis GSM1 is involved in ABI4-regulated ABA signaling under high-glucose condition in early seedling growth. *Plant Sci.* 287:110183. doi: 10.1016/j.plantsci.2019.110183

Conflict of Interest: The authors declare that the research was conducted in the absence of any commercial or financial relationships that could be construed as a potential conflict of interest.

Publisher's Note: All claims expressed in this article are solely those of the authors and do not necessarily represent those of their affiliated organizations, or those of the publisher, the editors and the reviewers. Any product that may be evaluated in this article, or claim that may be made by its manufacturer, is not guaranteed or endorsed by the publisher.

frontiers | Frontiers in Plant Science

ORIGINAL RESEARCH
published: 02 May 2022
doi: 10.3389/fpls.2022.862171

The Root Hair Development of Pectin Polygalacturonase PGX2 Activation Tagging Line in Response to Phosphate Deficiency

Qing Zhang†, Aiwen Deng†, Min Xiang, Qiuyan Lan, Xiaokun Li, Shuai Yuan, Xin Gou, Shuang Hao, Juan Du and Chaowen Xiao**

Key Laboratory of Bio-Resource and Eco-Environment of Ministry of Education, College of Life Sciences, Sichuan University, Chengdu, China

OPEN ACCESS

Edited by:
Kris Vissenberg, University of Antwerp, Belgium

Reviewed by:
Cecilia Borassi, Wageningen University and Research, Netherlands
Steffen Vanneste, Ghent University, Belgium

***Correspondence:**
Juan Du
juandu@scu.edu.cn
Chaowen Xiao
cwxiao@scu.edu.cn

†These authors have contributed equally to this work and share first authorship

Specialty section:
This article was submitted to Plant Cell Biology, a section of the journal Frontiers in Plant Science

Received: *25 January 2022*
Accepted: *19 April 2022*
Published: *02 May 2022*

Citation:
Zhang Q, Deng A, Xiang M, Lan Q, Li X, Yuan S, Gou X, Hao S, Du J and Xiao C (2022) The Root Hair Development of Pectin Polygalacturonase PGX2 Activation Tagging Line in Response to Phosphate Deficiency. Front. Plant Sci. 13:862171. doi: 10.3389/fpls.2022.862171

Pectin, cellulose, and hemicellulose constitute the primary cell wall in eudicots and function in multiple developmental processes in plants. Root hairs are outgrowths of specialized epidermal cells that absorb water and nutrients from the soil. Cell wall architecture influences root hair development, but how cell wall remodeling might enable enhanced root hair formation in response to phosphate (P) deficiency remains relatively unclear. Here, we found that POLYGALACTURONASE INVOLVED IN EXPANSION 2 (PGX2) functions in conditional root hair development. Under low P conditions, a *PGX2* activation tagged line (*PGX2*^{AT}) displays bubble-like root hairs and abnormal callose deposition and superoxide accumulation in roots. We found that the polar localization and trafficking of PIN2 are altered in *PGX2*^{AT} roots in response to P deficiency. We also found that actin filaments were less compact but more stable in *PGX2*^{AT} root hair cells and that actin filament skewness in *PGX2*^{AT} root hairs was recovered by treatment with 1-N-naphthylphthalamic acid (NPA), an auxin transport inhibitor. These results demonstrate that activation tagging of *PGX2* affects cell wall remodeling, auxin signaling, and actin microfilament orientation, which may cooperatively regulate root hair development in response to P starvation.

Keywords: cell wall, pectin, polygalacturonase, phosphate deficiency, root hair development, *Arabidopsis thaliana*

INTRODUCTION

Phosphate (P) is an essential mineral macronutrient for the normal growth and development of plants. In nature, phosphate widely exists in insoluble organic compounds in the soil, and soluble inorganic P is relatively unavailable for uptake by plants (Holford, 1997). Therefore, limited phosphate availability negatively affects global crop yields (Lopez-Arredondo et al., 2014). In P-deficient soil, plants can adapt to acquire this nutrient by reorganizing their root system architectures (Lopez-Bucio et al., 2002; Peret et al., 2014). These root architectural changes include the development and growth of primary roots, lateral roots, and root hairs, which allow plants to better adapt to soil environments (Bates and Lynch, 1995; Williamson et al., 2001; Lopez-Bucio et al., 2002). Root hairs expand out from root epidermal cells and

facilitate the uptake of water and nutrients from the soil by increasing the root surface area. In P-deficient conditions, plants can increase root hair number and length to enhance overall root absorption capacity and efficiency (Bates and Lynch, 2000). Thus, root hairs play a crucial role in plant survival under nutrient starvation conditions.

The hairs that extend from root hair cells, or trichoblasts, exhibit polarized growth in which cell length is much greater than cell width, making root hairs a good model for investigating anisotropic cell expansion and polarity (Hepler et al., 2001). Root hairs initiate from bulges that form on the rootward side of the outer periclinal walls of trichoblasts, followed by the establishment of tip growth from these bulges. The formation of root hairs is collectively determined by the transcriptional regulation of cell fate, hormones, and polarity factors (Balcerowicz et al., 2015). Two classes of proteins Rop GTPase and respiratory burst oxidase homolog (RBOH) have been shown to function in root hair growth in Arabidopsis. Rop2 GTPase acts as a positive regulatory switch in root hair initiation (Jones et al., 2002). RbohC/RHD2 derives reactive oxygen species (ROS) activity to regulate root hair elongation in a Ca^{2+}-dependent manner (Foreman et al., 2003; Takeda et al., 2008; Monshausen et al., 2009). An increasing number of research reveals that phytohormone auxin plays a key role in promoting root hair formation and elongation by triggering cell division and expansion (Lopez-Bucio et al., 2002; Kapulnik et al., 2011; Bhosale et al., 2018). Several auxin response mutants of *aux1*, *axr1*, *axr2,* and *axr3* in Arabidopsis have a pronounced effect on root hair length, indicating that auxin is required for normal root hair elongation (Pitts et al., 1998). Auxin can regulate *ROOT HAIR DEFECTIVE 6-LIKE 2* (*RSL2*) gene expression and ROS homeostasis to affect root hair growth (Mangano et al., 2018). Auxin can also induce receptor-like kinase ERULUS (ERU) activity to control root hair growth by modulating pectin dynamics (Schoenaers et al., 2018). Meanwhile, auxin integrates hormonal pathways and environmental factors to modulate root hair growth (Lee and Cho, 2013). Importantly, phosphate availability causes changes in hormone sensitivity in Arabidopsis root hair (Lopez-Bucio et al., 2002), and the activities of PIN-FORMED (PIN) proteins are involved in regulating root hair cell morphology (Ganguly et al., 2010). Mutants disrupting auxin synthesis (TRYPTOPHAN AMINOTRANSFERASE OF ARABIDOPSIS1, TAA) and transport (AUXIN RESISTANT1, AUX1) genes attenuate the response of root hairs to low P conditions (Bhosale et al., 2018). Additionally, hormone synthesis, transport, and sensitivity in roots are affected by P-deficient nutrient conditions, and thus, root architecture is reorganized in response to changes of phosphate availability (Lopez-Bucio et al., 2002).

In the auxin signaling pathway, polar auxin movement depends on auxin influx carrier proteins such as AUX1 and PINs, which mediate auxin transport across the plasma membrane (Friml, 2010). Arabidopsis AUX1 transports auxin from non-hair cells to developing hair cells to sustain root hair outgrowth (Jones et al., 2009), and rice OsAUX1 functions to mobilize auxin from the root apex to the differentiation zone to promote root hair elongation (Giri et al., 2018). PIN proteins are required for organ formation and plant development (Sabatini et al., 1999; Adamowski and Friml, 2015; Lee et al., 2020). PINs regulate cell division and expansion by controlling auxin distribution in plant roots (Blilou et al., 2005; Glanc et al., 2018). The expression of several PINs including PIN1, PIN2, and PIN3 in root hair cells greatly inhibits root hair growth, most likely by changing auxin level and PIN trafficking in the root hair cells (Ganguly et al., 2010). PIN2 generates an auxin gradient in epidermal cells that is crucial for root polarity (Nacry et al., 2005; Abas et al., 2006), and PIN3 is involved in both root hair growth and lateral root development (Lee and Cho, 2006; Chen et al., 2015). Auxin response factors (ARFs) control auxin-mediated transcriptional regulation of auxin-responsive genes (Tiwari et al., 2003), and ARF7 and ARF19 in Arabidopsis modulate root formation in response to P starvation (Huang et al., 2018). In addition to the role of auxin on root hair formation, actin cytoskeleton is also required for root hair morphogenesis (Kost et al., 1999; Hussey et al., 2006; Scheuring et al., 2016). The organization of actin microfilaments and their dynamics are essential for regulating cell expansion during root hair formation (Baluska et al., 2000; Wan et al., 2017; Wang et al., 2020); rapid cell elongation is concomitant with highly dynamic actin reorganization in roots (Takatsuka et al., 2018). Therefore, both auxin and actin drive root hair morphogenesis.

In plants, cell size and shape are determined by the deposition and mechanics of cell walls. The deposition of polysaccharides, including cellulose, hemicelluloses, and pectins, and structural remodeling of the wall are required for root cell formation (Park et al., 2011; Pena et al., 2012; Schoenaers et al., 2018). Some genes that control cell wall formation are involved in regulating root growth. Cellulose synthase-like proteins and xyloglucan-modifying proteins called xyloglucan endotransglucosylases/hydrolases (XTHs) have been shown to function in root growth (Favery et al., 2001; Vissenberg et al., 2005; Park et al., 2011). The modification and degradation of pectins mediated by pectin methylesterases (PMEs), pectin methylesterase inhibitors (PMEIs), and polygalacturonases (PGs) directly control the physicochemical properties of pectin, thereby influencing root growth (Levesque-Tremblay et al., 2015; Geng et al., 2017; Schoenaers et al., 2018).

Transcriptome data have shown that the expression of pectin-related genes changes in the roots of auxin-deficient Arabidopsis mutants or in response to low phosphate conditions (Yi et al., 2010; Hoehenwarter et al., 2016). Salazar-Haneo et al. used a coexpression-based approach and identified a class of P deficiency-induced genes encoding cell wall-modifying proteins that potentially function in root hair development (Salazar-Henao et al., 2016). Among these, a pectin degradation gene, *POLYGALACTURONASE INVOLVED IN EXPANSION 1* (*PGX1*), was predicted to respond to P starvation (Salazar-Henao et al., 2016); PGX1 was previously found to function in hypocotyl elongation and flower development in Arabidopsis (Xiao et al., 2014). Our previously studies showed that overexpression of *PGX2* in *PGX2*^{AT} seedlings inhibits primary root growth (Xiao et al., 2017), and alteration of *PGX3* gene expression affects stomatal development and rosette expansion

(Rui et al., 2017). In addition, *ARABIDOPSIS DEHISCENCE ZONE POLYGALACTURONASE1* (*ADPG1*) and *ADPG2* regulate floral organ abscission and anther dehiscence (Ogawa et al., 2009). Recently, another polygalacturonase, PG45 functions in leaf curvature (Yang et al., 2021). These characterized polygalacturonase genes are from different clades of phylogenetic tree (Xiao et al., 2014) and play important functions in multiple different organs during plant growth and development. However, the molecular mechanisms by which pectin degradation is associated with root growth in response to P deficiency remain elusive.

In an effort to understand how pectin degradation affects root hair development in response to P deficiency and auxin signaling, seedlings were grown under low P conditions or treated with 1-naphthaleneacetic acid (NAA) and 1-N-naphthylphthalamic acid (NPA), to observe the responses of root hairs to P availability. We found that the *PGX2* activation tagged line ($PGX2^{AT}$) but not overexpression and mutant lines of other tested PG genes displayed a phenotype of bubble-like root hairs under low P conditions, which was consistent with results from pectinase treatments *in vitro*. The activation tagging of *PGX2* triggered the production of superoxide and inhibited callose and anthocyanin accumulation in $PGX2^{AT}$ seedlings. Both NAA and NPA application inhibited the formation of bubble-like root hairs in $PGX2^{AT}$ roots. The trafficking and distribution of the auxin efflux carrier PIN2 were also altered in the roots of $PGX2^{AT}$ seedlings but were rescued with P deficiency. Moreover, actin filaments were less bundled and more stable in $PGX2^{AT}$ root hair cells than in the Col controls. In addition, we also found that *PGX2* transcript was downregulated in auxin pathway mutants. Together, these data link cell wall remodeling, the phytohormone auxin, and the actin cytoskeleton in regulating root hair morphogenesis in response to P starvation.

MATERIALS AND METHODS

Plant Materials and Growth Conditions

Arabidopsis thaliana Columbia (Col-0) ecotype was used as the wild-type control in this study. The $PGX2^{AT}$ activation tag line and $PGX1^{OE-1}$, $PGX1^{OE-48}$, $PGX3^{OE}$, *pgx1-1* (WiscDsLox262B06), *pgx1-2* (Salk_026818), *pgx2* (Salk_071023), and *pgx3* (Salk _010192) plants were described on previously published papers (Xiao et al., 2014, 2017; Rui et al., 2017). Transgenic plants were constructed by transforming *Lifeact-GFP* into Col and $PGX2^{AT}$ plants with *Agrobacterium tumefaciens* strain GV3101 using the floral dipping method (Clough and Bent, 1998). Positive transformants were screened on half-strength (½) MS plates containing 2.2 g/l MS salts (Caisson Laboratories, Cat#M519), 0.6 g/l MES, 1% (w/v) sucrose, 0.8% (w/v) agar-agar, and 25 μg/ml hygromycin (Phyto Technology, Cat#H397). *PIN2-GFP* $PGX2^{AT}$ plants were generated by crossing $PGX2^{AT}$ with *PIN2-GFP* plants. Homozygous plants were identified by GFP fluorescence screening. Sterilized seeds were sown on ½ MS plates for 3 days; then, seedlings were transferred into normal ½ MS plates (+P, 480 μm) or low-phosphorus ½ MS (MS salt without phosphate, Caisson Laboratories, Cat#MSP11) plates supplemented with 10 μm KH_2PO_4 and 49.5 μm K_2SO_4 (-P, 10 μm) for another 4 days. Seedlings were grown in a 22°C chamber with a 16-h-light (100 to 150 $\mu mol\, m^{-2}\ s^{-1}$)/8-h-dark lighting regime, and adult plants in soil were grown in a greenhouse under the same lighting conditions.

Root Hair Growth Phenotype

To measure primary root length, Arabidopsis seedlings grown on ½ MS plates were scanned with an HP Scanjet G4050 scanner and primary root lengths were measured using ImageJ. For measurements of root hair length, seedlings were photographed directly using a stereomicroscope (Leica M205FA), and root hair lengths were measured using ImageJ. To clearly observe root hair phenotype, root hairs were imaged using an epiflorescence microscope (Leica DM4B), and the width of each root hair base was measured using ImageJ and the number of root hairs with bubble-like morphology was counted. To observe the growth phenotype of root hairs after NPA and NAA treatments, 3-day-old seedlings grown on ½ MS plates containing 5 μm NPA (Sigma-Aldrich, Cat#33371) or 50 nm NAA (Sigma-Aldrich, Cat#N0640) were transferred into normal or low-phosphorus ½ MS plates supplemented with 5 μm NPA or 50 nm NAA to grow for another 4 days. Roots hairs were photographed under an epiflorescence microscope (Leica DM4B), and GFP fluorescence from *Lifeact-GFP* seedlings was detected using a spinning-disk confocal microscope with a 488-nm excitation laser and 525/50-nm emission filter with a 100x objective (Zeiss, Observer SD).

Gene Expression Analysis

Seedlings were collected and total RNA was extracted using a Plant RNA Kit (Omega). RNA concentration was measured by spectrophotometer (NanoDrop™ One^{C}), and first-strand cDNA was synthesized using qScript cDNA SuperMix (Takara) with 500 ng DNase I-treated RNA. qPCR was performed using SYBR Green FastMix (Takara) with cDNA and gene-specific primers on a Bio-Rad CFX96 Touch Real-Time PCR machine. *ACT2* or *EF1α* was amplified as an internal control. Data were analyzed using Bio-Rad CFX manager software and relative gene expression levels were calculated relative to *ACT2* or *EF1α* using the ΔΔCT method. Genes and primer sequences used for qPCR are listed in **Supplementary Tables 1, 2**.

Chemical Treatments

For exogenous pectinase treatment, Arabidopsis seedlings grown for 4 days after transferring on normal or P-deficient ½ MS medium plates were collected, and 7-day-old seedlings were incubated with liquid ½ MS medium containing 25 U/ml pectinase (Sigma-Aldrich, Cat#P2611) for 20 min at 30°C. Then, seedlings were washed by liquid ½ MS medium and photographed under an epifluorescence microscope (Leica DM4B).

To detect callose deposition in roots, aniline blue staining was performed according to a previously described method (Muller et al., 2015). Briefly, 7-day-old seedlings was stained

with 0.1% (w/v) aniline blue (Sigma-Aldrich, Cat#415049) in 100 mm phosphate buffer (pH 7.2) for 1.5 h. Root samples were placed in 20% (v/v) glycerol to observe under a spinning-disk confocal microscope with a 405-nm excitation laser and 445/50-nm emission filter with a 20x objective (Zeiss, Observer SD).

PI Staining

To clearly observe root hair phenotype, 7-day-old Col and *PGX2*^{AT} seedlings grown under normal and phosphate deficient conditions were stained with 1 ml 20 μg/ml propidium iodide (PI, Life Technologies, Cat#P3566) solution for 20 s in dark. The images of stained root hairs were recorded using a spinning-disk confocal microscope with a 561-nm excitation laser and 605/70-nm emission filter with a 100x objective (Zeiss, Observer SD). For superoxide detection, 7-day-old seedlings were incubated in 100 mm phosphate buffer (pH 7.2) containing with 0.5 mg/ml Nitro Blue Tetrazolium (NBT; Sigma-Aldrich, Cat#N6876) for 45 min, and images were recorded using a stereomicroscope (Leica M205FA).

Brefeldin A (BFA) treatment was performed as previously described method (Lin et al., 2020) with minor modifications. Seven-day-old seedlings grown on ½ MS medium plates were transferred to liquid ½ MS medium containing 50 μm BFA (Abmole, Cat#M2294) and incubated for 30 min. Seedlings were then washed with liquid ½ MS medium for 1.5 h. The roots were observed and imaged under a spinning-disk confocal microscope (Zeiss, Observer SD). Cells with visible BFA bodies were counted from epidermal cells of seedling roots. For actin inhibitor treatment, seedlings were incubated in liquid ½ MS medium containing 100 nm Latrunculin A (Lat A, Thermo Fisher, Cat#L12370) for 1 h, then washed by liquid ½ MS medium, and images of actin filaments were taken using a spinning-disk confocal microscope with a 488-nm excitation laser and 525/50-nm emission filter with a 100x objective (Zeiss, Observer SD).

Immunolabeling

Seven-day-old Arabidopsis Col and *PGX2*^{AT} seedlings grown on normal or P-deficient ½ MS medium plates were soaked in an isotonic fixation buffer containing 50 mm PIPES, 5 mm $MgSO_4$, 5 mm EGTA, 4% (v/v) paraformaldehyde, 0.1% (v/v) glutaraldehyde, and 1% (w/v) sucrose, pH 6.9 for 30 min, then transferred to the same fixation buffer for 90 min, and subsequently washed with 50 mm PIPES buffer (pH 6.9) three times. Seedling samples were blocked with PIPES buffer containing 3% (w/v) non-fat milk for 1 h. After washing by PIPES buffer three times, seedlings were incubated with a primary antibody (Agrisera; JIM5, Cat#AS184194; JIM7, Cat#AS184195; 1:10) at 4°C overnight. After washing by PIPES buffer, the samples were incubated with Alexa Fluor 488-conjugated goat anti-rat IgG secondary antibody (KPL, Cat#5230; 1:500) for 1 h at room temperature. The samples were then mounted on a slide in PIPES buffer and visualized using a spinning-disk confocal microscope with a 488-nm excitation laser and 525/50-nm emission filter with a 100x objective (Zeiss, Observer SD). The quantification of fluorescence intensity in immunolabeling images was performed by ZEN software (Zeiss), and the selected regions were used to quantify fluorescence intensity and the final fluorescence value was subtracted the background value.

Measurements of Uronic Acids and Methanol Release

Preparation of alcohol insoluble residue (AIR) enriched in cell walls and measurements of uronic acid content and pectin methylesterification degree were performed as described by Du et al. (2020).

Confocal Imaging of Lifeact-GFP and PIN2-GFP

Images of Lifeact-GFP and PIN2-GFP in root hairs and root tips were recorded under a spinning-disk confocal microscope with a 488-nm excitation laser and 525/50-nm emission filter with a 100x objective (Zeiss, Observer SD). Parameters representing actin filament density, skewness, and orientation were analyzed and quantified by ImageJ (Higaki, 2017). Briefly, original images were opened, cell regions were manually segmented, and cell region area and the angle of actin filaments relative to the cell growth axis were measured. Skeletonized images were obtained from the original images and masked with manually segmented cell region images. The parameters of actin filaments were quantified using the masked skeleton images. Fluorescence signal intensity of PIN2-GFP at the plasma membrane (PM) and intracellular compartments was quantified by ImageJ (Jensen, 2013). PM-associated GFP fluorescence was determined in regions of interest (ROIs) using the rectangle and/or freehand line tools in ImageJ. The intracellular signal of PIN2-GFP was determined by measuring multiple ROIs as the total intracellular fluorescence intensity, which excludes signals from the nuclei and nonspecific background. The resulting data were normalized to the mock control, and the signal ratio of PM to intracellular compartments was presented. For quantification of the BFA-induced internalization of PIN2-GFP, the level of internalized PIN2-GFP was presented as the number of GFP-labeled BFA bodies per cell (French et al., 2008).

RESULTS

A *PGX2*^{AT} Activation Tagged Line Has Bubble-Like Root Hairs Under P-Deficient Conditions

Plants can respond quickly to phosphate deficiency by increasing root hair length and density to enhance phosphate acquisition (Lopez-Bucio et al., 2002; Lynch, 2011). Cell wall remodeling plays a critical role in this process (Ogden et al., 2018). To explore how cell wall remodeling mediated by pectin-degrading polygalacturonases (PGs) affects root hair development, we screened a series of PG-related mutants for root hair phenotypes in response to P deficiency. Firstly, we detected gene expression in roots of *PGX1*^{OE1}, *PGX3*^{OE}, and *PGX2*^{AT}

seedlings. qPCR results showed that *PGX1* expression was comparable to wild type, *PGX3* expression was enhanced in *PGX3*^{OE} line, and *PGX2* was slightly increased in the roots of *PGX2*^{AT}, but its expression was significantly enhanced in the whole *PGX2*^{AT} seedlings (**Supplementary Figures 1A–D**). Neither overexpression nor loss of function for two polygalacturonase genes, *PGX1* and *PGX3*, showed significantly different root hair phenotypes compared with wild-type Col controls (**Supplementary Figure 1E**). The *PGX2* activation tagged line (*PGX2*^{AT}) displayed obvious bubble-like root hairs in response to P deficiency (**Figures 1A–C**), whereas the morphology of root hairs in *pgx2* mutant was similar to that of Col control (**Supplementary Figure 1E**). *PGX2*^{AT} seedlings had longer root hairs under normal and phosphate deficient conditions with similar growth rate (**Supplementary Figure 2**). We next quantified the width of the root hair base and found that *PGX2*^{AT} root hairs were wider than Col under normal conditions, and root hairs were the widest in P-deficient conditions (**Figure 1D**). To confirm that the bubble-like phenotype of root hairs resulted from pectin degradation in response to P deficiency, we incubated

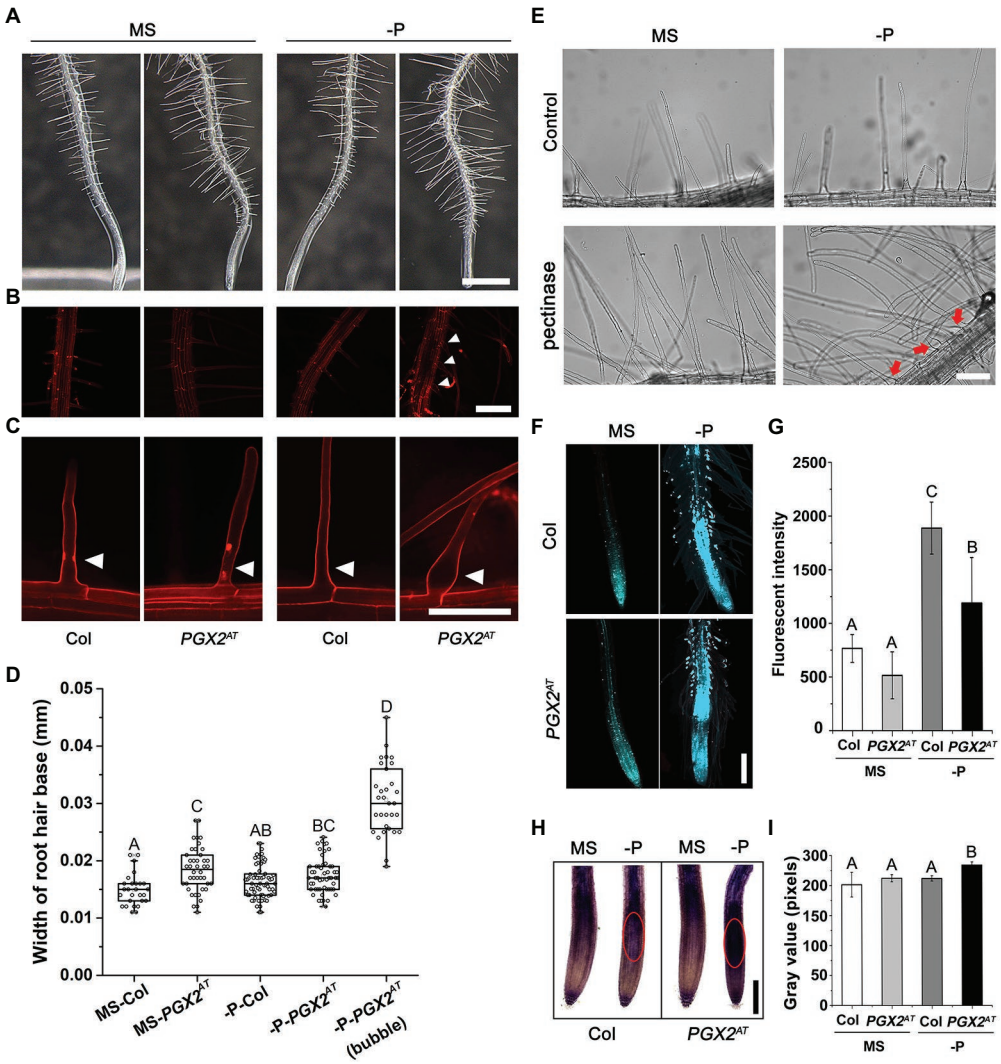

FIGURE 1 | Root hairs of *PGX2* activation tag (*PGX2*^{AT}) seedlings are sensitive to low phosphate conditions. **(A)** Primary roots with root hairs of 7-day-old Col and *PGX2*^{AT} seedlings grown in ½ MS medium plates under normal (MS) and phosphate deficient (-P) conditions. Three-day-old seedlings were transferred from normal MS plates into normal MS or -P conditions for another 4 days. Images were taken on the 4th day after seedling transfer. Bar = 1 mm. **(B)** Zoomed in images from **(A)** focusing on root hair regions by PI staining. Bar = 200 μm. **(C)** PI staining of root hairs in Col and *PGX2*^{AT} seedlings. Red and white arrowheads indicate positions of root hair bases. Bar = 0.1 mm. **(D)** Widths of root hair bases in Col and *PGX2*^{AT} seedlings grown in normal MS or -P conditions ($n \geq 27$ root hairs). **(E)** Pectinase treatment of Col seedlings after transferring to normal MS or -P conditions to grow for 4 days. Red arrows indicate bubble-like root hair bases. Bar = 100 μm. **(F)** Aniline blue staining for callose in roots of Col and *PGX2*^{AT} seedlings. Images were taken on the 4th day after seedling transfer. Bar = 200 μm. **(G)** Arbitrary fluorescent intensity of images for aniline blue staining ($n = 10$ seedlings per each genotype). **(H)** NBT staining for superoxide in root tips of Col and *PGX2*^{AT} seedlings. Red circles show highly stained regions. Images were taken in the 4th day after seedling transfer. Bar = 200 μm. **(I)** Gray value of NBT color intensity ($n = 10$ seedlings per each genotype). Error bars represent SD. Uppercase letters indicate significantly different groups as determined by one-way ANOVA with *post-hoc* Duncan's test ($p < 0.05$).

Col seedlings in liquid MS media with exogenous pectinase. The results revealed that the application of exogenous pectinase facilitated the formation of irreversibly bubble-like root hairs in Col seedlings grown under P-deficient conditions (**Figure 1E**). We also observed that the primary roots of *PGX2*^{AT} seedlings were shorter than those of Col in both normal and P-deficient conditions (**Supplementary Figures 3A,B**), whereas P deficiency has a similar negative effect on root growth in both genotypes (**Supplementary Figure 3C**). These data reveal the activation tagging of *PGX2* promotes cell expansion in root hairs.

In order to further investigate the response of *PGX2*^{AT} seedlings to P deficiency, we performed aniline blue and NBT staining in roots and found that callose deposition was decreased in root hairs, and superoxide accumulated more in root tips of *PGX2*^{AT} seedlings than in Col controls (**Figures 1F–I**). In general, P deficiency triggers anthocyanin accumulation in wild-type Arabidopsis (Jiang et al., 2007); however, there was less anthocyanin accumulation in *PGX2*^{AT} seedlings than in Col controls under low P conditions (**Supplementary Figure 4**). These experimental results show that *PGX2*^{AT} seedlings have different callose and anthocyanin deposition in response to nutrient stress.

The Pectin Physiological and Biochemical Properties Are Altered in *PGX2*^{AT} Line

In our previous studies, PGX1, PGX2, and PGX3 have been characterized as polygalacturonases that cleave pectin molecules and modulate demethylesterified HG abundance (Xiao et al., 2014, 2017; Rui et al., 2017). To determine whether PGX2-mediated pectin degradation affects pectin accumulation and pectin methylesterification, we measured uronic acid content and methanol released from the cell wall, which are used to calculate the degree of pectin methylesterification. Total uronic acid content in the cell walls of *PGX2*^{AT} seedlings was significantly lower, while the degree of pectin methylesterification in *PGX2*^{AT} seedlings increased compared to Col controls (**Figures 2A,B**). However, these differences were attenuated when seedlings were grown under P-deficient conditions (**Figures 2A,B**). To further examine whether the pectin modification is affected in the root hair wall of *PGX2*^{AT} seedlings, we performed immunolabeling experiments with JIM5 and JIM7 antibodies, which recognize low- and high-methylesterified HG, respectively (Willats et al., 2001; Guillemin et al., 2005). There was higher JIM5 signal intensity in *PGX2*^{AT} root hairs than in Col when seedlings were grown in both normal MS- and P-deficient conditions, whereas there was no obvious difference in JIM7 signal intensity (**Figures 2C–F**). These data suggest that PGX2 influences pectin degradation and modification, and that P deficiency might interfere in its effects to some degree in *PGX2*^{AT} seedlings.

Auxin Is Required to Maintain Normal Root Hair Width

Previous studies have shown that auxin plays an important role in root hair development by regulating cell expansion or cell division (Kapulnik et al., 2011; Bhosale et al., 2018; Schoenaers et al., 2018). Auxin promotes root hair growth in response to P deficiency in Arabidopsis and rice (Balzergue et al., 2017; Giri et al., 2018). Moreover, cell wall integrity signaling trigged by cell wall remodeling is closely related to hormone signaling pathway (Novakovic et al., 2018). PGX2 is a polygalacturonase to control cell expansion by pectin degradation (Xiao et al., 2017) and the *PGX2*^{AT} activation tagged line displayed a bubble-like root hair phenotype when seedlings were grown under P-deficient conditions (**Figure 1**). To explore whether auxin is also involved in this process along with cell wall regulators, especially in response to P deficiency, we analyzed the expression of genes associated with auxin signaling, P deficiency response, root hair development, and cell wall integrity (**Supplementary Table 2**). Gene expression was measured by qPCR, which showed that the expression levels of *LOW PHOSPHATE ROOT 1* (*LPR1*), *TIP GROWTH DEFECTIVE 1* (*TIP1*), *ROOT HAIR DEFECTIVE 1* (*RHD1*), *PIN1*, *ARF7*, and *ARF19* were upregulated in *PGX2*^{AT} seedlings grown under both normal and P-deficient conditions (**Figure 3A**). Importantly, *ARF19* showed the highest expression level of the genes measured in *PGX2*^{AT} seedlings under low P conditions (**Figure 3A**). *ARF19* functions in the auxin-mediated transcription that controls root hair growth (Michniewicz et al., 2007; Schoenaers et al., 2018). The auxin transporter PIN proteins are central components of the auxin efflux machinery that precisely regulate polar auxin transport (Sabatini et al., 1999). In addition, several genes associated with root hair formation, such as *TIP1*, *RHD1*, and *ROOT HAIR DEFECTIVE 6-LIKE 2* (*RSL2*), were upregulated in *PGX2*^{AT}, which was further enhanced with P deficiency (**Figure 3A**). However, there were no significant differences in the expression of *FERONIA* (*FER*), *THESEUS 1* (*THE1*), or *MECHANOSENSITIVE CHANNEL OF SMALL CONDUCTANCE LIKE 3* (*MSL3*) genes associated with cell wall integrity in Col seedlings under low P or in *PGX2*^{AT} seedlings under normal or low P conditions (**Figure 3A**).

To next investigate whether changes in auxin signaling and auxin transport conversely affect *PGX2* gene expression, we evaluated *PGX2* transcript levels in auxin signaling- or transport-deficient *arf7*, *arf19*, *arf7arf19*, *pin1*, *pin2*, and *pin3* mutants by qPCR. Expression of *PGX2* in all mutants was reduced, especially in *pin2* and *pin3* mutants, when seedlings were grown on normal MS medium plates (**Figure 3B**). Under P-deficient conditions, *PGX2* gene expression was significantly decreased in *arf7arf19* mutants but was still lower in *pin2* and *pin3* mutants than in Col (**Figure 3B**). These results indicate that *PGX2* expression might be regulated by auxin. The base of the root hairs in these mutants was measured and *arf7arf19*, *pin1*, and *pin3* mutants had wider root hairs in normal MS medium, and *arf7arf19*, *pin2*, and *pin3* mutants had wider root hairs under P-deficient conditions than the Col controls (**Figure 3C**). Both *arf7arf19* and *pin3* mutants displayed increased root hair cell width in both normal and P-deficient conditions compared with Col, whereas *pin2* mutants had wider root hairs only under P deficiency conditions. These experimental results imply that the alteration of *PGX2* gene expression in *PGX2*^{AT} seedlings may have an effect on auxin signaling and that *PGX2* expression may also be regulated by auxin during root hair formation.

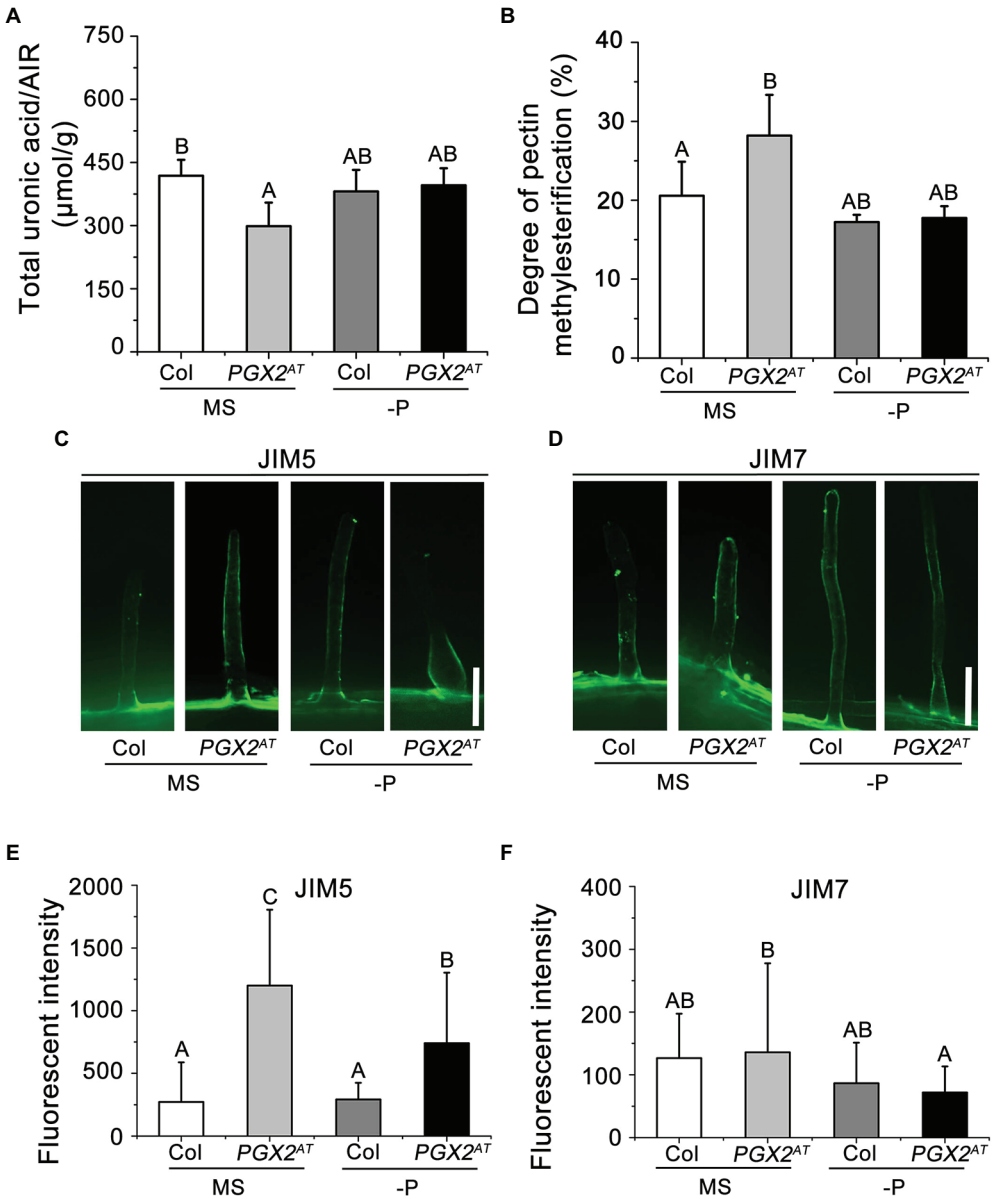

FIGURE 2 | The pectin content and degree of pectin methylesterification are altered in *PGX2*^{AT} seedlings. **(A,B)** Total uronic acid content and degree of pectin methylesterification of seedlings grown in normal MS and low phosphate (-P) conditions ($n = 5$ technical replicates). **(C,D)** Immunolabeling in root hair cells of Col and *PGX2*^{AT} seedlings after transferring for 4 days by JIM5 and JIM7, respectively. Bars = 50 μm. **(E,F)** Arbitrary fluorescent intensity of immunolabeling images for JIM5 and JIM7 antibodies ($n \geq 13$ root hairs per each genotype). Error bars represent SD. Uppercase letters on top of bar charts indicate significantly different groups as determined by one-way ANOVA with *post-hoc* Duncan's test ($p < 0.05$).

NAA and NPA Application Alleviates the *PGX2*^{AT} Root Hair Phenotype Under P-Deficient Conditions

Our experimental results showed that *PGX2*^{AT} seedlings have bubble-like root hair cells under P-deficient conditions (**Figure 1**). To assess the effect of auxin on the regulation of root hair shape, NAA or NPA was added into the growth medium. The application of 50 nm NAA or 5 μm NPA inhibited the bubble-like root hair phenotype of *PGX2*^{AT} seedlings under P-deficient conditions; however, we occasionally observed bulging at the middle or tip of some root hairs under low P conditions in NPA-treated *PGX2*^{AT} seedlings (**Figure 4A**). Quantification of basal bubble-like root hairs revealed that *PGX2*^{AT} root hairs were wider after NAA treatment under normal growth conditions compared to control plants, but this difference was offset under low P treatment conditions (**Figure 4B**). Moreover, there was no significant difference in basal root hair width between Col and *PGX2*^{AT} seedlings after NPA treatment under either normal or P-deficient conditions (**Figure 4B**) and NPA treatment markedly reduced the formation of bubble-like root hair cells under P-deficient conditions (**Figures 4C,D**).

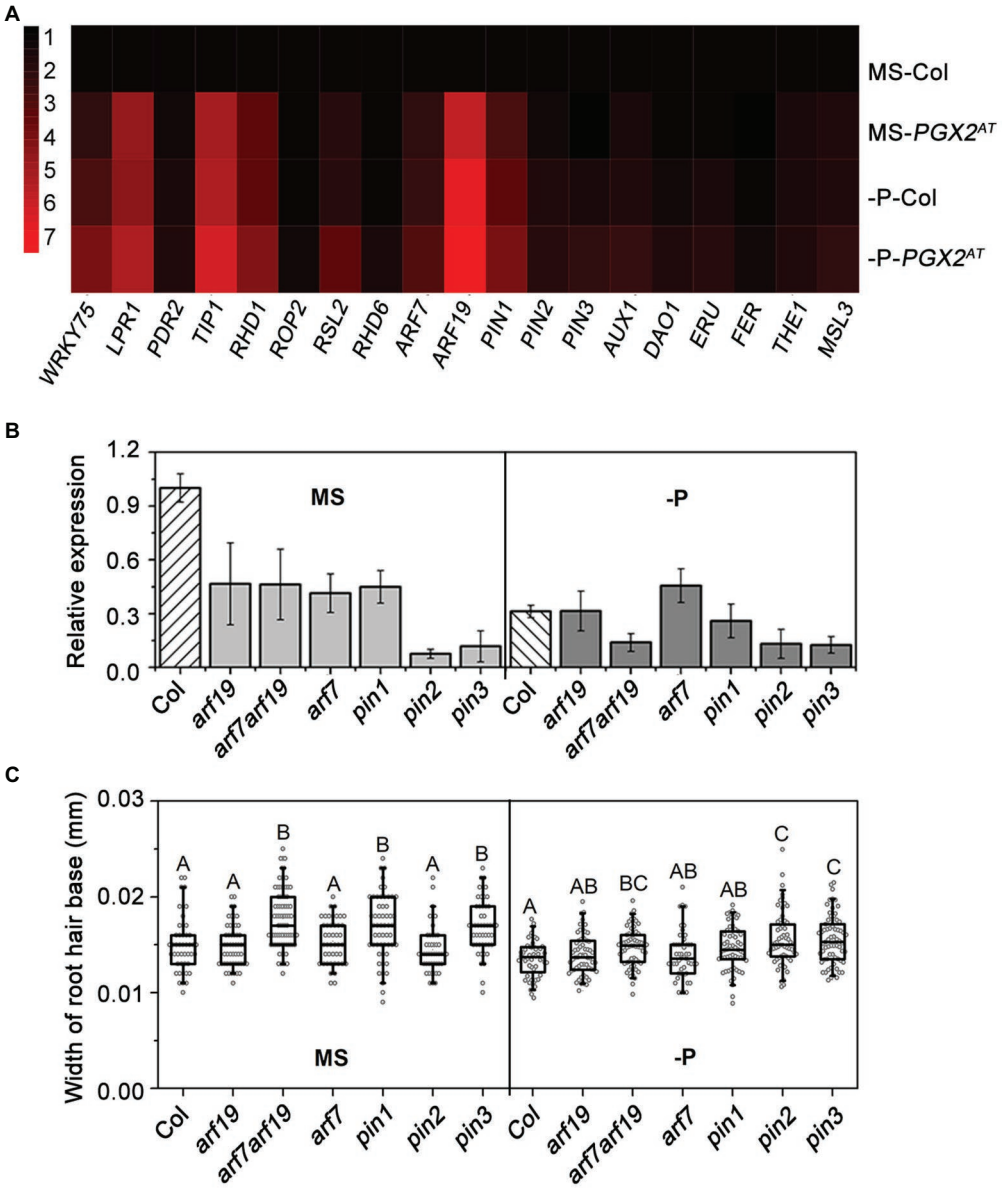

FIGURE 3 | Relative gene expression level and width of root hair base. **(A)** Relative expression of genes related to phosphate deficient response, root hair development, auxin and cell wall integrity signaling by RT-qPCR in Col, and *PGX2*^{AT} seedlings ($n = 3$ technical replicates). **(B)** Relative gene expression level of *PGX2* in auxin-related mutants with phosphate deficient (-P) conditions compared to MS controls ($n = 3$ technical replicates). **(C)** Widths of root hair bases of auxin-related mutants grown in MS control and phosphate deficient (-P) conditions ($n \geq 48$ root hairs). All data were collected in seedlings 4 days after transfer. Uppercase letters on top of boxplots indicate significantly different groups as determined by one-way ANOVA with *post-hoc* Duncan's test ($p < 0.01$).

We also measured root hair length of seedlings with NPA treatment under low P conditions. *PGX2*^{AT} seedlings had longer root hairs than Col controls in both normal and P-deficient conditions, whereas NPA application facilitated longitudinal cell expansion in *PGX2*^{AT} seedlings in response to P deficiency (**Supplementary Figure 5**). These results show that an imbalance in auxin levels induced the formation of bubble-like root hairs in *PGX2*^{AT} plants, further highlighting the role of auxin and cell wall remodeling during root hair morphogenesis, especially in response to P deficiency.

PIN2 Trafficking Is Altered in *PGX2*^{AT} Seedlings in Response to P Deficiency

We showed that NAA and NPA treatments affected root hair morphology in *PGX2*^{AT} seedlings (**Figure 4**) and that *PGX2* expression levels in *pin1*, *pin2*, and *pin3* mutants were decreased under both normal and P-deficient conditions (**Figure 3B**). These three mutants had wider root hairs, and the widths of root hair bases in *pin2* mutants significantly increased in response to P deficiency (**Figure 3C**). PIN2 functions in root hair development concomitantly with cellular trafficking and

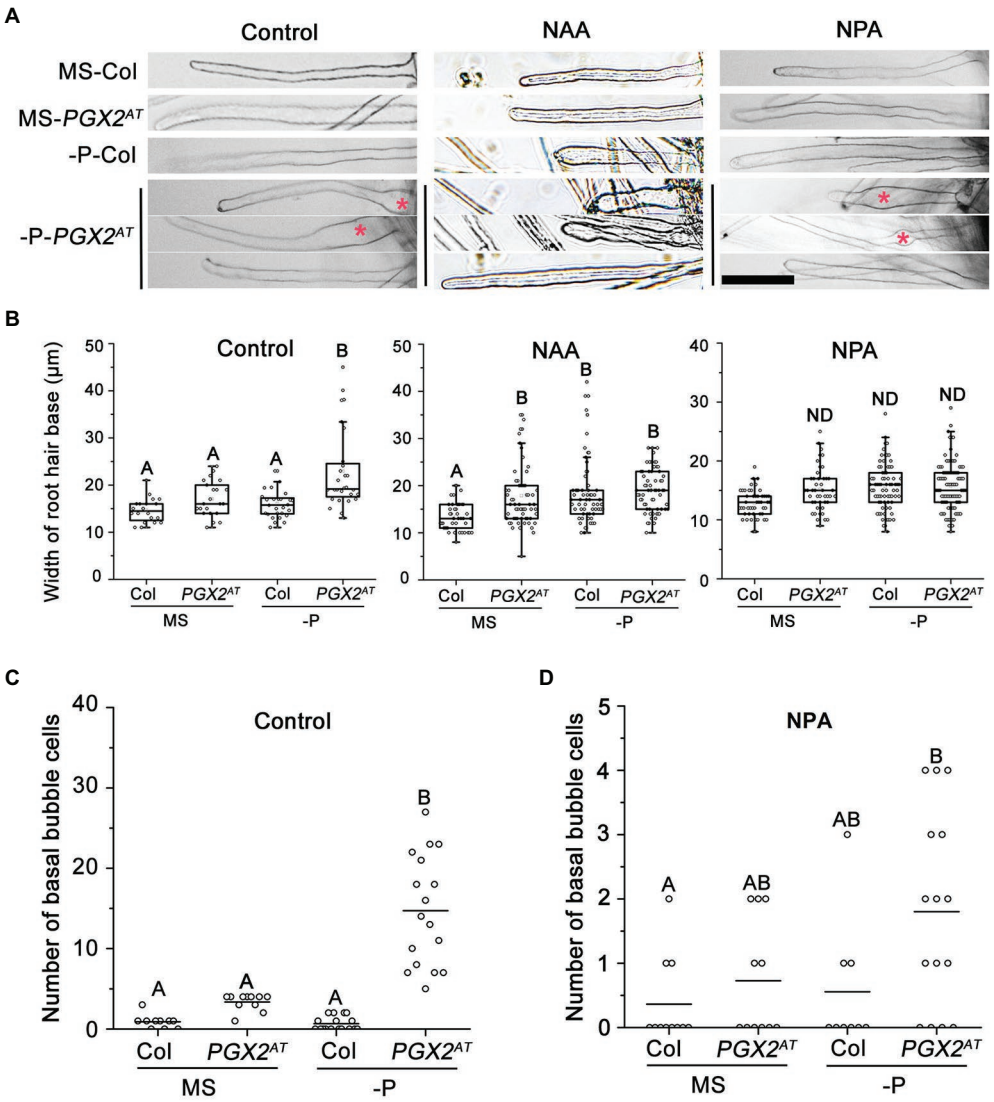

FIGURE 4 | NAA/NPA treatments inhibit bubble-like phenotype in root hair bases of *PGX2*^{AT} seedlings. **(A)** Both NAA and NPA treatments resulted in the occurrence of a few bubble-like root hairs at the top or middle under phosphate deficient (-P) conditions. Bars = 100 μm. **(B)** Widths of root hair bases in Col and *PGX2*^{AT} seedlings grown in MS control and phosphate deficient (-P) conditions with NAA or NPA application ($n \geq 20$ root hairs from at least 7 seedlings). **(C,D)** Number of basal bubble-like cells in Col and *PGX2*^{AT} seedlings grown in MS control and phosphate deficient (-P) conditions without (Control) or with NPA application ($n \geq 9$ seedlings). Uppercase letters indicate significantly different groups as determined by one-way ANOVA with *post-hoc* Duncan's test ($p < 0.01$). ND, no statistical difference.

polar transport (Lee and Cho, 2013; Pandya-Kumar et al., 2014). This evidence prompted us to further investigate whether PIN2 localization and transport are disrupted in root cells of *PGX2*^{AT} seedlings. We generated *35S::PIN2-GFP PGX2*^{AT} plants by crossing *35S::PIN2-GFP* line to *PGX2*^{AT}. We grew *35S::PIN2-GFP* Col and *35S::PIN2-GFP PGX2*^{AT} seedlings on normal and P-deficient medium plates, and then analyzed GFP localization and intensity. We found that in *PGX2*^{AT} seedling roots, PIN2-GFP was no longer polarized in root epidermal cells, especially in response to P deficiency, when compared with the polarized localization of PIN2-GFP in Col root cells (**Figures 5A,D**).

For auxin transport, the localization on plasma membrane (PM) of PIN proteins largely depends on dynamic vesicle recycling between the PM and endosomes (Dhonukshe et al., 2007). However, it is unknown whether the altered PIN2-GFP polarization in *PGX2*^{AT} root cells is associated with changes in PIN2 recycling. Brefeldin A (BFA) is a vesicle-trafficking inhibitor that interferes with PIN recycling and induces the accumulation of PIN proteins in "BFA bodies" (Geldner et al., 2001). We incubated *35S::PIN2-GFP* Col and *35S::PIN2-GFP PGX2*^{AT} seedlings with BFA for 30 min and then washed out the BFA for 1.5 h to allow PIN2 to repolarize in the plasma membrane (**Figures 5B,C,E,F**). After the application of BFA,

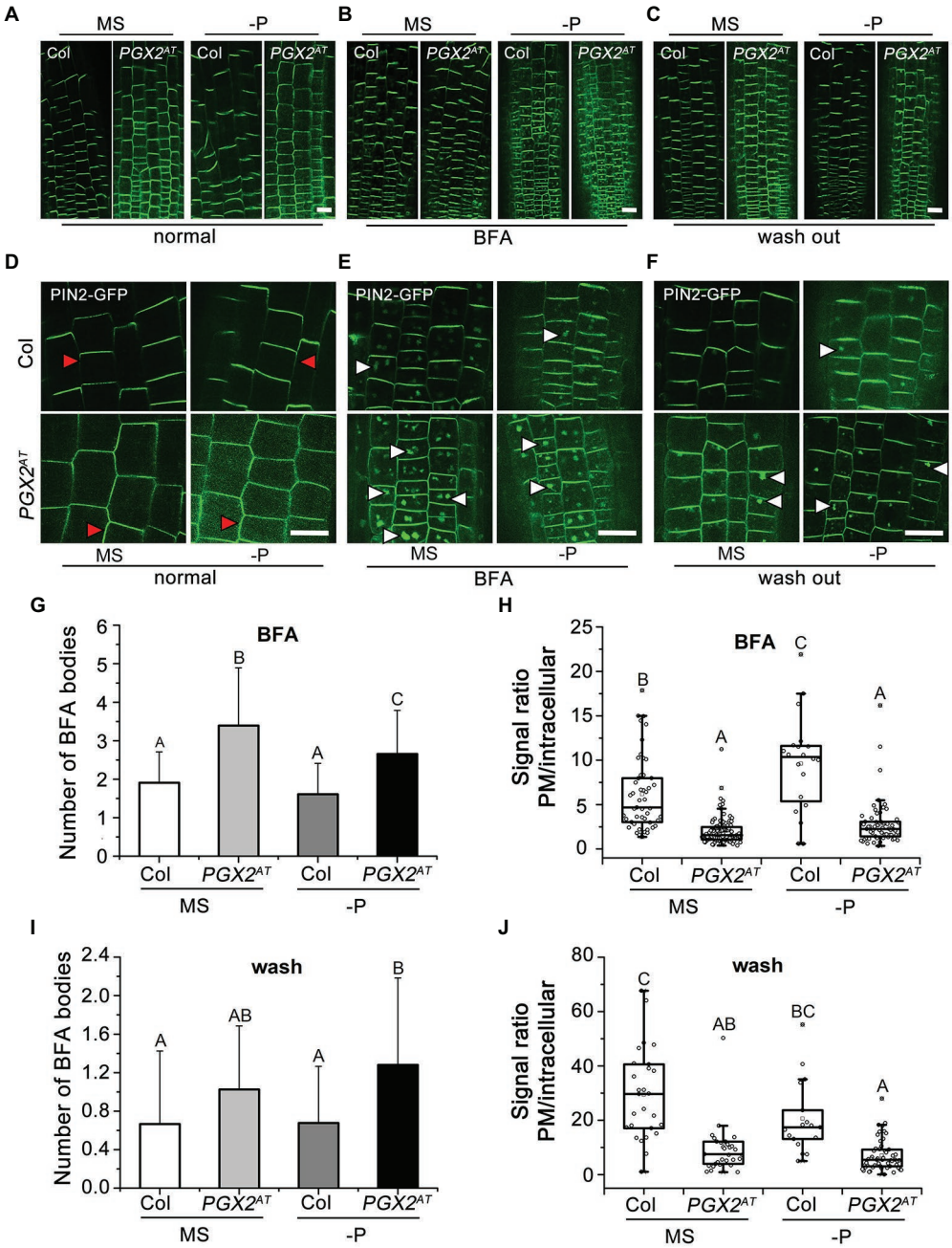

FIGURE 5 | The abundance of plasma membrane (PM)-localized PIN2 protein is reduced in *PGX2*^{AT} seedlings. **(A–C)** PIN2-GFP patterns in transgenic plants of *PIN2-GFP* Col and *PIN2-GFP PGX2*^{AT} seedling roots. PIN2-GFP images were taken after transferring for 4 days in those seedlings before **(A)** and after **(B)** BFA treatment for 30 min, and after BFA was washed out for 90 min **(C)**. Bars = 50 μm. **(D–F)** Images recorded with higher magnification under a confocal microscope. Red arrowheads indicate plasma membrane-localized PIN2-GFP; white arrowheads indicate intercellular PIN2-GFP. Bars = 50 μm. **(G,H)** Numbers of BFA bodies and signal ratio of PM to intracellular PIN2-GFP with BFA treatments ($n \geq 50$ cells from at least 10 seedlings). **(I,J)** Numbers of BFA bodies and signal ratio of PM to intracellular PIN2-GFP after washing BFA ($n \geq 28$ cells from at least 10 seedlings). Uppercase letters indicate significantly different groups as determined by one-way ANOVA with *post-hoc* Duncan's test ($p < 0.01$).

there was a similar trend of increased BFA body number and reduced PM-localized PIN2-GFP fluorescence in *PGX2*^{AT} root cells under both normal MS and P-deficient conditions (**Figures 5G,H**). The signal ratio of PM-localized to intracellular PIN2-GFP in *PGX2*^{AT} root cells was lower than that in Col in response to P deficiency (**Figure 5H**). After BFA was washed out, the number of BFA bodies in *PGX2*^{AT} root cells remained higher than in Col controls under P-deficient conditions (**Figure 5I**), and the fluorescent signal ratio of PM-localized to intracellular PIN2-GFP was lower under both normal and

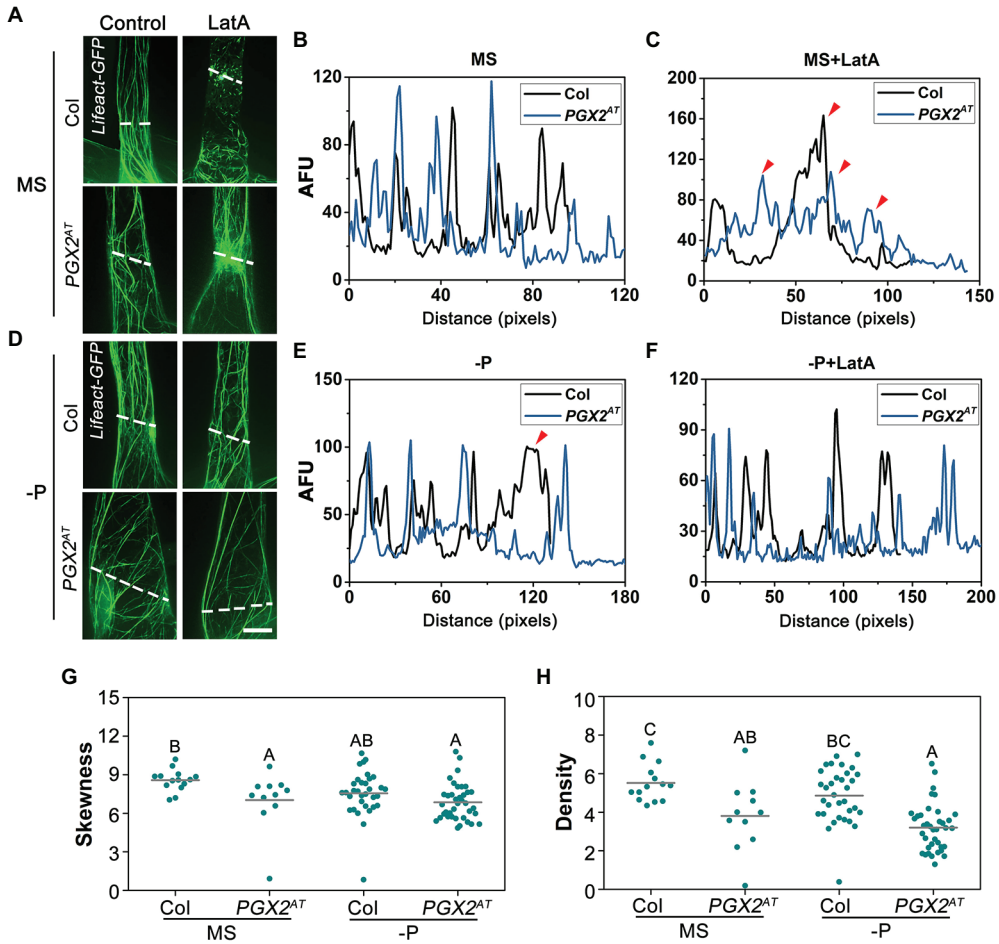

FIGURE 6 | Actin filaments in root hair cells of *PGX2*^{AT} seedlings show less skewness and more stable to LatA treatment. **(A,D)** *Lifeact-GFP* images of root hairs in 7-day-old *Lifeact-GFP* Col and *Lifeact-GFP PGX2*^{AT} seedlings under normal and P-deficient conditions without (Control) or with 100 nm LatA treatment. Bar = 10 μm. **(B,C,E,F)** Profiles of fluorescent intensity along lines (perpendicular to cell growth axis) for Col (black line) and *PGX2*^{AT} (blue line) cells in **(A)**. AFU, arbitrary fluorescence units. Arrows indicate differences between two lines. **(G,H)** Skewness and density of actin filaments decrease in *PGX2*^{AT} seedlings ($n \geq 11$ cells). Uppercase letters indicate significantly different groups as determined by one-way ANOVA with *post-hoc* Duncan test ($p < 0.01$).

P-deficient conditions (**Figure 5J**). These results indicate that activation tagging of *PGX2* affects polar transport and distribution of PIN2 in the PM, and that this effect is enhanced by P deficiency in *PGX2*^{AT} seedlings.

Actin Filaments Are More Stable and Less Bundled in *PGX2*^{AT} Than in Col Root Cells

The actin cytoskeleton is critical for vesicle trafficking and exocytosis in targeting PIN proteins to the plasma membrane during root hair development (Geldner et al., 2001; Ketelaar et al., 2003; Nagawa et al., 2012). Moreover, the organization and dynamics of actin filaments can influence root hair development in a PIN-independent fashion (Baluska et al., 2000; Pei et al., 2012; Ketelaar, 2013; Wang et al., 2020). Given the roles of the actin cytoskeleton and PGX2 in cell expansion and/or cell elongation (Xiao et al., 2017; Takatsuka et al., 2018; Arieti and Staiger, 2020), we generated transgenic plants expressing *Lifeact-GFP* in Col and *PGX2*^{AT} backgrounds to examine the dynamics and sensitivity of actin filaments to LatA, which depolymerizes actin filaments. On normal MS medium, a few actin filaments in *PGX2*^{AT} root hair cells were relatively intact after LatA treatment, whereas most actin filaments were fragmented in Col controls (**Figures 6A–C**). On P-deficient MS plates, actin filaments in both Col and *PGX2*^{AT} root hair cells were more resistant to LatA treatment (**Figures 6D–F**). We also noticed that actin filaments in root hairs of *PGX2*^{AT} seedlings grown on normal MS plates were more disorganized (**Figure 6A**) and that their distribution was different from that in Col root hairs under P-deficient conditions, which was possibly due to the bubble-like cell deformation of *PGX2*^{AT} root hairs (**Figure 6D**). Next, we quantified the skewness, which represents actin filament bundling or aggregation and density, and is indicated by the dispersion of the Lifeact-GFP signal. The degree of skewness and density of actin filaments was lower in *PGX2*^{AT} root hair cells than in Col controls

(**Figures 6G,H**), indicating that actin filaments in *PGX2*^{AT} root hairs are less bundled. However, the parameters of parallelness and angle that represent the direction of actin filaments did not show any difference between Col and *PGX2*^{AT} root hairs (**Supplementary Figures 6A,B**). Together, these data suggest that PGX2-mediated cell wall remodeling can feed back on actin orientation and dynamics, which is affected by P-deficient stress.

Low Actin Filament Skewness Is Rescued by NPA Application in *PGX2*^{AT} Root Hairs

Auxin and auxin transport inhibitors have been shown to affect actin dynamics and cell growth in roots. Although NAA application can drastically inhibit cell elongation concomitantly with actin filament bundling, NPA treatment can reduce cell elongation, leading to partial depolymerization of actin filaments with punctuated structures (Michniewicz et al., 2007). To observe whether actin filaments labeled with *Lifeact-GFP* are affected by NPA treatment, we grew transgenic lines expressing *Lifeact-GFP* in the Col and *PGX2*^{AT} genetic backgrounds on MS plates supplemented with 5 μm NPA for 7 days before imaging root cells by confocal microscope. The results showed a lower density and more parallel actin filaments in *PGX2*^{AT} than in Col root hair cells, whereas there was no significant difference in skewness and angle of actin filaments between the two lines (**Figure 7**). It is worth noting that the decreased actin filament skewness in *PGX2*^{AT} root hair cells was recovered with NPA application (**Figure 7**). Additionally, we did not observe bubble-like root hairs in *PGX2*^{AT} seedlings after NPA treatment under low P conditions (**Figure 7**), which is consistent with our other experimental results (**Figure 4**). These results reveal NPA treatment affected root cell expansion and actin filament skewness in *PGX2*^{AT} seedlings.

DISCUSSION

Several Arabidopsis PG genes from the large polygalacturonase gene family have been recently reported to function in hypocotyl elongation, leaf and flower morphogenesis, pollen and pollen tube development, and stem growth (Ogawa et al., 2009; Xiao et al., 2014, 2017; Rui et al., 2017; Hocq et al., 2020; Yang et al., 2021). Importantly, we previously reported that the polygalacturonase gene, *PGX2*, affects primary root length (Xiao et al., 2017). However, there are no reports on the functions of PG genes in root hair formation. In this study, we found that *PGX2*^{AT} seedlings had a bubble-like root hair phenotype in response to phosphate deficiency (**Figure 1**). Under low phosphate conditions, plants can remodel their root systems, including by regulating root hair development, to acquire more nutrients (Bates and Lynch, 1995; Lin et al., 2020). The reorganization of root system architecture is largely dependent on the remodeling of cell walls (Williamson et al., 2001; Ogden et al., 2018). Among different cell wall components, pectin is highly hydrated and flexible, which assists its role in controlling cell expansion and/or elongation during root growth (Levesque-Tremblay et al., 2015; Geng et al., 2017; Schoenaers et al., 2018). Here, we found that P-deficient stress triggers the formation of bubble-like root hairs in *PGX2*^{AT} seedlings, which was confirmed by the application of pectinase *in vitro* (**Figure 1**). These data indicate that P deficiency enhances the PGX2-dependent cell wall loosening in root hairs. *PGX2*^{AT} plants exhibited different stress responses, including decreased callose and anthocyanin deposition, and increased superoxide accumulation under P-deficient conditions (**Figure 1**). Together, these results suggest that PGX2 plays an important role in root hair development and that pectin degradation mediated by PGX2 is involved in multiple physiological processes.

The polygalacturonase activity of PGX2 allows it to cleave pectin molecules *in vivo* and *in vitro* (Xiao et al., 2017). Here, we found that *PGX2*^{AT} seedlings had lower pectin content but higher pectin methylesterification levels, supporting the role of PGX2 in pectin degradation and modification. However, this action of PGX2 on pectin was weakened under P-deficient conditions (**Figures 2A,B**). Interestingly, JIM5 fluorescence intensity was higher in *PGX2*^{AT} root hairs under both normal and P-deficient conditions (**Figures 2C,E**), but no change was observed in the JIM7 labeling pattern (**Figure 2F**), which indicated more demethylesterified HG in the *PGX2*^{AT} than Col seedlings. The methylesterification status in root hairs was monitored by immunolabeling with specific antibodies, while the methylesterification level was measured by biochemical method from isolated cell wall materials of whole seedlings. The different pectin methylesterification degree from biochemical measurement and immunolabeling may be attributable to differential accessibility in different tissue walls in *PGX2*^{AT} plants. In addition, the degree of methylesterification may vary in different parts of the plant.

Auxin acts as an organizing node that coordinates environmental cues to regulate root hair development, and PIN proteins are a key class of factors controlling the polar growth of root hairs (Blilou et al., 2005; Michniewicz et al., 2007; Lee and Cho, 2013). In our study, the expression levels of genes associated with auxin signaling pathways, such as *RSL2*, *ARF7*, *ARF19*, and *PIN1*, were upregulated in *PGX2*^{AT} seedlings, and their expression was further enhanced in response to low P (**Figure 3A**). Additionally, the expression of *PGX2* was significantly decreased in auxin signaling mutants (**Figure 3B**). Our results also showed that *PGX2*^{AT} seedlings had more low-methylesterified HG in root hairs (**Figures 2C,E**) and that low P conditions promoted the expression of genes associated with auxin signaling in *PGX2*^{AT} seedlings (**Figure 3A**). Moreover, the exogenous application of auxin NAA and auxin inhibitor NPA, which interferes with auxin signaling, limited the formation of bubble-like root hairs in *PGX2*^{AT} seedlings under low P conditions (**Figure 4**). These results indicate a possible functional interaction between auxin and pectin (Braybrook and Peaucelle, 2013), and further exploration of the molecular mechanisms by which auxin acts on pectin to regulate wall properties will deepen our understanding of this relationship.

Polarized PIN2 localization in the plasma membrane and its trafficking has been shown to respond to low P conditions (Kumar et al., 2015). The polar distribution of PM-localized PIN2 proteins in *PGX2*^{AT} root cells was obviously different from that in Col controls; PIN2 proteins were distributed uniformly around cells, unlike in Col controls (**Figure 5**). BFA treatment interrupted PIN2 trafficking and more BFA bodies accumulated

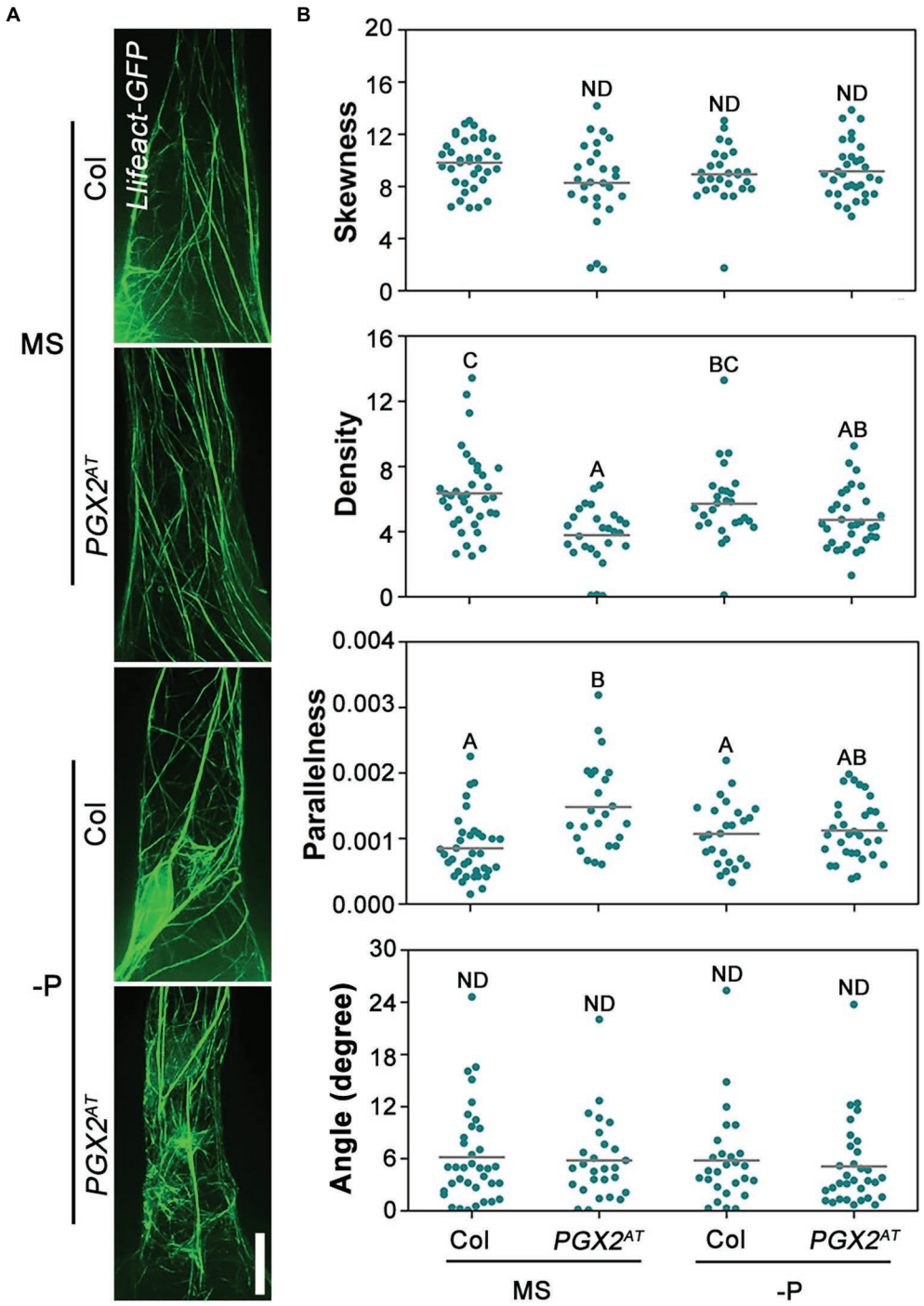

FIGURE 7 | Actin filament skewness is recovered in *PGX2*^{AT} root hair cells after NPA treatment. **(A)** Actin filaments in root hairs of *Lifeact-GFP* Col and *Lifeact-GFP PGX2*^{AT} transgenic seedlings in the 4th day after transferring into normal MS or P-deficient conditions. The 5 μm NPA was added into media for seedling growth. Bars = 10 μm. **(B)** Skewness, density, parallelness, and angle of actin filaments were quantified by ImageJ ($n \geq 27$ cells). Uppercase letters indicate significantly different groups as determined by one-way ANOVA with *post-hoc* Duncan testing ($p < 0.01$). ND, no statistical difference.

inside the cells of *PGX2*^{AT} roots under both normal and low P conditions. However, a few BFA bodies remained in the *PGX2*^{AT} cells after washing, which was especially obvious under low P conditions (**Figure 2**). These data indicate that PGX2-mediated cell wall remodeling affects polar localization and trafficking of PIN2 proteins in root cells, and these processes respond to P deficiency. In addition, given that the alteration of localization and trafficking of PIN2 proteins in *PGX2*^{AT} root

cells in P-deficient conditions, PIN2 endocytosis might be influenced by PGX2 in response to P deficiency. This may be explained that loosening of the cell wall causes changes in the wall-PM connections that help regulate membrane recycling.

To better adapt to low P soil environments, plant root systems undergo structural and wall remodeling (Lopez-Bucio et al., 2002), and actin filament bundling and dynamics in cells can respond to these alterations (Kumar et al., 2015). Here, we found that *PGX2*^{AT} root hair cells had disorganized but stable actin filaments after treatment with LatA under normal MS conditions. Actin filaments in *PGX2*^{AT} root hair cells were more disorganized under low P conditions, possibly contributing to the deformation of root cells. Interestingly, actin filaments in both Col and *PGX2*^{AT} root hair cells were more resistant to LatA treatment under low P conditions (**Figures 6A–F**). These data indicate that P deficiency can increase the stability of actin filaments in *PGX2*^{AT} seedlings, likely as part of a compensatory effect. Through further assessment of actin filament arrangement in the root hairs, *PGX2*^{AT} root hair cells had lower skewness of actin filaments than Col (**Figure 6G**), indicating that actin filaments were less bundled in *PGX2*^{AT} root hair cells. Additionally, we also observed actin filament arrangement after NPA treatment and found that the lower skewness of actin filaments in *PGX2*^{AT} was recovered (**Figure 7**), suggesting that NPA application increases actin filament bundling in *PGX2*^{AT} root hair cells.

CONCLUSION

In this study, we attempt to determine the key role of cell wall remodeling mediated by pectin degradation in plant root hair development, especially in response to low phosphate environments. Our results found that the activation tagging line *PGX2*^{AT} had altered pectin content and pectin methylesterification level. In low phosphate conditions, *PGX2*^{AT} seedlings displayed a bubble-like root hair phenotype, which was consistent with the pectinase treatment *in vitro*. Hormone auxin and cytoskeleton actin have been shown to play critical roles in root hair development. However, how cell wall remodeling cooperating with auxin signaling and actin in root hair development remains elusive. Our results found that the application of NAA or NPA inhibited the formation of bubble-like root hairs, and the polar localization and trafficking of the PIN2 protein was also affected in *PGX2*^{AT} root cells. In addition, actin filaments were less bundled and more stable in *PGX2*^{AT} root hair cells, and the decreased skewness of actin filaments in *PGX2*^{AT} root hairs was recovered with NPA treatment, which also inhibited the formation of bubble-like root hairs of *PGX2*^{AT} seedlings under low phosphate conditions. Taken together, our study demonstrates the molecular mechanism of how cell wall remodeling by pectin degradation, together with auxin signaling and cytoskeleton actin, cooperatively regulates root hair development in response to phosphate starvation. This provides a new view of the strategy for plants to adapt to low-nutrient environments.

DATA AVAILABILITY STATEMENT

The raw data supporting the conclusions of this article will be made available by the authors, without undue reservation.

AUTHOR CONTRIBUTIONS

CX designed the research. QZ, AD, MX, QL, XL, SY, XG, and SH performed experiments. QZ, AD, MX, JD, and CX analyzed the data and wrote the article. All authors contributed to the article and approved the submitted version.

FUNDING

This work was supported by Joint Science and Technology Support Program of Sichuan University and Panzhihua City (2019CDPZH-19) to JD, the Fundamental Research Funds for the Central Universities (SCU2021D006), the Institutional Research Fund from Sichuan University (2020SCUNL302), and the National Natural Science Foundation of China (32170357) to CX.

ACKNOWLEDGMENTS

The authors thank several laboratories for providing seeds and plasmids. PIN2-GFP seeds were from Yang Dong in Chinese Academy of Sciences; Lifeact-GFP plasmid was from Elison B. Blancaflor in Noble Research Institute; *pin1*, *pin2,* and *pin3* mutant seeds were from Jing Zhang in China Agriculture University; and *arf7*, *arf19,* and *arf7arf19* mutant seeds were from Feng Ren in Central China Normal University. The authors thank Charles T. Anderson for critical comments on this article.

SUPPLEMENTARY MATERIAL

The Supplementary Material for this article can be found online at: https://www.frontiersin.org/articles/10.3389/fpls.2022.862171/full#supplementary-material

REFERENCES

Abas, L., Benjamins, R., Malenica, N., Paciorek, T., Wirniewska, J., Moulinier-Anzola, J. C., et al. (2006). Intracellular trafficking and proteolysis of the Arabidopsis auxin-efflux facilitator PIN2 are involved in root gravitropism. *Nat. Cell Biol.* 8, 249–256. doi: 10.1038/ncb1369

Adamowski, M., and Friml, J. (2015). PIN-dependent auxin transport: action, regulation, and evolution. *Plant Cell* 27, 20–32. doi: 10.1105/tpc.114.134874

Arieti, R. S., and Staiger, C. J. (2020). Auxin-induced actin cytoskeleton rearrangements require AUX1. *New Phytol.* 226, 441–459. doi: 10.1111/nph.16382

Balcerowicz, D., Schoenaers, S., and Vissenberg, K. (2015). Cell fate determination and the switch from diffuse growth to planar polarity in *Arabidopsis* root epidermal cells. *Front. Plant Sci.* 6:1163. doi: 10.3389/fpls.2015.01163

Baluska, F., Salaj, J., Mathur, J., Braun, M., Jasper, F., Samaj, J., et al. (2000). Root hair formation: F-actin-dependent tip growth is initiated by local

assembly of profilin-supported F-actin meshworks accumulated within expansin-enriched bulges. *Dev. Biol.* 227, 618–632. doi: 10.1006/dbio.2000.9908

Balzergue, C., Dartevelle, T., Godon, C., Laugier, E., Meisrimler, C., Teulon, J. M., et al. (2017). Low phosphate activates STOP1-ALMT1 to rapidly inhibit root cell elongation. *Nat. Commun.* 8, 1–16. doi: 10.1038/ncomms15300

Bates, T. R., and Lynch, J. P. (1995). Stimulation of root hair elongation in *Arabidopsis thaliana* by low-phosphorus availability. *Plant Physiol.* 19, 529–538. doi: 10.1111/j.1365-3040.1996.tb00386.x

Bates, T. R., and Lynch, J. P. (2000). The efficiency of *Arabidopsis thaliana* root hairs in phosphorus acquisition. *Am. J. Bot.* 87, 964–970. doi: 10.2307/2656995

Bhosale, R., Giri, J., Pandey, B. K., Giehl, R. F. H., Hartmann, A., Traini, R., et al. (2018). A mechanistic framework for auxin dependent Arabidopsis root hair elongation to low external phosphate. *Nat. Commun.* 9:1409. doi: 10.1038/S41467-018-03851-3

Blilou, I., Xu, J., Wildwater, M., Willemsen, V., Paponov, I., Friml, J., et al. (2005). The PIN auxin efflux facilitator network controls growth and patterning in Arabidopsis roots. *Nature* 433, 39–44. doi: 10.1038/nature03184

Braybrook, S. A., and Peaucelle, A. (2013). Mechano-chemical aspects of organ formation in *Arabidopsis thaliana*: the relationship between auxin and pectin. *PLoS One* 8:e57813. doi: 10.1371/journal.pone.0057813

Chen, Q., Liu, Y., Maere, S., Lee, E., Van Isterdael, G., Xie, Z., et al. (2015). A coherent transcriptional feed-forward motif model for mediating auxin-sensitive PIN3 expression during lateral root development. *Nat. Commun.* 6:8821. doi: 10.1038/ncomms9821

Clough, S. J., and Bent, A. F. (1998). Floral dip: a simplified method for agrobacterium-mediated transformation of *Arabidopsis thaliana*. *Plant J.* 16, 735–743. doi: 10.1046/J.1365-313x.1998.00343.X

Dhonukshe, P., Aniento, F., Hwang, I., Robinson, D. G., Mravec, J., Stierhof, Y. D., et al. (2007). Clathrin-mediated constitutive endocytosis of PIN auxin efflux carriers in Arabidopsis. *Curr. Biol.* 17, 520–527. doi: 10.1016/j.cub.2007.01.052

Du, J., Kirui, A., Huang, S., Wang, L., Barnes, W. J., Kiemle, S. N., et al. (2020). Mutations in the pectin methyltransferase QUASIMODO2 influence cellulose biosynthesis and wall integrity in Arabidopsis. *Plant Cell* 32, 3576–3597. doi: 10.1105/tpc.20.00252

Favery, B., Ryan, E., Foreman, J., Linstead, P., Boudonck, K., Steer, M., et al. (2001). KOJAK encodes a cellulose synthase-like protein required for root hair cell morphogenesis in Arabidopsis. *Genes Dev.* 15, 79–89. doi: 10.1101/Gad.188801

Foreman, J., Demidchik, V., Bothwell, J. H., Mylona, P., Miedema, H., Torres, M. A., et al. (2003). Reactive oxygen species produced by NADPH oxidase regulate plant cell growth. *Nature* 422, 442–446. doi: 10.1038/nature01485

French, A. P., Mills, S., Swarup, R., Bennett, M. J., and Pridmore, T. P. (2008). Colocalization of fluorescent markers in confocal microscope images of plant cells. *Nat. Protoc.* 3, 619–628. doi: 10.1038/nprot.2008.31

Friml, J. (2010). Subcellular trafficking of PIN auxin efflux carriers in auxin transport. *Eur. J. Cell Biol.* 89, 231–235. doi: 10.1016/j.ejcb.2009.11.003

Ganguly, A., Lee, S. H., Cho, M., Lee, O. R., Yoo, H., and Cho, H. T. (2010). Differential auxin-transporting activities of PIN-FORMED proteins in Arabidopsis root hair cells. *Plant Physiol.* 153, 1046–1061. doi: 10.1104/pp.110.156505

Geldner, N., Friml, J., Stierhof, Y. D., Jurgens, G., and Palme, K. (2001). Auxin transport inhibitors block PIN1 cycling and vesicle trafficking. *Nature* 413, 425–428. doi: 10.1038/35096571

Geng, X. Y., Horst, W. J., Golz, J. F., Lee, J. E., Ding, Z. J., and Yang, Z. B. (2017). LEUNIG_HOMOLOG transcriptional co-repressor mediates aluminium sensitivity through PECTIN METHYLESTERASE46-modulated root cell wall pectin methylesterification in Arabidopsis. *Plant J.* 90, 491–504. doi: 10.1111/tpj.13506

Giri, J., Bhosale, R., Huang, G., Pandey, B. K., Parker, H., Zappala, S., et al. (2018). Rice auxin influx carrier OsAUX1 facilitates root hair elongation in response to low external phosphate. *Nat. Commun.* 9, 1408–1407. doi: 10.1038/s41467-018-03850-4

Glanc, M., Fendrych, M., and Friml, J. (2018). Mechanistic framework for cell-intrinsic re-establishment of PIN2 polarity after cell division. *Nature Plants* 4, 1082–1088. doi: 10.1038/s41477-018-0318-3

Guillemin, F., Guillon, F., Bonnin, E., Devaux, M. F., Chevalier, T., Knox, J. P., et al. (2005). Distribution of pectic epitopes in cell walls of the sugar beet root. *Planta* 222, 355–371. doi: 10.1007/s00425-005-1535-3

Hepler, P. K., Vidali, L., and Cheung, A. Y. (2001). Polarized cell growth in higher plants. *Annu. Rev. Cell Dev. Biol.* 17, 159–187. doi: 10.1146/annurev.cellbio.17.1.159

Higaki, T. (2017). Quantitative evaluation of cytoskeletal organizations by microscopic image analysis. *Plant Morphol.* 29, 15–21. doi: 10.5685/plmorphol.29.15

Hocq, L., Guinand, S., Habrylo, O., Voxeur, A., Tabi, W., Safran, J., et al. (2020). The exogenous application of AtPGLR, an endo-polygalacturonase, triggers pollen tube burst and repair. *Plant J.* 103, 617–633. doi: 10.1111/tpj.14753

Hoehenwarter, W., Monchgesang, S., Neumann, S., Majovsky, P., Abel, S., and Muller, J. (2016). Comparative expression profiling reveals a role of the root apoplast in local phosphate response. *BMC Plant Biol.* 16, 106–121. doi: 10.1186/S12870-016-0790-8

Holford, I. C. R. (1997). Soil phosphorus: its measurement, and its uptake by plants. *Aust. J. Soil Res.* 35, 227–239. doi: 10.1071/S96047

Huang, K. L., Ma, G. J., Zhang, M. L., Xiong, H., Wu, H., Zhao, C. Z., et al. (2018). The ARF7 and ARF19 transcription factors positively regulate PHOSPHATE STARVATION RESPONSE1 in Arabidopsis roots. *Plant Physiol.* 178, 413–427. doi: 10.1104/pp.17.01713

Hussey, P. J., Ketelaar, T., and Deeks, M. J. (2006). Control of the actin cytoskeleton in plant cell growth. *Annu. Rev. Plant Biol.* 57, 109–125. doi: 10.1146/annurev.arplant.57.032905.105206

Jensen, E. C. (2013). Quantitative analysis of histological staining and fluorescence using ImageJ. *Anat. Rec.* 296, 378–381. doi: 10.1002/ar.22641

Jiang, C., Gao, X., Liao, L., Harberd, N. P., and Fu, X. (2007). Phosphate starvation root architecture and anthocyanin accumulation responses are modulated by the gibberellin-DELLA signaling pathway in Arabidopsis. *Plant Physiol.* 145, 1460–1470. doi: 10.1104/pp.107.103788

Jones, A. R., Kramer, E. M., Knox, K., Swarup, R., Bennett, M. J., Lazarus, C. M., et al. (2009). Auxin transport through non-hair cells sustains root-hair development. *Nat. Cell Biol.* 11, 78–84. doi: 10.1038/ncb1815

Jones, M. A., Shen, J. J., Fu, Y., Li, H., Yang, Z., and Grierson, C. S. (2002). The Arabidopsis Rop2 GTPase is a positive regulator of both root hair initiation and tip growth. *Plant Cell* 14, 763–776. doi: 10.1105/tpc.010359

Kapulnik, Y., Resnick, N., Mayzlish-Gati, E., Kaplan, Y., Wininger, S., Hershenhorn, J., et al. (2011). Strigolactones interact with ethylene and auxin in regulating root-hair elongation in Arabidopsis. *J. Exp. Bot.* 62, 2915–2924. doi: 10.1093/jxb/erq464

Ketelaar, T. (2013). The actin cytoskeleton in root hairs: all is fine at the tip. *Curr. Opin. Plant Biol.* 16, 749–756. doi: 10.1016/j.pbi.2013.10.003

Ketelaar, T., de Ruijter, N. C., and Emons, A. M. (2003). Unstable F-actin specifies the area and microtubule direction of cell expansion in Arabidopsis root hairs. *Plant Cell* 15, 285–292. doi: 10.1105/tpc.007039

Kost, B., Mathur, J., and Chua, N. H. (1999). Cytoskeleton in plant development. *Curr. Opin. Plant Biol.* 2, 462–470. doi: 10.1016/S1369-5266(99)00024-2

Kumar, M., Pandya-Kumar, N., Dam, A., Haor, H., Mayzlish-Gati, E., Belausov, E., et al. (2015). Arabidopsis response to low-phosphate conditions includes active changes in actin filaments and PIN2 polarization and is dependent on strigolactone signalling. *J. Exp. Bot.* 66, 1499–1510. doi: 10.1093/jxb/eru513

Lee, S. H., and Cho, H. T. (2006). PINOID positively regulates auxin efflux in Arabidopsis root hair cells and tobacco cells. *Plant Cell* 18, 1604–1616. doi: 10.1105/tpc.105.035972

Lee, R. D. W., and Cho, H. T. (2013). Auxin, the organizer of the hormonal/environmental signals for root hair growth. *Front. Plant Sci.* 4:448. doi: 10.3389/Fpls.2013.00448

Lee, H. J., Kim, H. S., Park, J. M., Cho, H. S., and Jeon, J. H. (2020). PIN-mediated polar auxin transport facilitates root-obstacle avoidance. *New Phytol.* 225, 1285–1296. doi: 10.1111/nph.16076

Levesque-Tremblay, G., Pelloux, J., Braybrook, S. A., and Muller, K. (2015). Tuning of pectin methylesterification: consequences for cell wall biomechanics and development. *Planta* 242, 791–811. doi: 10.1007/s00425-015-2358-5

Lin, D. L., Yao, H. Y., Jia, L. H., Tan, J. F., Xu, Z. H., Zheng, W. M., et al. (2020). Phospholipase D-derived phosphatidic acid promotes root hair development under phosphorus deficiency by suppressing vacuolar degradation of PIN-FORMED2. *New Phytol.* 226, 142–155. doi: 10.1111/nph.16330

Lopez-Arredondo, D. L., Leyva-Gonzalez, M. A., Gonzalez-Morales, S. I., Lopez-Bucio, J., and Herrera-Estrella, L. (2014). Phosphate nutrition: improving low-phosphate tolerance in crops. *Annu. Rev. Plant Biol.* 65, 95–123. doi: 10.1146/annurev-arplant-050213-035949

Lopez-Bucio, J., Hernandez-Abreu, E., Sanchez-Calderon, L., Nieto-Jacobo, M. F., Simpson, J., and Herrera-Estrella, L. (2002). Phosphate availability alters architecture and causes changes in hormone sensitivity in the Arabidopsis root system. *Plant Physiol.* 129, 244–256. doi: 10.1104/pp.010934

Lynch, J. P. (2011). Root phenes for enhanced soil exploration and phosphorus acquisition: tools for future crops. *Plant Physiol.* 156, 1041–1049. doi: 10.1104/pp.111.175414

Mangano, S., Denita-Juarez, S. P., Marzol, E., Borassi, C., and Estevez, J. M. (2018). High auxin and high phosphate impact on RSL2 expression and ROS-homeostasis linked to root hair growth in *Arabidopsis thaliana*. *Front. Plant Sci.* 9:1164. doi: 10.3389/fpls.2018.01164

Michniewicz, M., Brewer, P. B., and Friml, J. I. (2007). Polar auxin transport and asymmetric auxin distribution. *Arabidopsis Book* 5:e0108. doi: 10.1199/tab.0108

Monshausen, G. B., Bibikova, T. N., Weisenseel, M. H., and Gilroy, S. (2009). Ca2+ regulates reactive oxygen species production and pH during mechanosensing in Arabidopsis roots. *Plant Cell* 21, 2341–2356. doi: 10.1105/tpc.109.068395

Muller, J., Toev, T., Heisters, M., Teller, J., Moore, K. L., Hause, G., et al. (2015). Iron-dependent callose deposition adjusts root meristem maintenance to phosphate availability. *Dev. Cell* 33, 216–230. doi: 10.1016/j.devcel.2015.02.007

Nacry, P., Canivenc, G., Muller, B., Azmi, A., Van Onckelen, H., Rossignol, M., et al. (2005). A role for auxin redistribution in the responses of the root system architecture to phosphate starvation in Arabidopsis. *Plant Physiol.* 138, 2061–2074. doi: 10.1104/pp.105.060061

Nagawa, S., Xu, T., Lin, D., Dhonukshe, P., Zhang, X., Friml, J., et al. (2012). ROP GTPase-dependent actin microfilaments promote PIN1 polarization by localized inhibition of clathrin-dependent endocytosis. *PLoS Biol.* 10, e1001299–e1001211. doi: 10.1371/journal.pbio.1001299

Novakovic, L., Guo, T., Bacic, A., Sampathkumar, A., and Johnson, K. L. (2018). Hitting the wall-sensing and signaling pathways involved in plant cell wall remodeling in response to abiotic stress. *Plants* 7:89. doi: 10.3390/plants7040089

Ogawa, M., Kay, P., Wilson, S., and Swain, S. M. (2009). ARABIDOPSIS DEHISCENCE ZONE POLYGALACTURONASE1 (ADPG1), ADPG2, and QUARTET2 are polygalacturonases required for cell separation during reproductive development in Arabidopsis. *Plant Cell* 21, 216–233. doi: 10.1105/tpc.108.063768

Ogden, M., Hoefgen, R., Roessner, U., Persson, S., and Khan, G. A. (2018). Feeding the walls: how does nutrient availability regulate cell wall composition? *Int. J. Mol. Sci.* 19, 1–16. doi: 10.3390/ijms19092691

Pandya-Kumar, N., Shema, R., Kumar, M., Mayzlish-Gati, E., Levy, D., Zemach, H., et al. (2014). Strigolactone analog GR24 triggers changes in PIN2 polarity, vesicle trafficking and actin filament architecture. *New Phytol.* 202, 1184–1196. doi: 10.1111/nph.12744

Park, S., Szumlanski, A. L., Gu, F. W., Guo, F., and Nielsen, E. (2011). A role for CSLD3 during cell-wall synthesis in apical plasma membranes of tip-growing root-hair cells. *Nat. Cell Biol.* 13, 973–980. doi: 10.1038/ncb2294

Pei, W., Du, F., Zhang, Y., He, T., and Ren, H. (2012). Control of the actin cytoskeleton in root hair development. *Plant Sci.* 187, 10–18. doi: 10.1016/j.plantsci.2012.01.008

Pena, M. J., Kong, Y. Z., York, W. S., and O'Neill, M. A. (2012). A galacturonic acid-containing xyloglucan is involved in Arabidopsis root hair tip growth. *Plant Cell* 24, 4511–4524. doi: 10.1105/tpc.112.103390

Peret, B., Desnos, T., Jost, R., Kanno, S., Berkowitz, O., and Nussaume, L. (2014). Root architecture responses: In search of phosphate. *Plant Physiol.* 166, 1713–1723. doi: 10.1104/pp.114.244541

Pitts, R. J., Cernac, A., and Estelle, M. (1998). Auxin and ethylene promote root hair elongation in Arabidopsis. *Plant J.* 16, 553–560. doi: 10.1046/j.1365-313x.1998.00321.x

Rui, Y., Xiao, C., Yi, H., Kandemir, B., Wang, J. Z., Puri, V. M., et al. (2017). POLYGALACTURONASE INVOLVED IN EXPANSION3 functions in seedling development, rosette growth, and stomatal dynamics in *Arabidopsis thaliana*. *Plant Cell* 29, 2413–2432. doi: 10.1105/tpc.17.00568

Sabatini, S., Beis, D., Wolkenfelt, H., Murfett, J., Guilfoyle, T., Malamy, J., et al. (1999). An auxin-dependent distal organizer of pattern and polarity in the Arabidopsis root. *Cell* 99, 463–472. doi: 10.1016/S0092-8674(00)81535-4

Salazar-Henao, J. E., Lin, W. D., and Schmidt, W. (2016). Discriminative gene co-expression network analysis uncovers novel modules involved in the formation of phosphate deficiency-induced root hairs in Arabidopsis. *Sci. Rep.* 6, 1–11. doi: 10.1038/srep26820

Scheuring, D., Lofke, C., Kruger, F., Kittelmann, M., Eisa, A., Hughes, L., et al. (2016). Actin-dependent vacuolar occupancy of the cell determines auxin-induced growth repression. *P Natl. Acad. Sci. USA* 113, 452–457. doi: 10.1073/pnas.1517445113

Schoenaers, S., Balcerowicz, D., Breen, G., Hill, K., Zdanio, M., Mouille, G., et al. (2018). The auxin-regulated CrRLK1L kinase ERULUS controls cell wall composition during root hair tip growth. *Curr. Biol.* 28, 722–732.e6. doi: 10.1016/j.cub.2018.01.050

Takatsuka, H., Higaki, T., and Umeda, M. (2018). Actin reorganization triggers rapid cell elongation in roots. *Plant Physiol.* 178, 1130–1141. doi: 10.1104/pp.18.00557

Takeda, S., Gapper, C., Kaya, H., Bell, E., Kuchitsu, K., and Dolan, L. (2008). Local positive feedback regulation determines cell shape in root hair cells. *Science* 319, 1241–1244. doi: 10.1126/science.1152505

Tiwari, S. B., Hagen, G., and Guilfoyle, T. (2003). The roles of auxin response factor domains in auxin-responsive transcription. *Plant Cell* 15, 533–543. doi: 10.1105/tpc.008417

Vissenberg, K., Oyama, M., Osato, V., Yokoyama, R., Verbelen, J. P., and Nishitani, K. (2005). Differential expression of AtXTH17, AtXTH18, AtXTH19 and AtXTH20 genes in Arabidopsis roots. Physiological roles in specification in cell wall construction. *Plant Cell Physiol.* 46, 192–200. doi: 10.1093/pcp/pci013

Wan, Z. Y., Chai, S., Ge, F. R., Feng, Q. N., Zhang, Y., and Li, S. (2017). Arabidopsis PROTEIN S-ACYL TRANSFERASE4 mediates root hair growth. *Plant J.* 90, 249–260. doi: 10.1111/tpj.13484

Wang, X. L., Bi, S. T., Wang, L., Li, H. P., Gao, B. A., Huang, S. J., et al. (2020). GLABRA2 regulates actin bundling protein VILLIN1 in root hair growth in response to osmotic stress. *Plant Physiol.* 184, 176–193. doi: 10.1104/pp.20.00480

Willats, W. G., McCartney, L., and Knox, J. P. (2001). In-situ analysis of pectic polysaccharides in seed mucilage and at the root surface of *Arabidopsis thaliana*. *Planta* 213, 37–44. doi: 10.1007/s004250000481

Williamson, L. C., Ribrioux, S. P. C. P., Fitter, A. H., and Leyser, H. M. O. (2001). Phosphate availability regulates root system architecture in Arabidopsis. *Plant Physiol.* 126, 875–882. doi: 10.1104/Pp.126.2.875

Xiao, C., Barnes, W. J., Zamil, M. S., Yi, H., Puri, V. M., and Anderson, C. T. (2017). Activation tagging of Arabidopsis POLYGALACTURONASE INVOLVED IN EXPANSION2 promotes hypocotyl elongation, leaf EXPANSION, stem lignification, mechanical stiffening, and lodging. *Plant J.* 89, 1159–1173. doi: 10.1111/tpj.13453

Xiao, C., Somerville, C., and Anderson, C. T. (2014). POLYGALACTURONASE INVOLVED IN EXPANSION1 functions in cell elongation and flower development in Arabidopsis. *Plant Cell* 26, 1018–1035. doi: 10.1105/Tpc.114.123968

Yang, Y., Anderson, C. T., and Cao, J. (2021). POLYGALACTURONASE45 cleaves pectin and links cell proliferation and morphogenesis to leaf curvature in *Arabidopsis thaliana*. *Plant J.* 106, 1493–1508. doi: 10.1111/tpj.15308

Yi, K., Menand, B., Bell, E., and Dolan, L. (2010). A basic helix-loop-helix transcription factor controls cell growth and size in root hairs. *Nat. Genet.* 42, 264–267. doi: 10.1038/ng.529

Conflict of Interest: The authors declare that the research was conducted in the absence of any commercial or financial relationships that could be construed as a potential conflict of interest.

Publisher's Note: All claims expressed in this article are solely those of the authors and do not necessarily represent those of their affiliated organizations, or those of the publisher, the editors and the reviewers. Any product that may be evaluated in this article, or claim that may be made by its manufacturer, is not guaranteed or endorsed by the publisher.

frontiers | Frontiers in Plant Science

MINI REVIEW
published: 18 May 2022
doi: 10.3389/fpls.2022.880680

Wound-Induced Systemic Responses and Their Coordination by Electrical Signals

Kyounghee Lee[1,2] *and Pil Joon Seo*[1,2,3]*

[1]Department of Chemistry, Seoul National University, Seoul, South Korea, [2]Research Institute of Basic Sciences, Seoul National University, Seoul, South Korea, [3]Plant Genomics and Breeding Institute, Seoul National University, Seoul, South Korea

Wounding not only induces the expression of damage-responsive genes, but also initiates physiological changes, such as tissue repair, vascular reconnection, and *de novo* organogenesis in locally damaged tissues. Wound-induced signals also propagate from the site of wounding to distal organs to elicit a systemic response. Electrical signaling, which is the most conserved type of systemic signaling in eukaryotes, is triggered by wound-induced membrane potential changes. Changes in membrane potential spread toward systemic tissues in synergy with chemical and hydraulic signals. Here, we review current knowledge on wound-induced local and systemic responses in plants. We focus particularly on how wound-activated plasma membrane-localized ion channels and pumps propagate systemic information about wounding to induce downstream molecular responses in distal tissues. Finally, we propose future studies that could lead to a better understanding of plant electrical signals and their role in physiological responses to wounding.

Keywords: electrical signal, ion channel, ion pump, jasmonic acid, membrane potential, systemic signaling, wounding

OPEN ACCESS

Edited by:
Simon Gilroy, University of Wisconsin-Madison, United States

Reviewed by:
Michael M. Wudick, Heinrich Heine University of Düsseldorf, Germany
Masatsugu Toyota, Saitama University, Japan

***Correspondence:**
Pil Joon Seo
pjseo1@snu.ac.kr

Specialty section:
This article was submitted to Plant Cell Biology, a section of the journal Frontiers in Plant Science

Received: *21 February 2022*
Accepted: *28 April 2022*
Published: *18 May 2022*

Citation:
Lee K and Seo PJ (2022) Wound-Induced Systemic Responses and Their Coordination by Electrical Signals. Front. Plant Sci. 13:880680. doi: 10.3389/fpls.2022.880680

INTRODUCTION

Plants are sessile organisms that are constantly exposed to a variety of external stimuli. Wounding is one external stimulus that induces physical damages threating plant survival and also makes them more susceptible to pathogen invasion (Savatin et al., 2014). Wounding is caused by insect feeding, pathogen infection, animal grazing, wind, and heavy rain (Reymond et al., 2000; Sozen et al., 2020). To survive, plants have evolved sophisticated defense mechanisms, such as the activation of defense gene expression, tissue repair, and *de novo* tissue regeneration in regions of the tissue where wounding occurs (Reymond et al., 2000; Liu et al., 2014; Savatin et al., 2014; Matsuoka et al., 2021). Signals in response to wounding propagate from the site of wound perception to distal tissues. These signals typically travel long distances, and this process is referred to as a systemic response (Huber and Bauerle, 2016). Wounding triggers distal systemic responses in plants, such as accumulation of defensive proteinase inhibitors (PIs) and jasmonates (JAs) in systemic tissues (Koo et al., 2009; Kiep et al., 2015; Gilroy et al., 2016; Fichman and Mittler, 2020).

Long-distance signals transduce environmental information throughout the whole plant body, and three major types of long-distance signals have been proposed: (i) chemical; (ii) hydraulic; and (iii) electrical signals (Huber and Bauerle, 2016; Canales et al., 2017). In particular, plant electrical signaling is the most conserved long-distance signaling system, which travels to plant distal tissues through vascular tissues to systemically induce responses in a whole plant (Hedrich et al., 2016). It is capable of transmitting signals more quickly over long distances, compared with hormone signals (Choi et al., 2017; Moe-Lange et al., 2021). Electrical signals in plants can be divided into several sub-types: local electrical potential (LEP), action potential (AP), systemic potential (SP), and slow wave potential (SWP; also known as variation potential; Szechynska-Hebda et al., 2017; Mudrilov et al., 2021). LEP is a sub-threshold response induced by change in environmental conditions, such as humidity light and temperatures. While LEP is only locally generated and is not transferred to other parts of a plant, AP, SP, and SWP can transmit from the stimulated site to other parts of the plant. AP can be defined as a rapid and transient changes in cell membrane potential (depolarization and subsequent repolarization) in response to non-damaging stimuli. AP induces an all-or-nothing response, which occurs only above a threshold of stimuli. In contrast, SWP defined as a transient membrane depolarization with an irregular shape and a longer and delayed repolarization phase is a hydraulically propagating electrical signal exclusively found in plant cells. SWP is usually induced by severe tissue damage. SP is a most recently proposed type that has variable intensities according to stimuli. SP displays a transient hyperpolarization that is usually induced by herbivore feeding or adding cations to a damaged tissues (Zimmermann et al., 2009, 2016; Szechynska-Hebda et al., 2017). To date, SWP has been extensively investigated in plants. SWP is characterized by a decrease in magnitude as it spreads away from the stimulated site, and magnitude and shape of SWP vary with the intensity of the environmental stimulus (Huber and Bauerle, 2016). Notably, wound-induced changes in membrane potential possibly generate a unique profile of electrical signals (Mousavi et al., 2014; Farmer et al., 2020), which is possibly shaped by wound-activated ion channels and pumps (Gadsby, 2009; Kumari et al., 2019; Farmer et al., 2020).

Here, we summarize current knowledge about local and systemic wound responses in plants. We also discuss how wound-activated ion channels and pumps generate and propagate electrical signals to induce downstream wound responses. Finally, we propose future studies that could help to identify the novel roles of electrical signaling upon wounding.

RESPONSES TO WOUNDING

To mitigate the plant damages from wounding, plants not only trigger tissue healing and regeneration, but also activate multiple defense responses (Leon et al., 2001; Cheong et al., 2002). Signals that are generated by wounding are transmitted through long distances. The activation of defense genes in tissues located away from the site of wounding is a well-known systemic response (Huber and Bauerle, 2016). In this section, we summarize the cellular and molecular processes underlying local and systemic responses to wounding.

Local Responses to Wounding

The healing of injured tissue is a primary local response to wounding (Hoermayer and Friml, 2019; Marhava et al., 2019; Matsuoka et al., 2021). Upon wounding, plants rely on targeted cell division and expansion to restore their damaged tissues. For example, elimination of specific root cells by laser ablation promotes periclinal cell division of cells adjacent to the inner side of the injury site through the reactivation of stem cell transcriptional programs, ensuring the correct replacement of injured cells (Marhava et al., 2019). Moreover, excision of the root apical meristem triggers root tip regeneration *via* embryonic developmental process as well as hormone redistributions (Efroni et al., 2016). The root tip regeneration in *Arabidopsis* is known to rely on genetic program consisting of *PLETHORA 2* (*PLT2*) and *ETHYLENE RESPONSE FACTOR 115* (*ERF115;* Durgaprasad et al., 2019; Canher et al., 2020). The tissue repair is also pervasive in other tissues. Damage to vascular tissues leads to the formation of cambial cells from differentiated cells, which then re-differentiate into xylem and phloem vessels in an auxin-dependent manner (Sussex et al., 1972; Mazur et al., 2016; Matsuoka et al., 2021; **Figure 1**).

Wounding triggers neighboring cells to re-enter the cell cycle, frequently inducing callus from differentiated somatic cells (Ikeuchi et al., 2017; Iwase et al., 2021). The AP2/ERF transcription factor gene, *WOUND-INDUCED DEDIFFERENTIATION1* (*WIND1*), and its close homologs *WIND*2, *WIND3*, and *WIND4* are rapidly induced by wounding, and they promote callus formation by activating cytokinin responses (Iwase et al., 2011). Callus has the capacity for cell fate transition, which is essential for regenerating new organs (Iwase et al., 2021). In parallel, wounding frequently activates *de novo* organogenesis, sometimes independently of callus formation. For instance, cutting leaf explants triggers *de novo* root organogenesis (Liu et al., 2014). Up-regulation of JA biosynthesis and signaling subsequently stimulates auxin biosynthesis that precedes cell fate transition into root founder cell (Zhang et al., 2019; **Figure 1**).

Consistent with the fact that JA is a major wound-responsive phytohormone (Koo et al., 2009), JA-induced defense responses are mainly activated in local damaged tissues. JA biosynthesis is rapidly initiated within 30 s by 13-lipoxygenases (13-LOXs) in local damaged leaves, which catalyze the incorporation of an oxygen molecule to chloroplastic tri-unsaturated fatty acids (Glauser et al., 2009; Ahmad et al., 2016; Li et al., 2016; **Figure 1**). Following wound-induced increases in JA levels, the F-box protein, CORONATINE INSENSITIVE 1 (COI1), physically interacts with JASMONATE-ZIM DOMAIN (JAZ) proteins, which are repressors of JA signaling (Gfeller et al., 2010). JA-induced COI1–JAZ interaction triggers JAZ degradation through the ubiquitin-dependent pathway, de-repressing MYC2 transcription factor activity (Guo et al., 2018). MYC2 activates defense genes and therefore increases the capacity of plants to defend themselves against wounding as well as herbivory (Chauvin et al., 2013; Major et al., 2017).

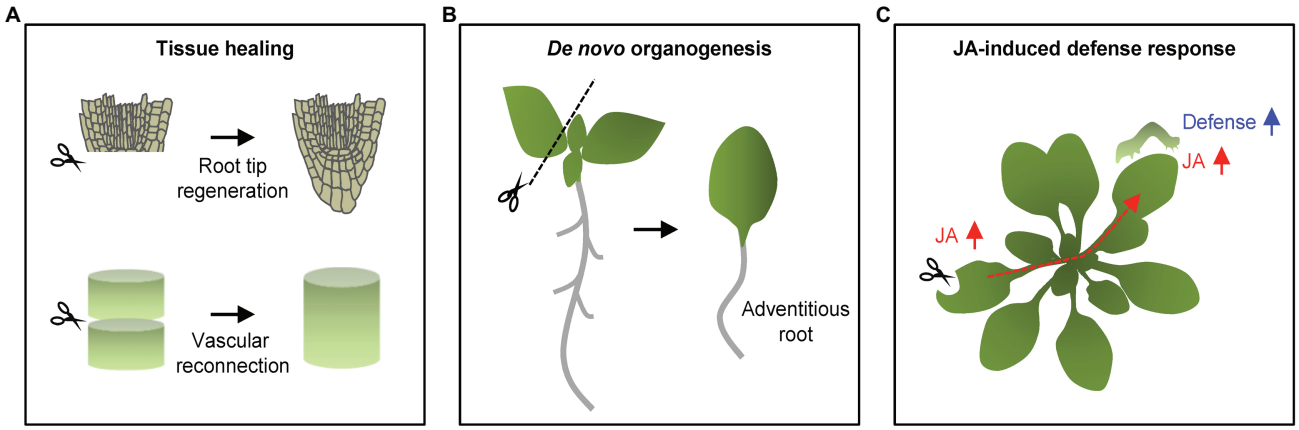

FIGURE 1 | Wound-induced local and systemic responses in plants. **(A)** Wound healing and tissue regeneration. Upon wounding, plants stimulate wound healing and tissue regeneration. Excision of the root apical meristem and vascular tissues leads to the tissue restoration in local damaged regions. **(B)** Wound-induced adventitious root formation. Wounding occasionally results in cell fate changes as shown by the adventitious root formation from detached leaf explants. **(C)** Wound-induced defense responses. Wounding also increases defense capacity in both local and systemic tissues. Jasmonic acid (JA) is a pivotal phytohormone stimulating plant defense responses not only in damaged local tissues, but also distal plant organs. Long-distance signals propagate through vasculatures in order to confer systemic defense resistance in a whole plant.

Systemic Responses to Wounding

Upon injury, wound-responsive genes are also induced in undamaged systemic tissues to protect plants against potential future damages. Accumulation of JA is essential to elicit defensive traits in systemic tissues. JA accumulation in systemic tissues significantly increases 120 s after wounding (Glauser et al., 2009). Among the four 13-LOXs, LOX6 contributes the most to JA biosynthesis in *Arabidopsis* systemic leaves (Chauvin et al., 2013). JA-inducible PIs protect plant systemic tissues from herbivores by reducing the activity of digestive enzymes in insect guts (Howe, 2004). In tomato, expression of *PI* genes is induced in systemic tissues within 2 h after wounding, and their induction is impaired in JA signaling mutants (Li et al., 2002). Application of methyl JA to one leaf induces *PI* gene expression in both local and systemic leaves even in the absence of wounding (Farmer and Ryan, 1990; Devoto and Turner, 2003).

Extracellular signals such as cell wall-derived oligogalacturonides (OGs) and peptides have been characterized as typical systemic signals of wounding, which are known as Damage-Associated Molecular Patterns (DAMPs). For instance, systemin, a 18-amino acid peptide, was identified in tomato after wounding or insect attack as a cleavage product released into the apoplast from the 200-amino acid precursor prosystemin protein (Sun et al., 2011). Systemin triggers systemic responses by acting upstream of JA (Sun et al., 2011). Ectopic expression of prosystemin triggers the constitutive expression of *PI* genes in the absence of wounding, and the increased *PI* levels are reduced in JA-deficient mutants (Sun et al., 2011). In addition to *PIs*, expression of *PATHOGENESIS-RELATED* (*PR*) genes, encoding PR-1, PR-10, chitinase, thaumatin-like protein, and plant defensin, is induced in systemic tissues to enhance plant survival and resistance against further herbivore attack (Kang et al., 2021).

LONG-DISTANCE SIGNALS IN RESPONSE TO WOUNDING

As noted, wound-induced defense responses propagate from injured local tissues to systemic tissues through long-distance signals. Long-distance signals are divided into three types: chemical, hydraulic, and electrical (Huber and Bauerle, 2016; Moe-Lange et al., 2021). Chemical signaling usually employs reactive oxygen species (ROS) and calcium ion (Ca^{2+}; Moe-Lange et al., 2021). Wounding rapidly triggers the production of ROS in local and systemic tissues that is dependent on the NADPH oxidase, RESPIRATORY BURST OXIDASE HOMOLOG D (RBOHD; Miller et al., 2009; Prasad et al., 2019). Transgenic plants expressing luciferase driven by a ROS-responsive *ZAT12* gene promoter show that ROS signaling propagates into systemic tissues at a rate of ~8 cm/min, and this rate is substantially delayed in p*ZAT12::Luc/rbohD* plants (Miller et al., 2009). An increase in cytosolic Ca^{2+} is another hallmark of long-distance signaling (Shao et al., 2020). Wounding elevates cytosolic Ca^{2+} within seconds at the injured site, which generates a Ca^{2+} wave that travels into systemic tissues through vasculature tissues at rates of ~6 cm/min (Tian et al., 2020). The Glu-activated GLUTAMATE RECEPTOR-LIKE (GLR) ion channel family expressed in phloem and xylem is responsible for the increases in intracellular Ca^{2+} concentration in local and systemic tissues (Gilroy et al., 2016; Toyota et al., 2018). Notably, accumulation of Ca^{2+} is required for systemic JA induction, and consistently, blocking Ca^{2+} entry inhibits JA-induced defense responses (Tian et al., 2020). Moreover, hydraulic signaling is a class of long-distance signaling that is closely associated with initial Ca^{2+} entry into cells (Gilroy et al., 2016). Wounding causes rapid axial changes of hydrostatic pressure in the xylem and then, converts it to slower, radially dispersed changes of pressure associated with activation of a clade 3 GLR-dependent signaling

pathway that prepares distal leaves for imminent attack (Farmer et al., 2014).

Electrical signaling is another crucial type of long-distance signaling generated by a rapid collapse of membrane potential in response to wounding (Farmer et al., 2020). Among several sub-types of electrical signals, SWP is particularly triggered by local wounding and transmitted to undamaged tissues at a speed of ~7 cm/min through vascular connections in plants (Mousavi et al., 2013; Szechynska-Hebda et al., 2017; Nguyen et al., 2018; Kurenda et al., 2019). Although waves of SWP have variable dynamics, it is generally characterized by a rapid (< 2 s) and massive (>50 mV) depolarization phase, and a slow (> 5 min) repolarization phase after wounding in *Arabidopsis* (Nguyen et al., 2018; Kumari et al., 2019). Notably, SWP has a diverse range of intensities, propagation speed and amplitude depending on the severity of the injury and distance from the injured site (Huber and Bauerle, 2016). The variable SWP dynamics are likely decoded into appropriate defense responses in plants.

Although the long distance signals are closely interconnected (Farmer et al., 2020), SWPs act as key early responses that initiate wound-induced systemic responses, which precede increases in cytosolic Ca^{2+} accumulation and JA biosynthesis in distal tissues (Vega-Munoz et al., 2020; Moe-Lange et al., 2021). Several plasma membrane-localized ion channels and pumps are characterized as core regulators in generating and propagating SWPs in response to wounding (Mousavi et al., 2013; Kumari et al., 2019; Moe-Lange et al., 2021).

Glutamate Receptor-Like Channels

The *GLR* genes encode putative glutamate receptors and Ca^{2+} permeable channels (Nguyen et al., 2018). The *Arabidopsis* genome contains 20 *GLR* genes that are divided into three clades (Ni et al., 2016). Among others, Clade 3 GLR members have key roles in the generation and propagation of SWP (Mousavi et al., 2013; Vega-Munoz et al., 2020). Upon wounding, the concentration of apoplastic Glu increases in local damaged tissues. The Glu excretion subsequently activates GLRs to induce Ca^{2+} influx, which is potentially linked to membrane depolarization (Mousavi et al., 2013; Toyota et al., 2018). In support, mutating clade 3 *GLR* genes, such as *GLR3.1*, *GLR3.2*, *GLR3.3*, or *GLR3.6*, reduces Ca^{2+} influx and also the duration of SWPs in local wounded leaves (Mousavi et al., 2013). Propagation of SWP is particularly dependent on two GLR members, GLR3.3 and GLR3.6, which are expressed in the phloem and xylem contact cells, respectively, as SWP propagation in distal leaves is abolished in *glr3.3 glr3.6* double mutants (Mousavi et al., 2013; Salvador-Recatala, 2016; Toyota et al., 2018; Li et al., 2021; Moe-Lange et al., 2021). Similarly, OsGLR3.4, which is a clade 3 GLR member in rice, also functions in wound-induced SWP propagation (Yu et al., 2022). Induction of SWPs in systemic leaves by mechanical stress in roots is significantly reduced in *osglr3.4* mutants, indicating the functional conservation of GLRs across diverse plant species (Yu et al., 2022). Given that the GLR ion channels stimulate an increase in intracellular Ca^{2+} concentration that propagates to distant organs, the intimate connection between electrical and Ca^{2+} signals synergistically leads to efficient activation of systemic responses (**Figure 2**).

Notably, different GLR members further fine-tune distribution of systemic electrical signals. GLR3.5 prevents the propagation of wound-induced electrical potentials to distal non-neighbor leaves. The *glr3.5* mutant propagates systemic electrical signal in non-neighbor leaves where wound-induced electrical signal is not transmitted in wild type (Salvador-Recatala, 2016). Collectively, electrical signaling is propagated throughout the plant, and distribution of the systemic information is elaborately regulated by GLR proteins.

Phosphorylation (P)-Type Proton ATPase 1

P-type ATPases facilitate movement of protons, ions, and molecules across membranes, and determine membrane potential in animal kingdom (Kumari et al., 2019). Notably, plasma membrane-localized H^+-ATPases within the P-type superfamily act as ion pumps and are involved in SWP propagation in plants (Falhof et al., 2016), and treatment with fusicoccin (FC), which activates plasma membrane H^+-ATPases, attenuates SWP duration (Kumari et al., 2019).

The *Arabidopsis* genome contains 11 members encoding H^+-ATPases (AHA; Robertson et al., 2004; Haruta et al., 2010; Lin et al., 2021). AHA1 primarily functions in regulating SWPs in response to wounding (Kumari et al., 2019; Shao et al., 2020). In contrast to GLRs, AHA1 negatively controls SWP duration (Kumari et al., 2019; **Figure 2**). *aha1* mutants extend the duration of the repolarization phase of SWPs in both local and systemic tissues, while the *AHA1* gain-of-function mutant, *ost2-2D*, reduces SWP repolarization duration in systemic leaves (Kumari et al., 2019). Consistent with changes in the duration of SWPs, prolonged Ca^{2+} transients and JA biosynthesis increase in systemic tissues of *aha1* mutants (Kumari et al., 2019).

It should be noted that, GLRs and AHA1 may function in common pathways for SWP generation, as revealed by double mutant studies (Kumari et al., 2019). The duration of the repolarization phase of *aha1* mutants was lower than that of wild type in both local and systemic tissues when crossed with *glr3.3* mutants (Kumari et al., 2019). In addition, co-treatment with Glu and the H^+-ATPase activating compound FC abolishes the amplitude and duration of SWP depolarization, demonstrating that constitutive activation of H^+-ATPase blocks Glu-induced depolarization (Shao et al., 2020).

Mechanosensitive Ion Channel-Like 10 (MSL10)

Mechanosensitive ion channels (MscS) respond to physical forces or plasma membrane deformation and generate mechanosensitive ion flux (Basu and Haswell, 2017; Canales Coutino and Mayor, 2021). MscS-Like (MSL) channels are the best-characterized MscS in diverse organisms (Basu and Haswell, 2017). Among 10 MSL proteins in *Arabidopsis* (Haswell et al., 2008), MSL10 is known to be directly gated by lateral membrane tension (Basu and Haswell, 2020) and has preference for anions with the conductance of about 100 pS (Basu and Haswell, 2020). Notably, the vasculature-expressed MSL10 protein functions in

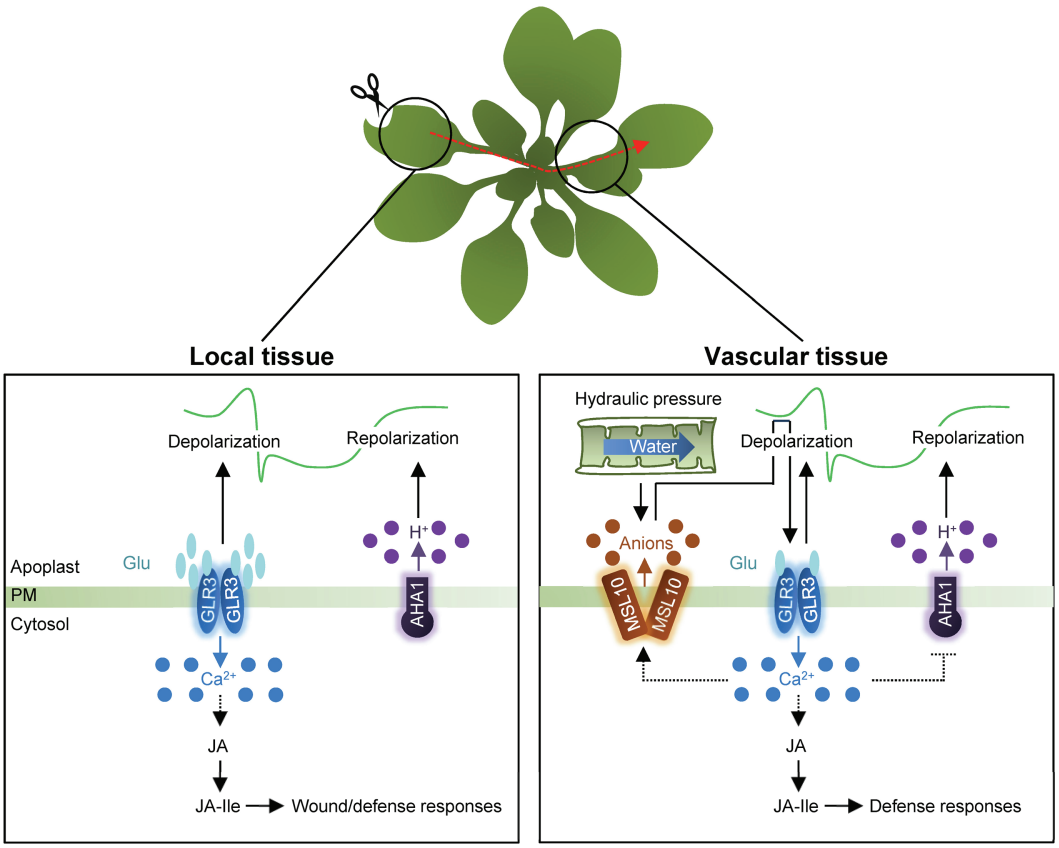

FIGURE 2 | Schematic representation of electrical signaling in local and systemic tissues. In local tissue, wounding triggers an increase in apoplastic Glu concentration and then, induces GLR-dependent Ca^{2+} influx as well as depolarization of membrane potential. The GLR proteins likely act as tetramers. Following depolarization, H^+-ATPase AHA1 is then required for membrane repolarization. The electrical signals systemically propagate through vasculature tissues in a connection with Ca^{2+} wave. Changes in turgor pressure affect membrane tension and activate the heptameric anion channel, MSL10, causing membrane depolarization through anion efflux. The membrane depolarization fully activates GLRs in response to wounding. GLR-dependent Ca^{2+} influx potentially causes activation of MSL10, simultaneously with the deactivation of AHA1. Synergistic propagation of Ca^{2+} waves and SWPs promotes JA biosynthesis to induce defense responses in systemic tissues. PM, plasma membrane.

systemic SWP propagation upon wounding in *Arabidopsis* (Moe-Lange et al., 2021). The mutation of *MSL10* significantly reduces the duration of SWP in systemic leaves, which also leads to reduced Ca^{2+} waves and *JASMONATE-ZIM-DOMAIN PROTEIN 10* expression in distal tissues of *msl10* mutants (Moe-Lange et al., 2021), indicating that the mechanosensitive ion channel MSL10 is required for wound-elicited electrical signals and systemic Ca^{2+} wave in distal tissues (**Figure 2**).

The *msl10* mutants display ~fourfold shortened systemic SWPs and reduced Ca^{2+} wave in distal tissues, similar to the effects observed in the *glr3.1*, *glr3.3*, and *glr3.6* single mutants (Moe-Lange et al., 2021). Considering that not only the spatial expression of *GLR3.1*, *GLR3.3*, and *GLR3.6* overlaps with that of *MSL10* in vasculature tissues, but also reduced SWP magnitudes of *msl10;glr3.3* and *msl10;glr3.6* double mutants are indistinguishable from those of their single mutants, MSL10 and GLRs function in overlapping genetic pathways (Moe-Lange et al., 2021). Taken together, wounding triggers the release of glutamate into the apoplasm, in turn activating Ca^{2+}-permeable GLR3s that also influence electrical propagation. In parallel, changes in turgor pressure affect membrane tension and activate MSL10, causing anion efflux and depolarization of membrane potential. Membrane depolarization promotes full activity of the GLRs in distal tissues in response to wounding. Synergistic propagation of Ca^{2+} waves and SWPs efficiently induces systemic wound responses for plant survival (Fromm and Lautner, 2007; Feng et al., 2021).

CONCLUSION AND PROSPECTS

Plants have evolved long-distance communication system that systemically coordinates plant growth and development, especially enabling them to cope with adverse environments. Electrochemical signals are likely to mediate intercellular and intracellular communication in association with environmental changes. In this context, this study focused particularly on wound-responsive electrical signaling. Despite advances in understanding on the role of electrical signaling in systemic wound responses, several key questions still

remain to be resolved. First, it is currently elusive how different environmental stimuli induce appropriate electrical signals with unique phase signatures. Functional and mechanical studies on ion channels and pumps that shape dynamics of SWPs would be required. Second, given that Glu-mediated activation of GLR ion channels plays a central role in the generation and systemic propagation of SWPs after wounding, it should be addressed whether subcellular localization of GLRs is related to the systemic signal propagation. Several GLR proteins are predicted to be targeted to the endoplasmic reticulum and play a potential function in secretory pathway (Davenport, 2002; Bassham et al., 2008; Nguyen et al., 2018), as shown by the rice GLR3.1 protein (Li et al., 2006). Localization-dependent GLR functions should be investigated to understand a possible linkage of intracellular and intercellular communications. Third, although wounding increase apoplastic Glu in local injured tissue, it should be answered how it is conveyed to the distal parts of the plant (Qiu et al., 2019). Additionally, a range of cellular Glu concentrations that trigger systemic calcium and electrical waves *via* GLR proteins should also be elucidated.

The SWP contains information about the severity of wounding and the distance from injured sites. Based on the information, plants induce appropriate wound responses by regulating intracellular Ca^{2+} concentration and endogenous JA levels in local and systemic tissues. Since current studies on wound-responsive electrical signals focus mainly on systemic aspects of defense responses and there is limited understanding on potential impact of SWPs in tissue healing and regeneration and pathogen resistance in local tissues (Kral et al., 2016; Hernandez-Coronado et al., 2022), it would be necessary to unravel the relevance of electrical signals in wound responses in local tissues in the near future.

The electrical signal intricately interacts with other systemic signals. Hydraulic signals contribute to propagation of SWP (Stahlberg and Cosgrove, 1996; Farmer et al., 2020). Altered hydrostatic pressure by wounding activates mechanosensitive elements that in turn affect membrane depolarization in systemic tissues (Moe-Lange et al., 2021). Similarly, ROS-dependent long-distance signaling also participates in SWP propagation (Farmer et al., 2020). Treatment with the NAD(P)H oxidase inhibitor, diphenyleneiodonium, reduces SWP duration in systemic tissues (Mousavi et al., 2013), indicating that ROS signaling potentially regulates SWP. Moreover, Ca^{2+} and SWP waves are also interdependent on each other. Despite the extensive connections among systemic signals, the molecular mechanisms underlying these interactions have been limitedly unveiled. It will be needed to identify molecular factors that are responsible for the crosstalk of systemic signals and ultimately comprehensive mechanisms that coordinate systemic signals to further understand efficiency and robustness of long-distance wound responses.

AUTHOR CONTRIBUTIONS

All authors listed have made a substantial, direct, and intellectual contribution to the work, and approved it for publication.

FUNDING

This work was supported by the Basic Science Research (NRF-2021R1I1A1A01054378 to KL; NRF-2022R1A2B5B02001266 to PJS) and Basic Research Laboratory (NRF-2020R1A4A2002901) programs funded by the National Research Foundation of Korea and by the Creative-Pioneering Researchers Program through Seoul National University (0409–20210288).

REFERENCES

Ahmad, P., Rasool, S., Gul, A., Sheikh, S. A., Akram, N. A., Ashraf, M., et al. (2016). Jasmonates: multifunctional roles in stress tolerance. *Front. Plant Sci.* 7:813. doi: 10.3389/fpls.2016.00813

Bassham, D. C., Brandizzi, F., Otegui, M. S., and Sanderfoot, A. A. (2008). The secretory system of *Arabidopsis*. *Arabidopsis Book* 6:e0116. doi: 10.1199/tab.0116

Basu, D., and Haswell, E. S. (2017). Plant mechanosensitive ion channels: an ocean of possibilities. *Curr. Opin. Plant Biol.* 40, 43–48. doi: 10.1016/j.pbi.2017.07.002

Basu, D., and Haswell, E. S. (2020). The mechanosensitive ion channel MSL10 potentiates responses to cell swelling in *Arabidopsis* seedlings. *Curr. Biol.* 30:e2716. doi: 10.1016/j.cub.2020.05.015

Canales Coutino, B., and Mayor, R. (2021). Mechanosensitive ion channels in cell migration. *Cells Dev.* 166:203683. doi: 10.1016/j.cdev.2021.203683

Canales, J., Henriquez-Valencia, C., and Brauchi, S. (2017). The integration of electrical signals originating in the root of vascular plants. *Front. Plant Sci.* 8:2173. doi: 10.3389/fpls.2017.02173

Canher, B., Heyman, J., Savina, M., Devendran, A., Eekhout, T., Vercauteren, I., et al. (2020). Rocks in the auxin stream: wound-induced auxin accumulation and *ERF115* expression synergistically drive stem cell regeneration. *Proc. Natl. Acad. Sci. U. S. A.* 117, 16667–16677. doi: 10.1073/pnas.2006620117

Chauvin, A., Caldelari, D., Wolfender, J. L., and Farmer, E. E. (2013). Four 13-lipoxygenases contribute to rapid jasmonate synthesis in wounded *Arabidopsis thaliana* leaves: a role for lipoxygenase 6 in responses to long-distance wound signals. *New Phytol.* 197, 566–575. doi: 10.1111/nph.12029

Cheong, Y. H., Chang, H. S., Gupta, R., Wang, X., Zhu, T., and Luan, S. (2002). Transcriptional profiling reveals novel interactions between wounding, pathogen, abiotic stress, and hormonal responses in *Arabidopsis*. *Plant Physiol.* 129, 661–677. doi: 10.1104/pp.002857

Choi, W. G., Miller, G., Wallace, I., Harper, J., Mittler, R., and Gilroy, S. (2017). Orchestrating rapid long-distance signaling in plants with Ca^{2+}, ROS and electrical signals. *Plant J.* 90, 698–707. doi: 10.1111/tpj.13492

Davenport, R. (2002). Glutamate receptors in plants. *Ann. Bot.* 90, 549–557. doi: 10.1093/aob/mcf228

Devoto, A., and Turner, J. G. (2003). Regulation of jasmonate-mediated plant responses in *Arabidopsis*. *Ann. Bot.* 92, 329–337. doi: 10.1093/aob/mcg151

Durgaprasad, K., Roy, M. V., Venugopal, M. A., Kareem, A., Raj, K., Willemsen, V., et al. (2019). Gradient expression of transcription factor imposes a boundary on organ regeneration potential in plants. *Cell Rep.* 29:e453. doi: 10.1016/j.celrep.2019.08.099

Efroni, I., Mello, A., Nawy, T., Ip, P. L., Rahni, R., Delrose, N., et al. (2016). Root regeneration triggers an embryo-like sequence guided by hormonal interactions. *Cell* 165, 1721–1733.

Falhof, J., Pedersen, J. T., Fuglsang, A. T., and Palmgren, M. (2016). Plasma membrane H(+)-ATPase regulation in the center of plant physiology. *Mol. Plant* 9, 323–337. doi: 10.1016/j.molp.2015.11.002

Farmer, E. E., Gao, Y. Q., Lenzoni, G., Wolfender, J. L., and Wu, Q. (2020). Wound- and mechanostimulated electrical signals control hormone responses. *New Phytol.* 227, 1037–1050. doi: 10.1111/nph.16646

Farmer, E. E., Gasperini, D., and Acosta, I. F. (2014). The squeeze cell hypothesis for the activation of jasmonate synthesis in response to wounding. *New Phytol.* 204, 282–288. doi: 10.1111/nph.12897

Farmer, E. E., and Ryan, C. A. (1990). Interplant communication: airborne methyl jasmonate induces synthesis of proteinase inhibitors in plant leaves. *Proc. Natl. Acad. Sci. U. S. A.* 87, 7713–7716. doi: 10.1073/pnas.87.19.7713

Feng, S., Pan, C., Ding, S., Ma, Q., Hu, C., Wang, P., et al. (2021). The glutamate receptor plays a role in defense against *Botrytis cinerea* through electrical signaling in tomato. *Appl. Sci.* 11:11217. doi: 10.3390/app112311217

Fichman, Y., and Mittler, R. (2020). Rapid systemic signaling during abiotic and biotic stresses: is the ROS wave master of all trades? *Plant J.* 102, 887–896. doi: 10.1111/tpj.14685

Fromm, J., and Lautner, S. (2007). Electrical signals and their physiological significance in plants. *Plant Cell Environ.* 30, 249–257. doi: 10.1111/j.1365-3040.2006.01614.x

Gadsby, D. C. (2009). Ion channels versus ion pumps: the principal difference, in principle. *Nat. Rev. Mol. Cell Biol.* 10, 344–352. doi: 10.1038/nrm2668

Gfeller, A., Liechti, R., and Farmer, E. E. (2010). *Arabidopsis* jasmonate signaling pathway. *Sci. Signal.* 3:cm4. doi: 10.1126/scisignal.3109cm4

Gilroy, S., Bialasek, M., Suzuki, N., Gorecka, M., Devireddy, A. R., Karpinski, S., et al. (2016). ROS, calcium, and electric signals: key mediators of rapid systemic signaling in plants. *Plant Physiol.* 171, 1606–1615. doi: 10.1104/pp.16.00434

Glauser, G., Dubugnon, L., Mousavi, S. A., Rudaz, S., Wolfender, J. L., and Farmer, E. E. (2009). Velocity estimates for signal propagation leading to systemic jasmonic acid accumulation in wounded *Arabidopsis*. *J. Biol. Chem.* 284, 34506–34513. doi: 10.1074/jbc.M109.061432

Guo, Q., Yoshida, Y., Major, I. T., Wang, K., Sugimoto, K., Kapali, G., et al. (2018). JAZ repressors of metabolic defense promote growth and reproductive fitness in *Arabidopsis*. *Proc. Natl. Acad. Sci. U. S. A.* 115, E10768–E10777. doi: 10.1073/pnas.1811828115

Haruta, M., Burch, H. L., Nelson, R. B., Barrett-Wilt, G., Kline, K. G., Mohsin, S. B., et al. (2010). Molecular characterization of mutant *Arabidopsis* plants with reduced plasma membrane proton pump activity. *J. Biol. Chem.* 285, 17918–17929. doi: 10.1074/jbc.M110.101733

Haswell, E. S., Peyronnet, R., Barbier-Brygoo, H., Meyerowitz, E. M., and Frachisse, J. M. (2008). Two MscS homologs provide mechanosensitive channel activities in the Arabidopsis root. *Curr. Biol.* 18, 730–734. doi: 10.1016/j.cub.2008.04.039

Hedrich, R., Salvador-Recatala, V., and Dreyer, I. (2016). Electrical wiring and long-distance plant communication. *Trends Plant Sci.* 21, 376–387. doi: 10.1016/j.tplants.2016.01.016

Hernandez-Coronado, M., Dias Araujo, P. C., Ip, P. L., Nunes, C. O., Rahni, R., Wudick, M. M., et al. (2022). Plant glutamate receptors mediate a bet-hedging strategy between regeneration and defense. *Dev. Cell* 57:e456. doi: 10.1016/j.devcel.2022.01.013

Hoermayer, L., and Friml, J. (2019). Targeted cell ablation-based insights into wound healing and restorative patterning. *Curr. Opin. Plant Biol.* 52, 124–130. doi: 10.1016/j.pbi.2019.08.006

Howe, G. A. (2004). Jasmonates as signals in the wound response. *J. Plant Growth Regul.* 23, 223–237. doi: 10.1007/s00344-004-0030-6

Huber, A. E., and Bauerle, T. L. (2016). Long-distance plant signaling pathways in response to multiple stressors: the gap in knowledge. *J. Exp. Bot.* 67, 2063–2079. doi: 10.1093/jxb/erw099

Ikeuchi, M., Iwase, A., Rymen, B., Lambolez, A., Kojima, M., Takebayashi, Y., et al. (2017). Wounding triggers callus formation via dynamic hormonal and transcriptional changes. *Plant Physiol.* 175, 1158–1174. doi: 10.1104/pp.17.01035

Iwase, A., Kondo, Y., Laohavisit, A., Takebayashi, A., Ikeuchi, M., Matsuoka, K., et al. (2021). WIND transcription factors orchestrate wound-induced callus formation, vascular reconnection and defense response in *Arabidopsis*. *New Phytol.* 232, 734–752. doi: 10.1111/nph.17594

Iwase, A., Mitsuda, N., Koyama, T., Hiratsu, K., Kojima, M., Arai, T., et al. (2011). The AP2/ERF transcription factor WIND1 controls cell dedifferentiation in *Arabidopsis*. *Curr. Biol.* 21, 508–514. doi: 10.1016/j.cub.2011.02.020

Kang, J. N., Lee, W. H., Won, S. Y., Chang, S., Hong, J. P., Oh, T. J., et al. (2021). Systemic expression of genes involved in the plant defense response induced by wounding in *Senna tora*. *Int. J. Mol. Sci.* 22:10073. doi: 10.3390/ijms221810073

Kiep, V., Vadassery, J., Lattke, J., Maass, J. P., Boland, W., Peiter, E., et al. (2015). Systemic cytosolic Ca^{2+} elevation is activated upon wounding and herbivory in *Arabidopsis*. *New Phytol.* 207, 996–1004. doi: 10.1111/nph.13493

Koo, A. J., Gao, X., Jones, A. D., and Howe, G. A. (2009). A rapid wound signal activates the systemic synthesis of bioactive jasmonates in *Arabidopsis*. *Plant J.* 59, 974–986. doi: 10.1111/j.1365-313X.2009.03924.x

Kral, N., Hanna Ougolnikova, A., and Sena, G. (2016). Externally imposed electric field enhances plant root tip regeneration. *Regeneration (Oxf)* 3, 156–167. doi: 10.1002/reg2.59

Kumari, A., Chetelat, A., Nguyen, C. T., and Farmer, E. E. (2019). *Arabidopsis* H(+)-ATPase AHA1 controls slow wave potential duration and wound-response jasmonate pathway activation. *Proc. Natl. Acad. Sci. U. S. A.* 116, 20226–20231. doi: 10.1073/pnas.1907379116

Kurenda, A., Nguyen, C. T., Chetelat, A., Stolz, S., and Farmer, E. E. (2019). Insect-damaged *Arabidopsis* moves like wounded *Mimosa pudica*. *Proc. Natl. Acad. Sci. U. S. A.* 116, 26066–26071. doi: 10.1073/pnas.1912386116

Leon, J., Rojo, E., and Sanchez-Serrano, J. J. (2001). Wound signalling in plants. *J. Exp. Bot.* 52, 1–9. doi: 10.1093/jexbot/52.354.1

Li, J. H., Fan, L. F., Zhao, D. J., Zhou, Q., Yao, J. P., Wang, Z. Y., et al. (2021). Plant electrical signals: A multidisciplinary challenge. *J. Plant Physiol.* 261:153418. doi: 10.1016/j.jplph.2021.153418

Li, Q., Lei, S., Du, K., Li, L., Pang, X., Wang, Z., et al. (2016). RNA-seq based transcriptomic analysis uncovers alpha-linolenic acid and jasmonic acid biosynthesis pathways respond to cold acclimation in *Camellia japonica*. *Sci. Rep.* 6:36463. doi: 10.1038/srep36463

Li, L., Li, C., Lee, G. I., and Howe, G. A. (2002). Distinct roles for jasmonate synthesis and action in the systemic wound response of tomato. *Proc. Natl. Acad. Sci. U. S. A.* 99, 6416–6421. doi: 10.1073/pnas.072072599

Li, J., Zhu, S., Song, X., Shen, Y., Chen, H., Yu, J., et al. (2006). A rice glutamate receptor-like gene is critical for the division and survival of individual cells in the root apical meristem. *Plant Cell* 18, 340–349. doi: 10.1105/tpc.105.037713

Lin, W., Zhou, X., Tang, W., Takahashi, K., Pan, X., Dai, J., et al. (2021). TMK-based cell-surface auxin signalling activates cell-wall acidification. *Nature* 599, 278–282. doi: 10.1038/s41586-021-03976-4

Liu, J., Sheng, L., Xu, Y., Li, J., Yang, Z., Huang, H., et al. (2014). WOX11 and 12 are involved in the first-step cell fate transition during *de novo* root organogenesis in *Arabidopsis*. *Plant Cell* 26, 1081–1093. doi: 10.1105/tpc.114.122887

Major, I. T., Yoshida, Y., Campos, M. L., Kapali, G., Xin, X. F., Sugimoto, K., et al. (2017). Regulation of growth-defense balance by the JASMONATE ZIM-DOMAIN (JAZ)-MYC transcriptional module. *New Phytol.* 215, 1533–1547. doi: 10.1111/nph.14638

Marhava, P., Hoermayer, L., Yoshida, S., Marhavy, P., Benkova, E., and Friml, J. (2019). Re-activation of stem cell pathways for pattern restoration in plant wound healing. *Cell* 177:e913, 957–969.e13. doi: 10.1016/j.cell.2019.04.015

Matsuoka, K., Sato, R., Matsukura, Y., Kawajiri, Y., Iino, H., Nozawa, N., et al. (2021). Wound-inducible *ANAC071* and *ANAC096* transcription factors promote cambial cell formation in incised *Arabidopsis* flowering stems. *Commun. Biol.* 4:369. doi: 10.1038/s42003-021-01895-8

Mazur, E., Benkova, E., and Friml, J. (2016). Vascular cambium regeneration and vessel formation in wounded inflorescence stems of *Arabidopsis*. *Sci. Rep.* 6:33754. doi: 10.1038/srep33754

Miller, G., Schlauch, K., Tam, R., Cortes, D., Torres, M. A., Shulaev, V., et al. (2009). The plant NADPH oxidase RBOHD mediates rapid systemic signaling in response to diverse stimuli. *Sci. Signal.* 2:ra45. doi: 10.1126/scisignal.2000448

Moe-Lange, J., Gappel, N. M., Machado, M., Wudick, M. M., Sies, C. S. A., Schott-Verdugo, S. N., et al. (2021). Interdependence of a mechanosensitive anion channel and glutamate receptors in distal wound signaling. *Sci. Adv.* 7:eabg4298. doi: 10.1126/sciadv.abg4298

Mousavi, S. A., Chauvin, A., Pascaud, F., Kellenberger, S., and Farmer, E. E. (2013). *GLUTAMATE RECEPTOR-LIKE* genes mediate leaf-to-leaf wound signalling. *Nature* 500, 422–426. doi: 10.1038/nature12478

Mousavi, S. A., Nguyen, C. T., Farmer, E. E., and Kellenberger, S. (2014). Measuring surface potential changes on leaves. *Nat. Protoc.* 9, 1997–2004. doi: 10.1038/nprot.2014.136

Mudrilov, M., Ladeynova, M., Grinberg, M., Balalaeva, I., and Vodeneev, V. (2021). Electrical signaling of plants under abiotic stressors: transmission

of stimulus-specific information. *Int. J. Mol. Sci.* 22:10715. doi: 10.3390/ijms221910715

Nguyen, C. T., Kurenda, A., Stolz, S., Chetelat, A., and Farmer, E. E. (2018). Identification of cell populations necessary for leaf-to-leaf electrical signaling in a wounded plant. *Proc. Natl. Acad. Sci. U. S. A.* 115, 10178–10183. doi: 10.1073/pnas.1807049115

Ni, J., Yu, Z., Du, G., Zhang, Y., Taylor, J. L., Shen, C., et al. (2016). Heterologous expression and functional analysis of rice GLUTAMATE RECEPTOR-LIKE family indicates its role in glutamate triggered calcium flux in rice roots. *Rice (N Y)* 9:9. doi: 10.1186/s12284-016-0081-x

Prasad, A., Sedlarova, M., Balukova, A., Rac, M., and Pospisil, P. (2019). Reactive oxygen species as a response to wounding: *in vivo* imaging in *Arabidopsis thaliana*. *Front. Plant Sci.* 10:1660. doi: 10.3389/fpls.2019.01660

Qiu, X. M., Sun, Y. Y., Ye, X. Y., and Li, Z. G. (2019). Signaling role of glutamate in plants. *Front. Plant Sci.* 10:1743. doi: 10.3389/fpls.2019.01743

Reymond, P., Weber, H., Damond, M., and Farmer, E. E. (2000). Differential gene expression in response to mechanical wounding and insect feeding in *Arabidopsis*. *Plant Cell* 12, 707–719. doi: 10.1105/tpc.12.5.707

Robertson, W. R., Clark, K., Young, J. C., and Sussman, M. R. (2004). An *Arabidopsis thaliana* plasma membrane proton pump is essential for pollen development. *Genetics* 168, 1677–1687. doi: 10.1534/genetics.104.032326

Salvador-Recatala, V. (2016). New roles for the *GLUTAMATE RECEPTOR-LIKE 3.3*, *3.5*, and *3.6* genes as on/off switches of wound-induced systemic electrical signals. *Plant Signal. Behav.* 11:e1161879. doi: 10.1080/15592324.2016.1161879

Savatin, D. V., Gramegna, G., Modesti, V., and Cervone, F. (2014). Wounding in the plant tissue: the defense of a dangerous passage. *Front. Plant Sci.* 5:470. doi: 10.3389/fpls.2014.00470

Shao, Q., Gao, Q., Lhamo, D., Zhang, H., and Luan, S. (2020). Two glutamate- and pH-regulated Ca^{2+} channels are required for systemic wound signaling in *Arabidopsis*. *Sci. Signal.* 13:eaba1453. doi: 10.1126/scisignal.aba1453

Sozen, C., Schenk, S. T., Boudsocq, M., Chardin, C., Almeida-Trapp, M., Krapp, A., et al. (2020). Wounding and insect feeding trigger two independent MAPK pathways with distinct regulation and kinetics. *Plant Cell* 32, 1988–2003. doi: 10.1105/tpc.19.00917

Stahlberg, R., and Cosgrove, D. J. (1996). Induction and ionic basis of slow wave potentials in seedlings of Pisum sativum L. *Planta* 200, 416–425. doi: 10.1093/aob/mcg151

Sun, J. Q., Jiang, H. L., and Li, C. Y. (2011). Systemin/Jasmonate-mediated systemic defense signaling in tomato. *Mol. Plant* 4, 607–615. doi: 10.1093/mp/ssr008

Sussex, I. M., Goldsmith, M. H., and Clutter, M. E. (1972). Wound recovery by pith cell redifferentiation: structural changes. *Am. J. Bot.* 59, 797–804. doi: 10.1002/j.1537-2197.1972.tb10154.x

Szechynska-Hebda, M., Lewandowska, M., and Karpinski, S. (2017). Electrical signaling, photosynthesis and systemic acquired acclimation. *Front. Physiol.* 8:684. doi: 10.3389/fphys.2017.00684

Tian, W., Wang, C., Gao, Q., Li, L., and Luan, S. (2020). Calcium spikes, waves and oscillations in plant development and biotic interactions. *Nat. Plants* 6, 750–759. doi: 10.1038/s41477-020-0667-6

Toyota, M., Spencer, D., Sawai-Toyota, S., Jiaqi, W., Zhang, T., Koo, A. J., et al. (2018). Glutamate triggers long-distance, calcium-based plant defense signaling. *Science* 361, 1112–1115. doi: 10.1126/science.aat7744

Vega-Munoz, I., Duran-Flores, D., Fernandez-Fernandez, A. D., Heyman, J., Ritter, A., and Stael, S. (2020). Breaking bad news: dynamic molecular mechanisms of wound response in plants. *Front. Plant Sci.* 11:610445. doi: 10.3389/fpls.2020.610445

Yu, B., Wu, Q., Li, X., Zeng, R., Min, Q., and Huang, J. (2022). GLUTAMATE RECEPTOR-like gene *OsGLR3.4* is required for plant growth and systemic wound signaling in rice (*Oryza sativa*). *New Phytol.* 233, 1238–1256. doi: 10.1111/nph.17859

Zhang, G., Zhao, F., Chen, L., Pan, Y., Sun, L., Bao, N., et al. (2019). Jasmonate-mediated wound signalling promotes plant regeneration. *Nat. Plants* 5, 491–497. doi: 10.1038/s41477-019-0408-x

Zimmermann, M. R., Maischak, H., Mithofer, A., Boland, W., and Felle, H. H. (2009). System potentials, a novel electrical long-distance apoplastic signal in plants, induced by wounding. *Plant Physiol.* 149, 1593–1600. doi: 10.1104/pp.108.133884

Zimmermann, M. R., Mithofer, A., Will, T., Felle, H. H., and Furch, A. C. (2016). Herbivore-triggered electrophysiological reactions: candidates for systemic signals in higher plants and the challenge of their identification. *Plant Physiol.* 170, 2407–2419. doi: 10.1104/pp.15.01736

Conflict of Interest: The authors declare that the research was conducted in the absence of any commercial or financial relationships that could be construed as a potential conflict of interest.

Publisher's Note: All claims expressed in this article are solely those of the authors and do not necessarily represent those of their affiliated organizations, or those of the publisher, the editors and the reviewers. Any product that may be evaluated in this article, or claim that may be made by its manufacturer, is not guaranteed or endorsed by the publisher.

frontiers | Frontiers in Plant Science

REVIEW
published: 02 June 2022
doi: 10.3389/fpls.2022.921148

The Ups and Downs of Plant *NLR* Expression During Pathogen Infection

Alicia Fick[1,2], Velushka Swart[1,2] and Noëlani van den Berg[1,2]*

[1]*Department of Biochemistry, Genetics and Microbiology, University of Pretoria, Pretoria, South Africa,* [2]*Forestry and Agricultural Biotechnology Institute, University of Pretoria, Pretoria, South Africa*

Plant Nucleotide binding-Leucine rich repeat (NLR) proteins play a significant role in pathogen detection and the activation of effector-triggered immunity. NLR regulation has mainly been studied at a protein level, with large knowledge gaps remaining regarding the transcriptional control of *NLR* genes. The mis-regulation of *NLR* gene expression may lead to the inability of plants to recognize pathogen infection, lower levels of immune response activation, and ultimately plant susceptibility. This highlights the importance of understanding all aspects of NLR regulation. Three main mechanisms have been shown to control *NLR* expression: epigenetic modifications, *cis* elements which bind transcription factors, and post-transcriptional modifications. In this review, we aim to provide an overview of these mechanisms known to control *NLR* expression, and those which contribute toward successful immune responses. Furthermore, we discuss how pathogens can interfere with *NLR* expression to increase pathogen virulence. Understanding how these molecular mechanisms control *NLR* expression would contribute significantly toward building a complete picture of how plant immune responses are activated during pathogen infection—knowledge which can be applied during crop breeding programs aimed to increase resistance toward numerous plant pathogens.

Keywords: pathogen infection, NLR, epigenetics, transcriptional regulatinon, NB-LRR, *cis* elements, NLR expression

OPEN ACCESS

Edited by:
Chang Liu,
University of Hohenheim, Germany

Reviewed by:
Pingtao Ding,
Leiden University, Netherlands
Liu Xiaokun,
Lushan Botanical Garden (CAS), China

****Correspondence:***
Alicia Fick
alicia.fick@up.ac.za

Specialty section:
This article was submitted to Plant Cell Biology, a section of the journal Frontiers in Plant Science

Received: *15 April 2022*
Accepted: *16 May 2022*
Published: *02 June 2022*

Citation:
Fick A, Swart V and van den Berg N (2022) The Ups and Downs of Plant NLR Expression During Pathogen Infection. Front. Plant Sci. 13:921148. doi: 10.3389/fpls.2022.921148

INTRODUCTION

Various pathogens, including bacteria, fungi, oomycetes, and viruses, constantly bombard plant species and may cause large crop losses in agricultural settings. Plants have in turn evolved a complex set of defense mechanisms to combat pathogen infection (Jones and Dangl, 2006). Understanding how these plant defense responses are regulated and activated during pathogen attack will accelerate crop breeding programs and may contribute to the development of transgenic crop species with the desired resistance characteristics (Wang et al., 2019). Research focused on unraveling plant immune responses has, unsurprisingly, been of particular interest for the past decade (Bezerra-Neto et al., 2020). All research studies have contributed to reveal an increasingly more complex system, with thousands of signaling molecules, receptors, and hormones, each playing a role in plant immune responses (Wan et al., 2012; Van den Berg et al., 2018; Adachi et al., 2019).

Jones and Dangl (2006) first explained plant immune responses with the well-known Zig-Zag model. This model explains that pathogens are first recognized when pathogen-associated molecular patterns (PAMPs) or damage-associated molecular patterns (DAMPs) are recognized by pattern recognition receptors (PRRs). After PAMP recognition, PRRs activate a low amplitude immune response, known as PAMP-triggered immunity (PTI). This immune response is often able to overcome infection by suppressing pathogen growth. However, some pathogens can overcome PTI responses. Plant Resistance (R) proteins may then recognize Avirulence effector (Avr) proteins, secreted by pathogens, and trigger effector-triggered immunity (ETI; Davis and Hahlbrock, 1987). A successful ETI response leads to the reactive oxygen species (ROS) and activation of the hypersensitive response (HR)—leading to localized plant cell death and the suppression of pathogen growth. When a R protein is either not present, or unable to recognize a corresponding Avr protein, effector-triggered susceptibility (ETS) is triggered, often leading to plant death (Cui et al., 2015).

This model can, however, be deceivingly simple (Naveed et al., 2020). For example, the model explains that a successful ETI response (able to overcome host-adapted pathogen attack) can only be activated when R proteins recognize a respective Avr protein. However, an increasing amount of evidence has suggested that the expression levels of *R* genes also contribute toward a successful immune response (Bradeen et al., 2009; Andam et al., 2020). When *R* gene expression is mis-regulated, the amplitude of ETI activation decreases, and an ETI response strong enough to suppress pathogen growth cannot be triggered (Umadevi and Anandaraj, 2017; Xu et al., 2018). Thus, even when a R protein is able to recognize a corresponding Avr protein, insufficient levels of this protein would lead to susceptibility. Understanding how *R* gene expression is regulated is thus the first step in untangling the mechanisms behind successful immune responses. In this review, we will focus on the regulatory mechanisms controlling *R* gene expression during pathogen infection, and how pathogens interfere and highjack these mechanisms for their own advantage.

THE MAIN CHARACTER: NLR PROTEINS

NLR proteins, also known as NB-LRRs, constitute the largest subclass of R proteins and are characterized based on containing a Nucleotide binding (NB/NB-ARC) domain and a Leucine rich repeat (LRR) domain. NLRs can further be classified based on either having a Coiled coil (CC) domain, a CC with an integrated RPW8 domain (CC_R), or a Toll/interleukin-1 receptor domain located at the protein's N-terminus, termed CNLs, C_RNLs, and TNLs, respectively (**Figure 1**; Takken and Goverse, 2012). These N-terminus domains are normally described to control homo- or heterodimerization events between NLRs (Xu et al., 2000; Maekawa et al., 2011). In NLR dimer pairs, one NLR often acts as a "sensor" NLR, able to recognize pathogen Avr proteins (Bonardi et al., 2011). The second NLR acts as a "helper" NLR, triggering the ETI response following activation by the sensor NLR. NB domains remain largely conserved between species and are often used during phylogenetic studies (Maiti et al., 2014). NB domains function as molecular switches for NLR proteins, determining whether the protein is in an active or inactive state. This molecular switch is controlled by ADP and ATP binding to the NB domain P-loop, with ATP binding to activate NLRs following Avr recognition (Steele et al., 2019). The LRR domain, however, is variable in length and shows large sequence variations since this domain is responsible for Avr recognition (Maule et al., 2007). The LRR domain also exerts a negative regulatory effect on the NLR, with loss of this domain leading to increased cell necrosis (Bentham et al., 2017).

The recognition of Avr proteins can either occur through direct binding to LRR domains, with the use of a guard protein, or through sensor NLR proteins (Chiang and Coaker, 2015). The use of a guard, or sensor NLRs, to recognize Avr proteins have been shown to significantly increase the variety of Avr proteins recognized by a particular NLR protein. Furthermore, many guard proteins including RIN4, are under the surveillance of multiple NLR proteins (Su et al., 2018). This increases the chances of Avr recognition and successful ETI activation. Arabidopsis RPP1 proteins serve as an example for NLR proteins which directly recognize Avr proteins (Botella et al., 1998). Some NLR proteins also contain integrated domains (ID), which may resemble Avr targets. For example, a WRKY domain was identified in the Arabidopsis RRS1-R protein which recognizes *Ralstonia solanacearum* effectors (Deslandes et al., 2002; Grund et al., 2019). *Ralstonia solanocearum* PopP2 and AvrRps4 effectors normally target WRKY transcription factors (TFs), which abolishes transcriptional activation of defense-related genes. However, when these effectors bind to RRS1-R proteins, the RRS1-R/RPP4 complex is activated and triggers defense responses (Ma et al., 2018). Thus, the WRKY ID acts as a decoy for *R. solanocearum* effectors.

MORE IS BETTER—SOMETIMES: *NLR* EXPRESSION

NLR regulation has mainly been studied on protein level, and very little is known regarding *NLR* transcriptional regulation (Yu et al., 2022). Studies focusing on the expression of *NLR* genes have highlighted the importance of proper timing and level of *NLR* expression to activate successful immune responses during pathogen attack (Liu et al., 2020a). The overexpression of *NLR* genes leads to stunted growth and Avr-independent cell death (Palma et al., 2010; Li et al., 2015). However, rice mutants in which the APIP4 *NLR* was knocked down showed increased susceptibility when infected with *Magnaporthe oryzae* (Zhang et al., 2020). Thus, enough NLR proteins need to be activated to trigger successful immune responses during pathogen infection. This indicates that *NLR* expression needs to be above a certain threshold (Bieri et al., 2004). These factors make it unsurprising to observe differences in *NLR* expression levels between resistant and susceptible plant genotypes when infected with a pathogen. For example, 22 *NLRs* were upregulated in *Raphanus sativus* resistant to *Plasmodiophora brassicae*, but not in a susceptible genotype during *P. brassicae* infection

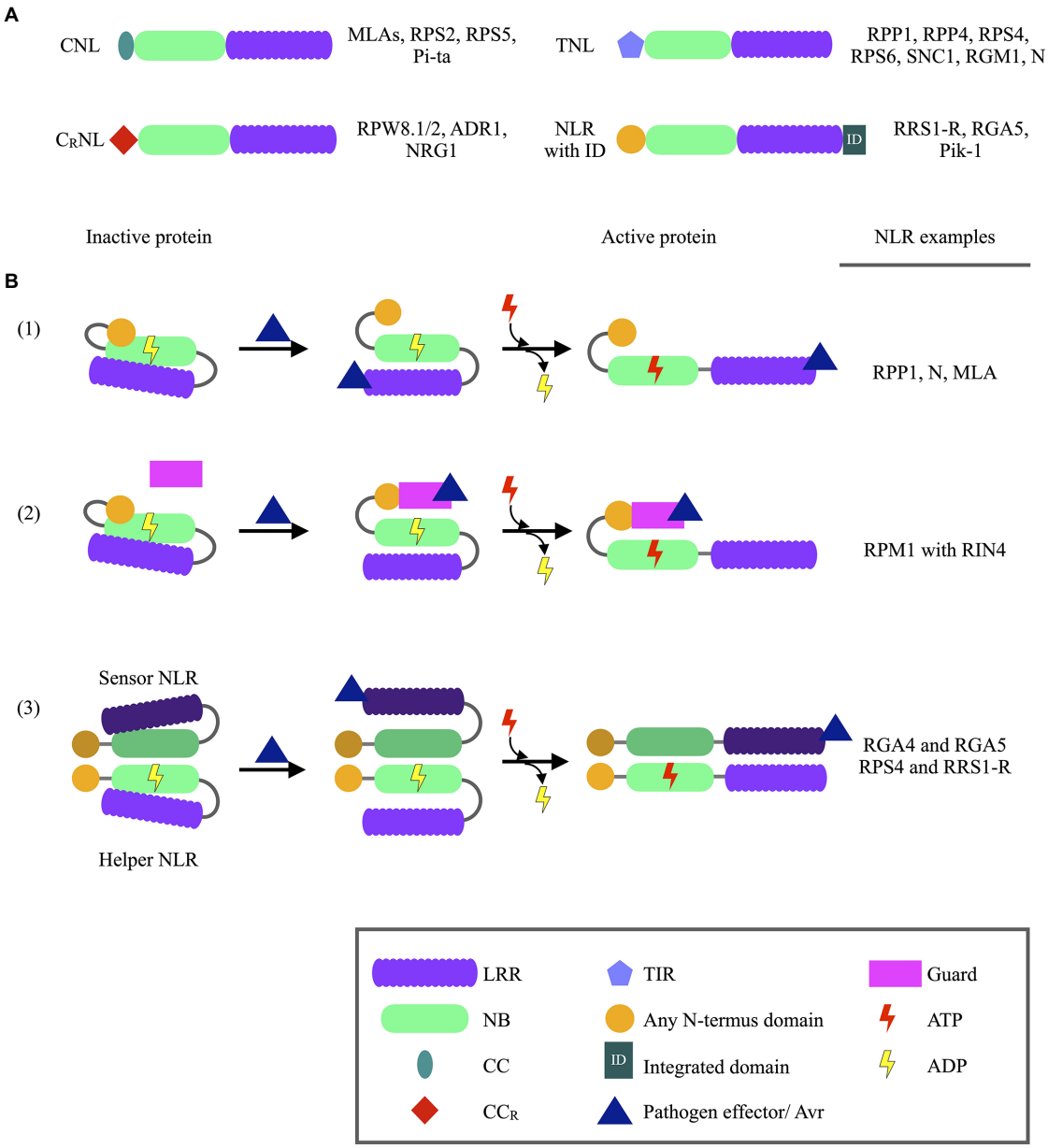

FIGURE 1 | Schematic representation of NLR protein domains and NLR activation, together with NLR protein examples. **(A)** Different structures of NLR proteins identified in plants, with NLR protein examples listed on the right of each schematic. **(B)** Models of Nucleotide binding-Leucine rich repeat (NLR) protein recognition of pathogen Avirulence (Avr) proteins. (1) Direct recognition of pathogen Avr protein through binding to LRR domains of NLR proteins. Avr recognition is followed by the exchange of ADP with ATP at the Nucleotide binding (NB) domain, which activates the protein and downstream immune responses. (2) Pathogen Avr proteins may bind to guard proteins which are under the surveillance of NLR proteins. Once Avr binding is recognized the NLR protein is activated through the binding of ATP, ultimately leading to immune response activation. (3) Avr recognition by NLR dimer pairs occurs when an Avr proteins binds to a sensor NLR. Structural changes of the sensor NLR induced by the Avr activates a helper NLR, subsequently leading to immune response activation. The binding of ATP to the sensor NLR is not required for NLR function (ADP—Adenosine diphosphate; ATP—Adenosine triphosphate; CC—Coiled coil; CC_R—Coiled coil domain with integrated RPW8 domain; LRR—Leucine rich repeat; NB—Nucleotide binding; TIR—Toll/interleukin-1 receptor).

(Wang et al., 2022a). Furthermore, significant differences in *NLR* expression were observed between a partially resistant and susceptible *Persea americana* rootstocks infected with *Phytophthora cinnamomi*, especially after 6 h post-inoculation (Fick et al., 2022). The expression of *NLR* genes is regulated by three main mechanisms: (1) epigenetic mechanisms, (2) *cis* elements and TFs, and (3) post-transcriptional modifications (**Figure 2**; Bezerra-Neto et al., 2020). Epigenetic mechanisms include histone modifications and DNA methylation, which influence chromatin density, and subsequently the ability of TFs and transcription machinery to bind to gene promoter sequences. TFs, which bind to *cis* elements in gene promoter sequences either exert

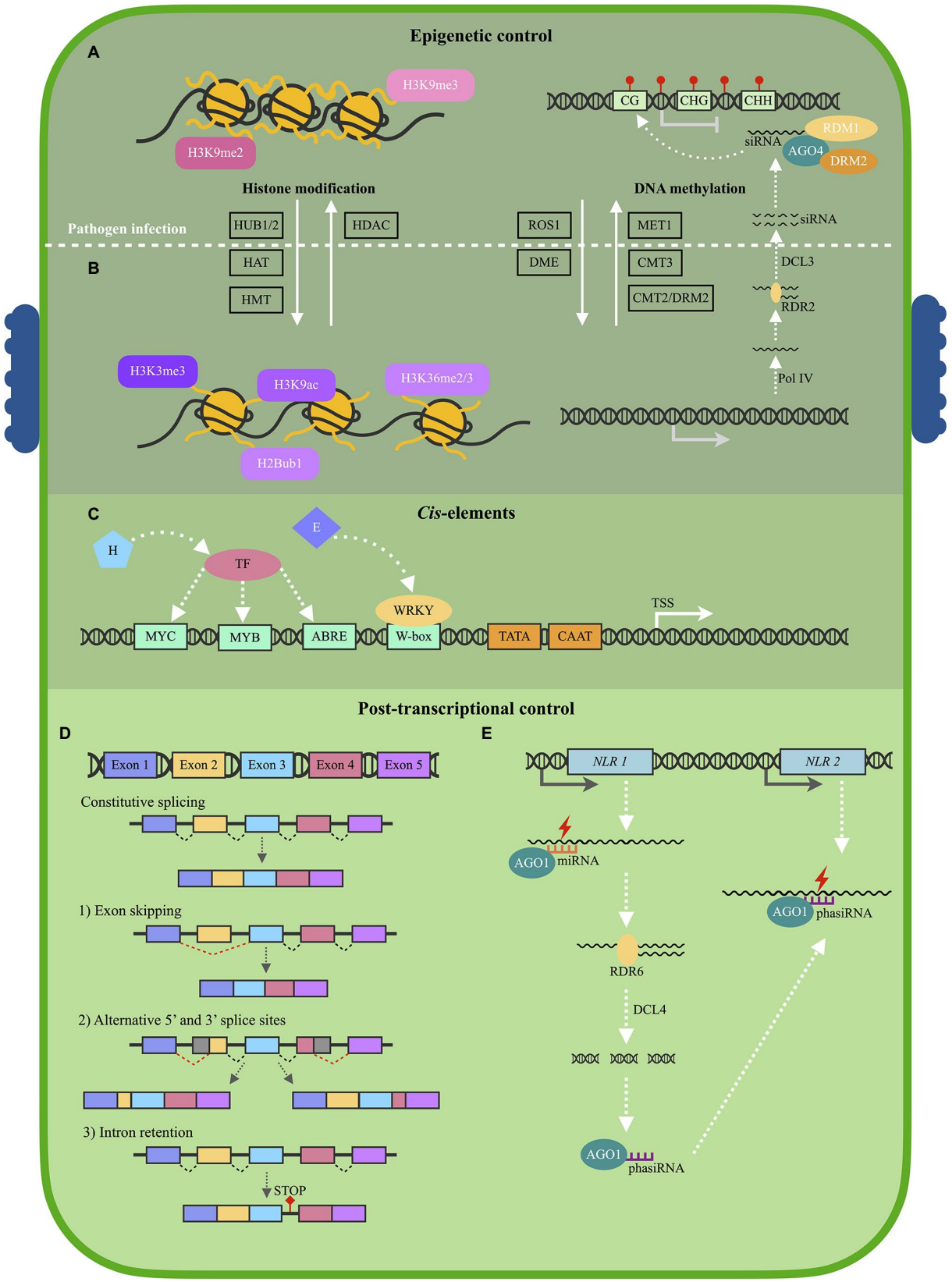

FIGURE 2 | Schematic illustration of the main regulatory mechanisms of plant *NLR* expression. **(A)** Before pathogen infection, a heterochromatin structure is

(Continued)

FIGURE 2 | maintained by histone methylation marks H3K9me2 and H3K9me3, which suppresses *Nucleotide binding-Leucine rich repeat* (*NLR*) expression. Histone deacetylases (HDAC) also contribute to a heterochromatin structure. The H3K9me3 mark is also associated with DNA methylation of CG, CHG, and CHH sites, established by the RNA-directed DNA methylation pathway. *De novo* DNA methylation is guided by small interfering RNA (siRNA) in association with Argonaute 4 (AGO4), Domains rearranged methyltransferase 2 (DRM2), and RNA-dependent DNA methylation 1 (RDM1) proteins. DNA methylation is further maintained by DNA methyltransferase 1 (MET1), CMT3 (Chromomethylase 3), and CMT2/DRM2. **(B)** Following pathogen infection, a euchromatin structure is adopted which allows for the activation of *NLR* expression. Histone marks H3K3me3 and H3K36me2/3 are established by Histone methyl transferases (HMT), H3K9ac by Histone acetyltransferases (HAT), and H2Bub1 by Histone monoubiquitination 1 and 2 (HUB1/2). Repressor of silencing 1 (ROS1) and DEMETER enzymes (DME) antagonize the RNA-directed DNA methylation pathway, and lower levels of DNA methylation is observed. **(C)** A euchromatin structure allows for Transcription factors (TFs) to bind to *cis* elements within *NLR* promoter sequences located upstream from the Transcription start site (TSS). Most TFs are activated following stress hormone (H) detection, but may also be activated by pathogen effectors **(E)**. The four most common *cis* elements identified within *NLR* promoter sequences include W-boxes, ABRE, MYB, and MYC elements. **(D)** Following *NLR* expression, alternative splicing (AS) patterns may contribute to different *NLR* mRNA isoforms, and thus, different levels of NLR proteins. AS may produce mRNAs containing (1) different exons, (2) different Untranslated regions (UTRs), (3) or a retained intron which may code for a stop codon, producing a truncated NLR protein following translation. **(E)** MicroRNA (miRNA) molecules in association with AGO1 can downregulate *NLR* expression by binding to *NLR* mRNAs to either block mRNA translation or cause mRNA degradation. Phased secondary RNA (phasiRNA) molecules can also be produced when diced *NLR* mRNAs are reverse transcribed by RNA-directed RNA polymerase 6 (RDR6) and diced by Dicer-like 4 (DCL4). These phasiRNA molecules may then target more *NLR* mRNA molecules to further contribute to *NLR* suppression (DCL3—Dicer-like 3; Pol IV—RNA polymerase IV).

a positive or negative regulatory effect on gene transcription. Furthermore, post-transcriptional modifications include alternative splicing patterns and small RNA, which can introduce stop codons, change protein structure or cause *NLR* mRNA degradation.

Epigenetic Control of *NLR* Genes

Epigenetic modifications regulate whether the chromatin is in a euchromatin (open) or heterochromatin (condensed) structure, thus controlling whether *NLR* transcription can be activated (**Figures 2A,B**). Histone modifications and DNA methylation patterns are dynamic molecular mechanisms able to change chromatin structure following pathogen infection (Zhang et al., 2018). Histone modifications have mostly been studied for Arabidopsis *NLR* genes. One histone modification often associated with transcriptional activation is the trimethylation of lysine 4 of histone H3 (H3K4me3) and is observed to regulate the expression of the Arabidopsis *RPP4* and *SNC1 NLR* genes (Kouzarides, 2007; Xia et al., 2013). This histone mark is established by the histone methyltransferase ATXR7, with the expression of both *NLRs* being reduced in *atxr7* mutants (Xia et al., 2013). Expression of *LAZ5*, another Arabidopsis *NLR* gene, is also controlled by histone methylation. Histone methyltransferase SDG8 is responsible for di- or trimethylating H3K36, activating *LAZ5* transcription (Palma et al., 2010). The di- and trimethylated H3K36 mark, is interestingly associated with alternative splicing patterns (discussed below) of *NLR* genes. H3K36me2/me3 levels were significantly higher at the 5' UTR (untranslated region) of the *ARG1 NLR* gene in resistant *Sorghum bicolor* genotypes when infected with *Colletotrichum sublineola* (Lee et al., 2022). H3K36me2/me3 was shown to increase the expression of *ARG1* and regulate alternative splicing patterns to produce a full-length *ARG1* mRNA transcript. In the susceptible *S. bicolor* genotype, lower H3K36me2/me3 marks and expression of *ARG1* was observed, together with truncated *ARG1* mRNA. This indicates that histone modifications also control *NLR* expression in an indirect manor at post-transcriptional levels.

Histone acetylation is also associated with active transcription of *NLR* genes (Luna et al., 2012). Histone acetylation is established by histone acetyltransferases (HATs) and removed by histone deacetylases (HDACs; Bannister and Kouzarides, 2011). Acetyl groups are negatively charged, and histone acetylation would thus result in the chromatin adopting a euchromatin structure (Luna et al., 2012). One HDAC, HDA9, in association with HOS15 was shown to regulate the expression of 62 *NLR* genes in Arabidopsis, with *hda9* and *hos15* mutants showing increased *NLR* expression levels and fewer H3K9ac marks (Yang et al., 2019). Overexpression of another HDAC protein, HDA19, was also shown to enhance Arabidopsis resistance toward the necrotrophic fungus *Alternaria brassicicola* (Zhou et al., 2005). Since NLR proteins activate the HR, decreased *NLR* expression could be hypothesized to lead to increased resistance toward necrotrophic pathogens. Histone deacetylation and thus, transcriptional repression might be favorable toward certain types of pathogens. *HDA19* expression was also induced by jasmonic acid (JA) and ethylene—signaling hormones produced in response to necrotrophic pathogens (Li et al., 2019). This shows that some histone modifying proteins are activated by either biotrophic- or necrotrophic pathogens, resulting in a different immune response which would prove more suitable toward a specific pathogen. Lastly, histone ubiquitylation is also associated with *NLR* transcription. HUB1 and HUB2, both E3 ubiquitin ligases, mono-ubiquitylates H2B to H2Bub1 during *Pseudomonas syringae* pv. *tomato* DC3000 infection of Arabidopsis. H2Bub1 levels increase, leading to the subsequent increase in expression of *RPP4* and *SNC1* (Zou et al., 2014).

The H3K9me2 histone mark is associated with transcriptional repression and is seen at the first intron region of the Arabidopsis *RPP7 NLR* gene (Tsuchiya and Eulgem, 2013). This mark influences alternative polyadenylation patterns of this *NLR* mRNA, influencing RPP7 protein structure and ultimately governs resistance levels toward *Hyaloperonospora arabidopsidis* (Eulgem et al., 2007; Tsuchiya and Eulgem, 2013). The H3K9me3 mark is also functionally associated with DNA methylation. DNA methylation of cytosine (position 5; 5mC) occurs at GC, CHG, or CHH (where H is A, C, or T) sites within plants, often aimed at silencing transposable elements (TEs) frequently found within *NLR* sequences (Miyao et al., 2003; Cuerda-Gil and Slotkin, 2016). *De novo* DNA methylation is mainly controlled by the RNA-directed DNA methylation pathway (RdDM) in plants (Law and Jacobsen, 2010). Small interfering RNAs (siRNAs) are produced during the canonical RdDM pathway when double-stranded RNA is synthesized by RNA-dependent RNA polymerase 2 (RDR2) and diced by Dicer-like 3 (DCL3). This double-stranded siRNA molecule is

then incorporated into Argonaute 4 (AGO4) as single-stranded siRNA. In association with the AGO4-siRNA complex, Domains rearranged methyltransferase 2 (DRM2) and RNA-dependent DNA methylation 1 (RDM1) establishes *de novo* DNA methylation (Wendte and Pikaard, 2017). Thereafter, DNA methylation is maintained by MET 1 (DNA methyltransferase 1) at CG sites, CMT3 (Chromomethylase 3) at CHG sites, and CMT2/DRM2 at CHH sites. DNA methylation defective Arabidopsis plants showed increased resistance levels toward *P. syringae* pv. *tomato* DC3000 and *H. arabidopsidis*, indicating that decreased levels of DNA methylation may lead to increased *NLR* expression and immune activation (Dowen Robert et al., 2012; López Sánchez et al., 2016).

The widespread loss of DNA methylation (hypomethylation) at TEs has been observed to occur during the activation of immune responses following pathogen infection (Annacondia et al., 2021). Demethylation of promoters leads to *cis* elements being more accessible to TFs, ultimately leading to increased *NLR* gene expression and disease resistance. In poplar trees infected with *Lonsdalea populi*, hypomethylation occurred at CH sites within promoter regions of defense-related genes (Xiao et al., 2021). Higher levels of hypomethylation were particularly noted in poplar trees with increased resistance toward *L. populi* when compared to susceptible trees. This observation suggests that hypomethylation results in increased defense-related gene expression which may ultimately lead to increased resistance levels. This could be explained by the observation that AGO4 is repressed after Arabidopsis treatment with PAMP flagellin-22 (flg22), and *Aegilops tauschii* infection with *Blumeria graminis* f. sp. *tritici* (Yu et al., 2013; Geng et al., 2019). The repression of AGO4 leads to lower levels of DNA methylation, which decreases transcriptional repression. Furthermore, ROS1 (Repressor of silencing 1) antagonizes RdDM mediated DNA methylation and promotes resistance toward *P. syringae* pv. *tomato* DC3000 (Halter et al., 2021). ROS1 has specifically been implicated in the regulation of some Arabidopsis *NLR* genes. In *ros1* mutants, four *NLR* genes showed decreased expression levels, due to active demethylation being repressed (Kong et al., 2020). ROS1 was also shown to demethylate promoter regions in which WRKY TFs bind (Halter et al., 2021). In particular, ROS1 demethylated promoter regions of *RGM1 TNL* after PTI activation by *P. syringae* pv. *tomato* DC3000 flagellin proteins. Lastly, DNA demethylation by DEMETER (DME) enzymes also contributes to enhanced resistance toward *Verticillium dahlia* and *P. syringae* pv. *tomato* infection in Arabidopsis (Zeng et al., 2021). In *dme* mutants, a hypermethylated region was associated with the *AtPRX34 TNL* gene. This gene showed lower expression levels following *P. syringae* pv. *tomato* infection in *dme* mutants when compared to wild-type plants. These results indicate that DME demethylates *NLR* sequences in response to bacterial and fungal infection.

Cis Elements of *NLR* Genes

Cis elements of *NLR* genes remain largely unknown due to these genes having unusually large promoter sequences (Yu et al., 2022). An *NLR* promoter sequence has often been defined as the 2 kb region upstream from the *NLR* transcription start site (**Figure 2C**). Multiple *cis* elements are frequently identified within *NLR* promoter sequences, many being pathogen-inducible *cis* elements (**Table 1**). These *cis* elements may be found in different arrangements within promoter sequences, resulting in complex gene regulatory mechanisms (Wang et al., 2021). Regulatory mechanisms are further complicated by the fact that the TFs which bind to these *cis* elements either exert a positive or negative regulatory effect on gene expression. Both a positive and negative *cis*-acting element were identified within the *SNC1 NLR* gene promoter using CRISPR/Cas9 directed mutations in Arabidopsis (Yu et al., 2022). This study further identified that two other *NLR* genes, *RPP4* and *SIKIC2*, are also affected by these mutations. This may indicate that these genes share the same *cis* elements. This hypothesis is supported by the fact that plant *NLRs* are often found within gene clusters and arranged in a head-to-head configuration (Narusaka et al., 2009; Van Wersch and Li, 2019). Many of these *NLRs* are often co-expressed following infection, further suggesting that these genes might be under the control of the same promoter, or promoters with the same *cis* elements (Liang et al., 2019; Yang et al., 2021).

It is important to remember that the abundance of TFs and certain arrangements of *cis* elements also influence gene expression levels, and the simple binding of a specific TF does not necessarily activate gene expression (Hoang et al., 2017). Thus, the identification of *NLR cis* elements alone cannot be used to predict the level of *NLR* expression, or when transcription will be activated. In tomato plants, a single nucleotide difference was identified in the promoter region of the *Sl5R-1 NLR* gene when compared between a Tomato spotted wilt virus (TSWV) resistant and susceptible plant (Qi et al., 2022). This single nucleotide deletion in resistant tomato plants resulted in a new TF binding site to be formed, which increases *Sl5R-1* expression and subsequent resistance. Importantly, *cis* elements are not the only regulatory sequences to control *NLR* expression—the tobacco *N TNL* contains two introns which contribute to increased expression levels of this gene during Tobacco mosaic virus (TMV) infection (Ikeda et al., 2021). Transient expression of the *N* gene without these introns showed lower levels of expression.

Cis elements identified most often in *NLR* promoter sequences include W-boxes, ABRE, MYB, and MYC elements (Mohr et al., 2010; Ding et al., 2020). W-boxes bind WRKY TFs, which is a large, diverse group of zinc finger TFs (Babu et al., 2006). These TFs are mostly activated by pathogen infection, effectors, and stress hormones, such as salicylic acid (SA) and JA. Following activation, a subset of WRKYs trigger the expression of PTI and ETI-related proteins, and the synthesis of stress hormones (Chen et al., 2019). Interestingly, an apple (*Malus domestica*) *NLR* gene, *MdNLR16*, is under the control of the MdWRKY79 TF which is responsive to sorbitol levels (Meng et al., 2018). Higher sorbitol levels lead to increased *MdNLR16* expression and subsequently enhanced resistance levels toward *Alternaria alternata*. ABRE elements are abscisic acid responsive elements which are recognized by bZIP proteins (Hobo et al., 1999). A single ABRE element, however, is not able to activate transcription, instead multiple elements are needed for transcriptional activation (Shen et al., 1996). Lastly, MYB and MYC elements have been shown to activate gene transcription in response to both abiotic

TABLE 1 | *Cis* elements identified in promoter sequences of plant *NLR* genes.

***Cis* element**	**Species**	**Putative function**	**Reference**
Common			
CAAT	*Pinus monticola*	Common element	Liu and Xiang, 2019
	Lagenaria siceraria		Wang et al., 2022b
	Triticum durum		Rampino et al., 2017
TATA-box	*P. monticola*	Core element	Liu and Xiang, 2019
	L. siceraria		Wang et al., 2022b
	Tomato		Qi et al., 2022
	T. durum		Rampino et al., 2017
Pathogen-inducible/stress			
ABRE	Rice	Abscisic acid responsive element	Ding et al., 2020
	L.a siceraria		Wang et al., 2022b
	T. durum		Rampino et al., 2017
AS-1 (TGACG)	Rice	Salicylic acid responsive element	Kong et al., 2018
	Vitis vinifera		Goyal et al., 2021
	Glycine max		Diao et al., 2021
BIHD-binding site (TGTCA)	*P. monticola*	Regulation of defense-related genes	Liu and Xiang, 2019
CGCG-box (ACGCGT)	*P. monticola*	Stress tolerance genes	Liu and Xiang, 2019
CGTCA-motif and TGACG-motif	*L. siceraria*	Methyl jasmonate responsive element	Wang et al., 2022b
	T. durum		Rampino et al., 2017
	G. max		Cui et al., 2017
E-box (CANNTG)	Rice	Jasmonic acid responsive element	Miyamoto et al., 2012
ERE-box (ATTTCAAA)	*P. monticola*	Ethylene responsive element	Liu and Xiang, 2019
	G. max		Diao et al., 2021
	Actinidia chinensis		Wang et al., 2020
	T. durum		Rampino et al., 2017
G-box	Rice	Regulation of defense-related genes	Kong et al., 2018
	T. durum		Rampino et al., 2017
GARE-motif, P-box, and TATC-box	*L. siceraria*	Gibberellin responsive element	Wang et al., 2022b
	T. durum		Rampino et al., 2017
	G. max		Cui et al., 2017
GCC-box (AGCCGCC)	Rice	Ethylene and pathogen responsive gene	Kong et al., 2018
	Saccharum spontaneum		Wang et al., 2021
GT1-box (GAAAAA)	*P. monticola*	Pathogen and salt-induced gene expression	Liu and Xiang, 2019
GTTGA	*Zea mays*	*Rhizoctonia solani* inducible	Li et al., 2017
H-box (CCTACCN7CT)	Rice	Regulation of defense-related genes	Kong et al., 2018
MYB recognition elements	Rice	Stress responsive elements	Kong et al., 2018
	S. spontaneum		Ding et al., 2020
	A. chinensis		Wang et al., 2020
Myb1-box (GTTAGTT)	*P. monticola*	Regulation of defense and drought-related genes	Liu and Xiang, 2019
	L. siceraria		Wang et al., 2022b
MYC elements	Rice	Stress responsive elements	Ding et al., 2020
STRE	Rice	Stress responsive elements	Ding et al., 2020
TATTT	*Z. mays*	*Rhizoctonia solani* inducible	Li et al., 2017
TC-rich repeats	*V. vinifera*	Stress responsive element	Goyal et al., 2021
	L. siceraria		Wang et al., 2022b
	G. max		Cui et al., 2017
TCA element	*V. vinifera*	Salicylic acid responsive element	Goyal et al., 2021
	G. max		Cui et al., 2017
TGA element	*V. vinifera*	Auxin responsive element	Goyal et al., 2021
	L. siceraria		Wang et al., 2022b
W-box (TTTGACY)	*P. monticola*	Regulation of defense-related genes	Liu and Xiang, 2019
	V. vinifera		Wang et al., 2021
	Arabidopsis		Wang et al., 2020
	S. spontaneum		
	A. chinensis		

(Continued)

TABLE 1 | Continued

Cis element	Species	Putative function	Reference
Other (Growth/development)			
ACACNNG	*P. monticola*	Abscisic acid induced gene expression	Liu and Xiang, 2019
ARR1-binding site (AGATT)	*P. monticola*	Cytokinin responsive gene	Liu and Xiang, 2019
MADS-box/ CArG-motif (CCW6GG)	*P. monticola*	Regulation of plant flowering time and vernalization genes	Liu and Xiang, 2019
Circadian motif (CAAN4ATC)	*P. monticola*	Circadian gene expression	Liu and Xiang, 2019
NtBBF1 binding site (ACTTTA)	*P. monticola*	Tissue-specific expression and auxin induction	Liu and Xiang, 2019
SRE (TTATCC)	*P.s monticola*	Activation of axillary bud outgrowth	Liu and Xiang, 2019
T-box (ACTTTG)	*P. monticola*	Light activated element	Liu and Xiang, 2019
WUS-binding site (TTAATGG)	*P. monticola*	Establishment and maintenance of stem cells in shoot and floral meristems	Liu and Xiang, 2019
W-box	*Malus domestica*	Sorbitol inducible element	Meng et al., 2018

and biotic stressors (Feng et al., 2013; Fang et al., 2018; Wu et al., 2019). *NLR cis* element identification studies have thus shown that the TFs controlling *NLR* expression is mostly activated by abiotic and biotic stress. *Cis* element studies may then also be used to identify putative NLR function. For example, in *Pinus monticola* Douglas ex D. Don (Western white pine trees), *cis* element identification of the *PmTNL2* gene suggested that this NLR might be important for both plant immune responses, as well as growth and development (Liu and Xiang, 2019).

Post-transcriptional Modifications of NLRs

Alternative splicing (AS) contributes significantly toward the diversity of the *NLR* transcriptome and NLR proteome—altering levels of different mRNA isoforms in response to developmental and environmental conditions (Kelemen et al., 2013). AS can result in *NLR* mRNAs to contain different exons, 5′- and 3′ untranslated regions, and introns which may introduce stop codons resulting in truncated NLR proteins (**Figure 2D**). The example used most often for AS of *NLR* genes is the N TNL protein associated with resistance toward TMV. The *N* gene produces either a short *N* mRNA (N_S) or a long *N* mRNA (N_L; Erickson et al., 1999). N_L contains an exon which encodes a stop codon, resulting in a truncated protein. N_S however is translated into a complete protein. Both these proteins are expressed during TMV infection and needed for full TMV resistance. One rice *CNL*, *Pi-ta*, produces up to 11 different protein isoforms as a result of AS (Costanzo and Jia, 2009). In response to *M. oryzae* infection, a resistant rice genotype showed increased expression levels of a Pi-ta protein with a C-terminus thioredoxin domain, when compared to a susceptible genotype.

In both barley and wheat, AS was seen to regulate whether and which IDs were present in NLR proteins in response to different experimental conditions (Halterman et al., 2003; Andersen et al., 2020). Different IDs may influence where NLR proteins localize to in the plant cell or may even cause the NLR protein to act as a decoy target for Avr proteins (Yang et al., 2014). It is worth noting that AS may also have an impact on proteins guarded by NLRs, suggesting that AS may regulate NLR activity in an indirect manner. For example, a NLR Rpi-vnt1.1 guards the GLYK (Glycerate 3-kinase) protein in potato (Gao et al., 2020). A truncated isoform of *GLYK*, which does not contain a chloroplast transit peptide-encoding sequence, is expressed in dark conditions, and cannot be recognized by a *Phytophthora infestans* Avr protein AVRvnt1. Thus, Rpi-vnt1.1 cannot activate immune responses. In light conditions, the full-length *GLYK* mRNA is expressed, and this protein isoform binds to the Avr during infection, leading to Rpi-vnt1.1 being activated to trigger ETI.

NLR repression can be regulated at a post-transcriptional level using siRNAs and micro RNAs (miRNAs; **Figure 2E**). miRNAs are non-coding RNAs between 20 and 24 nucleotides in length. They are encoded by *miRNA* genes, which are transcribed by RNA polymerase II to produce a long, primary miRNA (Xie et al., 2005). After processing, a precursor miRNA (pre-miRNA) is produced which forms a hairpin structure with a self-complementary stem loop. This pre-miRNA molecule is diced by DCL1 or DCL4, and produces a 22 nucleotide double-stranded miRNA, which is exported to the cytoplasm (Sun et al., 2019). An RNA-induced silencing complex (RISC) is then formed when the mature miRNA binds to an AGO1 protein. miRNAs guide AGO1 proteins to target mRNAs, either resulting in endonucleolytic cleavage and degradation or inhibition of translation. The P-loop domain, important for ATP binding and NLR protein activation, is a common target for miRNAs (Zhai et al., 2011; Fei et al., 2015).

NLR mRNA cleavage by miRNAs may also produce phasiRNAs (phased secondary small interfering RNAs), which then target and degrade other mRNAs with the same sequence (Liu et al., 2020b). Three *Medicago truncatula* miRNA families target mRNA transcripts of 74 *NLRs*, leading to the production of phasiRNAs which suppress the expression of 324 *NLR* genes (Zhai et al., 2011). Liu et al. (2014) showed that the barley miR9863 family targets *MLA1 CNL* transcripts, with the resulting phasiRNAs also leading to *MLA1* mRNAs being degraded. The authors suspect that this pathway prevents immune responses from being overloaded, and thus, *NLR* downregulation may have a positive effect on plant resistance levels. In Arabidopsis *miR472* knock-down mutants, increased resistance levels were observed toward *P. syringae*, and reduced resistance levels were observed when this miRNA was overexpressed (Boccara et al., 2014). This presents an interesting method of pathogen control—transient expression of miRNA targets in host plants may increase resistance levels toward various pathogens. In tomato, transient expression of short tandem target mimic RNAs increased resistance levels toward *P. infestans* and *P. syringae* (Canto-Pastor et al., 2019). These mimic RNAs acted

as targets for miR482/211b, which resulted in increased *NLR* expression and enhanced disease resistance.

OH NO YOU DO NOT: HOW PATHOGENS INTERFERE WITH *NLR* EXPRESSION

With multiple proteins contributing to the regulation of *NLR* expression, comes multiple opportunities for pathogen interference. Despite this, very few cases are documented in which pathogen Avr proteins influence *NLR* expression. However, Avr targets remain largely unknown, and it is yet to be discovered how *NLR* regulation is hijacked by pathogens (Wu et al., 2022). An average of 32% of Avr proteins from bacteria, fungi, and oomycetes localize in the plant cell nucleus, indicating that these Avr proteins may interfere with *NLR* transcription (Khan et al., 2018). Two cytoplasmic effectors from *M. oryzae*, MoHTR1, and MoHTR2, bind to effector binding elements (EBE) in rice gene promoters and function as transcription repressors (Kim et al., 2020). These EBEs were present in many defense-related gene promoters, and the binding of these effectors led to significant transcription reprogramming. Transient expression of *MoHTR1* and *MoHTR2* in rice not only led to increased susceptibility toward *M. oryzae*, but also to *Xanthomonas oryzae* pv. *oryzae* and *Cochliobolus miyabeanus*. It remains unclear whether these effectors bind host repressor proteins, or whether they interfere with the binding of transcription activators. A *Melampsora larici-populina* effector, Mlp124478, also interferes with the transcription of WRKY TFs which indirectly inhibits the activation of defense-related gene expression, including the *RPP8 NLR* (Ahmed et al., 2018). Some pathogen Avr proteins also interfere with the synthesis of stress hormones. SA metabolism is inhibited by *Phytophthora sojae* PsIsc1 and *Verticillium dahliae* VdIsc1 enzymatic effectors, which redirects the precursor molecule of SA from the plastid into the cytosol (Liu et al., 2014). The metabolism of SA decreases and thus SA-mediated immune responses cannot be activated. Since some TFs which bind to *NLR cis* elements are activated by SA, lower SA levels may disrupt the activation of *NLR* expression (Goyal et al., 2021).

From another perspective, the suppression of *NLR* expression may not be the ultimate goal of the pathogen. *Phytophthora* species are hemibiotrophic oomycetes, which switch from a biotrophic to necrotrophic phase during infection (Zuluaga et al., 2016). During the necrotrophic phase, increased *NLR* expression may be beneficial to the pathogen since NLRs activate the HR and thus, plant cell death. *P. sojae* RxLR effectors PSR1 and PSR2 suppress plant RNA silencing by interfering with the miRNA synthesis pathway, which increased susceptibility in *Nicotiana benthamiana* (Qiao et al., 2013). This may lead to higher NLR levels and activation of HR, resulting in a more favorable environment for necrotrophic pathogens. This hypothesis is further supported by the fact that PSR2 is only expressed during the later stages of infection, when *P. sojae* switches to a necrotrophic stage (Qiao et al., 2013). Furthermore, the *V. dahliae* VdSSR1 protein was shown to interfere with the nuclear exportation of AGO1-miRNA complexes in *N. benthamiana* (Zhu et al., 2022). Decreased AGO1-miRNA exportation would subsequently lead to decreased suppression of *NLR* expression, which may contribute to the observed increased susceptibility in transgenic plants expressing *VdSSR1* at higher levels. However, VdSSR1 expression data is needed to indicate whether this protein is only expressed during the necrotrophic stage of this hemibiotrophic fungus. Lastly, a necrotrophic fungus, *Botrytis cinerea*, is able to translocate siRNAs into plant cells and may redirect host siRNA machinery (Weiberg et al., 2013). *B. cinerea* siRNAs were associated with AGO1 proteins during infection of Arabidopsis, indicating that *B. cinerea* may hijack RISC to increase virulence (Ellendorff et al., 2009). It would be interesting to investigate whether these siRNA molecules cause siRNA-directed cleavage and degradation of *NLR* mRNA transcripts (Qiao et al., 2021). It may also be of interest to investigate whether pathogen-derived siRNAs influence DNA methylation patterns during infection.

CONCLUSION

NLR proteins play a significant role in activating plant immune responses during pathogen attack. The mis-regulation of NLR-encoding genes considerably impairs the plant's ability to detect pathogen Avr proteins, which ultimately leads to susceptibility. Thus, a comprehensive understanding of *NLR* gene regulation is of particular interest. Unfortunately, NLR protein regulation has mainly been studied on a post-translational level, with a large knowledge gap remaining regarding the transcriptional- and post-transcriptional regulation of these proteins. Identifying epigenetic marks, and *cis* elements which control *NLR* expression in response to pathogen attack provides the first step in unraveling these complex regulatory mechanisms. These mechanisms can further be compared between susceptible and resistant plant genotypes to understand the factors which contribute to a successful immune response. Furthermore, investigating how pathogens interfere with these mechanisms would provide much needed insight into plant–pathogen interactions. Ultimately, knowledge in these areas may be used during plant breeding programs which aim to produce genotypes with increased resistance toward a variety of pathogens. These mechanisms can also be used to drive the expression of trans-*NLR* genes in genetically modified crops, with the goal of increasing resistance toward both biotic and abiotic stresses.

AUTHOR CONTRIBUTIONS

AF conceptualized, drafted, and reviewed the manuscript. VS and NB reviewed and assisted in the drafting of the manuscript. All authors contributed to the article and approved the submitted version.

FUNDING

Funding was generously provided by the Hans Merensky Foundation.

REFERENCES

Adachi, H., Derevnina, L., and Kamoun, S. (2019). NLR singletons, pairs, and networks: evolution, assembly, and regulation of the intracellular immunoreceptor circuitry of plants. *Curr. Opin. Plant Biol.* 50, 121–131. doi: 10.1016/j.pbi.2019.04.007

Ahmed, M. B., Santos, K. C. G. D., Sanchez, I. B., Petre, B., Lorrain, C., Plourde, M. B., et al. (2018). A rust fungal effector binds plant DNA and modulates transcription. *Sci. Rep.* 8:14718. doi: 10.1038/s41598-018-32825-0

Andam, A., Azizi, A., Majdi, M., and Abdolahzadeh, J. (2020). Comparative expression profile of some putative resistance genes of chickpea genotypes in response to ascomycete fungus, *Ascochyta rabiei* (Pass.) Labr. *Rev. Bras. Bot.* 43, 123–130. doi: 10.1007/s40415-020-00576-w

Andersen, E. J., Nepal, M. P., Purintun, J. M., Nelson, D., Mermigka, G., and Sarris, P. F. (2020). Wheat disease resistance genes and their diversification through integrated domain fusions. *Front. Genet.* 11:898. doi: 10.3389/fgene.2020.00898

Annacondia, M. L., Markovic, D., Reig Valiente, J., Scaltsoyiannes, V., Pieterse, C., Ninkovic, V., et al. (2021). Aphid feeding induces the relaxation of epigenetic control and the associated regulation of the defence response in Arabidopsis. *New Phytol.* 230, 1185–1200. doi: 10.1111/nph.17226

Babu, M. M., Iyer, L. M., Balaji, S., and Aravind, L. (2006). The natural history of the WRKY-GCM1 zinc fingers and the relationship between transcription factors and transposons. *Nucleic Acids Res.* 34, 6505–6520. doi: 10.1093/nar/gkl888

Bannister, A. J., and Kouzarides, T. (2011). Regulation of chromatin by histone modifications. *Cell Res.* 21, 381–395. doi: 10.1038/cr.2011.22

Bentham, A., Burdett, H., Anderson, P. A., Williams, S. J., and Kobe, B. (2017). Animal NLRs provide structural insights into plant NLR function. *Ann. Bot.* 119, mcw171–mcw702. doi: 10.1093/aob/mcw171

Bezerra-Neto, J. P., Araújo, F. C., Ferreira-Neto, J. R. C., Silva, R. L. O., Borges, A. N. C., Matos, M. K. S., et al. (2020). "*NBS-LRR* genes—plant health sentinels: structure, roles, evolution and biotechnological applications," in *Applied Plant Biotechnology for Improving Resistance to Biotic Stress*. eds. P. Poltronieri and Y. Hong (Amsterdam, Netherlands: Academic Press), 63–120.

Bieri, S., Mauch, S., Shen, Q. H., Peart, J., Devoto, A., Casais, C., et al. (2004). RAR1 positively controls steady state levels of barley MLA resistance proteins and enables sufficient MLA6 accumulation for effective resistance. *Plant Cell* 16, 3480–3495. doi: 10.1105/tpc.104.026682

Boccara, M., Sarazin, A., Thiébeauld, O., Jay, F., Voinnet, O., Navarro, L., et al. (2014). The Arabidopsis miR472-RDR6 silencing pathway modulates PAMP- and effector triggered immunity through the post-transcriptional control of disease resistance genes. *PLoS Pathog.* 10:e1003883. doi: 10.1371/journal.ppat.1003883

Bonardi, V., Tang, S., Stallmann, A., Roberts, M., Cherkis, K., and Dangl Jeffery, L. (2011). Expanded functions for a family of plant intracellular immune receptors beyond specific recognition of pathogen effectors. *Proc. Natl. Acad. Sci.* 108, 16463–16468. doi: 10.1073/pnas.1113726108

Botella, M. A., Parker, J. E., Frost, L. N., Bittner-Eddy, P. D., Beynon, J. L., Daniels, M. J., et al. (1998). Three genes of the Arabidopsis *RPP1* complex resistance locus recognize distinct *Peronospora parasitica* avirulence determinants. *Plant Cell* 10, 1847–1860. doi: 10.1105/tpc.10.11.1847

Bradeen, J. M., Iorizzo, M., Mollov, D. S., Raasch, J., Kramer, L. C., Millett, B. P., et al. (2009). Higher copy numbers of the potato *RB* transgene correspond to enhanced transcript and late blight resistance levels. *Mol. Plant-Microbe Interact.* 22, 437–446. doi: 10.1094/MPMI-22-4-0437

Canto-Pastor, A., Santos Bruno, A. M. C., Valli Adrian, A., Summers, W., Schornack, S., and Baulcombe David, C. (2019). Enhanced resistance to bacterial and oomycete pathogens by short tandem target mimic RNAs in tomato. *Proc. Natl. Acad. Sci.* 116, 2755–2760. doi: 10.1073/pnas.1814380116

Chen, X., Li, C., Wang, H., and Guo, Z. (2019). WRKY transcription factors: evolution, binding, and action. *Phytopathol. Res.* 1:13. doi: 10.1186/s42483-019-0022-x

Chiang, Y. H., and Coaker, G. (2015). Effector triggered immunity: NLR immune perception and downstream defence responses. *The Arabidopsis Book* 2015:e0183. doi: 10.1199/tab.0183

Costanzo, S., and Jia, Y. (2009). Alternatively spliced transcripts of *Pi-ta* blast resistance gene in *Oryza sativa*. *Plant Sci.* 177, 468–478. doi: 10.1016/j.plantsci.2009.07.012

Cuerda-Gil, D., and Slotkin, R. K. (2016). Non-canonical RNA-directed DNA methylation. *Nat. Plants* 2:16163. doi: 10.1038/nplants.2016.163

Cui, H., Tsuda, K., and Parker, J. E. (2015). Effector triggered immunity: from pathogen perception to robust defence. *Ann. Rev. Plant Biol.* 66, 487–511. doi: 10.1146/annurev-arplant-050213-040012

Cui, X., Yan, Q., Gan, S., Xue, D., Dou, D., Guo, N., et al. (2017). Overexpression of gma-miR1510a/b suppresses the expression of a NB-LRR domain gene and reduces resistance to *Phytophthora sojae*. *Gene* 621, 32–39. doi: 10.1016/j.gene.2017.04.015

Davis, K. R., and Hahlbrock, K. (1987). Induction of defence responses in cultured parsley cells by plant cell wall fragments. *Plant Physiol.* 84, 1286–1290. doi: 10.1104/pp.84.4.1286

Deslandes, L., Olivier, J., Theulières, F., Hirsch, J., Feng, D. X., Bittner-Eddy, P., et al. (2002). Resistance to *Ralstonia solanacearum* in *Arabidopsis thaliana* is conferred by the recessive *RRS1-R* gene, a member of a novel family of resistance genes. *Proc. Natl. Acad. Sci.* 99, 2404–2409. doi: 10.1073/pnas.032485099

Diao, P., Sun, H., Bao, Z., Li, W., Niu, N., Li, W., et al. (2021). Expression of an antiviral gene *GmRUN1* from soybean is regulated via intron-mediated enhancement (IME). *Viruses* 13:2032. doi: 10.3390/v13102032

Ding, L., Xu, X., Kong, W., Xia, X., Zhang, S., Liu, L. W., et al. (2020). Genome-wide identification and expression analysis of rice *NLR* genes responsive to the infections of *Xanthomonas oryzae* pv. *oryzae* and *Magnaporthe oryzae*. *Physiol. Mol. Plant Pathol.* 111:101488. doi: 10.1016/j.pmpp.2020.101488

Dowen Robert, H., Pelizzola, M., Schmitz Robert, J., Lister, R., Dowen Jill, M., Nery Joseph, R., et al. (2012). Widespread dynamic DNA methylation in response to biotic stress. *Proc. Natl. Acad. Sci.* 109, E2183–E2191. doi: 10.1073/pnas.1209329109

Ellendorff, U., Fradin, E. F., De Jonge, R., and Thomma, B. P. (2009). RNA silencing is required for Arabidopsis defence against Verticillium wilt disease. *J. Exp. Bot.* 60, 591–602. doi: 10.1093/jxb/ern306

Erickson, F. L., Holzberg, S., Calderon-Urrea, A., Handley, V., Axtell, M., Corr, C., et al. (1999). The helicase domain of the TMV replicase proteins induces the N-mediated defence response in tobacco. *Plant J.* 18, 67–75. doi: 10.1046/j.1365-313x.1999.00426.x

Eulgem, T., Tsuchiya, T., Wang, X. J., Beasley, B., Cuzick, A., Tör, M., et al. (2007). EDM2 is required for RPP7-dependent disease resistance in Arabidopsis and affects *RPP7* transcript levels. *Plant J.* 49, 829–839. doi: 10.1111/j.1365-313X.2006.02999.x

Fang, Q., Wang, Q., Mao, H., Xu, J., Wang, Y., Hu, H., et al. (2018). AtDIV2, an R-R-type MYB transcription factor of Arabidopsis, negatively regulates salt stress by modulating ABA signalling. *Plant Cell Rep.* 37, 1499–1511. doi: 10.1007/s00299-018-2321-6

Fei, Q., Li, P., Teng, C., and Meyers, B. C. (2015). Secondary siRNAs from *Medicago* NB-LRRs modulated via miRNA-target interactions and their abundances. *Plant J.* 83, 451–465. doi: 10.1111/tpj.12900

Feng, H. L., Ma, N. N., Meng, X., Zhang, S., Wang, J. R., Chai, S., et al. (2013). A novel tomato MYC-type ICE1-like transcription factor, SlICE1a, confers cold, osmotic and salt tolerance in transgenic tobacco. *Plant Physiol. Biochem.* 73, 309–320. doi: 10.1016/j.plaphy.2013.09.014

Fick, A., Swart, V., Backer, R., Bombarely, A., Engelbrecht, J., and Van den Berg, N. (2022). Partially resistant avocado rootstock Dusa® shows prolonged upregulation of *nucleotide binding-Leucine rich repeat* genes in response to *Phytophthora cinnamomi* infection. *Front. Plant Sci.* 13:793644. doi: 10.3389/fpls.2022.793644

Gao, C., Xu, H., Huang, J., Sun, B., Zhang, F., Savage, Z., et al. (2020). Pathogen manipulation of chloroplast function triggers a light-dependent immune recognition. *Proc. Natl. Acad. Sci.* 117, 9613–9620. doi: 10.1073/pnas.2002759117

Geng, S., Kong, X., Song, G., Jia, M., Guan, J., Wang, F., et al. (2019). DNA methylation dynamics during the interaction of wheat progenitor *Aegilops*

tauschii with the obligate biotrophic fungus *Blumeria graminis* f. sp. *tritici*. *New Phytol.* 221, 1023–1035. doi: 10.1111/nph.15432

Goyal, N., Bhatia, G., Garewal, N., Upadhyay, A., and Singh, K. (2021). Identification of defence related gene families and their response against powdery and downy mildew infections in *Vitis vinifera*. *BMC Genomics* 22:776. doi: 10.1186/s12864-021-08081-4

Grund, E., Tremousaygue, D., and Deslandes, L. (2019). Plant NLRs with integrated domains: unity makes strength. *Plant Physiol.* 179, 1227–1235. doi: 10.1104/pp.18.01134

Halter, T., Wang, J., Amesefe, D., Lastrucci, E., Charvin, M., Singla Rastogi, M., et al. (2021). The Arabidopsis active demethylase ROS1 *cis*-regulates defence genes by erasing DNA methylation at promoter-regulatory regions. *eLife* 10:e62994. doi: 10.7554/eLife.62994

Halterman, D. A., Wei, F., and Wise, R. P. (2003). Powdery mildew-induced *Mla* mRNAs are alternatively spliced and contain multiple upstream open reading frames. *Plant Physiol.* 131, 558–567. doi: 10.1104/pp.014407

Hoang, X. L. T., Nhi, D. N. H., Thu, N. B. A., Thao, N. P., and Tran, L. S. P. (2017). Transcription factors and their roles in signal transduction in plants under abiotic stresses. *Curr. Genomics* 18, 483–497. doi: 10.2174/1389202918666170227150057

Hobo, T., Asada, M., Kowyama, Y., and Hattori, T. (1999). ACGT-containing abscisic acid response element (ABRE) and coupling element 3 (CE3) are functionally equivalent. *Plant J.* 19, 679–689. doi: 10.1046/j.1365-313x.1999.00565.x

Ikeda, C., Taku, K., Miyazaki, T., Shirai, R., Nelson, R. S., Nyunoya, H., et al. (2021). Cooperative roles of introns 1 and 2 of tobacco resistance gene *N* in enhanced *N* transcript expression and antiviral defence responses. *Sci. Rep.* 11:15424. doi: 10.1038/s41598-021-94713-4

Jones, J. D. G., and Dangl, J. L. (2006). The plant immune system. *Nature* 444, 323–329. doi: 10.1038/nature05286

Kelemen, O., Convertini, P., Zhang, Z., Wen, Y., Shen, M., Falaleeva, M., et al. (2013). Function of alternative splicing. *Gene* 514, 1–30. doi: 10.1016/j.gene.2012.07.083

Khan, M., Seto, D., Subramaniam, R., and Desveaux, D. (2018). Oh, the places they'll go! A survey of phytopathogen effectors and their host targets. *Plant J.* 93, 651–663. doi: 10.1111/tpj.13780

Kim, S., Kim, C. Y., Park, S. Y., Kim, K. T., Jeon, J., Chung, H., et al. (2020). Two nuclear effectors of the rice blast fungus modulate host immunity via transcriptional reprogramming. *Nat. Commun.* 11:5845. doi: 10.1038/s41467-020-19624-w

Kong, W., Ding, L., Cheng, J., and Wang, B. (2018). Identification and expression analysis of genes with pathogen-inducible *cis*-regulatory elements in the promoter regions in *Oryza sativa*. *Springer* 11:52. doi: 10.1186/s12284-018-0243-0

Kong, W., Xia, X., Wang, Q., Liu, L.-W., Zhang, S., Ding, L., et al. (2020). Impact of DNA demethylases on the DNA methylation and transcription of Arabidopsis *NLR* genes. *Front. Genet.* 11:460. doi: 10.3389/fgene.2020.00460

Kouzarides, T. (2007). Chromatin modifications and their function. *Cell* 128, 693–705. doi: 10.1016/j.cell.2007.02.005

Law, J. A., and Jacobsen, S. E. (2010). Establishing, maintaining and modifying DNA methylation patterns in plants and animals. *Nat. Rev. Genet.* 11, 204–220. doi: 10.1038/nrg2719

Lee, S., Fu, F., Liao, C. J., Mewa, D. B., Adeyanju, A., Ejeta, G., et al. (2022). Broad-spectrum fungal resistance in sorghum is conferred through the complex regulation of an immune receptor gene embedded in a natural antisense transcript. *Plant Cell* 34, 1641–1665. doi: 10.1093/plcell/koab305

Li, N., Chen, J., Yang, F., Wei, S., Kong, L., Ding, X., et al. (2017). Identification of two novel *Rhizoctonia solani*-inducible *cis*-acting elements in the promoter of the maize gene, *GRMZM2G315431*. *Sci. Rep.* 7:42059. doi: 10.1038/srep42059

Li, N., Han, X., Feng, D., Yuan, D., and Huang, L. J. (2019). Signalling crosstalk between salicylic acid and ethylene/jasmonate in plant defence: do we understand what they are whispering? *Int. J. Mol. Sci.* 20:671. doi: 10.3390/ijms20030671

Li, X., Wu, J., Yin, L., Zhang, Y., Qu, J., and Lu, J. (2015). Comparative transcriptome analysis reveals defence-related genes and pathways against downy mildew in *Vitis amurensis* grapevine. *Plant Physiol. Biochem.* 95, 1–14. doi: 10.1016/j.plaphy.2015.06.016

Liang, W., Van Wersch, S., Tong, M., and Li, X. (2019). TIR-NB-LRR immune receptor SOC3 pairs with truncated TIR-NB protein CHS1 or TN2 to monitor the homeostasis of E3 ligase SAUL1. *New Phytol.* 221, 2054–2066. doi: 10.1111/nph.15534

Liu, T., Song, T., Zhang, X., Yuan, H., Su, L., Li, W., et al. (2014). Unconventionally secreted effectors of two filamentous pathogens target plant salicylate biosynthesis. *Nat. Commun.* 5:4686. doi: 10.1038/ncomms5686

Liu, Y., Teng, C., Xia, R., and Meyers, B. C. (2020b). PhasiRNAs in plants: their biogenesis, genic sources, and roles in stress responses, development, and reproduction. *Plant Cell* 32, 3059–3080. doi: 10.1105/tpc.20.00335

Liu, J. J., and Xiang, Y. (2019). Characterization of the western white pine TIR-NBS-LRR (*PmTNL2*) gene by transcript profiling and promoter analysis. *Genome* 62, 477–488. doi: 10.1139/gen-2019-0035

Liu, X., Zhao, C., Yang, L., Zhuang, M., Zhang, Y., Wang, Y., et al. (2020a). A time-resolved dual transcriptome analysis reveals the molecular regulating network underlying the compatible/incompatible interactions between cabbage (*Brassica oleracea*) and *Fusarium oxysporum* f. sp. *conglutinans*. *Plant Soil* 448, 455–478. doi: 10.1007/s11104-020-04437-z

López Sánchez, A., Stassen, J. H., Furci, L., Smith, L. M., and Ton, J. (2016). The role of DNA (de)methylation in immune responsiveness of Arabidopsis. *Plant J.* 88, 361–374. doi: 10.1111/tpj.13252

Luna, E., Bruce, T. J. A., Roberts, M. R., Flors, V., and Ton, J. (2012). Next-generation systemic acquired resistance. *Plant Physiol.* 158, 844–853. doi: 10.1104/pp.111.187468

Ma, Y., Guo, H., Hu, L., Martinez, P. P., Moschou, P. N., Cevik, V., et al. (2018). Distinct modes of derepression of an Arabidopsis immune receptor complex by two different bacterial effectors. *Proc. Natl. Acad. Sci.* 115, 10218–10227. doi: 10.1073/pnas.1811858115

Maekawa, T., Cheng, W., Spiridon, L. N., Töller, A., Lukasik, E., Saijo, Y., et al. (2011). Coiled-coil domain-dependent homodimerization of intracellular barley immune receptors defines a minimal functional module for triggering cell death. *Cell Host Microbe* 9, 187–199. doi: 10.1016/j.chom.2011.02.008

Maiti, S., Basak, J., and Pal, A. (2014). "Current understanding on plant R-genes/proteins and mechanisms of defence responses against biotic stresses," in *Review of Plant Pathology*. eds. B. N. Chakraborty and U. Chakraborty (Jodhpur, India: Scientific Publishers), 93–126.

Maule, A. J., Caranta, C., and Boulton, M. I. (2007). Sources of natural resistance to plant viruses: status and prospects. *Mol. Plant Pathol.* 8, 223–231. doi: 10.1111/j.1364-3703.2007.00386.x

Meng, D., Li, C., Park, H. J., González, J., Wang, J., Dandekar, A. M., et al. (2018). Sorbitol modulates resistance to *Alternaria alternata* by regulating the expression of an *NLR* resistance gene in apple. *Plant Cell* 30, 1562–1581. doi: 10.1105/tpc.18.00231

Miyamoto, K., Shimizu, T., Lin, F., Sainsbury, F., Thuenemann, E., Lomonossoff, G., et al. (2012). Identification of an E-box motif responsible for the expression of jasmonic acid-induced chitinase gene *OsChia4a* in rice. *J. Plant Physiol.* 169, 621–627. doi: 10.1016/j.jplph.2011.12.008

Miyao, A., Tanaka, K., Murata, K., Sawaki, H., Takeda, S., Abe, K., et al. (2003). Target site specificity of the Tos17 retrotransposon shows a preference for insertion within genes and against insertion in retrotransposon-rich regions of the genome. *Plant Cell* 15, 1771–1780. doi: 10.1105/tpc.012559

Mohr, T. J., Mammarella, N. D., Hoff, T., Woffenden, B. J., Jelesko, J. G., and McDowell, J. M. (2010). The Arabidopsis downy mildew resistance gene *RPP8* is induced by pathogens and salicylic acid and is regulated by W-box *cis*-elements. *Mol. Plant-Microbe Interact.* 23, 1303–1315. doi: 10.1094/MPMI-01-10-0022

Narusaka, M., Shirasu, K., Noutoshi, Y., Kubo, Y., Shiraishi, T., Iwabuchi, M., et al. (2009). RRS1 and RPS4 provide a dual resistance-gene system against fungal and bacterial pathogens. *Plant J.* 60, 218–226. doi: 10.1111/j.1365-313X.2009.03949.x

Naveed, Z. A., Wei, X., Chen, J., Mubeen, H., and Ali, G. S. (2020). The PTI to ETI continuum in *Phytophthora*-plant interactions. *Front. Plant Sci.* 11:593905. doi: 10.3389/fpls.2020.593905

Palma, K., Thorgrimsen, S., Malinovsky, F. G., Fiil, B. K., Nielsen, H. B., Brodersen, P., et al. (2010). Autoimmunity in Arabidopsis *acd11* is mediated by epigenetic regulation of an immune receptor. *PLoS Pathog.* 6:e1001137. doi: 10.1371/journal.ppat.1001137

Qi, S., Shen, Y., Wang, X., Zhang, S., Li, Y., Islam, M. M., et al. (2022). A new *NLR* gene for resistance to tomato spotted wilt virus in tomato (*Solanum lycopersicum*). *Theor. Appl. Genet.* 135, 1493–1509. doi: 10.1007/s00122-022-04049-4

Qiao, Y., Liu, L., Xiong, Q., Flores, C., Wong, J., Shi, J., et al. (2013). Oomycete pathogens encode RNA silencing suppressors. *Nat. Genet.* 45, 330–333. doi: 10.1038/ng.2525

Qiao, Y., Xia, R., Zhai, J., Hou, Y., Feng, L., Zhai, Y., et al. (2021). Small RNAs in plant immunity and virulence of filamentous pathogens. *Annu. Rev. Phytopathol.* 59, 265–288. doi: 10.1146/annurev-phyto-121520-023514

Rampino, P., De Pascali, M., De Caroli, M., Luvisi, A., De Bellis, L., Piro, G., et al. (2017). *Td4IN2*: a drought-responsive durum wheat (*Triticum durum* Desf.) gene coding for a resistance like protein with serine/threonine protein kinase, nucleotide binding site and leucine rich domains. *Plant Physiol. Biochem.* 120, 223–231. doi: 10.1016/j.plaphy.2017.10.010

Shen, Q., Zhang, P., and Ho, T. H. (1996). Modular nature of abscisic acid (ABA) response complexes: composite promoter units that are necessary and sufficient for ABA induction of gene expression in barley. *Plant Cell* 8, 1107–1119. doi: 10.1105/tpc.8.7.1107

Steele, J. F. C., Hughes, R. K., and Banfield, M. J. (2019). Structural and biochemical studies of an NB-ARC domain from a plant NLR immune receptor. *PLoS One* 14:e0221226. doi: 10.1371/journal.pone.0221226

Su, J., Spears, B. J., Kim, S. H., and Gassmann, W. (2018). Constant vigilance: plant functions guarded by resistance proteins. *Plant J.* 93, 637–650. doi: 10.1111/tpj.13798

Sun, X., Lin, L., and Sui, N. (2019). Regulation mechanism of microRNA in plant response to abiotic stress and breeding. *Mol. Biol. Rep.* 46, 1447–1457. doi: 10.1007/s11033-018-4511-2

Takken, F. L., and Goverse, A. (2012). How to build a pathogen detector: structural basis of NB-LRR function. *Curr. Opin. Plant Biol.* 15, 375–384. doi: 10.1016/j.pbi.2012.05.001

Tsuchiya, T., and Eulgem, T. (2013). An alternative polyadenylation mechanism co-opted to the Arabidopsis *RPP7* gene through intronic retrotransposon domestication. *Proc. Natl. Acad. Sci.* 110, E3535–E3543. doi: 10.1073/pnas.1312545110

Umadevi, P., and Anandaraj, M. (2017). Genotype specific host resistance for *Phytophthora* in black pepper (*Piper nigrum* L.). *Physiol. Mol. Plant Pathol.* 100, 237–241. doi: 10.1016/j.pmpp.2017.10.011

Van den Berg, N., Mahomed, W., Olivier, N. A., Swart, V., and Crampton, B. G. (2018). Transcriptome analysis of an incompatible *Persea americana-Phytophthora cinnamomi* interaction reveals the involvement of SA- and JA-pathways in a successful defence response. *PLoS One* 13:e0205705. doi: 10.1371/journal.pone.0205705

Van Wersch, S., and Li, X. (2019). Stronger when together: clustering of plant *NLR* disease resistance genes. *Trends Plant Sci.* 24, 688–699. doi: 10.1016/j.tplants.2019.05.005

Wan, H., Yuan, W., Ye, Q., Wang, R., Ruan, M., Li, Z., et al. (2012). Analysis of TIR- and non-TIR-*NBS-LRR* disease resistance gene analogous in pepper: characterization, genetic variation, functional divergence and expression patterns. *BMC Genomics* 13:502. doi: 10.1186/1471-2164-13-502

Wang, J., Hu, T., Wang, W., Hu, H., Wei, Q., Yan, Y., et al. (2022a). Comparative transcriptome analysis reveals distinct responsive biological processes in radish genotypes contrasting for *Plasmodiophora brassicae* interaction. *Gene* 817:146170. doi: 10.1016/j.gene.2021.146170

Wang, T., Jia, Z. H., Zhang, J. Y., Liu, M., Guo, Z. R., and Wang, G. (2020). Identification and analysis of *NBS-LRR* genes in *Actinidia chinensis* genome. *Plan. Theory* 9:1350. doi: 10.3390/plants9101350

Wang, Z., Xu, F., Ren, H., Lu, G., Que, Y., and Xu, L. (2021). Genome-wide characterization of *NLRs* in *Saccharum spontaneum* L. and their responses to leaf blight in *Saccharum*. *Agronomy* 11:153. doi: 10.3390/agronomy11010153

Wang, J., Yang, C., Wu, X., Wang, Y., Wang, B., Wu, X., et al. (2022b). Genome-wide characterization of *NBS-LRR* family genes and expression analysis under powdery mildew stress in *Lagenaria siceraria*. *Physiol. Mol. Plant Pathol.* 118:101798. doi: 10.1016/j.pmpp.2022.101798

Wang, L., Zhao, L., Zhang, X., Zhang, Q., Jia, Y., Wang, G., et al. (2019). Large-scale identification and functional analysis of *NLR* genes in blast resistance in the Tetep rice genome sequence. *Proc. Natl. Acad. Sci.* 116, 18479–18487. doi: 10.1073/pnas.1910229116

Weiberg, A., Wang, M., Lin, F. M., Zhao, H., Zhang, Z., Kaloshian, I., et al. (2013). Fungal small RNAs suppress plant immunity by hijacking host RNA interference pathways. *Science* 342, 118–123. doi: 10.1126/science.1239705

Wendte, J. M., and Pikaard, C. S. (2017). The RNAs of RNA-directed DNA methylation. *Biochim. Biophys. Acta Gene Regul. Mech.* 1860, 140–148. doi: 10.1016/j.bbagrm.2016.08.004

Wu, J., Jiang, Y., Liang, Y., Chen, L., Chen, W., and Cheng, B. (2019). Expression of the maize MYB transcription factor *ZmMYB3R* enhances drought and salt stress tolerance in transgenic plants. *Plant Physiol. Biochem.* 137, 179–188. doi: 10.1016/j.plaphy.2019.02.010

Wu, Y., Xie, L., Jiang, Y., and Li, T. (2022). Prediction of effector proteins and their implications in pathogenicity of phytopathogenic filamentous fungi: a review. *Int. J. Biol. Macromol.* 206, 188–202. doi: 10.1016/j.ijbiomac.2022.02.133

Xia, S., Cheng, Y. T., Huang, S., Win, J., Soards, A., Jinn, T. L., et al. (2013). Regulation of transcription of nucleotide binding-Leucine rich repeat encoding genes *SNC1* and *RPP4* via H3K4 trimethylation. *Plant Physiol.* 162, 1694–1705. doi: 10.1104/pp.113.214551

Xiao, D., Zhou, K., Yang, X., Yang, Y., Ma, Y., and Wang, Y. (2021). Crosstalk of DNA methylation triggered by pathogen in poplars with different resistances. *Front. Microbiol.* 12:750089. doi: 10.3389/fmicb.2021.750089

Xie, Z., Allen, E., Fahlgren, N., Calamar, A., Givan, S. A., and Carrington, J. C. (2005). Expression of Arabidopsis *MIRNA* genes. *Plant Physiol.* 138, 2145–2154. doi: 10.1104/pp.105.062943

Xu, Y., Liu, F., Zhu, S., and Li, X. (2018). The maize NBS-LRR gene *ZmNBS25* enhances disease resistance in rice and Arabidopsis. *Front. Plant Sci.* 9:1033. doi: 10.3389/fpls.2018.01033

Xu, Y., Tao, X., Shen, B., Horng, T., Medzhitov, R., Manley, J. L., et al. (2000). Structural basis for signal transduction by the toll/interleukin-1 receptor domains. *Nature* 408, 111–115. doi: 10.1038/35040600

Yang, S., Tang, F., and Zhu, H. (2014). Alternative splicing in plant immunity. *Int. J. Mol. Sci.* 15, 10424–10445. doi: 10.3390/ijms150610424

Yang, L., Wang, Z., and Hua, J. (2021). A meta-analysis reveals opposite effects of biotic and abiotic stresses on transcript levels of Arabidopsis intracellular immune receptor genes. *Front. Plant Sci.* 12:625729. doi: 10.3389/fpls.2021.625729

Yang, L., Xiangsong, C., Wang, Z., Sun, Q., Hong, A., Zhang, A., et al. (2019). HOS15 and HDA9 negatively regulate immunity through histone deacetylation of intracellular immune receptor *NLR* genes in Arabidopsis. *New Phytol.* 226, 507–522. doi: 10.1111/nph.16380

Yu, A., Lepère, G., Jay, F., Wang, J., Bapaume, L., Wang, Y., et al. (2013). Dynamics and biological relevance of DNA demethylation in Arabidopsis antibacterial defence. *Proc. Natl. Acad. Sci. U. S. A.* 110, 2389–2394. doi: 10.1073/pnas.1211757110

Yu, H., Yang, L., Li, Z., Sun, F., Li, B., Guo, S., et al. (2022). *In situ* deletions reveal regulatory components for expression of an intracellular immune receptor gene and its co-expressed genes in Arabidopsis. *Plant Cell Environ.* 45, 1862–1875. doi: 10.1111/pce.14293

Zeng, W., Huang, H., Lin, X., Zhu, C., Kosami, K. I., Huang, C., et al. (2021). Roles of DEMETER in regulating DNA methylation in vegetative tissues and pathogen resistance. *J. Integr. Plant Biol.* 63, 691–706. doi: 10.1111/jipb.13037

Zhai, J., Jeong, D. H., De Paoli, E., Park, S., Rosen, B. D., Li, Y., et al. (2011). MicroRNAs as master regulators of the plant *NB-LRR* defence gene family via the production of phased, trans-acting siRNAs. *Genes Dev.* 25, 2540–2553. doi: 10.1101/gad.177527.111

Zhang, C., Fang, H., Shi, X., He, F., Wang, R., Fan, J., et al. (2020). A fungal effector and a rice NLR protein have antagonistic effects on a Bowman-Birk trypsin inhibitor. *Plant Biotechnol. J.* 18, 2354–2363. doi: 10.1111/pbi.13400

Zhang, H., Lang, Z., and Zhu, J. K. (2018). Dynamics and function of DNA methylation in plants. *Nat. Rev. Mol. Cell Biol.* 19, 489–506. doi: 10.1038/s41580-018-0016-z

Zhou, C., Zhang, L., Duan, J., Miki, B., and Wu, K. (2005). HISTONE DEACETYLASE19 is involved in jasmonic acid and ethylene signalling of pathogen response in Arabidopsis. *Plant Cell* 17, 1196–1204. doi: 10.1105/tpc.104.028514

Zhu, C., Liu, J. H., Zhao, J. H., Liu, T., Chen, Y. Y., Wang, C. H., et al. (2022). A fungal effector suppresses the nuclear export of AGO1-miRNA complex to promote infection in plants. *Proc. Natl. Acad. Sci.* 119:e2114583119. doi: 10.1073/pnas.2114583119

Zou, B., Yang, D. L., Shi, Z., Dong, H., and Hua, J. (2014). Monoubiquitination of histone 2B at the disease resistance gene locus regulates its expression and impacts immune responses in Arabidopsis. *Plant Physiol.* 165, 309–318. doi: 10.1104/pp.113.227801

Zuluaga, A. P., Vega-Arreguín, J. C., Fei, Z., Ponnala, L., Lee, S. J., Matas, A. J., et al. (2016). Transcriptional dynamics of *Phytophthora infestans* during sequential stages of hemibiotrophic infection of tomato. *Mol. Plant Pathol.* 17, 29–41. doi: 10.1111/mpp.12263

Conflict of Interest: The authors declare that the research was conducted in the absence of any commercial or financial relationships that could be construed as a potential conflict of interest.

Publisher's Note: All claims expressed in this article are solely those of the authors and do not necessarily represent those of their affiliated organizations, or those of the publisher, the editors and the reviewers. Any product that may be evaluated in this article, or claim that may be made by its manufacturer, is not guaranteed or endorsed by the publisher.

frontiers | Frontiers in Plant Science

ORIGINAL RESEARCH
published: 24 June 2022
doi: 10.3389/fpls.2022.883961

Network and Evolutionary Analysis Reveals Candidate Genes of Membrane Trafficking Involved in Maize Seed Development and Immune Response

Chunyan Zheng[1†], Yin Yu[1†], Guiling Deng[1], Hanjie Li[1] and Faqiang Li[2]*

[1] College of Life Sciences, South China Agricultural University, Guangzhou, China, [2] Guangdong Provincial Key Laboratory of Protein Function and Regulation in Agricultural Organisms, College of Life Sciences, South China Agricultural University, Guangzhou, China

OPEN ACCESS

Edited by:
Nan Yao,
Sun Yat-sen University, China

Reviewed by:
Yonglun Zeng,
The Chinese University of Hong Kong, China
Yuanhu Xuan,
Shenyang Agricultural University, China
Xiangguo Liu,
Institute of Agricultural Biotechnology, Jilin Academy of Agricultural Sciences (CAAS), China

***Correspondence:**
Faqiang Li
fqli@scau.edu.cn

[†] These authors have contributed equally to this work

Specialty section:
This article was submitted to Plant Cell Biology, a section of the journal Frontiers in Plant Science

Received: 25 February 2022
Accepted: 29 March 2022
Published: 24 June 2022

Citation:
Zheng C, Yu Y, Deng G, Li H and Li F (2022) Network and Evolutionary Analysis Reveals Candidate Genes of Membrane Trafficking Involved in Maize Seed Development and Immune Response. Front. Plant Sci. 13:883961. doi: 10.3389/fpls.2022.883961

The plant membrane-trafficking system plays a crucial role in maintaining proper cellular functions and responding to various developmental and environmental cues. Thus far, our knowledge of the maize membrane-trafficking system is still limited. In this study, we systematically identified 479 membrane-trafficking genes from the maize genome using orthology search and studied their functions by integrating transcriptome and evolution analyses. These genes encode the components of coated vesicles, AP complexes, autophagy, ESCRTs, retromers, Rab GTPases, tethering factors, and SNAREs. The maize genes exhibited diverse but coordinated expression patterns, with 249 genes showing elevated expression in reproductive tissues. Further WGCNA analysis revealed that five COPII components and four Rab GTPases had high connectivity with protein biosynthesis during endosperm development and that eight components of autophagy, ESCRT, Rab, and SNARE were strongly co-upregulated with defense-related genes and/or with secondary metabolic processes to confer basal resistance to *Fusarium graminearum*. In addition, we identified 39 membrane-trafficking genes with strong selection signals during maize domestication and/or improvement. Among them, *ZmSec23a* and *ZmVPS37A* were selected for kernel oil production during improvement and pathogen resistance during domestication, respectively. In summary, these findings will provide important hints for future appreciation of the functions of membrane-trafficking genes in maize.

Keywords: membrane trafficking, maize, WGCNA, endosperm development, pathogen resistance, evolution, domestication, improvement

INTRODUCTION

Like other eukaryotic organisms, plants have evolved a sophisticated membrane-trafficking system to control most, if not all, cellular events (Surpin and Raikhel, 2004). The system connects distinctive membrane-bound organelles through vesicle transport, thus maintaining proper cellular functions and responding to various developmental signals and environmental cues

(Inada and Ueda, 2014; Gu et al., 2017; Wang et al., 2020b). The membrane-trafficking system is principally involved in two major routes, namely, the secretory and endocytic pathways. During the secretory pathway, proteins synthesized in the endoplasmic reticulum (ER) are transported to the Golgi apparatus, the trans-Golgi network (TGN), and ultimately reach the plasma membrane (PM) and/or apoplast or are directed to the vacuole *via* a Golgi–TGN–multivesicular endosome (MVE) pathway (Paez Valencia et al., 2016). During the endocytic pathway, PM-localized and extracellular proteins are first internalized and transported to the TGN/early endosome (EE), and then recycled back to the PM or further transported to the vacuole for degradation (Rodriguez-Furlan et al., 2019). Besides these two routes, cytoplasmic components can be degraded by a highly conserved catabolic process called autophagy, in which cargoes are engulfed by cup-shaped double-membrane vesicles termed autophagosomes and delivered to the vacuole for degradation (Marshall and Vierstra, 2018).

Both secretory and endocytic routes share conserved sequential events and involve several major molecular machineries governing these processes. First, protein cargoes are selectively recruited into the vesicles budding from the donor membrane facilitated by coat proteins (clathrin, COPI, and COPII coatomers) and adaptor protein complexes (AP-1 to AP-5). Some small GTPases, such as ADP ribosylation factor (ARF) and secretion associated and Ras-related 1 (Sar1) GTPases, are also required for this step and play critical roles in the recruitment of coat proteins (Paez Valencia et al., 2016). Different from the secretory and endocytic routes, the formation of an autophagosome requires no coat proteins and the cargoes are recognized selectively by a batch of cargo receptors (Marshall and Vierstra, 2018). Following their formation, vesicles are transported toward the target organelles along the cytoskeleton (Bhandari and Brandizzi, 2020). When reaching the target compartments, inbound vesicles are recognized and caught by tethering factors. Once tethered, vesicles are fused with target membranes mediated by soluble *N*-ethylmaleimide-sensitive-factor attachment protein receptors (SNARE) complexes. Usually, each donor and acceptor membrane contact is bridged by a specific tethering complex (Paez Valencia et al., 2016). For example, class C core vacuole/endosome tethering (CORVET) and homotypic fusion and vacuole protein sorting (HOPS) complexes mediate the tethering with the lysosome/vacuole, and conserved oligomeric Golgi (COG), a multi-subunit vesicle tethering complex, is involved in retrograde trafficking within the Golgi. Importantly, regulatory small GTPases, Rabs, regulate the steps of vesicle transport and tethering by selectively recruiting specific tethering or other effectors (Minamino and Ueda, 2019). The final step of endomembrane trafficking involves recycling the transport machinery components back to the donor membrane mediated by the retromer complex (Heucken and Ivanov, 2018). Moreover, PM proteins may also be ubiquitinated during endocytosis and sorted into intraluminal vesicles (ILVs) inside multivesicular bodies (MVBs) regulated by an endosomal sorting complex required for transport (ESCRT) machinery (Gao et al., 2017).

Through the coordination of secretory, endocytic, and autophagic routes, plants can fine-tune the levels of proteins, lipids, and other cellular components in response to various physiological and environmental changes. For example, plants can effectively modulate their protein receptors, transporters, and channels at the PM to facilitate environmental sensing, nutrient uptake, and intercellular communication. In the past decades, studies with *Arabidopsis* and rice have revealed the important roles of endomembrane trafficking in coordinating plant development and in response to various biotic and abiotic environmental stresses (Inada and Ueda, 2014; Gu et al., 2017; Wang et al., 2020b). The trafficking and deposition of seed storage proteins (SSPs) offer an outstanding example for us to appreciate how an endomembrane system changes morphologically and functionally to accommodate seed development (Zheng et al., 2022). The *Arabidopsis* major SSPs (2S albumins and 12S globulins) are first synthesized in the ER and then transported to the protein storage vacuoles (PSVs) *via* the ER–Golgi–TGN–MVE pathway in the embryo. In contrast, rice SSPs are predominantly accumulated in the sub-aleurone layer of endosperm (He et al., 2021). Once synthesized, rice SSPs can either remain inside the ER as protein bodies (PBs) or be exported to specialized PSVs. During seed development in both *Arabidopsis* and rice, numerous components of coat complexes, Rab GTPases, tethering factors, SNAREs, and retromers appear to participate in SSP transport because SSPs are often missorted to the apoplast when these factors are absent (He et al., 2021; Zheng et al., 2022).

The endomembrane-trafficking system also plays a vital role in the rapid response to pathogen infection. Upon infection, PM-localized immune receptors undergo endocytosis while antimicrobial peptides and cell wall components are secreted to the pathogen infection sites (Inada and Ueda, 2014; Gu et al., 2017). For example, the SYP1 group of Qa-SNARE localizes to the PM and is responsible for the membrane fusion with the PM. Studies with *Arabidopsis pen1* and Barley (*Hordeum vulgare*) *ror2-1* mutants have revealed the contribution of SYP121 to the penetration resistance against non-adapted powdery mildew fungi (Collins et al., 2003; Kwon et al., 2008). Tobacco (*Nicotiana benthamiana*) SYP132 was reported to be involved in multiple forms of plant defenses and the secretion of pathogenesis-related protein PR1a (Kalde et al., 2007). Moreover, the secretion of PR1 in *Arabidopsis* was also found to be negatively regulated by SNAREs BET12 and MEMB12, which are involved in protein trafficking in the early secretory pathway (Chung et al., 2018). As a unique catabolic process, autophagy plays multiple roles during plant–microbe interactions, including pathogen clearance, execution of pathogen-induced cell death, and modulation of innate immune signaling pathways (Hofius et al., 2017). Therefore, plant autophagy machinery is also a pivotal target of pathogens during infection.

Until now, our knowledge about the plant endomembrane-trafficking system has mainly been obtained from *Arabidopsis*, and the studies with rice allowed us to appreciate the contributions of this system to SSP transport during seed development (He et al., 2021). Although maize is the leading grain crop worldwide, few studies on its membrane-trafficking

system have been reported. For example, overexpression of *ZmVPS29*, a retromer complex component, conferred a slender kernel morphology (Chen et al., 2020b), and disruption of supernumerary aleurone 1 (SAL1, an ESCRT component) and Discolored1 (DSC1, an ADP-ribosylation factor GTPase) resulted in abnormal seed development (Shen et al., 2003; Takacs et al., 2012). The importance of the membrane-trafficking system was also revealed by a comparative genomic analysis of wild, landrace, and modern maize (Hufford et al., 2012), in which 31 factors involved in membrane trafficking were found to be selected during maize domestication and/or improvement, implying their strong connections with important agronomical traits. Therefore, it is important to understand the biological functions of maize membrane-trafficking factors. Here, the maize membrane-trafficking genes were identified using bioinformatic methods and publicly available data and characterized by the integration of co-expression network analysis and evolution analysis. These findings will provide important hints for future research to unravel the roles of these genes in maize development and responding to biotic and abiotic stresses.

MATERIALS AND METHODS

Identification of Membrane-Trafficking Genes

Two methods were used to identify maize membrane-trafficking genes. First, the maize genome and protein databases were downloaded from the Ensembl Plants database[1] (B73 RefGen version 3 and version 4). The protein sequences of *Arabidopsis* membrane-trafficking components were retrieved from the TAIR10 database[2] and employed as queries to search against local databases using BLASTP and TBLASTN methods (E value $\leq$ 1.0e-30). The orthology relationships between maize and *Arabidopsis* genes were further confirmed using the orthologs identification tool in the MCENet server[3] (Tian et al., 2018). Second, the hidden Markov model (HMM) profiles of available membrane-trafficking components were retrieved from Pfam[4] and used to search against the local maize protein database using the BLASTP method. The redundant sequences obtained from both methods were manually removed.

Phylogenetic Analysis and Conserved Domains of the Vesicle-Trafficking Proteins

Full-length protein sequences of maize and *Arabidopsis* membrane-trafficking proteins were aligned using ClustalW with default parameters, and phylogenetic trees were generated by MEGA (version 6.0) software using the neighbor-joining method with 1,000 bootstrap replications. The resulting Newick trees were visualized with the Evolview-v2 online server.[5] All the conserved domains of membrane-trafficking proteins were identified using the NCBI Batch CD-Search database[6] (Lu et al., 2020) and Pfam website with default parameters. The conserved domains were visualized with TBtools (Chen et al., 2020a).

Construction of Gene Co-expression Network Analysis

An R package, WGCNA, was used to construct gene co-expression networks (Langfelder and Horvath, 2008). For network analysis, two transcriptomic datasets, B73 different tissue RNA-seq data and Illumina HiSeq data (GEO accession: GSE92448), were collected and filtered to remove lower-quality reads and reads with expression variance of <20% (Stelpflug et al., 2016; Kebede et al., 2018). In the weighted gene network analysis, each node represented a gene, and the edge was determined by the similarity of paired genes. Pearson correlation coefficients were calculated based on the similarity of paired gene expression and then transformed into an adjacency matrix of connection strength, which was used to calculate the topographical overlap matrix (TOM). A 1-TOM was calculated using hierarchical clustering, which defined gene modules corresponding to the basis of dissimilarity of gene connectivity. The total connectivity and intramodular connectivity, KME (for eigengene-based connectivity), and the KME P-value were calculated. The eigengene value for each module (ME) with phenotypic traits was calculated, and the most significant module was considered the core module. Each module had a unique color. Gene connectivity in modules balanced the number of edges of a node and was further visualized in Gephi-0.9.2 software.[7] Gene Ontology (GO) categories of co-expression interactions with membrane-trafficking genes in the module were performed using R 3.6.4 packages clusterProfiler (Yu et al., 2012).

Gene Expression Pattern Analysis

To analyze the spatiotemporal expression pattern of maize membrane-trafficking genes, the expression data were retrieved from the previously described RNA-seq dataset (Stelpflug et al., 2016). To analyze the expression level of *ZmSec23a* in the seeds of regular and high oil inbred lines, the expression data in 15 DAP kernels of 368 maize inbred lines were downloaded from Yan's lab website[8] (Fu et al., 2013). The expression heatmaps were generated using the R.3.6.4 platform.[9]

Identification of Membrane-Trafficking Genes Selected During Maize Domestication and Improvement

The single nucleotide polymorphism (SNP) data were downloaded from the HapMapV3 study for 1,210 maize lines (HapMapV3.2.1)[10] (Bukowski et al., 2018). After filtering out SNPs with $\leq$50% missing data, 28,803,913 SNPs were

[1]http://plants.ensembl.org/index.html
[2]http://www.arabidopsis.org/
[3]http://bioinformatics.cau.edu.cn/MCENet/index.php
[4]http://pfam.sanger.ac.uk/
[5]https://www.evolgenius.info
[6]https://www.ncbi.nlm.nih.gov/Structure/bwrpsb/bwrpsb.cgi
[7]https://gephi.org/users/download/
[8]www.maizego.org
[9]http://www.R-project.org
[10]https://cbsusrv04.tc.cornell.edu/users/panzea/download.aspx?Filegroupid=15

obtained. Moreover, 3.6 million SNPs were retrieved from the 368 RNA-seq association mapping panel, which include 32 high oil lines[11] (Fu et al., 2013). After filtering with a minor allele frequency of ≥5% using the TASSEL software (Bradbury et al., 2007), 557,977 higher-quality SNPs were obtained.

The identification of genomic selective sweep regions and selected vesicle membrane-trafficking genes during maize domestication and improvement was conducted as described in the previous report (Lin et al., 2014). Briefly, the nucleotide diversity (π) ratio and the fixation index (*Fst*) during domestication (teosinte vs. landrace) and improvement (landrace vs. improved) processes were calculated using VCFtools (Danecek et al., 2011), with a window size of 10 kb and step size of 2 kb. The top 5% of π ratio (1.55 and 1.22 for domestication and improvement, respectively) and the top 5% *Fst* values (0.25 and 0.089 for domestication and improvement, respectively) were set as the thresholds for putative selection signals. When the values of π or *Fst* of the genomic region exceeded the threshold, the detected membrane-trafficking genes in the region were defined as "domestication" or "improvement."

Linkage Disequilibrium Analysis and Haplotype Analysis Within Genes

Single nucleotide polymorphisms (MAFs ≥ 0.05) and full-length DNA sequences of candidate genes were extracted from wild teosintes, landraces, improved cultivars, and high oil accessions. These SNPs were used to calculate the square values of the correlation coefficient (r^2) between each SNP pair to measure the linkage disequilibrium (LD) using HaploView version 4.2 (Barrett et al., 2005). Haplotypes were generated using DnaSP version 5 (Librado and Rozas, 2009). For haplotype network analysis of *ZmSec23a* (*Zm00001d009150*), a sample of 20 teosintes, 22 landraces, 58 maize inbred lines, 23 high oil materials, and 345 regular inbred lines was used to construct the haplotype network using POPART version 1.7 (Leigh and Bryant, 2015).

Cis-Element Analysis

Putative promoter regions containing 6,000 bp of 5′ genomic sequences immediately upstream of the start code of the *ZmVPS37A* gene were extracted from the teosinte and maize genome database[12] and were submitted to PlantCARE[13] for *cis*-element analysis.

Plant Growth and Fungal Strains Infection

Teosinte (*Zea mays* ssp. *Parviglumis,* accessions: W71-2), landrace (303WX), and B73 inbred lines were grown in a greenhouse at 25°C under a light/dark 16/8-h photoperiod. The *Fusarium graminearum* wild-type strain PH-1 used in this study was cultured at 25°C on a carnation leaf agar for 1 week and then transferred and incubated in liquid carboxymethyl cellulose (CMC) medium with gentle shaking (100 rpm) for three more days. The conidium was subsequently collected by filtering through the two layers of Miracloth (Millipore, 475855) and the number of conidia was counted using a hemocytometer. For the inoculation assay, in the stalk of maize V2 stage seedlings, a hole was created 2 cm above the soil using a sterile toothpick, 40 μl suspension conidia (1×10^6 conidia/ml) or ddH_2O (mock) was injected into the hole with a needleless syringe, and then it was placed in a greenhouse for 7 days (70% humidity, 25°C, a light/dark 16/8-h photoperiod).

Quantitative Real-Time Polymerase Chain Reaction

Maize stalk tissues were collected and frozen immediately in liquid nitrogen, and total RNA samples were isolated using the Plant RNA extraction kit (TIANDZ, Inc., Beijing, China). One microgram of total RNA was converted to cDNA using HiScript II RT SuperMix for qPCR (Vazyme, Nanjing, China) according to the manufacturer's instructions. qRT-PCR reactions were performed with the Bio-Rad CFX96^{TM} real-time PCR system using ChamQ Universal SYBR qPCR Master Mix (Vazyme, Nanjing, China). Maize *Ubc9* was used as an internal control (forward primer, 5′-acgaaggtcttccatccaaacatc-3′; reverse primer, 5′-gtttcatgggcaacaccacaatcg-3′), and the relative expression levels for target genes were calculated using the $2^{-\Delta\Delta Ct}$ method. qRT-PCRs were all performed with three biological replicates. The primers used for *ZmVPS37A* are as follows: *ZmVPS37A*-F 5′-gagctggagatttcctctcttc-3′ and *ZmVPS37A*-R 5′-gaagactgcggactatctgaagc-3′.

RESULTS

Genome-Wide Identification of Membrane-Trafficking Factors in Maize

Prior studies by Paul et al. (2014) and Li et al. (2015) defined the maize genomic loci that encode components of secretory and endocytic pathways and autophagy pathways, respectively. Here, with the improved maize genome sequence available [RefGen_v4, Jiao et al. (2012)], we exhaustively search for membrane-trafficking components using BLASTP and TBLASTN[14] with the full-length amino acid sequences of *Arabidopsis* membrane-trafficking factors as baits (Bassham et al., 2008; Paul et al., 2014; Gao et al., 2017). By sequence alignment and phylogenetic and domain analyses, the membrane-trafficking genes in the maize genome are defined (**Figure 1**, **Supplementary Figures 1–9**, and **Supplementary Datasets 1–7**). Totally, we obtained 479 maize genes involved in membrane trafficking, including 11 genes encoding components for clathrin-coated vesicle (CCV), 35 for AP1-5 complexes, 26 for COP-I complex, 30 for COP-II complex, 10 for ARF GTPases, 52 for autophagy machinery, 63 for ESCRTs machinery, 96 for tethering complexes, 11 for retromer complex, 76 factors for Rab GTPase protein family, and 69 for SNARE protein family.

The factors are highly comparable in their protein length and the number of orthologs between maize and *Arabidopsis*

[11]http://maizego.org/Resources.html

[12]http://www.maizego.org

[13]http://bioinformatics.psb.ugent.be/webtools/plantcare/html/

[14]https://plants.ensembl.org/Zea_mays/Info/Annotation/

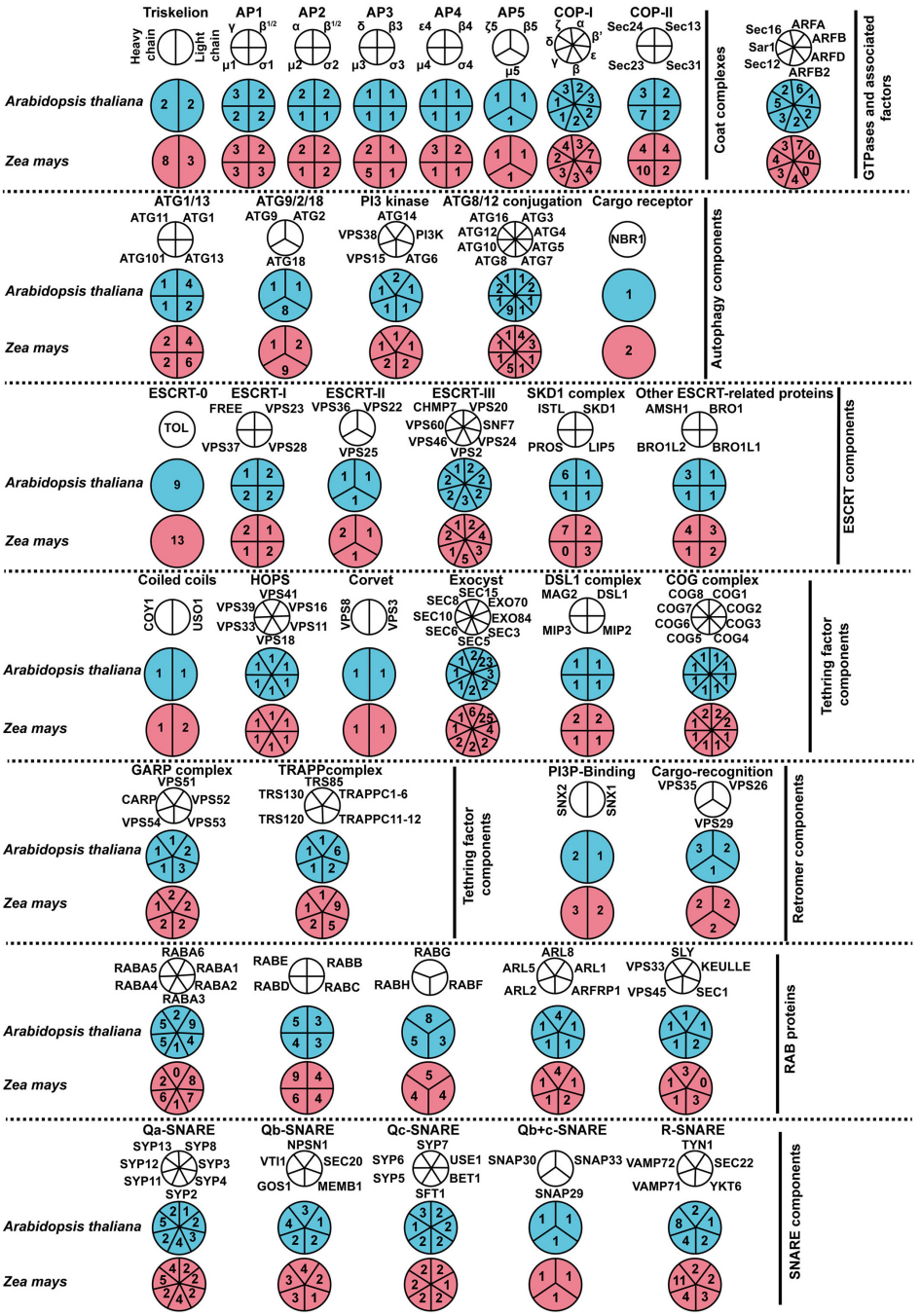

FIGURE 1 | An overview of endomembrane-trafficking components in *Arabidopsis thaliana* and *Zea mays*. Coulson plot depicting components of coat complexes, autophagy machinery, ESCRT machinery, tethering factors, retromer proteins, Rab proteins, and SNARE proteins in *A. thaliana* and *Z. mays*. Legends at the top of each column refer to the subunits of complexes. Numbers indicate relevant paralog counts. Homologs of these factors were identified and listed in **Supplementary Datasets 1–7**.

(**Supplementary Figures 1–9** and **Supplementary Datasets 1–7**). However, we observed a significantly higher copy number for certain factors in maize than in *Arabidopsis*. For example, there are seven, four, and three gene copies for the B-COP β' and ε subunits, and F-COP γ subunit, respectively, while there are only three, two, and one genes for the relevant *Arabidopsis* factors. Another clear example is the genes encoding clathrin heavy chain proteins, with eight and two gene copies in maize and *Arabidopsis* genomes, respectively. Notably, an interesting exception is that *Arabidopsis* possesses a slightly expanded set of Rab11 (RabA), with 26 paralogs as compared to 24 paralogs in the maize genome (**Supplementary Figure 8** and

Supplementary Dataset 6). Moreover, we could not detect any orthologs of PROS (an ESCRT component) and RABA6 protein in maize (**Supplementary Datasets 3, 6**).

Domain architecture is critical for protein function and is therefore mostly retained by orthologs during evolution for their function performance. Thus, we compared the domain architectures of maize factors with their relevant *Arabidopsis* components as an additional criterion to assign orthology. Using NCBI Conserved Domain (CDD[15]) and Pfam website,[16] we observed that 81.84% (392/479) of maize factors possess the same domain architecture as their *Arabidopsis* orthologs, which indicates that the membrane-trafficking system is largely conserved in monocotyledonous and dicotyledonous plants. In addition, we found that 6.47% (31/479) of maize orthologous genes are predicted to encode truncated proteins with defective domain structures. For examples, four genes [*Zm00001d009915* (*ZmCHC3a*), *Zm00001d026086* (*ZmCHC3b*), *Zm00001d021067* (*ZmCHC4a*), and *Zm00001d012897* (*ZmCHC5b*)] are predicted to encode truncated clathrin heavy chain protein (**Supplementary Figure 1**), and two genes [*Zm00001d013458* (*ZmATG3b*) and *Zm00001d003156* (*ZmATG3d*)] are predicted to encode truncated autophagy component ATG3 (**Supplementary Figure 4**). Further gene expression analysis with MaizeGDB[17] revealed that no cDNAs have been detected for these six genes, indicating that they are likely pseudogenes (data not shown).

In some cases, we observed the presence of additional domains in some maize factors when compared with their *Arabidopsis* orthologs, e.g., for SNARE protein SYP3 or ESCRT component SNF7. *Arabidopsis* Qa-SNARE protein AtSYP31 (AT5G05760) and AtSYP32 (AT3G24350) contain a t-SNARE domain at their C-terminal regions, while an additional syntaxin-5 domain is detected at the N-terminal regions of maize orthologs ZmSYP31 (Zm00001d008758) and ZmSYP32 (Zm00001d039614) (**Supplementary Figure 9**). A similar scenario is also detected for one of the maize ESCRT SNF7 proteins (Zm00001d044480), which contains an additional leucine-rich repeat N-terminal domain besides the C-terminal SNF7 domain (**Supplementary Figure 5**). These extra domains might provide another layer of regulatory feature for these maize membrane-trafficking factors.

RNA-Seq Analysis of Maize Membrane-Trafficking Gene Expression

To investigate the spatiotemporal expression patterns of maize membrane-trafficking genes, we performed a gene co-expression (clustering) analysis using a previously described RNA-seq dataset derived from 64 different tissues/stages of the maize inbred line B73 (Stelpflug et al., 2016; **Figure 2** and **Supplementary Figures 10–16**). We observed 3–12 clusters in all protein complexes or families analyzed, indicating that the expression profiles of these genes varied considerably. Notably, with few exceptions (e.g., *ZmGOS11*), most genes encoding SNARE proteins are grouped into nine clusters, which largely coincide with their subcellular localization (**Figure 2**). The first and last clusters mostly contained genes encoding TGN/PM-localized SNAREs, including *ZmSYP1*, *ZmVAMP72*, *ZmNPSN1*, and *ZmTYN11*, but showed distinct expression patterns, indicating that these two sets of *SNARE* genes might have tissue-specific functions. The genes in the second cluster (TGN-Vac) displayed elevated expression in root and some reproductive tissues (silk and tassel), whereas the genes in the third (TGN-vac or PM), fourth (Golgi), and sixth (ER-Golgi-Vac) clusters showed enhanced expression in endosperm but not in embryo. Interestingly, we also detected increased mRNA abundance in endosperm for multiple membrane-trafficking genes (175 loci) other than SNAREs (**Supplementary Figures 10–16**). It was similar to the earlier observation for maize autophagy machinery (Li et al., 2015), indicating that the membrane-trafficking system, including the autophagy pathway, might participate in the maturation of maize endosperm during seed development. The fifth cluster contained seven *SNARE* genes (*ZmSNAP33*, *ZmVAMP728*, *ZmVAMP729*, *ZmVAMP712*, *ZmSYP125*, *ZmSYP123*, and *ZmSYP23*), which all expressed preferentially in anthers above all other tissues, implying their roles during anther and/or pollen development.

Besides the analysis of spatiotemporal expression patterns, our RNA-seq analyses also detected differential expression at the isoform level for multiple membrane-trafficking genes. For example, VAMP72, which is a subgroup of VAMP7 specific to green plants and is largely involved in trafficking at the PM, had eleven isoforms in the maize genome and could be subdivided into five groups based on their expression patterns (**Figure 2**). The first group, encompassing *ZmVAMP727* and *ZmVAMP7210*, displayed elevated expression in root and leaf tissues. However, the second group, containing *ZmVAMP721*, *ZmVAMP723*, and *ZmVAMP725*, had enhanced expression patterns in whole seed and endosperm tissues, suggesting a role in regulating seed development. The third group included *ZmVAMP728* and *ZmVAMP729*; they were expressed exclusively in anther tissue, implying their specific role in pollen development. The fourth group contained *ZmVAMP722* and *ZmVAMP726*, which were expressed preferentially at the very early stage of seed development. The last group (*ZmVAMP724a* and *ZmVAMP724b*) had ubiquitous expression patterns.

Identification of Membrane-Trafficking Genes Involving Seed Development

Our spatiotemporal expression analysis revealed that 257 membrane-trafficking genes displayed elevated expression in the endosperm, embryo, or whole seed tissues, suggesting that they might play important roles in seed development (**Figure 2** and **Supplementary Figures 10–16**). To further investigate the contributions of these genes in maize seed development, we performed a weighted gene co-expression network analysis (WGCNA) to analyze the co-expression relationships among 16,888 differentially expressed genes identified from the above-mentioned RNA-seq dataset (Stelpflug et al., 2016). In total, 27 color-coded gene modules were identified according to the similarity of gene expression patterns

[15]https://www.ncbi.nlm.nih.gov/Structure/cdd/cdd.shtml

[16]http://pfam.xfam.org/

[17]https://maizegdb.org/

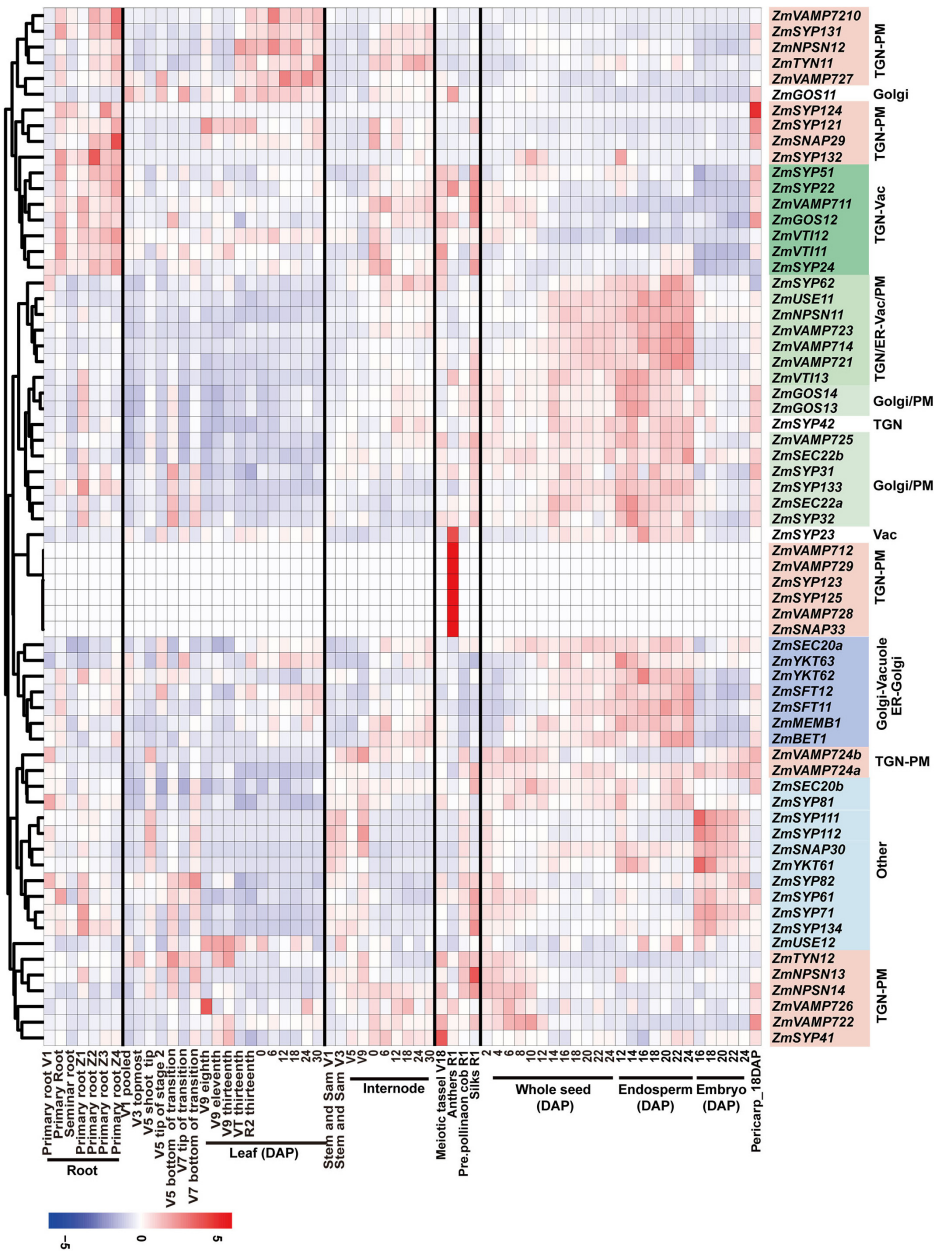

FIGURE 2 | The spatiotemporal expression profiles of maize genes encoding SNARE proteins. The expression patterns of SNARE-encoding genes are analyzed based on the reads per kilobase per one million reads (RPKM) of 64 maize tissue-specific samples. The blue, white, and red colors indicate the low, medium, and high gene expression values, respectively.

(**Supplementary Figure 17A** and **Supplementary Table 1**). The module-tissue correlation analysis showed that modules turquoise and yellow positively correlated with early and late endosperm development, respectively (r = 0.36, p = 9.45e–4; r = 0.39, p = 3.44e–4, respectively) (**Supplementary Figure 17B**). The genes of module turquoise peaked at the endosperm of 12 DAP (days after pollination), whereas those in module yellow were expressed highly at the endosperm of 24 DAP (**Supplementary Figures 17C,D**). Moreover, module black was correlated with embryo development (r = 0.66, p = 2.46e–11), and module dark red was correlated with early seed development (r = 0.56, p = 5.56e–8).

In early endosperm-specific module turquoise, 114 genes encoding membrane-trafficking factors were identified among 3,850 annotated genes, including 18 for CCV and AP complexes, 15 for COPI complex, 15 for COPII complex, three ARF GTPases, six for ESCRT complex, three for retromer complex, 30 for tethering factors, 16 for Rab GTPases, and 8 for SNARE proteins (**Supplementary Table 1**). Further analysis of the subnetwork harboring components with a weighted value

over 0.2 revealed that genes encoding five COPII components (ZmSec13a, ZmSec13b, ZmSec24a, ZmSec23i, and ZmSec23j), four Rab GTPases (ZmRABA1f, ZmRABE1b, ZmRABE1c, and ZmRABE1k), one Golgi/PM localized SNARE protein (ZmSec22), and one ESCRT-II component (ZmVPS25) have higher connectivity with other genes (**Figures 3A,B**). The COPII complex is responsible for the transport of newly synthesized protein from ER to *cis*-Golgi, and RabE GTPases are well-known regulators for vesicle transport from the Golgi apparatus to the PM (Speth et al., 2009). The GO enrichment analysis revealed that the genes involved in protein biosynthesis and assembly, ribosome biogenesis, and translation apparatus are overrepresented (**Figure 3C**), suggesting the role(s) of these membrane-trafficking components in the delivery of nascent biosynthesized proteins during early endosperm development.

Identification of Membrane-Trafficking Components Responsible for Pathogen Defense in Maize

To investigate the membrane-trafficking genes responsible for pathogen defense during Gibberella ear rot disease caused by *F. graminearum*, we also performed a WGCNA to identify gene modules between resistance inbred line CO441 and susceptible line B73 (Kebede et al., 2018). In total, 15 modules were identified among 12,528 differential expression genes across eight experimental conditions (**Supplementary Figure 18A** and **Supplementary Table 2**). According to the module-trait correlation analysis (**Supplementary Figure 18B**), modules red and magenta showed a highly positive correlation with disease defense of resistance line CO441 (r = 0.54, p = 0.04; r = 0.57, p = 0.03, respectively). The genes within module red were highly expressed in resistance line CO441 at 1–2 days after fungi infection (**Supplementary Figure 18C**). In contrast, genes within module green were highly expressed in susceptible line B73 (r = 0.7, p = 0.04) and peaked at 2 days after fungi infection (**Supplementary Figure 18D**).

In module green, four membrane-trafficking genes, which encode two ESCRT components (ZmTOL9 and ZmISTL6), one SNARE protein ZmSYP121, and a SNARE-interacting protein ZmSec1b were identified among 603 annotated genes with a weighted value over 0.3 (**Supplementary Figures 19A,B**). These genes were strongly co-upregulated with several defense genes in B73 2 days after fungi infection (**Supplementary Figure 19C**). Within the subnetwork containing these four genes, genes involved in defense, SA biosynthesis, jasmonic acid

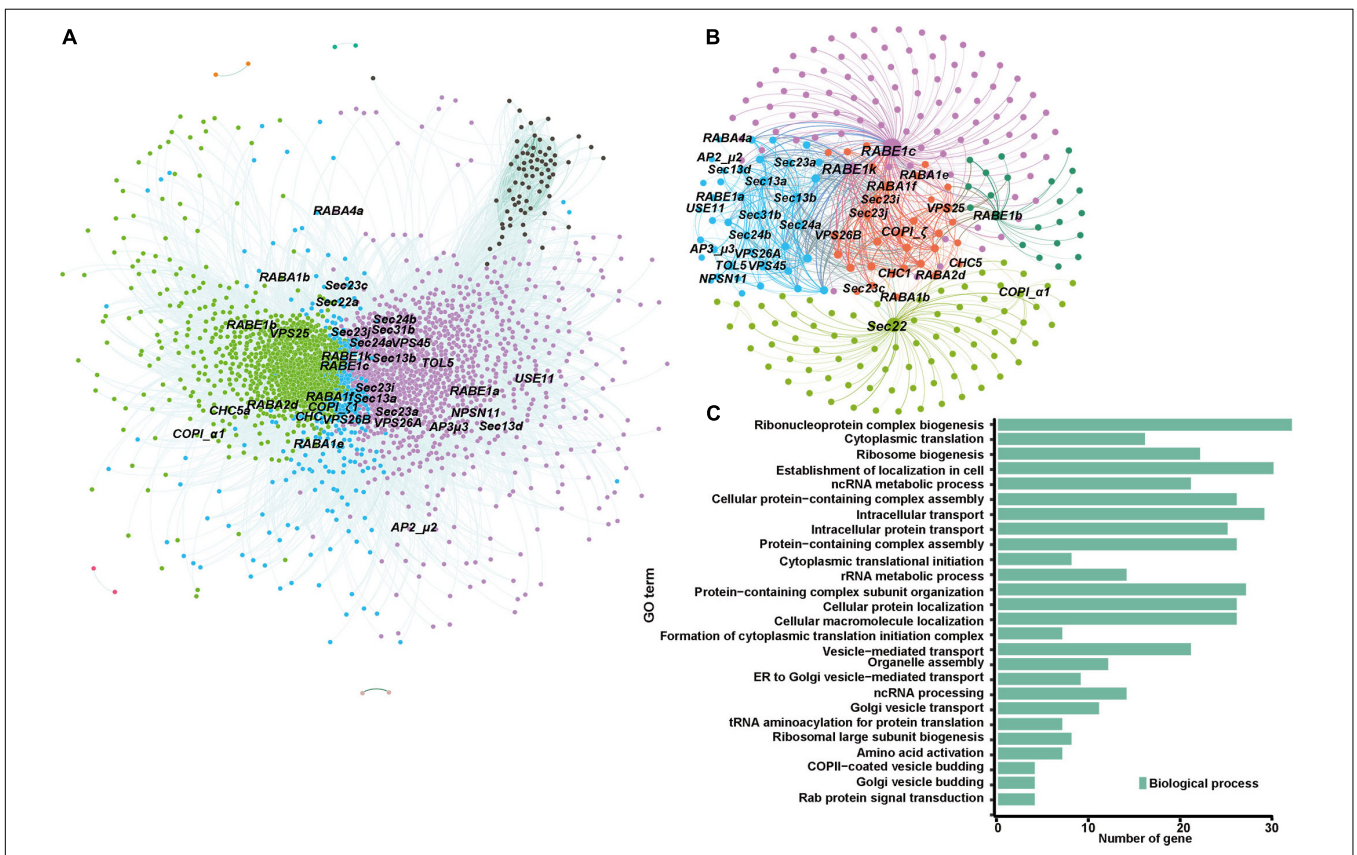

FIGURE 3 | Co-expression of membrane-trafficking genes during maize seed development. Nodes are color coded based on the consensus modules identified using the R language WGCNA package. Edges are constructed between genes with a correlation coefficient (r) > 0.2. **(A)** Co-expression network visualization for module turquoise identified in **Supplementary Figure 17**. **(B)** The subnetwork with membrane-trafficking genes in module turquoise for visualization (r > 0.2). **(C)** Gene ontology (GO) enrichment analysis of the subnetwork co-expressed genes.

signaling, and amino acid biological process are overrepresented (**Supplementary Figure 19D**), implying the role of these four factors in response to pathogen infection. The identification of *ZmSyp121* here further confirmed its conserved role in pathogen defense in both monocotyledonous and dicotyledonous plants (Collins et al., 2003).

We then analyzed module red and identified eight membrane-trafficking genes among 671 annotated genes (weighted value > 0.15) (**Figures 4A,B**). These factors all showed a stronger and more rapid gene expression in resistant line CO441 than in B73 upon pathogen infection, along with many defense genes, such as *PR1* and *PR10* (**Figure 4C**). Among these genes, those encoding SNARE protein SYP131, Rab GTPase RABH1c, and autophagy component ATG18f showed a higher degree of connectivity (>10). The *Arabidopsis* orthologs of SYP131 and RabH1b have been reported to be involved in the vesicle trafficking of callose (Gamir et al., 2018; He et al., 2018). The identification of *ZmSYP131* and *ZmRABH1c* here suggested that maize orthologs might have a similar function in callose deposition upon fungi infection. The identification of *ZmATG18f* also suggested the role of autophagy in the pathogen defense of maize. Further, GO analysis of the subnetwork containing these eight genes revealed an enrichment of defense genes (**Figure 4D**). Moreover, GO terms related to the biological process of biotic stress such as lipid biosynthetic process, isoprenoid biosynthetic process, and trypotophon metabolic process were also specifically enriched, indicating that membrane-trafficking factors likely coordinated with the defense-related metabolic processes and transported defense proteins and antimicrobial metabolites to the infected regions. In summary, the WGCNA analysis above revealed that the maize genes encoding membrane-trafficking factors were upregulated together with defense-related genes,

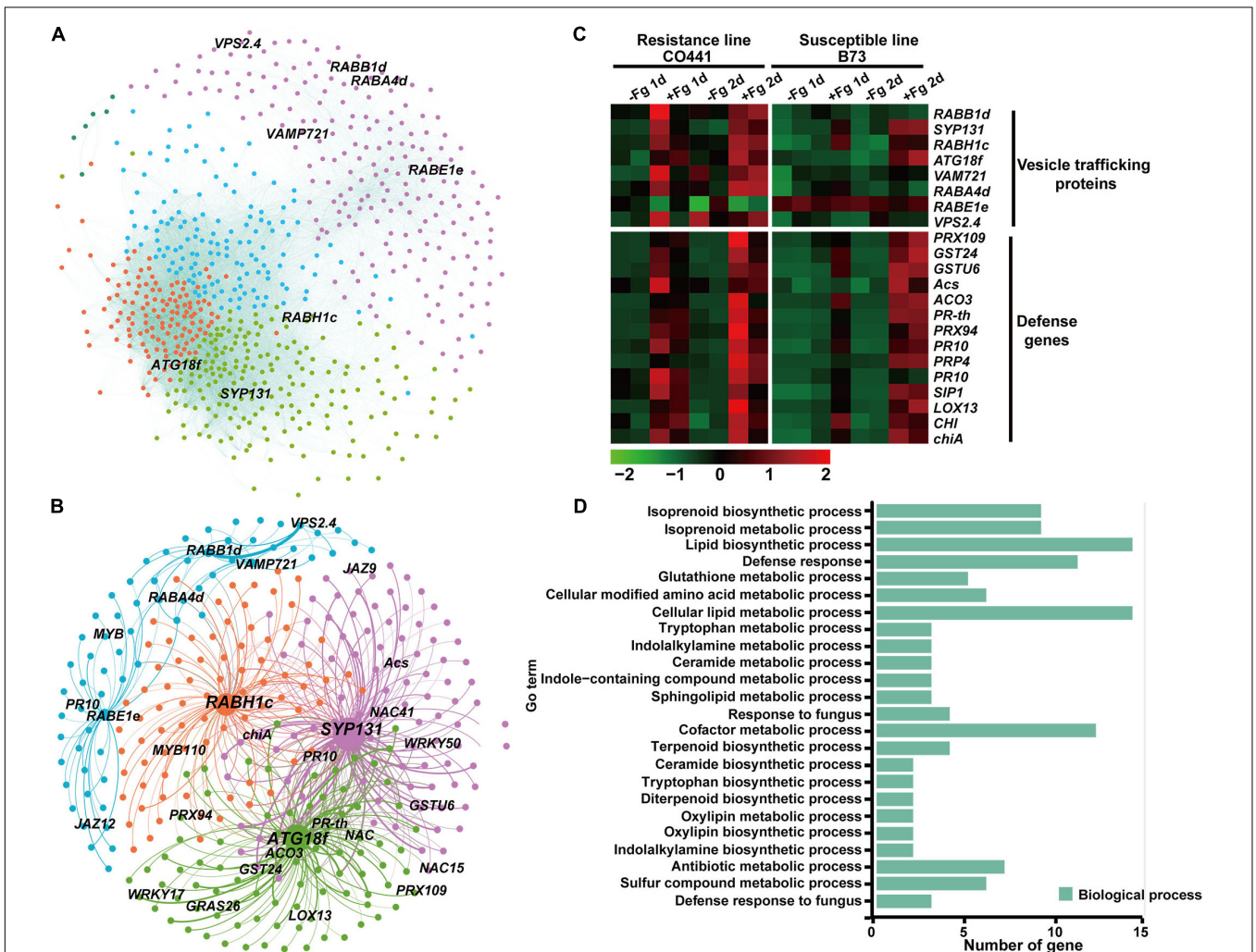

FIGURE 4 | Co-expression of membrane-trafficking genes responding to Gibberella ear rot disease in two maize inbred lines. **(A)** Co-expression network of module red. Nodes are color coded based on the consensus modules identified using the R language WGCNA package. Edges are constructed between genes with a correlation coefficient (r) > 0.15. **(B)** The subnetwork with membrane-trafficking genes for visualization in module red. **(C)** Expression profiles of defense and membrane-trafficking genes in module red upon Gibberella infection. The values in red and green indicate gene increases and decreases in expression, respectively. **(D)** Gene ontology (GO) enrichment analysis of co-expressed genes of module red.

TABLE 1 | Membrane-trafficking genes selected during maize domestication and improvement.

	Zea mays ID	Chr.	Position	Top 5% *Fst*	Top 5% π ratio	Annotation
Domestication	*Zm00001d052028*[a]	4	173834001-173850000	0.32	1.771	*ZmVPS15b*
	Zm00001d022584[a]	7	174832000-174858000	0.361	10.577	*ZmTYN11*
	Zm00001d023738[a]	10	17782000-178400000	0.479	3.832	*ZmVPS26B**
	Zm00001d021067[a]	7	135926000-136002000	0.489	4.348	*ZmCHC4a*
	Zm00001d046020[a]	9	54474000-54620000	0.39	3.139	*ZmTOL11*
	Zm00001d005215[a]	2	159788000-159848000	0.409	2.889	*ZmRABD1c*
	Zm00001d015890[a]	5	126234000-126294000	0.645	2.412	*ZmSec1a*
	GRMZM2G360867[a]	1	72404000-72516000	0.441	3.79	*ZmRABE1j*
	Zm00001d011984[a]	8	160366000-160470000	0.425	2.931	*ZmATG6b**
	Zm00001d022172[a]	7	166126000-166198000	0.567	4.651	*ZmARFRP2**
	Zm00001d027962[a]	1	18046000-18130000	0.589	2.154	*ZmVPS37A**
	Zm00001d032710[a]	1	232184000-232276000	0.614	7.41	*ZmVPS2.4**
	Zm00001d021551[a]	7	150440000-150572000	0.444	2.639	*ZmRabH1d**
	Zm00001d023910[a]	10	26982000-27084000	0.525	2.639	*ZmAP5/μ5**
	Zm00001d036161[a]	6	72344000-72418000	0.515	2.640	*Zmβ'3-COPI**
	Zm00001d043288[a]	3	191668000-191678000	0.341	1.895	*ZmCOG1a**
	Zm00001d034364[a]	1	285830000-285840000	0.309	2.784	*ZmTRS85**
	Zm00001d033776[a]	1	268656000-268668000	0.400	2.852	*ZmVPS39*
	Zm00001d038059[a]	6	142706000-142716000	0.352	1.551	*ZmCOG5*
	Zm00001d042303[b]	3	158480001-158500000	0.487	1.535	*ZmATG6a**
	Zm00001d015102[b]	5	73180001-73284000	0.335	1.825	*ZmGOS12**
	Zm00001d007075[b]	2	215490001-215528000	0.269	1.684	*ZmSec31a**
	Zm00001d018355[b]	5	213270001-213318000	0.442	2.062	*ZmATG18e**
	Zm00001d024239[b]	10	59888000-59978000	0.493	2.170	*ZmATG8d*
	Zm00001d045434[b]	9	22254001-22270000	0.299	6.133	*ZmSec1c*
Improvement	*Zm00001d033058*[a]	1	245198000-245304000	0.155	1.874	*ZmSec20a*
	Zm00001d016686[a]	5	168500000-168562000	0.141	2.127	*ZmSNAP33*
	Zm00001d034949[a]	1	300880000-301008000	0.16	2.16	*ZmRABF2c*
	Zm00001d006474[a]	2	203384000-203406000	0.157	2.154	*ZmATG8a*
	Zm00001d009150[a]	8	38490000-38546000	0.211	1.721	*ZmSec23a**
	Zm00001d033714[a]	1	267240000-267272000	0.126	1.565	*ZmISTL6**
	Zm00001d025044[a]	10	100866000-100876000	0.117	3.101	*ZmVPS54a*
	Zm00001d023867[a]	10	24958000-24968000	0.156	1.985	*ZmUSO1**
	Zm00001d043269[b]	3	191006000-191018000	0.092	2.272	*ZmVPS28B**
	Zm00001d047464[b]	9	128998000-129008000	0.117	1.496	*ZmAP1/2B2'**
	Zm00001d011347[b]	8	142642001-142702000	0.155	1.413	*ZmATG7**
	Zm00001d021913[b]	7	160350001-160370000	0.137	1.143	*ZmSFT11**
	Zm00001d037004[b]	6	105584001-105610000	0.129	1.359	*ZmRABA1b**
	Zm00001d004807[b]	2	136600000-136772000	0.147	1.537	*Zmβ1-COP-I*

Chr, chromosome number. [a,b] *Denote the gene status of identified loci either as a candidate gene or in selected regions, respectively. Asterisks indicate the loci that have been identified in previous analyses. GRMZM2G360867 is not available in Z. mays RefGen_V4.*

which conferred basal resistance to *F. graminearum* in B73, but also with genes involved in various secondary metabolic processes to further improve resistance capability in CO441 line.

Multiple Membrane-Trafficking Genes Are Selected During Maize Domestication and Improvement

The identification of selected genetic loci during domestication and improvement of crops is important for breeding elite varieties and can further facilitate appreciation of the contributions of selected loci to important agronomic traits (Zhou et al., 2015). Molecular evidence for selective sweeps on multiple membrane-trafficking genes during maize domestication and improvement has been reported in several previous studies (Hufford et al., 2012; Jiao et al., 2012; Liu et al., 2015). With more comprehensive and better annotated B73 genome datasets and the complete list of membrane-trafficking genes, we searched the larger and more diverse maize HapMap 3 genotype dataset (Bukowski et al., 2018), which covers 20 wild relatives (*Zea mays* spp. *Parviglumis*), 23 landraces, and 59 improved cultivars (**Supplementary Table 3**), for genomic regions showing positive selection signals during domestication and improvement through statistical analyses of high population

differentiation (*Fst*) and low level of nucleotide diversity (π) (**Table 1**). The top 5% of *Fst* and π ratio were set as thresholds to identify potentially selected regions. During maize domestication (teosinte vs. landrace), 15,760 windows were found as candidate regions (*Fst* ≥ 0.26; π teosinte/π landrace ≥ 1.55). A total of 25 out of 479 membrane-trafficking genes were found to be associated with domestication (**Figures 5A,C** and **Table 1**), including five genes encoding components of the autophagy machinery, three for ESCRT complex, four for Coat and AP complexes, one for retromer complex, four for tethering factors, six for ARF and Rab GTPases, and two for SNARE proteins. In the comparison of maize landrace and improved populations, 14,729 slide windows were revealed by two methods (*Fst* ≥ 0.08; π landrace/π improved ≥ 1.39). Similarly, a total of 14 membrane-trafficking genes were identified to be improvement genes (**Figures 5B,D** and **Table 1**), including two for autophagy factors, three for SNARE proteins, two for Rab GTPases, two for tethering factors, three for coat complexes, and two for ESCRT components.

Out of the 39 selected membrane-trafficking genes identified in our study, 22 have been identified in previous evolutionary analyses (Hufford et al., 2012; Jiao et al., 2012; Liu et al., 2015). Moreover, nine out of 39 selected membrane-trafficking genes were detected by QTL mapping or genome-wide association studies (**Supplementary Table 4**), which further implicates the potential roles of these genes in maize development and biotic and/or abiotic stress responses. For example, four of them are implicated in biotic stress responses [*Zm00001d042303* (*ZmATG6a*), *Zm00001d027962* (*ZmVPS37A*), *Zm00001d015102* (*ZmGOS13*), and *Zm00001d011347* (*ZmATG7*)], and three for ear and seed development [*Zm00001d011984* (*ZmATG6b*), *Zm00001d042215* (*ZmATG18e*), and *Zm00001d009150* (*ZmSec23a*)], and one for leaf senescence [*Zm00001d042215* (*ZmATG18e*)].

ZmSec23a Is a Maize Improvement Gene Involved in Seed Development

Among 114 genes involved in seed development, *ZmSec23a* on chromosome 8 was also found to have strong selection signals with high-level population differentiation between landrace and improved lines (*Fst* = 0.211, π landrace/π improved = 1.721) (**Figure 6A** and **Table 1**). Given that ZmSec23a is an important COPII component that might regulate the protein biosynthesis during seed development, we first analyzed its mRNA levels using previously reported RNA-sequencing data (Stelpflug et al., 2016). As shown in **Figure 6B**, *ZmSec23a* showed elevated expression in the endosperm and seed tissues. Interestingly, we also found that *ZmSec23a* exhibited increased mRNA abundance in high oil lines compared with regular materials (**Figure 6C**).

To gain deeper insights into the evolution of *ZmSec23a*, we then performed haplotype analysis with 468 selected teosintes (20), landraces (22), improved regular lines (403), and high oil lines (23) and identified 24 different haplotypes in its coding region. Among these haplotypes, Hap_20 and Hap_22 are enriched with high oil lines (**Figure 6D**), with 18 out of 22 being high oil lines. These two haplotypes not only carry the lead SNP (chr8: 38521846; G/T allele) detected by a previous genome association study (Li et al., 2013) but also carry the G/A, C/T, and T/C variants. Interestingly, these variants were also found in Hap_4, which mainly consists of teosintes and landraces, but not modern cultivars (**Figure 6D**). However, the haplotype network analysis failed to detect the close relationship between Hap_4 and Hap_20/22 (**Figure 6E**). Moreover, several alleles (Chr8: 38526804, T/C; Chr8: 38526831, G/A; Chr8:38528117, T/C; and Chr8: 38530903, C/T) within the gene region of *ZmSec23a* have different degrees of linkage disequilibrium with the lead SNP (G/T allele) from domestication to improvement, or from regular inbred lines to high oil materials (**Supplementary Figure 20**), indicating that these alleles of *Zmsec23a* could also be associated with high oil content.

ZmVPS37A Is a Domestication Gene Involved in Pathogen Defense

Another noticeable selected gene is *ZmVPS37A*. As a component of ESCRT machinery, *Arabidopsis* VPS37-1 is required for the endocytosis of plant immune receptor FLS2 after flagellin elicitation and for flg22-triggered stomatal closure to prevent bacterial entrance (Spallek et al., 2013). Moreover, *ZmVPS37A* is significantly associated with variation in Rp1-D21-induced HR (Olukolu et al., 2014). In this study, we found that the genetic diversity of *ZmVPS37A* in landrace was significantly lower than that in teosinte (*Fst* = 0.589, π landrace/π teosinte = 2.154, **Figures 5**, **7A** and **Table 1**), indicating that it is a domestication gene. To understand why *ZmVPS37A* is selected, we infected the stem tissues of teosinte (W71-2), landrace (303WX), and B73 seedlings with *F. graminearum*. As shown in **Figure 7B**, teosinte exhibited better resistance than 303WX and B73, while B73 displayed obvious lesions and severe stalk rot symptoms. qRT-PCR analysis revealed that the transcript level of *ZmVPS37A* in teosinte and 303WX was about 1.54-fold compared to B73 control after *F. graminearum* infection (**Figure 7C**). Analysis of the *cis*-regulatory elements in the promoter regions of *ZmVPS37A* further identified more stress-related elements in teosinte than in B73 (**Supplementary Figure 21**). These observations suggest that *ZmVPS37A*, like its *Arabidopsis* homolog, is critical for pathogen defense and likely lost its defense function during domestication as a trade-off between plant growth and defense.

DISCUSSION

As a fundamental cellular process, membrane trafficking in eukaryotic cells is sophisticatedly regulated in response to developmental signals and environmental cues. Previous research has reported that a set of SNARE genes, including *PEN1 (SYP121)*, *VAMP721/722*, and *SNAP33/34*, comprise a conserved regulon together with other ∼50 genes and function as a module in plant innate immunity (Humphry et al., 2010). Moreover, studies on plant autophagy have also revealed the coordinated expression pattern of *ATG* genes, as numerous *ATG* genes are upregulated in senescing tissues, seeds, and under nutrient-limiting conditions (Li et al., 2015;

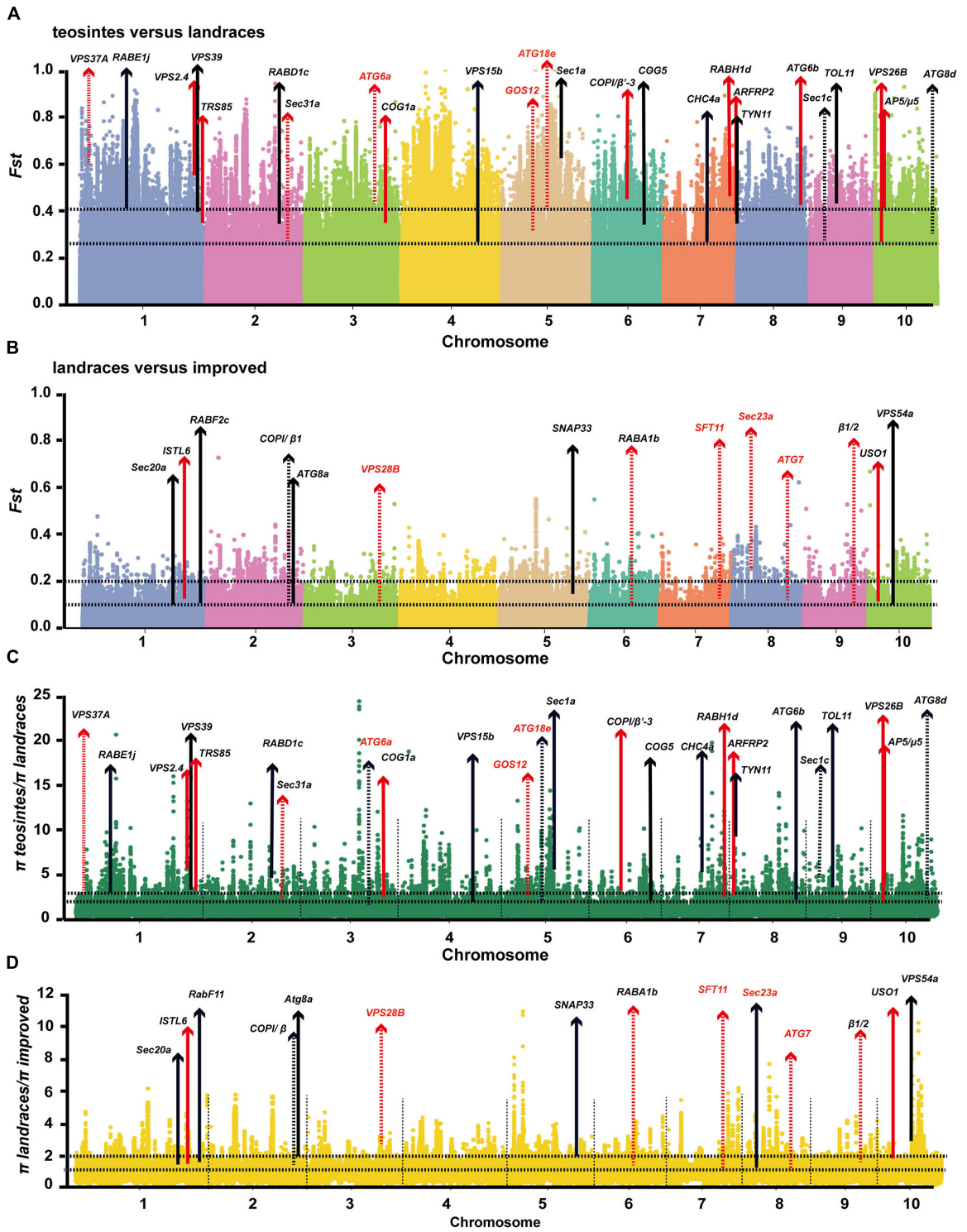

FIGURE 5 | Profiling of selected membrane-trafficking genes during maize domestication and improvement. **(A–D)** Genome-wide selective signals (*Fst* and π ratio) analysis of teosinte, landrace, and improved using a 20-kb sliding window and 10-kb steps. The chromosome numbers are set along the x-axis. The top and bottom horizontal black dashed lines in each panel represent the top 1% (*Fst* ≥ 0.41; π teosinte/π landrace ≥ 2.56; *Fst* ≥ 0.14; π landrace/π improved ≥ 1.99) and top 5% (*Fst* ≥ 0.26; π teosinte/π landrace ≥ 1.55; *Fst* ≥ 0.08; π landrace/π improved ≥ 1.39) of cutoffs, respectively. Arrows indicate that membrane trafficking genes were selected during maize domestication and improvement. Red arrows represent these genes that have also been identified in previous evolutionary analyses (Hufford et al., 2012). Dashed lines indicate domestication or improvement of genes falling within the selected region. Solid lines indicate domestication and improvement candidates.

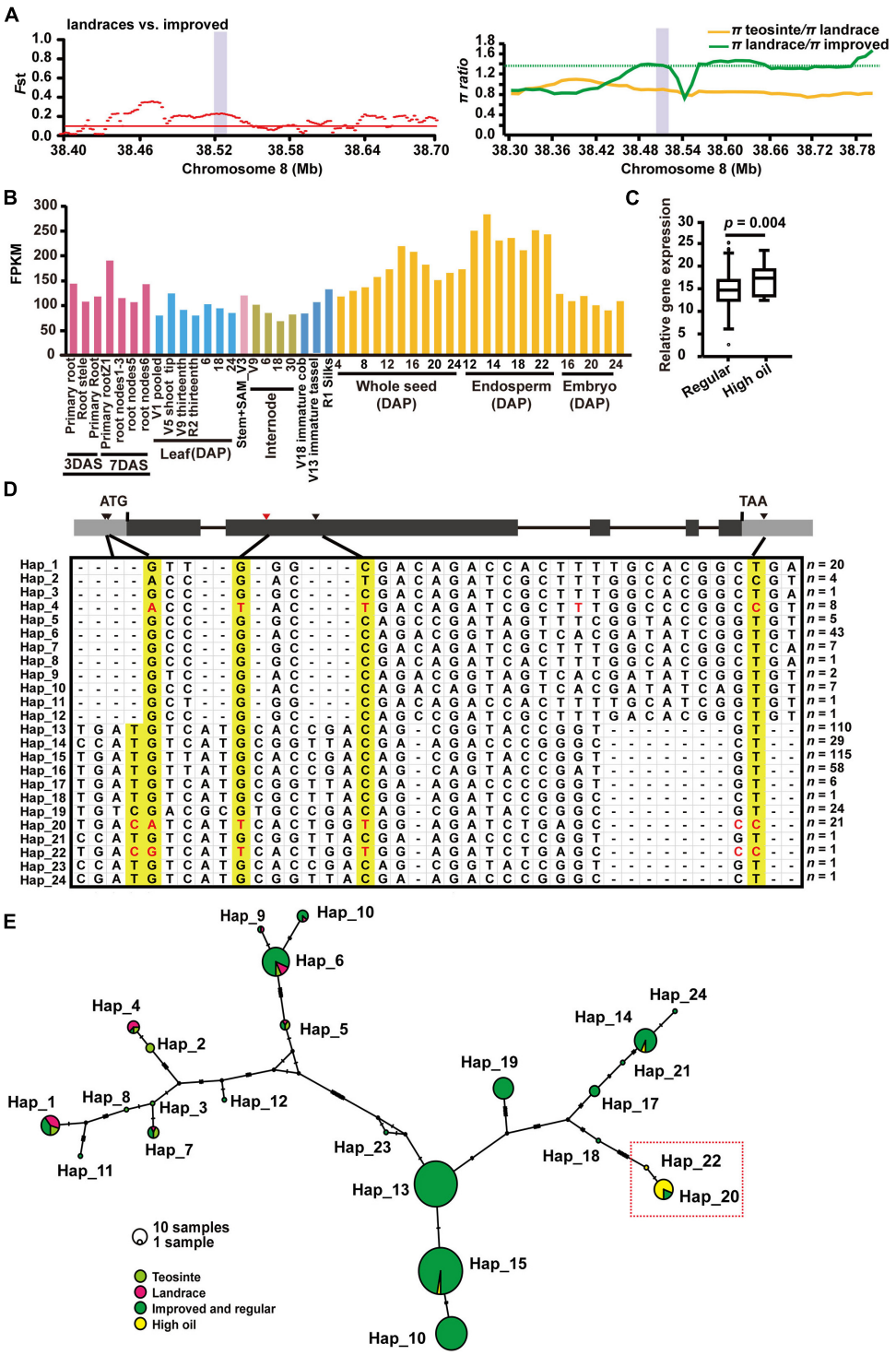

FIGURE 6 | *ZmSec23a* is selected during maize improvement and is strongly associated with seed oil content. **(A)** *Fst* (left) and π (right) values in landraces and improved cultivators across the 0.3-Mb and 0.48-Mb genomic regions surrounding *ZmSec23a*, respectively, which is indicated by the purple bar. **(B)** The spatiotemporal expression profile of *ZmSec23a*. **(C)** Gene expression analysis of *ZmSec23a* in high oil lines and regular materials. Statistical differences between regular materials and high oil lines were calculated by a two-tailed Student's *t*-test ($p < 0.05$). For the box, the central line indicates the median, and the box bounds mean the 25th and 75th percentiles. **(D)** Haplotype analysis of *ZmSec23a* among teosintes (20), landraces (22), improved lines (403), and high oil lines (23). Yellow colors denote the selected alleles of the *ZmSec23a* gene in maize improved high oil germplasms. **(E)** Genetic relatedness of *ZmSec23a* haplotypes based on the median-joining network constructed using PopART version 1.7. Each haplotype is represented by a circle, with its size proportional to the number of maize lines within it. Light green, teosintes; magenta, landraces; dark green, improved and regular cultivars; yellow, high oil materials.

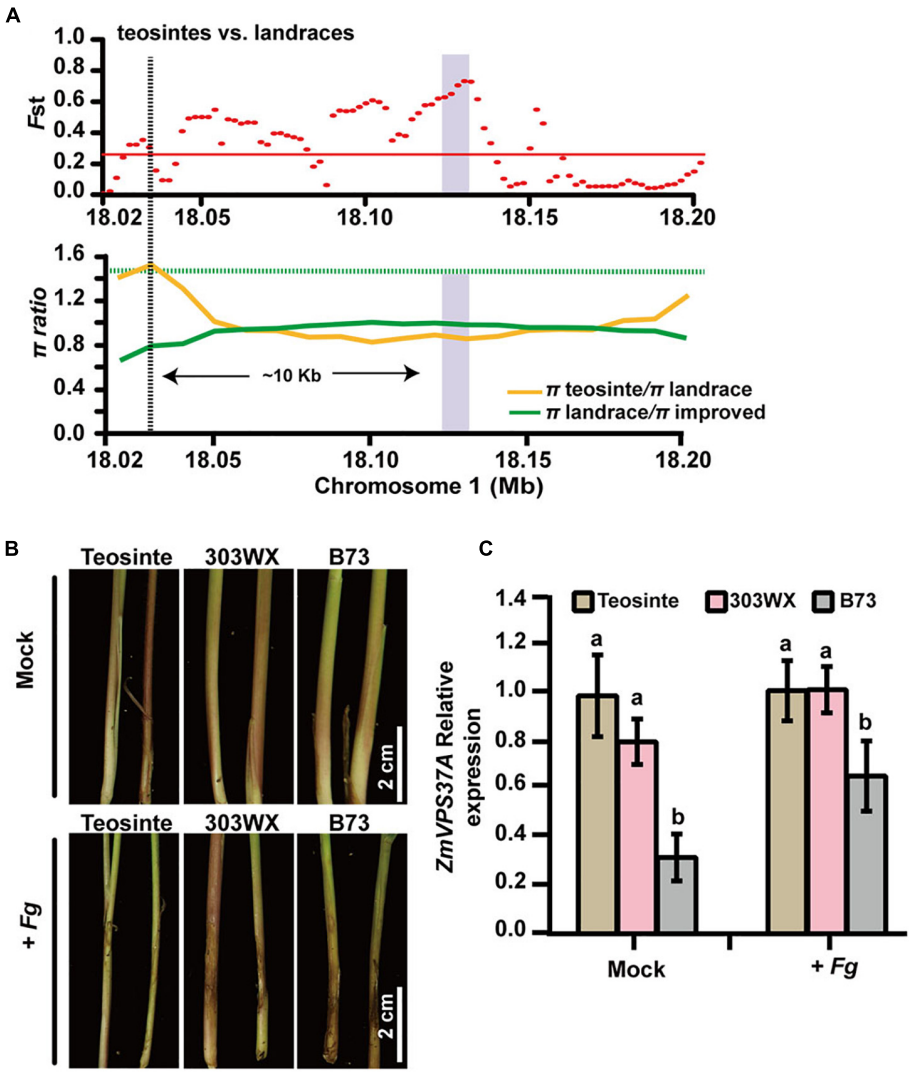

FIGURE 7 | *ZmVPS37A* is a domestication gene involved in pathogen defense. **(A)** *Fst* (upper) and π (lower) values in teosinte and landrace across the 0.18-Mb genomic region surrounding the *ZmVPS37A* gene, which is indicated by the purple bar. **(B)** The stalk phenotypes of teosinte, 303WX, and B73 seedlings 7 days after inoculation by *Fusarium graminearum* PH-1. **(C)** Gene expression analysis of *ZmVPS37A* responding to *F. graminearum* PH-1 48 h after infection. Values are mean ± s.d. Significant differences are shown by different letters ($p < 0.05$).

Marshall and Vierstra, 2018). Here, our in-depth RNA-seq analysis showed that genes encoding the same SNARE protein complex have similar expression patterns, implying that some regulons might exist to coordinate their expressions (**Figure 2**). Our RNA-seq analysis also revealed the tissue specificities of SNARE complexes, indicating the subfunctionalization of expression patterns, and possibly functions too. For example, PM-localized SYP12 syntaxins assemble with other SNAREs, including TGN-localized VAMP72 and SNAP3, into a SNARE complex to mediate the vesicle fusion at the PM. The genes encoding the components of such a SNARE complex could be classified into four groups based on their expression patterns. However, one group (ZmVAMP722/726, ZmNPSN13/14, ZmSYP41, and ZmTYN12) appears to have a constitutive expression pattern, and others show strong root, endosperm, or pollen specificities. During pollen development and pollen tube growth, endomembrane trafficking is one of the essential processes to sustain the growth-promoting membrane dynamics during the reproductive process. ZmVAMP712/728/729, ZmSYP123/125, and ZmSNAP33 compose a pollen-specific group, implying their roles in pollen development. Clearly, the identification of the transcription factors that regulate SNARE genes is required for a full appreciation of the importance of their contributions to plant growth.

Our transcriptomic analysis also revealed that the transcript levels of 114 and 34 membrane-trafficking genes are upregulated in early and late endosperm tissues, respectively (**Supplementary Table 1**, modules turquoise and yellow, respectively). During seed maturation, the endosperm undergoes three major changes: coenocyte, cellularization, and differentiation (Dai et al., 2021).

The involvement of the endomembrane system during endosperm cellularization has been revealed recently by a high temporal-resolution RNA-seq analysis, which shows that multiple membrane-trafficking genes are upregulated at the cellularization stage (Yi et al., 2019). Our study also showed that the genes encoding multiple COPII components, Rab GTPases, and one SNARE are grouped together with those involved in protein assembly and biogenesis by GO enrichment analysis (**Figure 3**), indicating that these membrane-trafficking components might be essential for protein transport for the cellularization of the endosperm.

The ESCRT is conserved machinery responsible for the formation of intraluminal vesicles (ILVs) to degrade the monoubiquitinated membrane proteins (Gao et al., 2017). Previous studies with rice *OsVPS22* and maize *ZmSAL1* have demonstrated that ESCRT components are essential for seed development (Shen et al., 2003; Zhang et al., 2013). Recent research in barely endosperm has shown that the transcript abundance of three ESCRT genes, namely, *HvTOL1*, *HvTOL2*, and *HvTOL8*, is upregulated in endosperm upon pollination, suggesting their potential roles in vacuolar transport of cargo during early endosperm development (Roustan et al., 2020). In maize, *ZmSKD1* is significantly upregulated under salt and drought conditions as well as in immature seeds (Xia et al., 2013). In this study, our WGCNA analysis revealed that several ESCRT components are involved in the response to abiotic stress (**Figure 4** and **Supplementary Figure 19**). For example, *TOL7* (ESCRT-0 component) and *ISTL6* (SKD1 complex) were found to be upregulated upon fungi infection and were strongly correlated with defense genes and other metabolic processes involved in SA biosynthesis and jasmonic acid signaling pathways (**Figure 4** and **Supplementary Figure 19**), further confirming the important role of ESCRT machinery in maize development and growth.

Many components of the membrane-trafficking system with similar or divergent functions are the consequences of gene duplication, expansion, and neofunctionalization. The proven functionally important differences in the membrane-trafficking system are often accompanied by the emergence of new paralogs of trafficking protein families and/or gene neofunctionalization (More et al., 2020). Therefore, exploring the diversity and the selection of membrane-trafficking genes during maize domestication and improvement was chosen as the subject of this study. The previous genomic analysis of maize genetic diversity has identified the number of genes with strong selection signals during maize evolution from teosinte to modern cultivar by resequencing 73 maize accession genomes (Hufford et al., 2012). Among these genes, a total of 15 and 16 vesicle components are found in domestication and improvement regions, respectively (Hufford et al., 2012). In this study, comparative genomic analysis of teosintes, landraces, and cultivators was conducted renewedly to identify artificially selected vesicle components based on genetic variation diversity. Interestingly, we obtained additional 25 and 14 membrane-trafficking genes, which were located in domestication and improvement regions, respectively (**Figure 3**). In the maize genome, nine copies of *ZmSec23* were present, and they displayed different spatiotemporal expression patterns, indicating their diverse functions (**Supplementary Figure 12**). One of them, *ZmSec23a*, was identified as an improvement gene critical for oil production during seed development (**Figure 6**). Interestingly, the functional diversity of *Sec23* paralogs has been reported previously in *Arabidopsis* by Chung et al. (2016). AtSec23a, the homolog of ZmSec23a, was found to interact specifically with AtSar1a and be upregulated under ER stress (Zeng et al., 2015; Chung et al., 2016). A unique amino acid, Cys484, in AtSec23a required for the interaction with AtSar1a was found to be conserved in ZmSec23a (Cys470) (data not shown). Therefore, whether any maize Sar1 isoform interacts with ZmSec23a to participate in seed development will be an interesting avenue for future research.

Among the selected genes, seven are for the autophagy pathway, of which four of them have been already identified by QTL mapping or associated studies (**Supplementary Table 4**). For example, *ZmATG7* was found within selected improvement regions in our study and has also been identified as one of the targeted genomic regions during modern maize breeding in a genome-wide association study with 350 inbred lines (Wang et al., 2020a). A non-synonymous variant (Chr8_142693004, G-A, and S662L) in *ZmATG7* shows significant changes in allele frequency across the breeding eras of modern maize, suggesting *ZmATG7* is a particularly interesting candidate for the selection for biotic resistance. Moreover, *ZmATG18e* (*Zm00001d042215*) has been identified as a novel locus for leaf senescence regulation, with lower *ZmATG18e* expression significantly delaying leaf senescence (Feng et al., 2021). All these studies suggested the important role(s) of autophagy in maize development and stress resistance.

DATA AVAILABILITY STATEMENT

The datasets presented in this study can be found in online repositories. The names of the repository/repositories and accession number(s) can be found below: The data used for WGCNA analysis were derived from the GEO and NCBI database. The RNA-seq data of maize B73 different tissues/stages have been reported previously (Stelpflug et al., 2016) and were deposited in SAR (accession numbers PRJNA171684 and SRP010680). The Illumina HiSeq data of Gibberella ear rot disease caused by *Fusarium graminearum* have been deposited in GEO (GSE92448) and SAR (accession numbers PRJNA357594 and SRP095179) (Kebede et al., 2018).

AUTHOR CONTRIBUTIONS

FL designed the research. CZ and YY conducted the experiments. CZ, YY, GD, and HL performed the data analysis. FL and CZ wrote the manuscript. All authors contributed to the article and approved the submitted version.

FUNDING

This study was supported by the National Natural Science Foundation of China (grants 31970307 and 31770356) and

Natural Science Foundation of Guangdong Province (grant 2021A1515011036) to FL.

ACKNOWLEDGMENTS

We thank all the members of the Li laboratory for helpful discussions and manuscript preparation, Jun Huang for the teosinte seeds, and Rui Xia for providing access to the server to conduct a series of computations.

SUPPLEMENTARY MATERIAL

The Supplementary Material for this article can be found online at: https://www.frontiersin.org/articles/10.3389/fpls.2022.883961/full#supplementary-material

REFERENCES

Barrett, J. C., Fry, B., Maller, J., and Daly, M. J. (2005). Haploview: analysis and visualization of LD and haplotype maps. *Bioinformatics* 21, 263–265. doi: 10.1093/bioinformatics/bth457

Bassham, D. C., Brandizzi, F., Otegui, M. S., and Sanderfoot, A. A. (2008). The secretory system of *Arabidopsis*. *Arabidopsis Book* 6:e0116. doi: 10.1199/tab.0116

Bhandari, D. D., and Brandizzi, F. (2020). Plant endomembranes and cytoskeleton: moving targets in immunity. *Curr. Opin. Plant Biol.* 58, 8–16. doi: 10.1016/j.pbi.2020.09.003

Bradbury, P. J., Zhang, Z., Kroon, D. E., Casstevens, T. M., Ramdoss, Y., and Buckler, E. S. (2007). TASSEL: software for association mapping of complex traits in diverse samples. *Bioinformatics* 23, 2633–2635. doi: 10.1093/bioinformatics/btm308

Bukowski, R., Guo, X., Lu, Y., Zou, C., He, B., Rong, Z., et al. (2018). Construction of the third-generation *Zea mays* haplotype map. *Gigascience* 7, 1–12. doi: 10.1093/gigascience/gix134

Chen, L., Li, Y. X., Li, C. H., Shi, Y. S., Song, Y. C., Zhang, D. F., et al. (2020b). The retromer protein ZmVPS29 regulates maize kernel morphology likely through an auxin-dependent process(es). *Plant Biotechnol. J.* 18, 1004–1014. doi: 10.1111/pbi.13267

Chen, C. J., Chen, H., Zhang, Y., Thomas, H. R., Frank, M. H., He, Y. H., et al. (2020a). TBtools: an integrative toolkit developed for interactive analyses of big biological data. *Mol. Plant* 13, 1194–1202. doi: 10.1016/j.molp.2020.06.009

Chung, K. B., Zeng, Y. L., Li, Y. M., Ji, C. Y., Xia, Y. J., and Jiang, L. W. (2018). Signal motif-dependent ER export of the Qc-SNARE BET12 interacts with MEMB12 and affects PR1 trafficking in *Arabidopsis*. *J. Cell Sci.* 131:jcs202838. doi: 10.1242/jcs.202838

Chung, K. P., Zeng, Y. L., and Jiang, L. W. (2016). COPII paralogs in plants: functional redundancy or diversity? *Trends Plant Sci.* 21, 758–769. doi: 10.1016/j.tplants.2016.05.010

Collins, N. C., Thordal-Christensen, H., Lipka, V., Bau, S., Kombrink, E., Qiu, J. L., et al. (2003). SNARE-protein-mediated disease resistance at the plant cell wall. *Nature* 425, 973–977. doi: 10.1038/nature02076

Dai, D. W., Ma, Z. Y., and Song, R. T. (2021). Maize endosperm development. *J. Integr. Plant Biol.* 63, 613–627. doi: 10.1111/jipb.13069

Danecek, P., Auton, A., Abecasis, G., Albers, C. A., Banks, E., DePristo, M. A., et al. (2011). The variant call format and VCFtools. *Bioinformatics* 27, 2156–2158. doi: 10.1093/bioinformatics/btr330

Feng, X., Liu, L. L., Li, Z. G., Sun, F., Wu, X. Y., Hao, D. Y., et al. (2021). Potential interaction between autophagy and auxin during maize leaf senescence. *J. Exp. Bot.* 72, 3554–3568. doi: 10.1093/jxb/erab094

Fu, J. J., Cheng, Y. B., Linghu, J. J., Yang, X. H., Kang, L. K., Zhang, Z. X., et al. (2013). RNA sequencing reveals the complex regulatory network in the maize kernel. *Nat. Commun.* 4:2832. doi: 10.1038/ncomms3832

Gamir, J., Pastor, V., Sanchez-Bel, P., Agut, B., Mateu, D., Garcia-Andrade, J., et al. (2018). Starch degradation, abscisic acid and vesicular trafficking are important elements in callose priming by indole-3-carboxylic acid in response to *Plectosphaerella cucumerina* infection. *Plant J.* 96, 518–531. doi: 10.1111/tpj.14045

Gao, C. J., Zhuang, X., Shen, J. B., and Jiang, L. W. (2017). Plant ESCRT Complexes: moving beyond endosomal sorting. *Trends Plant Sci.* 22, 986–998. doi: 10.1016/j.tplants.2017.08.003

Gu, Y. N., Zavaliev, R., and Dong, X. N. (2017). Membrane trafficking in plant immunity. *Mol. Plant* 10, 1026–1034. doi: 10.1016/j.molp.2017.07.001

He, M., Lan, M., Zhang, B. C., Zhou, Y. Y., Wang, Y. Q., Zhu, L., et al. (2018). Rab-H1b is essential for trafficking of cellulose synthase and for hypocotyl growth in *Arabidopsis thaliana*. *J. Integr. Plant Biol.* 60, 1051–1069. doi: 10.1111/jipb.12694

He, W., Wang, L., Lin, Q. L., and Yu, F. (2021). Rice seed storage proteins: biosynthetic pathways and the effects of environmental factors. *J. Integr. Plant Biol.* 63, 1999–2019. doi: 10.1111/jipb.13176

Heucken, N., and Ivanov, R. (2018). The retromer, sorting nexins and the plant endomembrane protein trafficking. *J. Cell Sci.* 131:jcs203695. doi: 10.1242/jcs.203695

Hofius, D., Li, L., Hafren, A., and Coll, N. S. (2017). Autophagy as an emerging arena for plant-pathogen interactions. *Curr. Opin. Plant Biol.* 38, 117–123. doi: 10.1016/j.pbi.2017.04.017

Hufford, M. B., Xu, X., van Heerwaarden, J., Pyhajarvi, T., Chia, J. M., Cartwright, R. A., et al. (2012). Comparative population genomics of maize domestication and improvement. *Nat. Genet.* 44, 808–811. doi: 10.1038/ng.2309

Humphry, M., Bednarek, P., Kemmerling, B., Koh, S., Stein, M., Gobel, U., et al. (2010). A regulon conserved in monocot and dicot plants defines a functional module in antifungal plant immunity. *Proc. Natl. Acad. Sci. U. S. A.* 107, 21896–21901. doi: 10.1073/pnas.1003619107

Inada, N., and Ueda, T. (2014). Membrane trafficking pathways and their roles in plant-microbe interactions. *Plant Cell Physiol.* 55, 672–686. doi: 10.1093/pcp/pcu046

Jiao, Y., Zhao, H. N., Ren, L. H., Song, W. B., Zeng, B., Guo, J. J., et al. (2012). Genome-wide genetic changes during modern breeding of maize. *Nat. Genet.* 44, 812–815. doi: 10.1038/ng.2312

Kalde, M., Nuhse, T. S., Findlay, K., and Peck, S. C. (2007). The syntaxin SYP132 contributes to plant resistance against bacteria and secretion of pathogenesis-related protein 1. *Proc. Natl. Acad. Sci. U. S. A.* 104, 11850–11855. doi: 10.1073/pnas.0701083104

Kebede, A. Z., Johnston, A., Schneiderman, D., Bosnich, W., and Harris, L. J. (2018). Transcriptome profiling of two maize inbreds with distinct responses to Gibberella ear rot disease to identify candidate resistance genes. *BMC Genomics* 19:131. doi: 10.1186/s12864-018-4513-4

Kwon, C., Neu, C., Pajonk, S., Yun, H. S., Lipka, U., Humphry, M., et al. (2008). Co-option of a default secretory pathway for plant immune responses. *Nature* 451, 835–840. doi: 10.1038/nature06545

Langfelder, P., and Horvath, S. (2008). WGCNA: an R package for weighted correlation network analysis. *BMC Bioinformatics* 9:559. doi: 10.1186/1471-2105-9-559

Leigh, J. W., and Bryant, D. (2015). POPART: full-feature software for haplotype network construction. *Methods Ecol. Evol.* 6, 1110–1116. doi: 10.1111/2041-210X.12410

Li, F. Q., Chung, T., Pennington, J. G., Federico, M. L., Kaeppler, H. F., Kaeppler, S. M., et al. (2015). Autophagic recycling plays a central role in maize nitrogen remobilization. *Plant Cell* 27, 1389–1408. doi: 10.1105/tpc.15.00158

Li, H., Peng, Z. Y., Yang, X. H., Wang, W. D., Fu, J. J., Wang, J. H., et al. (2013). Genome-wide association study dissects the genetic architecture of oil biosynthesis in maize kernels. *Nat. Genet.* 45, 43–50. doi: 10.1038/ng.2484

Librado, P., and Rozas, J. (2009). DnaSP v5: a software for comprehensive analysis of DNA polymorphism data. *Bioinformatics* 25, 1451–1452. doi: 10.1093/bioinformatics/btp187

Lin, T., Zhu, G. T., Zhang, J., Xu, X. H., Yu, Q. H., Zheng, Z., et al. (2014). Genomic analyses provide insights into the history of tomato breeding. *Nat. Genet.* 46, 1220–1226. doi: 10.1038/ng.3117

Liu, H. J., Wang, X. Q., Warburton, M. L., Wen, W. W., Jin, M. L., Deng, M., et al. (2015). Genomic, transcriptomic, and phenomic variation reveals the complex adaptation of modern maize breeding. *Mol. Plant* 8, 871–884. doi: 10.1016/j.molp.2015.01.016

Lu, S. N., Wang, J. Y., Chitsaz, F., Derbyshire, M. K., Geer, R. C., Gonzales, N. R., et al. (2020). CDD/SPARCLE: the conserved domain database in 2020. *Nucleic Acids Res.* 48, D265–D268. doi: 10.1093/nar/gkz991

Marshall, R. S., and Vierstra, R. D. (2018). Autophagy: the master of bulk and selective recycling. *Annu. Rev. Plant Biol.* 29, 173–208. doi: 10.1146/annurev-arplant-042817-040606

Minamino, N., and Ueda, T. (2019). RAB GTPases and their effectors in plant endosomal transport. *Curr. Opin. Plant Biol.* 52, 61–68. doi: 10.1016/j.pbi.2019.07.007

More, K., Klinger, C. M., Barlow, L. D., and Dacks, J. B. (2020). Evolution and natural history of membrane trafficking in eukaryotes. *Curr. Biol.* 30, R553–R564. doi: 10.1016/j.cub.2020.03.068

Olukolu, B. A., Wang, G. F., Vontimitta, V., Venkata, B. P., Marla, S., Ji, J., et al. (2014). A genome-wide association study of the maize hypersensitive defense response identifies genes that cluster in related pathways. *PLoS Genet.* 10:e1004562. doi: 10.1371/journal.pgen.1004562

Paez Valencia, J., Goodman, K., and Otegui, M. S. (2016). Endocytosis and endosomal trafficking in plants. *Annu. Rev. Plant Biol.* 67, 309–335. doi: 10.1146/annurev-arplant-043015-112242

Paul, P., Simm, S., Mirus, O., Scharf, K. D., Fragkostefanakis, S., and Schleiff, E. (2014). The complexity of vesicle transport factors in plants examined by orthology search. *PLoS One* 9:e97745. doi: 10.1371/journal.pone.0097745

Rodriguez-Furlan, C., Minina, E. A., and Hicks, G. R. (2019). Remove, recycle, degrade: regulating plasma membrane protein accumulation. *Plant Cell* 31, 2833–2854. doi: 10.1105/tpc.19.00433

Roustan, V., Hilscher, J., Weidinger, M., Reipert, S., Shabrangy, A., Gebert, C., et al. (2020). Protein sorting into protein bodies during barley endosperm development is putatively regulated by cytoskeleton members, MVBs and the HvSNF7s. *Sci. Rep.* 10:1864. doi: 10.1038/s41598-020-58740-x

Shen, B., Li, C., Min, Z., Meeley, R. B., Tarczynski, M. C., and Olsen, O. A. (2003). *sal1* determines the number of aleurone cell layers in maize endosperm and encodes a class E vacuolar sorting protein. *Proc. Natl. Acad. Sci. U. S. A.* 100, 6552–6557. doi: 10.1073/pnas.0732023100

Spallek, T., Beck, M., Ben Khaled, S., Salomon, S., Bourdais, G., Schellmann, S., et al. (2013). ESCRT-I mediates FLS2 endosomal sorting and plant immunity. *PLoS Genet.* 9:e1004035. doi: 10.1371/journal.pgen.1004035

Speth, E. B., Imboden, L., Hauck, P., and He, S. Y. (2009). Subcellular localization and functional analysis of the *Arabidopsis* GTPase RabE. *Plant Physiol.* 149, 1824–1837. doi: 10.1104/pp.108.132092

Stelpflug, S. C., Sekhon, R. S., Vaillancourt, B., Hirsch, C. N., Buell, C. R., de Leon, N., et al. (2016). An expanded maize gene expression atlas based on RNA sequencing and its use to explore root development. *Plant Genome* 9, 1–16. doi: 10.3835/plantgenome2015.04.0025

Surpin, M., and Raikhel, N. (2004). Traffic jams affect plant development and signal transduction. *Nat. Rev. Mol. Cell Biol.* 5, 100–109. doi: 10.1038/nrm1311

Takacs, E. M., Suzuki, M., and Scanlon, M. J. (2012). Discolored1 (DSC1) is an ADP-ribosylation factor-GTPase activating protein required to maintain differentiation of maize kernel structures. *Front. Plant Sci.* 3:115. doi: 10.3389/fpls.2012.00115

Tian, T., You, Q., Yan, H. Y., Xu, W. Y., and Su, Z. (2018). MCENet: a database for maize conditional co-expression network and network characterization collaborated with multi-dimensional omics levels. *J. Genet. Genomics* 45, 351–360. doi: 10.1016/j.jgg.2018.05.007

Wang, B. B., Lin, Z. C., Li, X., Zhao, Y. P., Zhao, B. B., Wu, G. X., et al. (2020a). Genome-wide selection and genetic improvement during modern maize breeding. *Nat. Genet.* 52, 565–571. doi: 10.1038/s41588-020-0616-3

Wang, X. F., Xu, M., Gao, C. J., Zeng, Y. L., Cui, Y., Shen, W. J., et al. (2020b). The roles of endomembrane trafficking in plant abiotic stress responses. *J. Integr. Plant Biol.* 62, 55–69. doi: 10.1111/jipb.12895

Xia, Z. L., Wei, Y. Y., Sun, K. L., Wu, J. Y., Wang, Y. X., and Wu, K. (2013). The maize AAA-type protein SKD1 confers enhanced salt and drought stress tolerance in transgenic tobacco by interacting with Lyst-interacting protein 5. *PLoS One* 8:e69787. doi: 10.1371/journal.pone.0069787

Yi, F., Gu, W., Chen, J., Song, N., Gao, X., Zhang, X. B., et al. (2019). High temporal-resolution transcriptome landscape of early maize seed development. *Plant Cell* 31, 974–992. doi: 10.1105/tpc.18.00961

Yu, G. C., Wang, L. G., Han, Y. Y., and He, Q. Y. (2012). clusterProfiler: an R package for comparing biological themes among gene clusters. *OMICS* 16, 284–287. doi: 10.1089/omi.2011.0118

Zeng, Y. L., Chung, K. B., Li, B. Y., Lai, C. M., Lam, S. K., Wang, X. F., et al. (2015). Unique COPII component AtSar1a/AtSec23a pair is required for the distinct function of protein ER export in *Arabidopsis thaliana*. *Proc. Natl. Acad. Sci. U. S. A.* 112, 14360–14365. doi: 10.1073/pnas.1519333112

Zhang, X. Q., Hou, P., Zhu, H. T., Li, G. D., Liu, X. G., and Xie, X. M. (2013). Knockout of the VPS22 component of the ESCRT-II complex in rice (*Oryza sativa* L.) causes chalky endosperm and early seedling lethality. *Mol. Biol. Rep.* 40, 3475–3481. doi: 10.1007/s11033-012-2422-1

Zheng, P., Zheng, C. Y., Otegui, M. S., and Li, F. Q. (2022). Endomembrane mediated trafficking of seed storage proteins: from *Arabidopsis* to cereal crops. *J. Exp. Bot.* 73, 1312–1326. doi: 10.1093/jxb/erab519

Zhou, Z. K., Jiang, Y., Wang, Z., Gou, Z. H., Lyu, J., Li, W. Y., et al. (2015). Resequencing 302 wild and cultivated accessions identifies genes related to domestication and improvement in soybean. *Nat. Biotechnol.* 33, 408–414. doi: 10.1038/nbt.3096

Conflict of Interest: The authors declare that the research was conducted in the absence of any commercial or financial relationships that could be construed as a potential conflict of interest.

Publisher's Note: All claims expressed in this article are solely those of the authors and do not necessarily represent those of their affiliated organizations, or those of the publisher, the editors and the reviewers. Any product that may be evaluated in this article, or claim that may be made by its manufacturer, is not guaranteed or endorsed by the publisher.

Advantages of publishing in Frontiers

OPEN ACCESS
Articles are free to read for greatest visibility and readership

FAST PUBLICATION
Around 90 days from submission to decision

HIGH QUALITY PEER-REVIEW
Rigorous, collaborative, and constructive peer-review

TRANSPARENT PEER-REVIEW
Editors and reviewers acknowledged by name on published articles

Frontiers
Avenue du Tribunal-Fédéral 34
1005 Lausanne | Switzerland

Visit us: www.frontiersin.org
Contact us: frontiersin.org/about/contact

REPRODUCIBILITY OF RESEARCH
Support open data and methods to enhance research reproducibility

DIGITAL PUBLISHING
Articles designed for optimal readership across devices

FOLLOW US
@frontiersin

IMPACT METRICS
Advanced article metrics track visibility across digital media

EXTENSIVE PROMOTION
Marketing and promotion of impactful research

LOOP RESEARCH NETWORK
Our network increases your article's readership